

|                   |                  |    |              |   |            |         |                        |                   |
|-------------------|------------------|----|--------------|---|------------|---------|------------------------|-------------------|
| MATER.<br>TEHNOL. | LETNIK<br>VOLUME | 49 | ŠTEV.<br>NO. | 4 | STR.<br>P. | 479–661 | LJUBLJANA<br>SLOVENIJA | JULY–AUG.<br>2015 |
|-------------------|------------------|----|--------------|---|------------|---------|------------------------|-------------------|

## VSEBINA – CONTENTS

## PREGLEDNI ČLANEK – REVIEW ARTICLE

**Impact-toughness investigations of duplex stainless steels**

Preiskave udarne žilavosti dupleksnega nerjavnega jekla

S. Topolska, J. Łabanowski . . . . . 481

## IZVIRNI ZNANSTVENI ČLANKI – ORIGINAL SCIENTIFIC ARTICLES

**Effects of the artificial-aging temperature and time on the mechanical properties and springback behavior of AA6061**

Vpliv temperature in časa umetnega staranja na mehanske lastnosti in vzmetnost AA6061

A. Polat, M. Avsar, F. Ozturk . . . . . 487

**Monitoring of polyurethane dispersions after the synthesis**

Spremljanje poliuretanskih disperzij po sintezi

M. Očepek, J. Zabret, J. Kecej, P. Venturini, J. Golob . . . . . 495

**Spectroscopic and porosimetric analyses of Roman pottery from an archaeological site near Mošnje, Slovenia**

Spektroskopske in porozimetrične preiskave rimske lončenine z arheološkega najdišča pri Mošnjah, Slovenija

S. Kramar, J. Lux . . . . . 503

**Non-linear finite-element simulations of the tensile tests of textile composites**

Nelinearna simulacija nateznih preizkusov tekstilnih kompozitov s končnimi elementi

T. Kroupa, K. Kunc, R. Zemčik, T. Mandys . . . . . 509

**Influence of the type and number of prepreg layers on the flexural strength and fatigue life of honeycomb sandwich structures**

Vpliv vrste in števila plasti na utrditev upogibne trdnosti in zdržljivosti pri utrujanju satastih sendvičnih konstrukcij

L. Fojtl, S. Rusnakova, M. Zaludek, V. Rusnák . . . . . 515

**Potential for obtaining an ultrafine microstructure of low-carbon steel using accumulative roll bonding**

Možnosti doseganja ultradrobnozrnate mikrostrukture pri spajanju maloogljčnega jekla z akumulativnim valjanjem

T. Kubina, J. Gubiš . . . . . 521

**Optimization of the annealing of plaster moulds for the manufacture of metallic foams with an irregular cell structure**

Optimiranje postopka žarjenja mavčnih form za izdelavo kovinskih pen z nepravilno strukturo celic

I. Kroupová, P. Lichý, F. Radkovský, J. Beňo, V. Bednářová, I. Lána . . . . . 527

**The kinetics of small-impurity grain-boundary-segregation formation in cold-rolled deep-drawing 08C-Al and IF steels during post-deformation annealing**

Kinetika nastanka segregacije nečistoč po mejah zrn med žarjenjem po hladnem valjanju jekel 08C-Al in IF za globoki vlek

A. Rashkovskiy, A. Kovalev, D. Wainstein, I. Rodionova, Y. Bykova, D. Zakharova . . . . . 531

**Application of a control-measuring apparatus and peltier modules in the bulk-metallic-glass production using the pressure-casting method**

Uporaba kontrolno-merilne naprave in peltierjevih modulov pri izdelavi masivnih kovinskih stekel po postopku tlačnega litja

W. Pilarczyk, A. Pilarczyk . . . . . 537

**Evaluation of the structural changes in 9 % Cr creep-resistant steel using an electrochemical technique**

Ocena sprememb strukture v jeklu z 9 % Cr, odpornem proti lezenju, z uporabo elektrokemijske tehnike

J. Rapouch, J. Bystriansky, V. Sefl, M. Svobodova . . . . . 543

**Effect of the by-pass cement-kiln dust and fluidized-bed-combustion fly ash on the properties of fine-grained alkali-activated slag-based composites**

Vpliv prahu iz peči za cement in letečega pepela iz vrtnčaste plasti na lastnosti drobnozrnatega, z alkalijami aktiviranega kompozita na osnovi žlindre

V. Bílek Jr., L. Pařízek, L. Kalina . . . . . 549

**Microstructure, magnetic and mechanical properties of the bulk amorphous alloy Fe<sub>61</sub>Co<sub>10</sub>Ti<sub>4</sub>Y<sub>5</sub>B<sub>20</sub>**Mikrostruktura, magnetne in mehanske lastnosti masivne amorfnе zlitine Fe<sub>61</sub>Co<sub>10</sub>Ti<sub>4</sub>Y<sub>5</sub>B<sub>20</sub>

K. Bloch, M. Nabialek, J. Gondro . . . . . 553

**Modified cement-based mortars: crack initiation and volume changes**

Modificirane malte na osnovi cementa: iniciacija razpok in volumenske spremembe

I. Havlikova, V. Bilek Jr., L. Topolar, H. Simonova, P. Schmid, Z. Kersner . . . . . 557

|                                                                                                                                                                                                                                                                                                                                                                   |     |
|-------------------------------------------------------------------------------------------------------------------------------------------------------------------------------------------------------------------------------------------------------------------------------------------------------------------------------------------------------------------|-----|
| <b>Fracture properties of plain and steel-polypropylene-fiber-reinforced high-performance concrete</b><br>Lastnosti loma navadnega in visokozmogljivega betona, ojačanega s polipropilenskimi vlakni<br>P. Smarzewski, D. Barnat-Hunek . . . . .                                                                                                                  | 563 |
| <b>Preparation of porous ceramic materials based on CaZrO<sub>3</sub></b><br>Priprava porozne keramike na osnovi CaZrO <sub>3</sub><br>E. Śnieżek, J. Szczerba, I. Jastrzębska, E. Kleczyk, Z. Pędzich . . . . .                                                                                                                                                  | 573 |
| <b>DP780 dual-phase-steel spot welds: critical fusion-zone size ensuring the pull-out failure mode</b><br>Točkasti zvari jekla DP780 z dvofazno strukturo: kritična velikost staljene cone, ki zagotavlja porušenje z izpuljenjem<br>M. Pouranvari, S. P. H. Marashi, H. L. Jaber . . . . .                                                                       | 579 |
| <b>Application of computed tomography in comparison with the standardized methods for determining the permeability of cement-composite structures</b><br>Uporaba računalniške tomografije v primerjavi s standardiziranimi metodami določanja prepustnosti cementnih kompozitnih struktur<br>T. Komárková, M. Králíková, P. Kovács, D. Kocáb, T. Stavař . . . . . | 587 |
| <b>Properties of polymer-filled aluminium foams under moderate strain-rate loading conditions</b><br>Lastnosti aluminijevih pen, napoljenih s polimernimi materiali, pri zmernih obremenitvah<br>T. Doktor, P. Zlámal, T. Fíla, P. Koudelka, D. Kytýř, O. Jiroušek . . . . .                                                                                      | 597 |
| <b>Quality of the structure of ash bodies based on different types of ash</b><br>Kvaliteta strukture telesa iz pepela na osnovi različnih vrst pepela<br>V. Cerny . . . . .                                                                                                                                                                                       | 601 |
| <b>Sintered board materials based on recycled glass</b><br>Sintrani ploščati materiali na osnovi recikliranega stekla<br>T. Melichar, J. Bydžovský . . . . .                                                                                                                                                                                                      | 607 |
| <b>Mechanical and wetting properties of nanosilica/epoxy-coated stainless steel</b><br>Mehanske in površinske lastnosti premaza iz silicijevih nanodelcev in epoksidne smole na nerjavnem jeklu<br>M. Conradi, G. Intihar, M. Zorko . . . . .                                                                                                                     | 613 |
| <b>STROKOVNI ČLANKI – PROFESSIONAL ARTICLES</b>                                                                                                                                                                                                                                                                                                                   |     |
| <b>Development of composite salt cores for foundry applications</b><br>Razvoj kompozitnih slanih jeder za uporabo v livarstvu<br>J. Beňo, E. Adámková, F. Mikšovský, P. Jelínek . . . . .                                                                                                                                                                         | 619 |
| <b>Carbide morphology and ferrite grain size after accelerated carbide spheroidisation and refinement (ASR) of C45 steel</b><br>Morfolologija karbidov in velikost feritnih zrn po pospešeni sferoidizaciji in rafinaciji (ASR) jekla C45<br>J. Dlouhy, D. Hauserova, Z. Novy . . . . .                                                                           | 625 |
| <b>Use of micromachining to shape the structure and electrical properties of the front electrode of a silicon solar cell</b><br>Uporaba mikroobdelovanja za oblikovanje strukture in električnih lastnosti prednje elektrode silicijeve sončne celice<br>M. Musztyfaga-Staszuk . . . . .                                                                          | 629 |
| <b>Fabrication of TiO<sub>2</sub> nanotubes for bioapplications</b><br>Izdelava TiO <sub>2</sub> -nanocevk za biomedicinsko uporabo<br>M. Kulkarni, K. Mrak-Poljšak, A. Flašker, A. Mazare, P. Schmuki, A. Kos, S. Čučnik, S. Sodin-Šemrl, A. Iglič . . . . .                                                                                                     | 635 |
| <b>Assessment of the impact-echo method for monitoring the long-standing frost resistance of ceramic tiles</b><br>Ocena metode impact-echo za kontrolo dolgotrajne odpornosti keramičnih ploščic proti zmrzali<br>M. Matysik, I. Plskova, Z. Chobola . . . . .                                                                                                    | 639 |
| <b>Investigation on new creep- and oxidation-resistant materials</b><br>Preiskava novega materiala, odpornega proti lezenju in oksidaciji<br>O. Khalaj, B. Masek, H. Jirkova, A. Roneseva, J. Svoboda . . . . .                                                                                                                                                   | 645 |
| <b>Effect of preheating on mechanical properties in induction sintering of metal-powder material Fe and w(Cu) = 3 %</b><br>Vpliv predgrevanja na mehanske lastnosti indukcijsko sintranega materiala, izdelanega iz kovinskega prahu Fe in w(Cu) = 3 %<br>G. Akpınar, E. Atik . . . . .                                                                           | 653 |

# IMPACT-TOUGHNESS INVESTIGATIONS OF DUPLEX STAINLESS STEELS

## PREISKAVE UDARNE ŽILAVOSTI DUPEKSNEGA NERJAVNEGA JEKLA

Santina Topolska<sup>1</sup>, Jerzy Łabanowski<sup>2</sup>

<sup>1</sup>Silesian University of Technology, Institute of Engineering Materials and Biomaterials, Konarskiego Street 18a, 44-100 Gliwice, Poland

<sup>2</sup>Gdańsk University of Technology, Faculty of Mechanical Engineering, Narutowicza St. 11/12, 80-233 Gdańsk, Poland  
santina.topolska@polsl.pl

*Prejem rokopisa – received: 2014-07-30; sprejem za objavo – accepted for publication: 2014-09-15*

doi:10.17222/mit.2014.133

Duplex stainless steels are very attractive constructional materials for use in aggressive environments because of their several advantages over austenitic stainless steels. Duplex steels have excellent pitting and crevice corrosion resistance, are highly resistant to chloride stress-corrosion cracking and are about twice as strong as common austenitic steels. Better properties are associated with their microstructures consisting of ferrite and austenite grains. However, with certain thermal treatments, these excellent properties may be reduced due to undesired changes in the steel microstructure, related mainly to different solid-state-precipitation processes. The impact toughness of the commercial 2205 duplex stainless steel and the higher-alloy super-duplex 2507 steel was investigated. Both steels were submitted to the ageing treatment in a temperature range between 500 °C and 900 °C with the exposure times of 6 min, 1 h and 10 h; in addition, light microscope examinations, hardness measurements and impact-toughness tests were performed. The main objective of the investigations was to determine the effect of the change in the microstructure on the mechanical properties of the steel.

Keywords: duplex stainless steels, heat treatment, impact toughness

Dupleksna nerjavna jekla so zanimiv konstrukcijski material za uporabo v agresivnem okolju, ker imajo nekaj prednosti v primerjavi z avstenitnimi nerjavnimi jekli. Dupleksna jekla imajo odlično odpornost proti jamičasti in špranjski koroziji, so odporna proti napetostnim korozijskim pokanjem v kloridnem okolju in so okrog dvakrat bolj trdna kot avstenitna nerjavna jekla. Boljše lastnosti so povezane z njihovo mikrostrukturo iz zrn ferita in perlita. Vendar pa se njihove odlične lastnosti lahko poslabšajo zaradi neželenih sprememb v mikrostrukturi jekla, ki so predvsem v povezavi s procesi izločanja iz trdne raztopine. Preiskovana je bila udarna žilavost komercialnega dupleksnega nerjavnega jekla 2205 in bolj legiranega super dupleksnega jekla 2507. Obe jekli sta bili starani v temperaturnem območju med 500 °C in 900 °C v trajanju 6 min, 1 h in 10 h. Izvršene so bile preiskave s svetlobnim mikroskopom in meritve trdote ter udarne žilavosti. Glavni namen preiskave je bil določiti vpliv sprememb v mikrostrukturi na mehanske lastnosti jekla.

Ključne besede: dupleksna nerjavna jekla, toplotna obdelava, udarna žilavost

## 1 INTRODUCTION

The microstructure of duplex stainless steel consists of austenite and ferrite phases, combining beneficial properties of both kinds of steel, showing a good corrosion resistance, a good weldability and a high strength. The properties of duplex steels depend on their chemical compositions and microstructures. These steels have 22 % to 27 % chromium, 3 % to 7 % nickel and up to 4.5 % molybdenum and are usually used for chemical tankers, desalination plants, chemical and petrochemical units, pipelines and oil and gas separators.<sup>1-3</sup>

Duplex stainless steels are a family of grades with different corrosion-resistance levels depending on their chemistry and they are divided into four groups.<sup>4</sup> The first group, the lean duplex steels (like 2304) contain no nominal molybdenum addition, but 21.5 % to 24.5 % Cr, 3 % to 5.5 % Ni and 0.05 % to 0.60 % Mo. The second and the most common group includes the typical 2205 duplex steel with 21 % to 23 % Cr, 4.5 % to 6.5 % Ni and 2.5 % to 3.5% Mo. The third group includes alloys

255 and DP-3 with 24 % to 27 % Cr, 4.5 % to 7.5 % Ni and 2.9 % to 7.5 % Mo. Higher-alloy super-duplex 2507 grades consist of 24 % to 26 % Cr, 6 % to 8 % Ni, 3 % to 5 % Mo.

Two most commonly used duplex steels, 2205 and 2507, were chosen for the investigation. The mechanical properties of these duplex grades are excellent in the temperature range from –50 °C to 300 °C. At elevated temperatures different precipitates may form and cause detrimental changes in the steel properties, especially the toughness.<sup>5</sup> During the tempering in the temperature range of 500–900 °C changes in the microstructure and a precipitation of intermetallic phases can be observed; these reduce the mechanical properties and the corrosion resistance. In certain temperature ranges the first precipitates form rapidly.<sup>6,7</sup> In **Figure 1** an isothermal precipitation diagram for 2205 and 2507 duplex stainless steels (2304 grade is presented for comparison) is depicted. It shows that, in a relatively short time of 1–2 min, the chromium carbide and nitride precipitation process starts. The kinetics of the carbide and nitride formation is

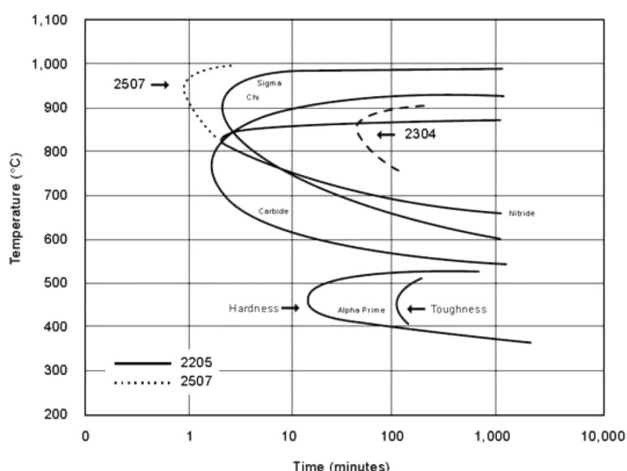


**Figure 1:** Isothermal precipitation diagram for duplex stainless steels, annealed at 1050 °C<sup>4</sup>

**Slika 1:** Izotermni diagram izločanja v dupleksnem nerjavnem jeklu, žarjenem na 1050 °C<sup>4</sup>

affected by chromium, molybdenum and nickel. This is why the kinetics of all the nitrogen-alloyed duplex stainless-steel grades is similar to that of steel 2205 with regard to these precipitates. A sigma and chi precipitation occurs at higher temperatures. Super-duplex grades that are highly alloyed with chromium, molybdenum and nickel will have more rapid sigma and chi kinetics than steel 2205.

**Table 1:** Secondary phases forming in duplex stainless steels (temperatures above 500 °C)<sup>8</sup>

**Tabela 1:** Sekundarne faze, ki nastajajo v dupleksnem nerjavnem jeklu (temperature nad 500 °C)<sup>8</sup>

| Type of precipitate       | Nominal chemical formula                     | Temperature range (°C) |
|---------------------------|----------------------------------------------|------------------------|
| Ferrite ( $\alpha$ )      | —                                            | —                      |
| Austenite ( $\gamma$ )    | —                                            | —                      |
| $\sigma$                  | Fe-Cr-Mo                                     | 600–1000               |
| Chromium nitride          | $\text{Cr}_2\text{N}$                        | 700–900                |
| Chromium nitride          | $\text{CrN}$                                 | 1000                   |
| $\chi$                    | $\text{Fe}_{36}\text{Cr}_{12}\text{Mo}_{10}$ | 700–900                |
| R                         | Fe-Cr-Mo                                     | 550–800                |
| $\pi$                     | $\text{Fe}_7\text{Mo}_{13}\text{N}_4$        | 550–600                |
| $\tau$                    | —                                            | 550–650                |
| $\text{M}_7\text{C}_3$    | —                                            | 550–650                |
| $\text{M}_{23}\text{C}_6$ | —                                            | —                      |

The most important secondary phases during the manufacturing and welding of duplex steels are  $\sigma$ ,  $\chi$ , secondary austenite and chromium nitrides. All these phases are formed above 500 °C. The sigma and chi precipitation occurs at slightly higher temperatures but in approximately equal precipitation time as the carbide and nitride precipitation. **Table 1** lists the secondary phases found in duplex stainless steels and weld metals above 500 °C.<sup>8</sup> Below 500 °C the precipitation reactions are comparatively slow, having little effect on the embrittlement. The 475 °C embrittlement is due to the decomposition of ferrite between 350 °C and 525 °C, into

the  $\alpha'$  phase which precipitates in the ferrite phase and causes a hardening and embrittlement of the ferrite.<sup>4</sup>

Numerous research studies describe the precipitation phenomena in Cr-Ni stainless steels,<sup>6,9–13</sup> however, there is yet no clear evidence on the amount of acceptable secondary phases in a steel microstructure. The objective of the investigations was to study the effect of heat treatment of duplex and super-duplex steels on their mechanical properties, impact toughness and strength, and to analyze the changes in the steel microstructure.

## 2 EXPERIMENTAL PROCEDURE

Commercial grades 2205 and 2507, with their chemical compositions shown in **Table 2**, were investigated. The specimens were cut from plates 12 mm, pre-annealed at 1050 °C and isothermally tempered in a vacuum furnace for 6 min, 1 h and 10 h at temperatures from 500 °C to 900 °C and water quenched. The microstructure was examined after chemical etching in Murakami and Beraha's reagents. The amount of the phases was assessed with a magnetic ferritoscopic analysis and a quantitative microstructure analysis.

**Table 2:** Chemical compositions of tested 2205 and 2507 duplex stainless steels

**Tabela 2:** Kemijska sestava preizkušanih dupleksnih nerjavnih jekel 2205 in 2507

| Duplex grade | w/%   |      |       |      |      |      |
|--------------|-------|------|-------|------|------|------|
|              | C     | Mn   | Cr    | Ni   | Mo   | N    |
| 2205 S31803  | 0.017 | 1.50 | 21.9  | 5.7  | 3.0  | 0.17 |
| 2507 S32550  | 0.030 | 0.87 | 25.12 | 5.82 | 3.59 | 0.29 |

The initial Vickers hardness of the base materials was 254 HV10 for the 2205 steel grade and 270 HV10 for the 2507 steel grade. Charpy V impact tests were performed at ambient temperature (+20 °C) on the specimens with a notch that was orthogonal to the plate's longitudinal direction. The as-delivered specimens had high fracture energy ( $\approx$  300 J).

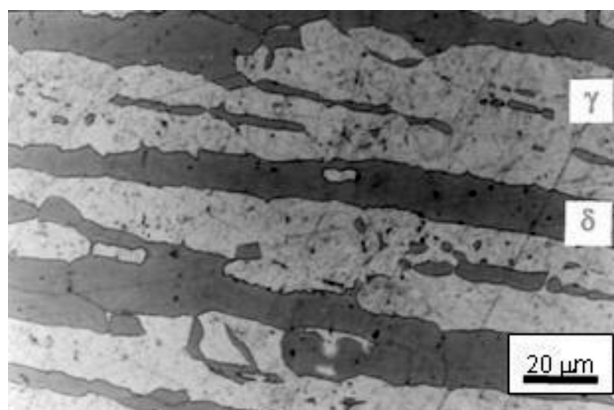


**Figure 2:** Microstructure of the as-delivered 2205 duplex stainless steel

**Slika 2:** Mikrostruktura dupleksnega nerjavnega jekla 2205 v dobavljenem stanju

### 3 RESULTS AND DISCUSSION

Due to the used treatments different phases (intermetallic phases,  $\text{Cr}_2\text{N}$  and secondary austenite) were formed, with the  $\sigma$ -phase as the most important one beside ferrite and austenite and with the largest volume fraction. **Figure 2** presents the microstructure of the as-received 2205 duplex steel with an elongated lamellar shape of the rolled ferrite and austenite (the light etched phase is austenite and the dark etched one is ferrite). In the as-received state, the microstructure of grade 2507 is similar to that of grade 2205. The ferrite content in the microstructure of steel 2205 was 44–47 % and in steel 2507 it was 52–55 %. The specimens of both steels being aged at 500 °C, even in the case of the longest aging time, do not exhibit any significant phase transformation; only the amount of ferrite is slightly decreased due to the nucleation of secondary austenite  $\gamma_2$ .

In duplex steels, the ferrite is unstable at elevated temperatures (600 °C and 900 °C) because of the high diffusion rates of dissolved alloying elements, which were 100 times faster than in the case of austenite. Moreover, the ferrite is enriched in chromium and molybdenum, thus promoting the formation of intermetallic phases.

On the other hand, the formation of secondary austenite is independent of the  $\sigma$ -phase precipitation although these two transformations occur simultaneously and are both related to the ferrite phase. The mechanism of the  $\sigma$ -phase formation depends on the temperature; below 900 °C and after a longer ageing period, the  $\sigma$ -phase is formed by the eutectoid reaction  $\delta \rightarrow \sigma + \gamma_2$ . First, the  $\sigma$ -phase forms inside the ferrite grains, then it starts to form at the ferrite/ferrite or ferrite/austenite grain boundaries. At 900 °C and above this temperature ferrite transforms into the  $\sigma$ -phase without an austenite formation and the composition of the  $\sigma$ -phase is close to ferrite.

Comparing the two considered duplex steel grades, it is evident that grade 2205 is less prone to the  $\sigma$ -phase precipitation than grade 2507. In grade 2205, the precipitation of the  $\sigma$ -phase is observed after 10 h of ageing at the temperatures of 600 °C and 700 °C. The specimens of grade 2205 aged at 800 °C show the  $\sigma$ -phase precipitation after less than 1 h (**Figure 3**) and due to the ageing at 900 °C the  $\sigma$ -phase formation occurs in less than 6 min. In the case of super-duplex steel 2507, the precipitation of small aggregations of the  $\sigma$ -phase was observed already after 6 min of ageing at 700 °C. The specimens aged at 800 °C and 900 °C (**Figure 4**)

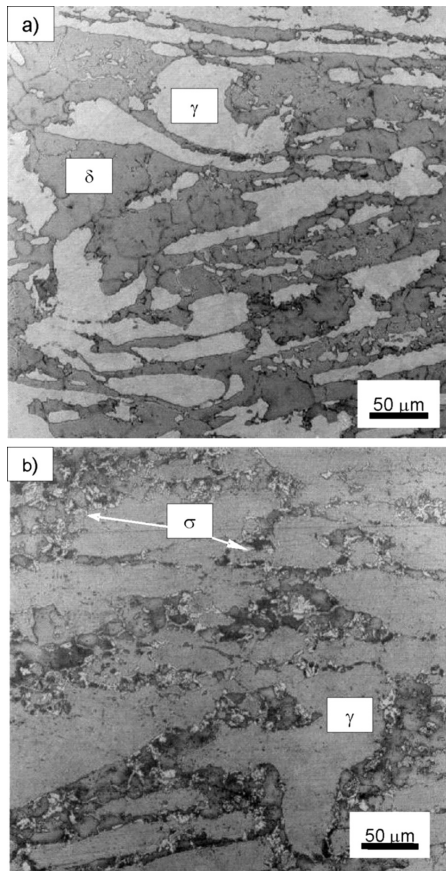


**Figure 3:** Formation of  $\sigma$ -phase (eutectoid reaction) in 2205 duplex-steel grade aged at 800 °C for: a) 6 min, b) 1 h

**Slika 3:** Tvorba  $\sigma$ -faze (eutektoidna reakcija) v dupleksnem nerjavnem jeklu 2205, staranjem na 800 °C: a) 6 min, b) 1 h

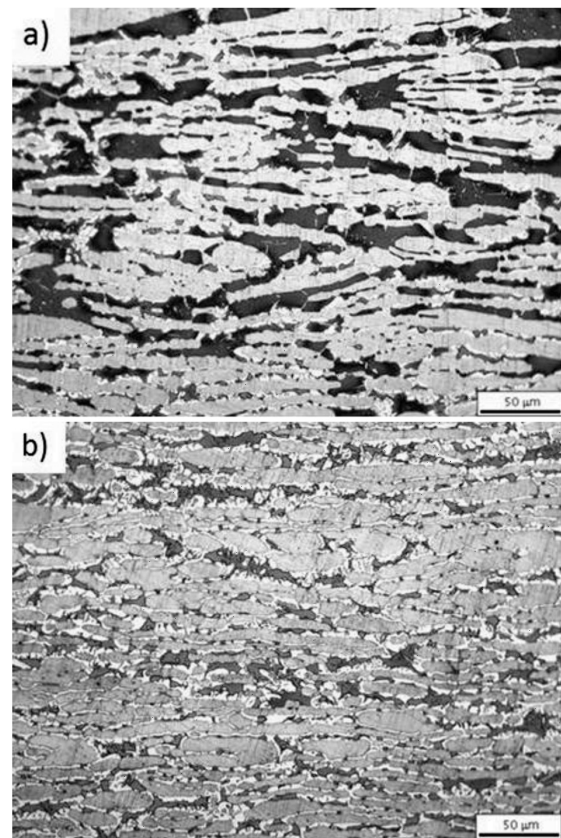


**Figure 4:** Formation of  $\sigma$ -phase (directly from ferrite) in 2507 duplex steel grade aged at 900 °C for: a) 6 min, b) 1 h

**Slika 4:** Tvorba  $\sigma$ -faze (neposredno iz ferita) v dupleksnem nerjavnem jeklu 2507, staranjem na 900 °C: a) 6 min, b) 1 h

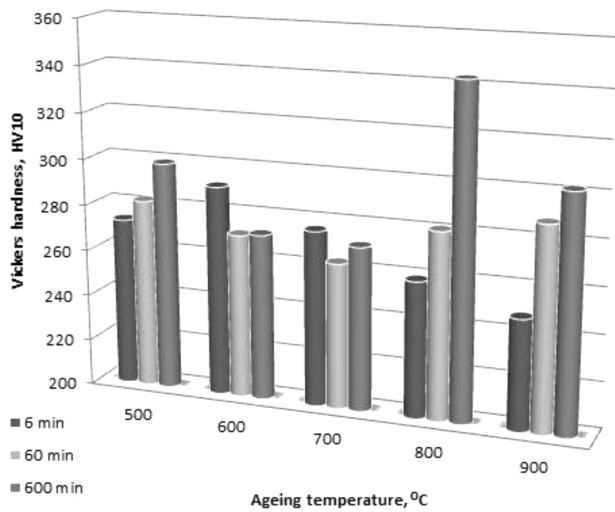


Figure 5: Influence of the ageing time and temperature on the hardness of 2205 duplex stainless steel

Slika 5: Vpliv časa in temperature staranja na trdoto dupleksnega nerjavnega jekla 2205

show, already after 6 min, advanced ferrite-phase disintegration. In the cases of lower ageing temperatures (500 °C, 600 °C) and shorter aging times (6 min, 60 min) no  $\sigma$ -phase was observed in the microstructures.

The next detailed investigations were conducted to determine the correlation between certain mechanical properties (hardness and embrittlement) and the microstructure. The  $\alpha'$ -phase precipitations caused a slight hardness increase in both investigated duplex steels being aged at 500 °C. In steel grade 2205 the ageing at 600 °C and 700 °C caused a small decrease in the steel hardness (Figure 5), probably due to the creation of the  $\gamma_2$ -phase. Further ageing at higher temperatures causes a precipitation of the  $\sigma$ -phase and a significant hardness increase. The maximum hardness values were 348 HV10

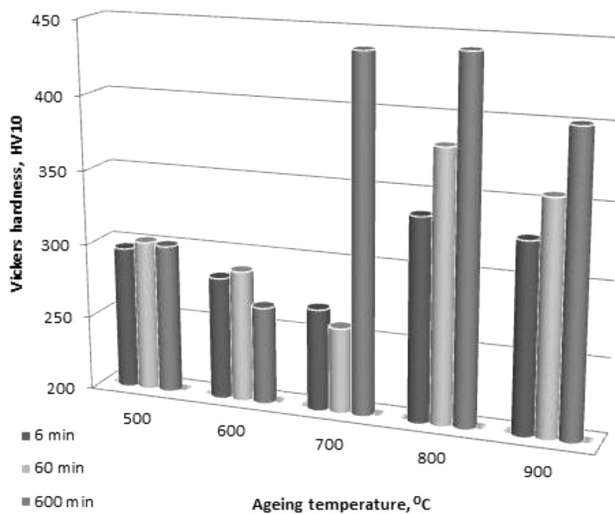


Figure 6: Influence of the ageing time and temperature on the hardness of 2507 super-duplex stainless steel

Slika 6: Vpliv časa in temperature staranja na trdoto super dupleksnega nerjavnega jekla 2507

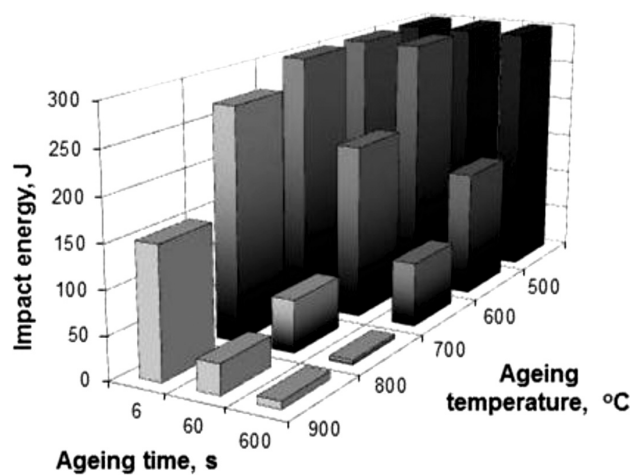


Figure 7: Influence of the ageing time and temperature on the impact energy of 2205 duplex stainless steel

Slika 7: Vpliv časa in temperature staranja na energijo udarca dupleksnega nerjavnega jekla 2205

for steel 2205 after 10 h of ageing at 800 °C and 94 HV10 for duplex steel grade 2507. The ageing at 600 °C caused a small decrease in the steel hardness, while the ageing at 700 °C significantly increased the hardness (Figure 6). The super-duplex 2507 steel showed the highest hardness of 438–441 HV10 after 10 h of ageing at 700 °C and 800 °C and the hardness increase for steel grade 2507 was 171 HV10. The ageing of both analyzed steel grades at 900 °C increased the hardness less than the ageing at 800 °C, probably due to a smaller amount of precipitates. Unlike the hardness, the embrittlement behavior of the analyzed specimens of duplex steel grades was different and the 2205 duplex was less sensitive to embrittlement (Figure 7). A short time (6 min) of ageing at the temperatures up to 800 °C did not remarkably decrease the impact energy. At 900 °C the impact energy fell to a value of 150 J. The ageing for 1 h caused

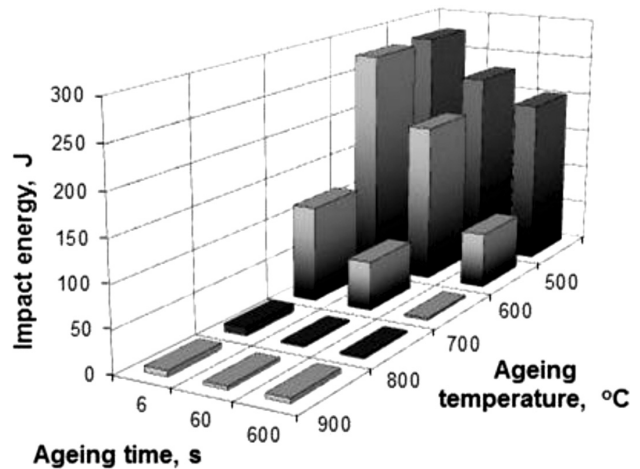
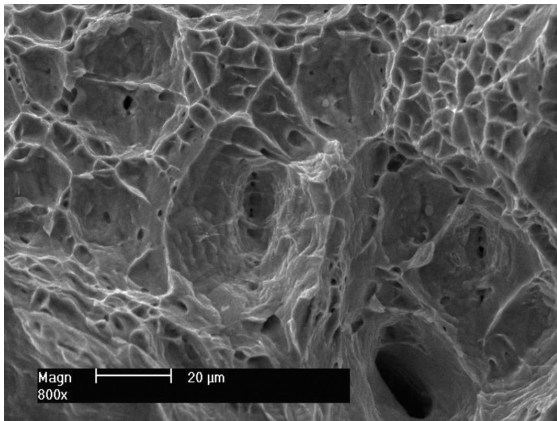
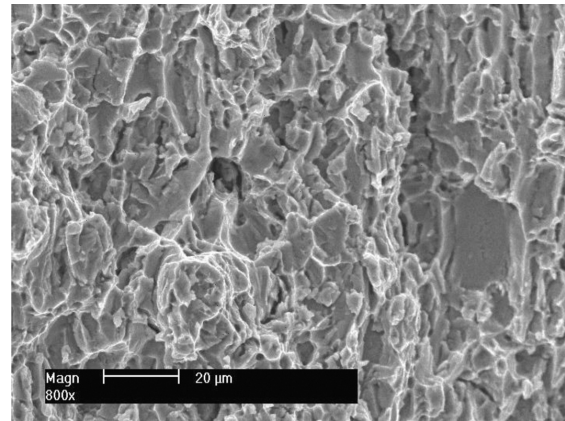


Figure 8: Influence of the ageing time and temperature on the impact energy of 2507 super-duplex stainless steel

Slika 8: Vpliv časa in temperature staranja na energijo udarca super dupleksnega nerjavnega jekla 2507



**Figure 9:** Fracture surface of the specimen aged at 500 °C for 1 h  
**Slika 9:** Površina preloma vzorca, staranega 1 h na 500 °C



**Figure 11:** Fracture surface of the specimen aged at 900 °C for 1 h  
**Slika 11:** Površina preloma vzorca, staranega 1 h na 900 °C

a decrease in the impact energy starting at 700 °C and the greatest change occurred at 800 °C. During the ageing for 10 h at 500 °C the high toughness remained at the level of 300 J, while at higher temperatures a significant decrease in the impact energy was observed. The 2507 super-duplex steel showed a high toughness after the ageing for 6 min at 500 °C and 600 °C (**Figure 8**) and at 700 °C the impact energy decreased by more than half. With the average ageing time (1 h), the impact energy decreased from about 250 J at 500 °C to almost zero at 800 °C and 900 °C. Finally, after 10 h of ageing the impact energy was on a decrease from 200 J at 500 °C to 100 J at 600 °C, approaching zero at the temperatures above 600 °C. It should be stated that higher temperatures remarkably reduce the steel plasticity and may cause an almost complete decrease in the toughness.

The change in the mechanical properties was investigated with scanning electron microscopy with the main aim to determine the correlation between the impact toughness and fracture mode by examining the fractures of Charpy V specimens. The macroscopic observation of fracture surfaces showed many secondary cracks or splits. The literature information<sup>14</sup>, according to which

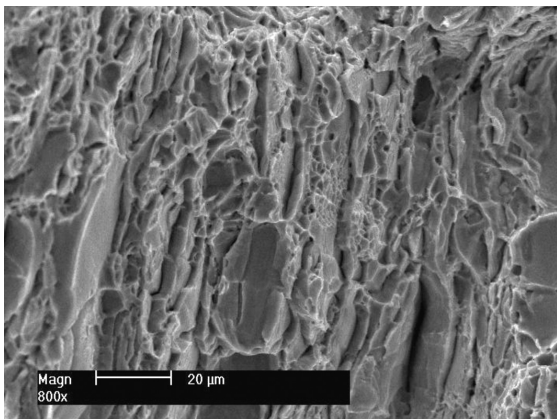


**Figure 10:** Fracture surface of the specimen aged at 700 °C for 1 h  
**Slika 10:** Površina preloma vzorca, staranega 1 h na 700 °C

the splits propagate through the ferrite phase or ferrite-austenite boundaries, was confirmed. The fractures of the samples tempered at 600 °C and 700 °C for up to 1 h were ductile and had dimpled fracture surfaces, with the dimples being elongated in the stress direction (**Figure 9**). With higher ageing temperatures and longer annealing times the fractures were mixed. The sample annealed at 700 °C showed a cleavage fracture and small areas with dimples (**Figure 10**). Brittle fracture was found on the samples treated at 800 °C and 900 °C (**Figure 11**).

#### 4 CONCLUSIONS

The research was focused on the potential and future applications of duplex steels,<sup>15</sup> as for many of them the mechanical properties are of an essential importance. The results indicate a negative effect of the changes to the microstructures of duplex steels on their mechanical

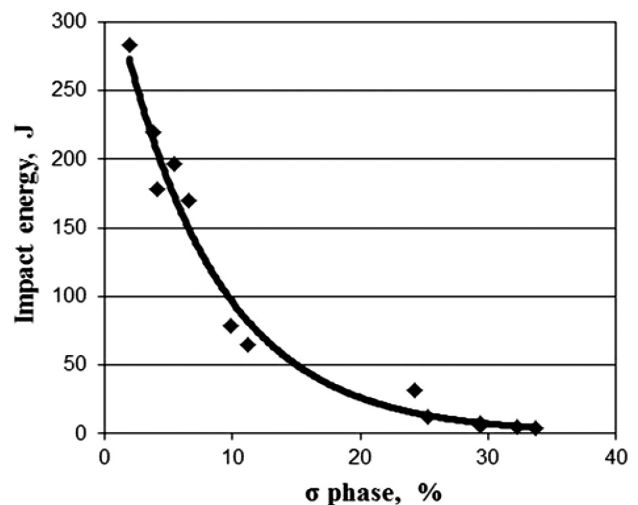


**Figure 12:** Influence of the  $\sigma$ -phase content on the impact energy of 2205 duplex stainless steel

**Slika 12:** Vpliv vsebnosti  $\sigma$ -faze na energijo udarca pri dupleksnem nerjavnem jeklu 2205

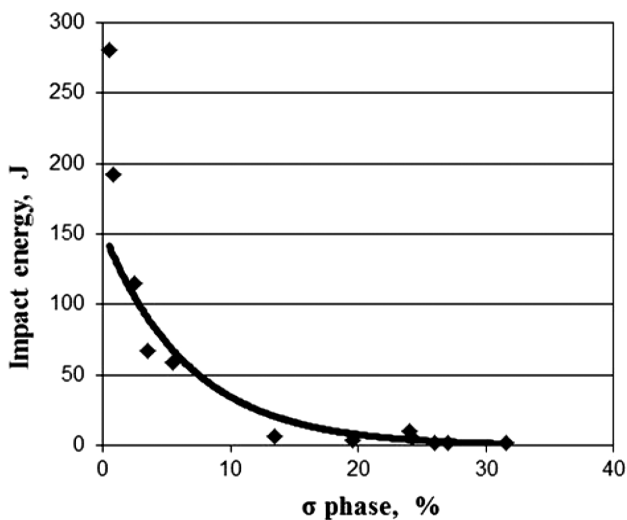


**Figure 13:** Influence of the  $\sigma$ -phase content on the impact energy of 2507 super-duplex stainless steel

**Slika 13:** Vpliv vsebnosti  $\sigma$ -faze na energijo udarca pri super dupleksnem nerjavnem jeklu 2507

properties. Precipitates, mainly the  $\sigma$ -phase, decrease the plasticity of duplex 2205 and super-duplex 2507 stainless steels as, due to small amounts of the  $\sigma$ -phase in the steel microstructures, the toughness of both steels decrease considerably. This is a result of the brittleness of the closed-packed  $\sigma$ -phase lattice. **Figures 12 and 13** show diagrams of the influence of the  $\sigma$ -phase amounts in the microstructures of the 2205 and 2507 duplex steels on the impact energy. To determine the amounts of this phase a multi-scan image-analysis system and metallographic specimens were used.

The obtained results can be analyzed with respect to the requirements of Ship Classification Societies. According to the common material-design criterion for wrought products, the impact energy obtained on the Charpy V specimens should be higher than 27 J or 40 J, depending on the testing temperature and the transverse or longitudinal direction of the specimens. It is obvious that the examined 2205 steel could be used at room temperature provided its  $\sigma$ -phase content accounts for up to 14 % ( $KV > 40$  J) and the super-duplex 2507 steel could be used with the  $\sigma$ -phase accounting for up to 8 % of the microstructure (**Figures 12 and 13**). The usually accepted amount of the  $\sigma$ -phase is about 4 %<sup>2</sup> but some researches<sup>16</sup> claim that even smaller amounts of the  $\sigma$ -phase lead to a significant decrease in the toughness and a rapid decrease to the value unacceptable for industrial applications. This statement is compatible with the

results presented in our work. Even a very small amount of the  $\sigma$ -phase in a microstructure caused a measurable decrease in the toughness of the two analyzed steels. The 2507 super-duplex steel is more prone to embrittlement, which is an important criterion for the design and exploitation of steels for the maritime and energy-related technical applications. An undesired and unpredictable temperature growth over 500 °C, lasting for a longer time could cause errors during the processing of duplex stainless steels and accidents during the use of the products.

The results of these investigations confirm that high-temperature service of duplex stainless steels should be avoided. The precipitation of secondary phases strongly influences the mechanical properties, and for the use of steel grade 2205, only limited amounts of the  $\sigma$ -phase are acceptable.

## 5 REFERENCES

- 1 J. Charles, *Welding in the World*, 36 (1995), 89–97
- 2 J. Łabanowski, *Apparatus and Chemical Engineering*, 36 (1997) 2, 3–10 (in Polish)
- 3 A. Gwiazda, *Applied Mechanics and Materials*, 474 (2014), 417–422, doi:10.4028/www.scientific.net/AMM.474.417
- 4 Practical guidelines for the fabrication duplex stainless steels, International Molybdenum Association, London 2001, 48
- 5 J. Frodigh, J. Nicholls, *Mechanical properties of Sandvik duplex stainless steels*, AB Sandvik Steel, Sandviken 1994, 81
- 6 X. G. Wang, D. Dumortier, Y. Riquier, *Structural evolution of zeron 100 duplex stainless steel between 550 and 1100 °C*, Proc. of Conf. Duplex stainless steels '91, Beaune, France, 1991, 127–134
- 7 L. Karlsson, L. Ryen, S. Pak, *Welding Journal*, 1 (1995), 115–122
- 8 L. Karlsson, *Welding in the world*, 43 (1999) 5, 20–40
- 9 T. Otarola, S. Hollner, B. Bonnefois, M. Anglada, L. Coudreuse, A. Mateo, *Engineering Failure Analysis*, 12 (2005), 930–941, doi:10.1016/j.engfailanal.2004.12.022
- 10 T. H. Chen, K. L. Weng, J. R. Yang, *Materials Science Engineering*, A338 (2002), 259–270, doi:10.1016/S0921-5093(02)00093-X
- 11 J. Nowacki, P. Rybicki, *Journal of Achievements in Materials and Manufacturing Engineering*, 17 (2006) 1–2, 113–116
- 12 J. Łabanowski, *Journal of Achievements in Materials and Manufacturing Engineering*, 20 (2007) 1–2, 255–258
- 13 J. Nowacki, A. Łukojć, *Journal of Materials Processing Technology*, 164–165 (2005), 1074–1081, doi:10.1016/j.jmatprotec.2005.02.243
- 14 H. Sieurin, R. Sandström, *Engineering Fracture Mechanics*, 73 (2006) 4, 377–390, doi:10.1016/j.engfracmech.2005.03.009
- 15 A. Gwiazda, *Advanced Materials Research*, 837 (2014), 393–398, doi:10.4028/www.scientific.net/AMR.837.393
- 16 J. Charles, *The duplex stainless steels: materials to meet your needs*, Proc. of Conf. Duplex stainless steels '91, Beaune, France, 1991, 3–48



# EFFECTS OF THE ARTIFICIAL-AGING TEMPERATURE AND TIME ON THE MECHANICAL PROPERTIES AND SPRINGBACK BEHAVIOR OF AA6061

## VPLIV TEMPERATURE IN ČASA UMETNEGA STARANJA NA MEHANSKE LASTNOSTI IN VZMETNOST AA6061

Aytekin Polat<sup>1</sup>, Mustafa Avsar<sup>1</sup>, Fahrettin Ozturk<sup>2</sup>

<sup>1</sup>Department of Mechanical Engineering, Nigde University, Nigde, Turkey

<sup>2</sup>Department of Mechanical Engineering, The Petroleum Institute, Abu Dhabi, United Arab Emirates  
apolat@nigde.edu.tr

*Prejem rokopisa – received: 2013-09-20; sprejem za objavo – accepted for publication: 2014-09-08*

doi:10.17222/mit.2013.154

In this study, the effects of the artificial-aging temperature and time on the mechanical properties and springback behavior of AA6061 are investigated. The results reveal that the yield strength, the tensile strength and the elongations decreased with the increasing artificial-aging temperature, but increased with the increasing artificial-aging time up to the peak age. The springback of the alloy increased significantly with the increasing artificial-aging time at the artificial-aging temperature ranging from 160 °C to 180 °C and decreased with the artificial-aging time at 200 °C. The springback angle in the as-received condition is lower than in all the aged conditions.

Keywords: aluminum alloy, AA6061, artificial aging, mechanical properties, springback

V tej študiji so bili preiskovani vplivi temperature in časa umetnega staranja na mehanske lastnosti in vzmetnost AA6061. Rezultati so pokazali zmanjšanje meje tečenja, natezne trdnosti in raztezka pri naraščanju temperature umetnega staranja ter povečevanje teh vrednosti do maksimuma pri podaljšanju časa staranja. Vzmetnost zlitine občutno narašča z naraščanjem časa umetnega staranja v območju temperatur od 160 °C do 180 °C in se zmanjša s časom umetnega staranja pri 200 °C. Kot vzmetnosti v dobavljenem stanju je manjši kot pri vseh starih razmerah.

Gljučne besede: aluminijeva zlitina, AA6061, umetno staranje, mehanske lastnosti, vzmetnost

## 1 INTRODUCTION

The 6xxx-series aluminum alloys are widely used in many industries such as aerospace, automotive and food industry due to their high strength-to-mass ratio, good corrosion resistance, good mechanical properties or a combination of these properties.<sup>1</sup> In these alloys, all the alloying elements and impurities contribute, to various degrees, to the strengthening of aluminum matrix through solution hardening and dispersion hardening. Mg and Si are the major solid-solution strengtheners. They increase the strength of an alloy by precipitation hardening (also called age hardening).<sup>2</sup> Precipitation hardening is a heat-treatment process used to improve the mechanical properties of the age-hardenable alloys. The process produces fine particles of an impurity phase and these precipitates impede the movement of dislocations. Any obstacles that make dislocation movement difficult harden the materials. There has been a considerable industrial interest in these alloys because two thirds of all the extruded products are made of aluminum, and 90 % of these are made of the 6xxx series alloys. The AA6061 alloy is one of the most widely used aluminum alloys from the 6xxx series.<sup>3</sup> It is an age-hardenable alloy, whose mechanical properties are mainly controlled with the hardening precipitates contained in the material.

When the material is subjected to a solution heat treatment followed by quenching and artificial aging, its mechanical properties reach their highest levels and become very good compared to the other aluminum alloys.

Since the AA6061 alloy is a precipitation-hardenable material, its hardness, strength, and work-hardening capability are determined by the level of the solutes in the solid-solution matrix and the amount, type, density, size and nature of the second-phase particles.<sup>4</sup> The precipitation sequence for the 6xxx alloys, which is generally accepted in the literature<sup>5-7</sup> is: SSSS → atomic clusters (Si clusters and Mg clusters) → dissolution of Mg clusters → Mg, Si co-clusters → precipitates of an unknown structure (GP-I zones) →  $\beta''$  (GP-II zones) →  $B'$  and  $\beta' \rightarrow \beta$  (stable  $Mg_2Si$ ). Here SSSS represents the supersaturated solute solution and GP stands for Guinier-Prestone zones.

The most effective hardening phase for these types of materials is  $\beta''$ . The formation of a stable  $\beta$  phase ( $Mg_2Si$ ) is preceded by a chain of transformations involving various coherent and semi-coherent meta-stable phases. Specifically, the sequence is: the formation of independent clusters of the Mg and Si atoms from the supersaturated solute solution, the formation of co-clusters that contain both Si and Mg,<sup>4</sup> the formation and

growth of  $\beta''$  needle-shaped precipitates, the transformation of the  $\beta''$  precipitates into  $\beta'$  lath-shaped precipitates and  $\beta'$  rod-shaped precipitates, followed, after long annealing times, by the formation of an incoherent, stable  $\beta$ . The co-clusters form after the dissolution of the Mg clusters; these were also found in naturally aged alloys. Compared to the co-clusters, the GP-I zones are thermally more stable; they contain more solute atoms and are spherical, with typical sizes of 1–3 nm.<sup>8</sup> The pre- $\beta''$  phases are coherent, while  $\beta'$  is semi-coherent (coherent with the Al matrix along the axis of the needle). The rod-shaped phases  $\beta'$  and  $\beta'$  form consecutively. These phases are typical for over-aged structures. The needle-shaped  $\beta''$  ( $Mg_5Si_6$ ) precipitates are associated with peak-aged states.<sup>8</sup> The precipitate particles and solute atoms generally formed in these alloys are obstacles to the dislocation accumulation and arrangement. They affect the development of a dislocation substructure with a special distribution of dislocation accumulation, the flexibility of dislocation movements, the initial trapping behavior of dislocations and the rate of dynamic recovery.<sup>9</sup>

Since the chemical compositions, volume fractions and morphologies of intermetallic phases exert significant effects on the mechanical properties of the 6xxx-type Al-alloys,<sup>10</sup> it is also important to know where, when and what kind of intermetallic may form during a solidification process. Hence, the improvement of the metallurgical process and the use of heat-treatable aluminum alloys as structural materials are then strongly related to the understanding of the influence of the precipitation process and an intermetallic with its physical and mechanical properties on the behavior of the Al alloys. The 6000-series alloys generally have a lower formability than the 5000-series Al–Mg alloys. However, they can obtain a higher strength after the paint-baking process.<sup>11</sup> This is the major advantage of the 6000-series alloys.

The objectives of the present study were as follows:

a) to develop a suitable age-hardening heat-treatment

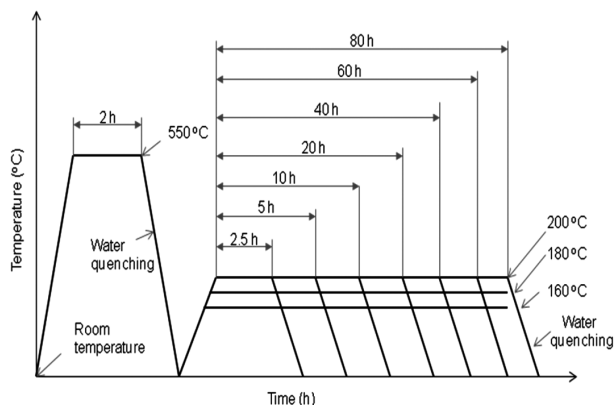


**Figure 1:** Schematic representations of the aging-treatment procedures

**Slika 1:** Shematski prikaz postopkov staranja

process with specified parameters for AA6061, b) to investigate the effects of the artificial aging temperature and time on the mechanical properties and springback behavior of AA6061, c) to discuss the relationship between the springback behavior and the mechanical properties.

## 2 MATERIALS AND EXPERIMENTAL PROCEDURE

In this study, a commercially available AA6061-O with a thickness 1 mm produced by AMAG rolling was used in its as-received condition. The chemical composition of the alloy is given in **Table 1**.

**Table 1:** Chemical composition of AA6061 in mass fractions, w/%  
**Tabela 1:** Kemijska sestava AA6061 v masnih deležih, w/%

| Mg   | Si   | Cu   | Mn   | Fe   | Cr   | Zn   | Al      |
|------|------|------|------|------|------|------|---------|
| 0.80 | 0.63 | 0.21 | 0.08 | 0.38 | 0.17 | 0.03 | balance |

All the 6061 Al-alloy specimens, except those in the as-received condition, were solution heat treated at 550 °C for 2 h followed by quenching in water at room temperature (*RT*). After the solution heat treatment, all the AA6061 specimens were kept in a refrigerator to avoid natural aging of the alloy at room temperature. Following the solution heat treatment, the specimens were artificially age hardened in a furnace at (160, 180, and 200) °C for periods of (2.5, 5, 10, 20, 40, 60, and 80) h and subsequently quenched in water. The aging-treatment procedure is illustrated in **Figure 1**.

Uniaxial tensile tests were performed at *RT*. The tensile-test samples were prepared by water-jet cutting according to the ASTM E8 standard along 0° (rolling), 45° (diagonal), and 90° (transverse) directions. The deformation speed was chosen as 25 mm/min and the gage length was 50 mm. The tests were conducted with a Shimadzu Autograph 100 kN tensile-testing machine and the deformation was measured with a video-type extensometer. Two lines were scribed on the gage length. Basically, the video-type extensometer followed these two lines during the test and calculates the strains.

For the springback measurements, a V-shaped die with a 60° angle integrated with the tensile-testing machine was used. Rectangular test samples were prepared in the rolling direction. All the tests were done at *RT* using a constant deformation speed of 25 mm/min. The hardness was measured using a Mitutoyo HV-112 Vickers-hardness tester with a 10 kg load. Three measurements were made for each sample under each experimental condition and the results were averaged.

## 3 RESULTS AND DISCUSSION

First, the mechanical properties of the as-received alloy at *RT* and the 0.0083 s<sup>-1</sup> strain rate were determined. The results were as follows: Young's Modulus *E*

= 68.9 GPa, the yield strength (YS) was 55.2 MPa, the ultimate tensile strength (UTS) was 124 MPa, hardening coefficient  $K$  was 332 MPa, hardening exponent  $n$  was 0.296, normal anisotropy  $r_n$  was 0.68, the total elongation (TE) was 25 % and Vickers hardness was 53 HV.

### 3.1 Effects of the artificial-aging temperature and time on the hardness of AA6061

The hardness variations for the alloy with various aging temperatures and times are displayed in **Figure 2**. This figure indicates that the hardness of AA6061 depends strongly on both the aging time and the temperature. At each aging temperature, the hardness of the alloy first increases with the aging time and reaches its maximum value. After reaching its maximum value, the hardness of the alloy begins to decrease gradually with the aging time. The increase in the hardness can be explained with the diffusion-assisted mechanism and also with the hindrance of dislocation by impurity atoms, i.e., the foreign particles of the second phase since the material, after being quenched from 550 °C (solution heat treatment), has an excessive vacancy concentration. Beyond the peak hardness, the hardness value drops. The decrease in the hardness is associated with an increase in the inter-particle spacing among precipitates, which makes the dislocation bowing much easier.<sup>12,13</sup> Moreover, the coarsening of the silicon phase results in a reduction of the hardness values.

The hardness of the alloy immediately after the solutionizing is 54 HV. The alloy achieves its maximum hardness at 160 °C when aged for 40 h. At this aging temperature and time, the alloy produces a hardness structure that is attributed to the acceleration of Mg<sub>2</sub>Si and other strengthened phases.<sup>14</sup> At this aging temperature and time, the microstructure of the alloy is refined by the heat treatment into a fine dispersion of Mg<sub>2</sub>Si and

other strengthening phases with  $\beta''$  as the strengthening phase<sup>15</sup> which is coherent, along with the semi-coherent clusters of  $\beta$ (Mg<sub>2</sub>Si). The solute atoms form clusters serving as a barrier to the movement of dislocation and, hence, a higher hardness is obtained.

At a higher aging temperature, the alloy is expected to develop hardness at a shorter aging time because the rate of precipitation of the second phase atoms is faster. With the particles of the second-phase precipitates, solute atoms and grain boundaries<sup>16,17</sup> a higher hardness is expected to develop in the alloy.

### 3.2 Effects of the artificial-aging temperature and time on the yield and tensile strengths of AA6061

The variation in the yield and tensile strengths of the alloy, when exposed to different aging temperatures for different intervals of the time, is shown in **Figures 3** and **4**, respectively.

At each aging temperature, it can be observed that initially the yield and tensile strengths of the alloy increase with the aging time and reach their peak values. After reaching the peak values, continuous decreases in the yield and tensile strengths are observed with the aging time. The peak-strength values of the alloy for the aging temperatures of (160, 180 and 190) °C were obtained when the alloy was aged for (60, 10 and 5) h, respectively. The initial increases in the yield and tensile strengths are due to the vacancy-assisted diffusion mechanism and the formation of a high volume fraction of GP zones followed by the formation of metastable  $\beta''$  and  $\beta'$  precipitates, disturbing the regularity in the lattices. Siddiqui et al.<sup>18</sup> showed that as the aging temperature and time increase, the density of GP zones also increases. Hence, the degree of irregularity in the lattices causes an increase in the mechanical properties of the Al-Mg-Si alloy. The strengthening effect of the AA6061

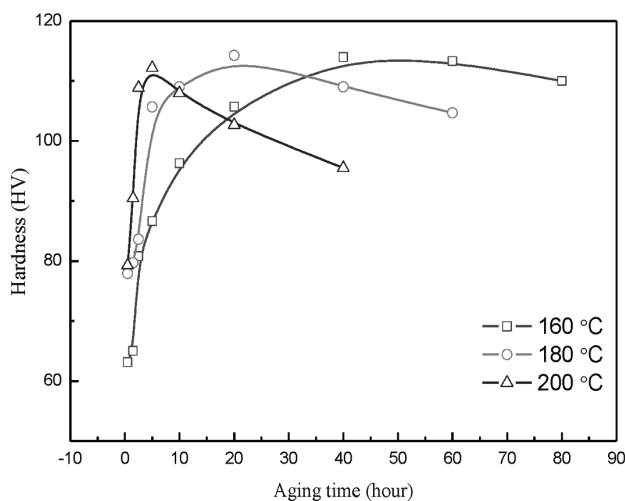


**Figure 2:** Effects of artificial-aging temperature and time on hardness of AA6061 alloy

**Slika 2:** Vpliv temperature in časa umetnega staranja na trdoto zlitine AA6061

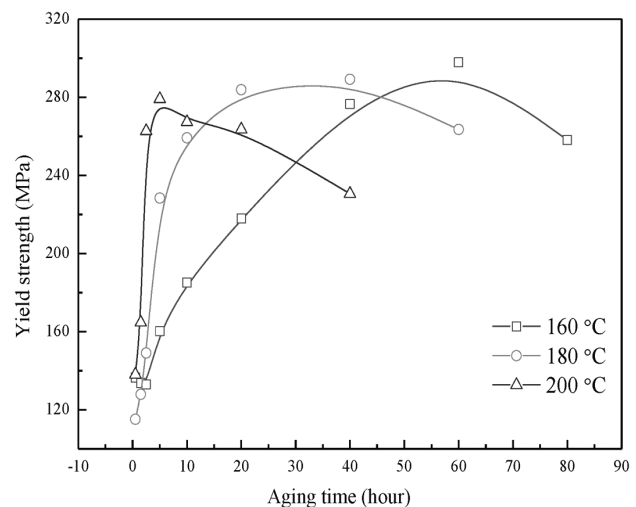


**Figure 3:** Effects of artificial-aging temperature and time on yield strength (YS) of AA6061 alloy

**Slika 3:** Vpliv temperature in časa umetnega staranja na mejo tečenja (YS) zlitine AA6061

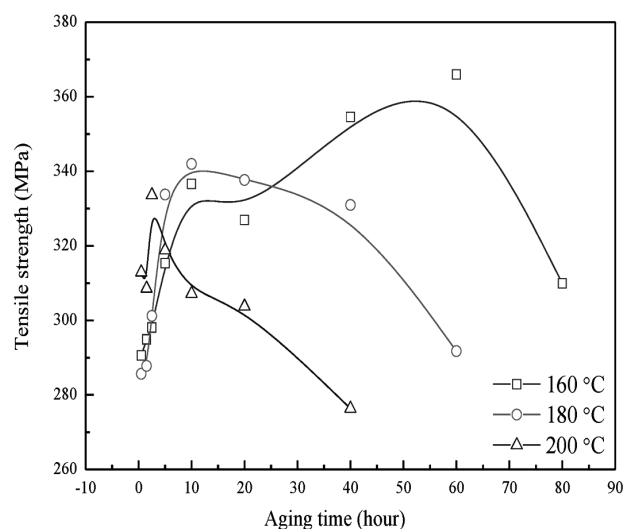


**Figure 4:** Effects of artificial-aging temperature and time on tensile strength (*TS*) of AA6061 alloy

**Slika 4:** Vpliv temperature in časa umetnega staranja na natezno trdnost (*TS*) zlitine AA6061

alloy can also be interpreted as a result of an interference with the motion of dislocation due to the presence of foreign particles of any other phase.

In the aging process performed at high temperatures, the yield and tensile strengths reach their peak values in a very short period of time because the rate of precipitation of the second-phase atoms is faster, and precipitates form quickly. As the aging temperature decreases, this period is prolonged. In addition, at high temperatures, the drops in the yield and tensile strengths after the peak values are very fast and occur in a very short time, while at low temperatures they are slower and occur after a long time.

The difference between the tensile strength after a shorter aging time, for example, 5 h and that obtained

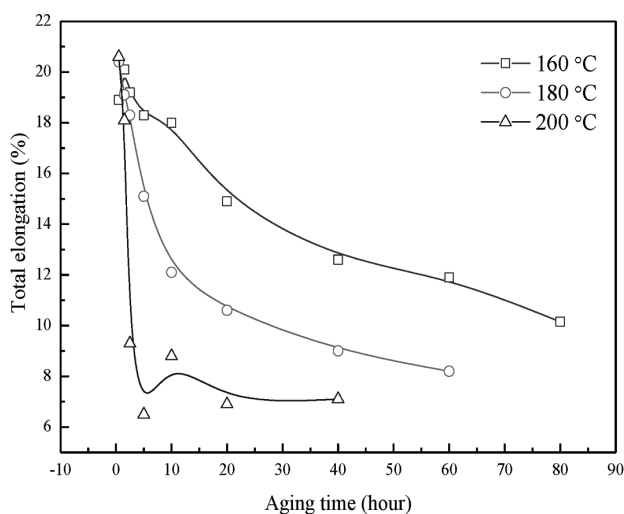


**Figure 5:** Effects of artificial-aging temperature and time on the total elongation (*TE*) of AA6061 alloy

**Slika 5:** Vpliv temperature in časa umetnega staranja na celotni raztezek (*TE*) zlitine AA6061

over a longer time of 10 h at 180 °C may be due to the incoherent precipitates that appeared in the early hours and disappeared later due to the diffusion of the precipitates and the homogenization of the matrix. However, since the diffusion/precipitation processes are slower at lower temperatures than at higher temperatures, the precipitates appeared in the aluminum matrix only after the aging for longer periods.<sup>19,20</sup>

The alloy achieves its maximum yield-strength values at the aging temperatures of (160, 180 and 190) °C when aged for (60, 40 and 5) h, respectively, thereafter, a decrease occurs as the aging time progresses. For example, at 180 °C, the yield strength decreases significantly from its maximum value of 290 MPa to a value of less than 260 MPa after another 20 h of aging. This could be due to coalescence of the precipitates into larger particles and a bigger grain size, causing fewer obstacles to the movement of dislocation, and also due to the annealing out of the defects.

The variation in the ductility of AA6061 with the artificial aging temperature and time is shown in **Figure 5**. The ductility follows an inverse relation with the strength, as expected. The elongation of AA6061 decreases gradually with both the increasing aging temperature and the time. The over-aged specimen has a ductility as low as 7 % when precipitation hardened at 200 °C for 40 h. Since the elongations of the aged specimens in all the conditions are larger than that of the as-received specimen (a 25 % elongation) it can be said that the aging has a negative effect on the ductility of the alloy. But low-temperature aging has a positive effect in terms of the total elongation as seen in **Figure 5**.

### 3.3 Effects of the artificial-aging temperature and time on the springback behavior of AA6061

In the sheet-metal forming process, springback has always been a serious problem. Basically, the elastic recovery occurs after removing the tools. Springback produces a decrease in the quality of the formed parts (a poor dimensional accuracy of the formed parts), therefore, representing a major defect in the sheet-metal forming processes. The factors such as material properties (elastic modulus, yield stress, hardening exponent, slope of the true stress/strain curve, or tangent modulus,  $d\sigma/de$ , and normal anisotropy), process variables (load, thickness of the sheet metal, die angle, punch radius and die gap) and lubrication affect the springback behavior. The springback of aluminum alloys has been a subject of major interest in sheet-metal forming. Numerous studies focus on springback from experimental, analytical or numerical viewpoints. A complete review on springback studies is presented by Wagoner.<sup>21</sup> Although much progress has been done, there are still needs for further research to solve this problem. The material properties affecting the springback must be strictly determined to prevent undesired shapes. Trial and error methods are still being

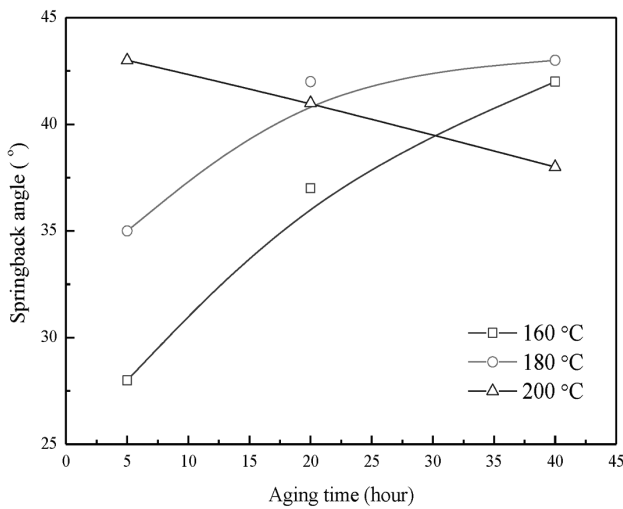


**Figure 6:** Effects of artificial-aging temperature and time on springback behavior of AA6061 alloy

**Slika 6:** Vpliv temperature in časa umetnega staranja na vzmetnost zlitine AA6061

used to establish suitable procedures for solving these elastic-distortion problems.

In this research, a springback evaluation of the AA6061 specimens artificially age hardened at (160, 180 and 200) °C for periods of (5, 20, 4) h was carried out in a V-shaped die with an angle of 60 ° at RT and a strain rate of 0.0083 s<sup>-1</sup>. **Figure 6** shows the effects of the artificial-aging temperature and time on the springback-angle variation of AA6061. The springback angle of the alloy increases with the increasing artificial-aging temperature and time; however, it decreases with the increasing aging time at 200 °C.

The specimen in the as-received condition exhibited a smaller springback angle (7 °) than the aged specimens in all the conditions. It is considered that this

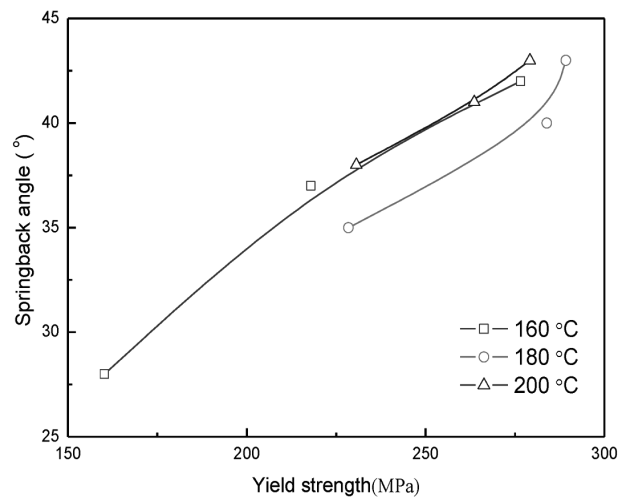


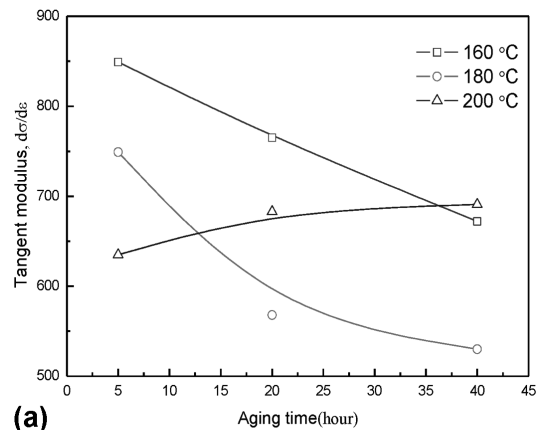
**Figure 7:** Variation of springback angle versus yield strength at various aging temperatures

**Slika 7:** Spreminjanje kota vzmetnosti od natezne trdnosti pri različnih temperaturah staranja

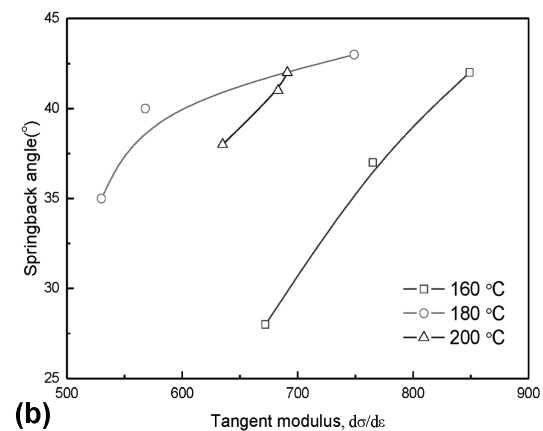
phenomenon is related to the changes in the properties of the material. The material properties that control the amount of the springback that occurs after the forming operation are the elastic modulus, the yield strength, the slope of the true stress/strain curve, or the tangent modulus, the normal anisotropy, and the strain-hardening exponent.

**Figure 7** shows the variations in the yield strength versus springback at various aging temperatures. From the figure it is evident that the yield strength of the alloy increases with the increasing aging time at 160 °C and 180 °C; however, it decreases with the increasing aging time at 200 °C. It can be concluded that the springback increases as the yield strength of the material increases.

With the increasing yield strength, the value of the flow stress and the stored elastic energy, being at the same strain level, increase. Since the stored elastic energy is high for a metal sheet with a higher yield strength, the changes in the strain produced by the elastic recovery are larger when the externally applied bending forces are released. The elastic recovery, i.e., the springback, being at the same strain level, is larger for a sheet metal with a larger yield strength.



**(a)**



**(b)**

**Figure 8:** Variation of: a) tangent modulus versus aging time, b) springback angle versus tangent modulus at various aging temperatures

**Slika 8:** Spreminjanje: a) tangentnega modula od časa staranja, b) kota vzmetnosti od tangentnega modula pri različnih temperaturah staranja

The effect of the tangent modulus on the amount of springback is shown in **Figures 8a** and **8b**. It is seen that a higher tangent modulus causes a larger springback for all the aging temperatures. Since the tangent modulus of the aged specimens is larger than that of the specimen in the as-received condition for the same plastic strain, an extra reverse-bending force is introduced after the bending of the aged specimens, which is expected to increase the springback angle. Ozturk et al.<sup>22</sup> observed a similar behavior where the strain-hardening rate decreases substantially with the increasing aging time. They also found that the anisotropy in the rolling direction decreased, while in the transverse direction it increased with the aging time.

Material scientists are focused on increasing the normal anisotropy using a favorable texture with a better formability, and therefore, it is necessary to understand the effect of normal anisotropy on the springback. The effect of normal anisotropy on the springback was studied by Liu<sup>23</sup> and Verma<sup>24</sup>. They showed that the springback increases when the normal anisotropy increases. In

the present work, the effect of the aging parameter on the amount of normal anisotropy and the springback angle is shown in **Figures 9a** and **9b**.

The specimen in the as-received condition exhibited a larger normal anisotropy ( $r_n = 0.68$ ) than the aged specimens in all the conditions. According to the studies of Liu<sup>23</sup> and Verma<sup>24</sup>, this indicates that aging has a positive effect on the springback angle of the alloy because the normal anisotropy is decreased by the aging parameters. The strain hardening is an ability of a material to strengthen or harden with the increasing strain level and it is one of the most important properties influencing the formability of sheet metals. In the materials with a high value, the flow stress increases rapidly with strain. A high value is also an indication of a good formability in a stretching operation. In the region of a uniform elongation, the strain-hardening coefficient is defined as  $n = \ln\sigma/\ln\epsilon$  where  $\sigma$  is the true stress and  $\epsilon$  is the true strain.

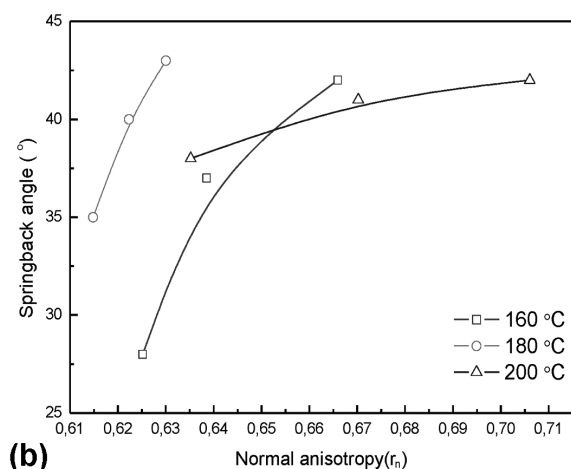
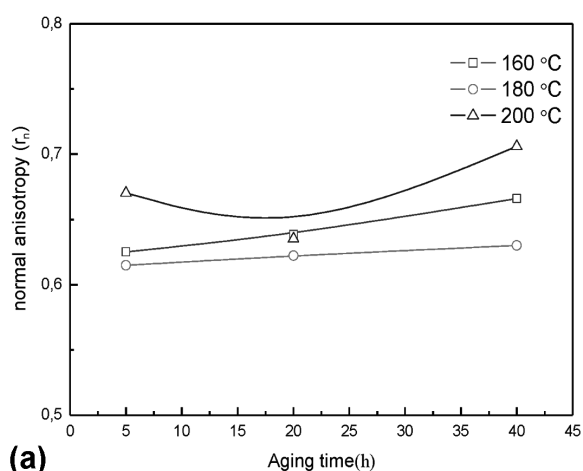


**Figure 9:** Variation of: a) normal anisotropy versus aging time, b) normal anisotropy versus springback angle at various aging temperatures  
**Slika 9:** Spreminjanje: a) normalne anizotropije od časa staranja, b) normalne anizotropije od kota vzmetnosti pri različnih temperaturah staranja

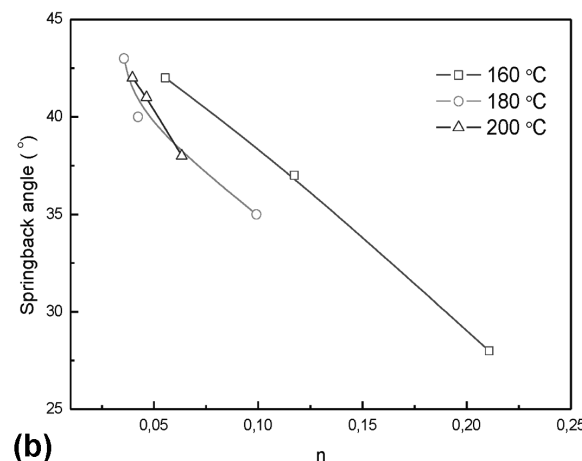
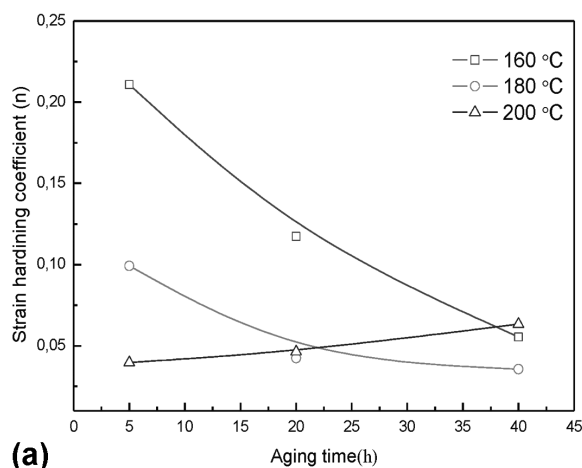


**Figure 10:** Variation of: a) hardening coefficient ( $n$ ) versus aging time, b) springback angle versus strain-hardening coefficient at various aging temperatures

**Slika 10:** Spreminjanje: a) koeficienta utrjevanja ( $n$ ) od časa staranja, b) kota vzmetnosti od koeficienta napetostnega utrjevanja pri različnih temperaturah staranja

**Figure 10** shows the relationships between the springback angle and the strain-hardening exponent of the aluminum alloy at different aging temperatures.

The springback angle is found to decrease with the increasing strain-hardening exponent for all of the aging temperatures. It is well-known that the larger the hardening exponent, the lower is the stress needed to achieve the same deformation during the V bending of sheet metal. Thus, according to the elastic unloading springback principle, the springback is larger for a sheet with a low  $n$  or vice-versa.

Since the hardening exponent of the aged specimens in all the conditions is larger than that of the as-received specimen, it seems that aging has a negative effect on the springback angle of the alloy.

#### 4 CONCLUSIONS

In this study, the effects of the artificial-aging temperature and time on the mechanical properties and springback properties of AA6061 are studied. The following conclusions are made.

The peak-strength values of the alloy for the aging temperatures of (160, 180 and 190) °C were obtained when the alloy was aged for (60, 10 and 5) h, respectively.

The aging between 5 h and 40 h at 180 °C is the most suitable combination of time and temperature exhibiting the maximum hardness, yield strength and tensile strength of the alloy.

A decrease in the mechanical properties of the alloy in the over-aging conditions (an increase in the artificial-aging temperature and time) occurred because of the coalescence of the precipitates into larger particles, a bigger grain size, and also due to the annealing of the defects.

The specimen in the as-received condition exhibited a smaller springback angle than the aged specimens in all the conditions.

#### 5 REFERENCES

- <sup>1</sup> S. J. Murtha, SAE International Journal of Materials and Manufacturing, 104 (1995), 657–666, doi:10.4271/950718
- <sup>2</sup> F. Ozturk, A. Sisman, S. Toros, S. Kilic, R. C. Picu, Materials and Design, 31 (2010), 972–975, doi:10.1016/j.matdes.2009.08.017
- <sup>3</sup> J. Buha, R. N. Lumley, A. G. Crosky, Metallurgical Materials Transactions, 37A (2006), 3119–3130, doi:10.1007/s11661-006-0192-x
- <sup>4</sup> G. A. Edwards, K. Stiller, G. L. Dunlop, M. J. Couper, Acta Materialia, 46 (1998), 3893–3904, doi:10.1016/S1359-6454(98)00059-7
- <sup>5</sup> J. Buha, R. N. Lumley, A. G. Crosky, K. Hono, Acta Materialia, 55 (2007), 3015–3024, doi:10.1016/j.actamat.2007.01.006
- <sup>6</sup> C. D. Marioara, H. Nordmark, S. J. Andersen, R. Holmestad, Journal of Materials Science, 41 (2006), 471–78, doi:10.1007/s10853-005-2470-1
- <sup>7</sup> S. Pogetsher, H. Antrekowitsch, H. Leitner, T. Ebner, P. J. Uggo-witzer, Acta Materialia, 59 (2011), 3352–3363, doi:10.1016/j.actamat.2011.02.010
- <sup>8</sup> S. J. Anderson, H. W. Zandbergen, J. E. Jansen, C. Taeholt, U. Tundal, O. Reiso, Acta Materialia, 46 (1998), 3283–3298, doi:10.1016/S1359-6454(97)00493-X
- <sup>9</sup> S. K. Panigrahi, R. Jayaganthan, Materials Science and Engineering A, 528 (2011), 3147–3160, doi:10.1016/j.msea.2011.01.010
- <sup>10</sup> G. Mrówka-Nowotnik, J. Sieniawski, Journal of Materials Processing Technology, 162–163 (2005), 367–372, doi:10.1016/j.jmatprotec.2005.02.115
- <sup>11</sup> G. B. Burger, A. K. Gupta, P. W. Jeffrey, D. J. Llyod, Materials Characterization, 35 (1995), 23–39, doi:10.1016/1044-5803(95)00065-8
- <sup>12</sup> O. El Sebaie, A. M. Samuel, F. H. Samuel, H. W. Doty, Materials Science and Engineering A, 480 (2008), 342–355, doi:10.1016/j.msea.2007.07.039
- <sup>13</sup> D. D. Risanti, M. Yin, P. E. J. Rivera Diazdel Castillo, S. Vau der Zwang, Materials Science and Engineering A, 523 (2009), 99–111, doi:10.1016/j.msea.2009.06.044
- <sup>14</sup> M. Tiryakioglu, J. Campbell, J. T. Staley, Materials Science and Engineering A, 361 (2003), 240–248, doi:10.1016/S0921-5093(03)00514-8
- <sup>15</sup> A. K. Gupta, D. J. Lloyd, S. A. Court, Materials Science and Engineering A, 316 (2001), 11–17, doi:10.1016/S0921-5093(01)01247-3
- <sup>16</sup> A. M. Kliauga, E. A. Vieira, M. Ferrante, Materials Science and Engineering A, 480 (2008), 5–16, doi:10.1016/j.msea.2007.07.091
- <sup>17</sup> G. E. Dieter, Mechanical metallurgy, 2nd ed., McGraw-Hill International Book Company, 1981
- <sup>18</sup> R. A. Siddiqui, H. A. Abdullah, K. R. Al-Belushi, Journal of Materials Processing Technology, 102 (2000), 234–240, doi:10.1016/S0924-0136(99)00476-8
- <sup>19</sup> D. A. Porter, K. E. Easterling, Phase Transformations in Metals and Alloys, Van Nostrand Reinhold Co. Ltd., New York, NY 1981, 162–168
- <sup>20</sup> W. D. J. Callister, Materials Science and Engineering, John Wiley and Sons Inc., 1997
- <sup>21</sup> R. H. Wagoner, Fundamental aspects of spring-back in sheet metal forming, Proceedings of NUMISHEET, Jeju Island, Korea, 2002, 13–24
- <sup>22</sup> F. Ozturk, E. Esener, S. Toros, R. C. Picu, Materials and Design, 31 (2010) 10, 4847–4852, doi:10.1016/j.matdes.2010.05.050
- <sup>23</sup> D. K. Liu, Journal of Materials Processing Technology, 66 (1997), 9–17, doi:10.1016/S0924-0136(96)02453-3
- <sup>24</sup> R. K. Verma, A. Haldar, Journal of Materials Processing Technology, 190 (2007), 300–304, doi:10.1016/j.jmatprotec.2007.02.033





# MONITORING OF POLYURETHANE DISPERSIONS AFTER THE SYNTHESIS

## SPREMLJANJE POLIURETANSKIH DISPERZIJ PO SINTEZI

**Martin Ocepek<sup>1</sup>, Jožefa Zabret<sup>1</sup>, Janez Kecelj<sup>1</sup>, Peter Venturini<sup>2</sup>, Janvit Golob<sup>3</sup>**

<sup>1</sup>Helios TBLUS, d. o. o., Količevo 65, 1230 Domžale, Slovenia

<sup>2</sup>Helios Domžale, d. d., Količevo 2, 1230 Domžale, Slovenia

<sup>3</sup>University of Ljubljana, Faculty of Chemistry and Chemical Technology, Aškerčeva cesta 5, 1000 Ljubljana, Slovenia  
martin.ocepek@helios.si

*Prejem rokopisa – received: 2014-06-05; sprejem za objavo – accepted for publication: 2014-09-30*

doi:10.17222/mit.2014.086

Chemical and physical parameters of the aqueous polyurethane dispersion (PUD) were studied after the synthesis. A prepolymer mixing process with a limited-chain extension step was used in order to examine the polymer and dispersion behavior with respect to the ageing time. Measurements of free isocyanate groups were performed with the aid of Fourier transform infrared spectroscopy (FT-IR). The pseudo-first-order kinetics of NCO disappearance was proposed and the value of the corresponding constant was determined. Additionally, particle size, particle size distribution, pH, conductivity and molecular mass were monitored and compared.

Keywords: polyurethane dispersion, colloid, FT-IR

V raziskavi smo preučevali spreminjanje kemijskih in fizikalnih parametrov vodne poliuretanske disperzije (PUD) po sintezi. Disperzijo smo sintetizirali po postopku vmešavanja prepolimera z omejenim podaljševanjem verig za preučevanje polimerne disperzije z ozirom na čas po sintezi. Merjenje prostih izocianatnih skupin smo izvedli z metodo Fourierjeve transformacijske infrardeče spektroskopije (FT-IR). Predpostavili smo kinetični model psevdoprvega reda z ozirom na reakcije izocianatnih skupin ter določili vrednost kinetične konstante. Dodatno smo spremljali in primerjali povprečne velikosti delcev, porazdelitev velikosti delcev, pH, prevodnost in molekulska maso.

Ključne besede: poliuretanska disperzija, koloid, FT-IR

## 1 INTRODUCTION

Polyurethane dispersions (PUDs) are one of the options to replace conventional solvent-borne polyurethane materials for resins. The replacement is required by the directives of the European Union in order to use environmentally friendly and non-hazardous materials.<sup>1,2</sup> The main advantages of PUD-based coatings are relatively good mechanical and chemical resistances, achieved only with physical drying at room temperature. However, these properties can be influenced using various polyols, isocyanates and their combinations with different ratios. The required high molecular mass is achieved with a chain extension with multifunctional amines.<sup>3-7</sup>

Many processes are used for a PUD preparation, although prepolymer mixing and acetone processes dominate in industrial applications. A prepolymer mixing process is mostly employed for the preparation of PUDs as coating binders. Using an acetone process, the PUDs for adhesives are synthesized.<sup>8-11</sup> The prepolymer process can be subdivided. Firstly, a polymerization of diols and diisocyanates is performed in an organic solvent. Typically, N-methyl-2-pyrrolidone (NMP) is used as it can efficiently dissolve the internal emulsifying monomer – 2.2-bis(hydroxymethyl)propionic acid (DMPA) – and reduce the viscosity of the prepolymer. In a coating application NMP also serves as a coalescing agent,

reducing the minimum film-forming temperature.<sup>11</sup> Prior to dispersing, a neutralization of the pending carboxyl functional groups has to be performed in order to increase the hydrophilicity of the polymer chains. Afterwards, an isocyanate (NCO)-terminated prepolymer is dispersed in cold water, using high-shear forces. In the final stage, a water-soluble diamine is added as the chain extender to increase the molecular mass.<sup>3,5-8,11-15</sup> During all the stages of the synthesis numerous side reactions can occur due to the NCO reactivity.<sup>5,12,16</sup>

Due to the system complexity, where many principles are in place but only a few have an important influence on the final macroscopic material properties, this field of research is rather more of an industrial importance.<sup>17,18</sup> In recent studies, the main focus was put on hardening two-component aqueous polyurethane coatings where the reactions and the mechanism itself are similar to those of a bulk PUD. However, the conditions (e.g., the water content) for coating hardening are significantly different. Consequently, the reported kinetic results are probably not applicable to dispersions.

Jang et al.<sup>14</sup> found that the efficiency of the reaction of a chain extender with unreacted NCO groups regarding prepolymer chains is around 50 % due to the limited diffusion of the chain-extender molecules into the core of the particles. Consequently, unreacted NCO groups

**Table 1:** Relative reactivity of NCO group against different hydrogen-active compounds<sup>5,12</sup>**Tabela 1:** Relativne reaktivnosti NCO-skupine z različno aktivnimi vodikovimi spojinami<sup>5,12</sup>

| Functional group                  | Formula               | Relative reaction rate | Linkage                        |
|-----------------------------------|-----------------------|------------------------|--------------------------------|
| Primary aliphatic amine           | R-NH <sub>2</sub>     | 2500                   | Urea                           |
| Secondary aliphatic amine         | R <sub>2</sub> -NH    | 500–1250               | Urea                           |
| Primary hydroxyl                  | R-CH <sub>2</sub> -OH | 2.5                    | Urethane                       |
| Water                             | HOH                   | 2.5                    | Urea                           |
| Carboxylic acid (non-dissociated) | R-COOH                | 1                      | Amide, (+ CO <sub>2</sub> (g)) |
| Secondary hydroxyl                | R <sub>2</sub> -CH-OH | 0.75                   | Urethane                       |
| Urea                              | R-NH-CO-NH-R          | 0.375                  | Biuret                         |
| 20Urethane                        | R-NH-COOR             | 0.0025                 | Allophanate                    |

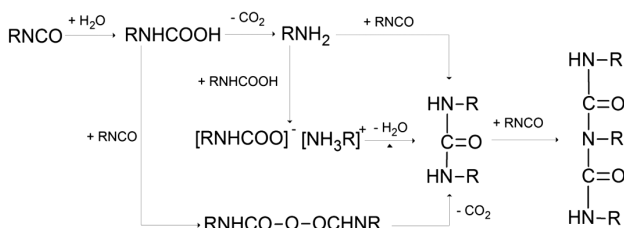
stay buried inside the particles. However, this thesis was only confirmed with the measurements of the molecular mass. In another study<sup>4</sup> researchers showed that only 60 % of the theoretical amount of diamine is sufficient to achieve a NCO conversion below the FT-IR detection. The reported results seem somehow contradictory. However, differences might be attributed to polyol selection and synthesis parameters or the reported results might have been influenced by the characterization methods.

From the engineering point of view, NCO conversion kinetics is at least of the same importance as the NCO thermodynamic background. The relative reactivity of isocyanate with hydrogen-active compounds can be found in **Table 1**. According to these data, one can assume that the disappearance of unreacted NCO groups (after an amine-chain extension reaction) is mainly due to the reaction with water. **Figure 1** presents a possible mechanism. The main products are urea linkages and gaseous CO<sub>2</sub>. Additionally, some biuret formation is expected.<sup>19</sup> The reaction with carboxylic groups is retarded due to a steric hindrance and a dissociation.<sup>5</sup>

The widely used dibutylamine back-titration method<sup>7</sup> was found inappropriate for the measurements of the residual NCO groups since high amounts of amine and water are involved. Therefore, those data were obtained by means of FT-IR spectroscopy, which represents a powerful tool to monitor NCO groups in an aqueous environment.<sup>4,5,9,10,20</sup> A conversion of the NCO groups was obtained through integrated absorbance-peak areas:<sup>21–24</sup>

$$\int A(\tilde{\nu})d\tilde{\nu} = bc \int a(\tilde{\nu})d\tilde{\nu} = bcA \quad (1)$$

where  $A(\tilde{\nu})$  stands for the absorbance at a specific wavenumber (cm<sup>-1</sup>),  $a(\tilde{\nu})$  (L mol<sup>-1</sup> cm<sup>-1</sup> = 0.1 m<sup>2</sup> mol<sup>-1</sup>) is

**Figure 1:** Reaction mechanism of isocyanate with water<sup>19</sup>**Slika 1:** Mehanizem reakcije izocianatne skupine z vodo<sup>19</sup>

the molar absorption coefficient, specific for a particular functional group at a specific wavelength,  $b$  (cm) is the path length through the sample,  $c$  (mol L<sup>-1</sup>) represents the molar concentration and  $A$  (L mol<sup>-1</sup> cm<sup>2</sup>) represent the integrated absorption coefficient.

The purpose of this research is to monitor the reaction between water and prepolymer terminal NCO groups. The reaction kinetics is studied using Fourier transform infrared spectroscopy. For this purpose, only 50 % of the theoretical amount of bifunctional amine is used in the chain-extension step. Simultaneously, important physico-chemical parameters of the dispersion is measured and evaluated through particle size, particle size distribution, pH, conductivity and relative molecular mass.

## 2 EXPERIMENTAL WORK

### 2.1 Materials

An ester-type polyol was previously prepared via a condensation polymerization from a technical grade including 1.6 hexanediol, adipic and isophthalic acid (**Table 2**). A linear macrodiol was proposed as only bi-functional monomers were used. The starting hydroxyl-to-carboxyl molar ratio was chosen to be 1.15 in order to ensure hydroxyl-terminated chains. The measured hydroxyl number of 57 mg KOH g<sup>-1</sup> corresponds to the average molecular mass of 2000 g mol<sup>-1</sup> at the acid number of 0.6 mg KOH g<sup>-1</sup>. The water content was below mass fraction 0.05 %. Polyester was melted and maintained at 50 °C for 6 h before use.

**Table 2:** Formulation for polyol synthesis and its properties**Tabela 2:** Receptura za sintezo poliola in njegove lastnosti

| Component                    | m/g                                | n/mol |
|------------------------------|------------------------------------|-------|
| 1.6 Hexanediol               | 236.91                             | 2.004 |
| Adipic acid                  | 183.70                             | 1.257 |
| Isophthalic acid             | 79.09                              | 0.486 |
| Properties                   |                                    |       |
| hydroxyl number              | (57 ± 1) mg KOH g <sup>-1</sup>    |       |
| acid number                  | (0.6 ± 0.1) mg KOH g <sup>-1</sup> |       |
| M <sub>n</sub> (titrimetric) | (2000 ± 50) g/mol                  |       |
| T <sub>g</sub>               | (-53 ± 1) °C                       |       |
| T <sub>m</sub>               | (25 ± 1) °C                        |       |

Isophorone diisocyanate (IPDI; Evonik Degussa), 2,2-bis(hydroxymethyl)propionic acid (DMPA; Perstorp), dibutyltin dilaurate (DBTDL; Air Products), all of a technical grade, N-methyl-2-pyrrolidone (NMP; Acros Organics), triethylamine (TEA; J.T. Baker) and isophoronediamine (IPDA; BASF), all of a laboratory grade, were used. Deionized water had the conductivity below  $20 \mu\text{S cm}^{-1}$ .

## 2.2 PUD synthesis

The formulation can be found in **Table 3**. The polymerization was carried in round-bottom 1 L, four-necked flask with a mechanical stirrer, condenser and digital thermometer connected to an automatically controlled electric-heating mantel. The system was kept in a nitrogen atmosphere during the whole synthesis process. At first, NMP, DMPA and the melted polyester polyol were put into the reactor and stirred at  $30 \text{ }^\circ\text{C}$  for 10 min to achieve homogenization. Afterwards, a mixture of IPDI and catalyst DBTDL was shot-added. After additional 5 min of homogenization, the first sample was taken out in order to verify the starting mass fraction of NCO groups. The di-*n*-dibutylamine back-titration method<sup>7</sup> was used. The mixture in the reactor was then heated up to  $82 \text{ }^\circ\text{C}$  in 30 min and maintained there for another hour, followed by cooling down to  $65 \text{ }^\circ\text{C}$ . The residual amount of NCO was determined before an equimolar amount of TEA (with respect to DMPA carboxyl groups) was shot-added. After 15 min of homogenization, a neutralized polymer was introduced into a double-jacketed dispersion vessel 2 L in a period of 10 min. High shear forces were applied during this time,

using a dissolver-disc stirrer with a diameter of 7 cm at 1800 r/min. A few drops of commercially available anti-foaming additive were used. Preliminary, the water in the double-jacketed dispersion vessel was cooled below  $20 \text{ }^\circ\text{C}$  and maintained at this temperature to the end of the process. Ten minutes after the end of dispersion, a pre-prepared IPDA-water mixture (**Table 4**) was added dropwise in a period of 30 min. The stirring was reduced to 1000 r/min. The end of the chain-extender addition was defined as the end of the synthesis, presenting time zero for the ageing study. After the synthesis, PUD was poured into a plastic container 1 L and kept at a temperature of  $(20 \pm 1) \text{ }^\circ\text{C}$  throughout the ageing study process. The container was sealed all the time, except when the samples were taken out.

## 2.3 Characterization

FT-IR spectra were measured with a Nicolet 6700 spectrophotometer, manufactured by Thermo Scientific. The samples were handled manually on a zinc-selenide (ZnSe) pellet. Care was taken that all the samples had the maximum absorbance-peak height (the ester peak) close to 1 since this parameter is defined as the condition for the most accurate quantitative measurement. The error was estimated to be below 10 % in this case.<sup>20,22</sup> The spectra at wavenumbers between  $650 \text{ cm}^{-1}$  and  $4000 \text{ cm}^{-1}$ , with a resolution of  $4 \text{ cm}^{-1}$ , were taken. The areas of the NCO peaks between  $2170 \text{ cm}^{-1}$  and  $2330 \text{ cm}^{-1}$  were normalized to the unchanging areas under the CH peaks at wavenumbers of  $2820\text{--}3010 \text{ cm}^{-1}$ . The instrument software was used for this purpose. Molecular mass averages ( $M_w$ ,  $M_n$ ) and their distributions ( $M_w/M_n$ ), relative to the polystyrene standards, were determined with size-exclusion chromatography (SEC) on an Agilent 1260 Infinity liquid chromatograph (Agilent Technologies) with a differential refractive-index detector at  $35 \text{ }^\circ\text{C}$ . The analyses were performed on a single pore-sized Phenogel linear column 5 mm ( $300 \text{ mm} \times 7.8 \text{ mm}$ ) with a styrene-divinylbenzene copolymer column packing. Tetrahydrofuran (THF) was used as an eluent with a flow rate of  $1.0 \text{ mL min}^{-1}$ . The samples were prepared in solutions and allowed to dissolve for three days. Prior to the analysis, the samples were filtered through a PTFE filter  $0.45 \mu\text{m}$ .  $100 \mu\text{L}$  of the prepared sample was injected into the column.

The conductivity and pH were measured without any sample preparation using a SevenMulti pH meter (Mettler Toledo). The pH electrode was calibrated using the standard buffer solutions (4.01, 7.00 and 10.01). The conductivity cell was calibrated using the standard electrolyte solution with  $1.413 \text{ mS cm}^{-1}$  at  $25 \text{ }^\circ\text{C}$ . Particle sizes were measured employing the dynamic light scattering (DLS) method at a scattering angle of  $173 \text{ }^\circ$ . A ZetaSizer (ZS) nano series, manufactured by Malvern, was used for these purposes. The samples were diluted in DI water to approximately volume fraction 0.1 % and poured into a proper cell. The Z-average<sup>25</sup> was obtained

**Table 3:** Formulation for PU prepolymer synthesis and its properties

**Tabela 3:** Receptura za sintezo PU-prepolimera in njegove lastnosti

| Component                           | <i>m/g</i>             | <i>n/mol</i>        |
|-------------------------------------|------------------------|---------------------|
| NMP                                 | 100.0                  | 1.009               |
| DMPA                                | 14.50                  | 0.108               |
| Polyester polyol ( <b>Table 2</b> ) | 137.90                 | 0.078               |
| DBTDL                               | 0.50                   | $7.9 \cdot 10^{-4}$ |
| IPDI                                | 78.80                  | 0.355               |
| TEA                                 | 10.7                   | 0.108               |
| Properties                          |                        |                     |
| residual free $w(\text{NCO})^*$     | 3.7 %                  |                     |
| $M_n$ (SEC)                         | (4540 $\pm$ 100) g/mol |                     |
| $M_w$ (SEC)                         | (7060 $\pm$ 100) g/mol |                     |
| $M_w/M_n$                           | 1.56 $\pm$ 0.02        |                     |

\**w* (mass fraction)

**Table 4:** Recipe for dispersing and chain-extension steps

**Tabela 4:** Receptura za dispergiranje in podaljševanje verig

| Component                      | <i>m/g</i> | <i>n/mol</i> |
|--------------------------------|------------|--------------|
| PU prepolymer                  | 298.0      | 0.130        |
| BYK 093 (antifoaming additive) | 1.0        | N/A          |
| IPDA                           | 11.1       | 0.065        |
| Water for IPDA                 | 50.0       | 2.778        |

using the Malvern software. Glass transition temperatures ( $T_g$ ) were determined with the differential scanning calorimeter (DSC) 1 STAR system (Mettler Toledo). The heat flow was measured under a heat rate of  $10 \text{ K min}^{-1}$  in a range from  $-70 \text{ }^\circ\text{C}$  to  $120 \text{ }^\circ\text{C}$ . The total solid content was determined gravimetrically, after 1 h at  $125 \text{ }^\circ\text{C}$ . The hydroxyl number was determined according to ASTM D 1957.

### 3 RESULTS AND DISCUSSION

The primary objective of this study was to track PUD properties with respect to the ageing time. According to the isocyanate reactivity, a reaction with water molecules is expected.<sup>15,19</sup> While solvent-borne PU polymers can be easily dissolved and analyzed with advanced methods (e.g., nuclear magnetic resonance),<sup>9,26</sup> a PUD analysis is limited due to a poor solubility of cross-linked and branched polymer chains. Colloidal physical parameters (e.g., particle size, particle size distribution, pH, conductivity) become of a greater importance in a PUD characterization. Nevertheless, the chemical changes can be monitored with FT-IR.<sup>4–14,21,26,27</sup>

#### 3.1 PUD design and properties

**Table 3** consists of the formulation and properties of the PU prepolymer before being dispersed. There is no doubt that PUD colloidal features depend upon the PU prepolymer. Among these features, the molecular mass, the DMPA content and its degree of neutralization might be the most important.<sup>14</sup> For the purpose of this investigation, the mass fraction 6.4 % of DMPA was used, based on the total prepolymer solids. 100 % neutralization was carried out by means of TEA as this compound was reported to be the most efficient.<sup>14</sup>

The PUD final properties can be found in **Table 5**. The DSC curves of polyester polyol and the final PUD in **Figure 2** prove that polyol was successfully polymerized since no melting-temperature-transition ( $T_m$ ) peak was detected for the PUD sample.  $T_g$  of polyol and PUD are practically identical at  $(-53 \pm 1) \text{ }^\circ\text{C}$ . The latter represents the ‘soft’ phase and, consequently, this PUD can be classified as a rubber-like elastomeric material at room temperature.<sup>12</sup> In general, PUs have another  $T_g$  at higher

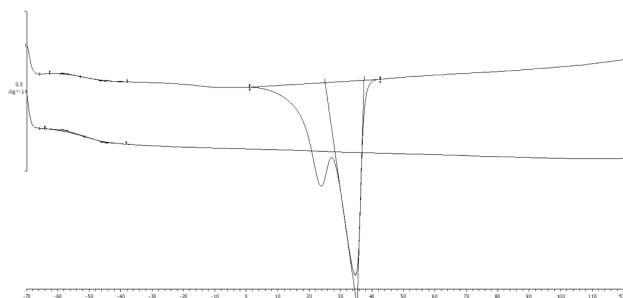


**Figure 2:** DSC curves (top – polyester polyol, bottom – final PUD)  
**Slika 2:** DSC-krivulji (zgoraj – poliesterški polioli, spodaj – končna PUD)

temperatures, representing the ‘hard’ phase.<sup>12</sup> However, the second  $T_g$  was not detected on the PUD sample. That might have been due to a higher NCO/OH ratio, resulting in pronounced amounts of hydrogen bonds,<sup>28</sup> severe crosslinking and branching, which all contribute to raising the second  $T_g$  above the measured conditions.<sup>12</sup>

**Table 5:** PUD final properties

**Tabela 5:** Končne lastnosti PUD

|           | Parameter         | Value                                |
|-----------|-------------------|--------------------------------------|
| Final PUD | total solids, w/% | 33.3                                 |
|           | soft phase $T_g$  | $(-53 \pm 1) \text{ }^\circ\text{C}$ |
|           | hard phase $T_g$  | not detected                         |

The NCO-terminated prepolymer had  $4540 \text{ g mol}^{-1}$  of  $M_n$  according to SEC and  $1580 \text{ g mol}^{-1}$  of  $M_g$  calculated from % NCO, assuming the ideal bifunctional NCO-terminated prepolymer. The almost three times higher  $M_n$  amount from SEC is somehow expected due to the formation of allophanate, resulting in some cross-linking.<sup>5,7</sup> The authors agree that the SEC result should be considered as the most reliable.

#### 3.2 FT-IR spectra evaluation and the kinetic model

In the cases where constant  $ab$  can be determined via calibration curves, the expression of concentration is trivial. However, this is not the case in this study. The path length ( $b$ ) is not constant due to the manual handling of a sample on the glass pellet. To avoid this variable, integrated absorbances under the NCO peaks were normalized to the CH peak, which is assumed to remain unchanged during the ageing. As a result, relative integrated absorbances were obtained. It was also assumed that absorption coefficients ( $\alpha$ ) did not significantly change during the monitoring. From the absorbance areas, the conversion of the NCO groups can be directly determined using:<sup>21</sup>

$$\alpha = \left[ 1 - \frac{(A_{\text{NCO}}/A_{\text{CH}})_t}{(A_{\text{NCO}}/A_{\text{CH}})_{t=0}} \right] \cdot 100 \quad (2)$$

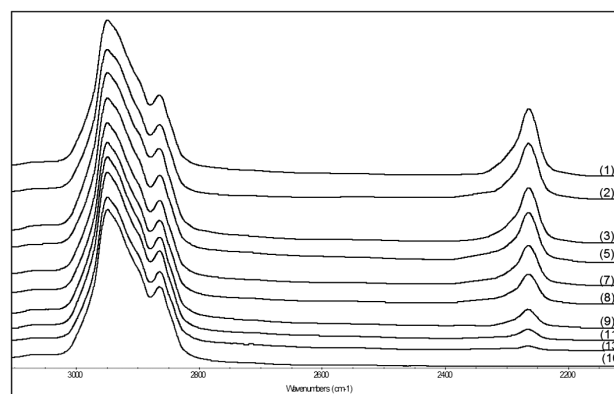


**Figure 3:** Selected FT-IR spectra of the observed PUD after the synthesis. For sample indices see **Table 6**.

**Slika 3:** Izbrani FT-IR-spektri PUD v času po sintezi. Oznake vzorcev se navezujejo na **tabelo 6**.

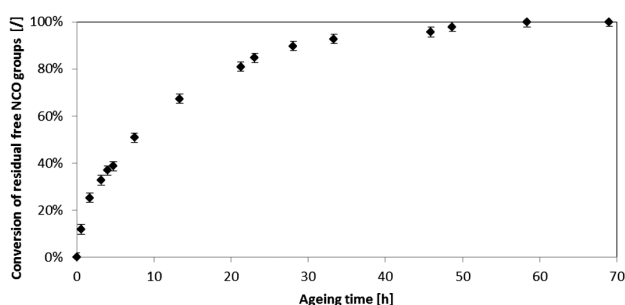


**Figure 4:** Conversion of residual free NCO groups after the synthesis  
**Slika 4:** Pretvorba prostih NCO-skupin po sintezi

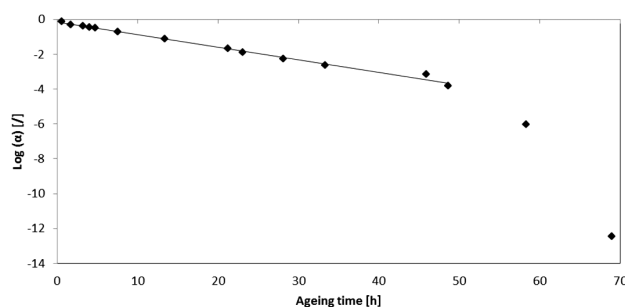


**Figure 5:** Conversion logarithm of residual NCO groups  
**Slika 5:** Logaritem pretvorbe prostih NCO-skupin

where  $\alpha$  is the NCO conversion (%),  $(A_{\text{NCO}}/A_{\text{CH}})_{t=0}$  is the relative integrated absorbance area at the ageing start and  $(A_{\text{NCO}}/A_{\text{CH}})_t$  is the relative integrated absorbance area at the specific time  $t$ . Using the proposed model, the standard calibration curve is not needed. That is especially true for the first-order kinetics where the starting concentration is not needed to obtain a conversion.<sup>23</sup> Another advantage of this approach is the elimination of the errors resulting from the water and NMP evaporation.

The selected FT-IR spectra in a period of three days after the synthesis are presented in **Figure 3**. The normalized area of Sample 1 (time 0) was taken as the starting point. The obtained results can be seen in **Figure 4**. The integrated areas and the associated conversions calculated using Equation (2) can be found in **Table 6**. For the purpose of determining the kinetic order, logarithms of the normalized areas were calculated and are presented in **Figure 5**. 90 % of the NCO conversion was detected after 33 h. In comparison with the previous study,<sup>17</sup> the NCO consumption in this study case is faster. The authors believe that the unlimited availability of water molecules is responsible for such a behavior. The

quantity below the FT-IR detection limit was achieved after 2.5–3 d. According to the data points in **Figure 5**, one might conclude that the first-order kinetic model does not fit. However, ignoring the last two points resulting from the FT-IR inaccuracy at very high conversions, the fitting line with a slope of  $-0.077 \text{ h}^{-1}$  and a root-mean-square deviation (*RMSD*) of 0.984 can be used to describe the data. Furthermore, neglecting the first point, a slope of  $-0.072 \text{ h}^{-1}$  with *RMSD* of 0.991 can be obtained. This fitting accuracy permits us to assume the first-order or at least the pseudo-first-order kinetics behavior. This is not in agreement with the reported second order at the beginning and the third order at higher conversions when the ratio of NCO to water OH was 1 : 1<sup>21</sup>. Again, the continuous water environment in PUDs governs the residual NCO group-reaction kinetics. To some extent, water diffusion can retard the reaction; however, this becomes significant only at a high conversion.

### 3.3 Molecular mass

The trend of the increasing molecular mass is visible from the SEC curve comparison in **Figure 6**. The

**Table 6:** Ageing-measurement data

**Tabela 6:** Podatki meritev staranja

| #  | time (h) | $A_{\text{NCO}}$ | $A_{\text{CH}}$ | $A_{\text{NCO}}/A_{\text{CH}}$ | $\alpha/\%$ | $\text{LN}(A_{\text{NCO}}/A_{\text{CH}})$ | pH   | conductivity (mS/cm) | $D_z/\text{nm}$ | $M_n/(\text{g/mol})$ | $M_w/(\text{g/mol})$ |
|----|----------|------------------|-----------------|--------------------------------|-------------|-------------------------------------------|------|----------------------|-----------------|----------------------|----------------------|
| 1  | 0        | 5.21             | 20.58           | 0.253                          | 0           | 0                                         | 8.07 | –                    | 88              | 5.710                | 10.110               |
| 2  | 0.583    | 5.65             | 25.33           | 0.223                          | 11.9        | -0.127                                    | 7.67 | 1.31                 | 90              | –                    | –                    |
| 3  | 1.70     | 2.75             | 14.55           | 0.189                          | 25.3        | -0.292                                    | 7.55 | 1.39                 | 92              | –                    | –                    |
| 4  | 3.17     | 7.61             | 44.70           | 0.170                          | 32.8        | -0.397                                    | 7.24 | 1.46                 | 89              | –                    | –                    |
| 5  | 4.00     | 7.67             | 48.02           | 0.160                          | 36.9        | -0.461                                    | 7.22 | 1.50                 | 89              | –                    | –                    |
| 6  | 4.75     | 3.47             | 22.38           | 0.155                          | 38.8        | -0.490                                    | 7.19 | 1.52                 | 88              | –                    | –                    |
| 7  | 7.50     | 7.23             | 58.06           | 0.125                          | 50.8        | -0.709                                    | 7.10 | 1.58                 | 90              | 11.410               | 25.410               |
| 8  | 13.3     | 8.32             | 100.7           | 0.083                          | 67.4        | -1.12                                     | 7.00 | 1.64                 | 87              | –                    | –                    |
| 9  | 21.3     | 1.58             | 32.73           | 0.048                          | 80.9        | -1.66                                     | 6.97 | 1.68                 | 89              | 13.490               | 30.670               |
| 10 | 23.1     | 1.13             | 29.10           | 0.039                          | 84.7        | -1.87                                     | 6.95 | 1.69                 | 88              | –                    | –                    |
| 11 | 28.1     | 1.09             | 42.00           | 0.026                          | 89.7        | -2.28                                     | 6.98 | 1.67                 | 88              | –                    | –                    |
| 12 | 33.3     | 1.11             | 60.54           | 0.018                          | 92.8        | -2.63                                     | 6.99 | 1.67                 | 86              | –                    | –                    |
| 13 | 45.9     | 0.18             | 16.49           | 0.011                          | 95.7        | -3.14                                     | 6.98 | 1.68                 | 87              | –                    | –                    |
| 14 | 48.7     | 0.081            | 14.66           | 0.006                          | 97.8        | -3.82                                     | 6.97 | 1.67                 | 90              | –                    | –                    |
| 15 | 58.3     | 0.02             | 33.19           | 0.001                          | 99.8*       | -6.04                                     | 6.98 | 1.67                 | 88              | –                    | –                    |
| 16 | 69.0     | 0                | 18.53           | 0.000                          | 100.0*      | -12.44                                    | 6.97 | 1.68                 | 90              | 21.560               | 64.540               |

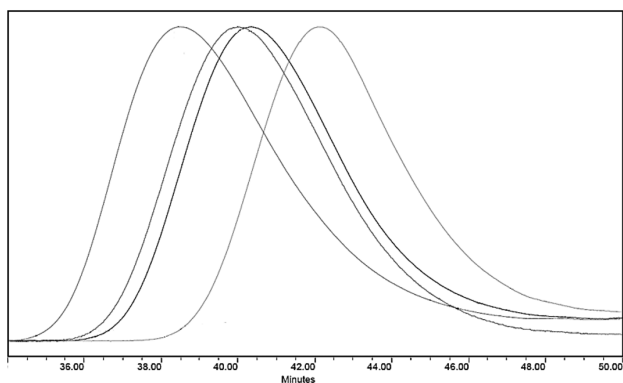


**Figure 6:** SEC results (from right to left: samples 1, 7, 9, 16)  
**Slika 6:** SEC-rezultati (od leve proti desni: vzorci 1, 7, 9, 16)

average molecular mass according to the polystyrene standards are presented in **Table 6**. The molecular mass is increasing during the ageing, as can be expected due to the formation of urea linkages, which are formed after the reaction between NCO and water.<sup>3,5,6,8,11–17</sup> The  $M_w/M_n$  ratio also increases from the initial 1.77 to 2.99 at the end. Nevertheless, the molecular mass distribution remains relatively narrow, indicating that the chain extension is relatively uniform. It is important to note that there were some problems with the sample solubility in THF, which was pronounced with the increasing molecular mass. Insoluble parts were filtered out. Consequently, those results should be taken with a reserve and can only serve as a relative comparison between the samples.

### 3.4 pH and conductivity

**Figure 7** shows the pH and conductivity changes during the ageing process. It can be seen that pH is decreasing to the 67 % conversion, followed by a constant value afterwards. As reported<sup>17,18</sup>, the pH drop is attributed to the formation of carbon acid from  $\text{CO}_2$  which is a side product of the NCO reaction with water.<sup>3,5,7,15–18</sup> A pH of  $(7.00 \pm 0.05)$  seems to be the equilibrium value in this system and is close to the reported value of 6.9.<sup>17</sup> Due to the fact that new ions are formed, it is quite clear

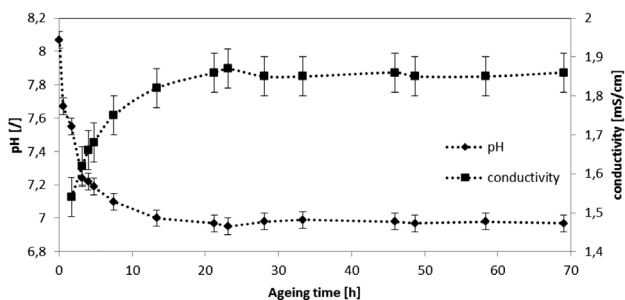


**Figure 7:** pH and conductivity changes during ageing. Dotted line is only drawn as a guide for the eye.

**Slika 7:** Spremembe pH in prevodnosti med staranjem. Prekinjena črta je narisana zgolj za lažje spremljanje.

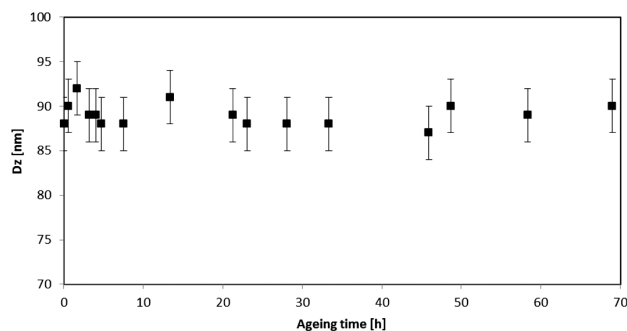


**Figure 8:** Average particle-size diameter ( $D_z$ ) during ageing  
**Slika 8:** Povprečne velikosti delcev ( $D_z$ ) med staranjem

that the conductivity increase is practically a mirror image of the pH curve. It has to be noted that a reliable conductivity measurement of the first sample was prevented by the air bubbles generated during the dispersing step.

### 3.5 Particle size

**Figures 8** and **9** reveal that the average particle size ( $D_z$ ) and particle size distribution did not significantly change during the ageing. Additionally, the DLS polydispersity index was below 0.1 in all the cases, meaning

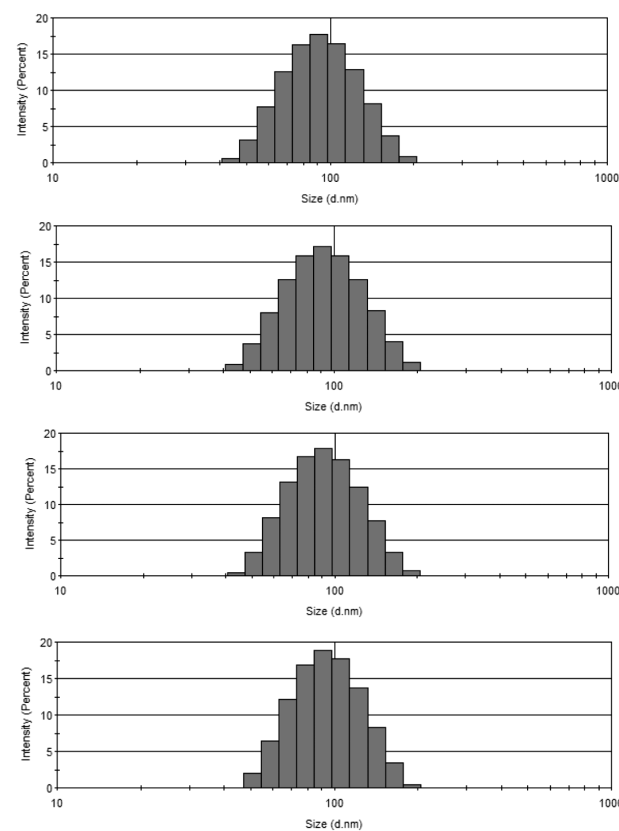


**Figure 9:** Selected DLS particle size distribution (from top to bottom: samples 1, 6, 13, 16)

**Slika 9:** Izbrani DLS-spektri porazdelitve velikosti delcev (od zgoraj navzdol: vzorci 1, 6, 13, 16)

that PUD can be considered to be monodisperse.<sup>26</sup> The same polydispersity (within a range 30 nm) was observed for all the samples. This result was expected since intra-particle events do not significantly influence the particle size. However, when the electrochemical or steric stability is affected, a particle agglomeration leads to bigger particles.<sup>5,25</sup>

#### 4 CONCLUSIONS

PUDs are probably the best option to replace solvent-borne polyurethanes where health risks must be decreased. Even though they have been known for decades, the final coating, or the adhesive quality, is seldom the same. This can be mostly attributed to the water's unique properties which transform a polymer solution into a colloidal dispersion. After the PUD synthesis, FT-IR spectroscopy detected a 85 % conversion of the residual NCO groups after one day, and a full conversion after 2.5–3 d. The data obtained was well described using a pseudo-first-order kinetic model. The kinetic constant was found to be  $(0.077 \pm 0.005) \text{ h}^{-1}$ . The colloid perspective confirmed the expected pH drop and the resulting conductivity increase. The average particle size and particle size distribution stayed unchanged, confirming that an increased molecular mass does not influence the colloidal particle size.

#### Acknowledgements

This operation was partly financed by the European Union, European Social Fund. The operation was carried out in the framework of the Operational Program for Human Resources Development for the Period 2007-2013, Priority axis 1: Promoting entrepreneurship and adaptability, Main type of activity 1.3: Scholarship scheme (contract No. 62231-268).

#### 5 REFERENCES

- <sup>1</sup> Council of the European Union, Solvent Emissions Directive 1999/13/EC, Official Journal of the European Union, L 085 (1999), 1–22
- <sup>2</sup> European Parliament, Council of the European Union, Paints Directive 2004/42/CE, Official Journal of the European Union, L 143 (2004), 87–96
- <sup>3</sup> B. K. Kim, *Colloid Polym. Sci.*, 274 (1996), 599–611, doi:10.1007/BF00653056
- <sup>4</sup> Y. K. Jhon, I. W. Cheong, J. H. Kim, *Colloids and Surfaces A: Physicochem. Eng. Aspects*, 179 (2001), 71–78, doi:10.1016/S0927-7757(00)00714-7
- <sup>5</sup> Z. Wicks, F. Jones, S. P. Pappas, *Organic Coatings: Science and Technology*, third ed., John Wiley and Sons, New York 2007, doi:10.1002/047007907X
- <sup>6</sup> O. Jaudouin, J. J. Robin, J. M. Lopez-Cuesta, D. Perrin, C. Imbert, *Poly. Int.*, 61 (2012) 4, 495–510, doi:10.1002/pi.4156
- <sup>7</sup> G. Oertel, *Polyurethane handbook*, Hanser Publishers, Munich 1985
- <sup>8</sup> S. A. Madbouly, J. U. Otaigbe, *Prog. Poly. Sci.*, 34 (2009), 1283–1332, doi:10.1016/j.progpolymsci.2009.08.002
- <sup>9</sup> H. Sardon, L. Irusta, M. J. Fernandez-Berridi, J. Luna, M. Lansalot, E. Bourgeat-Lami, *J. Appl. Polym. Sci.*, 120 (2011), 2054–2062, doi:10.1002/app.33308
- <sup>10</sup> H. Sardon, L. Irusta, M. J. Fernández-Berridi, *Prog. Org. Coat.*, 66 (2009), 291–295, doi:10.1016/j.porgcoat.2009.08.005
- <sup>11</sup> K. Noll, W. Thoma, K. Nachtkamp, W. Schroer, J. Pedain, US Patent No. 4876302, 1989
- <sup>12</sup> D. K. Chattopadhyay, K. V. S. N. Raju, *Prog. Polym. Sci.*, 32 (2007), 352–418, doi:10.1016/j.progpolymsci.2006.05.003
- <sup>13</sup> G. A. Howarth, *Surf. Coating Int. B: Coating Trans.*, 86 (2003), 111–118, doi:10.1007/BF02699621
- <sup>14</sup> J. Y. Jang, Y. K. Jhon, I. W. Cheong, J. H. Kim, *Colloids and Surfaces A: Physicochem. Eng. Aspects*, 196 (2002), 135–143, doi:10.1016/S0927-7757(01)00857-3
- <sup>15</sup> M. Ionescu, *Chemistry and Technology of Polyols for Polyurethanes*, Rapra Technology, Shropshire 2005
- <sup>16</sup> U. Meier-Westhues, *Polyurethanes Coatings, Adhesives and Sealants*, Vincentz Network, Hannover 2007
- <sup>17</sup> M. Melchior, M. Sonntag, C. Kobusch, E. Jurgens, *Prog. Org. Coat.*, 40 (2000), 99–109, doi:10.1016/S0300-9440(00)00123-5
- <sup>18</sup> W. Collong, A. Gobel, B. Kleuser, W. Lenhard, M. Sonntag, *Prog. Org. Coat.*, 45 (2002), 205–209, doi:10.1016/S0300-9440(02)00052-8
- <sup>19</sup> G. Shkapenko, G. T. Gmitter, E. E. Gruber, *Ind. Eng. Chem.*, 52 (1960) 7, 605–608, doi:10.1021/ie50607a031
- <sup>20</sup> M. Modesti, A. Lorenzetti, *Eur. Polym. J.*, 37 (2001), 949–954, doi:10.1016/S0014-3057(00)00209-3
- <sup>21</sup> J. L. Han, C. H. Yu, Y. H. Lin, K. H. Hsieh, *J. Appl. Polym. Sci.*, 107 (2008) 6, 3891–3902, doi:10.1002/app.27421
- <sup>22</sup> J. T. Vanderberg, *An Infrared Spectroscopy Atlas for the Coating Industry*, Federation of Societies for Coatings Technology, Chicago 1980
- <sup>23</sup> B. A. Hess, L. J. Schaad, P. Carsky, R. B. Zahradnik, *Chem. Rev.*, 86 (1986) 4, 709–730, doi:10.1021/cr00074a004
- <sup>24</sup> O. Levenspiel, *Chemical reaction engineering*, Wiley, New York 1972
- <sup>25</sup> International Standard ISO22412 – Particle Size Analysis: Dynamic Light Scattering, International Organization for Standardization, 2008
- <sup>26</sup> P. Krol, B. Krol, R. Stagracyński, K. Skrzypiec, *J. Appl. Polym. Sci.*, 127 (2013), 2508–2519, doi:10.1002/app.37552
- <sup>27</sup> K. Bagdi, K. Molnar, B. Pukanszky Jr., B. Pukanszky, *J. Therm. Anal. Calorim.*, 98 (2009), 825–832, doi:10.1007/s10973-009-0528-z
- <sup>28</sup> E. A. Collins, *Measurement of Particle Size and Particle Size Distribution*, In: P. A. Lovell, M. S. El-Aasser (Eds.), *Emulsion Polymerization and Emulsion Polymers*, John Wiley and Sons, Chichester 1997





# SPECTROSCOPIC AND POROSIMETRIC ANALYSES OF ROMAN POTTERY FROM AN ARCHAEOLOGICAL SITE NEAR MOŠNJE, SLOVENIA

## SPEKTROSKOPSKE IN POROZIMETRIČNE PREISKAVE RIMSKE LONČENINE Z ARHEOLOŠKEGA NAJDIŠČA PRI MOŠNJAH, SLOVENIJA

Sabina Kramar<sup>1</sup>, Judita Lux<sup>2</sup>

<sup>1</sup>Slovenian National Building and Civil Engineering Institute, Dimičeva 12, 1000 Ljubljana, Slovenia.

<sup>2</sup>Institute for the Protection of Cultural Heritage of Slovenia, Centre for Preventive Archaeology, Tomšičeva 7, 4000 Kranj, Slovenia  
sabina.kramar@zag.si

*Prejem rokopisa – received: 2014-07-16; sprejem za objavo – accepted for publication: 2014-07-31*

doi:10.17222/mit.2014.110

This study deals with spectroscopic and porosimetric analyses of pottery from a Roman villa rustica near Mošnje, Slovenia. Samples of coarse ware and fine ware, which according to archaeological considerations have been recognised as local or perhaps regional products, were investigated using FTIR spectroscopy, scanning electron microscopy, mercury-intrusion porosimetry and gas sorption. Based on their FTIR spectra, the pottery sherds can be divided into two main groups, depending on the presence or absence of calcite. The firing temperature was estimated according to the presence of an absorption band at around 3630 cm<sup>-1</sup>, associated with hydroxyl groups of minerals that are persistent up to 800 °C. The differences among the coarse and fine ware sherds related to the pore morphology and the pore volume in the matrix were observed, as was the extent of the vitrification. In general, the total porosity of the pottery sherds with coarse-grained calcite inclusions was lower than that of the fine pottery sherds. The fine ware samples also exhibited a significantly higher BET surface area than the coarse ware samples.

Keywords: Roman pottery, archaeological ceramics, FTIR, porosimetry, Mošnje

V prispevku so predstavljeni rezultati spektroskopskih in porozimetričnih analiz lončenine iz rimske vile rustike pri Mošnjah (Slovenija). Vzorce grobe in fine keramike, ki naj bi bila glede na arheološke raziskave lokalnega ali regionalnega izvora, smo preiskali s spektroskopijo FTIR, vrstično elektronsko mikroskopijo, živosrebreno porozimetrijo in plinsko sorpcijo. Glede na spektre FTIR lahko lončenino razdelimo v dve skupini, odvisno od tega, ali vsebuje kalcit. Temperatura žganja je bila ocenjena glede na prisotnost absorpcijskega traku hidroksilnih skupin pri okoli 3630 cm<sup>-1</sup>, ki je obstojen do 800 °C. Med grobo in fino keramiko so opazne razlike v obliki in volumnu por ter obsegu vitrifikacije. Na splošno je celotna poroznost lončenine z dodatkom debelozrnatega kalcita nižja kot pri fini keramiki. Slednja ima v primerjavi z grobo keramiko tudi občutno višjo specifično površino BET.

Ključne besede: rimska lončenina, arheološka keramika, FTIR, porozimetrija, Mošnje

## 1 INTRODUCTION

Analyses of the potteries that represent one of the most abundant types of archaeological find reveal information regarding the daily life and culture of ancient societies.<sup>1,2</sup> The mineralogical and chemical characterisation of pottery provides evidence for the technology involved in the manufacturing process and potentially the provenance of the raw material used.<sup>3-6</sup> Besides the raw materials, the nature and quality of the pottery depend on the firing temperature, the firing atmosphere or the kiln conditions, as well as the technical skill of the potter.<sup>7</sup>

Thermal transformations in clay materials during firing provide a means with which to estimate the firing temperature of the artefacts.<sup>8</sup> FTIR spectroscopy is considered as an important tool in the analysis of clay minerals and mineral transformation due to thermal effects, with the infrared spectra of the pottery revealing both the type of clay and the firing temperature.<sup>8-10</sup> An SEM examination of the pottery provides information

regarding not only the internal morphology that developed during the original firing in antiquity, but also the extent of the vitrification (the glassy phase) and the pore structure.<sup>11,12</sup>

Porosity is a fundamental attribute of pottery and can provide information about many aspects of archaeological manufacturing technologies, including the firing temperature, the type of clay and tempering materials, and the manufacturing and forming techniques employed, which all contribute to the degree of ceramic porosity exhibited.<sup>13</sup> Porosity also influences a wide range of ceramic use-related properties, such as strength, permeability, thermal insulation, as well as resistance to abrasion and thermal shock.<sup>14</sup>

Most pottery sherds found at the archaeological site near Mošnje, Slovenia date from the Augustian period (27 BC to 14 AD) to the 2<sup>nd</sup> Century, thus providing additional confirmation that the Roman villa rustica was built in the first half of the 1<sup>st</sup> Century and was in use

until the end of the 2<sup>nd</sup> Century, at the latest. The discovery of pottery fragments dating to prehistory, together with a number of bronze finds from the Early and Late Iron Ages, indicates settlement of the area prior to the arrival of the Romans. Furthermore, the presence of Late Roman pottery on the site that confirms the continuity of settlement somewhere nearby the villa, which by this time had already been abandoned.

It is widely known that both coarse ware and domestic tableware are usually of local manufacture and that such forms are typically not chronologically very sensitive.<sup>15</sup> The selected pottery samples, which according to the archaeological analysis have been recognised as local or perhaps regional products (i.e., not imported/terra sigillata), differ in their mineralogical and chemical composition, reflecting a variation in the manufacturing technology and the type of clay material used.<sup>16,17</sup> The sherds were classified into two distinct groups: (i) Group 1 – sherds made from clay with a high plasticity (calcite-tempered ware), containing abundant calcite and smaller amounts of quartz; (ii) Group 2 – sherds with a predominantly fine silicate fabric, part of the original clay, calcite-free and containing abundant quartz and illite/muscovite. Group 1 sherds are fairly homogenous, indicating that the technology of manufacture changed only slightly with time. The mineralogy and geochemistry of these sherds are also similar, suggesting that they must have been produced from the same source of raw materials, although the greater amount of quartz observed in two Late Roman sherds suggests a possible different clay-mass source in use at this time. In contrast, the Group 2 samples are highly heterogeneous, indicating the use of various sources of raw materials.

In the present study, samples of Roman coarse ware and fine ware from the archaeological site of Mošnje were chosen for spectroscopic and porosimetric analyses. FTIR spectroscopy, scanning electron microscopy, mercury-intrusion porosimetry and gas sorption were applied in order to characterise the porosity and estimate the firing temperature of the pottery.

## 2 EXPERIMENTAL

### 2.1 Materials

Seven samples – four of coarse ware and three of fine ware – previously studied with respect to their mineralogical and geochemical characteristics<sup>16,17</sup> were selected for the investigation. Information regarding the micro-location, type, surface colour and probable date of the pottery samples is provided in **Table 1**.

### 2.2 Methods

Samples were analysed via Fourier-transform infrared spectroscopy (FTIR) using a Perkin Elmer Spectrum 100 spectrometer. Sixty-four signal-averaged scans were acquired. Powder pellets were pressed from a mixture of sample and KBr at a ratio of about 1 : 200. The FTIR spectra were recorded with a spectral resolution of 4 cm<sup>-1</sup> in the range 4000–400 cm<sup>-1</sup>.

Freshly fractured surfaces of the pottery as well as polished thin sections were examined using the back-scattered electron (BSE) image mode on a scanning electron microscope (SEM) at low vacuum (between 10 Pa to 15 Pa), coupled to an energy-dispersive X-Ray (EDS) analyses, using JEOL 5500 LV equipment.

The pore systems of the samples were further investigated by means of mercury-intrusion porosimetry (MIP) and gas-sorption isotherms. Small representative fragments, approximately 1 cm<sup>3</sup> in size, were dried in an oven for 24 h at 105 °C and then analysed on a Pascal 240 porosimeter within the range from 0 MPa to 200 MPa. N<sub>2</sub> sorption isotherms were obtained at 77 K on a Micromeritics ASAP 2020 analyser under continuous adsorption conditions. Prior to these measurements, chip samples were heated at 200 °C for 2 h and outgassed to 1.33 · 10<sup>-3</sup> mbar using a Micromeritics Flowprep equipment. Gas-adsorption analysis across the relative pressure range of 0.05 to 0.3 was used to determine the total specific area or Brunauer–Emmet–Teller (BET) surface area of the samples.<sup>18,19</sup> The sample total pore volume and the micropore volume were calculated using a t-plot analysis, with the Barret–Joyner–Halenda (BJH) method employed to obtain the pore-size distribution curves.<sup>20</sup>

**Table 1:** Pottery samples from the archaeological site near Mošnje

**Tabela 1:** Vzorci lončenine z arheološkega najdišča pri Mošnjah

| Sample     | Location    | Type | Surface colour | Time frame                |                                       |
|------------|-------------|------|----------------|---------------------------|---------------------------------------|
|            | Grid square |      |                | Stratigraphic unit        | Munsell colour chart                  |
| K1 (4254)  | L10         | 187  | coarse ware    | 7.5YR5/1 (gray)           | 1.–3. (?) Century                     |
| K3 (3264)  | L10         | 137  | fine ware      | 7.5YR6/8 (reddish yellow) | 1.–3. Century                         |
| K6 (1722A) | N7, O7      | 162  | coarse ware    | 7.5YR6/4 (light brown)    | 1.–1. half of 2 <sup>nd</sup> Century |
| K7 (1909)  | L9          | 196  | fine ware      | 10YR4/1 (dark gray)       | 1.–2. Century                         |
| K8 (6366)  | L13         | 529  | coarse ware    | 10YR3/1 (very dark gray)  | 1.–2. Century                         |
| K10 (2447) | M9, N9      | 198  | coarse ware    | 10YR4/1 (dark gray)       | 1 <sup>st</sup> half of 1. Century    |
| K12 (1688) | N7, O7      | 162  | fine ware      | 5YR7/6 (reddish yellow)   | 1.–1. half of 2 <sup>nd</sup> Century |

### 3 RESULTS AND DISCUSSION

#### 3.1 FTIR analysis

On the basis of the FTIR spectra, all the analysed pottery sherds could be divided into two main groups according to the presence or absence of calcite. The obtained FTIR spectra are shown in **Figures 1** and **2**.

As can be seen in **Figure 1**, absorption bands at around (2515, 1797, 1426, 875 and 714)  $\text{cm}^{-1}$  that are characteristic of calcite were observed in the spectra of all the Group-1 samples (K1, K6, K8, and K10), which represent calcite-tempered coarse ware.<sup>16</sup> Another intense absorption band appears at around 1030  $\text{cm}^{-1}$ , indicative of clay minerals such as illite.<sup>9</sup> The small absorption band at 1164  $\text{cm}^{-1}$ , the shoulder at 1080  $\text{cm}^{-1}$ , the doublets at 798  $\text{cm}^{-1}$  and 779  $\text{cm}^{-1}$ , and the band at 694  $\text{cm}^{-1}$ , together indicate the presence of quartz in all the samples within the group.

According to the literature<sup>21</sup>, the absorption band at around 3630  $\text{cm}^{-1}$  is due to hydroxyl groups that persist up to 800 °C. The small absorption band at around 3630  $\text{cm}^{-1}$ , and which is assigned to the illite/muscovite, is clearly observed in sample K10, and slightly preserved in sample K1. This indicates that these two samples might have been fired below 800 °C, as already presumed in a previous study.<sup>16</sup> In contrast, those samples not exhibiting the absorption band at around 3630  $\text{cm}^{-1}$  were likely fired to temperatures of 800 °C or above (samples K6 and K8).

As shown in **Figure 2**, the spectra of the Group-2 samples that represent fine ware with predominant silicate grains (K3, K7, and K12) are, besides the absence of absorption bands, characteristic of calcite, characterised by a most intense band at about 1035  $\text{cm}^{-1}$ , which is attributed to the Si-O vibrations of silicate (clay) minerals. Sample K3 does not exhibit an absorption band at around 3630  $\text{cm}^{-1}$ , indicating a firing temperature higher than 800 °C. This band is slightly preserved in samples K7 and K12, indicating a lower firing temperature for these samples. The absorption

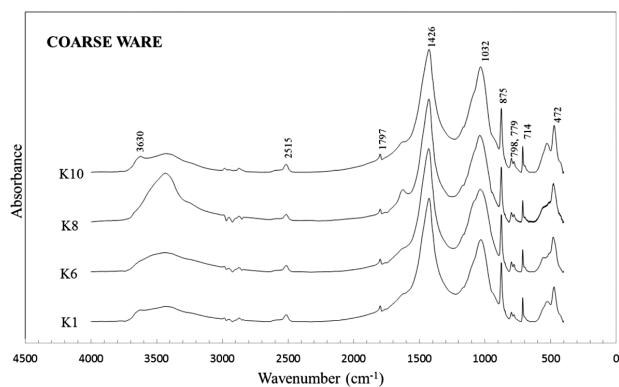


**Figure 1:** FTIR spectra of the calcite-tempered pottery sherds (coarse ware)

**Slika 1:** Spektri FTIR odlomkov lončenine z dodatkom kalcitnih zrn (groba keramika)

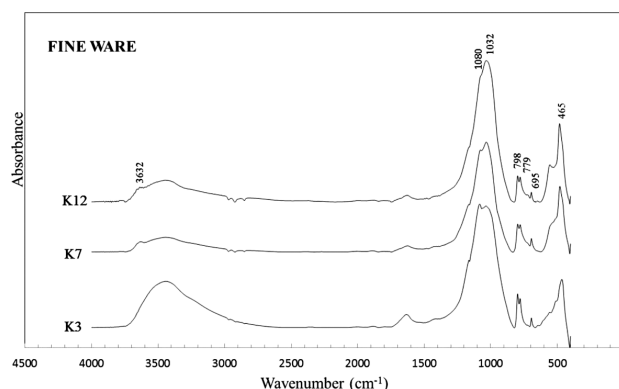


**Figure 2:** FTIR spectra of the pottery sherds with a predominantly fine silicate fabric (fine ware)

**Slika 2:** Spektri FTIR odlomkov lončenine, ki vsebujejo pretežno drobna silikatna zrna (fina keramika)

band at 1161  $\text{cm}^{-1}$ , the shoulder at 1080  $\text{cm}^{-1}$ , the doublets at 797  $\text{cm}^{-1}$  and 779  $\text{cm}^{-1}$ , and the band at 694  $\text{cm}^{-1}$ , are evidence of quartz in all the samples, with levels being especially high in sample K3. Sample K3 also has an additional shoulder at 1013  $\text{cm}^{-1}$ , suggesting the use of a different clay than that in samples K7 and K12. Together with those at around 720  $\text{cm}^{-1}$  and 646  $\text{cm}^{-1}$ , this band has been ascribed to feldspars previously identified in larger amounts in the same sample.<sup>16</sup>

#### 3.2 SEM

The examination of the fresh fracture surfaces and the polished sections provided some insight into the microstructure of the pottery sherds. As can be seen in the SEM microphotographs in **Figure 3**, the differences among the coarse and fine ware were observed in terms of their pore morphology and pore volume in the matrix. Information regarding the pottery's internal morphology, which developed during the original firing in antiquity, as well as the extent of vitrification, was revealed by the analysis of freshly fractured samples, as shown in **Figure 4**.

The coarse ware matrix is characterised by the occurrence of elongated pores or fissures and cracks around the calcite grains (**Figure 3a**). Samples K1 and especially K6 contain larger amounts of non-plastic inclusions (quartz, illite/muscovite) than do samples K8 and K10. The laminar habits of the phyllosilicates (illite/muscovite) in samples K1 and K6 are still preserved, which is also in accordance with the FTIR results, as the latter spectra included an absorption band associated with the hydroxyl group. Cultrone et al.<sup>22</sup> previously reported that samples fired at 700 °C and 800 °C still preserve the laminar habit of phyllosilicates, although muscovite crystals clearly exfoliate along basal planes, as also observed in sample K1. In this temperature range no clear evidence of sintering or partial melting should be detected, as vitrification occurs above 900 °C. In addition, according to Maniatis and Tite<sup>11</sup>, low refractory non-calcareous clays fired in oxidising conditions with no

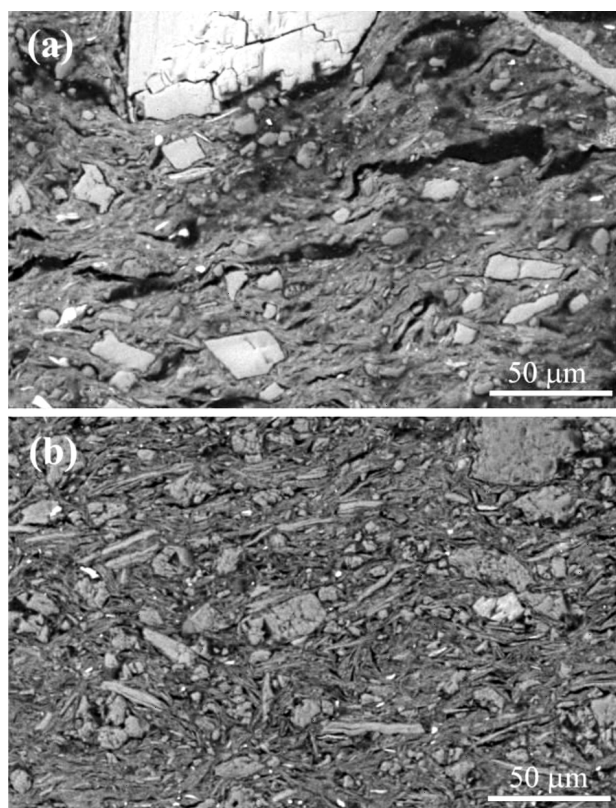


**Figure 3:** SEM photomicrographs of polished thin sections of pottery: a) elongated pores in sample K8, b) illite micromass in sample K7  
**Slika 3:** SEM-mikrofotografija poliranih zbruskov lončenine: a) podolgovate pore v vzorcu K8, b) ilitna mikromasa v vzorcu K7

vitriification stage were fired below 800 °C. Thus, samples K1 and K10 belong to the first group (NV), which contains pottery exhibiting no vitriification. Samples K6 and K8 could belong to the initial vitriification stage (IV) that is developed typically at firing temperatures in the range of 800–850 °C. This is suggested by the appearance of smooth-surfaced areas and the rounded edges of the clay plates (**Figure 4a**).

The matrix of the fine ware samples is relatively homogenous, with an illite micromass observed in samples K7 and K12 (**Figure 3b**). Among the fine ware samples, the preserved laminar habits of phyllosilicates presented in samples K7 and K12 (**Figure 4b**) indicate that these sherds were not subject to vitriification (NV). In contrast, the rounded particle edges in sample K3 are suggestive of the initial vitriification stage (IV).

### 3.3 Mercury-intrusion porosimetry

**Table 2** presents the sample parameters determined via mercury-intrusion porosimetry (total porosity, average pore diameter, bulk density and apparent density).

The porosity values range from 21.34 % to 44.03 %. In general, the total porosity of pottery sherds with coarse inclusions is lower (21.34–30.33 %) than that of the fine ware pottery sherds, in which the porosity ranges

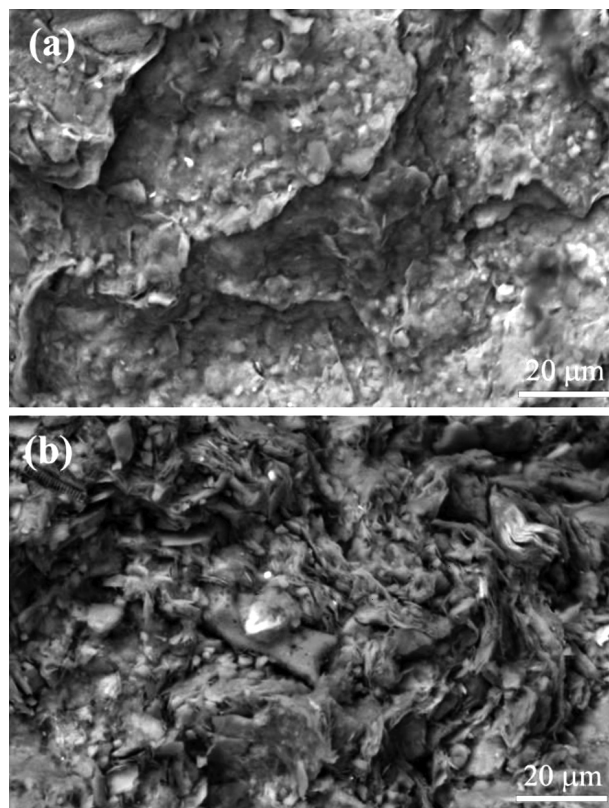


**Figure 4:** SEM photomicrographs demonstrating the degree of vitriification in the studied coarse ware and fine ware: a) smooth-surfaced areas could indicate initial vitriification in sample K8, b) preserved laminar habit of phyllosilicates indicates no vitriification in sample K12

**Slika 4:** SEM-mikrofotografija prikazuje stopnjo vitriifikacije pri grobi in fini keramiki: a) zaobljena površina lahko nakazuje začetno stopnjo vitriifikacije v vzorcu K8, b) ohranjena laminarna struktura filossilikatov nakazuje, da do vitriifikacije še ni prišlo, vzorec K12

from 36.49 % to 44.03 %. Furthermore, the average pore size diameter of the fine ware sherds is lower than that of the sherds with coarse inclusions. The sample bulk densities vary from 1.32 g/mL to 1.99 g/mL, whereas the apparent densities range from 2.52 g/mL to 2.68 g/mL.

**Table 2:** Porosity, average pore diameter, bulk density and apparent density of the investigated pottery samples

**Tabela 2:** Poroznost, povprečen premer por, volumenska in navidezna gostota preiskanih vzorcev lončenine

| Sample             | Porosity (%) | Average pore diameter (µm) | Bulk density (g/mL) | Apparent density (g/mL) |
|--------------------|--------------|----------------------------|---------------------|-------------------------|
| <b>Coarse ware</b> |              |                            |                     |                         |
| <b>K1</b>          | 21.43        | 5.54                       | 1.98                | 2.52                    |
| <b>K6</b>          | 30.33        | 0.22                       | 1.82                | 2.61                    |
| <b>K8</b>          | 21.34        | 4.60                       | 1.99                | 2.54                    |
| <b>K10</b>         | 29.15        | 58.94                      | 1.90                | 2.68                    |
| <b>Fine ware</b>   |              |                            |                     |                         |
| <b>K3</b>          | 44.03        | 0.66                       | 1.32                | 2.36                    |
| <b>K7</b>          | 36.49        | 0.38                       | 1.60                | 2.52                    |
| <b>K12</b>         | 37.11        | 0.37                       | 1.60                | 2.54                    |

All the samples with coarse inclusions exhibit a distinctive bimodal pore distribution, which is reflected

in a higher average pore diameter. These samples are also characterised by the presence of elongated pores in the matrix and sizeable cracks around the large calcite inclusions, as seen in SEM observations; these features thus contribute to the shift towards larger pores. Nevertheless, the main peak, with a higher intrusion, is observed at around 7.5  $\mu\text{m}$  to 10  $\mu\text{m}$  in all coarse ware samples with the exception of K10, where the distribution curve is shifted significantly to the right (85  $\mu\text{m}$ ). The minor intrusion peak occurs at around 0.07  $\mu\text{m}$  to 0.15  $\mu\text{m}$  in samples K8 and K10, while in samples K1 and K6 this peak is shifted slightly to the right at around 0.5  $\mu\text{m}$ . Samples K6 and K10, respectively, exhibit the lowest and highest average pore size diameters. Whereas the intrusion peaks at higher pore diameters are most probably related to the presence of fissures and pores in the matrix, the peaks at smaller pore diameters are associated with the composing clay minerals. The latter peaks occur at lower values in the group of pottery sherds containing calcite temper than in the non-tempered pottery, thus indicating the use of different types of raw clay in their manufacture. In samples K8 and K10 the minor peak is shifted to even smaller values, since these sherds were found to contain very little illite/muscovite.<sup>16</sup> Most porosity observed before 800 °C depends on the type of clay, as well as on the size and concentration of the inclusions.<sup>23</sup>

The porosities of the pottery sherds containing fine particles are unimodally distributed, with the largest intrusions being around 0.60  $\mu\text{m}$  (K7, K12) or 0.85  $\mu\text{m}$  (K3). While samples K7 and K12 have similar total porosities and average pore size diameters, sample K3 exhibits the highest porosity among all the samples, as well as an average pore size diameter larger than that of the other two samples. The latter were also found to have a higher percentage of phyllosilicates, as observed via SEM-EDS<sup>16</sup>, together with a different type of matrix to that seen in sample K3. The total specific surface is related to the grain size, with the smallest values found in sample K3.

Velraj et al.<sup>21</sup> have previously reported that samples containing coarse particles exhibit higher porosity, the reverse of the pattern observed here. Although a high firing temperature will lead to low porosity,<sup>7,24</sup> the fact that in the present study the porosity of the coarse ware is lower than that of the fine ware is most likely due to the type of clay used, with the former made of plastic montmorillonite-illite clays and the latter characterised by the predominance of illite, potentially mixed with other clay minerals.<sup>16</sup>

### 3.4 Gas sorption

The sample BET-specific surface area varies from 2.90  $\text{m}^2/\text{g}$  to 91.55  $\text{m}^2/\text{g}$ , with the fine ware sherds characterised by significantly higher values (36.25–91.55  $\text{m}^2/\text{g}$ ) than those of the coarse ware (2.90–7.97  $\text{m}^2/\text{g}$ ) (Table 3). On the other hand, the coarse ware samples

exhibit a larger average pore diameter. Two samples, K7 and K10, present a pore size distribution with weak maxima of approximately 4 nm and 20 nm, respectively, whereas those of the other samples are either unclear or smaller than the detection limit. The volume of pores accessible to gas is larger in the case of the fine ware sherds. Similar to the previous results, the lower BET surface area of the coarse ware is the result of the presence of a coarse calcite temper. In contrast, the various fine fabrics characterising the fine ware sherds contribute to their higher BET surface areas, with sample K7 composed of a medium sand fraction<sup>16</sup> having the lowest BET surface area, and K12 composed of a very fine sand fraction having the highest BET surface area.

All of the samples studied present a type-II physiosorption isotherm characteristic of non-porous and macroporous materials.<sup>25</sup>

**Table 3:** Results of  $\text{N}_2$ -adsorption measurements for the investigated pottery samples

**Tabela 3:** Rezultati  $\text{N}_2$ -adsorpcijskih meritev preiskanih vzorcev lončenine

| Sample      | BET surface area      | Total pore volume      | Average pore diameter | Micropore volume       |
|-------------|-----------------------|------------------------|-----------------------|------------------------|
| pha         | $\text{m}^2/\text{g}$ | $\text{cm}^3/\text{g}$ | nm                    | $\text{cm}^3/\text{g}$ |
| Coarse ware |                       |                        |                       |                        |
| K1          | 2.90                  | 0.0090                 | 12.41                 | 0.000052               |
| K6          | 4.35                  | 0.0113                 | 10.36                 | 0.000290               |
| K8          | 7.97                  | 0.0090                 | 12.41                 | 0.000572               |
| K10         | 3.78                  | 0.0165                 | 17.41                 | 0.000050               |
| Fine ware   |                       |                        |                       |                        |
| K3          | 86.37                 | 0.0976                 | 4.52                  | 0.009380               |
| K7          | 36.25                 | 0.0022                 | 4.98                  | 0.002232               |
| K12         | 91.55                 | 0.0836                 | 3.65                  | 0.012577               |

## 4 CONCLUSIONS

Samples of coarse ware and fine ware from an archaeological site near Mošnje (Slovenia), which according to previous analysis have been recognised as local or perhaps regional products, were investigated in order to characterise their porosity and estimate their firing temperature.

Based on FTIR spectra, the pottery sherds can be divided into two main groups, reflecting either the presence or absence of calcite. The firing temperature was estimated according to the presence of an absorption band at around 3630  $\text{cm}^{-1}$ , which is associated with hydroxyl groups persistent up to 800 °C. This band was observed in two coarse ware samples and two fine ware samples, indicating that these sherds might have been fired below 800 °C. In contrast, samples not exhibiting this absorption band would likely have been fired at temperatures of at least 800 °C or above.

Differences were observed among the coarse and fine ware samples in terms of their pore morphology and pore volume in the matrix, as well as the extent of the vitri-

fication. Two vitrification stages were recognised in the studied pottery samples: no vitrification and an initial vitrification stage. These results are consistent with the obtained FTIR data, as the absence of a vitrification stage is characteristic of pottery fired below 800 °C, whereas an initial vitrification stage is developed typically at firing temperatures in the range of 800–850 °C.

In general, the total porosity of the pottery sherds containing coarse inclusions was lower than that of the fine pottery shards, most probably due to the plastic clay used in the former. The fine ware samples had a significantly larger BET surface area than the coarse ware samples, which is mainly related to the fabric or temper grain size.

### Acknowledgements

This study was financially supported by the ARRS Program Group P2-0273.

### 5 REFERENCES

- <sup>1</sup> M. S. Tite, *Journal of Archaeological Method and Theory*, 6 (1999) 3, 181–233
- <sup>2</sup> R. Palanivel, U. Rajesh Kumar, *Rom. J. Phys.*, 56 (2011) 1–2, 195–208
- <sup>3</sup> C. Rathossi, P. Tsois-Katagas, C. Katagas, *Applied Clay Science*, 24 (2004) 3–4, 313–326, doi:10.1016/j.clay.2003.07.008
- <sup>4</sup> G. Barone, A. Lo Giudice, P. Mazzoleni, A. Pezzino, D. Barilaro, V. Crupi, M. Triscari, *Archaeometry*, 47 (2005) 4, 745–762, doi:10.1111/j.1475-4754.2005.00230.x
- <sup>5</sup> J. Barrios-Neira, L. Montealegre, L. A. López, L. Romero, *Applied Clay Science*, 42 (2009), 529–537, doi:10.1016/j.clay.2008.06.018
- <sup>6</sup> C. M. Belfiore, M. di Bella, M. Triscari, M. Viccaro, *Materials Characterisation*, 61 (2010) 4, 440–451, doi:10.1016/j.matchar.2010.01.012
- <sup>7</sup> M. S. Tite, *Archaeometry*, 11 (1969) 1, 134–143, doi:10.1111/j.1475-4754.1969.tb00636.x
- <sup>8</sup> R. Ravisankar, S. Kiruba, A. Chandrasekaran, A. Naseerutheen, M. Seran, P. D. Balaji, *Indian Journal of Science and Technology*, 3 (2010) 9, 1016–1019, doi:10.17485/ijst/2010/v3i9/29880
- <sup>9</sup> G. E. De Benedetto, R. Laviano, L. Sabbatini, P. G. Zambonin, *Journal of Cultural Heritage*, 3 (2002), 177–186, doi:10.1016/S1296-2074(02)01178-0
- <sup>10</sup> R. Palanivel, G. Velraj, *Indian Journal of Pure & Applied Physics*, 45 (2007), 501–508
- <sup>11</sup> Y. Maniatis, M. S. Tite, *Journal of Archaeological Science*, 8 (1981), 59–76, doi: 10.1016/0305-4403(81)90012-1
- <sup>12</sup> A. M. Musthafa, K. Janaki, G. Velraj, *Microchemical Journal*, 95 (2010) 2, 311–314, doi:10.1016/j.microc.2010.01.006
- <sup>13</sup> K. G. Harry, A. Johnson, *Journal of Archaeological Science*, 31 (2004), 1567–1575, doi:10.1016/j.jas.2004.03.020
- <sup>14</sup> P. M. Rice, *Pottery Analysis: a sourcebook*, University of Chicago Press, Chicago, IL and London 1987, 584
- <sup>15</sup> V. Vidrih Perko, *Arheološki vestnik*, 48 (1997), 341–358
- <sup>16</sup> S. Kramar, J. Lux, A. Mladenović, H. Pristacz, B. Mirtič, M. Saggadin, N. Rogan - Šmuc, *Applied Clay Science*, 57 (2012), 39–48, doi:10.1016/j.clay.2011.12.008
- <sup>17</sup> N. Rogan - Šmuc, M. Dolenc, J. Lux, S. Kramar, *Environmental Earth Sciences*, 71 (2014) 11, 4821–4833, doi:10.1007/s12665-013-2874-1
- <sup>18</sup> S. J. Gregg, K. S. W. Sing, *Adsorption, surface area and porosity*, 2nd ed., Academic Press, London 1982, 303
- <sup>19</sup> R. W. Adamson, A. P. Gast, *Physical chemistry of surfaces*, Chapter 17, 6th ed., Wiley, New York 1997, 808
- <sup>20</sup> E. P. Barret, L. G. Joyner, P. P. Halenda, *Journal of the American Chemical Society*, 73 (1951), 373–380, doi: 10.1021/ja01145a126
- <sup>21</sup> G. Velraj, K. Janaki, A. Mohamed Mushafa, R. Palanivel, *Applied Clay Science*, 43 (2009), 303–307, doi:10.1016/j.clay.2008.09.005
- <sup>22</sup> G. Cultrone, C. Rodriguez - Navarro, E. Sebastian, O. Cazalla, M. J. De la Torre, *European Journal of Mineralogy*, 13 (2001) 3, 621–634, doi:10.1127/0935-1221/2001/0013-0621
- <sup>23</sup> M. S. Tite, Y. Maniatis, *Transactions and Journal of the British Ceramics Society*, 74 (1975) 1, 19–22
- <sup>24</sup> M. Mureson, *Materials and Structures*, 6 (1973) 3, 203–208, doi: 10.1007/BF02479034
- <sup>25</sup> K. S. W. Sing, D. H. Everett, R. A. W. Haul, L. Moscou, R. A. Pietrotti, J. Rouquérol et al., *Pure and Applied Chemistry (IUPAC)*, 57 (1985), 603–619

# NON-LINEAR FINITE-ELEMENT SIMULATIONS OF THE TENSILE TESTS OF TEXTILE COMPOSITES

## NELINEARNA SIMULACIJA NATEZNIH PREIZKUSOV TEKSTILNIH KOMPOZITOV S KONČNIMI ELEMENTI

**Tomáš Kroupa, Kryštof Kunc, Robert Zemčík, Tomáš Mandys**

University of West Bohemia in Pilsen, NTIS – New Technologies for the Information Society, Univerzitní 22, 306 14, Plzeň, Czech Republic  
kroupa@kme.zcu.cz

*Prejem rokopisa – received: 2014-07-25; sprejem za objavo – accepted for publication: 2014-09-15*

doi:10.17222/mit.2014.117

The main aim of this paper is to find if it is possible to identify material parameters using only three force-displacement dependencies, each for a different angle between the loading force and the principal material directions. The tested materials are textiles made of epoxy resin and fibers in the form of a glass plain weave, a glass quasi-unidirectional weave, a carbon plain weave, a carbon quasi-unidirectional weave, an aramid plain weave and an aramid quasi-unidirectional weave. The plain weave has theoretically 50 % of the fibers in the first and 50 % in the second principal material direction. The quasi-unidirectional weave has theoretically 90 % of the fibers in the first and 10 % in the second principal material direction. Seven types of specimens for each material were subjected to experimental tests. The first principal material direction of each material forms an angle between 0 ° and 90 ° with a step of 15 ° with the applied loading force. The results show that it is possible to identify the material parameters with sufficient accuracy using only three force-displacement dependencies for five out of six materials.

Keywords: textile composite, cyclic tensile test, material parameters, plasticity, weave locking, identification, optimization

Namen članka je preiskava možnosti ugotavljanja parametrov materiala z uporabo samo treh odvisnosti sila-raztezek pri različnem kotu med silo obremenjevanja in glavno smerjo materiala. Preiskovani materiali so tekstil, izdelan iz epoksi smole in vlaken v obliki platnene vezave, kvazi usmerjene vezave, ogljikove platnene vezave, ogljikove kvazi usmerjene vezave, aramidne platnene vezave in aramidne kvazi usmerjene vezave. Platnena vezava ima teoretično 50 % vlaken v prvi in 50 % v drugi prednostni smeri usmerjenosti materiala. Kvazi usmerjena vezava ima teoretično 90 % v prvi in 10 % v drugi prednostni smeri usmerjenosti materiala. Sedem vrst vzorcev vsakega materiala je bilo preverjeno s preizkusi. Prva glavna usmerjenost pri vseh materialih je bila pod kotom med 0 ° in 90 ° s koraki po 15 ° glede na delovanje sile. Rezultati kažejo, da je bilo mogoče dovolj zanesljivo ugotoviti parametre materiala samo z uporabo treh odvisnosti sila-raztezek pri petih od šestih uporabljenih materialih.

Ključne besede: tekstilni kompozit, ciklični natezni preizkus, parametri materiala, plastičnost, zaklepanje vezave, identifikacija, optimizacija

## 1 INTRODUCTION

Various kinds of fibrous composite materials are used in modern applications. The main advantages over the classical metallic materials are the beneficial stiffness- and strength-to-mass ratios and the possibility to achieve desired anisotropic mechanical properties wherever necessary. Nevertheless, mathematical models used for designing such structures often require approaches different than those known for classical materials. One of these models is described in this paper. The presented model is kept as simple as possible in the order to keep the number of material parameters as low as possible. It is able to describe the non-linear elastic response, the plastic flow in shear only and the so-called locking of the principal material directions (warp and weft).

The main aim of this paper is to investigate if it is possible to identify material parameters using only three force-displacement dependencies, each for a different angle between the loading force and the principal material directions. The tested materials are the textiles made of epoxy resin and the fibers in the form of a plane

weave (GP), a glass quasi-unidirectional weave (GU), a carbon plane weave (CP), a carbon quasi-unidirectional weave (CU), an aramid plane weave (AP) and an aramid quasi-unidirectional weave (AU). The plain weave theoretically consists of 50 % of the fibers in the first and 50 % of the fibers in the second principal material direction; the quasi-unidirectional weave consists of 90 % of the fibers in the first and 10 % in the second principal material direction. Seven types of specimens of each material were subjected to experimental tests. The first principal material direction of each material forms an angle between 0 ° and 90 ° with a step of 15 ° with the applied loading force.

## 2 SPECIMENS

**Figure 1** shows the dimensions of the tested specimens where the investigated area is highlighted. It is the area between the extensometer clips where the elongation  $\Delta l$  of the specimens, the locking angle of the weave and the maximum equivalent plastic strain were measured or calculated.

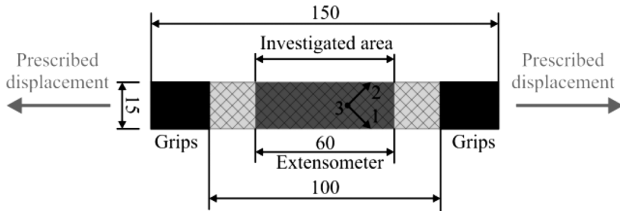


Figure 1: Dimensions of specimens  
Slika 1: Dimenzije vzorcev

Table 1 shows the thickness of the specimens of each material.

Table 1: Thickness of specimens  
Tabela 1: Debelina vzorcev

| Material | Thickness (mm) |
|----------|----------------|
| GP       | 1.8            |
| GU       | 1.8            |
| CP       | 2.0            |
| CU       | 1.5            |
| AP       | 2.2            |
| AU       | 2.0            |

2.1 Material model

The model assumes the state of plane stress and the finite-strain theory.

Three coordinate systems are used for the description of the material behavior. General coordinate system  $O(x,y,z)$  is used for designating the strains and stresses as  $\epsilon_{xy} = [\epsilon_x, \epsilon_y, \epsilon_{xy}]^T$  and  $\sigma_{xy} = [\sigma_x, \sigma_y, \tau_{xy}]^T$ . Coordinate system of undeformed configuration  $O(1,2,3)$  describes the principal material directions where the strains and stresses are designated as  $\epsilon_{12} = [\epsilon_1, \epsilon_2, \epsilon_{12}]^T$  and  $\sigma_{12} = [\sigma_1, \sigma_2, \tau_{12}]^T$ . Coordinate system of deformed configuration  $O(\xi, \eta, \zeta)$  describes the principal material directions of deformed material configuration and the strains and stresses are designated as  $\epsilon_{\xi\eta} = [\epsilon_\xi, \epsilon_\eta, \epsilon_{\xi\eta}]^T$  and  $\sigma_{\xi\eta} = [\sigma_\xi, \sigma_\eta, \tau_{\xi\eta}]^T$  (Figure 2). The transformation from system  $O(x,y,z)$  to system  $O(1,2,3)$  is performed using the rotation about axes  $z \equiv e_3$  by angle  $\theta$ . The strains are transformed using relation  $\epsilon_{12} = T_r \epsilon_{xy}$  and the stresses are transformed

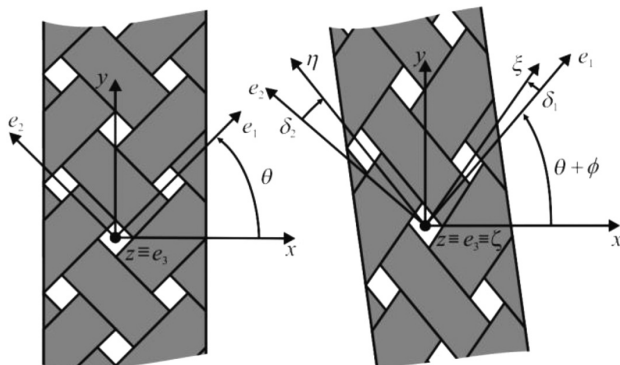


Figure 2: Coordinate systems  
Slika 2: Koordinatna sistema

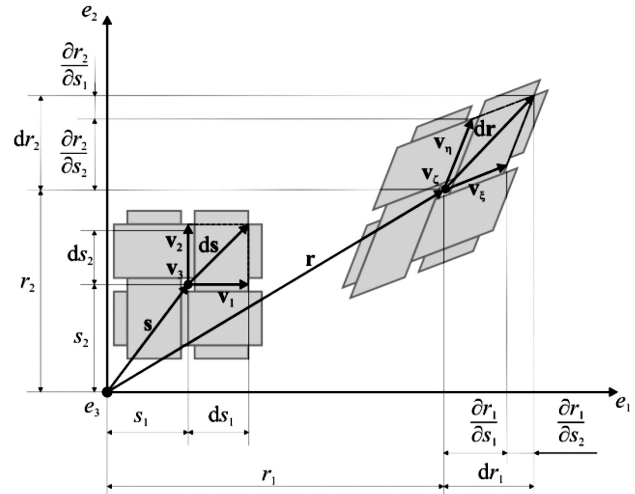


Figure 3: Undeformed and deformed configurations  
Slika 3: Nedeformirana in deformirana konfiguracija

using relation  $\sigma_{12} = T_r^{-T} \sigma_{xy}$  where the transformation matrix has the following form:

$$T_r = \begin{bmatrix} \cos^2 \theta & \sin^2 \theta & \sin \theta \cos \theta \\ \sin^2 \theta & \cos^2 \theta & -\sin \theta \cos \theta \\ -2 \sin \theta \cos \theta & 2 \sin \theta \cos \theta & \cos^2 \theta - \sin^2 \theta \end{bmatrix} \quad (1)$$

The transformation from system  $O(1,2,3)$  to system  $O(\xi, \eta, \zeta)$  is performed using deformation gradient:

$$F = \begin{bmatrix} F_{11} & F_{12} & 0 \\ F_{21} & F_{22} & 0 \\ 0 & 0 & F_{33} \end{bmatrix} = \begin{bmatrix} \frac{\partial r_1}{\partial s_1} & \frac{\partial r_1}{\partial s_2} & 0 \\ \frac{\partial r_2}{\partial s_1} & \frac{\partial r_2}{\partial s_2} & 0 \\ 0 & 0 & \frac{\partial r_3}{\partial s_3} \end{bmatrix} \quad (2)$$

which describes the deformation of the representative volume element of the weave (Figure 3).

Deformed principal material directions are described using vectors  $v_\xi = [F_{12}, F_{21}, 0]^T$  and  $v_\eta = [F_{12}, F_{22}, 0]^T$ ; these are used for defining transformation matrix:

$$T_d = \begin{bmatrix} F_{11} F_{11} & F_{21} F_{21} & F_{11} F_{21} \\ F_{12} F_{12} & F_{22} F_{22} & F_{12} F_{22} \\ 2 F_{11} F_{12} & 2 F_{21} F_{22} & F_{11} F_{22} + F_{21} F_{12} \end{bmatrix} \quad (3)$$

Subsequently, the transformation of the strains and stresses can be written as  $\epsilon_{\xi\eta} = T_d^{-T} \epsilon_{12}$  and  $\sigma_{\xi\eta} = T_d^{-T} \sigma_{12}$ .

The model is considered in similar way as in<sup>4</sup>, with the difference that plasticity is considered in shear only and nonlinearity in material directions  $\xi$  and  $\eta$  is modelled as non-linear elasticity. Hence, the stress-strain relation is proposed in the following form:

$$\begin{aligned} \sigma_\xi &= C_{11} \left( 1 + \frac{k_\xi}{2} \epsilon_\xi \right) \epsilon_\xi + C_{12} \epsilon_\eta \\ \sigma_\eta &= C_{22} \left( 1 + \frac{k_\eta}{2} \epsilon_\eta \right) \epsilon_\eta + C_{12} \epsilon_\xi \\ \tau_{\xi\eta} &= C_{33} \epsilon_{\xi\eta}^E \end{aligned} \quad (4)$$



where

$$C_{11} = \frac{E_\xi}{1 - \frac{E_\eta}{E_\xi} \nu_{\xi\eta}^2}, C_{22} = \frac{E_\eta}{1 - \frac{E_\xi}{E_\eta} \nu_{\xi\eta}^2}, C_{12} = \nu_{\xi\eta} \frac{E_\eta}{E_\xi}$$

and  $C_{33} = 2G_{\xi\eta}$ ,  $k_\xi$  and  $k_\eta$  are non-linear elastic parameters in the  $\xi$  and  $\eta$  directions,  $E_\xi$  and  $E_\eta$  are the Young's moduli in the  $\xi$  and  $\eta$  directions,  $G_{\xi\eta}$  is the shear modulus in the composite plane ( $\xi\eta$ ),  $\nu_{\xi\eta}$  is Poisson's ratio in the composite plane ( $\xi\eta$ ),  $\varepsilon_{\xi\eta}^E$  is the elastic part of the shear strain. Once the plastic flow is considered in the shear only the remaining strains  $\varepsilon_\xi$  and  $\varepsilon_\eta$  are normal elastic strains (no plastic part exists). The hardening function in the form of the power law is used:

$$\sigma^y = \sigma_0^y + \beta(\bar{\varepsilon}^P)^\alpha \tag{5}$$

where  $\sigma_0^y$  is the initial yield stress,  $\alpha$  and  $\beta$  are the shape parameters and  $\bar{\varepsilon}^P$  is the equivalent plastic strain. As mentioned before, the plastic flow is considered in the shear only, hence, the yield function has the following form:

$$\Phi = \left| \tau_{\xi\eta} \right| - \sigma^y \leq 0 \tag{6}$$

And the total shear strain is calculated as

$$\varepsilon_{\xi\eta} = \varepsilon_{\xi\eta}^E + \varepsilon_{\xi\eta}^P \tag{7}$$

Locking angle  $\delta$  is expressed as the sum of two angles, the first  $\delta_1$  is the angle formed by axes  $e_1$  and  $\xi$  and the second  $\delta_2$  is the angle formed by axes  $e_2$  and  $\eta$  (Figure 2).

### 2.2 FE model

The Abaqus 6.13-4 software is used for finite-element analyses. User subroutine UMAT is used for the implementation of the material model. The size of

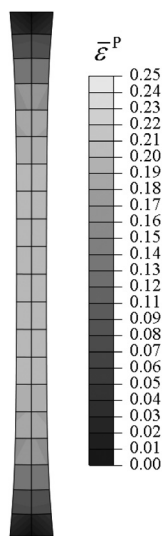


Figure 4: Deformed finite-element mesh with spatial distribution of the equivalent plastic strain for AP 45°

Slika 4: Deformirana mreža končnih elementov s prostorsko razporeditvijo enakovrednih napetosti za AP 45°

quadrilateral four-node plane-stress elements is 7.5 mm × 7.5 mm. The Newton-Raphson iteration scheme is used for solving the set of non-linear equations, resulting from the FE discretization.

Subroutines uexternaldb, disp, urdfil are used for controlling the cyclic loading process. The process is not trivial due to the high material nonlinearity. The specimens are loaded using the prescribed displacement of the grips and the elongation of a specimen is measured as the elongation of the area between the extensometer grips. Figure 4 shows the deformed finite-element mesh and the spatial distribution of  $\bar{\varepsilon}^P$  for specimen AP 45°.

### 2.3 Identification

Material parameters are identified using a combination of the finite-element model and experimental data<sup>5</sup>. The differences between the numerically and experimentally obtained force-displacement dependencies are minimized (Figure 5). The minimized function is proposed in the following form:

$$r_L = \sum_{\theta} \sum_{i=1}^N \left( \frac{F^E(\theta, \Delta l_i) - F^N(\theta, \Delta l_i)}{F_{max}^E(\theta)} \right)^2 \tag{8}$$

where  $N$  is the number of the time steps in the finite-element analysis,  $\theta$  is the angle of the used specimen type in a given identification,  $\Delta l_i$  is the elongation of the specimen in the  $i$ -th time step and the denominator is the maximum force in the experiment used as the weight coefficient.

In order to reduce the time consumption, the material parameters are identified in three separate steps.

1. Elastic parameters  $E_\xi$  and  $k_\xi$  are identified. Only angle  $\theta = 0^\circ$  is taken into account in (8).
2. Elastic parameters  $E_\eta$  and  $k_\eta$  are identified. Only angle  $\theta = 90^\circ$  is taken into account in (8).
3. Elastic parameter  $G_{\xi\eta}$  and plastic parameters  $\sigma_0^y$ ,  $\beta$  and  $\alpha$  are identified. Only angle  $\theta = 45^\circ$  for the materials with the plain weave and  $\theta = 15^\circ$  for the materials with the quasi-unidirectional weave are taken into account in (8).

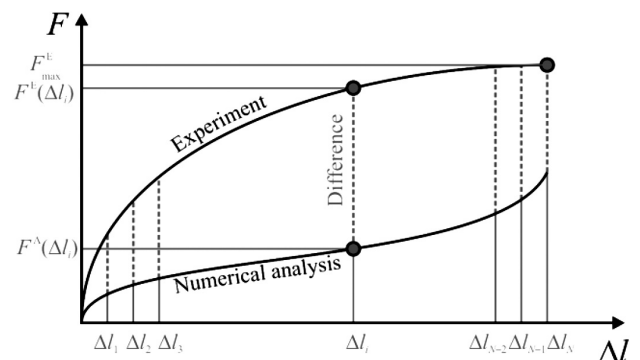


Figure 5: Difference between the finite-element result and the experiment

Slika 5: Razlika med rezultati končnih elementov in preizkusom

Poisson's ratio  $\nu_{\xi\eta}$  cannot be identified using the process mentioned above and must be identified separately. Therefore, the ratio (for each material) was measured using digital image correlation on the  $0^\circ$  specimens and was used as a constant in the identification process (Table 2).

Table 2: Poisson's ratios  
Tabela 2: Poissonovo razmerje

| Material | $\nu_{\xi\eta}$ |
|----------|-----------------|
| GP       | 0.24            |
| GU       | 0.24            |
| CP       | 0.19            |
| CU       | 0.19            |
| AP       | 0.31            |
| AU       | 0.31            |

Table 3: Identified material data  
Tabela 3: Ugotovljeni podatki materialov

|                    | GP   | GU   | CP   | CU    | AP    | AU   |
|--------------------|------|------|------|-------|-------|------|
| $E_{\xi}$ /GPa     | 17.7 | 40.1 | 51.3 | 139.4 | 28.9  | 48.4 |
| $E_{\eta}$ /GPa    | 17.1 | 12.6 | 51.2 | 8.7   | 29.9  | 8.4  |
| $k_{\xi}$          | -8.8 | -11  | 2.6  | -4.2  | -13   | -0.3 |
| $k_{\eta}$         | -25  | -88  | 3.8  | -54   | -12   | -4.8 |
| $G_{\xi\eta}$ /GPa | 2.2  | 4.1  | 3.0  | 4.1   | 1.2   | 1.5  |
| $\sigma_0$ /MPa    | 15.8 | 39.8 | 23.2 | 13.6  | 46.1  | 40.3 |
| $\beta$ /MPa       | 74.9 | 79.6 | 93.9 | 102.1 | 415.8 | 1585 |
| $\alpha$           | 0.23 | 1.27 | 0.28 | 0.26  | 1.86  | 2.2  |

Table 4: Maximum  $\bar{\epsilon}^p$   
Tabela 4: Maximum  $\bar{\epsilon}^p$

| Material | $\max(\bar{\epsilon}^p)$ | Specimen angle ( $^\circ$ ) |
|----------|--------------------------|-----------------------------|
| GP       | 0.111                    | 45                          |
| GU       | 0.019                    | 15                          |
| CP       | 0.131                    | 45                          |
| CU       | 0.007                    | 15                          |
| AP       | 0.250                    | 45                          |
| AU       | 0.131                    | 30                          |

Table 5: Locking angle  
Tabela 5: Kot zaklepanja

| Material | Type of specimen ( $^\circ$ ) | FEA max ( $\delta$ ) ( $^\circ$ ) | EXP max ( $\delta$ ) ( $^\circ$ ) |
|----------|-------------------------------|-----------------------------------|-----------------------------------|
| GP       | 45                            | 14                                | 15                                |
| GU       | 15                            | 3                                 | 4                                 |
| CP       | 45                            | 17                                | 26                                |
| CU       | 15                            | 1                                 | 10                                |
| AP       | 45                            | 34                                | 35                                |
| AU       | 15                            | 15                                | 20                                |

### 3 RESULTS

The identified material data (8 parameters) are listed in Table 3. Table 4 shows the maximum values of the equivalent plastic strain calculated in the models and the types of the specimens for which the maximum values were found. A comparison of the locking angles of the

weaves calculated in the models and the ones measured in the experiments is in Table 5. The results for all analysed materials are shown in Figures 6 to 13.

A slight deflection of the tensile dependencies for angles  $0^\circ$  and  $90^\circ$  is a natural result of the material non-linearity, the hardening and softening, and the fiber-tow entanglement<sup>4</sup>.

The resulting force-displacement dependencies for material GP are shown in Figure 6. Different shapes of the curves for  $0^\circ$  and  $90^\circ$  are caused by different numbers of the fibers in the warp ( $\xi$ ) and weft ( $\eta$ ) directions and different levels of the pre-stress of the material are caused by the processes of the entanglement of the weave and the injection of the epoxy matrix. Furthermore, it is not possible to precisely fit the pairs of the curves for  $15^\circ$ ,  $75^\circ$  and  $30^\circ$ ,  $60^\circ$  due to a large difference in the experimentally obtained results. This can be caused by different levels of damage in the warp and

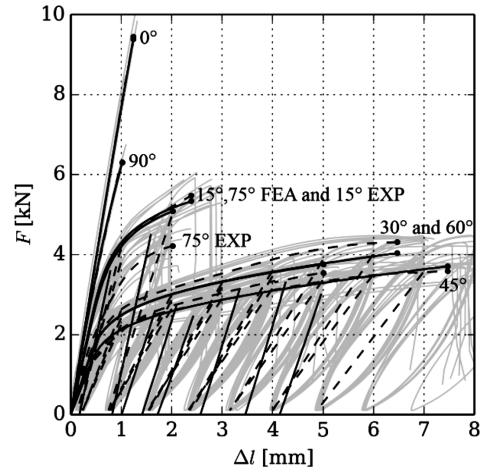


Figure 6: GP (solid line – FEA, dashed line – target/averaged experiments, gray – raw experiments)  
Slika 6: GP (polno – FEA, črtkano – ciljna vrednost/povprečje preizkusov, sivo – preizkusi)

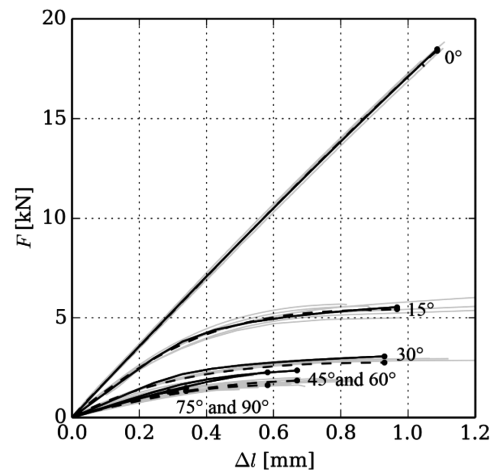
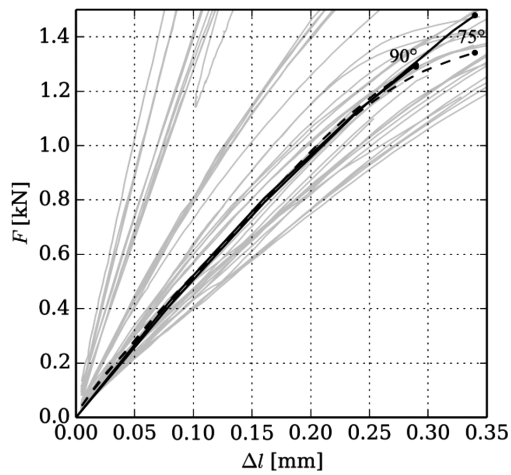
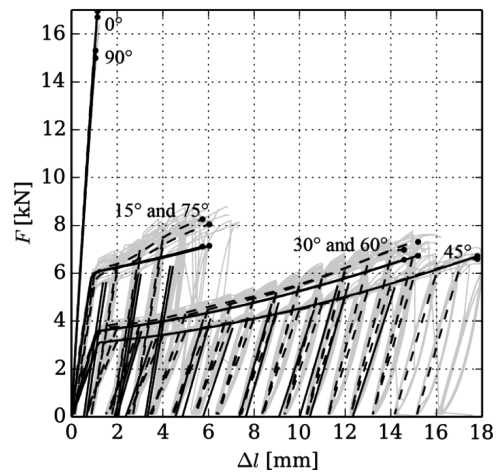


Figure 7: GU (solid line – FEA, dashed line – target/averaged experiments, gray – raw experiments)  
Slika 7: GU (polno – FEA, črtkano – ciljna vrednost/povprečje preizkusov, sivo – preizkusi)



**Figure 8:** GU zoomed view (solid line – FEA, dashed line – target/averaged experiments, gray – raw experiments)

**Slika 8:** GU povečan pogled (polno – FEA, črtkano – ciljna vrednost/povprečje preizkusov, sivo – preizkusi)



**Figure 11:** AP (solid line – FEA, dashed line – target/averaged experiments, gray – raw experiments)

**Slika 11:** AP (polno – FEA, črtkano – ciljna vrednost/povprečje preizkusov, sivo – preizkusi)

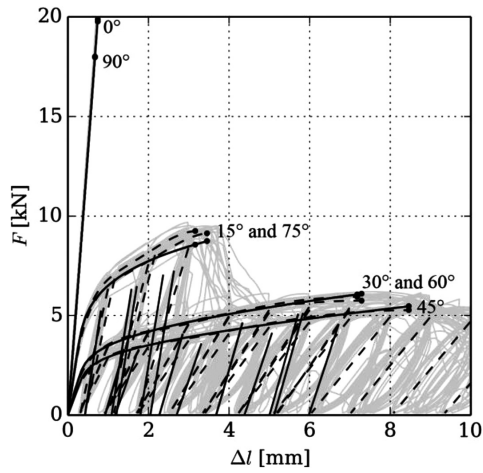


**Figure 9:** CP (solid line – FEA, dashed line – target/averaged experiments, gray – raw experiments)

**Slika 9:** CP (polno – FEA, črtkano – ciljna vrednost/povprečje preizkusov, sivo – preizkusi)

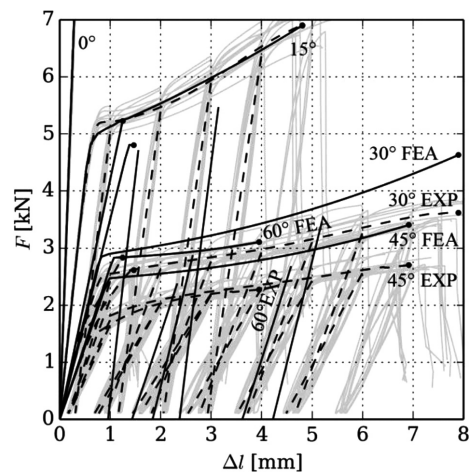


**Figure 12:** AU zoomed view (solid line – FEA, dashed line – target/averaged experiments, gray – raw experiments)

**Slika 12:** AU povečan pogled (polno – FEA, črtkano – ciljna vrednost/povprečje preizkusov, sivo – preizkusi)

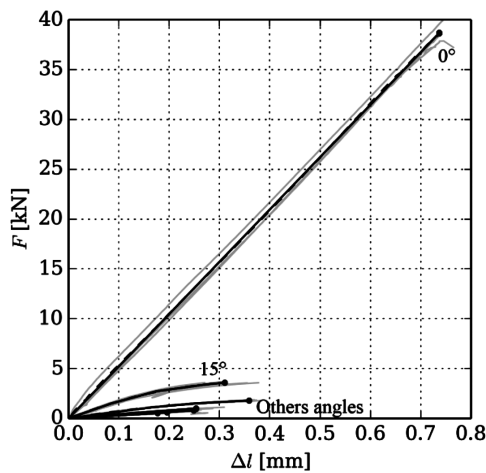


**Figure 10:** CU (solid line – FEA, dashed line – target/averaged experiments, gray – raw experiments)

**Slika 10:** CU (polno – FEA, črtkano – ciljna vrednost/povprečje preizkusov, sivo – preizkusi)

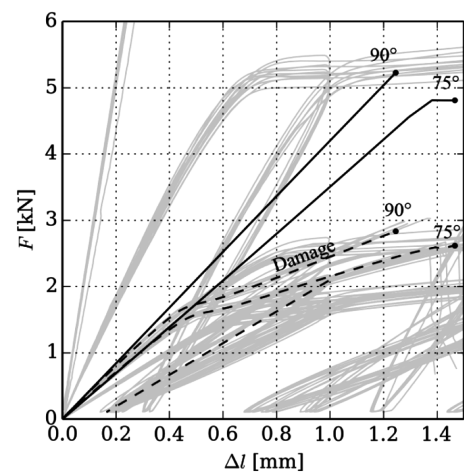


**Figure 13:** AU zoomed view (solid line – FEA, dashed line – target/averaged experiments, gray – raw experiments)

**Slika 13:** AU povečan pogled (polno – FEA, črtkano – ciljna vrednost/povprečje preizkusov, sivo – preizkusi)

weft directions that the model is not able to predict in the present state.

The results for GU (**Figure 7**) are fitted on  $0^\circ$ ,  $15^\circ$  and  $90^\circ$ . Nevertheless, even if the curves from the FEA and the experiments for angles  $0^\circ$  and  $90^\circ$  correspond perfectly, the curves for the other angles do not correspond. The difference between the curves for  $75^\circ$  obtained with the FEA and the experiment is shown in **Figure 8**. For comparison, the curve for  $90^\circ$  is included in the same graph (**Figure 8**).

We can say that the agreement between the FEA and the experiments for material CP (**Figure 9**) is sufficiently good. Exceptions are the tangents of the unload-load cycles and the impossibility of modeling a tensile test after reaching the maximum force-displacement dependencies (only the black dashed lines in **Figure 9**) that are the consequences of the behavior that is impossible to be captured using the model without damage.

Pure tensile curves without unload-load cycles were measured only for material CU. The results of the FEA show good agreement with the experiments. The results are similar to the ones obtained for the unidirectional carbon-epoxy material made from prepregs.

The best agreement was achieved for material AP (**Figure 11**) where the biggest differences between the FEA and the numerical results were found for  $15^\circ$  and  $75^\circ$ .

The lowest agreement between the FEA and the experimental results was achieved for the AU material. Non-negligible differences are visible for all the unfitted tensile curves, for the unload-load cycles and, unfortunately, even for the  $90^\circ$  dependency, where the model is inappropriate for damage modeling.

#### 4 CONCLUSION

A slight deflection of tensile dependencies for angles  $0^\circ$  and  $90^\circ$  is a natural result of the material nonlinearity, the hardening and softening and the fiber-tow entanglement.

Young's modulus  $E_1$  occasionally differs from  $E_2$ . This is caused by an inaccurate ratio of the fibers in the

tows in directions  $\xi$  and  $\eta$  or by a higher specimen preload in one of the mentioned directions, as a result of the manufacturing technology.

The force-displacement dependencies for the  $0^\circ$  and  $90^\circ$  specimens are usually non-linear as a result of the fiber-material nonlinearity (stiffening/softening) and the influence of the straightening of the originally wavy fiber tows (stiffening).

It was shown that it is possible to identify the material parameters for five out of six materials using only three force-displacement dependencies with a sufficient accuracy. However, damage modeling or degradation of the elastic material parameters is necessary for more precise simulations of the unload-load cycles.

Future work will be aimed at damage modeling, the compressive behavior of the materials and a precise determination of Poisson's ratios.

#### Acknowledgement

The work was supported by the European Regional Development Fund (ERDF), through project "NTIS – New Technologies for Information Society", European Centre of Excellence, CZ.1.05/1.1.00/02.0090 and the student research project of Ministry of Education of Czech Republic No. SGS-2013-036.

#### 5 REFERENCES

- <sup>1</sup> V. Laš, Mechanics of Composite Materials, University of Bohemia, Plzen 2004 (in Czech)
- <sup>2</sup> V. Laš, R. Zemčík, Progressive Damage of Unidirectional Composite Panels, Journal of Composite Materials, 42 (2008) 1, 25–44, doi:10.1177/0021998307086187
- <sup>3</sup> K. J. Bathe, Finite element procedures, Prentice hall, Upper Saddle River, New Jersey, USA 2007
- <sup>4</sup> S. Ogiwara, K. L. Reifsnider, Characterization of Nonlinear Behavior in Woven Composite Laminates, Applied Composite Materials, 9 (2002), 249–263, doi:10.1023/A:1016069220255
- <sup>5</sup> T. Kroupa, V. Laš, R. Zemčík, Improved nonlinear stress–strain relation for carbon–epoxy composites and identification of material parameters, Journal of Composite Materials, 45 (2011) 9, 1045–1057, doi:10.1177/0021998310380285

# INFLUENCE OF THE TYPE AND NUMBER OF PREPREG LAYERS ON THE FLEXURAL STRENGTH AND FATIGUE LIFE OF HONEYCOMB SANDWICH STRUCTURES

## VPLIV VRSTE IN ŠTEVILA PLASTI NA UTRDITEV UPOGIBNE TRDNOSTI IN ZDRŽLJIVOSTI PRI UTRUJANJU SATASTIH SENDVIČNIH KONSTRUKCIJ

Ladislav Fojtl<sup>1</sup>, Sona Rusnakova<sup>1</sup>, Milan Zaludek<sup>1</sup>, Vladimír Rusnák<sup>2</sup>

<sup>1</sup>Faculty of Technology, TBU in Zlín, Nad Stranemi 4511, 760 05 Zlín, Czech Republic

<sup>2</sup>Faculty of Metallurgy and Materials Engineering, VŠB-Technical University of Ostrava, 17. listopadu 15, 708 33 Ostrava-Poruba, Czech Republic  
fojtl@ft.utb.cz

*Prejem rokopisa – received: 2014-07-29; sprejem za objavo – accepted for publication: 2014-09-18*

doi:10.17222/mit.2014.124

This research paper deals with an investigation of the flexural properties measured in a three-point bending test depending on the type and number of the E-glass prepreg layers applied to the facing sides of the resulting sandwich structure used for floor panels in the transport industry. The values of the low-cycle fatigue were measured according to the values of the flexural strength obtained from the static test. Cycling was performed at (70, 60 and 50) % values of the ultimate flexural load. Moreover, a decrease in the flexural strength and stiffness depending on the number of cycles was also studied. For the production of samples, one type of aluminum honeycomb core and various phenolic prepreps with different numbers of layers were used. These samples were produced with two, in practice commonly used methods – compression molding and vacuum bagging. The measured results show that the production technology has a certain influence on the mechanical behavior in bending and the fatigue life of sandwich structures. The experimental results proved that the type of prepreg (defined by the reinforcing fabric and the amount of resin) and the number of layers also affect the properties of these structures. All the obtained results provide useful information for designing the sandwich structures for the transport industry.

Keywords: sandwich structure, honeycomb, prepreg, fatigue, flexural strength, flexural stiffness

Članek obravnava preiskave lastnosti pri upogibu, izmerjene s tritočkovnim upogibnim preizkusom, v odvisnosti od vrste in števila plasti E-stekla na utrditev, uporabljenih na čelni strani sendvičnih konstrukcij, ki se uporabljajo v transportu za talne plošče. Vrednosti malociklične utrujenosti so bile izmerjene skladno z vrednostmi upogibne trdnosti, dobljenimi pri statičnem preizkusu. Ciklično obremenjevanje je bilo izvršeno pri (70, 60 in 50) % vrednosti upogibne trdnosti. Poleg tega je bilo preučevano tudi zmanjšanje upogibne trdnosti in togosti v odvisnosti od števila ciklov. Za pripravo vzorcev je bila uporabljena ena vrsta sataste osnove iz aluminija in različne fenolne plasti za utrjenje z različnim številom plasti. Ti vzorci so bili izdelani z dvema običajnim metodama – s tlačnim litjem in vakuumskim pakiranjem. Izmerjeni rezultati kažejo, da ima tehnologija izdelave določen vpliv na mehansko vedenje pri upogibanju in utrujanju sendvičnih konstrukcij. Rezultati eksperimentov so pokazali, da vrsta plasti za utrjanje (določena s tkanino za utrjanje in količino smole) in število plasti tudi vplivata na lastnosti teh konstrukcij. Vsi dobljeni rezultati zagotavljajo koristne informacije za konstruiranje sendvičnih konstrukcij v transportni industriji.

Ključne besede: sendvične konstrukcije, satje, plast za utrjanje, utrujenost, upogibna trdnost, upogibna togost

## 1 INTRODUCTION

Sandwich structures belonging to a large group of composite materials are applied in many industry sectors such as transportation (interior or exterior parts), construction (insulation elements) and aviation (supporting elements or parts in the interior). With an expanding area of application, durability requirements on sandwich structures also increase. The most often used core materials are polymeric foams, honeycombs or, alternatively, cork and balsa, whereas the face materials are metals, aluminum sheets, HPL sheets and fiber laminates or prepreps (pre-impregnated laminates).<sup>1,2</sup>

Prepreps differ in the type of material (glass, Kevlar, carbon) and in the fabric weight depending on the type of the weave, in which the fibers are arranged. Further-

more, different types of resin such as phenol, epoxy, bismaleimide (BMI) and cyanide are used for the impregnation of prepreg fabrics.<sup>3</sup>

During their use, these structures are most often subjected to the bend or impact stress, where the maximum flexural stress is carried by the face material, while the core is barely stressed. This flexural stress leads to the compression of the structure on one side and the tension on the other side, while the core carries only the shear stress. It can be said that sandwich materials stand out particularly for a large flexural stiffness, a flexural strength and a high impact resistance, while having the minimum mass.<sup>4</sup>

In some applications, sandwich structures are subjected to repeated loading, where, more than in the previous cases, all the structural properties depend not only

on the materials used, but also on the quality of their connections with the unit. Cyclic loading produces a considerable decrease in the strength and modulus; this decrease is called the fatigue. The fatigue strength is strongly dependent on the quality of the connections of individual components creating a sandwich structure, namely, on the interface between the core and the prepreg fabrics. The start of a material failure during fatigue is characterized by the creation of small cracks (in most cases invisible to naked eye), which gradually connect and extend through the sample. In these cracks, a stress concentration causes their rapid growth continuing to a sudden fracture.<sup>2,5</sup>

The results of the experiments are used for a construction of  $S - N$  diagrams, which show the number of cycles ( $N$ ) that a structure can withstand at a certain loading value ( $S$ ). Due to these diagrams we can predict the durability of sandwich structures during their application.

The research of sandwich structures and their behavior during dynamic loading has been the subject of many studies for a long time. Previous research was focused on the influence of the thickness of the adhesive layer on the sandwich fatigue strength<sup>6,7</sup>, or on the study of the creation and propagation of the cracks in foam cores.<sup>8-11</sup>

However, no previous research was focused on the prepreg materials in combination with aluminum honeycombs, specifically on the dynamic behavior of these structures. The aim of the presented research is to investigate the influence of the type of pre-impregnated fabric and the number of layers in the facings on the static and cyclic flexural behaviors of honeycomb sandwich structures. The effect of the manufacturing technology on the static and dynamic properties of the prepared structures is also evaluated with the experimental measurements.

## 2 EXPERIMENTAL WORK

### 2.1 Materials

The researched sandwich structures were composed of different prepreg materials for the inner and outer facing layers and an aluminum honeycomb core with a hexagonal cell shape. E-glass prepreps PHG840N-G213-40 (P1) and PHG840N-F300-47 (P2), both impregnated with phenolic resin, were obtained from the Gurit company and honeycomb ECM 6.4-82 (H1) was from the Euro-Composites company. The latter prepreg was used to verify its excellent adhesion to aluminum honeycombs stated by the producer. The important parameters of the materials are presented in **Table 1**. The prepreg materials were chosen due to their use for rail interiors resulting from their excellent FST (fire-smoke-toxicity) behavior.

A total of four different sandwich structures were prepared from the above materials. Sample A was

formed of two outer layers of PHG840-G213-40, the ECM 6.4-82 core and one inner layer of the same prepreg. Sample B had the same composition, but two layers of PHG840-G213-40 were used for the inner layer. Sample C consisted of layers of both PHG840-G213-40 and PHG840N-F300-47 (the latter was closer to the core). These samples (A, B, C) were produced with vacuum bagging. The last sample, D, had absolutely the same composition as sample A, but was produced with compression molding.

**Table 1:** Parameters of prepreg materials and honeycomb

**Tabela 1:** Parametri plasti za utrditev in satje

| Materials | Fabric mass<br>g/m <sup>2</sup> | Resin mass<br>content w/% | Cell size<br>mm | Density<br>kg/m <sup>3</sup> |
|-----------|---------------------------------|---------------------------|-----------------|------------------------------|
| P1        | 820                             | 40                        | –               | –                            |
| P2        | 300                             | 47                        | –               | –                            |
| H1        | –                               | –                         | 6.4             | 82                           |

### 2.2 Preparation of sandwich samples

As mentioned above, samples A, B and C were prepared with vacuum bagging, while sample D with compression molding. The production using vacuum bagging followed the standard procedure, when, after achieving a sufficient value of vacuum (0.8 MPa), the whole assembly was placed into a curing oven. The samples were heated, in 60 min, from 23 °C to 130 °C and then held isothermally in the oven for 120 min. Conversely, compression molded sample D was placed into a laboratory press heated to 160 °C and compressed with a pressure of 2.5 MPa for 10 min.

### 2.3 Flexural tests

A static flexural test (a three-point bending test) was performed and evaluated according to EN 2746 on a ZWICK 1456 testing machine. The samples were placed on the supports (radius  $R = 5$  mm) with a distance of 120 mm between each other, and the crosshead speed was set to 10 mm/min. Totally, at least 5 samples were tested to obtain the average ultimate load for each type of structure. Fatigue tests were performed according to ČSN 640618 on an Instron 8871. The setting of this machine was based on the previously performed tests, according to which an appropriate loading frequency of 3 Hz was selected. This frequency was also selected to prevent a rise in the local temperature in a specimen during the testing.<sup>7</sup> The course of the loading was set to pressure pulsating, where the medium load of oscillation ( $F_o$ ) and the amplitude of the oscillation load ( $F_a$ ) were also set in the software (**Figure 1**).

The intensity of force  $F_o$  was derived from static ultimate load  $F_{max}$ . Specific values are given in **Table 2**. In both of these tests, flat sandwich samples with the dimensions of 150 mm × 20 mm were used. All the experiments were conducted at room temperature ((23 ± 1) °C).

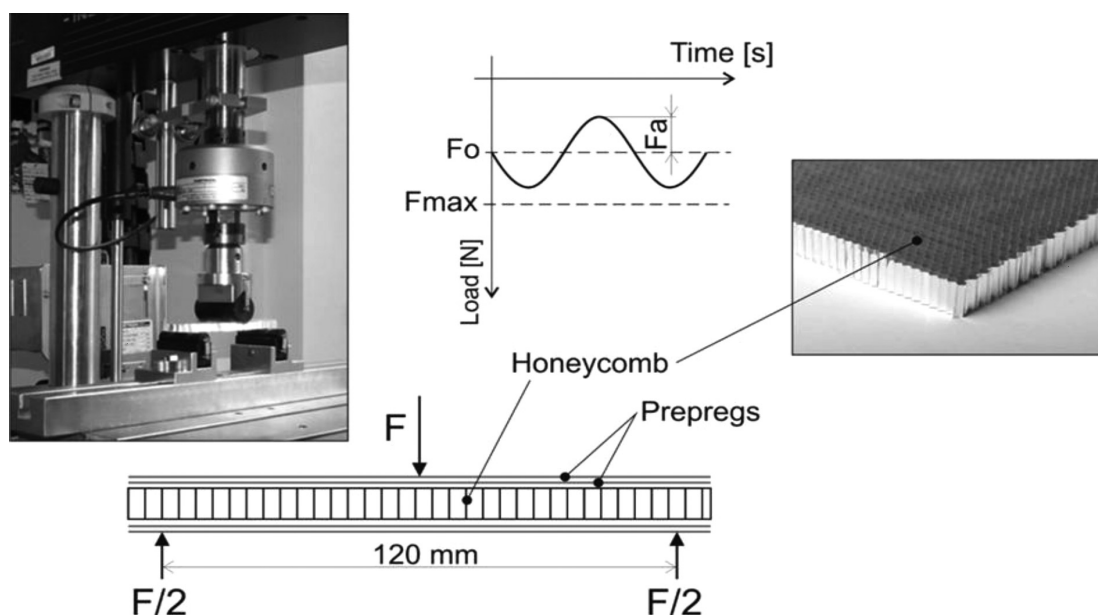


**Figure 1:** Set-up of the testing machine for flexural fatigue tests  
**Slika 1:** Sestav preizkusne naprave za preizkuse utrujanja pri upogibu

**Table 2:** Set-up of the loads for fatigue tests  
**Tabela 2:** Nastavitve obremenitev pri preizkusu utrujanja

|          | Medium load of oscillation $F_0$ (N) | Amplitude of oscillation load $F_a$ (N) |          | Medium load of oscillation $F_0$ (N) | Amplitude of oscillation load $F_a$ (N) |
|----------|--------------------------------------|-----------------------------------------|----------|--------------------------------------|-----------------------------------------|
| Sample A | 200                                  | $\pm 150$                               | Sample D | 210                                  | $\pm 160$                               |
|          | 175                                  | $\pm 125$                               |          | 180                                  | $\pm 130$                               |
|          | 150                                  | $\pm 100$                               |          | 155                                  | $\pm 105$                               |

### 3 RESULTS AND DISCUSSION

#### 3.1 Static flexural test

The three-point bending test was conducted to obtain the values of the average ultimate flexural loads ( $F_{max}$ ), which are shown in **Figure 2**, including the error bars (showing the minimum and maximum values) and the standard deviations. As can be seen, the highest value of the ultimate flexural load was measured for sample C

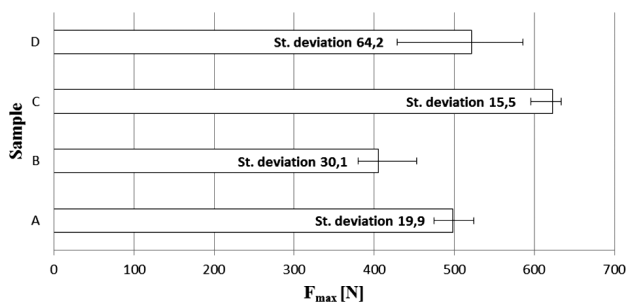


**Figure 2:** Average ultimate flexural loads for individual sandwich structures

**Slika 2:** Povprečje največjih upogibnih obremenitev za posamezne sendvične konstrukcije

having one layer of prepreg PHG840N-F300-47 in each facing. The results for this sample also show the lowest value of the standard deviation. In contrast, sample B, which has the same number of prepreg layers in the facings, shows about a 35 % lower value of the ultimate flexural load compared to sample C. It is also necessary to note that the fabric weight of the second prepreg is more than 2.5 times higher and that both preprags differ in the fabric weave style. Comparing samples A and D, manufactured with different technologies, we find that the samples manufactured with compression molding show higher average values of the ultimate flexural loads. However, these values are burdened with a higher variance leading to a three-time higher standard deviation compared to the values obtained for sample A.

#### 3.2 Flexural-fatigue test

The experiment for fatigue tests was based on the values of  $F_{max}$ . The medium loads of oscillation ( $F_0$ ) were set as (40, 35 and 30) % of the measured  $F_{max}$ , where the maximum applied loads during the sinusoidal loading ( $F_0 + F_a$ ) were equal to (70, 60 and 50) % of  $F_{max}$ . **Table 2** shows the specific-value set for cycling. Repeated loading was performed only for samples A and D to validate the influence of the production technology on the static and dynamic properties of the sandwich structures with identical material composition.

Fatigue curves were obtained from the measured data using an estimation of a logarithmic regression. This type of regression showed the highest value of reliability parameter  $R^2$ . The resulting curves obtained from the measured data are presented in **Figure 3**. For  $F_0 + F_a$  corresponding to 60 % of  $F_{max}$  sample A shows a greater number of cycles compared to sample D, similarly as in

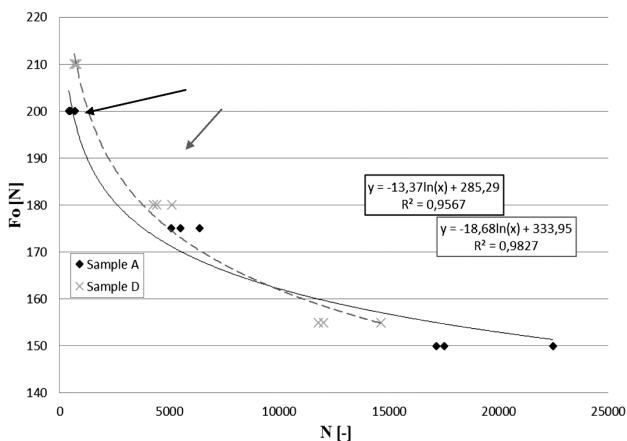


Figure 3: Fatigue curves for the samples produced with different production technologies

Slika 3: Krivulje utrujanja pri vzorcih, izdelanih po različnih tehnologijah

the case of  $F_o + F_a = 50\%$  of  $F_{max}$ . During this loading, sample A survived nearly 3000 cycles more than the other sample. In contrast, the number of cycles measured for  $F_o + F_a$  corresponding to 70% of  $F_{max}$  is not significantly different.

Furthermore, the cycling with the maximum applied load ( $F_o + F_a$ ) corresponding to 70% of  $F_{max}$  was performed for samples B and C in order to obtain the values of the flexural modulus and the tensile strength after (5000, 10000 and 15000) cycles. After these numbers of cycles, a single statistic flexural test was performed. The measured data are shown in the following figure, which also gives the results of the static test ( $N = 1$ ).

A decrease in the flexural modulus –  $E(f)$  – for samples B and C is depicted in Figure 4. Both samples show an almost identical decrease of 25% in the modulus after 5000 cycles. As can be seen, after 10000 and also after 15000 cycles, sample B does not exhibit any significant decline in the modulus. On the contrary, sample C shows a downward trend in the flexural modulus, by approximately 5% per each additional 5000-cycle set.

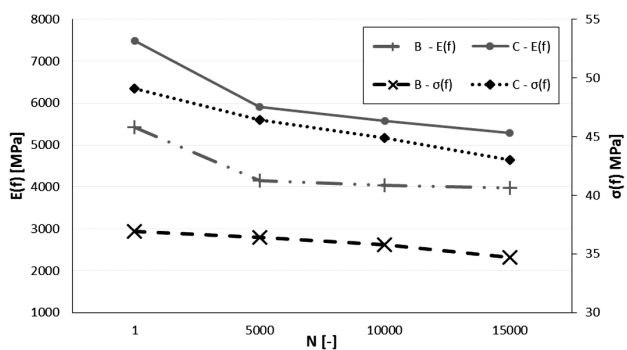


Figure 4: Decrease in flexural modulus –  $E(f)$  and flexural strength –  $\sigma(f)$  for samples B and C

Slika 4: Zmanjšanje modula upogiba  $E(f)$  in upogibne trdnosti  $\sigma(f)$  pri vzorcih B in C

The decline in the flexural strength –  $\sigma(f)$  – is not so significant. As depicted in the same figure, a more significant decrease again occurs in sample C with prepreg PHG840N-F300-47 containing the fabric with a lower areal weight and a greater amount of resin. This decrease is equal to approximately 2 MPa after every 5000 cycles. The strength after 15000 cycles decreased to 88% of the original value from the static test. Conversely, the decrease for sample B is in tenths of MPa, where the strength after 15000 cycles is equal to 94% of the original value obtained from the static test.

#### 4 CONCLUSIONS

The research evaluated the influences of the type and the number of the prepreg layers on the flexural properties and the bending fatigue. The results indicate that the type (characterized by the type of reinforcing fabric and resin content) significantly affects the lifetime of sandwich structures under cyclic bending. The experiments showed that the usage of a prepreg with a larger resin amount and a lower fabric weight leads to a significant increase in the fatigue lifetime, generally by 25%. This is apparently caused by the creation of a larger contact area between the prepreg fabric and the honeycomb cells due to the leak of a larger amount of resin and the formation of a larger radius of resin in the corner between the cells and the prepreg fabric. However, it must be noted that the fabric weave style in the prepreg can also influence the bending behavior of sandwich structures. The research further revealed that the technology with which a sandwich structure is prepared has a certain influence on the mechanical properties of this structure. It was found that the compression-molding technology, which is very productive and less demanding on the support materials in comparison to vacuum bagging negatively effects the fatigue lifetime. However, all the previous conclusions are valid only for the structures studied by the authors. In order to apply the results in practice and make the final conclusions, it is necessary to prepare new sandwich structures composed of different types of prepreg materials with a varying resin amount and also use honeycombs with different cell sizes.

#### Acknowledgement

This study was supported by an internal grant of TBU in Zlín, No. IGA/FT/2015/001, funded from the resources for specific university research. Furthermore, the article was written with the support of the Operational Program Research and Development for Innovations co-funded by the ERDF and the national budget of the Czech Republic, within the framework of project Centre of Polymer Systems (reg. number: CZ.1.05/2.1.00/03.0111).



## 5 REFERENCES

- <sup>1</sup> D. Zenkert, Nordic Industrial Fund, *The Handbook of Sandwich Construction*, 1st ed., EMAS Publishing, Worcestershire, UK 1997
- <sup>2</sup> T. N. Bitzer, *Honeycomb Technology: Materials, Design, Manufacturing, Applications and Testing*, 1st ed., Chapman & Hall, London, UK 1997
- <sup>3</sup> HexPly® Prepreg Technology [online], 2014, [cited 2014-28-05] Available from World Wide Web: <http://www.hexcel.com/resources/technology-manuals>
- <sup>4</sup> J. R. Vinson, *The Behavior of Sandwich Structures of Isotropic and Composite Materials*, 1st ed., CRC Press, New York, USA 1999
- <sup>5</sup> M. Burman, *Fatigue crack initiation and propagation in sandwich structures*, Dissertation thesis, Royal Institute of Technology, Stockholm, 1998
- <sup>6</sup> Y. Jen, L. Chang, Effect of thickness of face sheet on the bending fatigue strength of aluminum honeycomb sandwich beams, *Engineering Failure Analysis*, 16 (2009), 1282–1293, doi:10.1016/j.engfailanal.2008.08.004
- <sup>7</sup> Y. Jen, Ch. Ko, H. Lin, Effect of the amount of adhesive on the bending fatigue strength of adhesively bonded aluminum honeycomb sandwich beams, *International Journal of Fatigue*, 31 (2009), 455–462, doi:10.1016/j.ijfatigue.2008.07.008
- <sup>8</sup> B. Shafiq, A. Quispitupa, Fatigue characteristics of foam core sandwich composites, *International Journal of Fatigue*, 28 (2006), 96–102, doi:10.1016/j.ijfatigue.2005.05.002
- <sup>9</sup> M. Burman, D. Zenkert, Fatigue of foam core sandwich beams-1: undamaged specimens, *International Journal of Fatigue*, 19 (1997), 551–561, doi:10.1016/S0142-1123(97)00069-8
- <sup>10</sup> M. K. Farooq, A. El Maihi, S. Sahraoui, Modelling the flexural behaviour of sandwich composite materials under cyclic fatigue, *Materials & Design*, 25 (2004), 199–208, doi:10.1016/j.matdes.2003.09.022
- <sup>11</sup> N. Kulkarni, H. Mahfuz, S. Jeelani, L. A. Carlsson, Fatigue crack growth and life prediction of foam core sandwich composites under flexural loading, *Composite Structures*, 59 (2003), 499–505, doi:10.1016/S0263-8223(02)00249-0



# POTENTIAL FOR OBTAINING AN ULTRAFINE MICROSTRUCTURE OF LOW-CARBON STEEL USING ACCUMULATIVE ROLL BONDING

## MOŽNOSTI DOSEGANJA ULTRADROBNOZRNATE MIKROSTRUKTURE PRI SPAJANJU MALOOGLEJČNEGA JEKLA Z AKUMULATIVNIM VALJANJEM

**Tomáš Kubina, Jaroslav Gubiš**

COMTES FHT, Prumyslova 995, 334 41 Dobruška, Czech Republic  
tkubina@comtesfht.cz

*Prejem rokopisa – received: 2014-07-30; sprejem za objavo – accepted for publication: 2014-09-18*

doi:10.17222/mit.2014.136

The objective of the present work was to trial the ARB method on commercially available steels with the mass fraction of carbon 0.011 %. Specimens were prepared with great care, mainly with respect to their surfaces and shapes, to successfully achieve, at an elevated temperature, a mass reduction 50 % in a single pass. The specimens were protected against scale formation at testing temperatures of 500–600 °C. Due to the complexity of the ARB method, only two bonding cycles were completed. The initial mean grain size was  $(18 \pm 7)$  μm; after the first ARB cycle, the grains had a length of  $(24 \pm 10)$  μm and a width of  $(8 \pm 3)$  μm. The ultrafine-grained surface layer had a thickness of approximately 150–200 μm. After the second ARB cycle, the microstructure of this type was found in the centre of the specimens. After two passes the strength reached 660 MPa, but the elongation dropped to 3.3 %. The ultimate strength of the annealed feedstock was  $(290 \pm 3)$  MPa and its elongation was  $A_{50}$   $(49 \pm 2)$  %. Experience shows that a continuous bonding of the material would be more effectively achieved with coiling machines, preventing the problems arising from the cracks in the welded joints on the faces of the specimens.

Keywords: low-carbon steel, accumulative roll bonding, microstructure, mechanical properties

Cilj predstavljenega dela je bil preizkus ARB-metode pri komercialnih jeklih z masnim deležem ogljika 0,011 %. Vzorci so bili pripravljene z veliko pazljivostjo glede površine in oblike, da bi uspešno dosegli pri povišani temperaturi 50-odstotno zmanjšanje debeline v enem prehodu. Vzorci so bili zaščiteni pred nastankom škake pri temperaturah preizkusa 500–600 °C. Zaradi kompleksnosti ARB-metode sta bila dokončana samo dva cikla povezovanja. Začetna srednja velikost zrn je bila  $(18 \pm 7)$  μm, po prvem ARB-ciklu so bila zrna dolga  $(24 \pm 10)$  μm in široka  $(8 \pm 3)$  μm. Površinski sloj ultradrobnozrn je bil debel okrog 150–200 μm. Po drugem ARB-ciklu je bila podobna mikrostruktura tudi v sredini vzorca. Trdnost je po dveh prehodih dosegla 660 MPa, raztezek pa se je zmanjšal na 3,3 %. Končna trdnost žarjenega surovca je bila  $(290 \pm 3)$  MPa, raztezek  $A_{50}$  pa  $(49 \pm 2)$  %. Izkušnje kažejo, da bi bilo spajanje materiala bolj učinkovito z uporabo navijalcev, kar bi preprečilo težave s pojavom razpok v zvarjenih spojih na čelni strani vzorca.

Ključne besede: maloogljечно jeklo, spajanje z akumulativnim valjanjem, mikrostruktura, mehanske lastnosti

## 1 INTRODUCTION

Severe-plastic-deformation (SPD) methods belong to the techniques for producing fine-grained microstructures of metals, whereby a material's strength is improved by the grain-size strengthening mechanism. It is achieved by imparting extremely high stresses and applying a large plastic deformation with a shear stress to the metals. In conventional forming processes, such as forging, rolling or ordinary extrusion, the accumulated imparted strain  $\epsilon$  is normally less than 2. When a larger strain is applied, e.g., by rolling, the product becomes very thin and unsuitable for structural applications. To date, about a dozen methods for achieving fine-grained microstructures have been developed by applying a large plastic deformation with a strain level of more than 2, while preserving the workpiece dimensions.<sup>1</sup> When a large plastic strain is imparted, dislocations become absorbed by subgrain boundaries. Low-angle boundaries

thus become high-angle boundaries (a misorientation angle of  $\theta > 10^\circ$ ) and the grain size is decreased.<sup>2</sup> The most significant and currently most frequently used SPD methods include ARB (accumulative roll bonding), ECAP (equal-channel angular pressing) and its various variants and the HPT (high-pressure torsion) method.

ARB was developed by the team of prof. Saito in Japan in 1999. The method essentially involves stacking and bonding the stacked metal sheets by repeated cold rolling or warm rolling. The bonding is achieved by bringing the surfaces of metal sheets close together and by the resulting atomic-level interaction. Therefore, an essential precondition for creating a joint is a high quality of the surfaces. The surfaces of the metal sheets are prepared by grinding and degreasing. After the rolling, the rolled workpiece is split into halves and the surfaces of both parts are finished using the same procedure. The feedstock prepared in this manner is stacked again for the next processing cycle.<sup>3</sup>

In theory, a material can undergo the bonding, splitting and stacking sequences numerous times. Thus, the number of manufacturing cycles could be high as the material's final thickness does not change in the process. However, the achievable number of passes is limited by work-hardening processes and by surface-quality deterioration. Most references mention the maximum number of 5–10 passes.<sup>4–6</sup> The rolling is typically carried out at elevated temperatures below the material recrystallization temperature to prevent the release of the accumulated strain energy due to recrystallization. Typical rolling temperature for low-carbon steels are shown in **Table 1**. References<sup>7–9</sup> were selected according to the smallest grain size achieved. Otherwise, the effect of the process would be lost. On the other hand, low temperatures lead to an inadequate joint quality and to the cracking caused by impaired formability.

**Table 1:** Overview of the parameters and results achieved with the ARB method

**Tabela 1:** Pregled parametrov in rezultati, dobljeni z ARB-metodo

| Rolling temperature<br>°C | Number of cycles | Applied strain | Grain size |         | Source |
|---------------------------|------------------|----------------|------------|---------|--------|
|                           |                  |                | before     | after   |        |
|                           |                  |                | µm         | µm      |        |
| 500                       | 7                | 5.6            | 20         | 0.2–0.3 | 7      |
| 550                       | 8                | 6.4            | 5–27       | < 0.1   | 8      |
| 500                       | 5                | 6.4            | 30         | < 0.5   | 9      |

## 2 EXPERIMENTAL WORK

The experimental material was plain low-carbon steel supplied by the Třinecké železářny company. Its chemical composition (**Table 2**) was in accordance with the ČSN 41 1300 standard<sup>10</sup> and selected on the basis of the survey of the references. In the majority of the available studies<sup>3,4,11,12</sup> an IF steel was used and the composition of the present steel is closest to that of the IF steel. Continuously cast slabs of 150 mm × 150 mm × 350 mm were forged in a universal hydraulic press at 1200 °C. The finish-forging temperature was 900 °C. The dimensions of the final forgings were approximately 95 mm × 147 mm × 500 mm. The forgings were annealed in a roller-hearth furnace for 60 min at 1200 °C and then rolled at the same temperature to a thickness of 8 mm. The hot-rolled condition was chosen as the initial condition of the material. A two-high rolling mill with rolls of a 550 mm diameter was used for this purpose.

**Table 2:** Chemical composition of the initial continuously cast slab in mass fractions, w/%

**Tabela 2:** Kemijska sestava začetnega kontinuirno ulitega slaba v masnih deležih, w/%

| C     | Si    | Mn    | P     | S       | Cr    | Mo     |
|-------|-------|-------|-------|---------|-------|--------|
| 0.011 | 0.022 | 0.159 | 0.006 | 0.015   | 0.037 | 0.001  |
| Cu    | Al    | As    | B     | Ce      | N     | Fe     |
| 0.009 | 0.002 | 0.002 | 0.009 | < 0.003 | 0.003 | 99.691 |

Before the cold rolling the scale was removed from the hot-rolled sheets using a belt sander with the P80- and P320-grit abrasives. The sheets of 7.7 mm were cold-rolled to a thickness of 2 mm in a four-high rolling mill with diameter rolls 240 mm, coated with a protective film against decarburization and then recrystallization annealed at 700 °C for 2 h. The metal sheets treated in this manner were then used for making input specimens for the ARB process.

The future contact surfaces of these specimens were degreased using acetone and then roughened by grinding or scrubbing. The leading edges of the specimens were spot-welded together and the trailing ends were tied together with the wires running through pre-drilled holes. The leading edges were ground to a wedge shape to facilitate the entry into the roll gape. The deformation was carried out in a single step with a constant reduction of 50 % in all the passes. The specimens were heated in a HERAEUS electric furnace filled with nitrogen to suppress surface oxidation. As the furnace was stationed next to the rolling mill, the rolling temperature was only slightly lower than the soaking temperature (by 5 °C to 10 °C). The specimens prepared for the second pass were first descaled by pickling in Clark's solution, then the same sequence was used as with the specimens for the first pass: grinding with the P40-grit abrasive, spot welding the corners of the leading edge and tying the trailing ends with wires. Details of the procedure are given in<sup>13</sup>.

After the tests aimed at finding suitable processing conditions, a set of 10 specimens was made using a single cycle, of which 5 specimens were prepared for the second ARB cycle. The specimens were heated in the HERAEUS furnace at 515 °C in nitrogen with a flow rate of 40 L/min and after the soaking for 5 min the rolling was immediately performed.

The microstructures of all the rolled specimens at all the stages were examined using optical and electron microscopy. Metallographic sections were prepared by means of a Struers Discotom-6 grinding and polishing machine using the program for metallographic preparation of steels. The etchant used in all the cases was nital (5 % HNO<sub>3</sub> + ethanol + methanol). Micrographs were taken using a Nikon Epiphot 200 light microscope with the NIS Elements 2.3 software for image digital processing, analysing and assessing the grain size. EBSD mapping was carried out using a JEOL 7400F microscope with a field-emission cathode. The instrument is provided with a HKL NORDLYS high-speed EBSD camera. The specimens for EBSD mapping were electrolytically polished using a Movipol polisher. In order to determine the spatial grain orientation more accurately, the pole figures in individual EBSD maps were evaluated as well.

The hardness values for the hot-rolled, cold-rolled and recrystallized sheets were measured using a Struers Durascan automatic hardness tester with the Workflow software. The hardness-depth profiles of the specimens

were measured after one and two ARB cycles. Tension-test plots were obtained by means of a Zwick/Roell Z250 testing machine. The tension tests were carried out according to the ČSN EN ISO 6892-1 standard.<sup>14</sup>

### 3 RESULTS AND DISCUSSION

The quality of the joint was controlled primarily with the presence of the oxide layer, whose thickness depended on the access of oxygen to the surface, and on the duration and the temperature of the soaking. Various combinations of these parameters showed that the most effective means of heating the specimens was the electric furnace with nitrogen gas. Soaking for 5 min led to relatively sound joints which are described in the following section. In an effort to reduce the soaking time, induction heating was tried as well. The technical conditions, however, did not allow the nitrogen atmosphere to be used. This drawback outweighs the benefits of rapid heating. Induction heating also proved inadequate because it caused a non-uniform heating and cracking.

It is believed that to obtain a quality joint, a higher surface hardness is required as it supports the adhesion between the materials.<sup>12</sup> Another factor in selecting the surface-preparation method was its speed and ease of application because in the investigation no substantial impact of the surface-preparation technique on the joint quality was found. This was probably due to the fact that the study involved a large number of variables with a stronger impact on the quality of the joint than that of the sheet surface. As a result, grinding with a P40 abrasive wheel was selected for the surface preparation.

**Figure 1** shows the microstructure of the sheet annealed at 700 °C for 2 h with equiaxed grains and a uniform grain size of  $(15 \pm 7) \mu\text{m}$  on the transverse cross-section and of  $(18 \pm 7) \mu\text{m}$  on the longitudinal cross-section. The longitudinal cross-section shows that recrystallization transformed the deformed and elongated grains into finer and undeformed grains. The only discernible

trace of cold forming is the orientation of inclusions which was not changed by recrystallization.

The microstructure after the first ARB cycle is shown in **Figure 2**. Again, there is a surface layer of ultrafine grains with a thickness of 150–200  $\mu\text{m}$ . There is also a

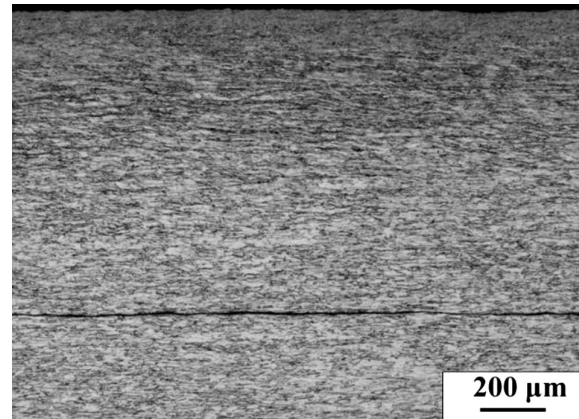


**Figure 2:** Surface layer and joint in the specimen after one ARB cycle  
**Slika 2:** Površinski sloj in spoj v vzorcu po enem ARB-ciklu

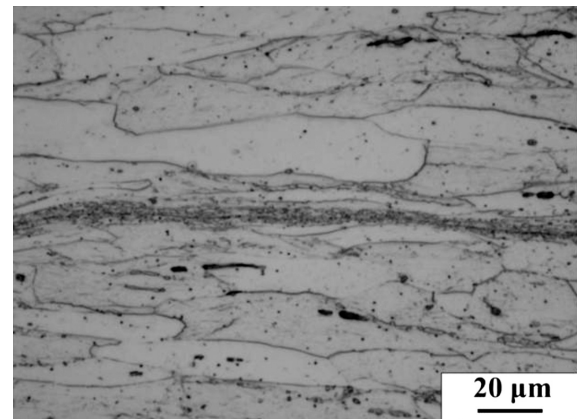


**Figure 3:** Detail of the joint in the specimen after one ARB cycle  
**Slika 3:** Detajl spoja v vzorcu po enem ARB-ciklu

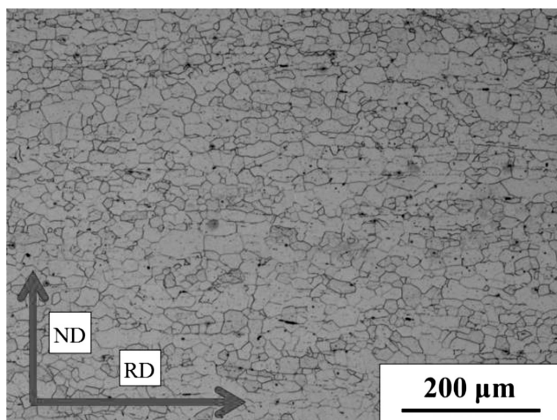


**Figure 1:** Microstructure of the longitudinal section through the recrystallization-annealed sheet

**Slika 1:** Mikrostruktura vzdolžnega prereza rekristalizacijsko žarjene pločevine

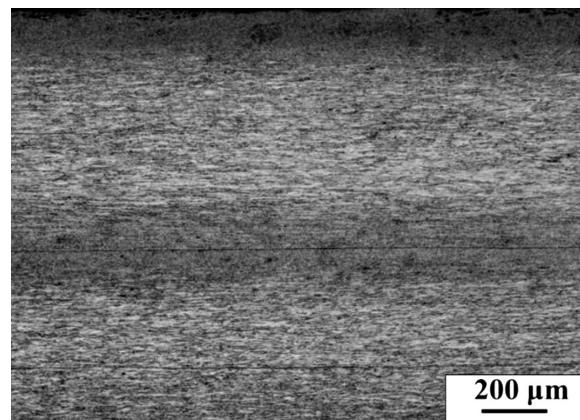


**Figure 4:** Microstructure of the sheet in the longitudinal direction after two ARB cycles

**Slika 4:** Mikrostruktura pločevine v vzdolžni smeri po dveh ARB-ciklih

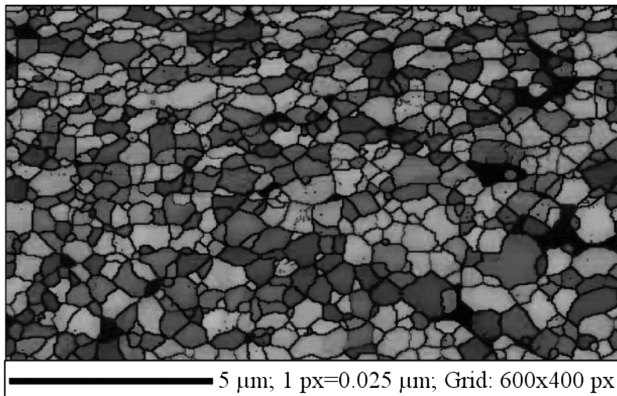


**Figure 5:** EBSD map of the area with fine grains in the specimen after two ARB cycles

**Slika 5:** EBSD-prikaz področja z drobnimi zrni v vzorcu po dveh ARB-ciklih

joint that appears to be of poor quality when viewed at a low magnification.

However, from **Figure 3** it is clear that the joint is of good quality, consisting of very fine grains and being free of oxide. The formation of the thin layer of very fine grains in the joint can be attributed to a high friction in the area of the joint and to a high residual shear stress and its formation is described in detail in<sup>7</sup>.

The microstructure after two ARB cycles is shown in **Figure 4**. The original sheets and the joint created in the first cycle are clear to see. The quality of the first joint appears to be better than that of the second one and this is probably caused by an expansion of the joint area in the process. One can also observe an increased thickness of the layer of ultrafine grains, while the thickness of the surface layer remains to be 150–200 μm. This layer has a similar thickness even in the joint area. A detailed examination of the joint in the ultrafine-grained area from the previous pass reveals a very good joint quality without any traces of the oxide layer.

The specimen after two ARB cycles contained ultrafine grains only in the surface layer, as shown in **Figure 5**. The grains had exclusively high-angle boundaries and a uniform size. The mean grain size in the fine-grained area of the specimen after two ARB cycles was  $700 \pm 300$  nm, with the typical size being between 500 nm and 600 nm.

As expected, the hot-rolled sheet had a low hardness,  $(94 \pm 2)$  HV<sub>10</sub>, low yield strength and ultimate strength but a very good elongation level. The upper yield point  $R_H$  was  $(269 \pm 17)$  MPa and the lower yield point  $R_L$  was  $(232 \pm 9)$  MPa; the ultimate strength  $R_m$  was  $(298 \pm 9)$  MPa and the  $A_{50}$  elongation was  $(40 \pm 2)$  %. The HV<sub>10</sub> hardness of the cold-rolled sheet was  $(196 \pm 2)$ , which is twice the initial level. No distinct yield point was present in the tensile-test plot of this sheet. Its strength was of  $(770 \pm 2)$  MPa, but the  $A_{50}$  elongation level was lowered to  $(1.8 \pm 0.1)$  %. This is evidence of intensive work hardening, while the low elongation reflects the loss of the material's ability to deform plastically.

In the recrystallization-annealed sheet the uniform and undeformed microstructure was restored, having the HV<sub>10</sub> hardness of  $(98 \pm 12)$ , which is the same as for the hot-rolled sheet. The  $R_{p0.2}$  proof stress decreased to  $(180 \pm 5)$  MPa and the ultimate strength to  $(290 \pm 3)$  MPa, while the  $A_{50}$  elongation level rose to  $(49 \pm 2)$  % and the distinct yield point vanished.

The HV<sub>0.1</sub> hardness after a single ARB cycle is 270 near the surface and decreases gradually to approximately 200 in the centre. With respect to the tensile properties, compared to the cold-rolled and recrystallization-annealed sheets, the expected increase in the ultimate and yield strengths and a decrease in the elongation took place. The ultimate strength of the sheet after a single ARB cycle was  $(611 \pm 36)$  MPa, the  $A_{50}$  elongation was lowered to  $(3.4 \pm 0.6)$  % and the yield strength was  $(609 \pm 20)$  MPa. The large scatter in the ultimate strength levels is possibly due to the variation in the thickness of the ultrafine-grained surface layer. A substandard quality of the joint in some locations of the tested specimen cannot be ruled out either.

The surface hardness measured in the specimens after two cycles is similar to that of the recrystallized specimen after a single cycle. The HV<sub>0.1</sub> hardness of the surface layer is essentially identical to that of the specimen after a single cycle; it is 270. However, the decrease in the hardness towards the specimen centre is slower. The minimum level is around 225. In addition, the hardness begins to rise again at a depth of approximately 0.7 μm, eventually reaching 245 and it is due to the ultrafine microstructure formed during the previous cycle in the centre of the specimen. In the specimen from the A2 series after two ARB cycles, the  $R_{p0.2}$  proof stress was  $(633 \pm 7)$  MPa, the strength was  $(650 \pm 19)$  MPa and the  $A_{50}$  elongation was  $(3.3 \pm 0.3)$  %. In **Figure 6** the tensile-test plots for the cold-rolled and recrystallized materials are compared with those for the specimens after one and two ARB cycles. A large increase in the strength after the first cycle is clear to see, as the initial

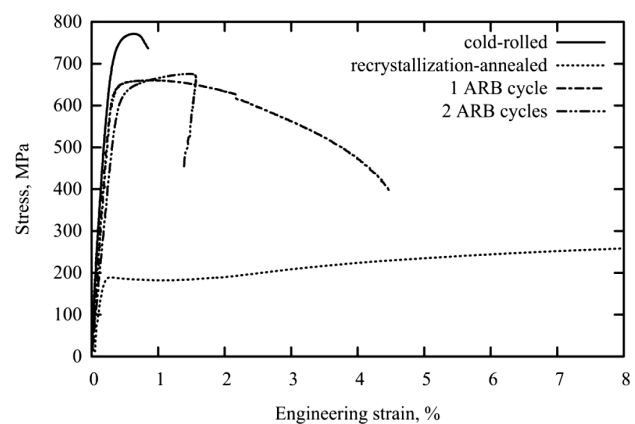


**Figure 6:** Comparison of the measured tensile curves after various treatments

**Slika 6:** Primerjava izmerjenih krivulj pri nateznem preizkusu po različnih obdelavah

value was doubled. The next cycle led to a further increase in the strength, though not as large. Still, the highest strength was found in the cold-rolled sheet, which can be attributed to a different condition of its microstructure.

#### 4 CONCLUSION

1. The conditions for rolling plain low-carbon steel and the ARB method used in a semi-commercial rolling mill in order to obtain a sound joint and ultrafine steel microstructure are investigated. As the appropriate rolling conditions, 5 min soaking at 515 °C in the electric furnace with nitrogen atmosphere and rolling at a 50 % reduction in a single pass were determined. As the suitable locations for the spot welds, the corners of a specimen leading edge were confirmed. In this way the longitudinal cracks that could initiate in the weld location were minimized. The heating in the furnace with an inert atmosphere provided reproducible conditions for the trials.
2. By means of the ARB rolling process, an ultrafine-grained surface layer with a thickness of 150–200 µm was obtained. The size of the smallest grains was 200 nm and the mean grain size was 700 nm. The grains were uniform, recrystallized and did not exhibit any notable orientation with regard to the rolling plane. In the next cycle, the ultrafine microstructure formed in the centre of the specimen; we assume that with more cycles it would spread throughout the specimen thickness.
3. The ultrafine-grained layer had an increased hardness of 300 HV<sub>0.1</sub>, the ultimate strength was doubled and the yield strength was almost tripled with respect to the annealed material. After two passes, the ultimate strength reached 660 MPa, while the elongation dropped to 3.3 %.
4. In future experiments, the method of joining the specimens will be welding as the latest trials showed that longitudinal cracks occur even on the appropriately located welds due to the effects of the heating in the vicinity of the weld. However, in this study induction heating was found to be unsuitable.
5. With the realised tests uniform heating was not achieved and, as a result, cracks appeared on the specimens. Rapid heating and an inert atmosphere are some of the conditions required for preventing an oxide layer from developing on the surfaces to be

joined. A fine-tuned induction heating would provide a uniform and rapid heating in inert gas and may offer a wide field of application.

6. The work hardening rapidly decreased the material plastic deformability. For this reason, heat-treatment options will be explored more closely in future experiments, with the aim to retain the ultra-fine microstructure and increase the elongation above 10 %.

#### Acknowledgement

The paper was prepared under the West-Bohemian Centre of Materials and Metallurgy project no. CZ.1.05/2.1.00/03.0077, with the support from the European Regional Development Fund.

#### 5 REFERENCES

- <sup>1</sup> A. Azushima et al., *CIRP Annals – Manufacturing Technology*, 57 (2008) 2, 716–735, doi:10.1016/j.cirp.2008.09.005
- <sup>2</sup> Z. R. Valiev, G. L. Terence, *Progress in Materials Science*, 51 (2006) 7, 881–981, doi:10.1016/j.pmatsci.2006.02.003
- <sup>3</sup> Y. Saito, H. Utsunomiya, N. Tsuji, T. Sakai, *Acta Metall. Mater.*, 47 (1999) 2, 579–583, doi:10.1016/S1359-6454(98)00365-6
- <sup>4</sup> N. Tsuji et al., *Scripta Materialia*, 47 (2000) 12, 893–899, doi:10.1016/S1359-6462(02)00282-8
- <sup>5</sup> S. Tamimi et al., *Materials and Design*, 30 (2009), 2556–2562, doi:10.1016/j.matdes.2008.09.039
- <sup>6</sup> Y. Okitsu, N. Takata, N. Tsuji, *Scripta Materialia*, 64 (2011) 9, 896–899, doi:10.1016/j.scriptamat.2011.01.026
- <sup>7</sup> N. Kamikawa, N. Tsuji, Y. Minamino, *Science and Technology of Advanced Materials*, 5 (2004) 1–2, 163–172, doi:10.1016/j.stam.2003.10.018
- <sup>8</sup> A. A. Tohidi, M. Ketabchi, A. Hassania, *Mater. Sci. Eng. A*, 577 (2013), 43–47, doi:10.1016/j.msea.2013.04.025
- <sup>9</sup> A. Kolahi, A. Akbarzadeh, M. R. Burnett, *Journal of Materials Processing Technology*, 209 (2009) 3, 1436–1444, doi:10.1016/j.jmatprotec.2008.03.064
- <sup>10</sup> ČSN 41 1300. 41 – Hutnictví - Materiálové Listy Ocelí 4113 – Oceli třídy 11, *Material data sheets*, 1986
- <sup>11</sup> S. Lee, Y. Saito et al., *Mater. Trans. JIM*, 43 (2000) 9, 2320–2325, doi:10.2320/matertrans.43.2320
- <sup>12</sup> G. Krallics, J. G. Lenard, *Journal of Materials Processing Technology*, 152 (2004), 154–161, doi:10.1016/j.jmatprotec.2004.03.015
- <sup>13</sup> J. Gubiš, *Vlastnosti ultrajemnozrné oceli připravené metodou intenzivní plastické deformace*, Diploma thesis, Institute of Chemical Technology Prague, Faculty of Chemical Technology, Department of Metallic Materials and Corrosion Engineering, Praha, 2014
- <sup>14</sup> ČSN EN ISO 6892-1, *Kovové materiály – Zkoušení tahem – Část 1: Zkušební metoda za pokojové teploty*, Praha: Úřad pro technickou normalizaci, metrologii a státní zkušebnictví, 2010, 64 pages





# OPTIMIZATION OF THE ANNEALING OF PLASTER MOULDS FOR THE MANUFACTURE OF METALLIC FOAMS WITH AN IRREGULAR CELL STRUCTURE

## OPTIMIRANJE POSTOPKA ŽARJENJA MAVČNIH FORM ZA IZDELAVO KOVINSKIH PEN Z NEPRAVILNO STRUKTURO CELIC

Ivana Kroupová<sup>1</sup>, Petr Lichý<sup>1</sup>, Filip Radkovský<sup>1</sup>, Jaroslav Beňo<sup>1</sup>,  
Vlasta Bednářová<sup>1</sup>, Ivo Lána<sup>2</sup>

<sup>1</sup>VŠB-Technical University of Ostrava, Faculty of Metallurgy and Materials Engineering, Department of Metallurgy and Foundry Engineering, 17. listopadu 15/2172, 708 33 Ostrava, Czech Republic

<sup>2</sup>Slévárna a modelárna Nové Ransko, s.r.o., Nové Ransko 234, 582 63 Ždírec nad Doubravou, Czech Republic  
ivana.kroupova@vsb.cz

*Prejem rokopisa – received: 2014-07-30; sprejem za objavo – accepted for publication: 2014-10-02*

doi:10.17222/mit.2014.132

Metallic foams are the materials, the research of which is still ongoing, with a broad applicability in many different areas (e.g., automotive industry, building industry, medicine, etc.). These materials have interesting potentials due to a combination of properties, which are, on the one hand, related to their metallic character and, on the other hand, to the porous structure. Since the discovery of porous metallic materials numerous methods of production have been developed. This work deals with the optimization of the foundry method for the manufacture of metallic foams using the evaporable polymeric pattern. This technology was used for the manufacture of metallic foams with an irregular cell structure and with fully open pores. Attention, in the experimental part, is devoted particularly to the chosen moulding material – plaster. We checked the suitability of the proposed procedure of manufacturing a plaster mould, the drying process and the subsequent annealing that significantly influence the final properties of the mould and, therefore, the quality of the resulting casting of the metallic foam.

Keywords: metallic foams, casting, irregular cell structure, plaster, annealing

Kovinske pene so materiali, ki se še preiskujejo in imajo široko področje uporabnosti na različnih področjih (npr. avtomobilska industrija, gradbena industrija, medicina in podobno). Ti materiali so perspektivni zaradi kombinacije lastnosti, ki imajo po eni strani kovinske lastnosti, po drugi pa porozno strukturo. Od odkritja poroznih kovinskih materialov so se razvile številne metode njihove izdelave. Delo obravnava optimizacijo litarne metode izdelave kovinske pene z uporabo izparljivega polimernega modela. Ta tehnologija je bila uporabljena za izdelavo kovinske pene z nepravilno celično strukturo in popolnoma odprtimi porami. V eksperimentalnem delu je pozornost usmerjena v izbiro mavca kot materiala za model. Preverjen je bil predlagani postopek izdelave mavčnega modela, postopka sušenja in žarjenja, ki imajo največji vpliv na končne lastnosti modela in na kvaliteto ulivanja kovinske pene.

Ključne besede: kovinske pene, ulitek, nepravilna struktura celic, mavec, žarjenje

## 1 INTRODUCTION

Metallic foams and porous metals are the materials that contain artificially created pores. These pores give them specific properties such as a large rigidity maintaining a low density, high temperature conductivity, the capability to absorb energy, etc.

The first mention of metal foams was recorded already at the beginning of the 20<sup>th</sup> century when these porous metal materials started to be used for engineering purposes. In the 1920s they began to be commercially produced by sintering metal powders and used for filters, batteries and self-lubricating bearings. A French patent from 1925 mentions metal foams made by foaming and thirty years later their commercial use was started in the United States. But extensive research-and-development activities started in the 1990s and they have been in progress up to now.

At the VSB – Technical University of Ostrava, the research dealing with the optimization of the production

of this unique material in a foundry is currently underway.

### 1.1 Present trends for metallic-foam manufactures

Since the discovery of the porous metallic materials numerous methods of production have been developed. Some technologies are similar to those for polymer foaming, others are developed with regard to the characteristic properties of metallic materials, such as their ability to be sintered or the fact that they can be deposited electrolytically.<sup>1</sup>

According to the state, in which a metal is processed, the manufacturing processes can be divided into four groups. Porous metallic materials can be made from:<sup>2,3</sup>

- a liquid metal (e.g., direct foaming with gas, blowing agents, powder-compact melting, casting, spray forming)
- a powdered metal (e.g., sintering of powders, fibres or hollow spheres, extrusion of polymer/metal mixtures, reaction sintering)

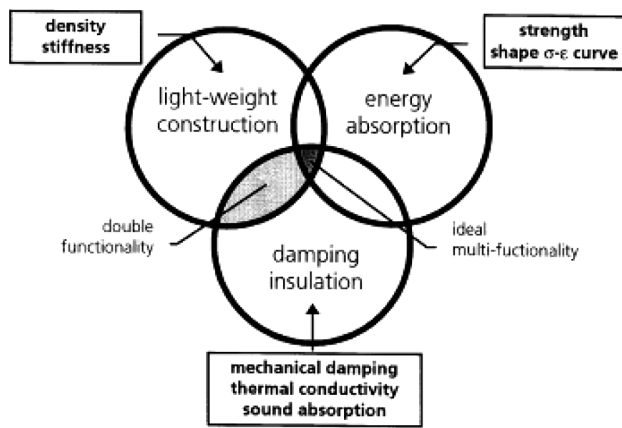


Figure 1: Application fields of structural metal foams<sup>4</sup>

Slika 1: Področja uporabnosti kovinskih pen<sup>4</sup>

- metal vapours (vapour deposition)
- metal ions (electrochemical deposition).

### 1.2 Properties and utilization of metallic foams

Foams and other highly porous materials with a cell structure are known for a combination of many interesting physical and mechanical properties, such as high stiffness at a low density, high thermal conductivity, the ability of energy absorption, etc. (Figure 1).<sup>4</sup> The use of a foam material is optimal in the cases when at least two or more its merits are used at the same time.

The most important parameters for these porous materials are the porosity, the pore diameter, the pore size, distribution, shape, orientation, the degree of the interconnection of the pores. Further, the characteristics of the base material – the alloy – or the density of the created material are also important.

The size, shape, distribution and degree of the interconnection of the pores influence the resulting properties of metal foams. These parameters affect, in particular,

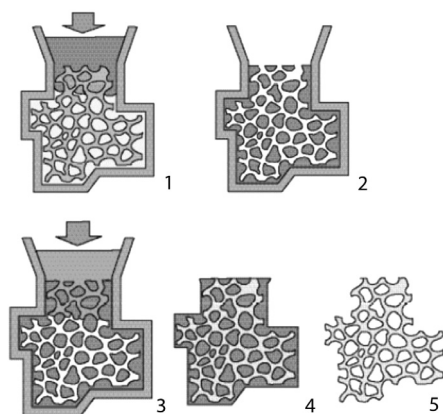


Figure 2: 1 – polymer foam infiltrated with plaster, 2 – removed polymer, 3 – infiltration with metal, 4 – metal foam in the mould, 5 – removed mould, final metal foam<sup>5</sup>

Slika 2: 1 – polimerna pena, prepojena z mavcem, 2 – odstranjeni polimer, 3 – prepojitev s kovino, 4 – kovinska pena in forma, 5 – odstranjena forma; končna kovinska pena<sup>5</sup>

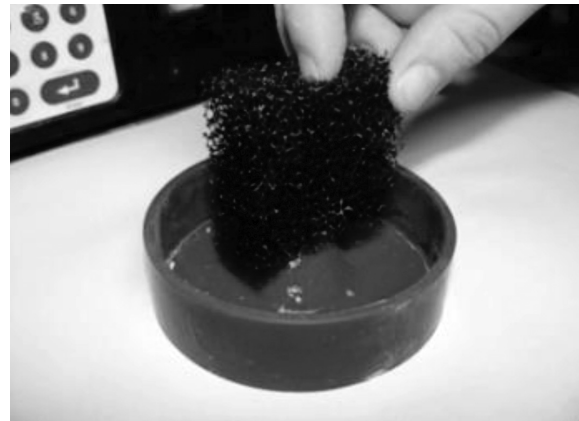


Figure 3: Polymer foam

Slika 3: Polimerna pena

the thermal conductivity of a material, its ability to dampen vibrations or to absorb energy.<sup>5</sup>

## 2 EXPERIMENTAL WORK

### 2.1 Casting method of the metallic foam

The most common foundry method for manufacturing metal foams with open pores is the method using a disposable evaporable polymeric pattern, creating polymeric foams (most commonly polyurethane foams – PU foams).

The process (Figure 2) consists of casting polymeric foam with a refractory material (Figures 3 and 4), followed by drying and annealing the mould when the foam pattern is evaporated. The molten metal is then poured in the resulting cavities. After removing the heat-resistant material the cast metal foam with open pores is obtained which is an exact copy of the foam pattern (Figures 5 and 6).

One of the key steps in this production process is the choice and processing of the material suitable for the manufacture of a mould – plaster in this case. In particular, the material for the mould manufacture must have



Figure 4: Plaster mould

Slika 4: Mavčna forma

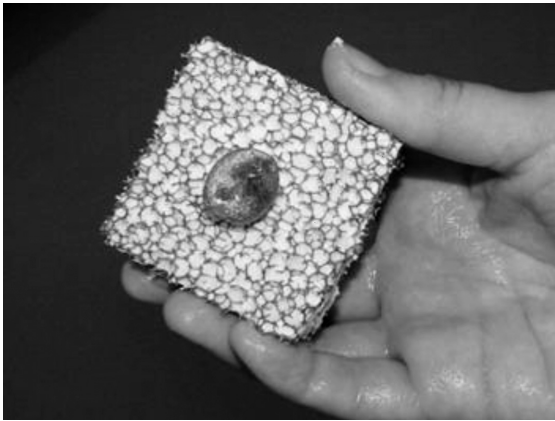


**Figure 5:** Metallic foam with remains of plaster mould  
**Slika 5:** Kovinska pena z ostanki mavčne forme

a sufficient heat resistance and the mixture must have a good fluidity to be able to fill all the small pores of the PU foam.

As the heat-resistant material for the manufacture of moulds, plaster Satin Cast 20 of the Kerr Lab firm was chosen for the casting of precious metals. This special plaster is a fine one and it can accurately copy the surface of a complex pattern. After casting the plaster shows an excellent collapsibility.

## 2.2 Plaster-mould manufacture

The plaster that serves as a filling material needs to be mixed in an exact proportion of water and plaster. One unit of water and two and a half units of plaster are used. It is appropriate to mix the plaster under a reduced pressure to avoid the formation of air bubbles which can negatively affect the plaster mould. Such a mould, after the thermal treatment, can crack or collapse under the influence of the expansion of the trapped air.

An Indu Mix device was used for mixing the plaster. It is fitted with a vibrating device that supports the elimination of air bubbles in the plaster after casting the plaster into the mould.

The plaster is mixed under a reduced pressure for five minutes followed by solidification in the presence of the vibrations for three minutes.

The making of a mould then consists of casting the pattern with the plaster and, at the same time, the plaster must fill all the pattern cavities. The pattern is stuck onto an accessory silicone hat that serves for creating a gate. A metal cover (cuvette) is put on the hat and the plaster is cast into the system prepared in such a way. The obtained moulds are left for two hours in the air and then they are dried at a temperature of 40 °C for 2 h.

After drying the moulds, the next step is their annealing. During annealing free water and chemically bound water are removed and the PU foam is evaporated.

For the casting of various alloys (Cu alloys, Al alloys) it is necessary to define different annealing cycles. When casting the Cu alloys with a higher melting

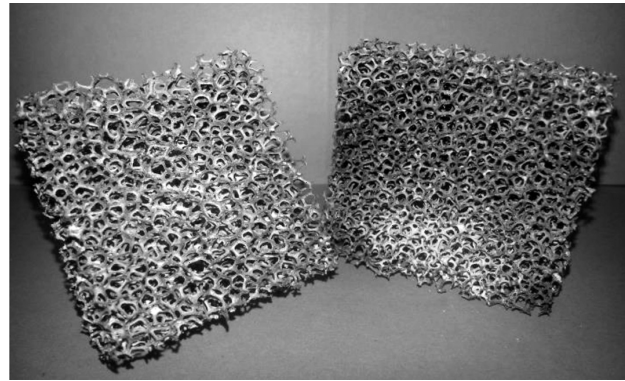


**Figure 6:** Metallic foam with an irregular cell structure with fully open pores  
**Slika 6:** Kovinska pena z nepravilno razporeditvijo celic s popolnoma odprtimi porami

temperature (a higher casting temperature) it is necessary to anneal the plaster moulds at higher temperatures to eliminate the thermal shock during the casting, and to increase the melt fluidity in the complex mould cavity. The annealing cycles can be seen in **Table 1**.

**Table 1:** Annealing cycles for plaster moulds

**Tabela 1:** Cikli žarjenja mavčne forme

|         | temperature, increase rate, soaking time | temperature, increase rate, soaking time | temperature, increase rate, soaking time |
|---------|------------------------------------------|------------------------------------------|------------------------------------------|
| cycle 1 | 120 °C<br>8 °C/min; 8 h                  | 320 °C<br>10 °C/min; 8 h                 | 800 °C<br>20 °C/min; 10 h                |
| cycle 2 | 120 °C<br>8 °C/min; 8 h                  | 550 °C<br>10 °C/min; 8 h                 | 1100 °C<br>20 °C/min; 10 h               |
| cycle 3 | 120 °C<br>8 °C/min; 8 h                  | 550 °C<br>10 °C/min; 8 h                 | 1000 °C<br>20 °C/min; 10 h               |

The most commonly used is the annealing cycle No. 1 suitable for the subsequent casting of Al alloys (a low melting temperature or a low casting temperature).

But for the casting of Cu and Fe alloys it is necessary to increase the annealing temperature, i.e., to heat the moulds to higher temperatures. Therefore, the annealing cycle No. 2 was recommended. However, this annealing cycle proved to be unsuitable – the moulds annealed at

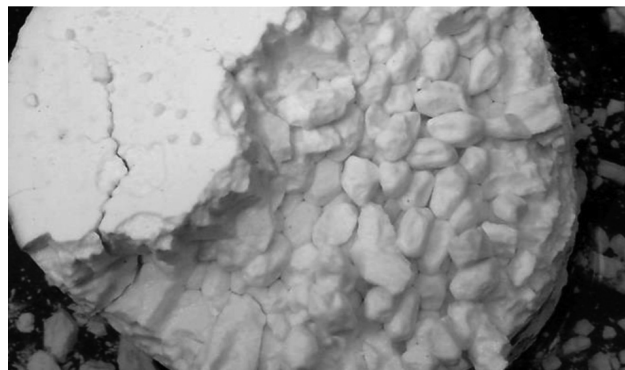


**Figure 7:** Plaster mould annealed at 1100 °C  
**Slika 7:** Mavčna forma, žarjena na 1100 °C

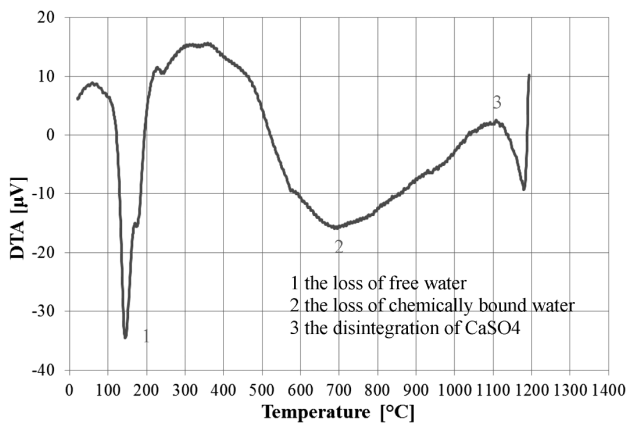


**Figure 8:** DTA of the Satin Cast plaster  
**Slika 8:** DTA mavca vrste Satin Cast

such high temperatures showed an impaired collapsibility after the metal casting (**Figure 7**).

A plaster sample was subjected to a differential thermal analysis (DTA) which showed that, at the temperature of 1100 °C,  $\text{CaSO}_4$  disintegrated into  $\text{CaO}$  and  $\text{SO}_3$  (a degradation of the mould).

After the evaluation of the plaster DTA the annealing cycle No. 3 was designed. The moulds annealed in such a way have a good collapsibility after the casting, but for casting the Cu and Fe alloys the mould temperature is too low. When casting these alloys, the metal fails to fill in the entire mould cavity due to a high-temperature jump. On the contrary, when casting the Al alloys the mould prepared in such a way is overheated.

### 3 RESULTS AND DISCUSSION

#### 3.1 Differential thermal analysis (DTA)

When designing individual annealing cycles it was found that after annealing a plaster mould at the temperature of 1100 °C this mould lost its collapsibility. Therefore, the plaster sample was subjected to a differential thermal analysis (**Figure 8**). This is based on the measurement of the temperature difference between the test sample and the reference sample (the standard).

The basic requirements for the reference sample are as follows: the inertness and stability (no phase transformation can be present) in the measured temperature interval.

After the differential thermal analysis (DTA) three significant changes can be observed on the resulting curve (**Figure 8**). The first range (150 °C) represents the loss of free water, while the second one represents the loss of chemically bound water (700 °C). The third area (1100 °C) shows the disintegration of  $\text{CaSO}_4$  into  $\text{CaO}$  and  $\text{SO}_3$  due to high temperatures. This process is irreversible and the moulds annealed in such a way are

unusable due to the loss of good collapsibility after the casting. If the annealing temperature is reduced to the maximum of 1000 °C,  $\text{CaSO}_4$  does not disintegrate and the plaster (together with the plaster mould) maintains its optimum properties.

### 4 CONCLUSION

With the technology using polymeric foam as a disposable combustible pattern, liquid metal is poured into a mould cavity that is an exact negative of the original foam pattern.

Proper choice and processing of a material suitable for manufacturing the mould are then essential for this production process. In particular, the material must show a sufficient heat-resistance and the mixture must have a good fluidity to fill in all the small pores of the polyurethane foam.

Thus, plaster (Satin Cast 20) is the ideal solution – it can accurately copy the complex shape of a foam pattern and, at the same time, resisting high temperatures. The key step of making the resulting plaster mould is then the annealing cycle. The annealing cycle must allow the moulds to be annealed at a sufficiently high temperature to avoid a heat shock or a misrun when the metal fails to fill in the entire mould cavity. At the same time, however, the annealing cycle should not exceed the temperature at which a degradation of the plaster mould occurs – in the case of the Satin Cast 20 plaster it is 1100 °C.

### Acknowledgements

This work was carried out within research project TA02011333 supported by the Technology Agency of the Czech Republic and project of specific research VŠB-TU Ostrava – SP 2014/61.

### 5 REFERENCES

- <sup>1</sup> P. Lichý, V. Bednářová, T. Elbel, Casting routes for porous metals production, *Archives of Foundry Engineering*, 12 (2012) 1, 71–74, doi:10.2478/v10266-012-0014-0
- <sup>2</sup> J. Banhart, Manufacturing routes for metallic foams, *Journal of Minerals, Metals and Materials*, 52 (2000) 12, 22–27, doi:10.1007/s11837-000-0062-8
- <sup>3</sup> V. Bednářová, P. Lichý, T. Elbel et al., Cast cellular metals with regular and irregular structures, *Mater. Tehnol.*, 48 (2014) 2, 175–179
- <sup>4</sup> J. Banhart, Manufacture, characterisation and application of cellular metals and metal foams, *Progress in Materials Science*, 46 (2001) 6, 559–632, doi:10.1016/S0079-6425(00)00020-5
- <sup>5</sup> D. Curran, Aluminium Foam Production Using Calcium Carbonate as a Foaming Agent [online], PhD. Thesis, University of Cambridge, Cambridge, 2003, 188 [cit. 2010-12-10]; [http://www.msm.cam.ac.uk/mmc/publications/thesis/2003-12\\_DCC\\_PhD\\_thesis.pdf](http://www.msm.cam.ac.uk/mmc/publications/thesis/2003-12_DCC_PhD_thesis.pdf)

# THE KINETICS OF SMALL-IMPURITY GRAIN-BOUNDARY-SEGREGATION FORMATION IN COLD-ROLLED DEEP-DRAWING 08C-AL AND IF STEELS DURING POST-DEFORMATION ANNEALING

## KINETIKA NASTANKA SEGREGACIJE NEČISTOČ PO MEJAH ZRN MED ŽARJENJEM PO HLADNEM VALJANJU JEKEL 08C-AL IN IF ZA GLOBOKI VLEK

**Alexander Rashkovskiy, Anatoly Kovalev, Dmitry Wainstein, Irina Rodionova,  
Yulia Bykova, Diana Zakharova**

I. P. Bardin Central Research Institute for Ferrous Metallurgy "CNIICHERMET", Radio str. 23/9, build. 2, off. 475, 105005 Moscow, Russian Federation  
a\_rashkovskiy@sprg.ru

*Prejem rokopisa – received: 2014-07-31; sprejem za objavo – accepted for publication: 2014-09-19*

doi:10.17222/mit.2014.145

An investigation of small-impurity grain-boundary-segregation (GBS) kinetics in deep-drawing steels (DDSs) allows us to improve the mechanical properties of these steels by optimizing the post-deformation heat-treatment parameters. The kinetics of the GBS formation for C, N, P and S was determined with a series of isothermal expositions of specimens in the spectrometer work chamber at temperatures of 250–650 °C. The surface chemical composition of the samples was measured with Auger electron spectroscopy (AES). Isodose C-curves of the GBS for each detected impurity were plotted. The time – temperature intervals of the preferential GB enrichment with C, N, P, S were determined for the 08C-AL steel with various reduction ratios and for the IF-steels with various concentrations of the micro-alloying elements Nb and Ti. It was found that cold rolling of the 08C-AL steel with a reduction ratio from 48 % to 80 % dramatically increases the preferential carbon GBS temperature from 350 °C to 450 °C due to the necessity of the carbon detachment from Cottrell atmospheres with the annealing of dislocations. The influence of the IF-steel micro-alloying with Nb and Ti on the concurrent multicomponent GBS of interstitial and substitution impurities is also demonstrated in the article.

**Keywords:** deep-drawing steels, IF-steels, grain-boundary segregation, Auger electron spectroscopy, annealing, dislocation structure, microalloying

Preiskava kinetike segregacije nečistoč po mejah zrn (GBS) v jeklih za globoki vlek (DDS) omogoča izboljšanje mehanskih lastnosti teh jekel z optimizacijo parametrov toplotne obdelave po hladni deformaciji. Kinetika nastanka GBS za C, N, P in S je bila določena s serijo izotermne izpostavitve vzorcev v delovni komori spektrometra pri temperaturah 250–650 °C. Kemijska sestava površine je bila izmerjena z Augerjevo elektronsko spektroskopijo (AES). Narisane so bile krivulje enakih odmerkov C za GBS za vsako odkrito nečistočo. Intervali čas – temperatura preferenčnih GB-obogatitev C, N, P, S so bili določeni za 08C-AL jeklo pri različnih stopnjah redukcije in za IF-jekla z različnimi koncentracijami mikrolegirnih elementov Nb in Ti. Ugotovljeno je, da pri hladnem valjanju 08C-AL-jekla s stopnjo redukcije med 48 % in 80 % naraste preferenčna temperatura GBS ogljika iz 350 °C na 450 °C zaradi potrebe razdvojitve ogljika iz Cottrellovega oblaka z žarjenjem dislokacij. V članku je prikazan tudi vpliv mikrolegiranja z Nb in Ti v IF-jeklu na sočasno večkomponentno GBS intersticijskih in substitucijskih nečistoč.

**Ključne besede:** jekla za globoki vlek, IF-jekla, segregacije po mejah zrn, Augerjeva elektronska spektroskopija, žarjenje, struktura dislokacij, mikrolegiranje

## 1 INTRODUCTION

The modern automotive industry increasingly demands the drawability of steels due to the necessity to decrease the weight of the car by thinning its body parts and due to the current fashions for the exterior of the car. The forming of rolled sheets with reduction ratios of up to 80 % requires a very high technological plasticity after heat treatment.

The mechanical properties of deep-drawing steels (DDS) are determined by the micro- and nanostructured parameters, such as the size and shape of grains, the texture, the concentration of the non-metallic inclusions, the dislocation structure and the perfection of the grain

boundaries. The necessary structure and composition of grain boundaries may be achieved by varying the post-deformation-annealing (PDA) regimes. That is why the PDA is the most critical stage of DDS production.

Multicomponent grain-boundary segregation (GBS) in steels is a concurrent process controlled by the thermodynamic and kinetic factors.<sup>1</sup> Each impurity (C, N, P, S, etc.) in a solid solution has its own time-temperature interval for the preferential enrichment of a GB. Typically, C and N, as the most mobile elements in steel, form GB segregations at temperatures of about 300–350 °C.<sup>2</sup> Other elements such as P, S, As, Sn and their analogues usually reach the GBs at higher temperatures. This phenomenon is exhibited by the most mobile impu-

**Table 1:** Chemical composition of 08C-Al steels in mass fractions, w/%**Tabela 1:** Kemijska sestava jekla 08C-Al v masnih deležih, w/%

| Melt # | C     | Si    | Mn   | P     | S      | Cr    | Ni    | Mo    | Cu    | Al    | N      | V     | Ti    | Nb    |
|--------|-------|-------|------|-------|--------|-------|-------|-------|-------|-------|--------|-------|-------|-------|
| 1      | 0.04  | 0.01  | 0.15 | 0.008 | 0.016  | 0.02  | 0.02  | 0.002 | 0.04  | 0.04  | 0.004  | 0.002 | 0.001 | 0.002 |
| 2      | 0.045 | 0.009 | 0.17 | 0.012 | 0.0186 | 0.030 | 0.025 | 0.005 | 0.035 | 0.039 | 0.0025 | 0.002 | –     | –     |

urities (C and N) migrating to grain boundaries, causing a decrease in the free energy of the GB. The elements of C and N occupying the possible sites at the interfaces at low temperatures prevent a further migration of any other elements to the GB from the solid solution (the grain volume). It was shown that the interstitial (C, N, B) and substitutional (P, S, etc.) atoms occupy different places at a GB.<sup>3</sup> The C and N in the solid solution ( $\alpha$ -Fe) in steels act as good surfactants with a high diffusion-mobility control of the behavior of other impurities.

The phosphorus in steel is a very strong surfactant element. Under favorable conditions it can enrich the GBs thousands of times compared to its bulk concentration. DDS and, especially, IF-steels contain very low amounts of carbon and other impurities (typically tens of ppm). When phosphorus adsorbs on the grain boundaries, it significantly decreases the cohesion of the grains and, correspondingly, reduces the damage resistance of the steel. So, we had to pay special attention to the P behavior during the DDS annealing relative to the C and N concentrations in the solid solution and the reduction ratios after cold rolling in the IF and 08C-Al steels for the maximum drawability grades of CR4 and CR5.<sup>4</sup>

## 2 MATERIALS AND METHODS

Four samples of cold-rolled 08C-Al steels (**Table 1**) with various reduction ratios (**Table 2**) and three samples of hot-rolled IF-steels (**Table 3**) with various Ti and Nb contents were investigated.

**Table 2:** Reduction ratio of 08C-Al samples**Tabela 2:** Stopnje redukcije vzorcev 08C-Al

| Melt | Sample | $\varepsilon_{c.r.}/\%$ |
|------|--------|-------------------------|
| 1    | 1-1    | 48                      |
|      | 1-2    | 58                      |
|      | 1-3    | 78                      |
| 2    | 2-4    | 80                      |

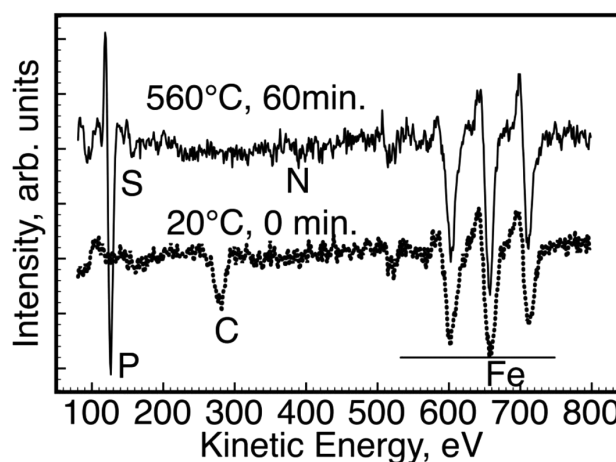
**Table 3:** Measured and required content of Ti and Nb in the investigated IF-steels**Tabela 3:** Izmerjena in zahtevana vsebnost Ti in Nb v preiskovanih IF-jeklih

| Sample # | Ti in steel (w%) | Ti req. (w%) | Nb in steel (w%) | Nb req. (w%) | P (w%)          | S (w%)          |
|----------|------------------|--------------|------------------|--------------|-----------------|-----------------|
| 3-1      | 0.029            | 0.0432       | 0.031            | 0.050        | $\approx 0.005$ | $\approx 0.005$ |
| 3-2      | 0.068            | 0.039        | 0.002            | 0.007        | 0.007           | 0.004           |
| 3-3      | 0.071            | 0.038        | 0.025            | 0.024        | 0.009           | 0.008           |

GBS processes are typically studied on the clean surfaces of heat-treated samples fractured in a vacuum. As the steels under investigation had a very high plasticity, together with a thickness after rolling of less than 1.2 mm, it was impossible to achieve a well-expressed brittle fracture, even at  $-196$  °C. So, we used a simulation of GBS kinetics segregation on a free surface of thin (0.1 mm) flat samples. This approach gives adequate results for the qualitative studies of isothermal segregation kinetics<sup>5,6</sup> when we do not need to precisely determine the segregation energies.

Multicomponent GBS kinetics was studied by annealing the samples one by one in an ESCALAB MK2 (VG, UK) spectrometer work chamber under UHV ( $10^{-8}$  Pa) at constant temperatures from 250 °C to 550 °C with a step of about 50 °C. The chemical composition of the surface was measured with Auger electron spectroscopy (AES) every 5–7 min. Then the isothermal  $C(t)$  curves for all the annealing temperatures were plotted and sectioned at the characteristic concentrations to obtain the isodose  $T(t)$  C-curves for the C, N and P segregation. The sample surfaces were cleaned with  $Ar^+$  ions before the AES measurements.

An example of the AES spectra acquired from a DDS sample surface is shown in **Figure 1**. One can clearly see that after the annealing of sample 3-2 at 560 °C for 60 min, the content of P on the surface is very noticeable. Similar spectra were obtained for all the investigated samples and annealings.

**Figure 1:** AES spectra of IF-steel before (bottom curve) and after (top curve) the tempering at 560 °C for 60 min**Slika 1:** AES-spekter jekla IF pred žarjenjem 60 min pri 560 °C (spodnja krivulja) in po njem (zgornja krivulja)

### 3 RESULTS AND DISCUSSION

#### 3.1 Influence of the degree of plastic deformation and structurally free carbon mobility on the trace-impurity segregation kinetics in DDS 08C-Al steels

An analysis of the carbon-segregation kinetics (**Figure 2a**) in dependence of the plastic-deformation degree for the samples of 08C-Al steel is demonstrated in **Figure 2b**. The temperature of the carbon segregation peak is shifted to higher values with the increasing plastic deformation degree. At a reduction ratio of 48 % (sample 1-1) the carbon segregation mostly occurs at 350 °C. At higher reduction ratios of 58 % (sample 1-2) and 74 % (sample 1-3) the maximum carbon GBS at 300–350 °C is suppressed. The plots in **Figure 2a** for 80 % (sample 2-4) of the 08C-Al steel reduction ratios were found at 400 °C ratio demonstrate that C and 450 °C correspondingly (**Figure 2a**). C and P are the antagonistic elements and the segregation of carbon at 410–440 °C suppresses the segregation of P. The dissolution of carbon GBS at the temperatures higher than the upper peak makes the segregation of P possible.

The maximum carbon concentrations for the 80 % reduction ratio were found at 360 °C and 440 °C (**Figure**

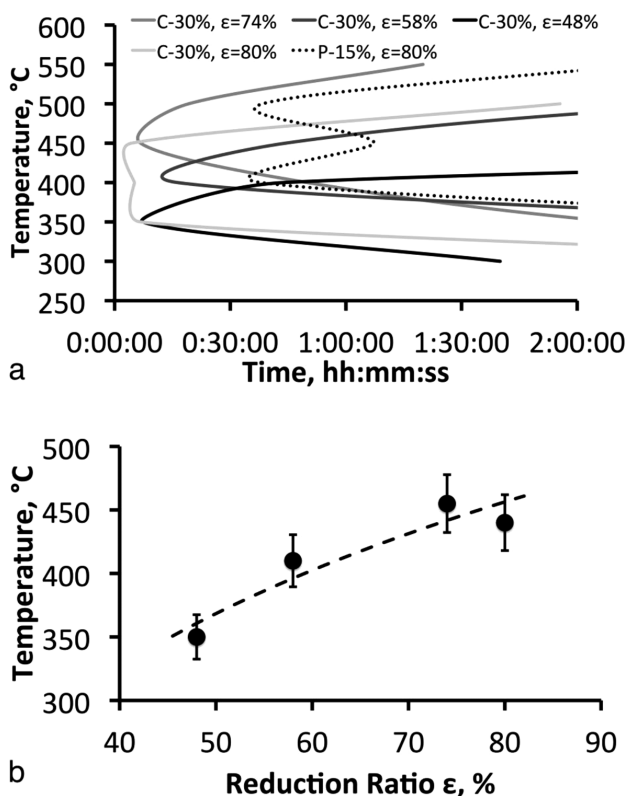


**Figure 2:** a) Isotherm diagram of isothermal segregation of C and P in 08C-Al steel with various reduction ratios, b) temperature of the most rapid segregation of C (C-curve peak nose) versus the reduction ratio after cold rolling

**Slika 2:** a) Diagram enakih odmerkov izotermnega izcejanja C in P v jeklu 08C-Al z različnimi stopnjami redukcije, b) temperatura najhitrejšega izcejanja C (vrh nosa krivulje C) v odvisnosti od stopnje redukcije po hladnem valjanju

**2a**). The annealing at temperatures higher than the upper peak dissolves the C segregation, vacating the grain boundaries for the other impurity migration (e.g., P). Such concurrent behavior of various impurity GBSs arises from the kinetic and thermodynamic factors.

On the one hand, the GBS kinetics of any element is closely connected to its concentration and mobility in a solid solution (the grain volume), while carbon, as a good surfactant with the highest diffusion coefficient in  $\alpha$ -Fe, controls the GBS of the other elements. On the other hand, increasing the cold-plastic-deformation degree provides the growth of the dislocations density and the concentration of other crystalline lattice defects. Since carbon atoms could be captured in Cottrell atmospheres the dislocations and grain boundaries become the concurrent sites for element binding. The dislocations have a preference due to the higher concentration and the shorter diffusion paths for the carbon atoms to reach the free site. So, the higher dislocation density (plastic deformation degree) the higher the amount of dissolved carbon in  $\alpha$ -Fe is blocked in these traps. The concentration of mobile carbon atoms in the solid solution becomes lower, and its GBS is suppressed. The detachment of the element from the dislocation traps requires excessive energy and/or a decreasing of the concentration of the traps.

Annealing of the dislocations is a way to release the carbon atoms from Cottrell's atmospheres and prevent the GBS segregation of harmful impurities. However, the time and temperature of the annealing should be adjusted according to the reduction ratio of the DDS rolled sheet.

#### 3.2 Influence of the concentration of carbide- and nitride-forming elements (Ti, Nb) on the trace impurities segregation kinetics in IF-steels

Due to the strong dependence of the segregation kinetics from cold plastic deformation degree we took the samples of IF-steels after hot rolling due to the more equilibrium state of the micro- and nanostructure.

Typically, IF-steels are alloyed with carbide- and nitride-forming elements: Ti and Nb. These elements should block the migration of the carbon and nitrogen to the GB. The authors<sup>7,8</sup> offer equations for a calculation of the required amount of Ti and Nb to stabilize the interstitials in IF steels:

$$\text{Ti} = 4\text{C} + 3.42\text{N} + 1.5\text{S}$$

while the optimal Nb content is:

$$\text{Nb} = (7.75\text{Ti} - 3.42\text{N} - 1.5\text{S})/4$$

**Table 3** shows the correspondence between the investigated IF-steel's chemical composition and the Ti and Nb alloying requirements for capturing the structural-free carbon and nitrogen.

We investigated three examples of Ti and Nb content (**Table 3**): Sample 3-1 – insufficient concentration of both Ti and Nb; Sample 3-2 – shortage of Nb; Sample

3-3 – concentrations of Ti and Nb that are sufficient to extract the carbon and nitrogen from the solid solution. These suggestions were based on the above equations.

**Figure 3a** represents the C-curves of the carbon and nitrogen segregation in Sample 3-1 (**Table 3**). There is significant amount of free C in this sample, and it segregates to the grain boundaries at 250–400 °C. This temperature range includes the non-stable segregation region stipulated by concurrent nitrogen GBS. Both C and N are occupying the interstitial positions at interfaces replacing each other. This process develops at 350–400 °C during the first 30 min of annealing. The carbon segregation is stable below 300 °C and the exposition times are less than 30 min. The nitrogen GBS is not stable below 300 °C and above 400 °C, and dissolves

after 30–45 min of isothermal exposition. The maximum nitrogen concentration was found at 450 °C after 15 min of annealing. Obviously, the amount of carbide- and nitride-forming elements in this sample (3-1) was insufficient to remove the interstitials from the solid solution and prevent their GBS.

Active phosphorus GBS was formed at temperatures above 400 °C, and it was dissolved above 550 °C. The inhibition of this segregation activity near 450 °C was stipulated by the active nitrogen migration to the GB. At 450–550 °C the nitrogen leaves the GB due to the more energy-efficient P segregation.

In the hot-rolled sample 3-2 no segregation of carbon was found, even after 90 min of annealing. There was found some GBS of nitrogen (**Figure 3b**), so there was

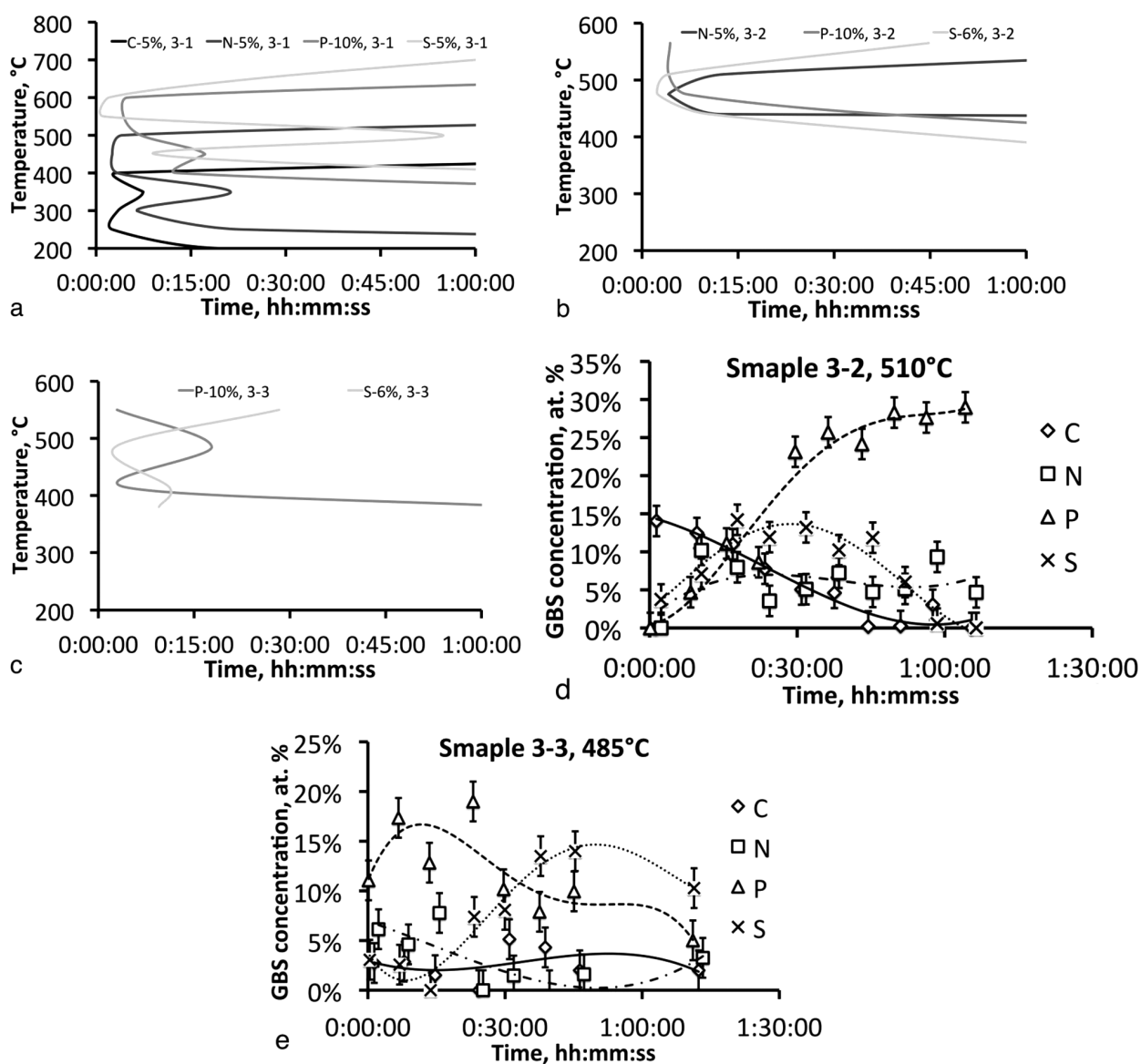


**Figure 3:** Concurrence between carbon, nitrogen, phosphorus and sulfur GBS in samples: a) 3-1, b) 3-2 and c) 3-3 of IF-steel, d), e) – diagrams of isothermal GBS formation for C, N, P and S for marked temperatures and samples

**Slika 3:** Ujemanje med GBS ogljika, dušika, fosforja in žvepla v vzorcih: a) 3-1, b) 3-2 in c) 3-3 v IF-jeklu, d), e) – diagrama nastanka izotermne GBS za C, N, P in S za označene temperature in vzorce



some nitrogen in the solid solution. Its concentration was about 5 % after annealing at 370 °C for 40 min. The same value was measured at 440 °C after 20 min. A maximum nitrogen concentration of 10 % was observed in this sample after annealing at 440 °C for 1 h. The nitrogen GBSs were stable up to 510 °C and they were dissolved after annealing for 30 min, even at 530 °C.

Below 440 °C all possible positions at the GB are occupied by nitrogen atoms, and no other impurities could migrate there. **Figure 3d** demonstrates that P and S are segregating in concurrence at temperatures above 370 °C. The range of preferential sulfur GBS is from 440 °C to 510 °C. Significant enrichment of the GB by P was observed above 480 °C (**Figure 3d**).

It was found that in spite of the higher P and S content in Sample 3-3 of hot-rolled IF-steel the optimal alloying with Ti and Nb does not only prevent C and N GBS, but it also restricts sulfur segregation. It was at the same level as in Sample 3-2. A comparison of **Figures 3b** and **3c** shows that only phosphorus behavior during the GBS process significantly differs in Sample 3-3. The maximum concentration of P at the GB of about 50 % was determined after annealing at 553 °C for 20 min. It means that such alloying of the IF-steel provides a similar degree of sulfur tiding, both in Samples 3-2 and 3-3, despite the two times higher sulfur content in Sample 3-3 (**Table 3**). The minimum sulfur GBS formation time (peak of C-curve) was determined at 485 °C (**Figure 3e**). The concurrence between P and S leads to a gap appearing at the isodose curve of P (**Figure 3c**) near this temperature. The phosphorus has two minimum segregation times, near 430 °C and above 550 °C. It escalates regularly in the absence of nitrogen and carbon segregation (lower peak), and dissolving of the sulfur at higher temperatures.

#### 4 CONCLUSIONS

1. Mobile carbon controls the kinetics of the harmful impurities' (P, S) grain-boundary segregation in DDS steels by both thermodynamic (energy) and concurrence (diffusion) mechanisms.
2. Plastic deformation increases the dislocation density, providing capture provides the formation of carbon atoms in Cottrell's atmospheres, decreasing the amount of mobile carbon in  $\alpha$ -Fe. The temperature of carbon GBS formation shifts to higher values by 50–150 °C depending on the plastic deformation degree due to the concurrence between the dislocation and the grain-boundaries systems.
3. In IF-steels with a low impurities content the GBS of P and S has a double-humped isodose segregation curve. It is stipulated by the following factors:
  - Preventing carbon and nitrogen GBS formation in the low-temperature range by its binding in Nb(CN) and Ti(CN). This facilitates the P and S migration to clean grain boundaries.
  - Annealing at 500–600 °C leads to the dissolution of P and S segregations.

The optimization of the microalloying and post-deformation annealing parameters for the DDS steels should take into account the multicomponent grain-boundary-segregation processes.

#### Acknowledgements

This research was partially supported by RFBR research project No. 13-02-12087 ofi\_m, RSF research project No. 14-12-00170, and Russian Federation President Scholarship #2040.2012.1.

#### 5 REFERENCES

- <sup>1</sup> M. Guttman, *Journal De Physique*, IV (1995) 5, 85–96, doi:10.1051/jp4:1995707
- <sup>2</sup> W. T. Nachtrab, Y. T. Chou, *Met. Trans. A*, 17 (1985) 11, 1995–2006, doi:10.1007/BF02644997
- <sup>3</sup> A. I. Kovalev, V. P. Mishina, G. V. Stsherbedinsky, D. L. Wainstein, *Vacuum*, 41 (1990) 7–9, 1794–1795, doi:10.1016/0042-207X(90)94094-7
- <sup>4</sup> ISO 3574:2012, Cold-reduced carbon steel sheet of commercial and drawing qualities, 2012
- <sup>5</sup> F. Bezuidehout, J. Du Plessis, P. E. Viljgen, *Surface Science*, 171 (1986), 392–399, doi:10.1016/0039-6028(86)91088-5
- <sup>6</sup> H. De Rugy, H. Viefhaus, *Surface Science*, 173 (1986), 418–438, doi:10.1016/0039-6028(86)90200-1
- <sup>7</sup> C. Capdevila, V. Amigo, F. G. Caballero, C. Garcia de Andres, M. D. Salvador, *Materials Transactions*, 51 (2010) 4, 625–634, doi:10.2320/matertrans.MG200909
- <sup>8</sup> M. Hua, C. I. Garcia, A. J. De Ardo, *Scr. Metall. Mater.*, 28 (1993), 973–978, doi:10.1016/0956-716X(93)90066-2



# APPLICATION OF A CONTROL-MEASURING APPARATUS AND PELTIER MODULES IN THE BULK-METALLIC-GLASS PRODUCTION USING THE PRESSURE-CASTING METHOD

## UPORABA KONTROLNO-MERILNE NAPRAVE IN PELTIERJEVIH MODULOV PRI IZDELAVI MASIVNIH KOVINSKIH STEKEL PO POSTOPKU TLAČNEGA LITJA

Wirginia Pilarczyk<sup>1</sup>, Adam Pilarczyk<sup>2</sup>

<sup>1</sup>Silesian University of Technology, Faculty of Mechanical Engineering, Institute of Engineering Materials and Biomaterials, Konarskiego Street 18a, 44-100 Gliwice, Poland

<sup>2</sup>Instytut Spawalnictwa, Bł. Czesława Street 16-18, 44-100 Gliwice, Poland  
wirginia.pilarczyk@polsl.pl

*Prejem rokopisa – received: 2014-07-31; sprejem za objavo – accepted for publication: 2014-09-30*

doi:10.17222/mit.2014.140

The primary objective of the article is to present an innovative workstation and the test results related to iron-based bulk metallic glasses made by pressure casting into a copper die that is cooled with Peltier modules. A production of bulk metallic glasses by pressure casting into a copper die, including an innovative cooling method is presented in this article. The equipment for the casting, including a modern high-frequency induction heater and a control-measuring apparatus, which enables the repeatability and maintenance of the process parameters, is discussed. Semiconductor Peltier modules for cooling the molds are presented. The tests show that the semiconductor Peltier modules are a suitable substitute for the water cooling of the molds. They enable the casting at 0 °C of the molds. Additionally, the ecological and economic aspects of the introduced new methods are presented. The application of the innovative cooling technology also has an influence on a simplification of the equipment construction for the casting process. The test results for the bulk metallic glasses based on iron and obtained with the designed devices are presented in this paper. A structure analysis using X-ray examination and microscopic observation was performed. The diffraction pattern and microscopic observation revealed that the studied as-cast Fe-Co-B-Si-Nb alloy is in the amorphous state. The test results confirmed the amorphous structure of the obtained materials.

Keywords: metallic materials, bulk metallic glasses, Peltier modules, Fe-based alloy, pressure casting into a copper die

Namen tega članka je predstavitev inovativne delovne postaje in rezultatov preizkusov masivnih kovinskih stekel na osnovi železa, izdelanih s tlačnim litjem v bakreno kokilo, hlajeno s Peltierjevimi moduli. V članku je predstavljena izdelava masivnih kovinskih stekel s tlačnim litjem v bakreno orodje z inovativno metodo ohlajanja. Obravnavana je oprema za litje, ki uporablja moderen visokofrekvenčni indukcijski grelnik, opremljen s kontrolno-merilnimi napravami, ki omogočajo ponovljivost in vzdrževanje procesnih parametrov. Predstavljeni so polprevodniški Peltierjevi moduli za hlajenje kokile. Preizkusi so pokazali, da so polprevodniški Peltierjevi moduli primeren nadomestek vodnega hlajenja kokil. Omogočajo ulivanje pri temperaturi kokile 0 °C. Dodatno so predstavljeni še ekološki in ekonomski vidiki nove metode. Uporaba inovativne tehnologije hlajenja vpliva tudi na poenostavitev konstrukcije naprave za ulivanje. V tem delu so predstavljeni rezultati preiskav masivnih kovinskih stekel na osnovi železa, dobljenih z novo konstruirano napravo. Analize strukture so bile izvršene z rentgensko preiskavo. Posnetki difrakcije in mikroskopska opazovanja so odkrila, da je zlitina Fe-Co-B-Si-Nb v litem stanju amorfná. Rezultati preiskav so potrdili amorfnó strukturo dobljenega materiala.

Ključne besede: kovinski materiali, masivna kovinska stekla, Peltierjevi moduli, zlitine na osnovi Fe, tlačno litje v bakreno kokilo

## 1 INTRODUCTION

Metallic glasses have an amorphous, i.e., formless structure. This structure is the intermediate between the crystalline and liquid states. In metallic glasses the arrangement of atoms is of a short-range order. Metallic glasses do not have a proper spatial arrangement of all the atoms, which is characteristic of crystals. Amorphous bodies are formed in the conditions of very intense cooling, during which the metallic fluid reaches the solid state without forming the crystalline structure. The positions of atoms are random, which is characteristic of fluids.<sup>1,2</sup>

Bulk metallic glasses (BMGs) have unique physical and mechanical properties. Generally, in some specific

cases the properties of metals in the amorphous state are diversified and better than the properties of the crystalline alloys of the same chemical composition. Due to a high chemical uniformity of their structure BMGs are characterised by a very high strength and corrosion resistance. The values of their Young's modulus are similar to those of their crystalline equivalents, yet they do not show the anisotropy of elastic properties and cannot accommodate a plastic strain. Metallic glasses have a lower electrical conductance than the crystalline alloys with the same chemical composition.<sup>3</sup>

The condition for the vitrification of cast metal alloys is cooling at an appropriate very high rate  $V_c$ . The manufacture of amorphous metal alloys uses specified

methods. The most popular methods of obtaining bulk metallic glasses include ultrafast splat-cooling, double-roll casting, laser-spin melting, alloy suction into a copper die or the pressure-casting method. The ultrafast splat-cooling technique consists of ejecting a metallic liquid drop onto a curved copper plate using a pressure shock wave. The pressure shock wave is used to provide the test piece with a specific velocity. This method enables obtaining a cooling rate of  $10^5$ – $10^9$  K/s. The effective cooling rate obtained by means of this method depends on the quality of the contact between the metallic liquid and the metal plate.<sup>1,4</sup>

The double-roll casting method consists of cooling a molten drop between two rotating cylinders. In the laser-spin melting method small drops are obtained using a target in the form of a rod rotating at a rate between 8000 r/min and 30000 r/min. The end of the target is heated using a CO<sub>2</sub> laser. According to the reference publications the exemplary cooling rate for 500 µm drops amounts to approximately 4000 K/s.<sup>4</sup>

The suction of a molten alloy into a copper die is a technique frequently used for cooling alloys in order to obtain bulk metallic glasses. This method consists of the arc melting of an alloy on the surface of a copper crucible with an opening located over the water-cooled copper die. Next, the molten alloy is sucked into the copper die using the pressure difference between a vacuum chamber containing the die and a pump connected to the die bottom. The suction of an alloy into the die was used, among others, for making Zr-Cu-Ni-Al amorphous rods (30 mm in diameter and 50 mm in length) as well as for obtaining the rods (12 mm in diameter) made of Nd-Fe-Al alloys.<sup>1,3</sup>

The present developmental state of bulk metallic glasses indicates that the nearest future will see further important applications of these materials. Today, bulk metallic glasses are used in the production of, among others, golf clubs, mobile telephones, springs and medical devices. Due to their unique properties bulk metallic glasses are very promising engineering materials.

Presently, in spite of a significant technological progress in the obtainment of amorphous phases, the method of metallic-liquid fast cooling belongs to the most effective methods enabling the production of bulk metallic glasses. It seems that casting by means of fast-cooling methods has a future application potential.

The presently used and most frequently described solutions utilise water as the copper-die cooling medium. Such a cooling system functions in an open circulation, i.e., the one in which the die is provided with the cooling water from the central service water system having a temperature between 10 °C and 20 °C, which, after passing through the die, is carried off to the sewage system. Such a solution, although the simplest, entails numerous inconveniences and limitations, for example, the casting can be performed only in the shops/rooms having access to the central service water system. The process itself

requires significant amounts of water. It is not possible to obtain the initial die temperature that is lower than that of the cooling medium.

The first two inconveniences can be eliminated by using a closed cooling system utilising a radiator and circulation-forcing pumps. Irrespective of the environmental conditions and the pump's efficiency, the cooling-medium temperature cannot be significantly reduced anyway, which is a significant limitation of this type of system.

Because of this, the authors of the article commenced a search for and an investigation on alternative sources of cooling a copper die used for casting metallic glasses.

The use of one of the basic thermoelectric phenomena, i.e., the Peltier effect has enabled the development of an innovative cooling system.

The Peltier effect is based on the phenomenon of the current-flow-induced change in the temperature at the junction of alternately arranged "n" and "p" semiconductors made of appropriately antimony- and selenium-doped bismuth telluride.

The tests involved the construction of a device presented in **Figure 1**, utilising the Peltier modules for copper-die cooling. The copper die with appropriately prepared grooves giving the right shape to the cast elements was composed of two parts being the mirror reflections of each other. The modules (100 W) required the use of radiators and fans on their hot sides. The efficiency of the radiators and fans significantly affected the die temperature. The configuration of the radiators and fans in the model device enabled obtaining the die temperature between ten and twenty degrees Celsius below zero at ambient room temperature. As a result, it was possible to obtain a significantly lower initial die temperature.

The main goal of the article is to describe the innovative equipment and present the test results for Fe-based bulk metallic glasses.

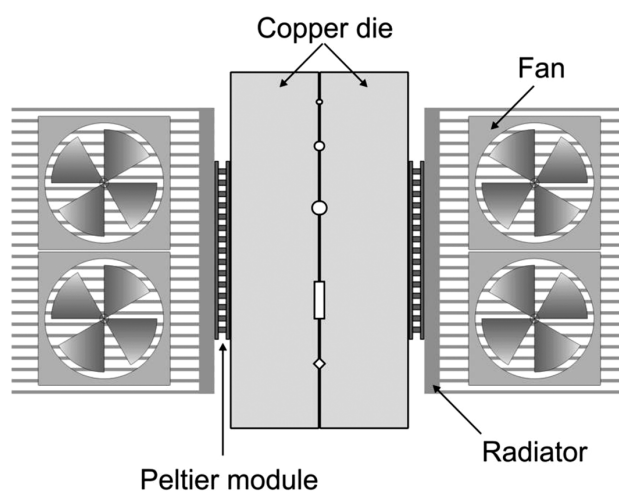


**Figure 1:** Scheme of the pressure-casting die with Peltier modules  
**Slika 1:** Shematski prikaz orodja za tlačno litje s Peltierjevimi moduli

## 2 TEST PROCEDURE

### 2.1 Test material

The material used in the tests was an alloy based on the iron matrix of the Fe-Co-B-Si-Nb system. An ingot with a pre-defined ( $\text{Fe}_{37.44}\text{Co}_{34.56}\text{B}_{19.2}\text{Si}_{4.8}\text{Nb}_{4.0}$ ) chemical composition was prepared by induction melting high-purity component elements Fe, Co, B, Si and Nb in a nitrogen atmosphere. The ingot with a homogenous structure underwent refining and remelting in a quartz crucible using an induction coil. Afterwards, the preliminary alloy was cast into the copper die using pressurised argon. As a result, rods with diameters of 1.5 mm and 3.0 mm were obtained.

Scheme of the station for making bulk metallic glasses is presented in **Figure 2**.

In order to carry out a technological process ensuring the test repeatability, the test station was provided with a necessary control-measuring apparatus. The module solutions supported by the LabView hardware and software, developed by National Instruments, enabled us to design a proper configuration of the related test station. The appropriate selection of the measurement modules integrated in a single housing as well as the possibility of controlling the modules using the LabView environment software ensured a failure-free and stable test-station operation and a relatively easy configuration modification.

### 2.2 Testing methods

Testing the structures of the elements made involved systematic tests of the phase composition  $\text{Fe}_{37.44}\text{Co}_{34.56}\text{B}_{19.2}\text{Si}_{4.8}\text{Nb}_{4.0}$  of the bulk metallic alloys in the form of rods. The tests utilised a Seifert-FPM-manufactured XRD 7 X-ray diffractometer provided with an X-ray lamp with a Co anode. The X-ray lamp voltage-current operational parameters amounted to 35 kV and 25 mA, respectively.

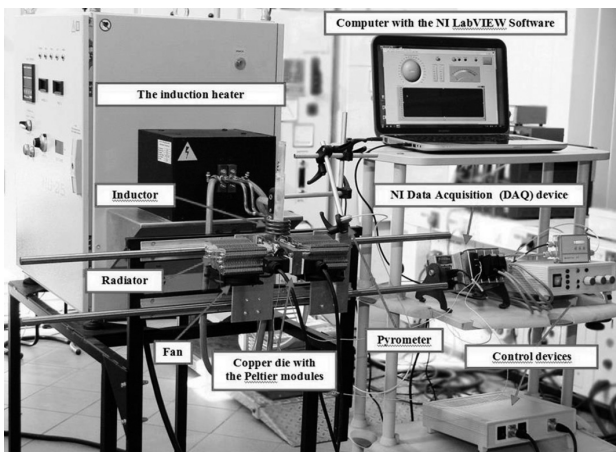


**Figure 2:** Scheme of the station for making bulk metallic glasses  
**Slika 2:** Prikaz postaje za izdelavo masivnih kovinskih stekel

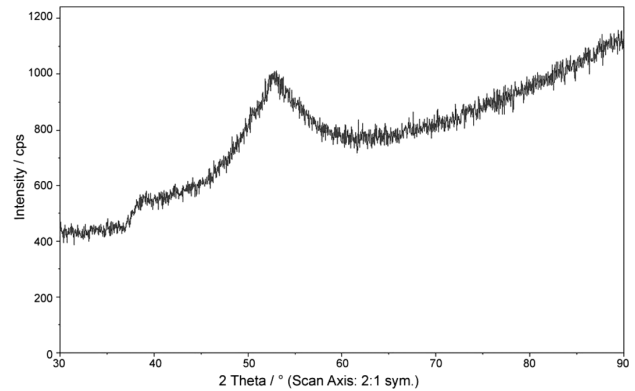


**Figure 3:** X-ray diffraction pattern of the  $\text{Fe}_{37.44}\text{Co}_{34.56}\text{B}_{19.2}\text{Si}_{4.8}\text{Nb}_{4.0}$  alloy rod with a diameter of 1.5 mm

**Slika 3:** Rentgenska difrakcija zlitine  $\text{Fe}_{37.44}\text{Co}_{34.56}\text{B}_{19.2}\text{Si}_{4.8}\text{Nb}_{4.0}$  v obliki palice premera 1,5 mm

The observations of the microstructure of the bulk metallic glasses obtained using pressure casting into the water-cooled copper die utilising the Peltier modules were performed with a Zeiss-manufactured Supra 25 scanning electron microscope provided with an X-ray microanalysis attachment.

## 3 TEST RESULTS AND DISCUSSION

**Figures 3 and 4** present the X-ray examination results for the  $\text{Fe}_{37.44}\text{Co}_{34.56}\text{B}_{19.2}\text{Si}_{4.8}\text{Nb}_{4.0}$  alloy rods. The analysis of X-ray spectra revealed a fully amorphous structure. A significant thickness value for a fully amorphous test piece indicates a good vitrification capacity of the alloy and properly adjusted and applied bulk-metallic-glass manufacturing conditions. The X-ray diffraction patterns revealed single low-intensity diffuse reflexes confirming the formation of an amorphous structure. The presence of nanocrystallites can be confirmed by means of a high-resolution electron microscope, yet this was not the primary objective of this work.

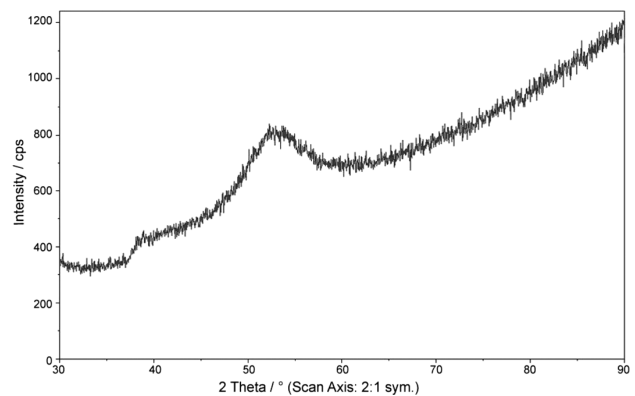


**Figure 4:** X-ray diffraction pattern of the  $\text{Fe}_{37.44}\text{Co}_{34.56}\text{B}_{19.2}\text{Si}_{4.8}\text{Nb}_{4.0}$  alloy rod with a diameter of 3 mm

**Slika 4:** Rentgenska difrakcija zlitine  $\text{Fe}_{37.44}\text{Co}_{34.56}\text{B}_{19.2}\text{Si}_{4.8}\text{Nb}_{4.0}$  v obliki palice premera 3 mm

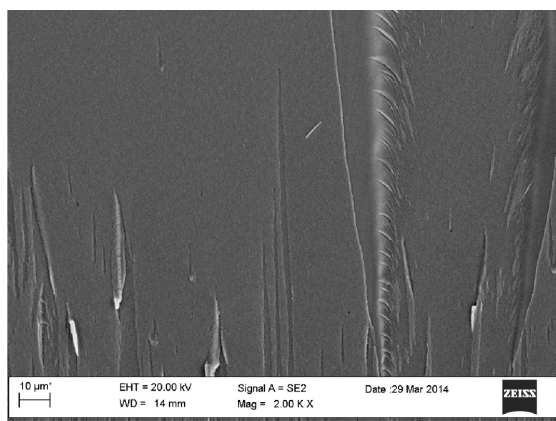


**Figure 5:** SEM micrograph of the fracture morphology of  $\text{Fe}_{37.44}\text{Co}_{34.56}\text{B}_{19.2}\text{Si}_{4.8}\text{Nb}_{4.0}$  amorphous rod in the as-cast state with a diameter of 1.5 mm

**Slika 5:** SEM-posnetek morfologije preloma amorfne palice s premerom 1,5 mm v litem stanju iz zlitine  $\text{Fe}_{37.44}\text{Co}_{34.56}\text{B}_{19.2}\text{Si}_{4.8}\text{Nb}_{4.0}$

**Figures 5 and 6** present the test-piece fractures formed during the bending of the  $\text{Fe}_{37.44}\text{Co}_{34.56}\text{B}_{19.2}\text{Si}_{4.8}\text{Nb}_{4.0}$  alloy rods. The microscopic examination revealed smooth inner surfaces of the test pieces. The smooth mirror-like fracture surfaces confirmed the presence of the amorphous state. In addition, on the surface of the amorphous test-piece fracture it was possible to observe the so-called "veiny patterns", being the characteristic elements of a ductile fracture, typical of the materials with an amorphous (formless) structure. It is justified to suppose that in the case of a crystalline-structure material the fracture surface would be rough.

The alloys were also checked with EDS to identify the chemical compositions of chosen areas. The chemical analysis of these areas show the presence of the Fe, Co, B, Si, and Nb elements. The curves of the X-ray dis-

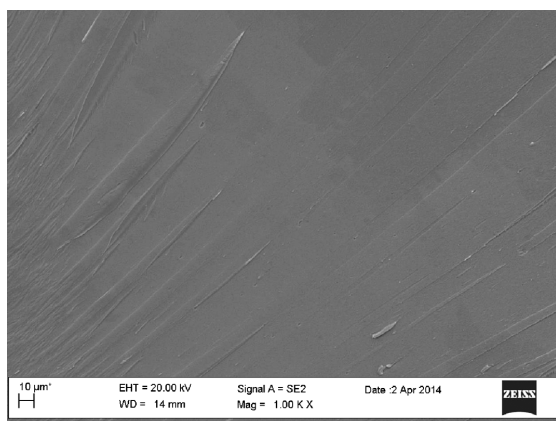


**Figure 6:** SEM micrograph of the fracture morphology of  $\text{Fe}_{37.44}\text{Co}_{34.56}\text{B}_{19.2}\text{Si}_{4.8}\text{Nb}_{4.0}$  amorphous rod in the as-cast state with a diameter of 3 mm

**Slika 6:** SEM-posnetek morfologije preloma amorfne palice s premerom 3 mm v litem stanju iz zlitine  $\text{Fe}_{37.44}\text{Co}_{34.56}\text{B}_{19.2}\text{Si}_{4.8}\text{Nb}_{4.0}$

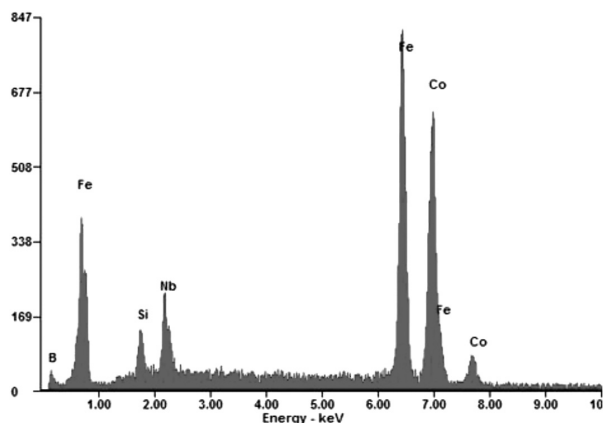


**Figure 7:** Plot of the X-ray dispersive-energy spectrometer measurement of the  $\text{Fe}_{37.44}\text{Co}_{34.56}\text{B}_{19.2}\text{Si}_{4.8}\text{Nb}_{4.0}$  alloy in the as-cast state with a diameter of 1.5 mm (the area from **Figure 5**)

**Slika 7:** Diagram rentgenske disperzije zlitine  $\text{Fe}_{37.44}\text{Co}_{34.56}\text{B}_{19.2}\text{Si}_{4.8}\text{Nb}_{4.0}$  v litem stanju premera 1,5 mm (področje s slike 5)

persive analysis of the  $\text{Fe}_{37.44}\text{Co}_{34.56}\text{B}_{19.2}\text{Si}_{4.8}\text{Nb}_{4.0}$  alloys are presented in **Figures 7 and 8**.

The alloy vitrification capacity is of critical importance when obtaining materials with amorphous structures. Another, equally important factor, is the critical cooling rate obtained with the manufacturing method applied. In order to obtain a fully amorphous test-piece structure it is necessary to use highly advanced, fast cooling techniques utilising the radial-heat offtake from the metal volume. Due to the significant geometrical dimensions of the test pieces, the cooling rates of the methods utilising the radial-heat offtake are lower than those achieved while making classical metallic glasses in the form of bands with thicknesses of several  $\mu\text{m}$ . The bulk-metallic-glass production technology usually involves the use of water-cooled copper dies. For this reason, the objectives of this work were to present a

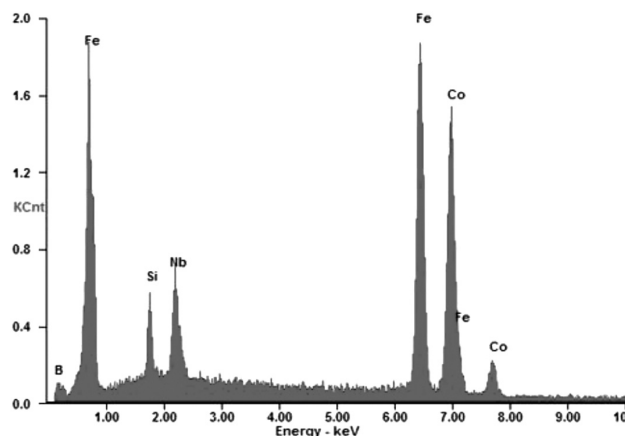


**Figure 8:** Plot of the X-ray dispersive-energy spectrometer measurement of the  $\text{Fe}_{37.44}\text{Co}_{34.56}\text{B}_{19.2}\text{Si}_{4.8}\text{Nb}_{4.0}$  alloy in the as-cast state with a diameter of 3 mm (the area from **Figure 6**)

**Slika 8:** Diagram rentgenske disperzije zlitine  $\text{Fe}_{37.44}\text{Co}_{34.56}\text{B}_{19.2}\text{Si}_{4.8}\text{Nb}_{4.0}$  v litem stanju premera 3 mm (področje s slike 6)

station and determine the copper-die cooling capacity using the Peltier modules as well as to present the test results for the bulk metallic glasses confirming their amorphous structure.

#### 4 CONCLUSIONS

- Test pieces in the form of rods (1.5 mm and 3 mm in diameter) were made by pressure casting an iron-based alloy into a copper die in argon atmosphere.
- X-ray diffractions and a microscopic examination revealed that it is possible to make iron-based bulk metallic glasses in the form of rods using the pressure-casting procedure involving an innovative casting-die cooling method.
- The use of the innovative cooling system based on thermoelectric Peltier modules enabled us to obtain the initial die temperature that was considerably lower than that obtained previously, using the water-based cooling solution. As a result, the cooling process was accelerated.
- In addition, the cooling system described above is environmentally friendly as it allows us to limit (eliminate) the water consumption. The current necessary for obtaining the minimum temperature is 10–20 W h.
- The apparatus design and the casting-die cooling method involving the Peltier modules are the subjects

of a patent application filed at the Polish Patent Office, the patent-application title being: Forma odlewnicza i sposób chłodzenia formy odlewniczej zwłaszcza do wytwarzania prętów i płytek z materiałów metalowych (Nr UP P.405786) /Casting Die and Casting Die Cooling Method Intended for Making Rods and Plates of Metallic Materials/.

#### Acknowledgement

This project was funded by the National Science Centre on the basis of decision DEC-2011/01/D/ST8/07327.

#### 5 REFERENCES

- <sup>1</sup> C. Suryanarayana, A. Inoue, Bulk metallic glasses, CRC Press, Taylor & Francis Group, 2011
- <sup>2</sup> W. Pilarczyk, J. Podwórny, The study of local structure of amorphous Fe-Co-B-Si-Nb alloy by atomic pair distribution function, *Solid State Phenomena*, 203–204 (2013), 386–389, doi:10.4028/www.scientific.net/SSP.203-204.386
- <sup>3</sup> K. Kurzydłowski, M. Lewandowska, *Engineering Construction and Functional Nanomaterials*, PWN, Warszawa 2010, 28–30 (in Polish)
- <sup>4</sup> K. Ziewicz, *Metallic glasses obtained from homogeneous liquid phase and immiscibility range of liquid*, Scientific Publishers of Pedagogic University, Kraków 2011, 28–33 (in Polish)





# EVALUATION OF THE STRUCTURAL CHANGES IN 9 % Cr CREEP-RESISTANT STEEL USING AN ELECTROCHEMICAL TECHNIQUE

## OCENA SPREMEMB STRUKTURE V JEKLU Z 9 % Cr, ODPORNEM PROTI LEZENJU, Z UPORABO ELEKTROKEMIJSKE TEHNIKE

Jiri Rapouch<sup>1</sup>, Jaroslav Bystriansky<sup>1</sup>, Vaclav Seřl<sup>1</sup>, Marie Svobodova<sup>2</sup>

<sup>1</sup>Department of Metals and Corrosion Engineering, Institute of Chemical Technology Prague, Technická 5, 166 28 Prague 6 – Dejvice, Czech Republic

<sup>2</sup>UJP Prague, a. s., Nad Kamínkou 1345, 156 10 Prague – Zbraslav, Czech Republic  
jiri.rapouch@vscht.cz

*Prejem rokopisa – received: 2014-08-01; sprejem za objavo – accepted for publication: 2014-09-23*

doi:10.17222/mit.2014.157

A correct prediction of the remaining lifetime of the components for power plants requires an evaluation of the material structural stability. In this work, the possibility of a non-destructive evaluation of the structural changes in 9 % Cr creep-resistant steel P92 after a long-term annealing was investigated using the electrochemical-polarization technique. Aging at 650 °C caused a significant precipitation and coarsening processes resulting in a redistribution of some alloying elements in the structure. The structural changes confirmed by scanning-electron-microscopy observations and a hardness measurement affected the shape of the measured potentiodynamic curves. Significant local peaks on this curve, in the active-to-passive transition area and in the transpassive region, were evaluated. Characteristic current densities in these regions showed very good correlation with the results of the structure observation and hardness testing.

Keywords: 9 % Cr creep-resistant steel, structural changes, electrochemical detection, polarization curve

Pravilna napoved preostale trajnostne dobe komponent v termoelektrarnah zahteva oceno stabilnosti strukture materiala. V tem delu je bila preiskovana možnost neporušne ocene sprememb v strukturi jekla z 9 % Cr, odpornega proti lezenju, z uporabo tehnike elektrokemijske polarizacije. Staranje pri 650 °C je povzročilo močno izločanje in procese rasti, kar je povzročilo prerazporeditev nekaterih legirnih elementov v strukturi. Spremembe v strukturi, potrjene pri opazovanju z vrstičnim elektronskim mikroskopom in pri merjenju trdote, so vplivale na obliko izmerjenih potenciodinamičnih krivulj. Ocenjeni so bili lokalni vrhovi na tej krivulji v območju prehoda iz aktivnega v pasivno in v transpasivnem območju. Značilna gostota tokov v teh območjih je pokazala dobro ujemanje z rezultati opazovanja strukture in z meritvami trdote.

Ključne besede: jeklo z 9 % Cr, odporno proti lezenju, spremembe strukture, elektrokemična detekcija, polarizacijska krivulja

## 1 INTRODUCTION

Modified steel with 9 % Cr P92 (9Cr-0.5Mo-1.8W-V-Nb) is nowadays often used for the structural components of power plants working under creep conditions (rotors, turbine blades, tubing).<sup>1-3</sup> A combination of a specific chemical composition and a suitable heat treatment provides these materials with a creep strength of up to 100 MPa at 600 °C (after 10<sup>5</sup> h) or even higher.<sup>4</sup> Their operation temperature is limited to about 620 °C; however, the possibilities of increasing it up to 650 °C are being studied. The limiting factor is their poor steam-oxidation resistance and also the acceleration of undesirable structural changes under these conditions.

The structure of the P92 steel after quenching and tempering consists of tempered martensite with a high dislocation density (10<sup>13</sup>–10<sup>14</sup> m<sup>-2</sup>).<sup>5</sup> The martensite laths and the former austenite grain boundaries are decorated with chromium-rich carbides M<sub>23</sub>C<sub>6</sub>, while the grain itself contains finely dispersed particles of the MX type (M = V, Nb, X = C, N). This structure provides the necessary creep resistance. Nevertheless, a long-term

exposure causes a coarsening or decomposition of some particles and the formation of new phases.<sup>6</sup> The phase with the highest effect on the creep properties is the Laves phase with the (Fe,Cr)<sub>2</sub>(Mo,W) formula, since it drains the structure of the solid-solution strengthening elements (Mo, W).<sup>7</sup> These phenomena significantly decrease the creep strength, the ductility, the corrosion and the oxidation resistance.

A correct prediction of the remaining lifetime of a component requires a quantification of these structural changes. Commonly, the mechanical attributes (the hardness, the tensile strength or the fracture toughness) are measured and compared to the initial values. Despite providing direct information about the mechanical attributes of a material, such testing requires samples of the studied component material; the component is cut into test samples, thus losing its function. Therefore, non-destructive methods providing similar quality information are being explored. For instance, electrochemical polarization provides an interesting method based on the change in the corrosion behavior of a material due to the

**Table 1:** Chemical composition of steel P92 in mass fractions (w/%)

**Tabela 1:** Kemijska sestava jekla P92 v masnih deležih (w/%)

|      |      |      |     |      |      |     |      |      |       |        |
|------|------|------|-----|------|------|-----|------|------|-------|--------|
| C    | Mn   | Si   | Cr  | Ni   | Mo   | W   | V    | Nb   | N     | B      |
| 0.11 | 0.48 | 0.37 | 8.6 | 0.09 | 0.33 | 1.6 | 0.23 | 0.06 | 0.037 | 0.0025 |

phases formed during the exposure.<sup>8-11</sup> The particles formed in the structure during the operation are, as mentioned above, rich in some alloying elements (Cr, Mo and W)<sup>12</sup> – all these elements dissolve in highly oxidative environments due to the transpassive mechanism.<sup>13</sup> A preferential dissolution of these phases alters the common steel polarization curve. In addition, electrochemical polarization could be utilized as a method complementary to the small-sample testing.<sup>14</sup> A previous study<sup>15</sup> suggests a possible utilization of the steel behavior in the transpassive region for detection purposes. This study deals with an evaluation of steel P92 after different heat treatments/long-term exposures using polarization techniques.

## 2 EXPERIMENT

The chemical composition of the P92 steel is shown in **Table 1**. The samples were in the state after a heat treatment or after a long-term exposure. **Table 2** shows their thermal histories.

The structures of the samples were studied using light microscope Olympus PME3 and scanning electron microscope Tescan Vega 3 equipped with an EDS probe. The samples were paper ground up to the P2500

**Table 2:** Thermal treatment

**Tabela 2:** Termična obdelava

| Denomination | Thermal history                          |
|--------------|------------------------------------------|
| Q            | quenched (1050 °C / water)               |
| QT           | quenched and tempered (780 °C / 120 min) |
| A1           | annealed at 650 °C for 1 h               |
| A2           | annealed at 650 °C for 10 h              |
| A3           | annealed at 650 °C for 100 h             |
| A4           | annealed at 650 °C for 1000 h            |
| A5           | annealed at 650 °C for 8000 h            |
| A6           | annealed at 650 °C for 15000 h           |
| A7           | annealed at 650 °C for 20000 h           |

roughness, polished with a diamond paste and etched in a mixture of 5 % Nital and Vilella-Bain (1:1). The chemical composition was determined using an EDS analyzer. The hardness of the samples was measured on the polished samples using the standard Vickers method with an applied load of 1 kg; the loading time was 10 s. The hardness of each sample was calculated from ten measurements.

The samples for the potentiodynamic measurements were first ground on a rotating disc with the abrasive paper with a roughness of up to P600. The potentiodynamic measurements were conducted in a corrosion cell

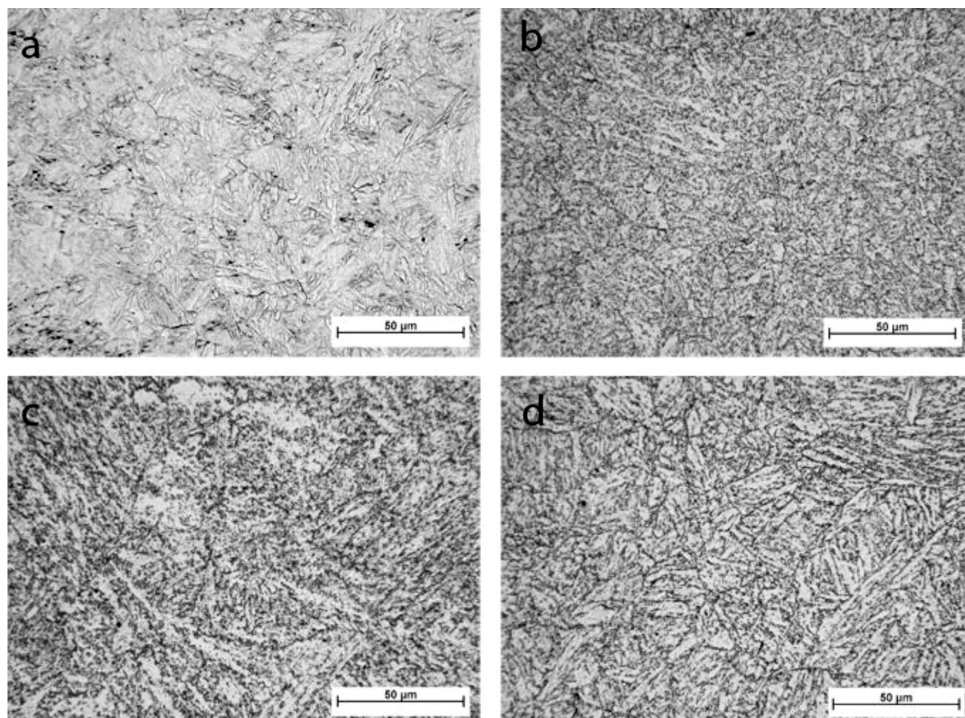


**Figure 1:** Microstructures of the samples: a) Q, b) QT, c) A4, d) A6

**Slika 1:** Mikrostruktura vzorcev: a) Q, b) QT, c) A4, d) A6

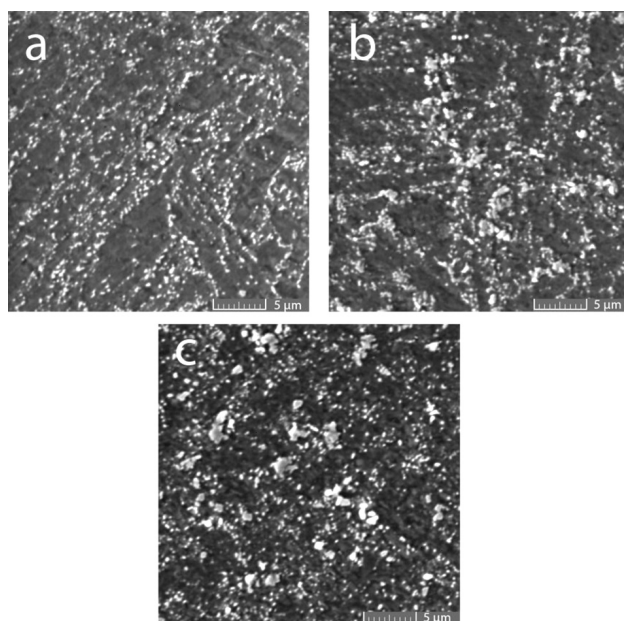


**Figure 2:** SEM images of the samples: a) A2, b) A4, c) A7  
**Slika 2:** SEM-posnetki vzorcev: a) A2, b) A4, c) A7

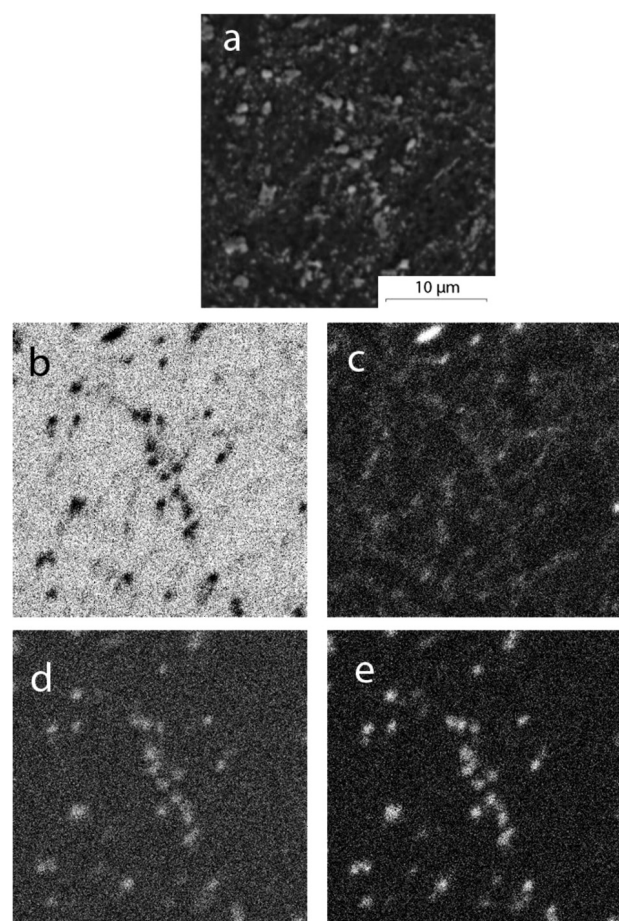


**Figure 3:** a) SEM image of sample A7; element maps for: b) Fe, c) Cr, d) Mo, e) W

**Slika 3:** a) SEM-posnetek vzorca A7; razporeditev elementov: b) Fe, c) Cr, d) Mo, e) W

with the classical three-electrode set-up with the sample being connected as the working electrode, a platinum wire as the auxiliary electrode and saturated silver/silver chloride as the reference electrode. The electrolyte was a solution of sulphuric acid of a 0.5 mol L<sup>-1</sup> concentration at ambient temperature. The measurement consisted of corrosion potential stabilization for 15 min, immediately followed by a polarization from cathodic region -0.05 V,  $E_{corr}$  up to 1.8 V. The sweep rate was 2 mV s<sup>-1</sup>. Potentiostat Gamry PC3 connected to a computer with a Gamry Instruments program was used in all the measurements. The polarization curves for samples A1-A7 were measured three times and the average values of the evaluated parameters were determined. All the presented data are related to the reference electrode described above.

### 3 RESULTS AND DISCUSSION

The microstructures of the selected samples are shown in **Figure 1**. The structure of the quenched sample (Q) consists of martensitic lath-shaped grains without any distinctive precipitates. The tempered sample (QT) has the desired structure of tempered martensite with fine precipitates on the former austenitic grain boundaries and martensitic lathes. The long-term annealing at 650 °C resulted in the coarsening of the grains (A4, A6), the phases and also in the formation of new particles.

Detailed structures are visible on the pictures obtained with scanning electron microscope (**Figure 2**). After about 1000 h of the exposure at 650 °C large precipitates form in the structure (sample A4); their size slowly increases with further annealing (A7). These particles were identified as a Laves phase rich in Mo and

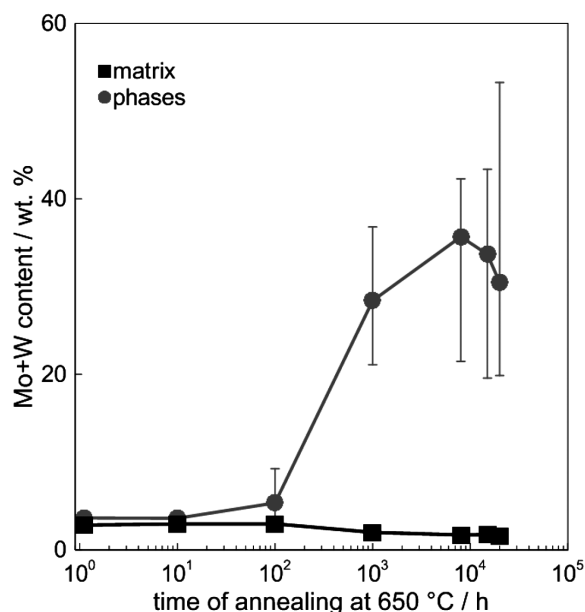


**Figure 4:** Effect of annealing on Mo+W content in matrix and in phases

**Slika 4:** Vpliv žarjenja na vsebnost Mo+W v osnovi in v fazah

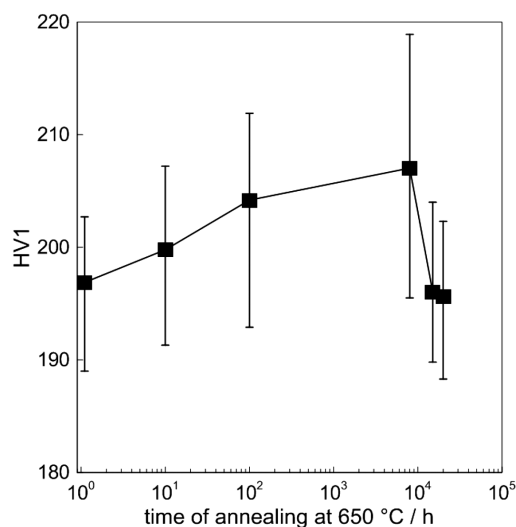


**Figure 5:** Effect of annealing on hardness  
**Slika 5:** Vpliv žarjenja na trdoto

W; the precipitation of this phase in the 9 % Cr steel was described by several authors.<sup>1-7</sup> The phase composition was verified by element mapping (Figure 3). It is apparent that the observed phases contain high amounts of both tungsten and molybdenum, while the chromium content is reduced compared to the surrounding material. In addition, the phases contain only very little iron.

Figure 4 shows the effect of the annealing time on the contents of molybdenum and tungsten in the forming phases and the adjacent matrix (determined from the EDS analysis). The element contents in the phases increase abruptly after 1000 h of the annealing, but further annealing has no significant effect. On the other hand, the contents of these elements in the matrix slowly decrease during the annealing. A decrease in the Mo and W contents during the operational exposure is well known<sup>4,6</sup> and it results in a decrease in the solid-solution strengthening and, thus, a reduction in the creep resistance.

The effect of the structural changes on the mechanical properties was verified with a hardness measurement (a load 1 kg). The average hardness of the quenched sample was 351 HV1, the tempering resulted in a decrease of this value, to 188 HV1. The effect of the subsequent annealing of the material is shown in Figure 5. It can be clearly seen that the hardness increases during the initial stages, probably due to the hardening processes occurring in the structure. The precipitation of the finely dispersed MX particles is assumed to be the most significant hardening process in the structure. Sample A5 (after 8000 h of annealing) has the highest hardness of 207 HV1. Further annealing at 650 °C causes a deterioration in the hardness, most likely due to the carbide coarsening and the formation of a brittle Laves phase.<sup>10</sup> While a decrease in the hardness was observed after the annealing for 15000 h (A6), the W- and Mo-rich phases were detected already after 1000 h

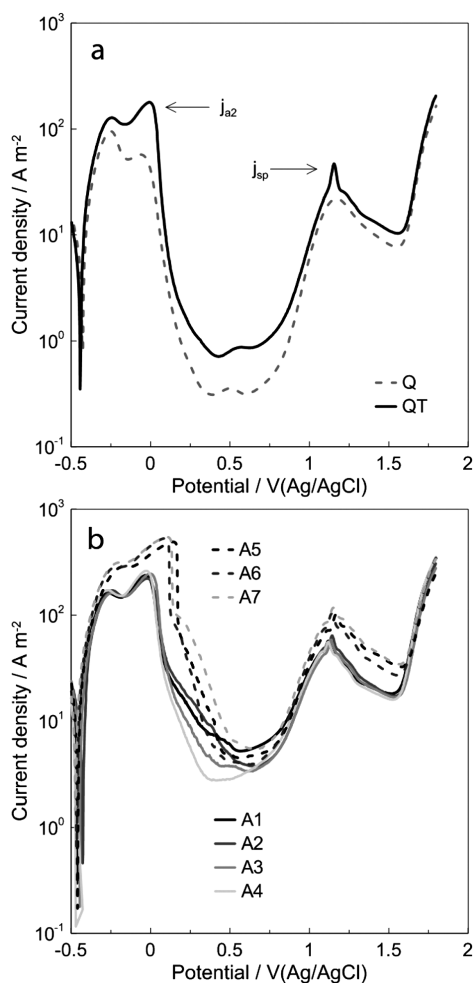


**Figure 6:** Potentiodynamic curves of samples: a) Q and QT, b) A1–A7  
**Slika 6:** Potenciodinamične krivulje vzorcev: a) Q in QT, b) A1–A7

(A4) (Figure 4). This discrepancy can be explained with the fact that the change in the hardness is not associated only with the precipitation of the W- and Mo-rich phases, but it is caused by many structural changes (the changes in the dislocation density, the coarsening of the  $M_{23}C_6$  particles, the precipitation of the MX particles).

An enrichment or formation of the phases with a high content of an alloying element was used for assessing the material with the electrochemical-polarization method. The typical polarization curves for the P92 steel quenched and tempered in a 0.5 mol L<sup>-1</sup> sulphuric acid are shown in Figure 6a. The active/passive transient on the curve exhibits itself as a second anodic maximum (the peak labeled as  $j_{a2}$ ). The transpassive-dissolution/secondary-passivity region is characterized by the local peak around the 1.25 V potential with current density  $j_{sp}$ . It is obvious from the plots that the tempering increases the current density of both the second anodic peak  $j_{a2}$  and the transpassive peak  $j_{sp}$ . The potentiodynamic curves of the annealed steel samples are shown in Figure 6b. The shape of these curves does not change, only the current-density levels in the studied regions increase.

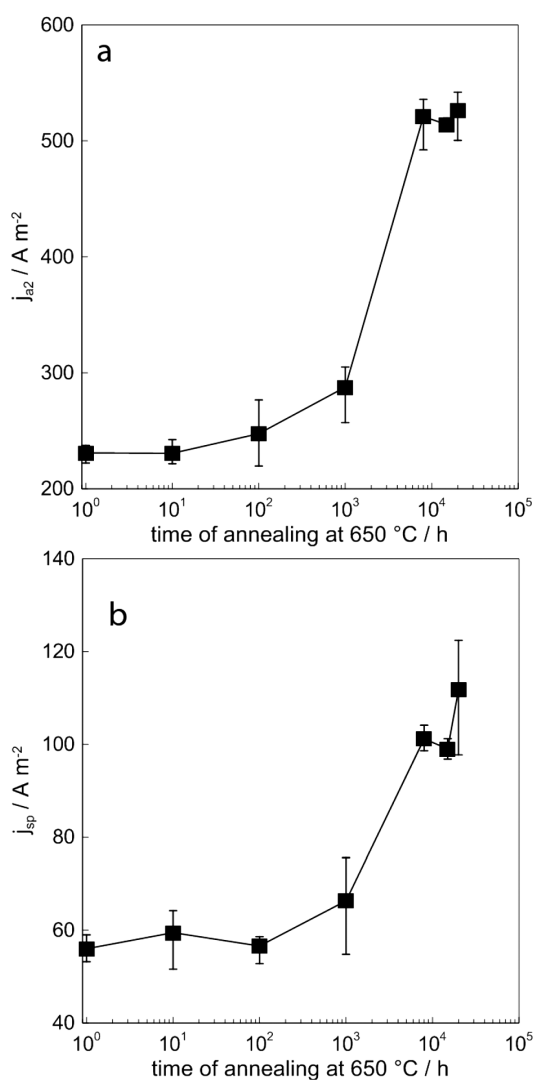


**Figure 7:** Effect of annealing at 650 °C on potentiodynamic-curve attributes: a)  $j_{a2}$ , b)  $j_{sp}$

**Slika 7:** Vpliv žarjenja pri 650 °C na značilnosti potenciodinamičnih krivulj: a)  $j_{a2}$ , b)  $j_{sp}$

The increase in the second anodic peak was discussed in many papers<sup>16,17</sup> and it is presumed that this effect corresponds to the formation of chromium-depleted regions around the  $M_{23}C_6$  carbides. The chromium content in carbides increases with further annealing which also significantly depletes the adjacent regions of chromium, resulting in an increase in the  $j_{a2}$  peak current density.

A similar trend was observed for the  $j_{sp}$  peaks at 1.25 V, where the current density also increases with the annealing time. This phenomenon can be explained with an increase in the number of minor phases rich with Cr, Mo and W, which can dissolve due to the transpassive mechanism at this potential. Chromium has the greatest effect on this phenomenon and it is known that its content in  $M_{23}C_6$  increases with the annealing time.<sup>12</sup> However, the effects of Mo and W in the Laves phases cannot be ignored, as shown in **Figure 4**. The relationships bet-

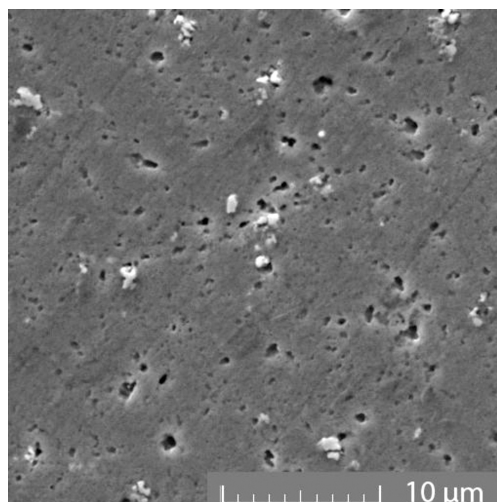


**Figure 8:** SEM image of the A7 sample after potentiostatic etching (1.25 V)

**Slika 8:** SEM-posnetek vzorca A7 po potenciostatičnem jedkanju (1,25 V)

ween  $j_{sp}$ ,  $j_{a2}$  and the annealing time are shown in **Figure 7**. Both these characteristics increase significantly after 8000 h and remain stable afterwards. In addition, it is necessary to emphasize that a sharp increase in  $j_{sp}$  corresponds to an intensive active dissolution of the matrix, therefore, increasing the area of the phases that are dissolved in the transpassive state at 1.25 V.

The observed trends between  $j_{a2}$ ,  $j_{sp}$  and the annealing time are in a good correlation with the hardness measurements, which also change significantly after 8000 h. The Laves phase starts to precipitate soon, after 1000 h (**Figure 2**), so it seems that the increase in the  $j_{sp}$  value corresponds mostly to the change in the  $M_{23}C_6$  chemical composition. To prove that the phases are being dissolved at 1.25 V, sample A7 was briefly potentiostatically etched. **Figure 8** shows a SEM image and it is clear that some phases in the matrix are partially dissolved.

#### 4 CONCLUSION

The recording of potentiodynamic curves in sulphuric acid seems to be an interesting method to assess the structural changes in creep-resistant steel P92. Two parts of the polarization curves were studied in detail – the second anodic peak in the active/passive transient region and the local-current maximum in the transpassive region. Both these peaks correspond to the changes in the structure during a long-term annealing and these further correlate with the hardness measurements. Therefore, the utilized polarization method is sensitive to both the behavior of the matrix ( $j_{a2}$ ) and the changes in secondary phases in the matrix ( $j_{sp}$ ). Due to its simplicity and non-destructivity, the electrochemical-polarization method could be an attractive choice when predicting the remaining lifetime of operating equipment.

## Acknowledgment

The authors gratefully acknowledge the financial support from the Ministry of Industry and Trade of the Czech Republic (project MPO FR-TI1/086) and the Technology Agency of the Czech Republic (project TA 02011179).

## 5 REFERENCES

- <sup>1</sup> R. O. Kaybyshev, V. N. Skorobogatykh, I. A. Shchenkova, *The Physics of Metals and Metallography*, 109 (2010), 186–200, doi:10.1134/S0031918X10020110
- <sup>2</sup> K. Maruyama, K. Sawada, J. Koike, *ISIJ International*, 41 (2001), 641–653, doi:10.2355/isijinternational.41.641
- <sup>3</sup> J. Hald, *International Journal of Pressure Vessels and Piping*, 85 (2008), 30–37, doi:10.1016/j.ijpvp.2007.06.010
- <sup>4</sup> V. Vodárek, Z. Kuboň, V. Foldyna, *Hutnické listy*, 4 (1997), 31–38
- <sup>5</sup> R. L. Klueh, *International Materials Reviews*, 50 (2005), 287–310, doi:10.1179/174328005X41140
- <sup>6</sup> M. Hättstrand, H. O. Andrén, *Micron*, 32 (2001), 789–797, doi:10.1016/S0968-4328(00)00086-X
- <sup>7</sup> A. Výrostková, V. Homolová, J. Pecha, *Materials Science and Engineering A*, 480 (2008), 289–298, doi:10.1016/j.msea.2007.07.036
- <sup>8</sup> M. A. Domínguez-Aguilar, R. C. Newman, *Corrosion Science*, 48 (2006), 2560–2576, doi:10.1016/j.corsci.2005.08.017
- <sup>9</sup> Y. Watanabe, T. Shoji, *Metallurgical Transactions A*, 22 (1991), 2097–2106, doi:10.1007/BF02669877
- <sup>10</sup> S. Komazaki, S. Kishi, T. Shoji, T. Kumazawa, K. Higuchi, K. Suzuki, *JSME International Journal A*, 45 (2002), 30–38, doi:10.1299/jseme.45.30
- <sup>11</sup> Y. Hyun, J. Lee, I. Kim, *Key Engineering Materials*, 270–273 (2004), 1206–1211, doi:10.4028/www.scientific.net/KEM.270-273.1206
- <sup>12</sup> L. M. Lundin, M. Hättstrand, H. Andrén, *Redistribution of Elements During Ageing and Creep Testing of 9-12% Chromium Steels*, Proc. of the 5th International Charles Parsons Turbine Conference, Cambridge, UK, 2000, 603–617
- <sup>13</sup> M. Bojinov, I. Betova, R. Raicheff, *Materials Science Forum*, 289–292 (1998), 1019–1028, doi:10.4028/www.scientific.net/MSF.289-292.1019
- <sup>14</sup> K. Milička, F. Dobeš, *International Journal of Pressure Vessels and Piping*, 83 (2006), 625–634, doi:10.1016/j.ijpvp.2006.07.009
- <sup>15</sup> J. Rapouch, J. Bystrianský, *Koroze a ochrana materiálu*, 56 (2012), 31–37, doi:10.2478/v10227-011-0006-7
- <sup>16</sup> T. L. Walzak, J. S. Sheasby, *Corrosion*, 39 (1983), 502–507, doi:10.5006/1.3577375
- <sup>17</sup> L. Felloni, S. Sostero Traverso, G. L. Zucchini, *Corrosion Science*, 13 (1973), 773–789, doi:10.1016/S0010-938X(73)80015-0

# EFFECT OF THE BY-PASS CEMENT-KILN DUST AND FLUIDIZED-BED-COMBUSTION FLY ASH ON THE PROPERTIES OF FINE-GRAINED ALKALI-ACTIVATED SLAG-BASED COMPOSITES

## VPLIV PRAHU IZ PEČI ZA CEMENT IN LETEČEGA PEPELA IZ VRTINČASTE PLASTI NA LASTNOSTI DROBNOZRNATEGA, Z ALKALIJAMI AKTIVIRANEGA KOMPOZITA NA OSNOVI ŽLINDRE

**Vlastimil Bílek Jr., Ladislav Pařízek, Lukáš Kalina**

Brno University of Technology, Faculty of Chemistry, Materials Research Centre, Purkyňova 118, 612 00 Brno, Czech Republic  
xcbilekv@fch.vutbr.cz

*Prejem rokopisa – received: 2014-08-01; sprejem za objavo – accepted for publication: 2014-09-23*

doi:10.17222/mit.2014.162

The aim of this work is to investigate the influence of the by-pass cement-kiln dust (CKD) and two types of the fluidized-bed-combustion (FBC) fly ash on the workability, shrinkage and mechanical properties (compressive and flexural strengths) of the water-glass-activated slag. The utilization of CKD and FBC is very problematic. One of the main reasons for this is a high lime and sulfate content in these wastes, which can lead to the formation of expansive hydration products and, consequently, to the cracking of ordinary Portland-cement (OPC) materials. On the other hand, these products might act against the high shrinkage of the alkali-activated slag (AAS). In order to investigate this assumption and the influence of these admixtures on the other properties mentioned above, fine-grained AAS-based composites were prepared. A ground, granulated blast-furnace slag (the reference binder) was partially replaced (0–50 %) by one type of CKD and two types of the FBC fly ash. A significant reduction in the shrinkage was observed on the samples containing an even lower amount of fly ash, while the composites with CKD did not show any notable shrinkage reduction. When using higher dosages of these admixtures the mechanical properties were reduced, but lower dosages did not have such effects, especially as regards the compressive strength. The workability was also strongly dependent on the admixture dosage. Its improvement was observed especially in the case when slag was replaced by up to 30 % of CKD.

Keywords: alkali-activated slag, by-pass cement-kiln dust, FBC fly ash, workability, strength, shrinkage

Namen tega dela je preiskati vpliv prahu iz peči za cement (CKD) in dveh vrst letečega pepela (FBC) iz zgorevanja v vrtinčasti plasti na obdelovalnost, krčenje in mehanske lastnosti (tlačna in upogibna trdnost) žlindre, aktivirane z vodnim steklom. Uporaba CKD in FBC je zelo problematična. Eden od glavnih razlogov za to je visoka vsebnost apna in sulfatov v teh odpadkih, kar lahko povzroči nastanek ekspanzijskih hidracijskih produktov in posledično pokanje portlandskih cementnih materialov (OPC). Po drugi strani pa ti produkti lahko zavirajo veliko krčenje žlindre, aktivirane z alkalijami (AAS). Da bi preverili te predpostavke in vpliv teh dodatkov na druge, zgoraj omenjene lastnosti, so bili pripravljene na osnovi AAS drobnozrnati kompoziti. Grobozrnata plavžna žlindra (referenčno vezivo) je bila delno nadomeščena (0–50 %) z eno vrsto CKD in dvema vrstama FBC letečega pepela. Opaženo je bilo občutno zmanjšanje krčenja pri vzorcih s celo majhnim deležem letečega pepela, medtem ko kompozit s CKD ni pokazal opaznega zmanjšanja krčenja. Pri uporabi večjih deležev obeh dodatkov so se poslabšale mehanske lastnosti, pri majhnem dodatku pa ni bilo takega vpliva na tlačno trdnost. Obdelovalnost je bila močno odvisna od količine dodatkov. Njeno izboljšanje je bilo posebno opazno v primeru, ko je bila žlindra nadomeščena z do 30 % CKD.

Ključne besede: z alkalijami aktivirana žlindra, prah iz peči za cement, FBC leteči pepel, obdelovalnost, trdnost, krčenje

## 1 INTRODUCTION

The binders based on AAS are considered as an ecological alternative to the OPC-based binders, which are most common in the concrete production. AAS, in comparison with Portland cement, can have a better durability, a lower hydration heat, a better resistance to elevated temperatures and an aggregate-matrix interphase and other benefits.<sup>1</sup> On the other hand, the main disadvantages of AAS are a very high shrinkage and a poor rheology, especially with respect to a relatively rapid setting in the case of a water-glass activation.<sup>2</sup>

CKD is a by-product of cement manufacturing with a highly variable composition, but it usually contains

significant amounts of alkali, chloride, sulfate and free lime.<sup>3</sup> Several works investigating the CKD use in the mortar and concrete production were published. It is usually concluded that a replacement of OPC higher than 5–10 % has an adverse effect on the compressive and tensile strengths.<sup>4</sup> FBC technology has many advantages in comparison with pulverized coal combustion,<sup>5</sup> but the ashes from FBC are very porous and they contain high amounts of very reactive free lime and anhydrite, which lead, on the one hand, to their self-cementing properties, but, on the other hand, to the problems with the workability and volume stability due to the formation of expansive-hydration products.<sup>6</sup>

## 2 EXPERIMENTAL WORK

### 2.1 Materials and sample preparation

A ground, granulated blast-furnace slag with a specific surface of 380 m<sup>2</sup>/kg was used as the reference binder (R). The slag was partially replaced (0–50 %) by one type of the by-pass CKD and two types of the FBC fly ash. The phase compositions of CKD and fly ashes were determined with X-ray diffraction (XRD). CKD mainly consisted of KCl, K<sub>2</sub>SO<sub>4</sub>, CaO and C<sub>2</sub>S. The main phases found in both fly ashes were anhydrite, quartz, glassy phase, free lime, portlandite and calcite. The fly ash designed as P contained more anhydrite, quartz and free lime, while the fly ash designed as L contained a higher amount of the glassy phase. The water glass with the silicate modulus equal to 1.85 was used as the alkaline activator. The weight ratio of Na<sub>2</sub>O/binder was kept constant at 0.042. The mass ratio of the Czech standard sand (three different fractions according to standard ČSN EN 196) to the binder was 2 : 1. The water-to-binder ratio (*w/b*) was kept constant at 0.40, only in the case of the mixtures with fly ash L, *w/b* had to be increased due to a very low workability. The binder compositions of the mortars prepared are shown in **Table 1**.

After approximately four minutes of mixing the workability of the mortar was measured using the flow-table spread test and then the mortar was cast into the molds. Prisms with the dimensions of 20 mm × 20 mm × 100 mm were prepared for the compressive- and flexural-strength tests and prisms with the dimensions of 25 mm × 25 mm × 285 mm and stainless-steel gauge studs in their front walls were prepared for the shrinkage tests.

### 2.2 Compressive- and flexural-strength testing

The prisms for the strength testing were demolded after 24 h and moist cured at a 99 % relative humidity and (23 ± 2) °C. Compressive strengths were tested at the ages of (1, 7 and 28) d. Three prisms were used for the flexural testing (three-point bending) of each mixture at each age and broken parts from these tests were used for the compressive-strength testing.

### 2.3 Shrinkage tests

The shrinkage tests were based on ASTM C596. After 24 h of moist curing the specimens were demolded, a comparator reading was taken and the speci-

mens were immersed for three days in tap water. Then the bars were removed from the water, their surfaces were dried with a wet towel and a zero reading was performed. After that the bars were stored in laboratory conditions ((45 ± 5) % relative humidity, (23 ± 2) °C) for 56 d and their length changes were measured. These shrinkage tests were rather tentative because only two samples of each mixture were measured.

## 3 RESULTS AND DISCUSSION

The average values of compressive  $f_c$  and flexural strength  $f_t$  for different ages with the standard errors of the mean are listed in **Table 2**. There are also the results of the workability testing expressed as the average values of the diameters of the mortar spread  $d$  in the same table. The data for the mortars designed as P10, L30 and L50 are not included because these mortars did not harden even after three days.

**Table 2:** Flexural  $f_t$  and compressive  $f_c$  strength development, standard errors of the mean (in parenthesis) and workability of the prepared composites

**Tabela 2:** Spreminjanje upogibne  $f_t$  in tlačne  $f_c$  trdnosti, povprečne standardne napake (v oklepaju) in obdelovalnost pripravljenih kompozitov

| Mortar | $f_t$ /MPa   |              |               | $f_c$ /MPa    |               |                | $d$ /mm |
|--------|--------------|--------------|---------------|---------------|---------------|----------------|---------|
|        | 24 h         | 7 d          | 28 d          | 24 h          | 7 d           | 28 d           |         |
| R      | 2.5<br>(0.1) | 7.3<br>(0.7) | 11.7<br>(0.4) | 10.0<br>(0.2) | 72.7<br>(1.7) | 107.4<br>(3.6) | 190     |
| CKD10  | 2.0<br>(0.1) | 2.4<br>(0.3) | 8.8<br>(0.1)  | 10.0<br>(0.2) | 62.0<br>(1.0) | 115.1<br>(2.8) | 220     |
| CKD20  | 1.3<br>(0.3) | 4.1<br>(0.7) | 7.6<br>(0.7)  | 6.0<br>(0.1)  | 46.5<br>(1.1) | 99.4<br>(0.9)  | 240     |
| CKD30  | 1.0<br>(0.0) | 3.9<br>(0.4) | 7.5<br>(0.4)  | 3.0<br>(0.1)  | 35.8<br>(0.6) | 72.0<br>(2.9)  | 225     |
| CKD40  | 1.0<br>(0.0) | 3.9<br>(0.2) | 5.9<br>(0.1)  | 2.6<br>(0.1)  | 33.9<br>(0.9) | 50.2<br>(1.9)  | 170     |
| CKD50  | 0.0<br>(0.0) | 2.6<br>(0.4) | 4.5<br>(0.2)  | 0.0<br>(0.0)  | 21.3<br>(0.4) | 26.3<br>(1.8)  | 120     |
| P2.5   | 1.6<br>(0.1) | 6.1<br>(0.1) | 8.4<br>(0.0)  | 6.6<br>(0.1)  | 67.6<br>(1.5) | 104.3<br>(2.2) | 155     |
| P5     | 1.5<br>(0.0) | 6.0<br>(0.2) | 7.4<br>(0.3)  | 5.8<br>(0.1)  | 60.2<br>(1.7) | 102.2<br>(1.1) | 115     |
| L10    | 1.2<br>(0.1) | 2.4<br>(0.1) | 7.4<br>(0.5)  | 4.8<br>(0.1)  | 11.1<br>(0.1) | 66.3<br>(2.4)  | 215*    |

\*  $w/b = 0.48$

Except for some cases of the CKD10 mixtures, the highest strengths were observed for the reference mortar.

**Table 1:** Binder compositions of the prepared composites in mass fractions, *w*%

**Tabela 1:** Sestava veziv pripravljenih kompozitov v masnih deležih, *w*%

| Mixture designation | R    | CKD10 | CKD20 | CKD30 | CKD40 | CKD50 |
|---------------------|------|-------|-------|-------|-------|-------|
| Slag                | 100  | 90    | 80    | 70    | 60    | 50    |
| Cement kiln dust    | 0    | 10    | 20    | 30    | 40    | 50    |
| Mixture designation | P2.5 | P5    | P10   | L10   | L30   | L50   |
| Slag                | 97.5 | 95    | 90    | 90    | 70    | 50    |
| FBC fly ash P       | 2.5  | 5     | 10    | 0     | 0     | 0     |
| FBC fly ash L       | 0    | 0     | 0     | 10    | 30    | 50    |



However, a significant strength gain was observed between 24 h and 7 d and also between 7 d and 28 d in the case of replacing the slag with up to 40 % of CKD and up to 5–10 % of the FBC fly ash. Higher dosages of these admixtures had a fatal effect on the mechanical properties of AAS, especially in the case of the FBC fly ash.

Both compressive and flexural strengths gradually decreased with the increasing slag replacement at all the ages. The strength reduction was the most severe at the early ages and in the case of the flexural strength. The strength reduction in the presence of CKD could have been caused not only by the decrease in the slag content, but also by a possible formation of chloro and sulfoaluminate phases, leading to a softening and an increased porosity.<sup>7</sup> Another reason can be the increase in the real *w/b* ratio if taking into account the CKD composition, which can also be a reason for the workability improvement at the replacement levels of up to 30 %. When more than 30 % of CKD was used, the workability became reduced, which can be attributed to the fast setting. The setting time was not measured but it was observed that these mortars set very soon after the filling of the molds. A shortening of the setting time was also observed with the increasing FBC-fly-ash dosages. The reason for this can be the formation of the primary CSH through the reaction between  $[\text{SiO}_4]^-$  from the water glass and  $\text{Ca}^{2+}$  released from the free lime present in the fly ash. The precipitation of portlandite is probably suppressed due to its higher solubility in comparison with CSH.<sup>8</sup> Anyway, the hydration of the alkali-activated slag in the presence of the FBC fly ash needs further investigation to explain the problems with the hardening of the mortars with the replacements of the slag by the FBC fly ash higher than 5–10 %. Perhaps most of  $[\text{SiO}_4]^-$  from the activator is consumed during the first minutes to form some type of calcium silicate which is cannot contribute to the strength gain or which suppresses further hydration.

On the other hand, at the later ages, especially the compressive strength grew faster in the case of the appropriately blended composites in comparison with the reference composites. From this point of view, it could be interesting to study the strength development over a longer period. This strength increase might be associated with the  $\text{C}_2\text{S}$  hydration and the pozzolanic reactions of the slag in the presence of the lime contained in CKD. The strength increase of the L10 mortar at the later ages might be due to the pozzolanic reactions of its glassy phase.

The shrinkage development is outlined in **Table 3**. The highest shrinkage rate was observed during the first three days after taking the specimens out of the water. After 14 d, only slight length changes were recorded.

When using CKD at a different replacement level, no clear trend in the shrinkage development was observed. Some mortars showed a slightly lower shrinkage than the

reference mortar, but the shrinkage values of the other mortars were higher. From the data obtained, CKD does not seem to affect the shrinkage reduction. However, the situation with both fly ashes is considerably different: in the case of a 2.5 % replacement of the slag by FBC fly ash P, the shrinkage of the reference mortar was reduced by more than 20 % and if 10 % of fly ash L was used, the shrinkage was reduced even by more than 70 %. Unfortunately, both P5 specimens were broken during demolding, so the data for them were not obtained. These preliminary results showed that the FBC fly ashes can be beneficial for the suppressing of the AAS shrinkage, but attention must be paid to the preservation of the other properties. Additional investigations through instrumental methods like scanning electron microscopy, calorimetry or XRD are planned for the future to clarify the role of the FBC fly ash in the AAS systems.

**Table 3:** Shrinkage development of the prepared composites

**Tabela 3:** Spreminjanje krčenja pripravljenih kompozitov

| Compo-<br>site | Days after water curing |      |      |      |      |      |
|----------------|-------------------------|------|------|------|------|------|
|                | 1                       | 3    | 7    | 14   | 28   | 56   |
| R              | 0.52                    | 0.74 | 0.81 | 0.83 | 0.85 | 0.86 |
| CKD10          | 0.58                    | 0.81 | 0.88 | 0.89 | 0.90 | 0.91 |
| CKD20          | 0.52                    | 0.84 | 0.84 | 0.84 | 0.84 | 0.84 |
| CKD30          | 0.36                    | 0.77 | 0.78 | 0.78 | 0.78 | 0.78 |
| CKD40          | 0.40                    | 0.75 | 0.81 | 0.81 | 0.81 | 0.81 |
| CKD50          | 0.40                    | 0.78 | 0.90 | 0.91 | 0.91 | 0.91 |
| P2.5           | 0.32                    | 0.55 | 0.61 | 0.66 | 0.67 | 0.67 |
| L10            | 0.05                    | 0.13 | 0.15 | 0.18 | 0.22 | 0.24 |

## 4 CONCLUSIONS

This pilot study investigated the effect of a partial replacement of the water-glass-activated blast-furnace slag with the CKD and FBC fly ashes on the workability, mechanical properties and the shrinkage. It was observed that CKD, in proper dosages, improved the workability, while the FBC fly ashes reduced it dramatically even at a low content. On the other hand, unlike CKD, the FBC fly ashes significantly reduced the shrinkage. Both these admixtures, at low replacement levels, had no or little adverse effect on the compressive strength, especially at later ages. In contrast, the flexural strength was affected more negatively. The FBC fly ashes at the dosages higher than 5–10 % had a fatal impact on the strength development.

## Acknowledgement

This outcome was achieved with the financial support of the junior specific research program at the Brno University of Technology, project No. FAST/FCH-J-14-2371.

## 5 REFERENCES

- <sup>1</sup> J. L. Provis, J. S. J. van Deventer (Eds.), *Alkali Activated Materials: State-of-the-art report*, RILEM TC 224-AAM, vol. 13, Springer, Dordrecht 2014, doi:10.1007/978-94-007-7672-2
- <sup>2</sup> M. Palacios, F. Puertas, *ACI Materials Journal*, 108 (2011), 73–78, doi:10.14359/51664218
- <sup>3</sup> P. Chaunsali, S. Peethamparan, *ACI Materials Journal*, 110 (2013), 297–304, doi:10.14359/51685663
- <sup>4</sup> R. Siddique, *Resources, Conservation and Recycling*, 48 (2006), 315–338, doi:10.1016/j.resconrec.2006.03.010
- <sup>5</sup> J. Koornneef, M. Junginger, A. Faaij, *Progress in Energy and Combustion Science*, 33 (2007), 19–55, doi:10.1016/j.pecs.2006.07.001
- <sup>6</sup> G. Sheng, J. Zhai, Q. Li, F. Li, *Fuel*, 86 (2007), 2625–2631, doi:10.1016/j.fuel.2007.02.018
- <sup>7</sup> R. Kunal, R. Siddique, A. Rajor, *Resources, Conservation and Recycling*, 61 (2012), 59–68, doi:10.1016/j.resconrec.2012.01.006
- <sup>8</sup> C. Shi, R. Day, *Cement and Concrete Research*, 25 (1995), 64–105, doi:10.1016/0008-8846(95)00126-W

# MICROSTRUCTURE, MAGNETIC AND MECHANICAL PROPERTIES OF THE BULK AMORPHOUS ALLOY



## MIKROSTRUKTURA, MAGNETNE IN MEHANSKE LASTNOSTI MASIVNE AMORFNE ZLITINE $\text{Fe}_{61}\text{Co}_{10}\text{Ti}_4\text{Y}_5\text{B}_{20}$

**Katarzyna Bloch, Marcin Nabialek, Joanna Gondro**

Czestochowa University of Technology, Faculty of Materials Processing Technology and Applied Physics, Institute of Physics, Czestochowa,  
Poland  
23kasia1@wp.pl

*Prejem rokopisa – received: 2014-08-01; sprejem za objavo – accepted for publication: 2014-09-30*

doi:10.17222/mit.2014.175

This paper presents the results of the studies into the microstructure, the magnetic and mechanical properties of bulk amorphous alloy samples. The samples were produced in the form of rods, using the suction-casting method. The structure and microstructure of the prepared samples were examined using an X-ray diffractometer, a scanning electron microscope and a computer tomograph. The magnetic and mechanical properties were studied using a Lakeshore vibrating-sample magnetometer, a Zwick testing machine and a FutureTech microhardness tester.

On the basis of the obtained results, it was found that, throughout their volumes, the investigated rods have an amorphous structure. Using computer tomography, three-dimensional images of the tested samples were reconstructed, enabling the imaging of the material defects occurring throughout the bulk volumes of the samples. Additionally, the tested Fe-based material should be included in the subset of the electrotechnical materials exhibiting good soft magnetic and mechanical properties. In view of their properties, these materials can be successfully used in energy-efficient transformers, replacing the conventional Fe-Si steel in this and other applications.

**Keywords:** bulk amorphous alloys, electron scanning microscopy, computer tomography, saturation magnetization, coercivity

Članek predstavlja rezultate študija mikrostrukture, magnetnih in mehanskih lastnosti vzorcev masivne amorfne zlitine. Le-ti so bili izdelani v obliki palic z uporabo ulivanja z nasesavanjem. Struktura in mikrostruktura pripravljenih vzorcev je bila preiskovana z rentgenskim difraktometrom, z vrstičnim elektronskim mikroskopom in z računalniškim tomografom. Magnetne in mehanske lastnosti so bile preiskovane z magnetometrom z vibrirajočim vzorcem Lakeshore, s preizkusno napravo Zwick in z merilnikom mikrotrdote FutureTech.

Dobljeni rezultati so pokazali, da imajo preiskovane palice po vsem volumnu amorfno strukturo. Z računalniško tomografijo so bile pripravljene 3D-slike preiskovanih vzorcev, kar omogoča ugotavljanje napak v materialu, ki se pojavljajo po vsem volumnu vzorca. Preizkušeni materiali na osnovi železa naj bi bili vključeni v podskupino materialov za elektrotehniko z dobrimi mehkomagnetnimi in mehanskimi lastnostmi. Glede na njihove lastnosti bi bili lahko ti materiali uspešno uporabljeni za energijsko učinkovite transformatorje, kjer bi nadomestili Fe-Si-jekla, in tudi na drugih področjih.

**Ključne besede:** masivne amorfne zlitine, vrstična elektronska mikroskopija, računalniška tomografija, nasičenje magnetenja, koercitivnost

## 1 INTRODUCTION

Industrial organizations are continuously searching for new materials that will exhibit much-improved properties over those that are currently used. Such materials include bulk amorphous alloys, which, compared with crystalline materials with the same chemical compositions, exhibit much more useful property parameters.<sup>1,2</sup> The reason for the improvement of these properties is the specific structure of the amorphous materials.<sup>3,4</sup> One of the most interesting groups of amorphous alloys includes some of the iron-based alloys, which exhibit excellent magnetic and mechanical properties.<sup>5-9</sup>

## 2 METHOD

In these investigations, the bulk amorphous alloy of  $\text{Fe}_{61}\text{Co}_{10}\text{Ti}_4\text{Y}_5\text{B}_{20}$  was used, in the form of rods with a

length of 2 cm and a diameter of 1 mm. The ingots of the alloy were obtained by arc-melting and mixing high-purity elements under an argon atmosphere. The amorphous rods were produced using the suction-casting method involving the quenching of the molten material in a water-cooled, copper die. In order to avoid oxidizing the samples, the whole production process was carried out in a protective argon atmosphere. The microstructure and structure of the alloy were investigated by means of X-ray diffractometry, electron scanning microscopy and computer tomography. The BRUKER X-ray diffractometer was equipped with a lamp with a Co-K $\alpha$  source. Investigations were carried out over the  $2\theta$  range from  $30^\circ$  to  $120^\circ$ , with a measurement step of  $0.02^\circ$  and the time per step of 5 s. Images of the material surface were obtained using a Zeiss SUPRA 35 high-resolution scanning electron microscope, utilizing the detection of secondary electrons (SE) and having an acceleration voltage of

25 kV. In order to analyse the chemical composition of the samples, an EDAX TRIDENT XM4 energy-dispersive X-ray Spectrometer (EDS) was used. A reconstruction of the surfaces of the samples was achieved using a BRUKER Mikro-CT SkyScan 1172 computer tomograph. The operating parameters, such as the voltage, the filter type and the exposure time were optimized to obtain the greatest contrast. The investigations were performed with a resolution (pixel size) of 2.38 mm, for the rotation angle of 360 °, a step of 0.3 ° and the exposure time of 1.2 ms. Diffraction rings were reduced by oscillating the measurement table with an amplitude setting of 50. All the reconstructions were obtained utilizing dedicated NRecon and CTAN (Bruker) software and the editing was visualized using DataViewer and CTVol (Bruker) software.

The microhardness of the samples was measured using the Vickers method and a FutureTech FM hardness tester, with a measurement time of 10 s and an applied force of 490.3 mN.

Three-point bending tests for metallic glasses were performed on the investigated material. A Zwick 005 testing machine was used for this test, with a crosshead speed of 1 mm/min; the spacing and diameter of the supports were 5 mm and 2 mm, respectively. The tension was calculated from the following equation:

$$\sigma = \frac{3Fl}{2bh^2} \text{ (MPa)} \quad (1)$$

where:  $F$  – force,  $l$  – support spacing,  $b$  – sample width,  $h$  – sample thickness.

Static hysteresis loops were obtained using a Lake-Shore 7103 vibrating-sample magnetometer (VSM). From the analysis of the static hysteresis loops, parameters such as the saturation magnetization, the coercivity and the stiffness parameter of the spin wave ( $D_{sp}$ ) were found.

### 3 RESULTS

**Figure 1** shows the X-ray diffraction pattern obtained for the sample of the  $\text{Fe}_{61}\text{Co}_{10}\text{Ti}_4\text{Y}_5\text{B}_{20}$  alloy.

In the obtained X-ray diffraction pattern, only a single broad maximum is present, indicating the amorphicity of the material.<sup>10</sup>

In **Figure 2**, SEM images of the surface of an investigated rod and the results obtained with an EDS ana-

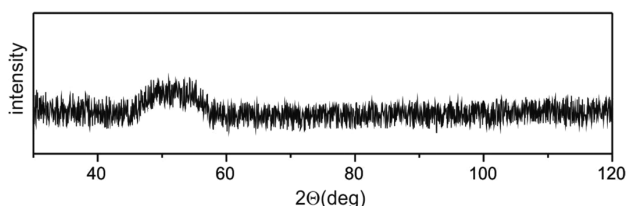


**Figure 1:** X-ray diffraction pattern for the bulk amorphous  $\text{Fe}_{61}\text{Co}_{10}\text{Ti}_4\text{Y}_5\text{B}_{20}$  alloy

**Slika 1:** Rentgenogram masivne amorfne zlitine  $\text{Fe}_{61}\text{Co}_{10}\text{Ti}_4\text{Y}_5\text{B}_{20}$

lysis, are presented. The SEM image of the surface reveals the consequence of an uneven cooling speed during the production process. Discontinuities along the longitudinal surface of the rod are the reason for an inhomogeneous stress distribution in the sample cross-section. The influence of these stresses on the type of breakthrough is visualised in **Figure 2b**. The zones with different breakthrough characteristics are marked with white circles. In **Figure 2e** three beams of the stress bands are visible, typical of those observed in the breakthroughs of the amorphous samples. Within the circumference zone of about 70 μm numerous gas bubbles can be seen, which were created during the production process of the rods. The elimination of the pores existing in this zone is difficult and requires maintenance of stable conditions during the whole production process. During the decohesion process, parallel displaced veins were created (**Figure 2c**). Within the boundaries of these veins, free volumes are visible due to the decomposition of the material. This can be connected with the fluctuations of the chemical composition and density existing in the alloy. Within the limits of the investigated breakthroughs, poorly developed scale-like structures were also observed (**Figure 2d**), indicating different levels of relaxation. Throughout the whole volume of the breakthrough, point imperfections were observed on the surface (**Figure 2f**).

The X-ray microanalysis demonstrated that these areas are not crystallites and that they have a different chemical composition, compared with the surrounding amorphous matrix. In the investigated areas, the Y and Fe atoms were subjected to regrouping processes. An increase in the Y content, to amount fraction 10 %, was observed with a simultaneous decrease in the Fe content of more than 3 %, compared with the nominal alloy composition. This result may indicate a tendency to create Y-rich conglomerates, which could be the origin of the

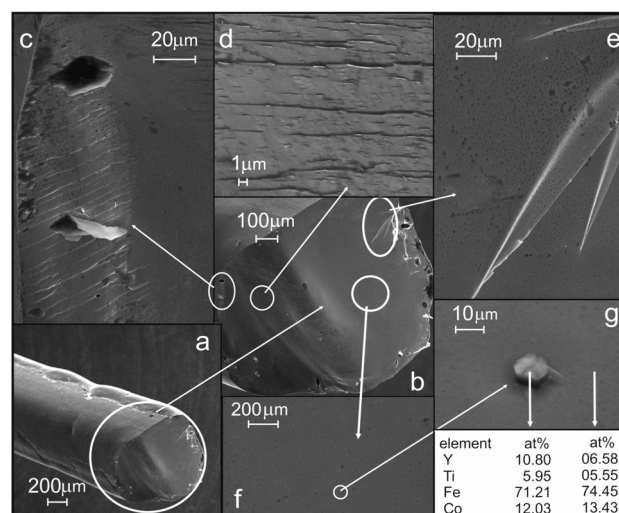


**Figure 2:** SEM images for the bulk amorphous  $\text{Fe}_{61}\text{Co}_{10}\text{Ti}_4\text{Y}_5\text{B}_{20}$  alloy

**Slika 2:** SEM-posnetki masivne amorfne zlitine  $\text{Fe}_{61}\text{Co}_{10}\text{Ti}_4\text{Y}_5\text{B}_{20}$

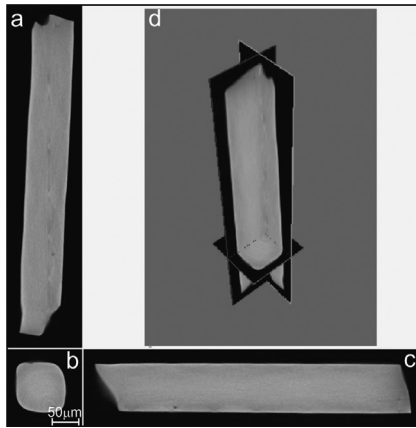


**Figure 3:** Cross-sections: a) lengthwise, b) transverse, c) sagittal and d) their spatial representation

**Slika 3:** Prezrez: a) vzdolžni, b) prečni, c) sagitalni in d) njihov prostorski prikaz

two metastable crystalline phases:  $Y_5Co$ ,  $Fe_{17}Y_2$  and  $\alpha$ -Fe phase, created during the primary crystallization.

The 3-D image reconstructions, obtained in three planes and then superposed, are presented in **Figure 3**.

The presented transmission images (**Figure 3**) are typical of a sample with one phase, which is in agreement with the X-ray results.

The magnetic parameters, including the saturation magnetization and the value of the coercive field were obtained from the analysis of the static hysteresis loops (**Figure 4**). The investigated alloy is a ferromagnetic material, exhibiting soft magnetic properties, with a relatively high value of the saturation magnetization and a small value of the coercivity. These properties make it attractive as a material for low-loss transformer cores working at high frequencies.

The Holstein-Primakoff paraprocess<sup>11</sup> is one of the high-field factors influencing the magnetization process in the range of the magnetic field above the anisotropy

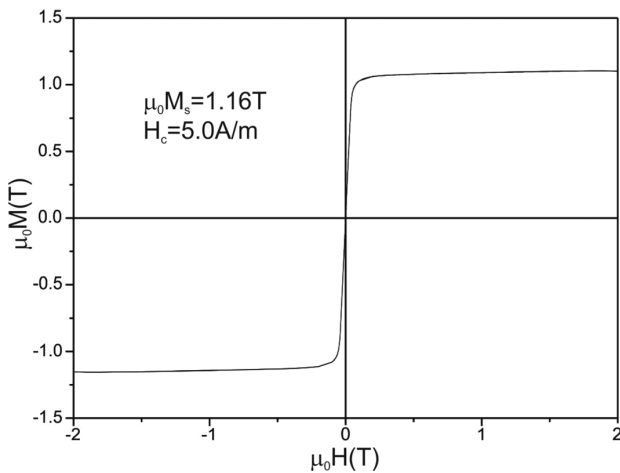


**Figure 4:** Static hysteresis loop for the  $Fe_{61}Co_{10}Ti_4Y_5B_{20}$  alloy in the form of a rod

**Slika 4:** Statična histerezna zanka zlitine  $Fe_{61}Co_{10}Ti_4Y_5B_{20}$  v obliki palice

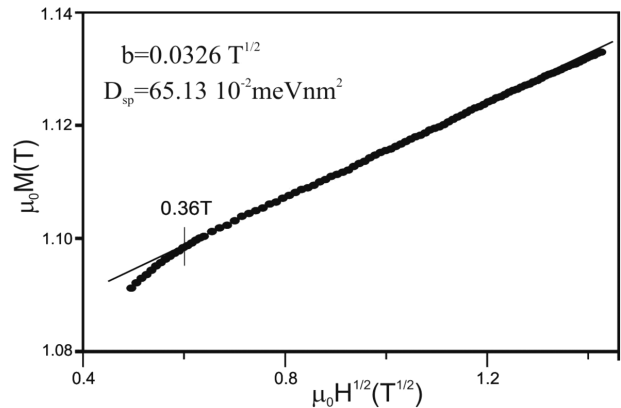


**Figure 5:** Magnetization as a function of the magnetic field for the bulk amorphous  $Fe_{61}Co_{10}Ti_4Y_5B_{20}$  alloy in the form of a rod

**Slika 5:** Magnetizacija v odvisnosti od magnetnega polja masivne amorfne zlitine  $Fe_{61}Co_{10}Ti_4Y_5B_{20}$  v obliki palice

field. A linear relation  $\mu_0M(\sqrt{\mu_0H})$  is presented in **Figure 5**.

On the basis of the following relationship:

$$b = 3.54g\mu_0\mu_B\sqrt{(1/4\pi D_{sp})^3 kt\sqrt{g\mu_B}} \quad (2)$$

(where:  $g$  – Lande split coefficient,  $\mu_B$  – Bohr magneton,  $\mu_0$  – magnetic permeability of a vacuum,  $k$  – Boltzmann constant,  $T$  – temperature,  $b$  – linear fit coefficient of the Holstein-Primakoff paraprocess<sup>11</sup>) the spin-wave stiffness parameter ( $D_{sp}$ ) was calculated; this parameter is described with the following equation:

$$D_{sp} = \sum S_i J(\vec{r}_i) \vec{r}_i^2 \cos^2(\vec{k}, \vec{r}_i) \quad (3)$$

where:  $S_i$  – spin in the  $r_i$  position against the central atom,  $J(r_i)$  – exchange integral between the central atom and an atom in the  $\vec{r}_i$  position,  $\vec{k}$  – wave vector.

In the case of the materials with an amorphous structure,  $\vec{r}_i$  denotes the locations of the closest magnetic atoms within the vicinity of the central atom. If the investigated alloy has a high value of this parameter this indicates the creation of short-range chemical order.

Exemplar imprints of the Vickers pyramids are presented in **Figure 6**.

The results of five microhardness measurements and their average value are listed in **Table 1**.

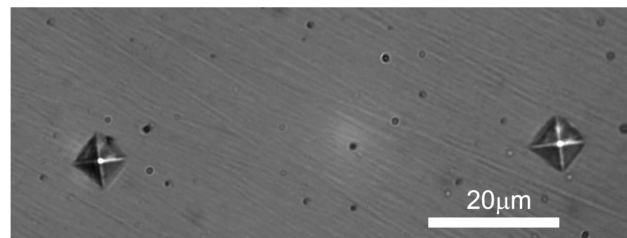


**Figure 6:** Vickers imprints obtained for the investigated alloy  
**Slika 6:** Odtiska meritve trdote po Vickersu na preiskovani zlitini

**Table 1:** Hardness-measurement results**Tabela 1:** Rezultati meritve trdote

| Item number | Microhardness (HV <sub>0.05</sub> ) |
|-------------|-------------------------------------|
| 1           | 1362                                |
| 2           | 1339                                |
| 3           | 1491                                |
| 4           | 1454                                |
| 5           | 1123                                |
| Average     | 1354                                |

The investigated amorphous alloy, Fe<sub>61</sub>Co<sub>10</sub>Ti<sub>4</sub>Y<sub>5</sub>B<sub>20</sub>, possesses a high average value of microhardness, more than 100 HV higher than the value for the Fe-B amorphous alloys<sup>12</sup>.

The investigated rod was subjected to the three-point bending test for metallic glasses. The maximum value of the bending strength parameter was found to be 465.75 MPa which is typical for this type of materials<sup>13–15</sup>.

#### 4 CONCLUSIONS

The investigation described in this paper involved the application of the suction-casting method of producing an alloy, with strict adherence to the rules for the production parameters. This resulted in a repeatable production process for the manufacture of a bulk amorphous alloy Fe<sub>61</sub>Co<sub>10</sub>Ti<sub>4</sub>Y<sub>5</sub>B<sub>20</sub> in the form of a rod with a length of 2 mm and a diameter of 1 mm.<sup>10</sup> On the basis of the structural and microstructural investigations, it can be concluded that regions of a slightly heterogeneous chemical composition occur within the volume of the sample, i.e., locally, the chemical composition varies slightly around the stoichiometric formula. On the surface of the breakthrough, numerous cylindrical 'islands' with a high Y content are present (**Figure 2g**). The fluctuations in the chemical composition and density are visible in the SEM images; such fluctuations can provide energetically favourable locations for the emergence of crystalline-phase nuclei, which are the result of the primary crystallization. In the breakthrough of the rod (**Figure 2**) various types of structures were observed. The variation from a smooth to a scale-like structure, with numerous breakdowns, indicates different stress distributions of the structure. 3-D reconstructions of the rod images did not reveal any imperfections in the form of the pores (**Figure 3**). The investigated material is ferromagnetic with a high value of the saturation magnetization and a low coer-

civity. These values are comparable to those obtained for FeSi steels used for transformer/inductor cores. However, the FeSi steels exhibit a high magnetostriction compared with the amorphous materials<sup>10</sup>. From the analysis of the high-field Holstein-Primakoff paraprocess, parameter  $D_{sp}$  was found, its value indicating a high concentration of magnetic atoms per unit volume, and confirming the high value of the saturation magnetization<sup>11</sup>. The investigated alloy has a microhardness value of approximately 1350 HV, which is slightly higher than that for the iron-based bulk amorphous alloys<sup>13–16</sup>. In conclusion, the investigated material has strong application prospects, especially in the electrotechnical industry where it may be used as a material for efficient magnetic cores.

#### 5 REFERENCES

- H. Chirac, N. Lupu, *Materials Science and Engineering A*, 375–377 (2004), 255–259, doi:10.1016/j.msea.2003.10.110
- K. Bloch, *Journal of Magnetism and Magnetic Materials*, 390 (2015), 118–122, doi:10.1016/j.jmmm.2015.04.032M
- A. Inoue, *Materials Science and Engineering*, 226–228 (1997), 357–363, doi:10.1016/S0921-5093(97)80049-4
- R. Hasegawa, *Journal of Magnetism and Magnetic Materials*, 41 (1984), 79–85, doi:10.1016/0304-8853(84)90142-2
- K. Bloch, M. Nabiałek, P. Pietrusiewicz, J. Gondro, M. Dośpiał, M. Szota, K. Gruszka, *Acta Physica Polonica A*, 126 (2014) 1, 108–109, doi:10.12693/APhysPolA.126.108
- K. Sobczyk, J. Świerczek, J. Gondro, J. Zbroszczyk, W. Ciużyńska, J. Olszewski, P. Brągiel, A. Łukiewska, J. Rzącki, M. Nabiałek, *Journal of Magnetism and Magnetic Materials*, 324 (2012), 540–549, doi:10.1016/j.jmmm.2011.08.038
- H. Jian, W. Luo, S. Tao, M. Yan, *Journal of Alloys and Compounds*, 505 (2010), 315–318, doi:10.1016/j.jallcom.2010.06.061
- M. Nabiałek, *Journal of Alloys and Compounds*, 642 (2015), 98–103, doi:10.1016/j.jallcom.2015.03.250
- K. Bloch, M. Nabiałek, *Acta Physica Polonica A*, 127 (2015), 413–414, doi:10.12693/APhysPolA.127.413
- D. Szewiczek, J. Tyrlik-Held, S. Lesz, *Journal of Materials Processing Technology*, 109 (2001), 190–195, doi:10.1016/S0924-0136(00)00795-0
- T. Holstein, H. Primakoff, *Physical Review*, 58 (1940), 1098–1113, doi:10.1103/PhysRev.58.1098
- A. Inoue, *Acta Materialia*, 48 (2000), 279–306, doi:10.1016/S1359-6454(99)00300-6
- D. Szewiczek, S. Lesz, *Journal of Materials Processing Technology*, 162–163 (2005), 254–259, doi:10.1016/j.jmatprotec.2005.02.017
- M. Nabiałek et al., *Journal of Alloys and Compounds*, 509S (2011), S155–S160, doi:10.1016/j.jallcom.2011.01.158
- M. Nabiałek et al., *Phys. Status Solidi C*, 7 (2010) 5, 1428–1431, doi:10.1002/pssc.200983393
- D. Jenko, *Mater. Tehnol.*, 45 (2011) 4, 303–310

# MODIFIED CEMENT-BASED MORTARS: CRACK INITIATION AND VOLUME CHANGES

## MODIFICIRANE MALTE NA OSNOVI CEMENTA: INICIACIJA RAZPOK IN VOLUMENSKA SPREMEMBE

Ivana Havlikova<sup>1</sup>, Vlastimil Bilek Jr.<sup>2</sup>, Libor Topolar<sup>1</sup>, Hana Simonova<sup>1</sup>,  
Pavel Schmid<sup>1</sup>, Zbynek Kersner<sup>1</sup>

<sup>1</sup>Brno University of Technology, Faculty of Civil Engineering, Veveri 331/95, 602 00 Brno, Czech Republic

<sup>2</sup>Ditto, Faculty of Chemistry, Purkynova 464/118, 612 00 Brno, Czech Republic  
havlikova.i@fce.vutbr.cz

*Prejem rokopisa – received: 2014-08-05; sprejem za objavo – accepted for publication: 2014-09-18*

doi:10.17222/mit.2014.179

The aim of this paper was to quantify the crack initiation and volume changes of three types of fine-grain cement-based composites: the reference one including Portland cement only and the other two with the mass fraction 20 % of Portland cement replaced by granulated blast-furnace slag or pulverized-coal fly ash. Half of the specimens from each mixture were cured according to ASTM C1260-94 and ASTM C1567-07, other specimens were cured in water. The length changes were measured during the curing (a test for the risk of the alkali-silica reactivity). Furthermore, a three-point-bending test was performed on these specimens to obtain the fracture parameters, which were determined using a double-*K* fracture model. It was found that the type of specimen curing has a significant effect on the volume changes and a moderate influence on the elasticity modulus, the crack initiation and fracture-toughness values.

Keywords: cement-based composite, slag, fly ash, alkali-silica reaction, crack initiation, double-*K* fracture model

Namen tega članka je oceniti iniciacijo razpoke in spremembe volumna treh vrst drobnozrnatih kompozitov na osnovi cementa: osnovna samo s cementom Portland, pri drugih dveh je bil masni delež 20 % cementa Portland nadomeščen z granulirano plavžno žlindro ali s prahom elektrofiltrskega pepela premoga. Polovica vzorcev iz vsake mešanice je bila strjena skladno z ASTM C1260-94 in ASTM C1567-07, drugi vzorci so bili strjeni v vodi. Med strjevanjem je bilo merjeno spreminjanje dolžine (preizkus za rizik reaktivnosti alkalija-silicijev dioksid). Poleg tega je bil izvršen pri teh vzorcih tritočkovni upogibni preizkus, da bi dobili parameter preloma, kar je bilo določeno z uporabo lomnega modela z dvojnim *K*. Ugotovljeno je bilo, da ima način strjevanja vzorcev močan vpliv na spremembe volumna in zmeren vpliv na modul elastičnosti, na iniciacijo razpoke, kot tudi na vrednosti lomne žilavosti.

Ključne besede: kompozit na osnovi cementa, žlindra, letечи pepel, reakcija med alkalijami in silicijevim dioksidom, iniciacija razpoke, lomni model z dvojnim *K*

## 1 INTRODUCTION

The utilization of supplementary cementing materials (SCM) in the Portland-cement-based composite manufacturing is a current topic in materials engineering. Besides the ecological and financial aspects, it also allows us to improve the mechanical properties and durability of a composite. One of the main durability problems is the risk of an alkali-silica reaction (ASR). ASR can be very harmful to a concrete construction because it is accompanied by a significant volume expansion. As a consequence, deleterious cracking of the aggregate and the binder phase can develop, leading even to a failure of the concrete structure. ASR can be suppressed through several ways, but some of them are impractical or expensive, such as the choice of non-alkali-reactive aggregates, restriction of the access of moisture to the concrete mass or the use of ASR inhibitors<sup>1</sup>. From this point of view, a very suitable possibility of ASR mitigation can be the use of SCM, which is also the topic of this paper.

In this paper, the authors examine the effect of replacing 20 % of the mass of Portland cement (PC) in a

fine-grained composite by selected admixtures on mechanical-fracture-parameter values and volume changes. The used admixtures are granulated blast-furnace slag and pulverized coal fly ash. Specimens of three different mixtures were prepared and, for comparison, two types of curing were used – the first one according to ASTM C1260-94<sup>2</sup> and ASTM C1567-07<sup>3</sup>, while the second one was performed in water. Length changes were measured to assess the effect of the admixtures on the suppression of ASR during this process. The result of the length-change measurement is the relative expansion at the age of 16 d.

The values of the mechanical-fracture parameters of quasi-brittle materials are usually determined via an evaluation of the records of the experiments on specimens with stress concentrators. In this paper, three-point-bending fracture tests were conducted on the above-mentioned specimens, which were evaluated using a double-*K* fracture model<sup>4</sup>. The advantage of this model is that it describes different levels of crack propagation: the initiation which corresponds with the beginning of a stable crack growth (at the level where the stress inten-

sity factor  $K_{Ic}^{ini}$  is reached) and the part featuring an unstable crack propagation (after the unstable-fracture toughness  $K_{Ic}^{un}$  has been reached). The results obtained with the double- $K$  model are the modulus of elasticity, the fracture toughness and the relative resistance to stable crack propagation.

## 2 EXPERIMENTAL PART

### 2.1 Materials and specimen preparation

Specimens with the nominal dimensions of 25 mm × 25 mm × 285 mm were prepared from three types of mixture. The first mixture was the reference (R), thus containing one part of PC CEM I 52.5 R to 2.25 parts of natural sand (0–4 mm) by mass. In the other two mixtures 20 % of PC was replaced with granulated blast-furnace slag (S) or pulverized-coal fly ash (F). All these admixtures originated from Czech plants. The water-to-binder ratio was 0.47 for all the mixtures. A total of 18 beams were prepared, thus, six specimens from each type of mixture.

### 2.2 Curing of specimens and the measuring of length changes

The specimens were cured and their length changes measured according to ASTM C1260-94 and ASTM C1567-07. The specimens were demolded 24 h after the mixing, fitted with gages and stored in tap water of 80 °C for another 24 h. Then a zero reading of the specimen length compared to the reference rod was taken. After this, a half of the total number of the specimens, i.e., three specimens from each mixture were cured for 14 d at 80 °C in a 1-N sodium hydroxide solution (H). For comparison, other specimens were cured for the same time in water (W) of the same temperature. To illustrate, **Figure 1** shows the classification and designation of the specimens by mixture and their curing conditions.

The relative length changes (in %) of the specimens were recorded during both types of curing and subtracted each workday. The relative expansion of the specimens

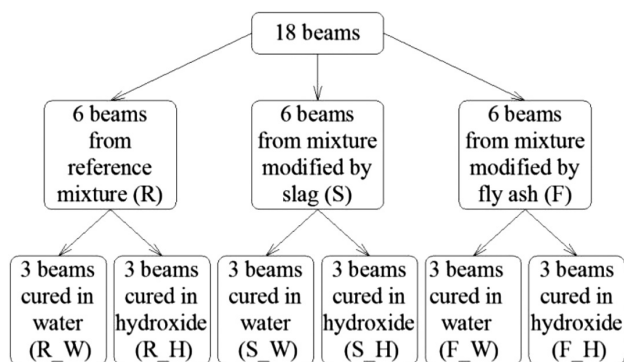


**Figure 1:** Classification of the specimens by mixture and curing condition

**Slika 1:** Delitev vzorcev po mešanicah in razmerah pri strjevanju

for the total age of 16 d  $\varepsilon_{16d}$ , was calculated using the following relation:

$$\varepsilon_{16d} = \frac{\Delta l - \Delta l_0}{l_k} \cdot 100(\%) \quad (1)$$

where  $\Delta l$  is the specimen length compared to the reference rod for the age of 16 d in mm,  $\Delta l_0$  is the specimen length compared to the reference rod at the zero reading in mm, and  $l_k$  is the effective gage length in mm (generally  $l_k = 250$  mm).

### 2.3 Fracture tests

A quantification of the mechanical fracture parameters was performed using tests on the specimens with stress concentrators. In this paper, three-point-bending tests were performed on the beams with a central-edge notch. The geometry of a specimen used in this test is shown in **Figure 2**, where  $D$  is the specimen depth,  $B$  is the width,  $L$  is the length,  $S$  is the span,  $a_0$  is the initial notch length,  $H_0$  is the thickness of the edge of the holder clip on the extensometer (for all the specimens  $H_0 = 2.5$  mm) and  $CMOD$  is the crack-mouth-opening displacement at load  $P$ . In this case, the specimens were cut from

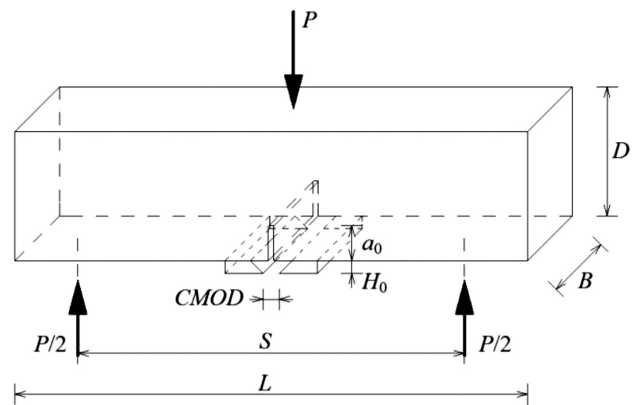


**Figure 2:** Three-point-bending-fracture test geometry  
**Slika 2:** Geometrija tritočkovnega upogibnega preloma

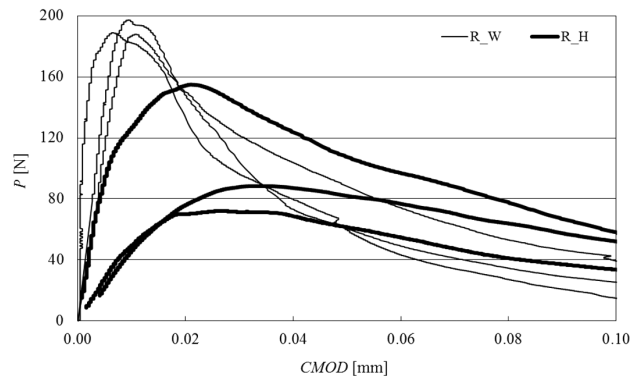


**Figure 3:**  $P - CMOD$  diagrams recorded during testing – the reference set

**Slika 3:** Diagrami  $P - CMOD$ , posneti med preizkušanjem – referenčna vrsta



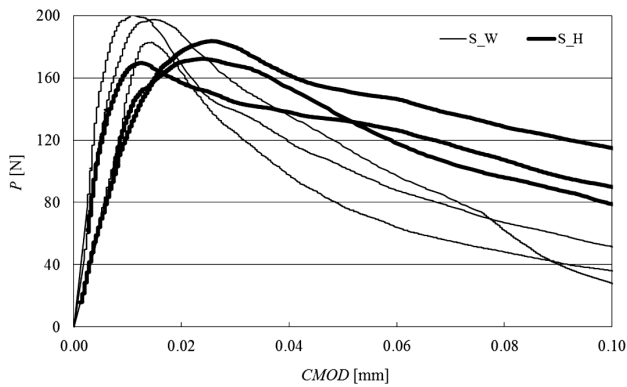


Figure 4:  $P - CMOD$  diagrams recorded during testing – the set of specimens with blast-furnace slag (S)

Slika 4: Diagrami  $P - CMOD$ , posneti med preizkušanjem – vrsta vzorcev s plavžno žilindro (S)

the original beams, the nominal dimensions of the specimens were 25 mm × 25 mm × 200 mm and the span length was 150 mm. The initial notch was made with a diamond-blade saw. Note that the depth of the notches was about 1/3 of the specimen depth. The specimen age was 28 d. Fracture tests were carried out using a Heckert FP 10/1 testing machine within a range of 0–400 N.

Load-versus-crack-mouth-opening-displacement ( $P - CMOD$ ) diagrams were recorded during the tests (Figure 3 for R, Figure 4 for the specimens of the mixture modified with S and Figure 5 for the specimens with F). From these diagrams we deduced the input data for the double- $K$  fracture model (Figure 6), namely, the maximum load  $P_{max}$  and its corresponding critical crack-mouth-opening displacement  $CMOD_c$ , and load  $P_i$  deduced from the linear part of a diagram and its corresponding crack-mouth-opening displacement  $CMOD_i$ .

### 2.4 Double- $K$ fracture model

In principle, a double- $K$  fracture model<sup>4</sup> combines the concept of cohesive forces acting on the faces of cracks during a fictitious (effective) crack increment with the criterion based on the stress-intensity factor.

As previously mentioned, the  $P - CMOD$  diagrams were used to determine the fracture parameters of the double- $K$  model. In this case, the unstable fracture toughness  $K_{Ic}^{un}$  was the first to be numerically determined, followed by a determination of the cohesive fracture toughness  $K_{Ic}^c$ . When both of these values were known, the following formula was used to calculate the initiation fracture toughness  $K_{Ic}^{ini}$ :

$$K_{Ic}^{ini} = K_{Ic}^{un} - K_{Ic}^c \quad (2)$$

Details regarding the calculation of both the unstable and cohesive fracture toughness can be found in numerous sources<sup>5,6</sup>.

To determine the cohesive part of the fracture toughness  $K_{Ic}^c$  it is necessary to accept the assumption of the distribution of the cohesive stress  $\sigma$  along the fictitious crack. Generally, in a cohesive crack model, the relation

between the cohesive stress  $\sigma$  and the effective crack-opening displacement  $w$  is referred to as the cohesive stress function  $\sigma(w)$ . The cohesive stress  $\sigma(CTOD_c)$  at the tip of the initial notch length  $a_0$  at the critical state can be obtained from the softening curve. In this paper, the exponential softening curve suggested by Reinhardt et al.<sup>7</sup> was used. The value of  $\sigma(CTOD_c)$  was determined using the following formula:

$$\sigma(CTOD_c) = f_t \left\{ \left[ 1 + \left( \frac{c_1 CTOD_c}{w_c} \right)^3 \right] \exp\left( \frac{-c_2 CTOD_c}{w_c} \right) - \frac{CTOD_c}{w_c} (1 + c_1^3) \exp(-c_2) \right\} \quad (3)$$

where  $f_t$  is the tensile strength in MPa,  $CTOD_c$  is the critical crack-tip-opening displacement in mm (the details regarding the calculation can be found in<sup>4</sup>),  $w_c$  is the maximum crack-tip-opening displacement in mm (in this case  $w_c = 0.06$  mm for all the specimens), and  $c_1, c_2$  are the material constants (in this case constants  $c_1 = 3$  and  $c_2 = 6.93$  were considered as recommended in<sup>4</sup>).

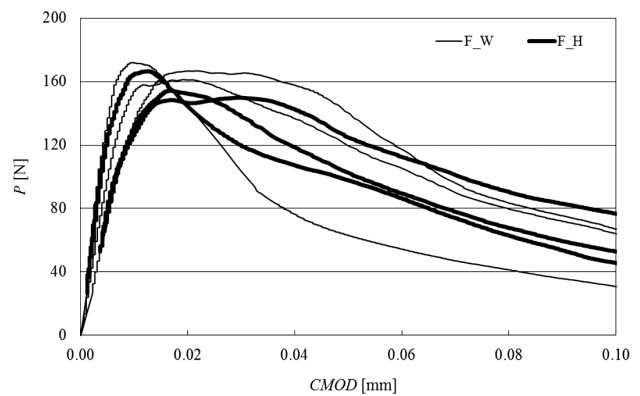


Figure 5:  $P - CMOD$  diagrams recorded during testing – the set of specimens with pulverized-coal fly ash (F)

Slika 5: Diagrami  $P - CMOD$ , posneti med preizkušanjem – vrsta vzorcev z elektrofiltrskim pepelom premoaga (F)

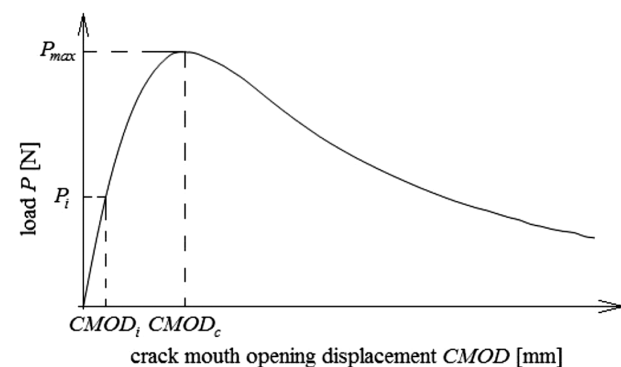


Figure 6: Deduction of the input data for the double- $K$  model from the  $P - CMOD$  diagram

Slika 6: Vhodni podatki za model z dvojnimi  $K$  iz diagrama  $P - CMOD$

The tensile-strength value was estimated using the measured compressive-strength value suggested by documentation<sup>8</sup>, using the following relationship:

$$f_t = 0.24f_{cu}^{2/3} \tag{4}$$

where  $f_{cu}$  is the compressive cube strength in MPa (in this case these values were estimated from the informative compressive tests on the fragments of the specimens after the fracture tests).

Finally, the value of the load  $P_{ini}$  was determined according to Equation (5). This value can be defined as the load level at the beginning of the stable crack propagation from the initial crack/notch:

$$P_{ini} = \frac{4WK_{Ic}^{ini}}{SF_1(\alpha_0)\sqrt{a_0}} \tag{5}$$

where  $W$  is the section modulus in  $m^3$  (determined as  $W = 1/6BD^2$ ),  $K_{Ic}^{ini}$  is the initial fracture toughness in  $Pa\ m^{1/2}$ ,  $S$  is the span length in  $m$ ,  $a_0$  is the initial notch length in  $m$ , and  $F_1(\alpha_0)$  is the geometry function determined using the following equation<sup>9</sup>:

$$F_1(\alpha_0) = \frac{1.99 - \alpha_0(1 - \alpha_0)(2.15 - 3.93\alpha_0 + 2.7\alpha_0^2)}{(1 + 2\alpha_0)(1 - \alpha_0)^{3/2}} \tag{6}$$

where  $\alpha_0$  is ratio  $a_0/D$ .

### 3 RESULTS

The mean values of the selected results are presented in the tables: elasticity modulus  $E$  (Table 1), fracture toughness  $K_{Ic}^{un}$  (Table 2), relative resistance to stable crack propagation  $K_{Ic}^{ini}/K_{Ic}^{un}$  (Table 3), load level at the beginning of the stable crack propagation from the initial notch  $P_{ini}$  (Table 4) and relative expansion at the age of 16 d  $\epsilon_{16d}$  which indicates the risk of alkali-silica reactivity (Table 5). The above-mentioned tables also give

**Table 1:** Mean values of elasticity modulus and their relative values (1.00...R\_|1.00...\_W)

**Tabela 1:** Srednje vrednosti modula elastičnosti in njihove relativne vrednosti (1.00...R\_|1.00...\_W)

| $E$ | W                        |                    | H                        |                    |
|-----|--------------------------|--------------------|--------------------------|--------------------|
|     | mean value (GPa) (COV/%) | relative value (-) | mean value (GPa) (COV/%) | relative value (-) |
| R   | 27.9 (13.7)              | 1.00 1.00          | 18.2 (23.0)              | 1.00 0.65          |
| S   | 24.8 (32.1)              | 0.89 1.00          | 18.6 (30.8)              | 1.02 0.75          |
| F   | 23.5 (31.5)              | 0.84 1.00          | 20.8 (26.0)              | 1.14 0.88          |

**Table 2:** Mean values of fracture toughness and their relative values (1.00...R\_|1.00...\_W)

**Tabela 2:** Srednje vrednosti lomne žilavosti in njihove relativne vrednosti (1.00...R\_|1.00...\_W)

| $K_{Ic}^{un}$ | W                                          |                    | H                        |                    |
|---------------|--------------------------------------------|--------------------|--------------------------|--------------------|
|               | mean value (MPa m <sup>1/2</sup> ) (COV/%) | relative value (-) | mean value (MPa) (COV/%) | relative value (-) |
| R             | 0.569 (4.3)                                | 1.00 1.00          | 0.624 (9.8)              | 1.00 1.10          |
| S             | 0.606 (16.0)                               | 1.06 1.00          | 0.613 (4.4)              | 0.98 1.01          |
| F             | 0.631 (6.2)                                | 1.11 1.00          | 0.616 (13.1)             | 0.99 0.98          |

the relative values of these parameters: first in relation to R, then in relation to the specimens cured in W.

**Table 3:** Mean values of relative resistance to stable crack propagation and their relative values (1.00...R\_|1.00...\_W)

**Tabela 3:** Srednje vrednosti relativne odpornosti proti stabilnemu napredovanju razpoke in njihove relativne vrednosti (1.00...R\_|1.00...\_W)

| $K_{Ic}^{ini}/K_{Ic}^{un}$ | W                      |                    | H                      |                    |
|----------------------------|------------------------|--------------------|------------------------|--------------------|
|                            | mean value (-) (COV/%) | relative value (-) | mean value (-) (COV/%) | relative value (-) |
| R                          | 0.542 (0.6)            | 1.00 1.00          | 0.340 (31.4)           | 1.00 0.63          |
| S                          | 0.555 (30.0)           | 1.02 1.00          | 0.384 (13.2)           | 1.13 0.69          |
| F                          | 0.384 (8.3)            | 0.71 1.00          | 0.347 (14.6)           | 1.02 0.90          |

**Table 4:** Mean values of load level at the beginning of stable crack propagation from the initial notch and their relative values (1.00...R\_|1.00...\_W)

**Tabela 4:** Srednje vrednosti obremenitve na začetku rasti razpoke od začetne zareze in njihove relativne vrednosti (1.00...R\_|1.00...\_W)

| $P_{ini}$ | W                      |                    | H                      |                   |
|-----------|------------------------|--------------------|------------------------|-------------------|
|           | mean value (N) (COV/%) | relative value (-) | mean value (N) (COV/%) | relative value(-) |
| R         | 122.2 (3.2)            | 1.00 1.00          | 59.7 (5.0)             | 1.00 0.49         |
| S         | 127.5 (11.7)           | 1.04 1.00          | 93.4 (17.4)            | 1.57 0.73         |
| F         | 93.7 (2.4)             | 0.77 1.00          | 81.4 (2.1)             | 1.36 0.87         |

**Table 5:** Mean values of relative expansion at the age of 16 d and their relative values (1.00...R\_|1.00...\_W)

**Tabela 5:** Srednje vrednosti relativne ekspanzije pri starosti 16 d in njihove relativne vrednosti (1.00...R\_|1.00...\_W)

| $\epsilon_{16d}$ | W                      |                    | H                      |                    |
|------------------|------------------------|--------------------|------------------------|--------------------|
|                  | mean value (%) (COV/%) | relative value (-) | mean value (%) (COV/%) | relative value (-) |
| R                | -0.0041 (-)            | 1.00 1.00          | 0.1901 (1.1)           | 1.00 46.0          |
| S                | -0.0018 (11.1)         | 0.44 1.00          | 0.1240 (2.3)           | 0.65 68.9          |
| F                | -0.0051 (39.4)         | 1.23 1.00          | 0.0988 (15.2)          | 0.52 19.5          |

### 4 DISCUSSION

It was found that the value of  $E$ , in the case of the specimens cured in W, was reduced by 11 % due to S and the use of F reduced this value by 16 % compared to the R value. In the case of the specimens cured in H, the use of S had no significant effect on the value of  $E$ , but the use of F increased this value by 14 % compared to the R value. The comparison of both types of specimen curing shows that the specimens cured in H had the values of  $E$ : R lower by 35 %, the values of the specimens containing S were lower by 25 % and the values of the specimen with F were lower by 12 %.

The value of  $K_{Ic}^{un}$  in the case of the specimens cured in W was increased by 6 % due to S and the use of F increased this value by 11 % compared to the R value. In the case of the specimens cured in H, the use of S or F had no significant effect on the value of  $K_{Ic}^{un}$  compared to the R value. The comparison of both types of specimen curing shows that R cured in H had higher values of

$K_{Ic}^{un}$  (by 10 %) and for the specimens with S or F this value was almost the same.

The value of the relative resistance to stable crack propagation ( $RSCP - K_{Ic}^{ini}/K_{Ic}^{un}$ ), in the case of the specimens cured in W, was reduced by 29 % due to the use of F, while the use of S had no significant effect on this resistance compared to the R value. In the case of the specimens cured in H, the use of F had no significant effect on  $RSCP$ , but using S increased this resistance by 13 % compared to the R value. The comparison of both types of specimen curing shows that the specimens cured in H had the  $RSCP$ : R value lower by 37 %, the value of the specimen with S was lower by 31 % and the value of the specimen with F was lower by 10 %.

The value of  $P_{ini}$ , in the case of the specimens cured in W, was increased by 4 % due to the use of S and F decreased this value by 23 % compared to the R value. In the case of the specimens cured in H, both S and F increased this value: S by 57 % and F by 36 % compared to the R value. The comparison of both types of specimen curing shows that the specimens cured in H had the values of  $P_{ini}$ : R lower by 51 %, the value of the specimen with S was lower by 27 % and the value of the specimen with F was lower by 13 %.

Further, in the case of the specimens cured in H, it can be assumed, according to the value of  $\varepsilon_{16d}$  for R, that the used natural sand can be considered as potentially reactive and dangerous in terms of the volume changes caused by ASR. The value of  $\varepsilon_{16d}$  for the specimens with F was almost half the value for R, namely, approximately 0.10 %. This value is the limit, above which the combination of the binder and the aggregates is considered to be potentially dangerous. S was slightly less effective on the suppression of ASR compared to F, but the reduction in the expansion was also quite significant, namely, 35 % compared to R. This observation is in agreement with the work of Thomas<sup>10</sup>. In the case of the specimens cured in W, no significant length changes were observed after the age of 16 d.

When comparing the risk of ASR and the values of  $E$  and  $RSCP$  for the specimens cured with W and H, an interesting relationship was noticed: the higher the alkali expansion, the lower were the  $E$  and  $RSCP$  values for each composite in comparison with the water storage, where the length changes were negligible. The reason can be the stress or even microcrack generation caused by the volume changes resulting from ASR.

## 5 CONCLUSIONS

In this paper, the authors investigated the effect of a mass fraction 20 % replacement of Portland cement, in a fine-grained composite, by granulated blast-furnace slag or pulverized-coal fly ash on the crack initiation (the resistance to stable crack propagation) and volume changes (the risk of alkali-silica reaction). It was observed that both used admixtures can significantly reduce the risk of an alkali-silica reaction, which is important for concrete durability. Fly ash was slightly more effective than slag. If the sodium hydroxide solution was replaced by water, all the composites were dimensionally stable. Further, it was found that the use of slag or fly ash and the type of specimen curing affect the crack initiation. The most resistant composite was the one containing slag and cured in water and the least resistant composite was the reference specimen cured in the sodium hydroxide solution.

## Acknowledgement

This outcome was achieved with the financial support of the junior specific research program at the Brno University of Technology, project No. FAST/FCH-J-14-2371.

## 6 REFERENCES

- 1 M. Berra, U. Costa, T. Mangialardi, A. E. Paolini, R. Turriziani, *Materials and Structures*, 46 (2013), 971–985, doi:10.1617/s11527-012-9947-6
- 2 ASTM International, ASTM C1260-94, 1994, doi:10.1520/C1260-94
- 3 ASTM International, ASTM C1567-07, 2007, doi:10.1520/C1567-07
- 4 S. Kumar, S. V. Barai, *Concrete Fracture Models and Applications*, Springer, Berlin 2011, 406, doi:10.1007/978-3-642-16764-5
- 5 S. Xu, H. W. Reinhardt, Z. Wu, Y. Zhao, *Otto-Graf-Journal*, 14 (2003), 131–157
- 6 X. Zhang, S. Xu, *Engineering Fracture Mechanics*, 78 (2011), 2115–2138, doi:10.1016/j.engfracmech.2011.03.014
- 7 H. W. Reinhardt, H. A. W. Cornelissen, D. A. Hordijk, *Journal of Structural Engineering*, 112 (1986), 2462–2477, doi:10.1061/(ASCE)0733-9445(1986)112:11(2462)
- 8 V. Cervenka, L. Jendele, J. Cervenka, *ATENA Program documentation – Part 1: theory*, Cervenka Consulting, Praha 2012
- 9 B. L. Karihaloo, *Fracture Mechanics of Concrete*, Longman Scientific & Technical, New York 1995
- 10 M. Thomas, *Cement and Concrete Research*, 41 (2011), 1224–1231, doi:10.1016/j.cemconres.2010.11.003



## FRACTURE PROPERTIES OF PLAIN AND STEEL-POLYPROPYLENE-FIBER-REINFORCED HIGH-PERFORMANCE CONCRETE

### LASTNOSTI LOMA NAVADNEGA IN VISOKOZMOGLJIVEGA BETONA, OJAČANEGA S POLIPROPILENSKIMI VLAKNI

**Piotr Smarzewski, Danuta Barnat-Hunek**

Lublin University of Technology, Faculty of Civil Engineering and Architecture, Nadbystrzycka Str. 40, 20-618 Lublin, Poland  
p.smarzewski@pollub.pl

*Prejem rokopisa – received: 2014-08-05; sprejem za objavo – accepted for publication: 2014-09-22*

doi:10.17222/mit.2014.180

The aim of this research was to establish the fracture properties of high-performance concrete (HPC) containing two widely used types of fibers. The experimental investigation consisted of the tests on cubes, cylinders and notched prismatic samples made of plain HPC and fiber HPC (FHCP) with variable contents of steel or/and polypropylene fibers ranging from 0.25 % to 1 %. Extensive data on compressive, splitting and flexural tensile behaviors, modulus of elasticity and fracture energy were recorded and analyzed. The experimental investigations showed that HPC in fracture mode I exhibit brittle/softening behavior. The FHPC materials showed a more ductile behavior compared to that of the HPC materials. Fiber bridges cracked on the fracture surface during the loading and delayed cracking, thus the element did not break. The results of the bending tests showed an extended post-peak softening behavior. The shape of the descending branch was dependent on geometrical and mechanical properties as well as the quantity of the fibers used. The results of the research were evaluated and it was shown that the fibers contributed considerably to the structural integrity and stability of the HPC elements, thereby improving their durable service life.

Keywords: hybrid fibers, steel fibers, polypropylene fibers, high-performance concrete, mechanical testing, fracture properties

Namen tega članka je bil ugotoviti lomne lastnosti visokozmogljivega betona (HPC), ki je vseboval dve vrsti vlaken. Eksperimentalno delo je bilo na kockah, valjih in zarezanih prizmatičnih vzorcih, izdelanih iz navadnega HPC in z vlakni ojačanega HPC (FHCP) s spremenljivo vsebnostjo od 0,25 % do 1 % jeklenih in/ali polipropilenskih vlaken. Ugotovljeni in analizirani so bili obsežni podatki o vedenju pri tlačni, cepilni in upogibni natezni obremenitvi, o modulu elastičnosti in energiji loma. Preizkusi so pokazali, da prelom HPC v načinu I izkazuje krhko/mehčalno vedenje. FHPC-materiali so pokazali bolj duktilno vedenje v primerjavi s HPC-materiali. Vlaknasti mostovi so pokali na površini loma med obremenitvijo in so zadrževali pokanje, zato se element ni porušil. Rezultati upogibnega preizkusa so pokazali povečano mehčanje po vrhu. Oblika pojemajočih korakov je bila odvisna od geometričnih in mehanskih lastnosti, kot tudi od količine uporabljenih vlaken. Rezultati preiskav so bili ocenjeni in pokazalo se je, da vlakna občutno prispevajo k strukturni integriteti in stabilnosti HPC-elementov in s tem podaljšajo dobo uporabnosti.

Ključne besede: hibridna vlakna, jeklena vlakna, polipropilenska vlakna, visokozmogljiv beton, mehanski preizkusi, lomne lastnosti

## 1 INTRODUCTION

High-performance concrete (HPC) is a material frequently used in the building industry due to its durability. Concrete technology has developed at a rapid pace over the last two decades and the material performance has been significantly improved. Initially, the attention of the researchers was only focused on increasing the compressive strength. Nowadays, HPC with a compressive strength exceeding 100 MPa can be readily designed and manufactured. However, the brittleness of concrete increases with an increase in its strength. The higher the strength of concrete, the lower is its ductility. Fibers are added to the matrix as a reinforcement to control the cracking, to increase the ductility and to improve the general ductility of a material.<sup>1-4</sup> Fiber-concrete research has been conducted for over fifty years<sup>5,6</sup> and future directions for its development are still being set.<sup>7-9</sup> Nowadays, there are numerous types of fibers made of different materials that are of different

geometric properties. With each type of fiber certain properties of concrete can be improved. In order to improve mechanical properties, especially the tensile and flexural strengths and long-term concrete shrinkage, steel fibers are usually used. Low-modulus polypropylene fibers can reduce early-age shrinkage and help control the phenomenon of the spalling of concrete during fire. One of the recent concepts is the hybridization of fibers, the optimum combination of several kinds of fibers with different properties to create a complex composite with a very high resistance to cracking in a wide range of crack width.<sup>10</sup> The hybrid-fiber-reinforced concrete is mainly used in underground waterproof projects, road and bridge engineering and seismic structures. A lot of research revealed that a hybrid of steel and polypropylene fiber in concrete exhibits composite advantages of the two-fiber material properties, improves the interface condition between cement and aggregate, enhances the medium continuity of concrete, and constrains the occurrence and development of concrete cracks.<sup>11-15</sup>

The basic parameter for measuring the fracture process in quasi-brittle materials is the fracture energy ( $G_F$ ). The most common way to measure the fracture energy of concrete materials is the method proposed by RILEM TC 50-FMC.<sup>16</sup> In order to analyze and compare the fracture behavior of high-performance concrete (HPC), steel-fiber-reinforced high-performance concrete (SFHPC), polypropylene-fiber-reinforced high-performance concrete (PFHPC) and hybrid (steel and polypropylene)-fiber-reinforced high-performance concrete (HFHPC), by varying the type, proportion and content of the fibers, it is necessary to evaluate the experimental fracture energy up to the value that is limited by the long sloping curve. This study evaluated the effects of the type and content of the fibers on the mechanical properties and fracture of FHPC. For this purpose, three-point bending tests on notched samples were carried out in accordance with RILEM TC 89-FMT<sup>17,18</sup> and the experimental fracture-energy values calculated up to the threshold criteria were compared.

**2 MATERIALS, SAMPLES AND THE TEST PROGRAM**

**2.1 Details of the materials and sample specifications**

The experimental examination was carried out on cubes, cylinders and notched prismatic samples made of HPC and FHPC with variable contents of steel fibers (SFHPC), polypropylene (PFHPC) or the hybrid (HFHPC). The following tests were conducted: compressive strength, splitting tensile strength, modulus of elasticity, and the three-point bending tests to determine the effects of the fiber type and its content on the compressive-tensile behavior, deflection and fracture energy. Sample specifications used in the test program are shown in **Table 1**.

**2.2 Mixture design and the sample-production process**

The following components were used in the recipes for the concrete mixtures: Portland cement CEM I 52.5 N-HSR/NA, two types of the coarse aggregate – granodiorite or granite, quartz sand, water, condensed silica fume and superplasticizer. The maximum size of the coarse aggregate was 8 mm. The silica fume in the form

of powder had a specific surface of 15–30 m<sup>2</sup>/g. Baumix steel fibers, hooked-end, with a 1100 MPa tensile strength, 200 GPa modulus of elasticity, 50 mm length and an aspect ratio of 50 were used. Polypropylene fibers Baucon had a length of 12 mm and a modulus of elasticity of 3.5 GPa.

The tests on the CEM I 52.5 N-HSR/NA cement were carried out according to the Polish standards.<sup>19,20</sup> A chemical analysis was performed, the cement composition was determined and the results obtained are shown in **Tables 2** and **3**. The determination of the particle-size distribution for the granodiorite and granite aggregates as well as quartz sand was performed in line with the standard.<sup>21</sup>

**Table 2:** Chemical composition of cement in mass fractions, w/%

**Tabela 2:** Kemijska sestava cementa v masnih deležih, w/%

| Cement component               | Content, w/% |
|--------------------------------|--------------|
| SiO <sub>2</sub>               | 20.92        |
| Al <sub>2</sub> O <sub>3</sub> | 3.50         |
| Fe <sub>2</sub> O <sub>3</sub> | 4.38         |
| CaO                            | 64.69        |
| MgO                            | 1.20         |
| SO <sub>3</sub>                | 3.07         |
| Na <sub>2</sub> O              | 0.22         |
| K <sub>2</sub> O               | 0.38         |
| Cl                             | 0.082        |
| Ignition loss                  | 1.27         |
| Ash                            | 0.26         |
| Total                          | 99.97        |

**Table 3:** Cement technical parameters

**Tabela 3:** Tehnični parametri cementa

| Cement characteristics                           | CEM I 52.5 N-HSR/NA |
|--------------------------------------------------|---------------------|
| Specific surface area (cm <sup>2</sup> /g)       | 4433                |
| Water demand (%)                                 | 30                  |
| Commencement of bonding (min)                    | 120                 |
| End of bonding (min)                             | 180                 |
| Volume stability according to Le Chateliere (mm) | 2.00                |
| Compressive strength after 2 d (MPa)             | 27.7                |
| Compressive strength after 28 d (MPa)            | 57.1                |
| Tensile strength after 2 d (MPa)                 | 5.29                |
| Tensile strength after 28 d (MPa)                | 8.23                |

**Table 1:** Sample specifications

**Tabela 1:** Specifikacija vzorcev

| Label                        | HPC1 | SFHPC     | HFHPC1         | HFHPC2         | HFHPC3         | PFHPC             | HPC2 |
|------------------------------|------|-----------|----------------|----------------|----------------|-------------------|------|
| Fiber type                   | –    | Steel (S) | Hybrid (S + P) | Hybrid (S + P) | Hybrid (S + P) | Polypropylene (P) | –    |
| $L_f$ /mm                    | –    | 50        | 50 / 12        | 50 / 12        | 50 / 12        | 12                | –    |
| $V_f$ /%                     | 0    | 1         | 0.75 + 0.25    | 0.5 + 0.5      | 0.25 + 0.75    | 1                 | 0    |
| Number of the tested samples |      |           |                |                |                |                   |      |
| Compression test             | 3    | 3         | 3              | 3              | 3              | 3                 | 3    |
| Splitting tensile test       | 3    | 3         | 3              | 3              | 3              | 3                 | 3    |
| Modulus of elasticity test   | 3    | 3         | 3              | 3              | 3              | 3                 | 3    |
| Three point bending test     | 3    | 3         | 3              | 3              | 3              | 3                 | 3    |

**Table 4:** Mixture proportions

**Tabela 4:** Razmerja mešanic

| Material            | Symbol, unit      | HPC1  | SFHPC | HFHPC1 | HFHPC2 | HFHPC3 | PFHPC | HPC2  |
|---------------------|-------------------|-------|-------|--------|--------|--------|-------|-------|
| Cement              | $c/(kg/m^3)$      | 670.5 | 670.5 | 670.5  | 670.5  | 670.5  | 670.5 | 670.5 |
| Quartz sand 0/2 mm  | $s/(kg/m^3)$      | 500   | 500   | 500    | 500    | 500    | 500   | 500   |
| Granodiorite 2/8 mm | $a_1/(kg/m^3)$    | 990   | 990   | 990    | –      | –      | –     | –     |
| Granite 2–8 mm      | $a_2/(kg/m^3)$    | –     | –     | –      | 990    | 990    | 990   | 990   |
| Silica fume         | $sf/(kg/m^3)$     | 74.5  | 74.5  | 74.5   | 74.5   | 74.5   | 74.5  | 74.5  |
|                     | $(sf/c)/\%$       | 11    | 11    | 11     | 11     | 11     | 11    | 11    |
| Superplasticizer    | $sp/(L/m^3)$      | 20    | 20    | 20     | 20     | 20     | 20    | 20    |
|                     | $sp/(c + sf)/\%$  | 2.7   | 2.7   | 2.7    | 2.7    | 2.7    | 2.7   | 2.7   |
| Water               | $w/(L/m^3)$       | 178   | 178   | 178    | 178    | 178    | 178   | 178   |
|                     | $w/(c + sf)$      | 0.24  | 0.24  | 0.24   | 0.24   | 0.24   | 0.24  | 0.24  |
| Steel fiber         | $w_{fs}/(kg/m^3)$ | –     | 78    | 58.5   | 29.25  | 19.5   | –     | –     |
|                     | $V_{fs}/\%$       | 0     | 1     | 0.75   | 0.5    | 0.25   | 0     | 0     |
| Polypropylene fiber | $w_{fp}/(kg/m^3)$ | –     | –     | 2.25   | 4.5    | 6.75   | 9     | –     |
|                     | $V_{fp}/\%$       | 0     | 0     | 0.25   | 0.5    | 0.75   | 1     | 0     |

In order to attain the same workability, the ISOFLEX CX 793 superplasticizer based on polycarboxylate ethers with a density of 1.065 g/cm<sup>3</sup> at 20 °C was used in all the concrete mixtures. The HPC and FHPC mix designs per cubic meter of the concrete used in the experimental program are shown in **Table 4**.

The mixtures were prepared using a typical concrete mixer with a capacity of 100 L. The mixing procedure was as follows: quartz sand and coarse aggregate were homogenized together and mixed with half a quantity of water. Then, cement, silica fume, the remaining water and, finally, the superplasticizer were added. After the components were thoroughly mixed, the fibers were gradually added by hand to obtain homogeneous and workable mixtures. Molds coated with an anti-adhesive substance were filled with the concrete batch that was compacted on a vibrating table. After the compacting, the samples were covered with a foil to minimize the loss of moisture. All the samples were stored at a temperature of about 23 °C until removing them from the moulds after 24 h and they were placed into a water tank for 7 d to cure. After 7 d the samples were removed from the tank to cure in the laboratory conditions for up to 28 d.

### 2.3 Test equipment and solutions

Compressive and splitting tensile tests were carried out after 28 d, in accordance with the standards,<sup>22,23</sup> using 100 mm cubes. A Walter-Bai AG servo-hydraulic closed-loop testing machine with a capacity of 3 MN was used.

The test method for the static modulus of elasticity of concrete in compression was performed on the cylinders with a 150 mm diameter and a height of 300 mm, measuring the deformation stress of the samples in the range from 0.5 MPa to 30 % of the concrete compressive strength. The examination was conducted by means of a Walter-Bai AG press and a modulus-measuring device with an extensometer in line with the recommendations of ASTM.<sup>24</sup>

Three-point bending tests were also performed after 28 d on a MTS 809 axial/torsional testing system machine, in accordance with RILEM TC 89-FMT,<sup>17</sup> using 80 mm × 150 mm × 700 mm prismatic samples (**Figure 1a**). In the mid-span of each sample, a single notch was made with a concreting flat iron sharpened at its tip, with a thickness of 3 mm and a depth of 50 mm, in order to locate the cracks. Before the testing, the samples were provided with plaques for fixing the clip gauge thereon.

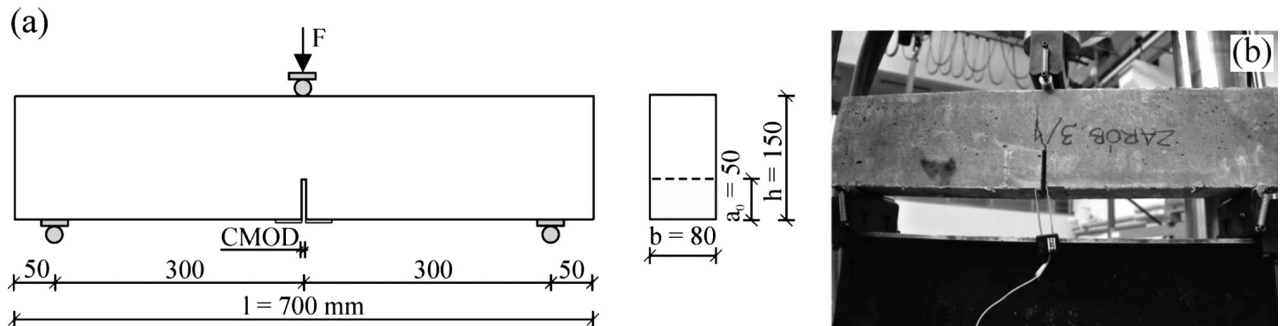


**Figure 1:** Three-point bending test: a) sample geometry and dimensions, b) experimental-set up

**Slika 1:** Tritočkovni upogibni preizkus: a) geometrija vzorca in dimenzije, b) eksperimentalni sestav

The tests were conducted by imposing a displacement rate of 0.05 mm/min. In order to measure the crack-mouth-opening displacement (CMOD), a strain gauge consisting of elastic plates separated by means of a non-conductive cube was used (Figure 1b). It was provided from the outside to the system for an automatic detection of the CMOD values corresponding to the loads applied.

### 3 RESULTS AND DISCUSSION

#### 3.1 Compressive strength

The cube compressive peak strength of each sample, the mean values of the compressive strength, the standard deviation and the coefficient of variation are given in Table 5. The cube compressive strength was insignificantly affected by adding steel and polypropylene fibers; however, a higher decrease in the compression strength was observed when the percent of the polypropylene-fiber volume added was higher. This was mainly due to the low modulus of elasticity of the propylene fibers and to some difficulties in dispersing the fibers in the mixtures. It should be noted that at a 1 % fiber volume in PFHPC, it had 73 % of the strength of the HPC2 fiber-free cube made of the same aggregate, whereas at the polypropylene-fiber volume of 0.75 % and the steel fibers of 0.25 %, the strength of the cube made of HFHPC was about 95 % of the HPC2 strength.

Table 5: Cube compressive strength

Tabela 5: Tlačna trdnost kock

| Mixture designation | Compressive strength MPa | Mean value MPa | Standard deviation MPa | Coefficient of variation % |
|---------------------|--------------------------|----------------|------------------------|----------------------------|
| HPC1                | 146.4                    | 151.0          | 4.1                    | 2.7                        |
|                     | 152.3                    |                |                        |                            |
|                     | 154.4                    |                |                        |                            |
| SFHPC               | 158.0                    | 154.9          | 2.9                    | 1.9                        |
|                     | 152.2                    |                |                        |                            |
|                     | 154.6                    |                |                        |                            |
| HFHPC1              | 142.5                    | 144.7          | 3.4                    | 2.3                        |
|                     | 143.1                    |                |                        |                            |
|                     | 148.6                    |                |                        |                            |
| HFHPC2              | 132.5                    | 133.9          | 3.8                    | 2.9                        |
|                     | 138.2                    |                |                        |                            |
|                     | 130.9                    |                |                        |                            |
| HFHPC3              | 124.1                    | 122.3          | 2.0                    | 1.7                        |
|                     | 120.1                    |                |                        |                            |
|                     | 122.7                    |                |                        |                            |
| PFHPC               | 94.8                     | 94.6           | 1.3                    | 1.4                        |
|                     | 95.8                     |                |                        |                            |
|                     | 93.2                     |                |                        |                            |
| HPC2                | 130.6                    | 129.5          | 3.8                    | 2.9                        |
|                     | 125.3                    |                |                        |                            |
|                     | 132.6                    |                |                        |                            |

#### 3.2 Splitting tensile strength

The cube peak-splitting tensile strength for each sample, the mean values of the splitting tensile strength, the standard deviation and the coefficient of variation are shown in Table 6. The addition of the fibers significantly affected the cube splitting tensile strength; however, a higher increase was observed at a higher percent of the steel fibers added. It was noted that at a 1 % steel-fiber volume in SFHPC, the cube strength increased by 55 % compared to the HPC1 fiber-free cube. A similar increase in the strength was observed for HFHPC at a 0.75 % steel-fiber volume and 0.25 % polypropylene-fiber volume. Lower increases in the strength of 12 % were obtained at a 1 % polypropylene-fiber volume in PFHPC compared to the HPC2 fiber-free cube.

Table 6: Cube splitting tensile strength

Tabela 6: Natezna trdnost cepljenja kock

| Mixture designation | Splitting tensile strength MPa | Mean value MPa | Standard deviation MPa | Coefficient of variation % |
|---------------------|--------------------------------|----------------|------------------------|----------------------------|
| HPC1                | 8.9                            | 8.9            | 0.4                    | 4.7                        |
|                     | 9.3                            |                |                        |                            |
|                     | 8.5                            |                |                        |                            |
| SFHPC               | 14.0                           | 13.8           | 0.1                    | 1.0                        |
|                     | 13.8                           |                |                        |                            |
|                     | 13.7                           |                |                        |                            |
| HFHPC1              | 13.8                           | 13.5           | 0.2                    | 1.7                        |
|                     | 13.3                           |                |                        |                            |
|                     | 13.5                           |                |                        |                            |
| HFHPC2              | 10.4                           | 10.0           | 0.4                    | 3.8                        |
|                     | 9.6                            |                |                        |                            |
|                     | 10.1                           |                |                        |                            |
| HFHPC3              | 9.5                            | 9.3            | 0.2                    | 1.9                        |
|                     | 9.3                            |                |                        |                            |
|                     | 9.2                            |                |                        |                            |
| PFHPC               | 7.4                            | 7.6            | 0.2                    | 3.1                        |
|                     | 7.7                            |                |                        |                            |
|                     | 7.9                            |                |                        |                            |
| HPC2                | 7.1                            | 6.8            | 0.3                    | 4.5                        |
|                     | 6.7                            |                |                        |                            |
|                     | 6.5                            |                |                        |                            |

#### 3.3 Modulus of elasticity

The cylinder modulus of elasticity for each sample, the mean values of the modulus of elasticity, the standard deviation and the coefficient of variation are shown in Table 7. The value of the cylinder elasticity modulus was only slightly affected by adding the steel fibers and it increased with their volume fraction added. This was mainly due to the high modulus of elasticity of the steel fibers. It should be noted that at a 1 % fiber volume in SFHPC, the cylinder modulus of elasticity was 4 % higher than that of the HPC1 fiber-free cylinder. At a lower content of the steel fibers, the modulus value was gradually decreased and at a 0.25 % fiber volume in the



cylinder made of HFHPC3, the modulus value was lower by 10 % compared to that of the HPC2 standard concrete.

**Table 7:** Cylinder modulus of elasticity

**Tabela 7:** Modul elastičnosti valjastih vzorcev

| Mixture designation | Modulus of elasticity MPa | Mean value MPa | Standard deviation MPa | Coefficient of variation % |
|---------------------|---------------------------|----------------|------------------------|----------------------------|
| HPC1                | 38381                     | 38371          | 279                    | 0.7                        |
|                     | 38645                     |                |                        |                            |
|                     | 38087                     |                |                        |                            |
| SFHPC               | 39767                     | 39740          | 261.1                  | 0.7                        |
|                     | 39466                     |                |                        |                            |
|                     | 39986                     |                |                        |                            |
| HFHPC1              | 34266                     | 34272          | 287.5                  | 0.8                        |
|                     | 33987                     |                |                        |                            |
|                     | 34562                     |                |                        |                            |
| IHFHPC2             | 32890                     | 32447          | 404.9                  | 1.2                        |
|                     | 32355                     |                |                        |                            |
|                     | 32096                     |                |                        |                            |
| HFHPC3              | 29870                     | 29632          | 323.4                  | 1.1                        |
|                     | 29264                     |                |                        |                            |
|                     | 29763                     |                |                        |                            |
| PFHPC               | 29641                     | 29425          | 232.5                  | 0.8                        |
|                     | 29455                     |                |                        |                            |
|                     | 29179                     |                |                        |                            |
| HPC2                | 32322                     | 32548          | 229.1                  | 0.7                        |
|                     | 32780                     |                |                        |                            |
|                     | 32542                     |                |                        |                            |

### 3.4 Flexural tensile behavior

The behavior of the HPC ordinary concrete samples during the bending test was almost linear-elastic up to the peak-load values, then the curve was sloping until the complete separation of the samples into two parts. The FRC samples showed a trilinear variation with the significant cracking between the first crack load and the peak load.

The typical experimental load ( $F$ ) – deflection ( $\delta$ ) curves for the selected samples SFHPC, PFHPC and HFHPC – recorded during the bending tests, are shown in **Figure 2**. The examination was carried out in two stages. During the first stage, the crack-mouth-opening displacement (CMOD) and deflection were measured until the cracking of the beams along the whole height. After dismantling the strain gauge only deflection was recorded.

A typical generic curve of the FRC samples is characterized with a linear curve up to the first crack, and then with the non-linear behavior up to the peak load. After reaching the peak load, the load-carrying capacity declines; however, the higher the loss of the strength, the lower is the steel-fiber content. As micro-cracks grow and join into larger macro-cracks, the long hooked-end fibers become engaged in crack bridging. Compared to the high-performance concrete, the peak load increases when steel fibers are used as shown in **Figure 3** and **Table 8**.

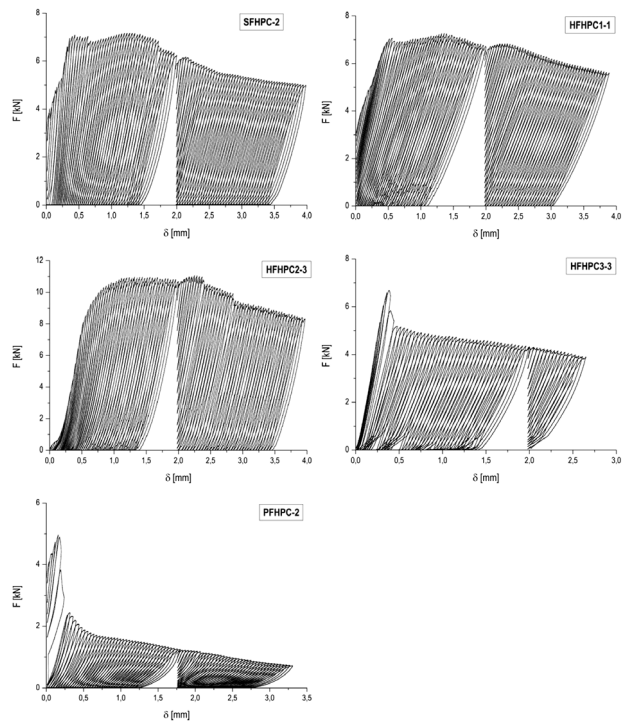


**Figure 2:** Typical experimental load-deflection curves for the FHPC notched prismatic samples

**Slika 2:** Značilne krivulje obremenitev – deformacija prizmatičnih FHPC-vzorcev z zarezo

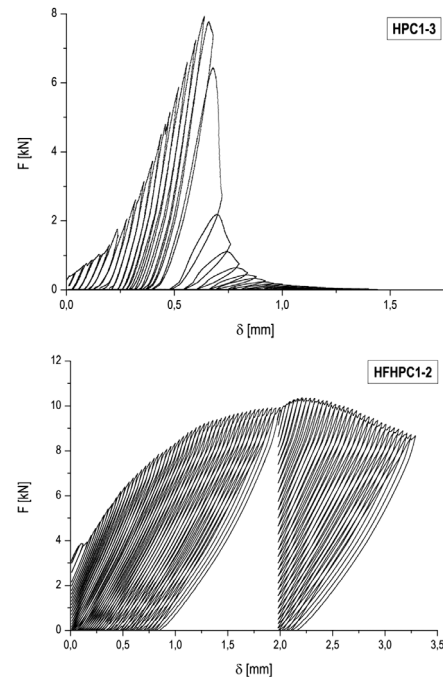


**Figure 3:** Typical experimental load-deflection curves for HPC and HFHPC

**Slika 3:** Značilne eksperimentalne krivulje obremenitev – deformacija za HPC in HFHPC

In particular, with respect to the typical curves for SFHPC, the peak load is increased by 17 %, compared to that of HPC1. An even higher increase of 92 % was

obtained for the HFHPC2 batch (from 0.5 % of steel fibers and 0.5 % of polypropylene) compared to HPC2.

The PFHPC samples with a low modulus of fibers of 1 % achieved similar peak-load values for the HPC2 samples. A very high coefficient of variation was observed for the steel-fiber-reinforced batch, which indicated that the decisive factor in obtaining the peak-load values was the amount of the longitudinally oriented fibers.

Table 8: Three-point bending tests

Tabela 8: Tritočkovni upogibni preizkusi

| Mixture designation | Peak load kN        | Mean value kN | Standard deviation kN | Coefficient of variation % |
|---------------------|---------------------|---------------|-----------------------|----------------------------|
| HPC1                | 7.5<br>7.0<br>7.9   | 7.5           | 0.4                   | 6.0                        |
| SFHPC               | 12.1<br>7.1<br>7.1  | 8.8           | 2.9                   | 32.9                       |
| HFHPC1              | 7.3<br>10.6<br>8.2  | 8.7           | 1.7                   | 19.6                       |
| HFHPC2              | 6.2<br>12.3<br>11.0 | 9.8           | 3.2                   | 32.7                       |
| HFHPC3              | 8.5<br>7.0<br>6.8   | 7.4           | 0.9                   | 12.5                       |
| PFHPC               | 5.1<br>5.0<br>5.4   | 5.2           | 0.2                   | 4.0                        |
| HPC2                | 5.0<br>5.0<br>5.3   | 5.1           | 0.2                   | 3.4                        |

### 3.5 Fracture properties

In order to describe the FHPC post-cracking enhancement, different toughness indexes were proposed. RILEM proposed the concept of an equivalent flexural tensile strength,  $f_{eq}$ .<sup>25</sup> Recently, RILEM proposed the concept of a residual flexural tensile strength,  $f_R$ , which is more readily assessed.<sup>26</sup> According to RILEM, recently recommended  $f_{eq,2}$  or  $f_{R,1}$  are used in the verification of the serviceability limit states, and  $f_{eq,3}$  or  $f_{R,4}$  are applied in the ultimate limit-state analysis.<sup>27</sup> These parameters are also used to determine the stress-strain curves which are useful in modeling the FHPC post-cracking behavior.

With regard to the experimental curves, the load at the limit of proportionality,  $F_L$ , the corresponding strength,  $f_{ict,L}$ , the equivalent flexural strengths,  $f_{eq,2}$  and  $f_{eq,3}$ , and the residual flexural strengths,  $f_{R,1}$  and  $f_{R,4}$ , relating to the mid-span deflections of 0.46 mm and 3.00 mm, were evaluated. The load at the limit of proportionality  $F_L$  is equal to the highest value of the load recorded up to a deflection of 0.05 mm. The strength corresponding to the limit of proportionality can be computed using the following equation:

$$f_{f_{a,L}} = \frac{2F_L l}{2b(h-a_0)^2} \text{ (MPa)} \quad (1)$$

where  $b = 80$  mm,  $h = 150$  mm and  $l = 600$  mm relate to the width, the height and the span of the samples tested,  $a_0 = 50$  mm is the notch depth and  $(h - a_0)$  is the distance between the tip of the notch and the top edge of a sample.

The parameters  $f_{eq,2}$  and  $f_{eq,3}$  were evaluated up to the deflections of  $\delta_2 = \delta_L + 0.65$  mm and  $\delta_3 = \delta_L + 2.65$  mm, where  $\delta_L$  is the deflection corresponding to  $F_L$ . The portion of the energy required by the fracture of the concrete corresponding to the OBA field in Figure 4 ( $D^{b_{OAB}}$ ) was not considered in assessing the equivalent flexural strength. Only the effect of the fibers was considered (ABCD –  $D^{f_{BZ,2}}$  and EFGH –  $D^{f_{BZ,3}}$  in Figure 4). The equivalent flexural strength was calculated from the following expressions:

$$f_{eq,2} = \frac{3l}{2b(h-a_0)^2} \frac{D^{f_{BZ,2}}}{0.5} \text{ (MPa)} \quad (2)$$

$$f_{eq,3} = \frac{3l}{2b(h-a_0)^2} \frac{D^{f_{BZ,3}}}{2.5} \text{ (MPa)} \quad (3)$$

The residual flexural tensile strengths  $f_{R,1}$  and  $f_{R,4}$  at the mid-span deflections of 0.46 mm and 3.00 mm, respectively, were computed according to:

$$f_{R,1} = \frac{3F_{R,1} l}{2b(h-a_0)^2} \text{ (MPa)} \quad (4)$$

$$f_{R,4} = \frac{3F_{R,4} l}{2b(h-a_0)^2} \text{ (MPa)} \quad (5)$$

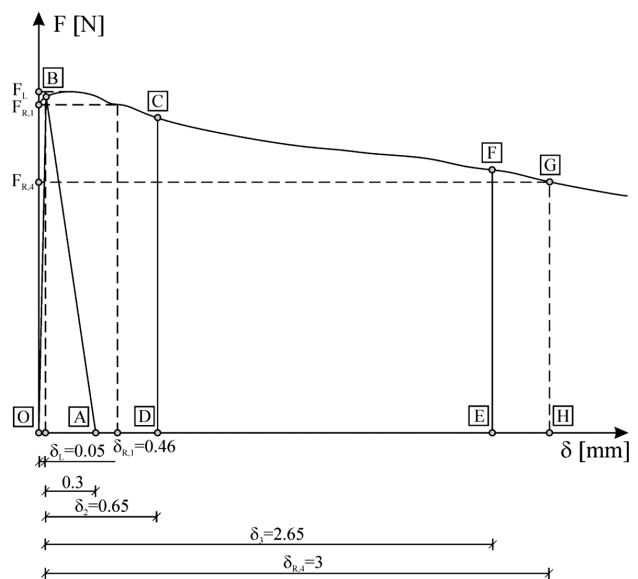


Figure 4: Evaluation of flexural-tensile-strength parameters according to RILEM TC 162-TDF

Slika 4: Vrednotenje parametrov upogibne natezne trdnosti skladno z RILEM TC 162-TDF

The energy dissipation in the fractured concrete is the most advantageous characteristic of FHPC due to the addition of the fibers to the material. The fracture energy ( $G_F$ ) was computed as the area under the stress-displacement curves. Assuming a linear stress distribution in relation to the fracture depth, the tensile stress was calculated according to the following formula:

$$\sigma = \frac{3Fl}{2b(h-a_0)^2} \text{ (MPa)} \quad (6)$$

where  $F$  is the load recorded during the three-point bending test.

The fracture energy was computed up to the predetermined load-deflection point based on the following formula:

$$G_F = \int_{\delta=0}^{\delta=\delta_{lim}} \sigma d\delta \text{ (N/mm)} \quad (7)$$

The fracture energy for the FRC samples needs to be computed in relation to the specified value of the displacement. A reliable cut-off point can be selected at a 10 mm displacement.<sup>28</sup> However, only a fracture dissipated up to a deflection of 3 mm seems to be interesting from the design viewpoint<sup>29</sup> and such a deflection value was adopted while computing energy in this work. The results of the strength parameters and the fracture energy are included in **Table 9**.

Referring to the data given in **Table 9**, it is noteworthy that the flexural-strength values obtained from Equations (2) and (3) lead to similar strength values in the cases of steel and hybrid fibers. The samples with the addition of polypropylene fibers only constitute an

exception. For all kinds of fibers, the equivalent flexural-strength values are lower than the strengths at the limit of proportionality given with Equation (1). The highest differences were observed for the polypropylene fibers. The obtained results emphasize the effect of the elasticity modulus on the variation in the HPC fracture properties. It can be seen that in FHPC the highest fracture energy was obtained with the addition of steel and polypropylene fibers, 0.5 % of each. The percentage volume of the steel fibers accounted for the fracture-energy increase. When decreasing the fiber content from 1 % to 0.75 %, the HFHPC-1 samples showed a decrease in the fracture energy by approximately 7 % compared to the SFHPC samples. The  $G_F$  values for the batches with the hybrid, steel-polypropylene fibers are due to the volume content of the low-modulus fibers. The higher the volume content of the low-modulus fibers, the lower are the  $G_F$  values obtained. The results of the fracture energy from **Table 9** show that the ductility of the FHPC material at a high level of the strain depends largely on the capability of the fibers to bridge the cracks. Stiffer steel fibers provide a higher resistance to the loads whereas polypropylene fibers of a low modulus of elasticity provide a higher resistance to shrinkage and temperature stress. Therefore, it seems appropriate to combine the fibers of high and low modulus which can result in a longer period of durable service life.

In the case of two batches of the HPC samples, a brittle fracture occurred through a separation of the elements into two parts (**Figure 5**).

The FHPC samples with cracks underwent a significant deflection; however, not in all the cases the brittle

**Table 9:** Tensile-strength parameters and experimental fracture energy

**Tabela 9:** Parametri natezne trdnosti in lomna energija pri preizkusih

| Mixture designation | $F_L$ /kN | $f_{ct,1}$ /MPa | $f_{eq,2}$ /MPa | $f_{eq,3}$ /MPa | $f_{R,1}$ /MPa | $f_{R,4}$ /MPa | $G_F$ /(N/mm) |
|---------------------|-----------|-----------------|-----------------|-----------------|----------------|----------------|---------------|
| SFHPC-1             | 12.1      | 13.5            | 6.4             | 12.3            | 5.7            | 12.6           | 32.3          |
| SFHPC-2             | 7.1       | 8.0             | 7.0             | 6.9             | 7.9            | 6.1            | 17.1          |
| SFHPC-3             | 7.1       | 8.0             | 7.4             | 7.5             | 7.9            | 6.1            | 19.0          |
| Mean value          | 8.8       | 9.7             | 6.9             | 8.9             | 7.2            | 8.3            | 22.8          |
| Standard deviation  | 2.9       | 2.9             | 0.5             | 3.0             | 1.3            | 3.7            | 8.3           |
| HFHPC1-1            | 7.3       | 8.2             | 6.6             | 7.5             | 6.8            | 7.1            | 18.8          |
| HFHPC1-2            | 10.6      | 11.9            | 6.1             | 9.7             | 6.8            | 10.6           | 24.9          |
| HFHPC1-3            | 8.2       | 9.2             | 7.8             | 8.3             | 8.4            | 9.1            | 19.9          |
| Mean value          | 8.7       | 9.8             | 6.8             | 8.5             | 7.3            | 8.9            | 21.2          |
| Standard deviation  | 1.7       | 1.9             | 0.9             | 1.1             | 0.9            | 1.8            | 3.2           |
| HFHPC2-1            | 6.2       | 7.0             | 6.1             | 6.6             | 6.2            | 6.1            | 16.6          |
| HFHPC2-2            | 12.3      | 13.8            | 7.3             | 14.8            | 7.9            | 11.6           | 29.1          |
| HFHPC2-3            | 11.0      | 12.4            | 7.1             | 11.1            | 5.6            | 10.5           | 28.3          |
| Mean value          | 9.8       | 11.1            | 6.8             | 10.8            | 6.6            | 9.4            | 24.7          |
| Standard deviation  | 3.2       | 3.6             | 0.6             | 4.1             | 1.2            | 2.9            | 7.0           |
| HFHPC3-1            | 8.5       | 9.6             | 8.4             | 8.8             | 8.9            | 8.1            | 22.1          |
| HFHPC3-2            | 7.0       | 7.9             | 6.6             | 5.9             | 7.5            | 6.5            | 14.8          |
| HFHPC3-3            | 6.8       | 7.7             | 6.5             | 5.8             | 6.2            | 4.2            | 14.3          |
| Mean value          | 7.4       | 8.4             | 7.2             | 6.8             | 7.5            | 6.3            | 17.1          |
| Standard deviation  | 0.9       | 1.0             | 1.1             | 1.7             | 1.3            | 2.0            | 4.4           |
| PFHPC-1             | 5.1       | 5.7             | 2.6             | 1.8             | 2.4            | 1.0            | 4.5           |
| PFHPC-2             | 5.0       | 5.6             | 2.5             | 1.7             | 2.3            | 0.9            | 4.0           |
| PFHPC-3             | 5.4       | 6.1             | 2.8             | 2.4             | 2.8            | 1.3            | 6.2           |
| Mean value          | 5.2       | 5.8             | 2.6             | 2.0             | 2.5            | 1.1            | 4.9           |
| Standard deviation  | 0.2       | 0.3             | 0.1             | 0.4             | 0.3            | 0.2            | 1.1           |

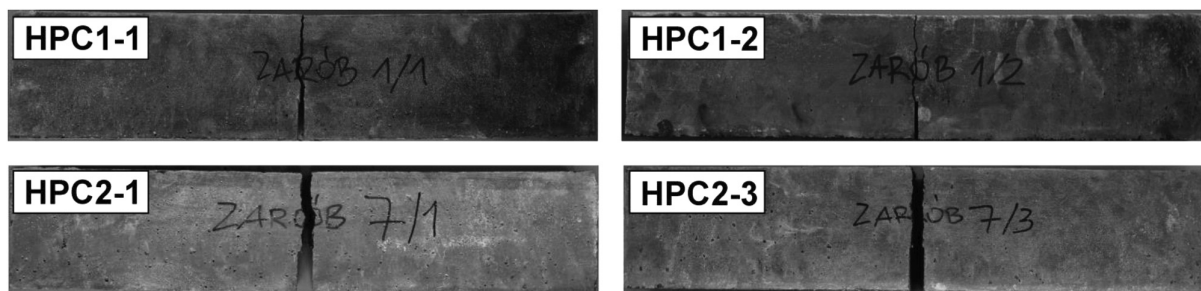


Figure 5: Notched HPC1 and HPC2 samples without fibers after the test  
Slika 5: Vzorci HPC1 in HPC2 z zarezo in brez vlaken po preizkusu



Figure 6: Notched FHPC samples after the test  
Slika 6: Vzorci FHPC z zarezo po preizkusu

destruction of the samples caused by a separation into two parts occurred (Figure 6) as some bridges were formed by the fibers on the crack surface and limited the split.

The samples with the fibers exhibited a more ductile behavior and the main crack ran from the crack-opening tip to the upper edge of the beam (Figure 7).

#### 4 CONCLUSIONS

The presence of steel fibers had an insignificant effect on the compressive strength of the high-performance concrete. Steel fibers increased the compressive strength by about 2.6 % at a 1 % fiber volume content. On the other hand, polypropylene fibers reduced the compression strength by about 37 % at 1 % fiber volumes. The addition of steel fibers in the amount of 0.5 % and the polypropylene amounting to 0.5 % caused an increase in the compressive strength by 3.4 % as compared to the standard high-performance concrete HPC2.

The presence of the fibers had a significant impact on the splitting tensile strength of the high-performance concrete. However, the polypropylene fibers improved the splitting tensile strength by only 12 % at a 1 % fiber volume content, while the steel fibers at the same fiber volume content caused an increase in this parameter by 55 %. In the case of hybrid fibers the increase depended on the steel-fiber volume content and it was (52, 47 and 37) % for the (0.75, 0.5 and 0.25) % steel fiber volumes, respectively.

The volume of the steel fibers was also a decisive factor regarding the modulus values for the high-perfor-

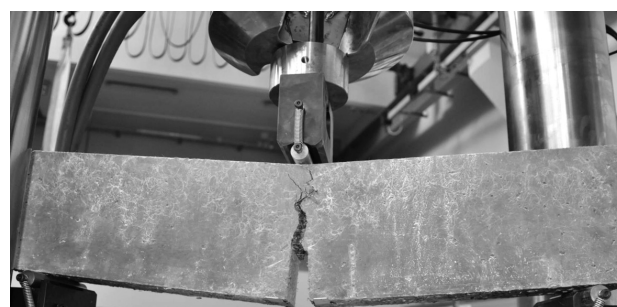


Figure 7: Crack opening on the HFHPC2-1 sample ( $V_{fs} = 0.5\%$ ,  $V_{fp} = 0.5\%$ )  
Slika 7: Odpiranje razpoke na vzorcu HFHPC2-1 ( $V_{fs} = 0.5\%$ ,  $V_{fp} = 0.5\%$ )

mance concretes. At the 1 % steel fiber volume there was a slight increase in the modulus by about 3.6 %. In all the other cases, there was a decrease in the modulus from 3 % to 12 %; the lower the decrease, the higher was the volume of the steel fibers of a high modulus. The above mentioned property was also affected by the type of the coarse aggregate.

All the samples of the SFHPC, HFHPC and PFHPC fibers showed a typical three-line variation in the load-deflection curves at flexure. The curves mostly consisted of a linear branch up to the first crack, followed by non-linear behavior up to the peak and the extensive descending/strain softening region.

The SFHPC samples showed the peak flexural load that is higher by 17 % compared to HPC1 at the 1 % fiber volume content. The PFHPC samples of a low elasticity showed a slight increase of about 2 % in the

HPC2 peak load at the 1 % fiber volume content. The highest increase in the peak flexural load of 92 % was observed with the addition of the steel fibers in the amount of 0.5 % and polypropylene fibers in the amount of 0.5 %. The SFHPC samples had the residual flexural strength at 17 % of their peak-load values at a deflection of 3 mm. The HFHPC and PFHPC samples which contained the fibers of a low elasticity modulus showed an abrupt decrease in the load capacity immediately after the peak load, while the load losses ranged from 10 % for HFHPC1 to 473 % for PFHPC, depending on the volume fraction of the polypropylene fibers.

Increasing the content of the polypropylene fibers reduces the fracture energy. The  $G_F$  values for the high-modulus fibers should be numerically higher than the corresponding values for the low-modulus fibers. However, the fracture energy is not a measure of the efficiency and effectiveness of the fibers in inhibiting the cracks. In the load-deflection curves it can be seen that similar extensibilities are caused by the low-modulus fibers and the high-modulus ones.

Adding fibers to concrete has a significant effect on the splitting tensile strength, modulus of elasticity, flexural strength, fracture behavior, fracture energy and ductility. The factors that influence these properties of FHPC are the modulus of elasticity and geometry, the content and properties of the fibers.

A critical evaluation of the load-deflection curves of HPC and FHPC proves that the fibers help significantly to preserve the structural integrity and stability of the high-performance concrete. A combination of steel and polypropylene fibers should contribute to a long-term durable service life of a construction.

## 5 REFERENCES

- <sup>1</sup> F. Bencardino, L. Rizzuti, G. Spadea, R. N. Swamy, Experimental evaluation of fiber reinforced concrete fracture properties, *Composites Part B: Engineering*, 41 (2010) 1, 17–24, doi:10.1016/j.compositesb.2009.09.002
- <sup>2</sup> RILEM PRO 31, Test and design method for steel fibre reinforced concrete –background and experience, Proceedings of RILEM TC 162-TDF workshop, 2003
- <sup>3</sup> RILEM PRO 39, Fibre-reinforced concretes, Proceedings of sixth RILEM symposium on fibre-reinforced concretes BEFIB 2004, 2004
- <sup>4</sup> M. di Prisco (Ed.), Fibre-reinforced concrete for strong, durable and cost-saving structures and infrastructures, Starrylink, Brescia 2007
- <sup>5</sup> A. M. Brandt, Cement Based Composites: Materials, Mechanical Properties and Performance, Taylor and Francis, London, New York 2009, 526
- <sup>6</sup> A. M. Brandt, Fibre reinforced cement-based (FRC) composites after over 40 years of development in building and civil engineering, *Composite Structures*, 86 (2008) 1–3, 3–9, doi:10.1016/j.compstruct.2008.03.006
- <sup>7</sup> J. C. Walraven, High performance fiber reinforced concrete: progress in knowledge and design codes, *Materials and Structures*, 42 (2009) 9, 1247–1260, doi:10.1617/s11527-009-9538-3
- <sup>8</sup> M. di Prisco, G. Plizzari, L. Vandewalle, Fibre reinforced concrete: new design perspectives, *Materials and Structures*, 42 (2009) 9, 1261–1281, doi:10.1617/s11527-009-9529-4
- <sup>9</sup> X. K. Li, L. Sun, Y. Y. Zhou, S. B. Zhao, A Review of Steel-polypropylene Hybrid Fiber Reinforced Concrete, *Applied Mechanics and Materials*, 238 (2012), 26–32, doi:10.4028/www.scientific.net/AMM.238.26
- <sup>10</sup> N. Banthia, R. Gupta, Hybrid fiber reinforced concrete (HyFRC): fiber synergy in high strength matrices, *Materials and Structures*, 37 (2004) 10, 707–716, doi:10.1007/BF02480516
- <sup>11</sup> K. Komloš, B. Babal, T. Nürnbergerova, Hybrid fiber-reinforced concrete under repeated loading, *Nuclear Engineering Design*, 156 (1995) 1–2, 195–200, doi:10.1016/0029-5493(94)00945-U
- <sup>12</sup> W. Sun, H. Qian, H. Chen, The effect of the combination of hybrid fibers and expansive agent on the physical properties of cementitious composites, *Journal of the Chinese Ceramic Society*, 2 (2000), 95–99
- <sup>13</sup> Y. Liu, W. Qiu, D. Li, The shrinkage of steel-polypropylene hybrid fiber reinforced concrete, *Materials Technology and Applications*, 33 (2003), 27–30
- <sup>14</sup> C. Yang, C. Huang, Y. Che, B. Wang, Mechanical properties and impermeability of hybrid fiber reinforced concrete, *Journal of Building Materials*, 1 (2008), 89–93
- <sup>15</sup> S. P. Singh, A. P. Singh, V. Bajaj, Strength and flexural toughness of concrete reinforced with steel-polypropylene hybrid fibers, *Asian Journal Of Civil Engineering (Building and Housing)*, 4 (2010), 495–507
- <sup>16</sup> RILEM TC 50-FMC, Determination of the fracture energy of mortar and concrete by means of three-point bend tests on notched beams, *Materials and Structures*, 18 (1985) 4, 287–290, doi:10.1007/BF02472918
- <sup>17</sup> RILEM TC 89-FMT, Fracture mechanics of concrete – test methods, Size-effect method for determining fracture energy and process zone size of concrete, *Materials and Structures*, 23 (1991), 461–465
- <sup>18</sup> G. Golewski, T. S. Sadowski, Role of coarse aggregate in destruction of concrete composites subjected to summarily loads, *IZT*, 2008, 174 (in Polish)
- <sup>19</sup> PN-EN 197-1:2002 Cement – Part 1: Composition, specifications and conformity criteria for common cements (in Polish)
- <sup>20</sup> PN-B-19707:2013-10 Cement – Special cement – Composition, specifications and conformity criteria (in Polish)
- <sup>21</sup> PN-EN 933-1:2000 Test for geometrical properties of aggregates – Part 1: Determination of particle size distribution – Sieving method (in Polish)
- <sup>22</sup> PN-EN 12390-3:2002 Testing hardened concrete – Part 3: Compressive strength of test specimens (in Polish)
- <sup>23</sup> PN-EN 12390-6:2001 Testing hardened concrete – Part 6: Tensile splitting strength of test specimens (in Polish)
- <sup>24</sup> ASTM C 469-02:2004 Standard Test Method for Static Modulus of Elasticity and Poisson's Ratio of Concrete in Compression
- <sup>25</sup> RILEM TC 162-TDF, Test and design method for steel fibre reinforced concrete, Recommendations for bending test, *Materials and Structures*, 33 (2000) 225, 3–5
- <sup>26</sup> RILEM TC 162-TDF, Test and design method for steel fibre reinforced concrete, Bending test, Final recommendation, *Materials and Structures*, 35 (2002) 253, 579–582
- <sup>27</sup> RILEM TC 162-TDF, Test and design method for steel fibre reinforced concrete,  $\sigma$ - $\epsilon$  design method, Final recommendation, *Materials and Structures*, 36 (2003) 262, 560–567
- <sup>28</sup> F. Ozalp, Y. Akkaya, C. Sengul, B. Akcay, M. A. Tasdemir, A. N. Kocaturk, Curing effect on fracture of high-performance cement based composites with hybrid steel fibers, Proceedings of sixth international conference on fracture mechanics of concrete and concrete structures – FraMCoS-6, Catania, Italy, 3 (2007), 1377–85
- <sup>29</sup> J. A. O. Barros, E. Pereira, A. Ribeiro, V. Cunha, Self-compacting steel fibre reinforced concrete for precast sandwich panels – experimental and numerical research, Proceedings of international workshop on advanced fiber reinforced concrete, Bergamo, Italy 2005, 169–80



# PREPARATION OF POROUS CERAMIC MATERIALS BASED ON $\text{CaZrO}_3$

## PRIPRAVA POROZNE KERAMIKE NA OSNOVI $\text{CaZrO}_3$

**Edyta Śnieżek, Jacek Szczerba, Ilona Jastrzębska, Elżbieta Kleczyk,  
Zbigniew Pędzich**

AGH University of Science and Technology, Faculty of Materials Science and Ceramics, al. A. Mickiewicza 30, 30-059 Krakow, Poland  
esniezek@agh.edu.pl

*Prejem rokopisa – received: 2014-08-08; sprejem za objavo – accepted for publication: 2014-09-22*

doi:10.17222/mit.2014.187

The present study was devoted to an investigation of the synthesis conditions and the influence of Sn ions on the production of a  $\text{CaZrO}_3$  porous structure. Porous ceramics based on  $\text{CaZrO}_3$  with a SnO addition were prepared by means of pressureless sintering. The study presents the influence of the type of the starting materials and the firing procedures on the microstructures of the  $\text{CaZrO}_3$  materials. Two different firing procedures were applied. The samples were obtained from pure chemical reagents  $\text{CaCO}_3$  or  $\text{CaO}$  and  $\text{ZrO}_2$ . SnO was added in the mass fraction of 2 %. The prepared materials were investigated in terms of phase composition with the XRD. The microstructure was analyzed using the SEM/EDS and mercury porosimetry methods. It was found that using  $\text{CaCO}_3$  in a one-step firing process at 1650 °C with a soaking time of 10 h allowed us to obtain porous zirconate ceramics with a porosity of about 44 %. The second synthesis, where  $\text{CaO}$  was used, allowed us to obtain a porosity of about 36 %. During the firing solid solutions containing Sn ions in  $\text{CaZrO}_3$  and  $\text{ZrO}_2$  were formed. No other compounds containing Sn ions were identified. It was found that these ions played a significant role in the formation of a stable porous microstructure. The final materials mainly consisted of  $\text{CaZrO}_3$  and a small amount of  $\text{ZrO}_2$ . The obtained porous  $\text{CaZrO}_3$  materials with an excellent oxidation and alkali resistance in a wide temperature range could be potential candidates for the use as membranes and filters.

Keywords: calcium zirconate, porous ceramics, solid solution

Ta študija je namenjena preiskavi razmer pri sintezi in vplivu ionov Sn na izdelavo porozne strukture  $\text{CaZrO}_3$ . Porozna keramika na osnovi  $\text{CaZrO}_3$  z dodatkom SnO je bila pripravljena s sintranjem brez tlaka. Študija predstavlja vpliv vrste izhodnega materiala in procesa žganja na mikrostrukturo materiala  $\text{CaZrO}_3$ . Uporabljena sta bila dva načina žganja. Vzorci so bili izdelani iz čistih kemijskih sestavin  $\text{CaCO}_3$  ali  $\text{CaO}$  in  $\text{ZrO}_2$ . Masni delež dodanega SnO je bil  $w = 2\%$ . Fazna sestava pripravljene materiala je bila analizirana z rentgensko difrakcijo. Mikrostruktura je bila analizirana s SEM/EDS in s porozimetrijo z živim srebrom. Ugotovljeno je, da uporaba  $\text{CaCO}_3$  v enostopenjskem postopku žarjenja 10 h na 1650 °C omogoča pridobitev porozne cirkonske keramike s poroznostjo okrog 44 %. Druga sinteza, kjer je bil uporabljen  $\text{CaO}$ , omogoča doseganje poroznosti okrog 36 %. Med žganjem je nastala trdna raztopina, ki je vsebovala ione Sn v  $\text{CaZrO}_3$  in v  $\text{ZrO}_2$ . Ni bila ugotovljena nobena druga sestavina, ki bi vsebovala ione Sn. Navedeno je, da ti ioni igrajo pomembno vlogo pri nastanku stabilne porozne mikrostrukture. Končni materiali so vsebovali pretežno  $\text{CaZrO}_3$  in majhno količino  $\text{ZrO}_2$ . Dobljen porozni keramični  $\text{CaZrO}_3$ -material z odlično odpornostjo proti oksidaciji in alkalijam v širokem temperaturnem intervalu je lahko potencialni kandidat za uporabo v obliki membrane in filtrov.

Ključne besede: kalcijev cirkonat, porozne keramike, trdna raztopina

## 1 INTRODUCTION

Zirconate materials with a perovskite structure are interesting for many engineering fields, especially for high-temperature structural applications. Due to their characteristics they can be applied in the sensors, mechanical filters or coatings used at high temperatures and in corrosive environments. It is interesting to obtain porous materials based on calcium zirconate ( $\text{CaZrO}_3$ ).

The synthesis conditions and properties of  $\text{CaZrO}_3$  can be modified with an addition of selected ions, such as scandium, indium, gallium, yttrium, aluminum, magnesium, etc.  $\text{CaZrO}_3$  doped with  $\text{Al}_2\text{O}_3$ ,  $\text{Y}_2\text{O}_3$  and  $\text{MgO}$  is an oxygen-ion conductor. Undoped  $\text{CaZrO}_3$  is a p-type semiconductor used at low temperatures (< 1200 °C). Moreover, trivalent cations, e.g., indium, scandium,

gallium change the conduct of  $\text{CaZrO}_3$  and in this state it acts as a proton conductor.<sup>1-6</sup>

Suzuki et al.<sup>7</sup> investigated porous, In-doped  $\text{CaZrO}_3/\text{MgO}$  composites with respect to the  $\text{CH}_4$ -sensitivity in air. The samples were prepared from a high-purity natural dolomite,  $\text{ZrO}_2$ ,  $\text{In}_2\text{O}_3$  and  $\text{LiF}$ . To obtain porous composites the samples were sintered in air at 1300 °C. It was found that the porous composite, consisting of  $\text{CaZrO}_3$ ,  $\text{MgO}$  and  $\text{CaIn}_2\text{O}_4$  (amount fraction  $x = 10\%$  of  $\text{In}_2\text{O}_3$ ), was characterized by the porosity of 57 %. A higher porosity (60 %) of the samples was obtained with an addition of  $x = 5\%$  of  $\text{In}_2\text{O}_3$ ; these samples were composed only of the  $\text{CaZrO}_3$  and  $\text{MgO}$  phases. The In-doping decreased the  $\text{CH}_4$ -sensitivity in argon, but it was effective at improving the  $\text{CH}_4$ -sensitivity in air.<sup>7</sup> The  $\text{CaZrO}_3/\text{MgO}$  composites without In obtained with the one-step heat treatment were also characterized by a

high porosity of 30–50 % which depended on the sintering temperature.<sup>8</sup>

The method of preparing the MgO-CaZrO<sub>3</sub>-β-Ca<sub>2</sub>SiO<sub>4</sub> porous materials with an interconnected porosity and a controlled size in the range of micrometers was presented in<sup>9</sup>. Dolomite-zirconia mixtures were used to obtain porous materials for refractory applications. The samples were fired in the temperature range from 800 °C to 1740 °C. After the final sintering at 1740 °C the porosity was at a significant level due to the decarbonization process associated with the loss of CO<sub>2</sub>.<sup>9</sup>

Individual properties of CaZrO<sub>3</sub> and SnO<sub>2</sub> may lead to an assumption that the Sn-doped CaZrO<sub>3</sub> has a stable porous structure. Therefore, it is interesting to study the synthesis process, the influence of the Sn ions on it and the structure of CaZrO<sub>3</sub> ceramics.

## 2 EXPERIMENTAL WORK

CaZrO<sub>3</sub> porous ceramics were prepared by means of a conventional solid-state reaction method. Calcium carbonate (CaCO<sub>3</sub>), zirconium dioxide (ZrO<sub>2</sub>) and tin oxide (SnO) were used as the starting raw materials. The characteristics of the starting raw materials are presented in **Table 1**. The firing was carried out in two ways: CaCO<sub>3</sub> was used with the first firing method (designation: ICZSn) and CaO was used with the second one (designation: IICZSn). The compositions of the materials were designed taking into account the CaCO<sub>3</sub> or CaO to ZrO<sub>2</sub> ratio corresponding to the CaZrO<sub>3</sub> stoichiometry. SnO was added in the mass fraction of 2 %. The oxides were mixed together for 2 h. The homogenized mixtures were pressed into pellets (a diameter 20 mm, a thickness 10 mm) at a pressure of 70 MPa. The synthesis of the two

series of the samples was carried out with pressureless sintering as shown in **Figure 1**. The pellets were heated up to 1650 °C with different heating rates, held at this temperature for 10 h and then cooled down in the furnace. Because CaCO<sub>3</sub> was used in the first firing, the samples were heated at two different heating rates: 2 °C/min up to 1000 °C and 5 °C/min up to the final temperature.

**Table 1:** Specification of the starting materials

**Tabela 1:** Pregled izhodnih materialov

|                              | Reagents                    |                                         |                               |
|------------------------------|-----------------------------|-----------------------------------------|-------------------------------|
|                              | CaCO <sub>3</sub><br>(POCH) | ZrO <sub>2</sub><br>(Acros<br>Organics) | SnO<br>(Aldrich<br>Chemistry) |
| Pure (%)                     | 98.5                        | 98.5                                    | 97                            |
| Median particle<br>size (μm) | 41.83                       | 4.53                                    | 23.66                         |

The phase composition of the sintered samples was examined using the powder X-ray diffraction (XRD) technique at room temperature. The measurements were performed with a Panalytical X'Pert-Pro diffractometer using Cu-Kα radiation at a 2θ angle ranging from 10 ° to 90 °. The obtained data were analyzed using the X'Pert Pro Highscore Plus software. The open porosity of the sintered samples was measured using the water-displacement method based on Archimedes' principle. The pore-size distribution was analyzed with the mercury-intrusion method (Porosimeter PoreMaster 60, Quantachrome Instruments). A cylindrical-pore model was used for the calculation. The changes in the microstructure of the products were discussed on the basis of SEM observations (NovaNanoSem 200) accompanied by an EDS chemical analysis of micro-areas.

## 3 RESULTS AND DISCUSSION

**Figure 2** shows the XRD analysis of the samples. The X-ray diffraction patterns of ICZSn and IICZSn indicated that CaZrO<sub>3</sub> in the amounts of 95 % and 99 %, respectively, was the main phase. Cubic ZrO<sub>2</sub> stabilized with calcium oxide (4 %) and monoclinic ZrO<sub>2</sub> (1 %) were identified in ICZSn. Furthermore, when CaO was used as the starting material (IICZSn) only cubic ZrO<sub>2</sub> (1 %) was determined. No phases containing tin were identified. This may indicate that the SnO<sub>2</sub>-ZrO<sub>2</sub> solid solution was created in accordance with reference<sup>10</sup>. An effective ionic radius of Sn<sup>4+</sup> (0.069 nm) is close to Zr<sup>4+</sup> (0.072 nm) and considerably lower than Ca<sup>2+</sup> (0.112 nm).<sup>11</sup>

It is worth mentioning that, in the Sn-O system, tin oxide is present in various forms, such as SnO, SnO<sub>2</sub>, Sn<sub>2</sub>O<sub>3</sub>, Sn<sub>3</sub>O<sub>4</sub> and Sn<sub>5</sub>O<sub>6</sub>. Only SnO and SnO<sub>2</sub> are stable. Above 270 °C, SnO decomposes into Sn<sub>3</sub>O<sub>4</sub> and metallic tin in accordance with Equation (1):

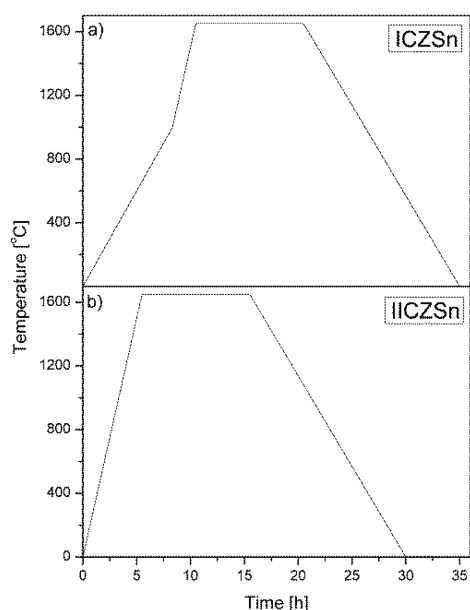


**Figure 1:** Firing curves: a) ICZSn, b) IICZSn

**Slika 1:** Krivulje žganja: a) ICZSn, b) IICZSn



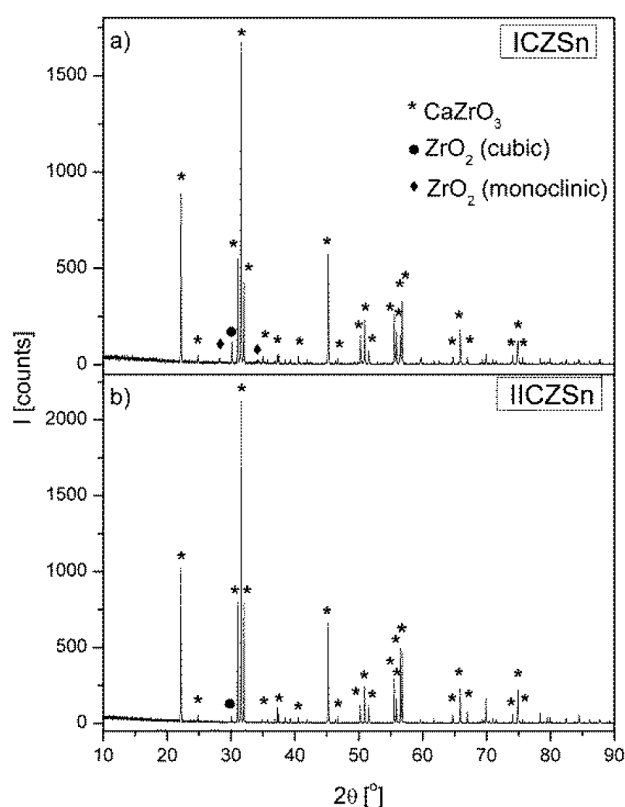


**Figure 2:** X-ray diffraction patterns of the samples prepared with a solid-state reaction: a) ICZSn, b) IICZSn

**Slika 2:** Rentgenski difrakcijski posnetek vzorcev, pripravljenih z reakcijo v trdnem: a) ICZSn, b) IICZSn

Above 450 °C Sn<sub>3</sub>O<sub>4</sub> melts incongruently into Sn and SnO<sub>2</sub>.<sup>12,13</sup>

The SEM micrographs of the samples are presented in **Figures 3 to 6**. The chemical compositions of the samples were confirmed with the EDS measurements (**Tables 2 and 3**). These allowed us to identify the most probable phase compositions of individual grains, CaZrO<sub>3</sub> (dark grey grains – point 1) and ZrO<sub>2</sub> (light grey phase – point 2). **Figures 4 and 6** present different forms of ZrO<sub>2</sub>. In ICZSn, ZrO<sub>2</sub> created clearly identifiable

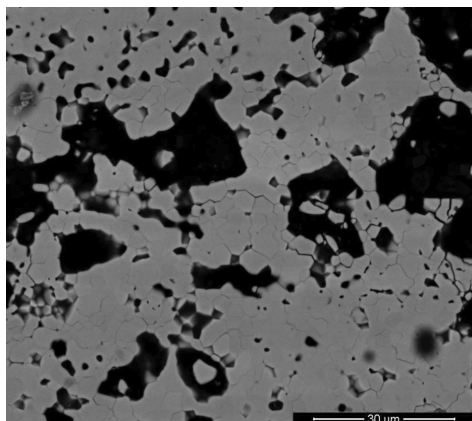


**Figure 3:** SEM micrograph of the ICZSn microstructure

**Slika 3:** SEM-posnetek mikrostrukture ICZSn

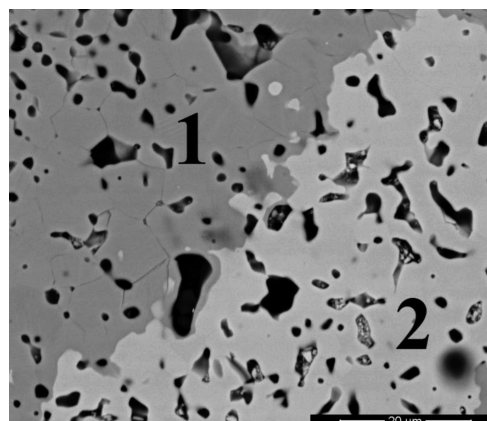


**Figure 4:** SEM micrograph of the ICZSn sample with marked points where the EDS analysis was performed

**Slika 4:** SEM-posnetek mikrostrukture vzorca ICZSn z označenima točkama, kjer je bila izvršena EDS-analiza

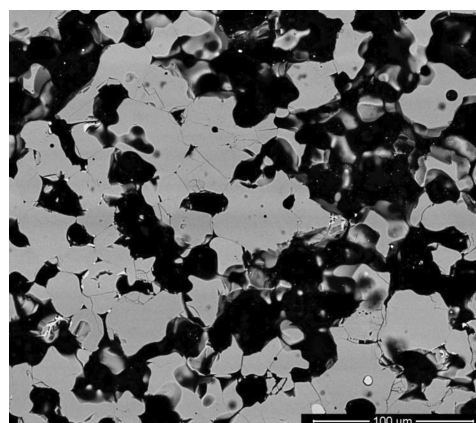


**Figure 5:** SEM micrograph of the IICZSn microstructure

**Slika 5:** SEM-posnetek mikrostrukture IICZSn

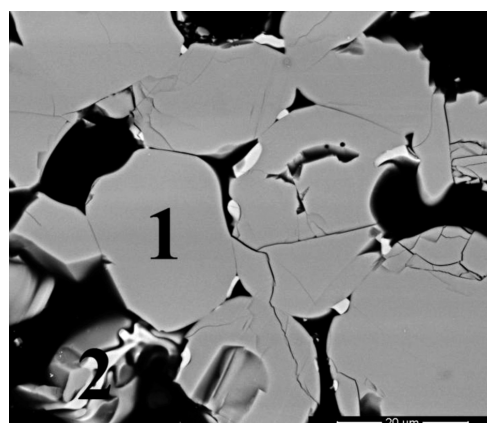


**Figure 6:** SEM micrograph of the IICZSn sample with marked points where the EDS analysis was performed

**Slika 6:** SEM-posnetek mikrostrukture vzorca IICZSn z označenima točkama, kjer je bila izvršena EDS-analiza

areas. In IICZSn, ZrO<sub>2</sub> occurred as individual inclusions. This can be explained with a higher concentration of ZrO<sub>2</sub> in the ICZSn samples (5 %). Furthermore, it can be established that the Sn ions incorporated in CaZrO<sub>3</sub> and

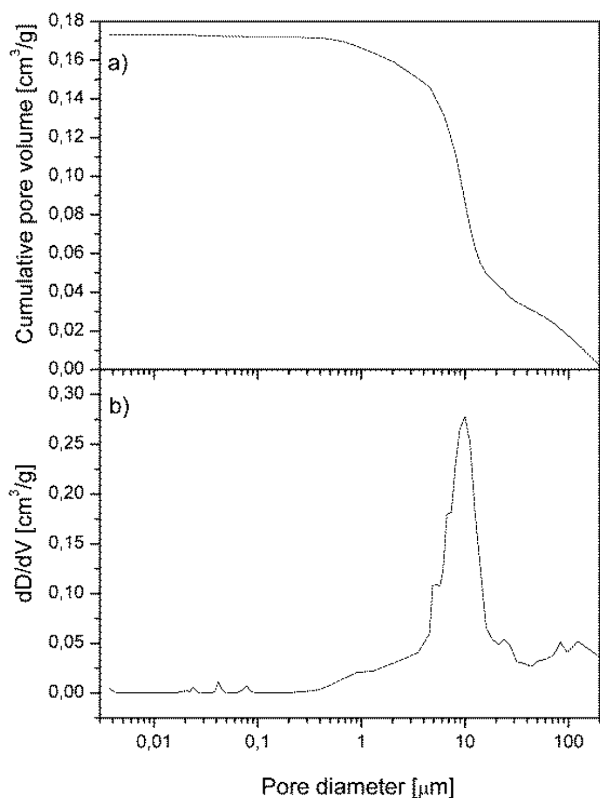


**Figure 7:** a) Cumulative pore-volume changes and b) pore-size distribution (pore-frequency curve) of the ICZSn sample

**Slika 7:** a) Kumulativna sprememba volumna por in b) razporeditev velikosti por (krivulja frekvence por) vzorca ICZSn

ZrO<sub>2</sub> are in different amounts. The SEM/EDS investigations confirmed the results of the XRD analysis. The average diameter of the CaZrO<sub>3</sub> grains changed from about 5–15 µm for ICZSn to 50 for IICZSn. The grain growth was associated with the type of the used raw material (CaCO<sub>3</sub>-ICZSn or CaO-IICZSn). Moreover, when only small amounts of ZrO<sub>2</sub> were observed in the samples (IICZSn – 1 %) the Sn ions were incorporated into the CaZrO<sub>3</sub> structure.

**Table 2:** Average chemical compositions (EDS) of CaZrO<sub>3</sub> and ZrO<sub>2</sub> grains according to **Figure 4**

**Tabela 2:** Povprečna kemijska sestava (EDS) CaZrO<sub>3</sub> in ZrO<sub>2</sub> zrn, skladno s **sliko 4**

| Point | Amount fraction, $x(\text{ICZSn})/\%$ |      |     |      |
|-------|---------------------------------------|------|-----|------|
|       | O                                     | Zr   | Sn  | Ca   |
| 1     | 53.9                                  | 23.8 | 0.4 | 21.9 |
| 2     | 57.9                                  | 33.6 | 0.7 | 7.8  |

**Table 3:** Average chemical compositions (EDS) of CaZrO<sub>3</sub> and ZrO<sub>2</sub> grains according to **Figure 6**

**Tabela 3:** Povprečna kemijska sestava (EDS) CaZrO<sub>3</sub> in ZrO<sub>2</sub> zrn, skladno s **sliko 6**

| Point | Amount fraction, $x(\text{IICZSn})/\%$ |      |     |      |
|-------|----------------------------------------|------|-----|------|
|       | O                                      | Zr   | Sn  | Ca   |
| 1     | 51.1                                   | 24.5 | 0.9 | 23.5 |
| 2     | 62.2                                   | 29.9 | 0.2 | 7.7  |

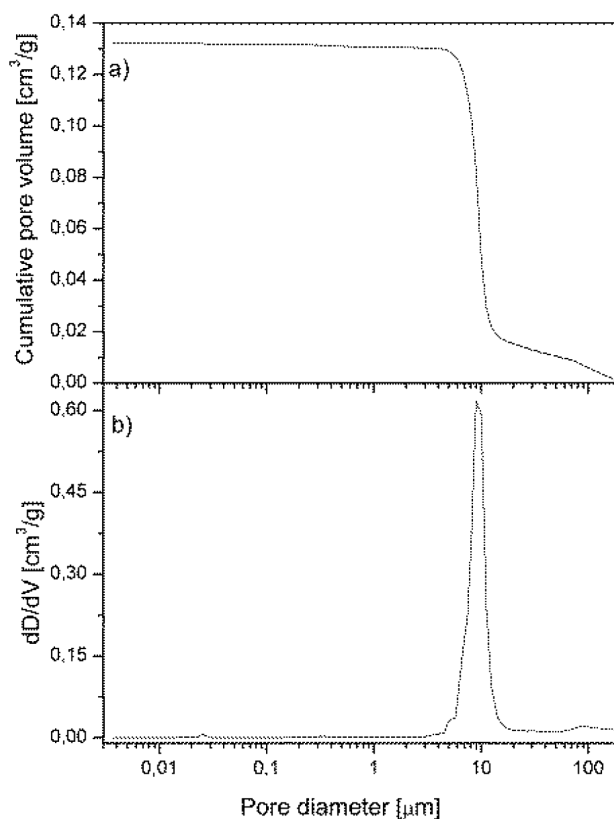


**Figure 8:** a) Cumulative pore-volume changes and b) pore-size distribution (pore-frequency curve) of the IICZSn sample

**Slika 8:** a) Kumulativna sprememba volumna por in b) razporeditev velikosti por (krivulja frekvence por) vzorca IICZSn

**Table 4:** Properties of ICZSn and IICZSn materials determined with mercury porosimetry

**Tabela 4:** Lastnosti materialov ICZSn in IICZSn, določene s porozimetrijo z živim srebrom

|        | Cumulative pore volume mm <sup>3</sup> /g | Median pore diameter µm | Bulk density g/cm <sup>3</sup> | Porosity % |
|--------|-------------------------------------------|-------------------------|--------------------------------|------------|
| ICZSn  | 173.6                                     | 10                      | 2.49                           | 43.2       |
| IICZSn | 132.3                                     | 9                       | 2.84                           | 37.6       |

The total pore volume and the median pore diameter of the samples analyzed with the mercury-intrusion method are shown in **Figures 7** and **8** and summarized in **Table 4**. The figures show slightly different types of curves but having the same mean pore size. The ICZSn sample (**Figure 7**) was characterized by one main pore population of about 10 µm in diameter. Two other populations were also distinctly detectable: of less than 0.1 µm and of about 100 µm. In contrast, the IICZSn sample had a very narrow pore-size distribution with the mean size of 9 µm (**Figure 8**). This proved that, in this case, the pores were more uniform and monomodal. This difference may have resulted from the CaCO<sub>3</sub> decarboxylation which occurred, as generally known, in the 600–950 °C temperature range. During the heating,

CaCO<sub>3</sub> decomposed into CaO (solid) and CO<sub>2</sub> (gas) according to Equation (2). The formed CaO reacted with ZrO<sub>2</sub> creating CaZrO<sub>3</sub>.



The porosity measured in accordance with Archimedes' principle varied from 44 % to 35 % for ICZSn and IICZSn, respectively, being in good agreement with the results of the mercury-intrusion analysis.

These porous materials, being comprised of CaZrO<sub>3</sub> and a small amount of ZrO<sub>2</sub> have an excellent oxidation and alkali resistance in a wide temperature range. The presented materials can be used as filters, membranes and insulation materials. Moreover, an incorporation of Sn ions in the CaZrO<sub>3</sub> and ZrO<sub>2</sub> structure can lead to obtaining unique electrical properties.

#### 4 CONCLUSIONS

The article focuses on porous CaZrO<sub>3</sub> materials with SnO additions. The presented results describe the influence of the starting raw materials and the firing procedure on the final properties of the CaZrO<sub>3</sub> ceramics. It is shown that using CaCO<sub>3</sub>, in comparison with CaO, allowed us to obtain a material with the porosity exceeding 40 %. A porous structure can be controlled by the synthesis conditions.

During the firing solid solutions containing Sn ions were formed in CaZrO<sub>3</sub> and ZrO<sub>2</sub>. The final materials ICZSn and IICZSn were composed of about 95 % and 99 % of CaZrO<sub>3</sub>, respectively, and ZrO<sub>2</sub>. No free CaO or Sn-containing inclusions (except for the CaZrO<sub>3</sub> solid solution) were detected with the performed XRD and SEM/EDS analyses. Porous CaZrO<sub>3</sub> materials could be potential candidates for the use as membranes and filters.

Moreover, a CaZrO<sub>3</sub> structure with incorporated Sn ions can reveal unique electrical properties.

#### Acknowledgement

The work was partially supported by the grant no. INNOTECH-K2/IN2/16/181920/NCBR/13.

#### 5 REFERENCES

- <sup>1</sup> C. C. Wang, S. A. Akbar, W. Chen, J. R. Schorr, *Sens. Actuators A*, 58 (1997), 237–243, doi:10.1016/S0924-4247(97)01394-0
- <sup>2</sup> C. Wang, W. H. Chen, S. A. Akbar, *J. Mater. Sci.*, 32 (1997), 2305–2312, doi:10.1023/A:1018580418264
- <sup>3</sup> K. Kobayashi, S. Yamaguchi, Y. Iguchi, *Solid State Ionics*, 108 (1998), 355–362, doi:10.1016/S0167-2738(98)00063-0
- <sup>4</sup> C. S. Prasanth, H. Padma Kumar, R. Pazhani, S. Solomon, J. K. Thomas, *J. Alloys Compd.*, 464 (2008), 306–309, doi:10.1016/j.jallcom.2007.09.098
- <sup>5</sup> S. C. Hwang, G. M. Choi, *Solid State Ionics*, 177 (2006), 3099–3103, doi:10.1016/j.ssi.2006.08.002
- <sup>6</sup> V. Longo, F. Marchini, F. Ricciardiello, A. de Pretis, *La Ceramica*, 34 (1981), 23–28
- <sup>7</sup> Y. Suzuki, M. Awano, N. Kondo, T. Ohjo, *J. Eur. Ceram. Soc.*, 22 (2002), 1177–1182, doi:10.1016/S0955-2219(01)00405-8
- <sup>8</sup> Y. Suzuki, P. E. D. Morgan, T. Ohjo, *J. Am. Ceram. Soc.*, 83 (2000), 2091–2093, doi:10.1111/j.1151-2916.2000.tb01519.x
- <sup>9</sup> J. L. Rodríguez, M. A. Rodríguez, S. De Aza, P. Pena, *J. Eur. Ceram. Soc.*, 21 (2001), 343–354, doi:10.1016/S0955-2219(00)00212-0
- <sup>10</sup> B. Gaillard-Allemand, R. Podor, M. Vilasi, Ch. Rapin, A. Maitre, P. Steinmetz, *J. Eur. Ceram. Soc.*, 22 (2002), 2297–2303, doi:10.1016/S0955-2219(02)00034-1
- <sup>11</sup> R. D. Shannon, *Acta Crystallogr. A*, 32 (1976), 751–767, doi:10.1107/S0567739476001551
- <sup>12</sup> G. H. Moh, *Chem. Erde*, 33 (1974), 243–275
- <sup>13</sup> S. Cahen, N. David, J. M. Fiorani, A. Maitre, M. Vilasi, *Thermochim. Acta*, 403 (2003), 275–285, doi:10.1016/S0040-6031(03)00059-5



## DP780 DUAL-PHASE-STEEL SPOT WELDS: CRITICAL FUSION-ZONE SIZE ENSURING THE PULL-OUT FAILURE MODE

### TOČKASTI ZVARI JEKLA DP780 Z DVOFAZNO STRUKTURO: KRITIČNA VELIKOST STALJENE CONE, KI ZAGOTAVLJA PORUŠENJE Z IZPULJENJEM

Majid Pouranvari<sup>1</sup>, Seyed Pirooz Hoveida Marashi<sup>2</sup>, Hassanen Latif Jaber<sup>3</sup>

<sup>1</sup>Materials and Metallurgical Engineering Department, Dezful Branch, Islamic Azad University, Dezful, Iran

<sup>2</sup>Mining and Metallurgical Engineering Department, Amirkabir University of Technology, Tehran, Iran

<sup>3</sup>Engineering College, University of Thi-Qar, Nasiriyah, Iraq  
mpouranvari@yahoo.com

*Prejem rokopisa – received: 2014-08-08; sprejem za objavo – accepted for publication: 2014-10-01*

doi:10.17222/mit.2014.184

This paper addresses the transition from the interfacial to the pull-out failure mode for DP780 dual-phase-steel resistance spot welds under tensile-shear and cross-tension loading conditions. It was studied whether industrial weld-size criteria can produce pull-out failure modes. Based on the failure mechanism of the spot welds in a cross-tension test, a simple analytical model is proposed to predict the critical FZ size to ensure the pull-out failure mode. According to the findings, the sheet thickness, the hardness ratio of the fusion zone to the sub-critical heat-affected zone, the amount of shrinkage voids in the fusion zone and the width of the HAZ are the main controlling factors for the transition from the interfacial to the pull-out failure mode in cross-tension loading. The fusion-zone size was proved to be the key factor controlling the cross-tension and tensile-shear strengths of DP780 resistance spot welds.

Keywords: advanced high-strength steel, resistance spot welding, failure mode

Ta članek obravnava prehod iz medploskovne porušitve v porušitve z izpuljenjem pri uporovnih točkastih zvarih dvofaznega jekla DP780 med natezno-strižnim in prečnim obremenjevanjem. Ugotovljeno je bilo, da lahko kriterij industrijske velikosti zvarov povzroči porušitev z izpuljenjem. Na osnovi mehanizma porušitve točkastih zvarov je predlagan enostaven model za napovedovanje kritične velikosti FZ, ki zagotavlja način porušitve z izpuljenjem. Glavni kontrolni faktorji za prehod iz medploskovne v porušitev z izpuljenjem pri prečni obremenitvi so debelina pločevine, razmerje trdote v talilni coni in v podkritični toplotno vplivani coni, količina praznin zaradi krčenja v talilni coni in širina HAZ. Širina talilne cone se je izkazala kot ključni faktor, ki kontrolira strižno in prečno natezno trdnost uporovnih točkastih zvarov pri DP780.

Ključne besede: napredno visokotrdnostno jeklo, uporovni točkasti zvar, način porušitve

## 1 INTRODUCTION

Due to a combination of excellent strength and proper formability, advanced high-strength steels (AHSSs) have a potential for improvement in the vehicle crash performance without an addition of excess weight.<sup>1</sup> Ferrite-martensite dual-phase (DP) advanced high-strength steels are currently used in the automotive industry. In this combination of two phases, martensite contributes its high strength and a ferrite matrix provides good elongation, creating a good combination of strength and ductility for the applications that require good formability. This unique composite microstructure has other interesting mechanical properties such as continuous yielding, a low ratio of the yield stress to the tensile strength and a high initial work-hardening rate.<sup>2-4</sup> However, higher alloying contents of these steels limit their weldability and the thermal cycle of a welding process destroys a carefully designed microstructure which deteriorates the mechanical properties of the weld.<sup>5</sup>

Resistance spot welding (RSW) is a vital joining process for the automotive production. Typically, there

are about 2000–5000 spot welds in a modern vehicle. Automotive structural assemblies use groups of spot welds to transfer load through the structure during a crash. Additionally, spot welds can act as fold-initiation sites to manage impact energy.<sup>6</sup> Vehicle crashworthiness, which is defined as the capability of a car structure to provide adequate protection to its passengers against injuries in the event of a crash, largely depends on the integrity and the mechanical performance of the spot welds.<sup>7-9</sup> Failure of spot welds may affect the vehicle's stiffness and NVH (noise, vibration and harshness) performance at the general level.<sup>10</sup> Therefore, the quality, performance and failure characteristics of resistance spot welds are important for determining the durability and safety design of vehicles.

The mode in which resistance spot welds fail can significantly affect their load-carrying capacity and energy-absorption capability. Generally, a resistance-spot-weld failure occurs in two modes: interfacial failure (IF) and pull-out failure (PF).<sup>11-13</sup> **Figure 1** shows a schematic representation of the failure modes of resistance spot welds. The interfacial failure mode propagates along the

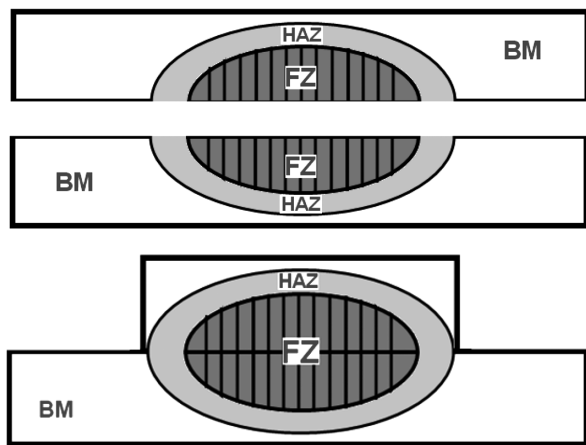


**Figure 1:** Schematic representation of typical failure modes that can occur during mechanical testing: a) interfacial, b) pull-out  
**Slika 1:** Shematska predstavitev značilnih porušitev, do katerih pride med mehanskim preizkušanjem: a) medploskovna, b) izpuljenje

centerline of a weld nugget, resulting in a sudden low-ductility failure. Because of its low ductility, the IF is generally considered an undesired failure mode for spot welds; hence, the IF mode is detrimental to weldability.<sup>5</sup> The resistance spot welds of the AHSS exhibit a higher tendency to fail in the interfacial failure mode than those of traditional steels (i.e., low-carbon and HSLA steels). Due to its significant impact on the joint reliability, the failure mode has been an interesting issue for some recent studies. The transition from the IF mode to the PF mode is generally related to the increase in the size of the fusion zone above the minimum value.<sup>5,14-19</sup> There are several sizing criteria for resistance spot welds including industrial standards. The effectiveness of these criteria for evaluating an AHSS spot weld, however, was not adequately addressed in the automotive welding community; it was simply adopted from the mild-steel practice and applied to AHSS spot welds.<sup>19</sup> The failure mode of the AHSS spot welds is a complex phenomenon which involves interactions among geometrical factors, weld metallurgical properties and the loading mode. Consequently, it is necessary to develop a spot-weld sizing criterion based on the failure mode to obtain an in-depth understanding of the factors governing the failure mode of spot welds.

In this paper, the microstructure and the failure mode of DP780 resistance spot welds under cross-tension and tensile-shear loading conditions are studied. The objectives of this study are: 1) to examine whether the existing weld-size criteria can provide for the pull-out failure mode of the DP780 spot welds; 2) to investigate the transition from the interfacial to the pull-out failure mode using both experimental and analytical approaches.

**2 EXPERIMENTAL PROCEDURE**

DP780 dual-phase steel sheets 2 mm thick were used as the base metal. **Table 1** shows the chemical compo-

sition and tensile properties of the investigated steel. Resistance spot welding was performed using a 120 kV A AC pedestal-type resistance-spot-welding machine, controlled with a PLC operating at 50 Hz. The welding was conducted using a 45-deg truncated-cone RWMA Class 2 electrode with an face diameter 8 mm.

**Table 1:** Chemical composition and mechanical properties of the investigated DP780 dual-phase steel in mass fractions, w/%

**Tabela 1:** Kemijska sestava in mehanske lastnosti preiskovanega dvo-faznega jekla DP780 v masnih deležih, w/%

| Chemical composition |      |      |      |      | Tensile properties |      |
|----------------------|------|------|------|------|--------------------|------|
| C                    | Mn   | Si   | Cr   | Mo   | TUS* (MPa)         | EL** |
| 0.16                 | 0.67 | 0.24 | 0.04 | 0.01 | 820                | 14   |

\*Yield strength, \*\*Elongation

To study the effects of the welding conditions on the weld performance, several welding schedules were used. The electrode force and the holding time were selected on the basis of the thickness of the base material and kept constant at 5.1 kN and 0.2 s, respectively. The welding current was increased step by step from 7 kA to 11.5 kA at the welding times of 0.5 s. The welding parameters were chosen below the expulsion limit to avoid the undesirable failure mode. Seven samples were prepared

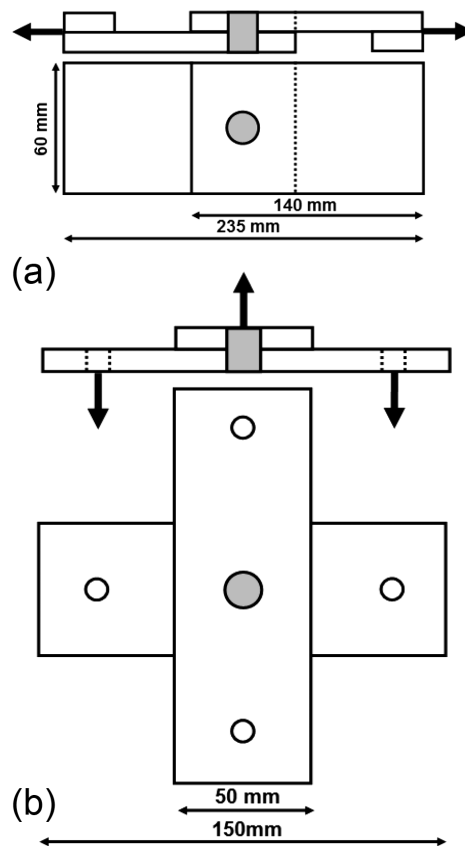


**Figure 2:** Test configuration and sample dimensions: a) tensile-shear test, b) cross-tension test

**Slika 2:** Izvedba preizkusov in dimenzije vzorcev: a) natezni strižni preizkus, b) prečni natezni preizkus

for each welding condition including three samples for the tensile-shear test, three samples for the cross-tension test and one sample for a metallographic investigation and measurement of the weld size.

The samples for the mechanical testing were prepared according to the AWS standard.<sup>20</sup> **Figure 2** shows the sample dimensions for the tensile-shear test and cross-tension test. The mechanical tests were performed at a cross head of 10 mm/min with an Instron universal testing machine. The failure modes of the spot-welded specimens were determined by examining the fractured samples. The fracture surfaces of the samples were examined with scanning electron microscopy (SEM).

Weld-nugget (fusion-zone) sizes were measured for all the samples on the metallographic cross-sections of the welds. A Vickers microhardness test was performed using an indenter load of 100 g for a period of 20 s to obtain the diagonal hardness profile from the center of the FZ to the BM. The hardness indentations were spaced 0.3 mm apart.

### 3 RESULTS AND DISCUSSION

#### 3.1 Failure mode

The failure modes of the samples were identified by examining the fracture surfaces. For the tensile-shear (TS) samples, it was observed that all the spot welds failed in the interfacial failure mode. On the other hand, both interfacial and pull-out failure modes were observed

during the cross-tension (CT) loading (**Figures 3a** and **3b**). **Figure 3c** shows the fracture surface of a weld failed in the IF mode demonstrating a cleavage-type fracture which indicates a low-fracture energy. Therefore, it is necessary to adjust the welding parameters so that obtaining the PF mode is guaranteed. The fracture surfaces of the spot welds failed in the IF mode exhibit some voids. An examination of the surface near the voids (**Figure 3d**) revealed a dendritic fracture surface indicating that these voids/cracks were formed due to solidification shrinkage.

It is well documented that the size of the fusion zone is the key physical weld attribute controlling the failure-mode transition of spot welds.<sup>5,12–19</sup> The effect of the welding current on the FZ size is shown in **Figure 4** indicating an enlargement of the weld nugget by increasing the welding current and generating a higher heat at the sheet/sheet interface. According to **Figure 4**, the failure mode during the CT loading was changed from the IF to the PF by increasing the welding current and the FZ size. In order to avoid the IF mode during the cross-tension test, the minimum welding current of 9 kA should be used for welding a DP780 steel sheet. The minimum FZ size required to obtain the PF mode during the CT loading was 6.6 mm. However, all the spot welds made with the welding current ranging from 7 kA to 11.5 kA and with the FZ size ranging from 3.4 mm to 9.2 mm failed in the IF mode indicating a higher tendency to the interfacial failure during the TS loading compared with that occurring during the CT loading.

Due to its significant impact on the joint reliability, the failure mode has been an interesting issue for some recent studies. The transition from the IF mode to the PF

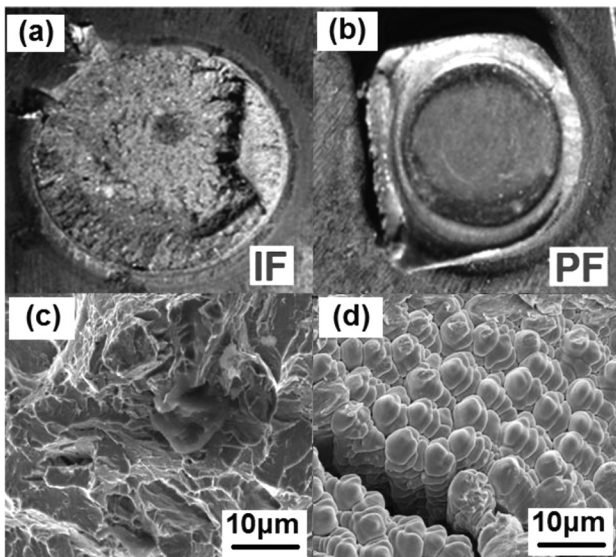


**Figure 3:** a) Typical interfacial-failure (IF) surface during cross-tension test, b) typical pullout failure (PF) during cross-tension test, c) SEM of fracture morphology of the spot welds failed in IF mode, d) morphology of solidification void found in the fracture surface of welds failed in IF mode

**Slika 3:** a) Značilna ploskev medploskovne porušitve (IF) med prečnim nateznim preizkusom, b) značilna porušitev z izpuljenjem (PF) med prečnim nateznim preizkusom, c) SEM-posnetek morfologije preloma točkastega zvara, porušenega v IF načinu, d) videz praznine pri strjevanju na površini preloma zvara, porušenega v IF načinu

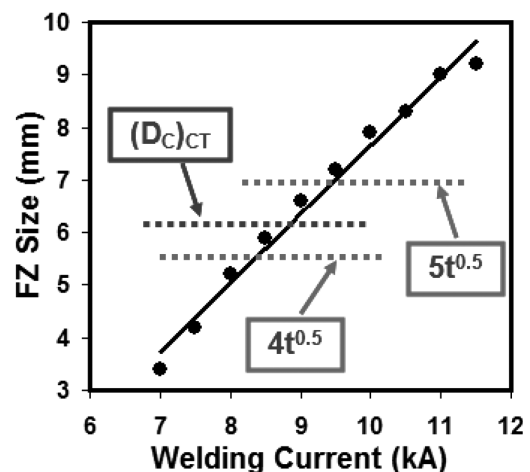


**Figure 4:** Effect of welding current on FZ size of DP780 resistance spot welds. Transition from interfacial to pull-out failure mode for CT loading is also shown. All spot welds were failed in IF mode during TS loading. Conventional weld-sizing recommendations of  $4t^{0.4}$  and  $5t^{0.4}$  and calculated  $(D_C)_{CT}$  are also superimposed.

**Slika 4:** Vpliv varilnega toka na velikost FZ v uporovnem točkastem zvaru DP780. Prikazan je tudi prehod iz medploskovne v porušitev z izpuljenjem pri CT-obremenitvi. Vsi točkasti zvari so bili porušeni v načinu IF pri TS-obremenitvi. Nadgrajena so tudi priporočila za velikost zvara  $4t^{0.4}$ ,  $5t^{0.4}$  in izračunan je  $(D_C)_{CT}$ .

mode is generally related to the increase in the size of the FZ above the minimum value. In the following sections, the failure-mode transition is compared with the existing criterion for sizing the weld nugget of a spot weld.

### 3.1.1 Industrial recommendations

For practical purposes, it is interesting to compare the experimentally determined minimum FZ size required to obtain the PF mode with the existing industrial standards for weld-nugget sizing. Various industrial standards recommend the minimum weld size for a given sheet thickness:

(I) AWS/ANSI/AISI<sup>20</sup> determines the weld-button sizing to ensure that the weld size is large enough to carry the desired load, on the basis of Equation (1):

$$D = 4t^{0.5} \tag{1}$$

where  $D$  is the weld-nugget size and  $t$  is the sheet thickness (mm).

(II) According to Japanese JIS Z 3140<sup>21</sup> and German DVS 2923<sup>22</sup> standards the required weld size is specified with Equation (2):

$$D = 5t^{0.5} \tag{2}$$

According to **Figure 4**, the weld-sizing criterion of  $4t^{0.5}$  is not sufficient to produce a weld with the PF mode during the TS and CT loading. Neither can the sizing of spot welds based on the  $5t^{0.5}$  criterion produce welds with the PF mode during the TS loading. However, the weld-sizing criterion of  $5t^{0.5}$  is sufficient to produce a weld with the PF mode during the CT loading.

### 3.1.2 Chao model

On the basis of the competition between the shear plastic deformation in the nugget circumference (i.e., the nugget pullout) and the crack propagation in the weld nugget (i.e., the interfacial failure mode), Chao<sup>23</sup> derived the equation for the critical weld-nugget size for the cross-tension test as follows:

$$D_c = 2.93 \left( \frac{\tau_{yBM}}{K_c^{FZ}} \right)^{2/3} t^{4/3} \tag{3}$$

where  $\tau_{yBM}$  is the shear strength of the base metal and  $K_c^{FZ}$  is the fracture toughness of the fusion zone.  $\tau_{yBM}$  and  $K_c^{FZ}$  can be obtained from the experimental data. Although Chao relates the critical weld size to the fracture toughness of the weld nugget and the fracture strength in the shear of the HAZ, he tried to show that his model is not material dependent. He suggested the following formula:

$$D_c = 3.41t^{4/3} \tag{4}$$

According to Equation (4), the minimum FZ size required to ensure the PF mode during the tensile-shear testing of 2 mm DP780 welds is 8.6 mm. According to **Figure 4**, the sizing based on this criterion can avoid the interfacial failure mode; however, the recommended

value is overestimated by nearly 30 % above the required weld size.

In the following sections the transition behavior during the TS and CT are explained in the light of the failure mechanism. It will be seen that the transition of the IF to the PF mode is governed by the fusion-zone size, the hardness characteristics of the welds and also by the loading condition.

### 3.1.3 New model for estimating the critical FZ size during the CT loading

**Figure 5** shows a simple model describing the stress distribution at the interface and circumference of a weld nugget during the CT test. According to **Figure 5**, the driving force for the IF is the tensile stress along the sheet/sheet interface, while the driving force for the PF is the shear stress around the weld nugget. For small weld nuggets, before the shear stress causes the nugget pullout, the tensile stress at the sheet/sheet interface reaches its critical value; as a result, the failure tends to occur in the interfacial failure mode. Therefore, in this section, a model is proposed to estimate the minimum fusion-zone size necessary to ensure the nugget pull-out-failure mode during the cross-tension test. In order to develop a model that predicts the failure mode, the first necessary step is to develop the equations for calculating the required force for each failure mode to happen.

Considering the nugget as a cylinder with a certain diameter ( $D$ ), the failure load in the interfacial failure mode during the cross-tension test,  $(P_{IF})_{CT}$ , can be expressed with Equation (5):

$$(P_{IF})_{CT} = \frac{\pi D^2}{4} \sigma_{FZ} \tag{5}$$

where  $\sigma_{FZ}$  is the tensile strength of the FZ.

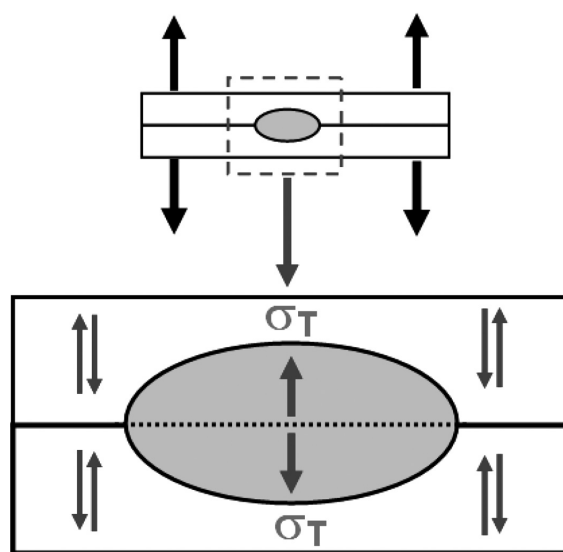


**Figure 5:** Simple model describing stress distribution in a spot weld during cross-tension test

**Slika 5:** Preprost model, ki prikazuje razporeditev napetosti v točkastem zvaru med prečnim nateznim preizkusom



One of the most probable defects during the resistance spot welding of the AHSSs is a shrinkage void<sup>5,19,24,25</sup> (**Figure 3a**). In the IF mode, the presence of voids decreases the effective FZ size and the load-bearing surface area, thus, decreasing the spot-weld failure strength. It is interesting to note that the AHSSs are highly prone to the shrinkage-void formation. This fact has been recognized as one of the main reasons for the high susceptibility of the AHSSs to the interfacial failure mode.<sup>5,19</sup> Therefore, the void level of RSWs should be taken into account when modeling the failure load in the interfacial failure mode. Here, similar to Sun et al.<sup>26</sup>, modeling the failure load of an aluminium spot weld during a cross-tension test, the void factor ( $V$ ) can be defined as follows:

$$V = \frac{A_{\text{total}} - A_{\text{Void}}}{A_{\text{total}}} \quad (6)$$

where  $A_{\text{total}}$  is the total area of the fusion zone on the faying interface and  $A_{\text{void}}$  is the projected area of the void in the fusion zone on the faying interface of the weld. Therefore, Equation (5) can be adjusted as follows:

$$F_{\text{IF}} = V \frac{\pi D^2}{4} \sigma_{\text{FZ}} \quad (7)$$

For the pull-out failure mode, it is assumed that a failure occurs when the shear stress at the circumference of one half of the cylindrical nugget reaches the ultimate shear strength of the softened HAZ (experimental investigations showed that the pull-out failure mode in the cross-tension test is initiated in the HAZ.)<sup>27,28</sup> Therefore, Equation (8) is suggested for the pull-out failure load in the cross-tension test, ( $P_{\text{PF}}$ )<sub>CT</sub>:

$$F_{\text{PF}} = \pi(D + 2X_{\text{HAZ}}) \cdot t \cdot \tau_{\text{SCHAZ}} \quad (8)$$

where  $\tau_{\text{SCHAZ}}$  is the ultimate shear strength of the pullout failure location (i.e., the sub-critical HAZ) and  $X_{\text{HAZ}}$  is the distance of the pullout-failure location from the fusion boundary. At the critical weld-nugget size,  $D_C$ , Equations (5) and (8) are equal. Therefore,  $D_C$  can be calculated using Equation (9):

$$(D_C)_{\text{CT}} = \frac{2t \cdot \tau_{\text{SCHAZ}}}{V\sigma_{\text{FZ}}} \left[ 1 + \left( 1 + \frac{2VX_{\text{HAZ}}}{t} \cdot \frac{\sigma_{\text{FZ}}}{\tau_{\text{SCHAZ}}} \right)^{0.5} \right] \quad (9)$$

The spot welds with  $D < D_C$  tend to fail via the interfacial mode, unlike the welds with  $D > D_C$  that tend to fail via the preferred pull-out mode.

A direct measurement of the mechanical properties of different regions of a spot weld is difficult. It is well known that there is a direct relationship between a material's tensile strength and its hardness. Also, the shear strength of a material can be linearly related to its tensile strength with the constant coefficient,  $f$ . Therefore, Equation (9) can be rewritten as follows:

$$(D_C)_{\text{CT}} = \frac{2t \cdot f}{VK} \left[ 1 + \left( 1 + \frac{2VKX_{\text{HAZ}}}{ft} \right)^{0.5} \right] \quad (10)$$

where  $K$  is the hardness ratio of the FZ to the sub-critical HAZ ( $H_{\text{FZ}}/H_{\text{SCHAZ}}$ ).

### 3.1.4 Critical FZ during the TS loading

In previous work,<sup>29</sup> in the light of the failure mechanism, using a simple stress analysis, an analytical mode was proposed to predict the failure mode of spot welds during the tensile-shear test. ( $D_C$ )<sub>TS</sub> was correlated to the hardness characteristics and void factor as follows:

$$(D_C)_{\text{TS}} = \frac{2t}{fVK} \left[ 1 + \left( 1 + \frac{2VfKX_{\text{HAZ}}}{t} \right)^{0.5} \right] \quad (11)$$

where  $t$  is the sheet thickness,  $K$  is the hardness ratio of the FZ to the sub-critical HAZ ( $H_{\text{FZ}}/H_{\text{SCHAZ}}$ ),  $V$  is the void factor,  $X_{\text{HAZ}}$  is the HAZ width and  $f$  is the ratio of the shear strength to the tensile strength of the metal.

## 3.2 Model validation

According to the proposed models, the hardness characteristics play the key role in determining the failure mode of resistance spot welds. Rapid heating and cool-

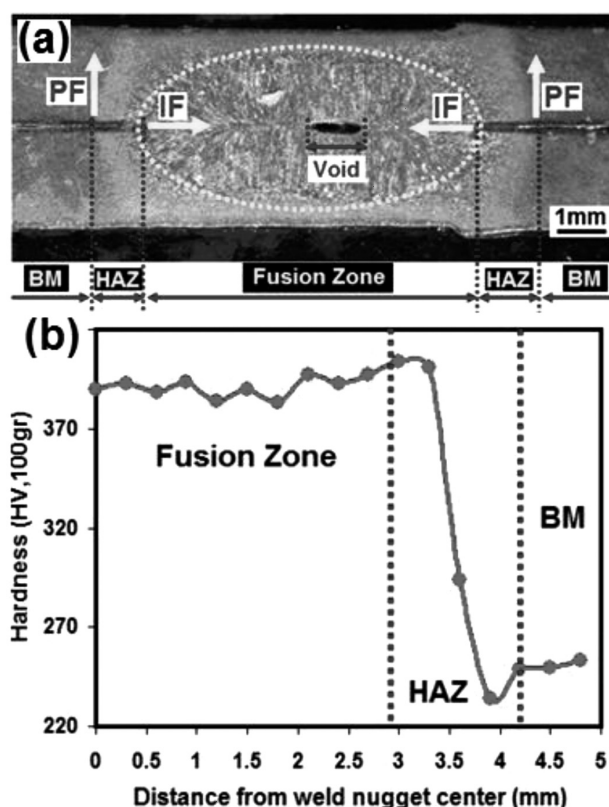


**Figure 6:** a) Typical macrostructure along the two main failure paths during cross-tension test and b) typical hardness profile of DP780 resistance spot welds

**Slika 6:** a) Značilna mikrostruktura vzdolž obeh poti preloma pri prečnem nateznem preizkusu in b) značilen potek trdote v uporovnem točkastem zvaru DP780

ing induced by the resistance-spot-welding thermal cycles significantly alter the microstructure in the joint zone. A typical macrostructure of DP780 spot welds is shown in **Figure 6a** indicating three distinct zones, namely, the fusion zone (FZ), the heat-affected zone (HAZ) and the base metal (BM). **Figure 6b** shows a typical hardness profile of the DP780 welds. The hardness profile exhibits three important phenomena:

- (i) A hardening of the FZ: The average hardness of the FZ is 380 HV which is higher compared to the base-metal hardness (i.e., 230 HV). The high hardness of the FZ can be attributed to the martensite formation in the FZ.
- (ii) A hardening in the HAZ: In the upper critical heat-affected zone (UCHAZ) where the peak temperatures are above  $A_{c1}$  during the welding, the base-metal microstructure transforms into austenite. On the subsequent cooling, austenite transforms into martensite. Therefore, in the UCHAZ, the local post-weld martensite content can be above the level of the as-manufactured steel, leading to a higher local hardness.<sup>30</sup>
- (iii) A softening in the HAZ: The sub-critical heat-affected zone (SCHAZ) where the peak temperatures are below  $A_{c1}$  exhibits a reduction in the hardness (softening) with respect to the BM. It is reported that the location of the minimum hardness in a softened HAZ corresponds to  $A_{c1}$ . It is well documented that this phenomena is due to the tempering with the pre-existing martensite in the sub-critical HAZ.<sup>5,30</sup>

According to the hardness profile, the average hardness values of the FZ and SCHAZ are 380 HV and 230 HV. The hardness ratio is calculated as 1.65. The void factor ( $V$ ) of the spot welds failed in the IF mode was determined using their fracture-surface macrograph. The average void factor of all the samples failed in the IF mode for the investigated DP780 spot welds is about 0.9 (i.e., 20 % of the area of the weld centerline plan exhibits a void). The average width of the HAZ ( $X_{HAZ}$ ) is around 1 mm. The ratio of the shear strength to the tensile strength ( $f$ ) is reported as 0.7–0.8. Here, an average value of 0.75 is considered. Now, the critical fusion zone ( $D_C$ ) can be estimated for both TS and CT loading conditions using Equations (10) and (11):

- (i) The critical fusion zone in the TS loading: According to Equation (10) the calculated  $D_C$  is 6.1 mm. As can be seen in **Figure 4**, at the welding current lower than 9 kA, the FZ size is lower than  $D_C$  and, consequently, the welds fail in the IF mode. On the other hand, the welds made at the welding current equal or higher than 9 kA exhibit a FZ that is higher than  $D_C$  and, hence, they fail in the PF mode. Indeed, the transition of the failure mode from the IF to the PF is well predicted using the proposed procedure.
- (ii) The critical fusion zone in the CT loading: According to Equation (9), the calculated  $(D_C)_{CT}$  is 9.7 mm. According to **Figure 4**, all the spot welds made in this study had the FZ size lower than 9.7 mm. There-

fore, it is not surprising that all the spot welds failed in the IF mode during the TS loading.

## 4 CONCLUSIONS

The failure-mode transition for the resistance spot-welded DP780 advanced high-strength steel during the tensile-shear loading and cross-tension loading is studied. The following conclusions can be drawn from this work:

1. The industrial weld-nugget sizing criterion of  $4t^{0.5}$  is not sufficient to ensure the pullout failure mode during the cross-tension and tensile-shear testing of DP780 resistance spot welds.
2. According to the theoretical analysis presented in this study the failure-mode transition of the DP780 spot welds in the cross-tension loading condition is governed by the sheet thickness, the FZ hardness, the sub-critical HAZ hardness, the shrinkage voids and the width of the HAZ.
3. The following relation is proposed to predict the minimum FZ size ( $D_C$ ) required to ensure the pull-out failure mode during the cross-tension test of the DP780 spot welds:

$$(D_C)_{CT} = \frac{2t \cdot f}{PK} \left[ 1 + \left( \frac{2VKX_{HAZ}}{ft} \right)^{0.5} \right]$$

where  $t$  is the sheet thickness,  $K$  is the hardness ratio of the FZ to the sub-critical HAZ ( $H_{FZ}/H_{SCHAZ}$ ),  $V$  is the void factor,  $X_{HAZ}$  is the HAZ width and  $f$  is the ratio of the shear strength to the tensile strength of the metal. The proposed analytical model successfully predicts the critical FZ size for the DP780 spot welds.

## 5 REFERENCES

- <sup>1</sup> M. Pouranvari, Influence of welding parameters on peak load and energy absorption of dissimilar resistance spot welds of DP600 and AISI1008 steels, *Can. Metall. Q.*, 50 (2011), 381–388, doi:10.1179/1879139511y.0000000008
- <sup>2</sup> A. Bag, K. K. Ray, E. S. Dwarakadasa, Influence of Martensite Content and Morphology on the Toughness and Fatigue Behaviour of High-Martensite Dual-Phase Steels, *Metall. Mater. Trans.*, 32A (2001), 2207–2217, doi:10.1007/s11661-001-0196-5
- <sup>3</sup> P. Movahed, S. Kolahgar, S. P. H. Marashi, M. Pouranvari, N. Parvin, The effect of intercritical heat treatment temperature on the tensile properties and work hardening behavior of ferrite–martensite dual phase steel sheets, *Mater. Sci. Eng. A*, 518 (2009), 1–6, doi:10.1016/j.msea.2009.05.046
- <sup>4</sup> M. Pouranvari, S. P. H. Marashi, S. M. Mousavizadeh, Failure mode transition and mechanical properties of similar and dissimilar resistance spot welds of DP600 and low carbon steels, *Sci. Technol. Weld. Join.*, 15 (2010), 625–631, doi:10.1179/136217110x12813393169534
- <sup>5</sup> M. Pouranvari, S. P. H. Marashi, Critical review of automotive steels spot welding: process, structure and properties, *Sci. Technol. Weld. Join.*, 18 (2013), 361–403, doi:10.1179/1362171813y.0000000120

- <sup>6</sup> W. Peterson, J. Borchelt, Maximizing Cross Tension Impact Properties of Spot Welds in 1.5 mm Low Carbon, Dual-phase, and Martensitic Steels, SAE Technical Paper Series, SAE 2000-01-2680, doi:10.4271/2000-01-2680
- <sup>7</sup> S. Simončič, P. Podržaj, Image-based electrode tip displacement in resistance spot welding, *Meas. Sci. Technol.*, 23 (2012), 1–7, doi:10.1088/0957-0233/23/6/065401
- <sup>8</sup> S. Simončič, P. Podržaj, Resistance spot weld strength estimation based on electrode tip displacement/velocity curve obtained by image processing, *Sci. Technol. Weld. Join.*, 19 (2014), 468–475, doi:10.1179/1362171814y.0000000212
- <sup>9</sup> P. Podržaj, S. Simončič, Resistance spot welding control based on the temperature measurement, *Sci. Technol. Weld. Join.*, 18 (2013), 551–557, doi:10.1179/1362171813y.0000000131
- <sup>10</sup> S. Donders, M. Brughmans, L. Hermans, N. Tzannetakis, The effect of spot weld failure on dynamic vehicle performance, *Sound and Vibration*, 39 (2005), 16–25
- <sup>11</sup> M. Pouranvari, S. P. H. Marashi, On the failure of low carbon steel resistance spot welds in quasi-static tensile-shear loading, *Mater. Des.*, 31 (2010), 3647–3652, doi:10.1016/j.matdes.2010.02.044
- <sup>12</sup> M. Pouranvari, H. R. Asgari, S. M. Mosavizadeh, P. H. Marashi, M. Goodarzi, Effect of weld nugget size on overload failure mode of resistance spot welds, *Sci. Technol. Weld. Join.*, 12 (2007), 217–225, doi:10.1179/174329307x164409
- <sup>13</sup> M. Pouranvari, S. P. H. Marashi, Factors affecting mechanical properties of resistance spot welds, *Mater. Sci. Technol.*, 26 (2010), 1137–1144, doi:10.1179/174328409x459301
- <sup>14</sup> M. Pouranvari, S. P. H. Marashi, Similar and dissimilar RSW of low carbon and austenitic stainless steels: effect of weld microstructure and hardness profile on failure mode, *Mater. Sci. Technol.*, 25 (2009), 1411–1416, doi:10.1179/026708309x12459430509292
- <sup>15</sup> M. Pouranvari, S. P. H. Marashi, Failure mode transition in AISI 304 resistance spot welds, *Weld. J.*, 91 (2012), 303–309
- <sup>16</sup> M. M. H. Abadi, M. Pouranvari, Failure-mode transition in resistance spot welded DP780 advanced high strength steel: effect of loading conditions, *Mater. Tehnol.*, 48 (2014) 1, 67–71
- <sup>17</sup> M. Pouranvari, S. M. Mousavizadeh, On the Failure Mode of M130 Martensitic Steel Resistance Spot Welds, *Mater. Tehnol.*, 47 (2013) 6, 771–776
- <sup>18</sup> M. Pouranvari, E. Ranjbarnoodeh, Dependence of Fracture Mode on Welding Variables in Resistance Spot Welding of DP980 Advanced High Strength Steel, *Mater. Tehnol.*, 46 (2012) 6, 665–671
- <sup>19</sup> X. Sun, E. V. Stephens, M. A. Khaleel, Effects of fusion zone size and failure mode on peak load and energy absorption of advanced high strength steel spot welds under lap shear loading conditions, *Eng. Fail. Anal.*, 15 (2008), 356–367, doi:10.1016/j.engfailanal.2007.01.018
- <sup>20</sup> Recommended Practices for Test Methods for Evaluating the Resistance Spot Welding Behavior of Automotive Sheet Steel Materials, ANSI/AWS/SAE D8.9-97, 1997
- <sup>21</sup> Japanese Industrial Standard, Method of Inspection for Spot Welds, JIS Z 3140, 1989
- <sup>22</sup> German Standard, Resistance Spot Welding, DVS 2923, 1986
- <sup>23</sup> Y. J. Chao, Failure mode of resistance spot welds: interfacial versus pullout, *Sci. Technol. Weld. Joining*, 8 (2003), 133–137
- <sup>24</sup> D. S. Safanama, S. P. H. Marashi, M. Pouranvari, Similar and dissimilar resistance spot welding of martensitic advanced high strength steel and low carbon steel: metallurgical characteristics and failure mode transition, *Sci. Technol. Weld. Joining*, 17 (2012), 288–294, doi:10.1179/1362171812y.0000000006
- <sup>25</sup> M. Pouranvari, Susceptibility to interfacial failure mode in similar and dissimilar resistance spot welds of DP600 dual phase steel and low carbon steel during cross-tension and tensile-shear loading conditions, *Mater. Sci. Eng. A*, 546 (2012), 129–138, doi:10.1016/j.msea.2012.03.040
- <sup>26</sup> X. Sun, E. V. Stephens, R. W. Davies, M. A. Khaleel, D. J. Spinella, Effects of failure modes on strength of aluminum resistance spot welds, *Weld. J.*, 83 (2004), 188–195
- <sup>27</sup> D. J. Radakovic, M. Tumuluru, An evaluation of the cross-tension test of resistance spot welds in high-strength dual-phase steels, *Weld. J.*, 91 (2012), 8–15
- <sup>28</sup> V. H. B. Hernandez, M. L. Kuntz, M. I. Khan, Y. Zhou, Influence of weld size and microstructure of dissimilar AHSS resistance spot welds, *Sci. Technol. Weld. Joining.*, 13 (2008), 769–776, doi:10.1179/136217108x325470
- <sup>29</sup> M. Pouranvari, S. P. H. Marashi, On failure mode of resistance spot welded DP980 advanced high strength steel, *Can. Metall. Q.*, 51 (2012), 447–455, doi:10.1179/1879139512y.0000000034
- <sup>30</sup> V. H. B. Hernandez, S. K. Panda, M. L. Kuntz, Y. Zhou, Nanoindentation and microstructure analysis of resistance spot welded dual phase steel, *Mater. Lett.*, 64 (2010), 207–210, doi:10.1016/j.matlet.2009.10.040



# APPLICATION OF COMPUTED TOMOGRAPHY IN COMPARISON WITH THE STANDARDIZED METHODS FOR DETERMINING THE PERMEABILITY OF CEMENT-COMPOSITE STRUCTURES

## UPORABA RAČUNALNIŠKE TOMOGRAFIJE V PRIMERJAVI S STANDARDIZIRANIMI METODAMI DOLOČANJA PREPUSTNOSTI CEMENTNIH KOMPOZITNIH STRUKTUR

**Tereza Komárková, Monika Králíková, Pavel Kovács, Dalibor Kocáb, Tomáš Stavař**

Brno University of Technology, Faculty of Civil Engineering, Veveří 331/95, 602 00 Brno, Czech Republic  
kralikovam@fce.vutbr.cz

*Prejem rokopisa – received: 2014-08-14; sprejem za objavo – accepted for publication: 2014-09-30*

doi:10.17222/mit.2014.194

The paper deals with various testing methods for evaluating the surface layer (the concrete cover) of concrete on which the durability of the whole composite depends. The key parameters for determining concrete permeability are the pore volume, size and distribution in the material and the relating water and air permeability. The aim of the experiment was to compare the results of the permeability measurement of the surface layer of concrete using standardized methods (depth of penetration of water under pressure, ISAT, GWT, TPT) with the outputs provided with computed tomography (CT). Based on the measurement results, CT appears to be an inappropriate method for evaluating the permeability of the surface layer of concrete. Circumstances that may limit the test method are described in detail in the article.

Keywords: concrete, durability, permeability, computed tomography

Članek obravnava različne preizkusne metode za oceno površinske plasti betona, od katere je odvisna vzdržljivost kompozita. Ključni parameter za določanje prepustnosti betona je ugotavljanje volumna, velikosti in razporeditve por v materialu ter z njimi povezana prepustnost vode in zraka. Namen eksperimenta je bil primerjati meritve prepustnosti površinskega sloja betona s standardiziranimi metodami (globina penetracije vode pod tlakom, ISAT, GWT, TPT) z rezultati, dobljenimi z računalniško tomografijo (CT). Na osnovi rezultatov meritev je videti, da CT ni primerna metoda za oceno prepustnosti površinskega sloja betona. V članku so podrobno opisane okoliščine, ki lahko omejujejo metodo preizkusa.

Ključne besede: beton, vzdržljivost, prepustnost, računalniška tomografija

## 1 INTRODUCTION

Concrete is used as a composite building material in most branches of the building industry and concrete structures are found in a number of places worldwide while the issue of their deterioration has been an increasing problem. This is illustrated by the fact that approximately 50 % of the expenses in the construction in Europe relates to repairs, maintenance and rehabilitation of concrete structures.<sup>1</sup> Very important criteria for a construction design are the intended purpose, the location and, especially, the environmental conditions which may affect it.

Durability is defined as resistance to weather, chemical attack, abrasion and other degradation processes.<sup>2</sup> With a correct construction design, its execution and subsequent treatment, the durability of the material can be much longer than the expected life cycle. The requirement for durability of building materials (including concrete) is now included in the CPR (Construction Products Regulation).<sup>3</sup>

Concrete durability can also be visualised according to Sommerville (**Figure 1**)<sup>4</sup>. Curve 1 in **Figure 1** shows

the minimum reduction in quality over time. The most frequently occurring progression of concrete durability is shown by curve 2 where there is an apparent deterioration over time but, thanks to repairs and maintenance, its quality can be remedied. The third curve characterises the concretes that are rarely used for building and it is clear that over time there can be a significant loss in their durability. In order to prevent a large durability reduction over time, it would be advisable to perform continuous monitoring of a construction, especially in terms of its maintenance and in some cases also during the construction. Unfortunately, this is not always possible and, therefore, a random quality assessment of concrete constructions is the only performable method today.<sup>1</sup>

The most important aspects influencing concrete deterioration are, for instance, seasonal temperature variations, cyclic freezing and thawing, precipitation, changes in relative humidity and pollutant concentrations in the atmosphere or in water. Generally speaking, contact with water is the main cause of concrete degradation. Water permeation into concrete is the key parameter influencing the degree of damage to concrete and it can be said, therefore, that in general terms the permeability

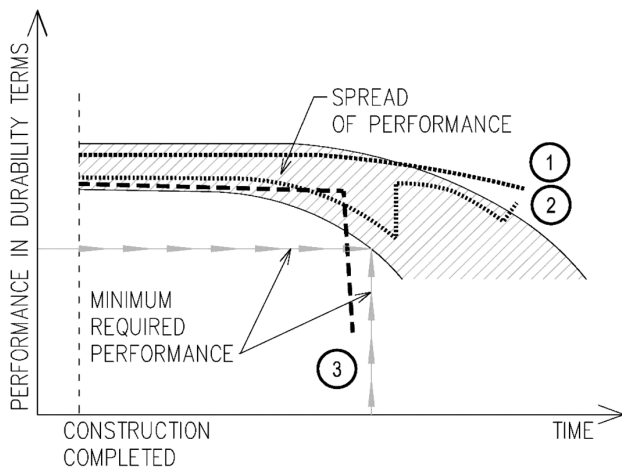


**Figure 1:** Loss of durability with time<sup>4</sup>  
**Slika 1:** Zmanjšanje zdržljivosti s časom<sup>4</sup>

of the concrete cover can be considered as the measure of its durability. The thickness of the concrete cover can be defined as 40–60 mm from the surface of the structure. This layer can be the one covering the reinforcement in the case of a steel-reinforced structure.

Given that water is being constantly transported as a liquid and steam, the speed of its permeation into the inner structure of the concrete is dependent on the physical structure of the cement paste. There is a large number of mechanisms having a damaging effect on concrete and they can be described, e.g., by means of a holistic diagram presented in **Figure 2**.<sup>1</sup>

For a determination of concrete durability (the concrete-cover quality) numerous standardised and non-standardised testing methods are used throughout Europe. These methods are mainly based on determining the permeability of the concrete-surface layer to those liquids and gasses that have substantial influences on the state of a reinforced concrete structure or a structural element.

Concrete-cover quality is closely connected with the internal structure and porosity of a material. Most of the commonly used methods are non-destructive or semi-destructive and on their basis it is possible to define the quality of a concrete cover but it is not possible to

precisely determine the internal structure of a concrete structure or a specimen as a whole. It was recently found that the use of computed tomography (CT) in the fields other than medicine is greatly beneficial. X-rays can be used for examining the specimens of virtually any material. Tomographic data enables us to display an internal structure at any level and, using appropriate software, to construct a 3D model of the object. The 3D model facilitates an easier visualisation of the distribution of detected defects within the shape of the object.

This paper describes in detail an experiment whose aim was to compare the results of the commonly used methods for determining the concrete-cover permeability to liquids and gasses (and thereon the dependent concrete durability) with the outcomes of a measurement performed with CT. The methodology and the advantages and disadvantages of the individual methods used are described in more detail in the following sections.

## 2 POSSIBILITIES OF DETERMINING PERMEABILITY OF CONCRETE COVER

One of the standardised methods for determining the permeability of the surface layer of concrete is the depth of penetration of water under pressure according to EN 12390-8.<sup>5</sup> The test is performed with cube-, cylinder- or prism-shaped specimens. The specimens submerged under water are tested at the age of 28 d when they are placed in a water-permeability apparatus so that they are loaded perpendicularly to the direction of compaction – the top face of a specimen is not tested. The specimens are exposed to water at a pressure of  $(500 \pm 50)$  kPa for  $(72 \pm 2)$  h. The specimens are split during the tensile splitting-strength test in order to reveal the maximum depth of the water penetration.

For the determination of the water permeability of concrete cover, a GWT (Germann Water Permeation Test) device is used. It is produced by the Danish company Germann Instruments and works on the principle of measuring the flow of water through a given area. The concrete-cover-permeability value can be obtained from the set water pressure and the volume of hardened cement paste within the overall volume of concrete. The

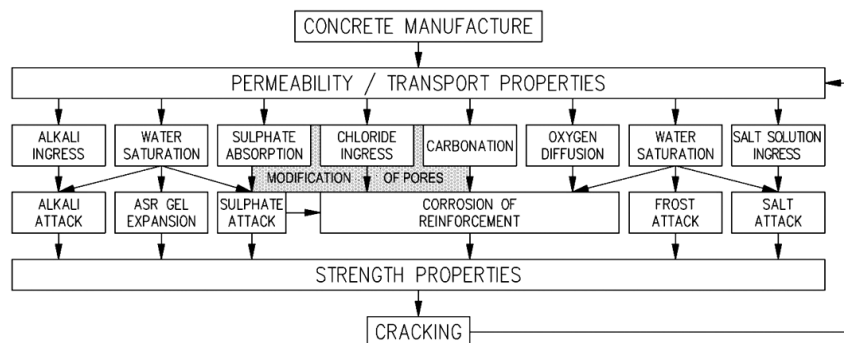


**Figure 2:** Causes of deterioration – physical-property interaction model  
**Slika 2:** Vzroki slabšanja – fizikalne lastnosti interakcijskega modela

measurement is affected by the inlet and outlet water pressure, its dynamic viscosity, density and acceleration due to gravity. The GWT measurement is performed by fixing a pressure chamber fitted with a gasket with freshly applied silicone sealant, securing it onto the tested area with clamps and filling it with distilled water. After 5 min of wetting the concrete surface, the measuring itself is started. The chamber is pressurised to 0.2 bar. A micrometric gauge is used to determine the volume of the absorbed water and, simultaneously, the time is being measured. The measurement ends when the gauge is fully extended, i.e., to 20 mm.<sup>6</sup>

The values of the initial surface permeability can also be obtained using the initial surface absorption test (ISAT). This method was developed in Italy as a method for measuring the state of the surface structure of concrete and it is specified in the British standard BS 1881-208:1996.<sup>7</sup> It involves measuring the volume of water under pressure penetrating into a specimen through a given area. This area is defined by the area of an acrylic cap which is sealed onto the surface of a concrete composite.

The water volume is determined by measuring the flow rate of the water travelling through a capillary system of a known volume. A transparent reservoir is connected to the inlet and the cap's outlet is connected to a glass capillary. The capillary is fitted with a scale. Individual parts are connected with rubber tubes and the cap's inlet is fitted with a valve to regulate the water flow from the reservoir.

To achieve the necessary pressure of 0.02 bar, the capillary with the scale as well as the reservoir are placed 200 mm above the concrete surface. Upon filling the cap, the inlet is closed and the water-flow measurement starts. Readings are performed upon the first contact with water and then after (10, 30 and 60) min. The number of scale units after the initial 5 s of the measurement determines the preliminary quality class of the concrete cover and also the period after which the data is recorded during the measurement: 30 s, 1 min or 2 min.<sup>6</sup> The obtained data is then compared with the classification table of concrete-cover water absorption based on the ISAT values (**Table 1**).<sup>8</sup>

Gas permeability of the concrete cover of a cement composite can be determined using a Torrent permeability tester (TPT) produced by the Swiss company Proceq. The principle of the test is the measurement of the air flow into the inner chamber of the device. A vacuum pump creates a vacuum of 1000 mbar, after which the pump is switched off and the air flow through the concrete into the inner chamber is observed. The device measures and calculates the permeability coefficient  $k_T$ , the depth of penetration of the vacuum and the pressure after the pressure equalisation between the inner and the outer chamber of the vacuum cap.<sup>6</sup> The method is specified in the Swiss standard SN 505 262/1.<sup>9</sup> The moisture content of a specimen (structure) plays an important role

in assessing concrete covers and for this reason a determination of the current moisture is also performed.<sup>10</sup> The principle of the measurement using TPT lies in determining the quality of a tested surface according to **Table 2**.<sup>11</sup>

All the above mentioned methods are mostly performed in laboratories although the determination of water and air permeability using GWT, ISAT and TPT can also be carried out in situ.

**Table 1:** Classification of water absorption by concrete cover based on ISAT values<sup>8</sup>

**Tabela 1:** Razporeditev absorpcije vode v površinski plasti betona z uporabo ISAT-vrednosti<sup>8</sup>

| Concrete absorption | ISAT results ( $\text{mL m}^{-2} \text{s}^{-1}$ ) |           |           |           |
|---------------------|---------------------------------------------------|-----------|-----------|-----------|
|                     | time after starting the test                      |           |           |           |
|                     | 10 min                                            | 30 min    | 60 min    | 120 min   |
| high                | > 0.5                                             | > 0.35    | > 0.2     | > 0.15    |
| medium              | 0.25–0.5                                          | 0.17–0.35 | 0.10–0.20 | 0.07–0.15 |
| low                 | < 0.25                                            | < 0.17    | < 0.10    | < 0.07    |

**Table 2:** Classification of the quality of concrete cover based on TPT values<sup>11</sup>

**Tabela 2:** Razporeditev kvalitete površine betona z uporabo TPT-vrednosti<sup>11</sup>

| Quality of concrete cover | index | $k_T/(10^{-16} \text{ m}^2)$ |
|---------------------------|-------|------------------------------|
| very poor                 | 5     | > 10                         |
| poor                      | 4     | 1.0–10                       |
| medium                    | 3     | 0.1–1.0                      |
| good                      | 2     | 0.01–0.1                     |
| very good                 | 1     | < 0.01                       |

### 3 COMPUTED TOMOGRAPHY

X-ray computed tomography is a modern imaging method allowing a visualisation and analysis of objects. The advantage of this method is that it is a non-destructive method providing a display of the internal structure of a specimen in slices. The basic principle of the measurement using CT is shown in **Figure 3**. The specimen is secured onto a rotary stage between the X-ray source and the detector array. The device records X-ray images at a certain angle while rotating the specimen by 360°. Tomographic reconstruction uses these X-ray scans to generate images representing the slices through the object (the so-called tomographic slices). Microtomography ( $\mu\text{CT}$ ) is the name for the tomography with a voxel resolution down to several micrometers, scanning internal structures of three-dimensional objects with a high spatial resolution.<sup>12,13</sup>

$\mu\text{CT}$  finds use in a variety of fields where knowing the internal structure of a specimen of a heterogeneous material is a necessity for the evaluation of its properties and a comparison with the existing results.

The X-ray micro- and nanotomography laboratory established as a part of the Central European institute CEITEC has, at its disposal, a unique micrographic station GE Phoenix v|tome|x L 240 (with a voxel resolu-

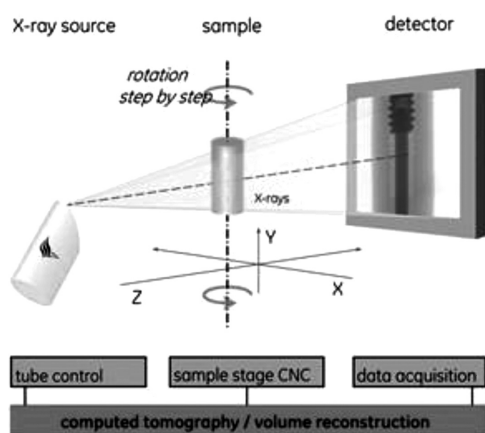


**Figure 3:** Diagram of the principle of scanning a specimen<sup>13</sup>  
**Slika 3:** Prikaz principa skeniranja vzorca<sup>13</sup>

tion of up to 5 μm for a 240 kV microfocus X-ray tube) shown in **Figure 4**, which has been in use since September 2012. For the analysis of X-ray images, the VGStudio MAX software, equipped with a module for a pore analysis is used.<sup>14</sup>

For most European methods evaluating the pore structure of a concrete composite, the overall air content and microscopic air content are decisive for the so-called  $A_{300}$  value, indicating the pores with a diameter of 0.3 mm (300 μm) and less.<sup>15</sup> Among all the above-mentioned methods, only CT allows us to determine the  $A_{300}$  value, the so-called effective air.<sup>16</sup>

#### 4 EXPERIMENT

The described experiment is focused on a comparison of the evaluations of the concrete-cover quality achieved with the commonly applied methods (GWT, ISAT, TPT) and the findings obtained with CT. The main effort of the experiment is to ascertain whether CT provides a sufficient predictive value when evaluating the quality of a concrete cover in comparison with the above-mentioned methods.



**Figure 4:** Microscope station GE Phoenix v|tome|x L 240<sup>16</sup>  
**Slika 4:** Mikroskopska postaja GE Phoenix v|tome|x L 240<sup>16</sup>

Four different mixtures were chosen for the testing. They were always three-part concrete, i.e., made of concrete without any additives and admixtures in order to observe the changes in the internal structure of the concrete due to the changes in the cement proportion. The individual mixtures differed in the water/cement ratio depending on how much the portion of the cement was increased while maintaining consistency S3 according to EN 206.<sup>17</sup> The mixture details are in **Table 3**. The components of the individual mixtures were identical, i.e., the same aggregates from the same locations, one type of cement from the same mill. Relevant properties of the components were checked against EN 196<sup>18</sup>, EN 933<sup>19</sup> and EN 1097<sup>20</sup>. **Table 3** shows that the values of the water/cement ratio decrease depending on the amount of cement in the mixture, where the cement dosage was increased by approximately 50 kg in each consecutive mixture.

At the age of 28 d the following specimens were tested:

- for the depth of penetration of water under pressure, 12 cubes with a size of 150 mm, designated with mixture-type codes R, 0/1, 0/2, 0/3 and numbers 1, 2, 3;
- using GWT, ISAT and TPT, a total of 12 specimens sized 300 mm × 300 mm × 150 mm, designated with mixture-type codes R, 0/1, 0/2, 0/3 and letters a, b, c;
- using the CT method, 4 samples were core drilled from the specimens used with the previous methods (GWT, ISAT and TPT); they were 50 mm in diameter and 60 mm in length; their dimensions were chosen on the basis of the requirement to check the surface layer of the concrete and the resolution settings of the software used.

**Table 3:** Compositions of the mixtures

**Tabela 3:** Sestava mešanic

| Component                               | Aggregates (kg) |                 |                  | Cement 42.5 R (kg) | Water (kg) | Water/cement ratio |
|-----------------------------------------|-----------------|-----------------|------------------|--------------------|------------|--------------------|
|                                         | 0–4 Bratčice    | 4–8 Olbramovice | 8–16 Olbramovice |                    |            |                    |
| Concrete mixture R – C12/15 X0 S3 D16   |                 |                 |                  |                    |            |                    |
| Concrete mixture                        | 953             | 173             | 675              | 248                | 201        | 0.75               |
| Concrete mixture 0/1 – C20/25 X0 S3 D16 |                 |                 |                  |                    |            |                    |
| Concrete mixture                        | 925             | 182             | 696              | 308                | 203        | 0.61               |
| Concrete mixture 0/2 – C30/37 X0 S3 D16 |                 |                 |                  |                    |            |                    |
| Concrete mixture                        | 889             | 174             | 693              | 357                | 201        | 0.53               |
| Concrete mixture 0/3 – C35/45 X0 S3 D16 |                 |                 |                  |                    |            |                    |
| Concrete mixture                        | 826             | 195             | 669              | 392                | 208        | 0.50               |

#### 5 RESULTS AND DISCUSSION

Mixture R exhibits the highest permeability as indicated by the average value of the depth of penetration of water under pressure – up to three times more than the



other mixtures. These results were expected for the given mixture design – its water/cement ratio was the highest (0.75) and it had the smallest amount of cement. Next, concretes 0/1 and 0/2 displayed lower values of the depth of penetration of water under pressure. Concrete mixture 0/3 had the lowest average value of the depth of penetration of water under pressure, which proved the tendency of the maximum depth of penetration to decrease in dependence of the increase in the amount of cement in the mixture (**Table 4** and **Figure 5**).

**Table 4:** Results of the depth of penetration of water under pressure  
**Tabela 4:** Rezultati globine penetracije vode pod tlakom

| Specimen | Depth of penetration (mm) | Average value of depth of penetration (mm) |
|----------|---------------------------|--------------------------------------------|
| R – 1    | 105                       | 102                                        |
| R – 2    | 90                        |                                            |
| R – 3    | 110                       |                                            |
| 0/1 – 1  | 30                        | 34                                         |
| 0/1 – 2  | 34                        |                                            |
| 0/1 – 3  | 38                        |                                            |
| 0/2 – 1  | 38                        | 35                                         |
| 0/2 – 2  | 29                        |                                            |
| 0/2 – 3  | 37                        |                                            |
| 0/3 – 1  | 31                        | 24                                         |
| 0/3 – 2  | 20                        |                                            |
| 0/3 – 3  | 22                        |                                            |

The evaluation of the results of GWT, ISAT and TPT revealed that the specimens made from mixture R (the cement content of 248 kg) had the lowest results for the water and air permeability. It is the mixture with the smallest portion of the cement and the highest water/cement ratio of 0.75.

Mixture 0/1 containing approximately 50 kg of cement more (the cement content of 308 kg) with the water/cement ratio of 0.61 displayed lower values of the concrete-cover permeability compared to mixture R. The

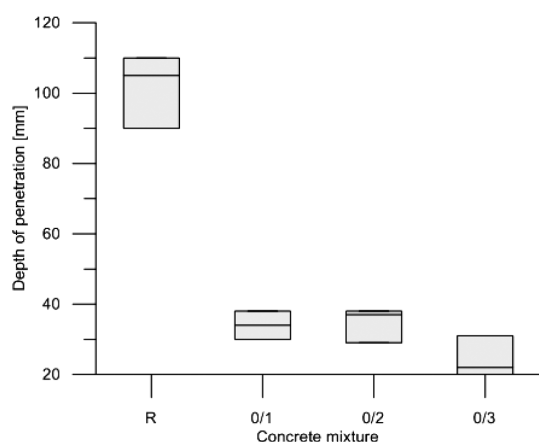


**Figure 5:** Dependence of average depth of penetration of water under pressure on mixture type

**Slika 5:** Odvisnost povprečne globine penetracije vode pod tlakom od vrste mešanice

quality improvement was proved with all the methods used.

Mixture 0/2 showed a slight increase in the concrete-cover quality compared to mixture 0/1. Mixture 0/2 has a higher cement content, again by approximately 50 kg (the cement content of 357 kg) compared to mixture 0/1 and a lower water/cement ratio of 0.53; however, the obtained values do not differ as significantly as in the cases of mixtures R and 0/1.

The last mixture, designated as 0/3, with the highest portion of the cement (the cement content of 392 kg) and the lowest water/cement ratio of 0.50 showed the best measurement results, reaching the values significantly lower than those for mixture 0/2.

The measurement results obtained with the GWT, ISAT and TPT methods (**Tables 5 to 7**) show an apparent tendency where the quality parameters of the water and air permeability improve as the cement content in the mixtures is increased while maintaining the same amount of water. The obtained results were presented in tables and afterwards corresponding graphs were created (**Figures 6 to 8**). For a better result interpretation it is necessary to take into account the number of performed measurements where the following numbers of tests were performed for each method:

- GWT – 6 measurements (two measurements were performed on each of the three specimens a, b, c);
- ISAT – 6 measurements (two measurements were performed on each of the three specimens a, b, c);

**Table 5:** GWT results

**Tabela 5:** Rezultati GWT

| Specimen | Permeability (mm/s) | Total average value (mm/s) |
|----------|---------------------|----------------------------|
| R – a    | 2.89E–03            | 3.66E–03                   |
|          | 3.47E–03            |                            |
| R – b    | 4.33E–03            |                            |
|          | 4.33E–03            |                            |
| R – c    | 3.47E–03            |                            |
|          | 3.47E–03            |                            |
| 0/1 – a  | 2.48E–03            | 1.90E–03                   |
|          | 1.58E–03            |                            |
| 0/1 – b  | 1.93E–03            |                            |
|          | 2.48E–03            |                            |
| 0/1 – c  | 1.24E–03            |                            |
|          | 1.73E–03            |                            |
| 0/2 – a  | 2.48E–03            | 1.79E–03                   |
|          | 1.33E–03            |                            |
| 0/2 – b  | 2.17E03             |                            |
|          | 1.58E–03            |                            |
| 0/2 – c  | 1.93E–03            |                            |
|          | 1.24E–03            |                            |
| 0/3 – a  | 3.10E–04            | 4.91E–04                   |
|          | 5.78E–04            |                            |
| 0/3 – b  | 4.81E–04            |                            |
|          | 4.56E–04            |                            |
| 0/3 – c  | 5.42E–04            |                            |
|          | 5.78E–04            |                            |

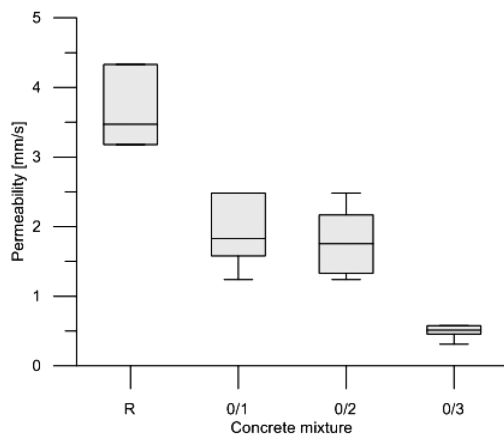


**Figure 6:** Dependency of permeability on mixture type using GWT  
**Slika 6:** Odvisnost prevodnosti od vrste mešanice, določene z GWT

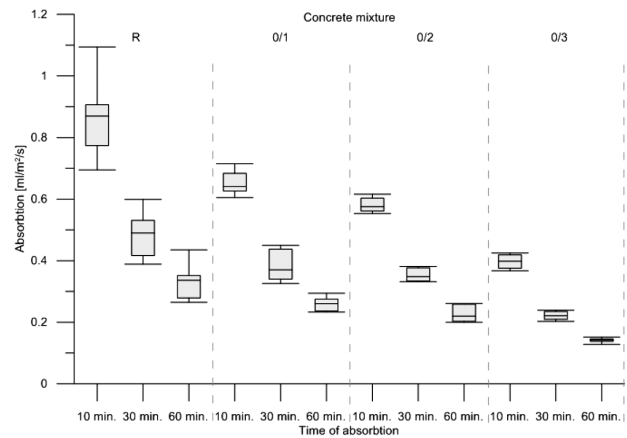


**Figure 7:** Dependency of permeability on mixture type using ISAT  
**Slika 7:** Odvisnost prepustnosti od vrste mešanice, določene z ISAT

- TPT – 9 measurements (three measurements were performed on each of the three specimens a, b, c).

Previous research revealed that the pores with a diameter of up to 300 μm present in a concrete cover are very advantageous since their size does not allow the appearance or development of microcracks which later cause concrete-cover degradation. Therefore, it is desirable, especially for the surface of steel-reinforced concrete, that the largest proportion of the pores includes the

ones of up to 300 μm. As far as this experiment is concerned, the information about the total air content and  $A_{300}$  can be determined from the data obtained using only μCT.

The requirements for the CT output data were the values of the total air content in the selected specimens and the volume of the pores of up to 300 μm in diameter – value  $A_{300}$ . Given the resolution, the bottom threshold for the pore diameter was set to 100 μm. The obtained

**Table 6:** ISAT results

**Tabela 6:** Rezultati ISAT

| Specimen | Permeability 10 min after the start of the test (mL/m <sup>2</sup> /s) |               | Absorption of concrete | Permeability 30 min after the start of the test (mL/m <sup>2</sup> /s) |               | Absorption of concrete | Permeability 60 min after the start of the test (mL/m <sup>2</sup> /s) |               | Absorption of concrete |
|----------|------------------------------------------------------------------------|---------------|------------------------|------------------------------------------------------------------------|---------------|------------------------|------------------------------------------------------------------------|---------------|------------------------|
|          | measured value                                                         | average value |                        | measured value                                                         | average value |                        | measured value                                                         | average value |                        |
| R – a    | 0.695                                                                  | 0.868         | high                   | 0.389                                                                  | 0.486         | high                   | 0.265                                                                  | 0.334         | high                   |
|          | 0.907                                                                  |               |                        | 0.500                                                                  |               |                        | 0.332                                                                  |               |                        |
| R – b    | 1.094                                                                  |               |                        | 0.599                                                                  |               |                        | 0.435                                                                  |               |                        |
|          | 0.846                                                                  |               |                        | 0.480                                                                  |               |                        | 0.340                                                                  |               |                        |
| R – c    | 0.774                                                                  |               |                        | 0.417                                                                  |               |                        | 0.279                                                                  |               |                        |
|          | 0.893                                                                  |               |                        | 0.531                                                                  |               |                        | 0.352                                                                  |               |                        |
| 0/1 – a  | 0.684                                                                  | 0.652         | high                   | 0.437                                                                  | 0.382         | high                   | 0.275                                                                  | 0.259         | high                   |
|          | 0.605                                                                  |               |                        | 0.326                                                                  |               |                        | 0.237                                                                  |               |                        |
| 0/1 – b  | 0.642                                                                  |               |                        | 0.375                                                                  |               |                        | 0.271                                                                  |               |                        |
|          | 0.626                                                                  |               |                        | 0.340                                                                  |               |                        | 0.233                                                                  |               |                        |
| 0/1 – c  | 0.640                                                                  |               |                        | 0.365                                                                  |               |                        | 0.249                                                                  |               |                        |
|          | 0.715                                                                  |               |                        | 0.450                                                                  |               |                        | 0.294                                                                  |               |                        |
| 0/2 – a  | 0.560                                                                  | 0.580         | high                   | 0.376                                                                  | 0.353         | high                   | 0.259                                                                  | 0.227         | high                   |
|          | 0.567                                                                  |               |                        | 0.380                                                                  |               |                        | 0.261                                                                  |               |                        |
| 0/2 – b  | 0.615                                                                  |               |                        | 0.352                                                                  |               |                        | 0.223                                                                  |               |                        |
|          | 0.603                                                                  |               |                        | 0.344                                                                  |               |                        | 0.200                                                                  |               |                        |
| 0/2 – c  | 0.553                                                                  |               |                        | 0.334                                                                  |               |                        | 0.217                                                                  |               |                        |
|          | 0.583                                                                  |               |                        | 0.332                                                                  |               |                        | 0.203                                                                  |               |                        |
| 0/3 – a  | 0.403                                                                  | 0.396         | medium                 | 0.213                                                                  | 0.221         | medium                 | 0.140                                                                  | 0.141         | medium                 |
|          | 0.425                                                                  |               |                        | 0.229                                                                  |               |                        | 0.146                                                                  |               |                        |
| 0/3 – b  | 0.367                                                                  |               |                        | 0.209                                                                  |               |                        | 0.138                                                                  |               |                        |
|          | 0.375                                                                  |               |                        | 0.203                                                                  |               |                        | 0.128                                                                  |               |                        |
| 0/3 – c  | 0.419                                                                  |               |                        | 0.235                                                                  |               |                        | 0.144                                                                  |               |                        |
|          | 0.393                                                                  |               |                        | 0.239                                                                  |               |                        | 0.152                                                                  |               |                        |

**Table 7: TPT results**  
**Tabela 7: Rezultati TPT**

| Specimen | Current mass humidity (%) | Value of $k_T$ for current humidity ( $10^{-16} \text{ m}^2$ ) | Value of $k_T$ for current humidity ( $10^{-16} \text{ m}^2$ ) | Correction value of $k_T$ for $w = 3 \%$ ( $10^{-16} \text{ m}^2$ ) | Correction value of $k_T$ for $w = 3 \%$ ( $10^{-16} \text{ m}^2$ ) | Quality of concrete cover for $w = 3 \%$ |
|----------|---------------------------|----------------------------------------------------------------|----------------------------------------------------------------|---------------------------------------------------------------------|---------------------------------------------------------------------|------------------------------------------|
|          | average value             | measured value                                                 | average value                                                  | average value                                                       | total average value                                                 |                                          |
| R – a    | 3.72                      | 1.587                                                          | 1.634                                                          | 1.896                                                               | 1.577                                                               | poor                                     |
|          |                           | 2.603                                                          |                                                                |                                                                     |                                                                     |                                          |
|          |                           | 0.712                                                          |                                                                |                                                                     |                                                                     |                                          |
| R – b    | 3.68                      | 1.562                                                          | 1.172                                                          | 1.226                                                               |                                                                     |                                          |
|          |                           | 1.583                                                          |                                                                |                                                                     |                                                                     |                                          |
|          |                           | 0.371                                                          |                                                                |                                                                     |                                                                     |                                          |
| R – c    | 3.75                      | 2.185                                                          | 1.437                                                          | 1.610                                                               |                                                                     |                                          |
|          |                           | 1.015                                                          |                                                                |                                                                     |                                                                     |                                          |
|          |                           | 1.110                                                          |                                                                |                                                                     |                                                                     |                                          |
| 0/1 – a  | 3.90                      | 0.031                                                          | 0.047                                                          | 0.149                                                               |                                                                     |                                          |
|          |                           | 0.047                                                          |                                                                |                                                                     |                                                                     |                                          |
|          |                           | 0.062                                                          |                                                                |                                                                     |                                                                     |                                          |
| 0/1 – b  | 4.10                      | 0.041                                                          | 0.041                                                          | 0.179                                                               |                                                                     |                                          |
|          |                           | 0.038                                                          |                                                                |                                                                     |                                                                     |                                          |
|          |                           | 0.044                                                          |                                                                |                                                                     |                                                                     |                                          |
| 0/1 – c  | 4.20                      | 0.072                                                          | 0.067                                                          | 0.262                                                               |                                                                     |                                          |
|          |                           | –                                                              |                                                                |                                                                     |                                                                     |                                          |
|          |                           | 0.062                                                          |                                                                |                                                                     |                                                                     |                                          |
| 0/2 – a  | 4.00                      | 0.038                                                          | 0.030                                                          | 0.130                                                               |                                                                     |                                          |
|          |                           | 0.027                                                          |                                                                |                                                                     |                                                                     |                                          |
|          |                           | 0.024                                                          |                                                                |                                                                     |                                                                     |                                          |
| 0/2 – b  | 3.90                      | 0.052                                                          | 0.052                                                          | 0.159                                                               |                                                                     |                                          |
|          |                           | 0.031                                                          |                                                                |                                                                     |                                                                     |                                          |
|          |                           | 0.073                                                          |                                                                |                                                                     |                                                                     |                                          |
| 0/2 – c  | 4.00                      | 0.054                                                          | 0.045                                                          | 0.165                                                               |                                                                     |                                          |
|          |                           | 0.047                                                          |                                                                |                                                                     |                                                                     |                                          |
|          |                           | 0.033                                                          |                                                                |                                                                     |                                                                     |                                          |
| 0/3 – a  | 4.22                      | 0.032                                                          | 0.023                                                          | 0.158                                                               |                                                                     |                                          |
|          |                           | 0.015                                                          |                                                                |                                                                     |                                                                     |                                          |
|          |                           | 0.021                                                          |                                                                |                                                                     |                                                                     |                                          |
| 0/3 – b  | 4.15                      | 0.022                                                          | 0.016                                                          | 0.117                                                               |                                                                     |                                          |
|          |                           | 0.012                                                          |                                                                |                                                                     |                                                                     |                                          |
|          |                           | 0.013                                                          |                                                                |                                                                     |                                                                     |                                          |
| 0/3 – c  | 4.05                      | 0.014                                                          | 0.015                                                          | 0.097                                                               |                                                                     |                                          |
|          |                           | 0.021                                                          |                                                                |                                                                     |                                                                     |                                          |
|          |                           | 0.011                                                          |                                                                |                                                                     |                                                                     |                                          |

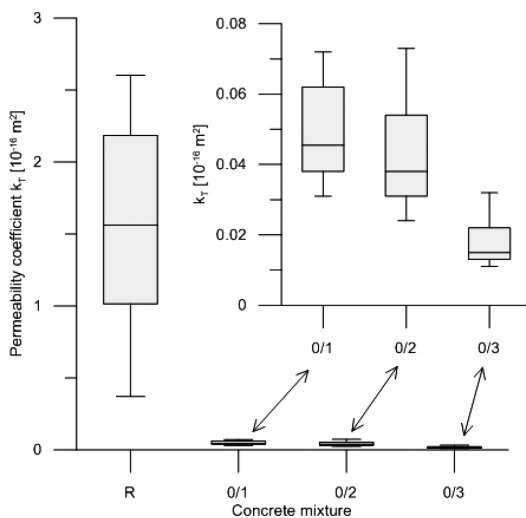


**Figure 8: Dependency of permeability on mixture type using TPT**  
**Slika 8: Odvisnost prepustnosti od vrste mešanice, določene s TPT**

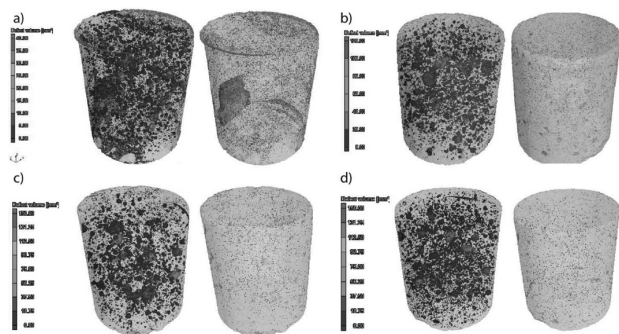
results are in **Table 8**. A great amount of the information was obtained mainly from 3D models (**Figure 9**), where, at the correct resolution settings, the pore distribution is clearly visible in the whole volumes of the specimens being scanned and only the pores of up to 300  $\mu\text{m}$  are indicated.

Only one sample with small dimensions, representing the whole mixture, was taken for CT scanning. For this reason, the test results may be distorted due to local defects.

Previous results<sup>21</sup>, where the effective-porosity value reached the average of 8 %, can be only partially compared with the results of this experiment. The reason for this is a different specimen size which determines the resolution settings of the scanner and the SW. Other factors influencing the evaluation of the experiment<sup>21</sup> include a different technology of the concrete production and a different composition of the concrete.

**Table 8:** CT results**Tabela 8:** Rezultati CT

| Concrete mixture | Pore diameter | Total volume of the specimen (mm <sup>3</sup> ) | Pore volume (mm <sup>3</sup> ) | Pore content (%) | Ratio for volume of pores < 300 µm (%) | Pore surface area (mm <sup>2</sup> ) | Ratio for pore surface area < 300 µm (%) |
|------------------|---------------|-------------------------------------------------|--------------------------------|------------------|----------------------------------------|--------------------------------------|------------------------------------------|
| R                | all           | 117388.26                                       | 2022.17                        | 1.69             | 2.74                                   | 23218.03                             | 14.86                                    |
|                  | below 300 µm  |                                                 | 55.40                          | 0.05             |                                        | 3449.69                              |                                          |
| 0/1              | all           | 118220.09                                       | 2226.60                        | 1.85             | 0.83                                   | 17407.05                             | 6.02                                     |
|                  | below 300 µm  |                                                 | 18.44                          | 0.02             |                                        | 1047.30                              |                                          |
| 0/2              | all           | 118296.94                                       | 2348.12                        | 1.95             | 0.71                                   | 15689.52                             | 6.14                                     |
|                  | below 300 µm  |                                                 | 16.67                          | 0.01             |                                        | 962.59                               |                                          |
| 0/3              | all           | 123547.70                                       | 2136.65                        | 1.70             | 0.86                                   | 19655.83                             | 5.02                                     |
|                  | below 300 µm  |                                                 | 18.46                          | 0.01             |                                        | 986.47                               |                                          |

**Figure 9:** 3D models of mixture specimens: a) R, b) 0/1, c) 0/2 and d) 0/3, left total air content, right pores up to 300 µm**Slika 9:** 3D-model vzorcev mešanice: a) R, b) 0/1, c) 0/2 in d) 0/3, levo: celotna vsebnost zraka, desno: pore do 300 µm

## 6 CONCLUSION

The experimental results proved that:

- the standardised methods (the depth of penetration of water under pressure, GWT, ISAT and TPT) appear to be well applicable for assessing the concrete-cover permeability. During the comparison of the test results of the individual methods, a tendency was observed, according to which a decrease in the concrete-cover permeability (an improvement in the concrete durability) is dependent on the amount of cement in the individual concrete mixtures;
- the evaluation of the concrete-cover permeability using the standardised methods (the depth of penetration of water under pressure, GWT, ISAT and TPT) does not correspond with the data obtained from the 3D model created by CT;
- an advantage of CT is a possibility of monitoring the internal structure of a composite material and detecting flaws or defects. Not only the pores, their diameter and distribution also influence the permeability of the surface layer of concrete and so do capillaries and microcracks. However, the results obtained with CT are very sensitive to the resolution settings of the device – with respect to the required pore-diameter range, it is necessary to adapt the specimen size used in a CT measurement. In order to

evaluate the experimental results with a greater precision, it is advisable to analyze a larger number of specimens from one sample of hardened concrete, which, given the financial requirements, is a subject for further experiments;

- on the basis of the measurement results obtained with CT, the method appears to be unsuitable for the evaluation of the permeability of the surface layer of concrete. The principle of the measurement using CT is useful for assessing concrete in other fields.<sup>22–28</sup>

## Acknowledgement

This paper was completed with the financial support of the Czech Science Foundation's project GA13-18870S and European Union's "Operational Programme Research and Development for Innovations", No. CZ.1.05/2.1.00/03.0097, as an activity of the regional Centre AdMaS "Advanced Materials, Structures and Technologies".

## 7 REFERENCES

- <sup>1</sup> A. E. Long, G. D. Henderson, F. R. Montgomery, Why assess the properties of near-surface concrete?, *Construction and Building Materials*, 15 (2001) 2–3, 65–79, doi:10.1016/S0950-0618(00)00056-8
- <sup>2</sup> B. Kucharczyková, Data for exercises of the subject BI03 – Diagnostic Methods in Civil Engineering, available from [www.szk.fce.vutbr.cz/](http://www.szk.fce.vutbr.cz/)
- <sup>3</sup> Regulation (EU) No 305/2011 of the European parliament, available from <http://eur-lex.europa.eu/LexUriServ/LexUriServ.do?uri=OJ:L:2011:088:0005:0043:EN:PDF>
- <sup>4</sup> G. Sommerville, The interdependence of research, durability and structural design, *Proceedings of a Symposium on Design Life of Buildings*, London, 1984, 233–250
- <sup>5</sup> EN 12390-8 Testing hardened concrete – Part 8: Depth of penetration of water under pressure, ÚNMZ, 2001
- <sup>6</sup> T. Vymazal, P. Bayer, P. Rovnaníková, Effect of water/cement ratio on permeability of surface layer of cement mortar for water and air, In: *Construction Materials*, Nitra 2013, 108–115
- <sup>7</sup> BS 1881: Part 5, *Methods of testing hardened concrete for other than strength*, BSI, 1996
- <sup>8</sup> R. Torrent, L. Fernandez Luco (Eds.), *Non-Destructive Evaluation of the Penetrability and Thickness of the Concrete Cover: State-of-the-Art Report of RILEM*, RILEM Publications S.A.R.L., 2007, 246

- <sup>9</sup> SN 505 262/1 Construction en béton – Spécifications complémentaires, Annexe E: Perméabilité à l'air dans les structures, NS, 2003
- <sup>10</sup> B. Kucharczyková, P. Misák, T. Vymazal, Determination and Evaluation of the Air Permeability Coefficient using Torrent Permeability Tester, *Russian Journal of Nondestructive Testing*, 46 (2010) 3, 226–233, doi:10.1134/S1061830910030113
- <sup>11</sup> J. Adánek, V. Juránková, O. Michalko, Monitoring of Sealing Technology Quality of Concrete by Determination of its Water and Gas Permeability, Proceedings of the 6th international workshop Strengthening and seal rocks and building structures in the early 21st century, Ostrava, 2001, 218–223
- <sup>12</sup> L. Hobst, P. Břelek, O. Anton, T. Zikmund, Monitoring of anomalous distribution of wires in the calibration samples of fiber concrete by computed tomography, *Beton TKS*, (2014) 3, 54–57
- <sup>13</sup> <http://blogs.sun.ac.za/ctscanner/introduction/>
- <sup>14</sup> T. Zikmund, M. Petrilak, J. Kaiser, X-ray computed tomography for casting analysis, defectoscopy and dimensional inspection, Proceedings of the Conference Testing and quality in construction, Brno, 2013, 429–438
- <sup>15</sup> EN 480-11 – Admixtures for concrete, mortar and grout – Test methods – Part 11: Determination of air void characteristics in hardened, ÚNMZ, 2006
- <sup>16</sup> <https://www.gemeasurement.com/>
- <sup>17</sup> EN 206 Concrete – Specification, performance, production and conformity, ÚNMZ, 2013
- <sup>18</sup> EN 196-6 Methods of testing cement – Part 6: Determination of fineness, ÚNMZ, 2010
- <sup>19</sup> EN 933 Tests for geometrical properties of aggregates, ÚNMZ, 2012
- <sup>20</sup> EN 1097 Tests for mechanical and physical properties of aggregates, ÚNMZ, 2011
- <sup>21</sup> É. Lublőy, L. G. Balázs, Potentials in use of X-ray computer tomography (CT) to study concrete, *Beton TKS*, (2013) 6, 43
- <sup>22</sup> K. Wan, Q. Xu, Local porosity distribution of cement paste characterized by X-ray micro-tomography, *Science China Technological Sciences*, 57 (2014) 5, 953–961, doi:10.1007/s11431-014-5513-5
- <sup>23</sup> D. Fukuda, M. Maruyama, Y. Nara, D. Hayashi, H. Ogawa, K. Kaneko, Observation of fracture sealing in high-strength and ultra-low-permeability concrete by micro-focus X-ray CT and SEM/EDX, *International Journal of Fracture*, 188 (2014) 2, 159–171, doi:10.1007/s10704-014-9952-6
- <sup>24</sup> S. Erdem, X-ray computed tomography and fractal analysis for the evaluation of segregation resistance, strength response and accelerated corrosion behaviour of self-compacting lightweight concrete, *Construction and Building Materials*, 61 (2014) 30, 10–17, doi:10.1016/j.conbuildmat.2014.02.070
- <sup>25</sup> T. Suzuki, H. Ogata, R. Takada, M. Aoki, M. Ohtsu, Use of acoustic emission and X-ray computed tomography for damage evaluation of freeze-thawed concrete, *Construction and Building Materials*, 24 (2010) 12, 2347–2352, doi:10.1016/j.conbuildmat.2010.05.005
- <sup>26</sup> A. C. Bordelon, J. R. Roesler, Spatial distribution of synthetic fibers in concrete with X-ray computed tomography, *Cement and Concrete Composites*, 53 (2014), 35–43, doi:10.1016/j.cemconcomp.2014.04.007
- <sup>27</sup> D. Braz, P. E. S. Almeida, L. M. G. Motta, R. C. Barroso, R. T. Lopes, Study of the concrete overlay (whitetopping) in paving using computed tomographic system, *Nuclear Instruments and Methods in Physics Research Section A: Accelerators, Spectrometers, Detectors and Associated Equipment*, 579 (2007) 1, 510–513, doi:10.1016/j.nima.2007.04.112
- <sup>28</sup> E. Gallucci, K. Scrivener, A. Groso, M. Stampanoni, G. Margaritondo, 3D experimental investigation of the microstructure of cement pastes using synchrotron X-ray microtomography ( $\mu$ CT), *Cement and Concrete Research*, 37 (2007) 3, 360–368, doi:10.1016/j.cemconres.2006.10.012



# PROPERTIES OF POLYMER-FILLED ALUMINIUM FOAMS UNDER MODERATE STRAIN-RATE LOADING CONDITIONS

## LASTNOSTI ALUMINIJEVIH PEN, NAPOLNJENIH S POLIMERNIMI MATERIALI, PRI ZMERNIH OBREMENITVAH

**Tomáš Doktor<sup>1,2</sup>, Petr Zlámal<sup>1</sup>, Tomáš Fíla<sup>1,2</sup>, Petr Koudelka<sup>1,2</sup>, Daniel Kytýř<sup>1</sup>,  
Ondřej Jiroušek<sup>2</sup>**

<sup>1</sup>Institute of Theoretical and Applied Mechanics, Academy of Sciences of the Czech Republic, Prosecká 76, 190 00 Prague, Czech Republic

<sup>2</sup>Czech Technical University in Prague, Faculty of Transportation Sciences, Konviktska 20, 110 00 Prague 1, Czech Republic  
doktor@itam.cas.cz

*Prejem rokopisa – received: 2014-08-15; sprejem za objavo – accepted for publication: 2014-09-26*

doi:10.17222/mit.2014.195

This paper deals with an experimental study of deformation response of open-cell aluminium foams under a moderate strain-rate compressive loading. Generally, porous metals show a promising potential in energy-absorption applications. However, the low strength of open-cell metal foams is a limiting parameter for such applications. Furthermore, the strain-rate sensitivity of mechanical properties is typically observed in closed-cell metal foams. On the other hand, open-cell foams provide a better control over the morphological parameters of a cellular structure. To enhance the properties of an open-cell microstructure an aluminium open-cell foam cured with polymeric filling was comparatively tested against the deformation-energy-absorption capabilities of the 'as-delivered' foam under a moderate strain-rate compressive loading. Prismatic samples with square cross-sections were prepared from the open-cell aluminium foam and a selected set of the samples was then filled with the thixotropic polyurethane putty. The specimens were tested with quasi-static compression, using a custom drop tower at several levels of the impact energy. The drop tests were instrumented with a tri-axial accelerometer and a high-speed camera to measure the mechanical response and the strain evolution during the impact. The comparison of the quasi-static behaviour with the results of the dynamic tests showed insignificant changes in the deformation curves in the case of the 'as-delivered' open-cell foam and an increasing energy-absorption capacity in the case of the samples equipped with the polymeric filling.

Keywords: interpenetrating-phase composite, compression, aluminium foam, polyurethane, moderate strain-rate loading

Članek opisuje eksperimentalno študijo o deformacijskem odzivu odprtoceličnih aluminijevih pen pri zmernih kompresijskih obremenitvah. Kovinske pene so obetajoč potencial pri absorpciji energije. Kljub temu manjša moč kovinske pene deluje omejujoče pri tovrstnih aplikacijah, obremenitvena občutljivost pa je pretežno opazovana pri zaprtoceličnih kovinskih penah. Po drugi strani pa odprtocelične pene omogočajo boljši nadzor nad morfološkimi parametri celične strukture. Da bi izboljšali lastnosti odprtoceličnih kovinskih pen, smo preizkusili polimerna polnila skupaj s peno. Primerjalna raziskava vzorcev odprtoceličnih aluminijevih pen je potekala v dveh skupinah: (i) 'kot dobavljeno' in (ii) polnjena s poliuretanskim polnilom. Iz odprtocelične aluminijeve pene smo pripravili romboedrske vzorce s kvadratnim prerezom. Druga skupina vzorcev je bila nato opremljena s tikstotropičnim poliuretanskim kitom. Vzorce smo preizkusili s kvazistatično kompresijo in z uporabo naključnega stolpa za padanje pri različnih stopnjah udarne energije. Preizkus padanja je bil omogočen s triosnim pospeševalnikom in kamero pri visoki hitrosti, ta pa je izmerila mehanski odziv razvoja obremenitve med udarcem. Primerjava kvazistatičnega vedenja z rezultati dinamičnega preizkusa je pokazala neznačilne spremembe deformacijskih krivulj v primeru odprtocelične pene, označene 'kot dobavljeno,' in povečano zmogljivost absorpcije energije v primeru vzorcev, ki so bili polnjeni s polimernim polnilom.

Ključne besede: kompozit z interpenetracijskimi fazami, stiskanje, aluminijeva pena, poliuretan, obremenjevanje z zmerno hitrostjo

## 1 INTRODUCTION

In the recent years, metal foams have been of renewed interest, particularly in the transport industry<sup>1</sup>. This interest led to an improvement in the production of metal foams that can be nowadays produced with many manufacturing techniques showing quite different results in the final product quality measured, e.g., the quality of the pore shape and size, the cell shape and wall thickness.

Structurally optimized cellular materials filled with a material sensitive to the strain rate<sup>2,3</sup> which form interpenetrating-phase composites (IPCs) have a broad range of applications ranging from lightweight crash-safe cars to structural protection against ballistic impact from projectiles or blast protection from explosives. The

influence of design parameters<sup>4,5</sup> (volume fraction of the polymeric filling, pore size, wall thickness or pore shape and connectivity) on the resulting material properties and energy-absorption capability still limits the applicability of this prospective material in various industries.

Dynamic impact response of IPCs is a key parameter in the applications of a material where shock resistance in impact loading is required. One of the experimental methods used to measure the energy absorbed in a material during impact loading is a drop test. This test, in which a dead weight is dropped onto a sample from predefined heights to load the sample with a predefined energy, is suitable for moderate strain rates depending on the drop height and weight of the impactor. The results of these tests are essential for the development of the

strain-rate-sensitive constitutive models for numerical modelling using, e.g., the finite-element (FE) method. A thorough validation of the material parameters of these constitutive models is required for a successful application of FE simulations in the later analysis, design and verification.

## 2 MATERIALS AND METHODS

### 2.1 Specimen preparation

In the experimental study an open-cell aluminium foam manufactured using the EN-AW-6101 aluminium alloy was tested. According to the data provided by the manufacturer of the foam the porosity reaches approximately 93 % with the pore size corresponding to  $6.3 \text{ cm}^{-1}$  (16 *ppi*, pores per inch). The cells are of a dodecahedral shape with the typical cell-edge thickness from 0.35 mm to 0.50 mm.

For a comparative study two groups of samples were prepared. Prismatic samples with dimensions of  $50 \text{ mm} \times 30 \text{ mm} \times 30 \text{ mm}$  were cut from the delivered slabs of the foam. One set of the samples was kept in the 'as-delivered' state while the second group was filled with one-component thixotropic polyurethane putty to form an IPC with the strain-rate-sensitive mechanical behaviour. A comparison between the plain aluminium foam and the filled structure is depicted in **Figure 1**.

In order to enable an optical strain evaluation one face of each sample was polished and sprayed using granite paint to create a random pattern for automatic displacement tracking.

### 2.2 Quasi-static tests

Quasi-static compression tests were performed in a custom uniaxial loading frame with a loading capacity of 2 kN. The loading tests were displacement driven and the

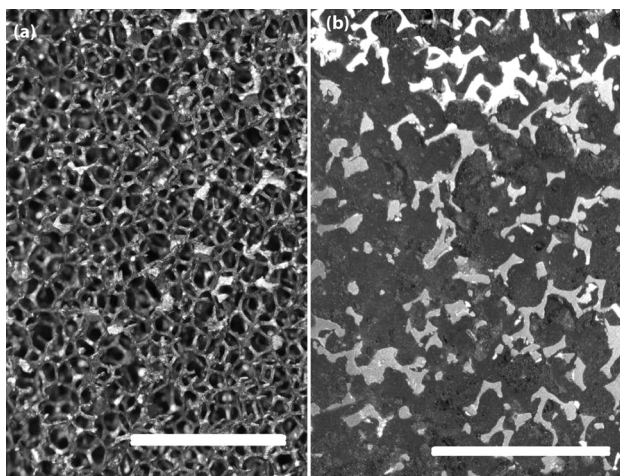


**Figure 1:** Open-cell aluminium foam: a) plain and b) filled with polyurethane. Scale bars correspond to 10 mm.

**Slika 1:** Odprtocelična aluminijeva pena: a) navadna in b) polnjena s poliuretanom. Dolžina črte ustreza 10 mm.

final displacement corresponded to a strain of 0.25–0.35. The loading rate set at  $20 \mu\text{m s}^{-1}$  corresponded to the strain rate of  $4 \cdot 10^{-4} \text{ s}^{-1}$ . Based on the results of the quasi-static compression, the amount of the absorbed energy was estimated in order to set an appropriate impact velocity for the low-energy impact tests. For the displacement tracking the loading scene was captured by a CCD camera (Manta G504B, Allied Vision Technologies, GmbH, Germany) attached to bi-telecentric lens (TCZR 072, Opto Engineering, Italy). A custom read-out software based on OpenCV library<sup>6</sup> was used for the image acquisition. The resolution of the acquired image data was  $2452 \text{ px} \times 2056 \text{ px}$  and the frame rate was  $2 \text{ s}^{-1}$  (frames per second, fps).

### 2.3 Low-energy impact tests

Low-energy compressive-impact tests were performed using our laboratory drop tower (**Figure 2**). Stress values were computed from the accelerograms acquired with a tri-axial accelerometer (EGCS3, Measurement Specialties, USA) connected to the read-out electronics (9234, National Instruments Corporation, USA) with a sampling rate of  $51.2 \cdot 10^3 \text{ s}^{-1}$ . The strain was measured optically using a high-speed CMOS camera (NX3, Integrated Design Tools, Inc., USA). The frame rate was  $4770 \text{ s}^{-1}$  and the resolution of the acquired images was  $536 \text{ px} \times 896 \text{ px}$ . The exposure time for the 'as-delivered' group and for the IPC specimens was  $49 \mu\text{s}$  and  $19 \mu\text{s}$ , respectively. A longer exposure time was required due to a higher diaphragm number, which enabled us to extend the depth of the field for the open cellular structure.

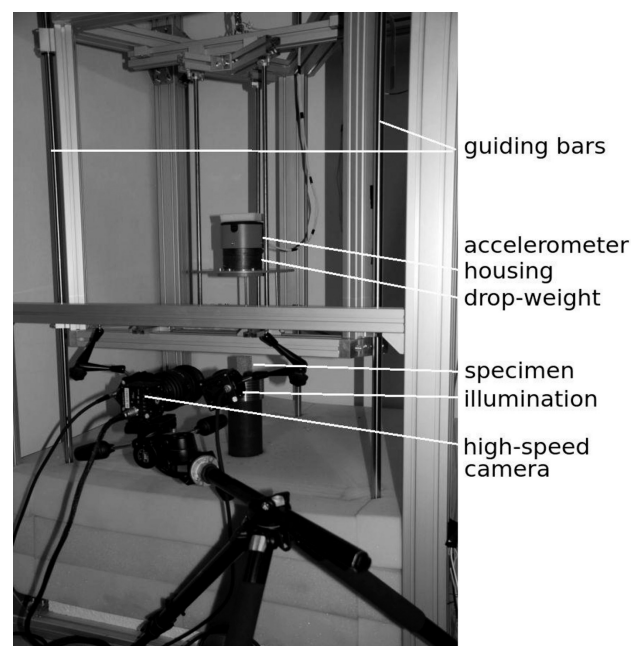


**Figure 2:** Drop tower and high-speed camera set-up

**Slika 2:** Nastavitev stolpa padanja in visokohitrostne kamere



For both the 'as delivered' and IPC specimens, the impact tests at three initial height levels were used: i) 600 mm and ii) 1000 mm. Additionally, the initial heights of iii) 1400 mm and iv) 1750 mm were used for the impact test of the filled specimen. The strain rates corresponding to the used hammer heights were (68.6, 88.6, 104.8 and 117.2)  $s^{-1}$ , respectively. The drop mass was 6504.57 g.

## 2.4 Strain measurement

For both the quasi-static compression and low-energy impact tests, an optical strain measurement was used. In the first image of the captured sequence tracking features were selected and arranged in two horizontal lines in the lower and upper parts of a specimen. Using a custom digital-image correlation software<sup>7</sup> based on the Lucas-Kanade tracking algorithm<sup>8</sup> displacement paths were tracked. During the tracking procedure the neighbourhood of each tracking feature is searched for the highest correlation coefficient in the subsequent image. From the tracked displacements the logarithmic strain was computed.

## 3 RESULTS AND DISCUSSION

From both the quasi-static and moderate strain-rate compression tests, stress-strain diagrams were obtained. The stress-strain curves are depicted in **Figure 3** (the plain open-cell foam) and **Figure 4** (the IPC). The stress-strain curves of the 'as-delivered' foam exhibit the deformation behaviour of a typical cellular metal. The initial linear elastic part is followed by a constant stress-plateau region caused by a collapse of the cell edges during the compression. Since the cell edges in the entire microstructure collapse gradually, the stress plateau exhibits an insignificant scatter. As expected, the

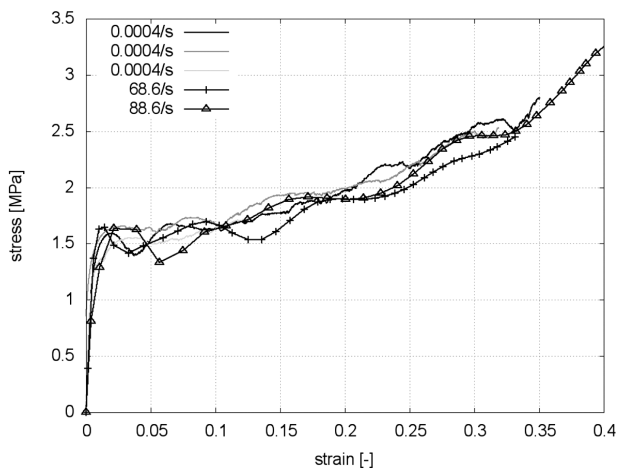


**Figure 3:** Stress-strain diagrams of open-cell aluminium foam – comparison of quasi-static and dynamic loading tests

**Slika 3:** Obremenitveni diagrami odprtocelične aluminijeve pene – primerjava kvazistatične obremenitve in dinamičnih preizkusov obremenitve

stress plateau is similar in both the quasi-static and dynamic loading.

The deformation curves for the IPC samples showed linear behaviour up to the stress level similar to the stress plateau of the plain foam, followed by an apparent deformation of the polymeric filling represented by a gradual increase in the stress in the compaction region. The amount of the deformation energy absorbed during the loading by the IPC samples increased in the non-zero strain-rate tests showing that such a material exhibits strain-rate-dependent mechanical characteristics.

From the stress-strain curves of the compression tests, the deformation energy absorbed in a sample was determined. To enable a comparison among all the groups of the specimens and levels of the strain rates, only the deformation curves up to 21 % were considered. The comparison is presented in **Table 1**.

**Table 1:** Comparison of absorbed deformation energies  
**Tabela 1:** Primerjava absorbirane energije deformacije

|                                   | Strain-energy density<br>( $J\ cm^{-3}$ ) |
|-----------------------------------|-------------------------------------------|
| Open-cell foam; quasi-static test | $0.339 \pm 0.014$                         |
| Open-cell foam; drop test         | $0.327 \pm 0.043$                         |
| IPC; quasi-static test            | $0.452 \pm 0.051$                         |
| IPC; drop test                    | $0.711 \pm 0.078$                         |

## 4 CONCLUSIONS

A comparative study on the strain-rate effects of the polymeric filling in an open-cell aluminium foam was performed. Deformation behaviour was assessed with quasi-static and moderate strain-rate compression tests. The results showed an increase in the absorbed impact energy in the case of the IPC, while the impact energy absorbed by the plain aluminium foam remains un-

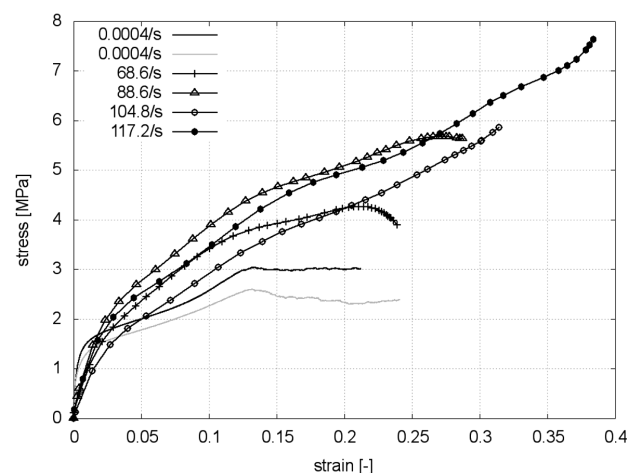


**Figure 4:** Stress-strain diagrams of open-cell aluminium foam filled with thixotropic polyurethane putty – comparison of quasi-static and dynamic loading tests

**Slika 4:** Obremenitveni diagrami odprtocelične aluminijeve pene, napolnjene s tiksotropičnim poliuretanskim kitom – primerjava kvazistatične obremenitve in dinamičnih preizkusov obremenitve

changed at the increasing strain rates. According to the comparison, the deformation energy absorbed by the IPC showed a 57 % increase at higher strain rates, while in case of the unfilled foam the deformation energy remained unchanged. We can conclude that to exploit the strain-rate-sensitive nature of the IPC, the density of the filling material should be optimized in order to improve its strength-to-mass ratio. In order to describe the strain-rate-dependent behaviour in a wider range of strain rates, the drop tower is not sufficient and a different technique, e.g., the Split-Hopkinson pressure bar should be employed in further investigations.

### Acknowledgements

The authors would like to express their gratitude to the Czech Science Foundation (research projects No. P105/12/0824 and 15-15480S). Institutional support of RVO: 68378297 is also gratefully acknowledged for the financial contribution to this research. We express special thanks to Dr. Jan Vyčichl who provided us with the base frame of the impact test device.

### 5 REFERENCES

- <sup>1</sup> J. Bahnhart, *Progress in Materials Science*, 46 (2001), 559–632, doi:10.1016/S0079-6425(00)00002-5
- <sup>2</sup> G. Subhash, Q. Liu, X. L. Gao, *International Journal of Impact Engineering*, 32 (2006), 1113–1126, doi:10.1016/j.ijimpeng.2004.11.006
- <sup>3</sup> M. C. Saha, H. Mahfuz, U. K. Chakravarty, M. Uddin, Md. E. Kabir, S. Jeelani, *Materials Science and Engineering A*, 406 (2005), 328–336, doi:10.1016/j.msea.2005.07.006
- <sup>4</sup> C. Periasamy, R. Jhaver, H. V. Tippur, *Materials Science and Engineering A*, 527 (2010), 2845–2856, doi:10.1016/j.msea.2010.01.066
- <sup>5</sup> C. Periasamy, H. V. Tippur, *Mechanics Research Communications*, 43 (2012), 57–65, doi:10.1016/j.mechrescom.2012.03.002
- <sup>6</sup> G. Bradski, *The OpenCV Library*, Dr. Dobb's Journal of Software Tools [online] (2000), article id 2236121, [posted 2008-01-15 19:21:54], Available from World Wide Web: <http://www.drdoobs.com/open-source/the-opencv-library/184404319>
- <sup>7</sup> I. Jandejsek, J. Valach, D. Vavrik, *Optimization and Calibration of Digital Image Correlation Method*, Proceedings of the 48<sup>th</sup> International Scientific Conference on Experimental Stress Analysis EAN 2010, Velke Losiny, Czech Republic, 2010, 121–126
- <sup>8</sup> B. D. Lucas, T. Kanade, *An Iterative Image Registration Technique with an Application to Stereo Vision*, Proceedings of Imaging Understanding Workshop, Vancouver, 1981, 121–130

# QUALITY OF THE STRUCTURE OF ASH BODIES BASED ON DIFFERENT TYPES OF ASH

## KVALITETA STRUKTURE TELESA IZ PEPELA NA OSNOVI RAZLIČNIH VRST PEPELA

Vit Cerny

Brno University of Technology, Faculty of Civil Engineering, Veveri 95, 602 00 Brno, Czech Republic  
cerny.v@fce.vutbr.cz

*Prejem rokopisa – received: 2014-08-21; sprejem za objavo – accepted for publication: 2014-09-25*

doi:10.17222/mit.2014.207

Artificial aggregates based on the self-firing process are often produced with an outdated technology without innovations and research. The knowledge of the production of ceramic materials is useful, but fly ash is quite a heterogeneous material influenced by the thermal processes occurring during the production; therefore, this problem has to be solved. The aim of the research work was to evaluate the influence of the character of fly ash on the formation, structure and properties of a sintered fly-ash body using laboratory firings. The main difference as regards the behavior is between the fly ash originating from high temperature and the one originating from fluidized-bed combustion. While the first type of ash contains mainly mullite and other high-temperature minerals, the fluidized-bed-combustion ash contains mainly anhydrite and free lime. These increase, for example, the manipulation strength of a fly-ash mix, but they also increase the amount of mixing water and weaken a sintered fly-ash body. The content of  $\text{Fe}_2\text{O}_3$  and its modifications and the proportion of  $\text{SiO}_2$  in the amorphous phase or mullite are important parameters for evaluating various types of high-temperature combustion fly ashes. The content of  $\text{Fe}_2\text{O}_3$  together with carbon finally works as a very effective fluxing agent. Thus, the surface of a specimen was sintered and the swelling was considerable due to the product gases of CO and  $\text{CO}_2$ . A higher proportion of  $\text{SiO}_2$  contained in the amorphous phase increases the strength and the quality of a fly-ash body. A higher proportion of  $\text{SiO}_2$  in the crystal phase requires a higher amount of heat for obtaining a solid structure.

Keywords: artificial aggregate, bottom ash, fly ash, FBC ash, sintering, clinkering

Umetna telesa, ki temeljijo na procesu zgorevanja, se pogosto izdelujejo po zaostali tehnologiji, brez inovacij in raziskav. Poznanje izdelave keramičnih materialov je koristno, vendar pa je letični pepel zelo heterogen material, na katerega vplivajo toplotni procesi med proizvodnjo, zato je ta problem potrebno rešiti. Namen te preiskave je bil oceniti vpliv značilnosti letičnega pepela na nastanek, strukturo in lastnosti teles iz sintranega letičnega pepela z laboratorijskim žganjem. Glavna razlika glede na vedenje je med letičim pepelom, ki izvira iz visokih temperatur in tistim, ki izvira iz zgorevanja v zvrtničeni plasti. Medtem ko prva vrsta pepela vsebuje pretežno mulit in druge visokotemperaturne minerale, vsebuje pepel iz zgorevanja v zvrtničeni plasti predvsem anhidrit in prosto apno. To na primer poveča manipulacijsko trdnost mešanice letičnega pepela, vendar poveča tudi količino mešalne vode in oslabi telo iz sintranega letičnega pepela. Vsebnost  $\text{Fe}_2\text{O}_3$  in njegovih modifikacij ter razmerja  $\text{SiO}_2$  v amorfnih fazi ali mulitu sta pomembna parametra pri oceni različnih vrst visokotemperaturnih letičih pepelov. Vsebnost  $\text{Fe}_2\text{O}_3$  skupaj z ogljikom deluje kot zelo učinkovito talilo. Površina vzorcev je bila sintrana in pojavilo se je občutno nabrekanje zaradi nastajanja plinov CO in  $\text{CO}_2$ . Večji delež vsebnosti  $\text{SiO}_2$  v amorfnih fazi je povečala trdnost in kvaliteto telesa iz letičnega pepela. Večja vsebnost  $\text{SiO}_2$  v kristalni fazi povzroča potrebo po večji količini toplote za pridobivanje trdne strukture.

Ključne besede: umetno telo, pepel, letični pepel, FBC-pepel, sintranje, negorljiv ostanek

## 1 INTRODUCTION

Even after its previous treatment, a big part of the produced fly ash is still stored at a storing place and the cost for its liquidation is still considerable.<sup>1</sup> Generally, the volume of suitable fly-ash types produced in our country highly exceeds the possibilities of its processing in the building industry.<sup>2</sup>

In the first period of realisation our building industry is able to use suitably sintered artificial aggregates in the volume of  $300\text{--}400 \cdot 10^3 \text{ m}^3$  annually.<sup>3</sup> After its application has been generally accepted in the building industry this volume may continually increase. A former experience confirmed this expectation when the complete production of the Dětmárovice agglomeration factory (the Corson technology) was troublefree and used mostly in the North Moravia region. Considering

the limited knowledge in this field, the operation and optimisation of this technology were very expensive and fly ash found its place in the traditional technologies of concrete production.<sup>4-6</sup>

The European and global trends in the new-technology development in the building industry require a production of high-quality light artificial aggregates, and its operation is increasing in the advanced countries.<sup>7,8</sup>

In Central and Eastern Europe, only Poland reacted to this trend by constructing a factory for the artificial-aggregate production using the sintered fly ash in Gdansk. The factory is equipped with licensed process equipment from Lytag, UK. However, the technology of this production process is even older than the Corson technology.<sup>9</sup>

The production technology for obtaining artificial aggregates by burning frequently uses the original format

of high-quality black-coal fly ash containing the optimum amount of unburned residues, burned with an external heat source and without the necessary correction of the fuel or the aggregate. Globally, there is no competition within this field and thus the involved companies do not commit to development and innovations. On that ground the procedures of obtaining artificial aggregates from sintered fly ash are relatively poorly explored and only a minimum scientific work is dedicated to the process of producing fly-ash bodies by burning. Therefore, if we consider the possibility of restoring the production in inland conditions it is necessary not only to innovate the existing technology but also, in particular, to commit to the study of reaction processes in the solid phase and the creation of fly-ash aggregates.

## 2 EXPERIMENTAL WORK

At the beginning the experimental activity was focused on the characterization of the selected types of ashes, representing the current production plants of the Czech Republic. We selected five samples of fly ashes obtained with the combustion of coal at temperatures of 1200–1600 °C, with its desulphurization taking place after the separation by means of a lime solution. We had one sample of black-coal fly ash (FFA), three samples of brown-coal fly ashes from the silos of three different power plants (FA1, FA2, FA3s) and one sample of a finer fly ash (2nd electrostatic separator) from the third plant (FA3f). There were also two samples from a power plant with the fluidized-bed combustion (FBC) of brown coal. This type of combustion takes place at the temperatures of around 850 °C and desulphurization is carried out in the furnace. One sample was from the electrostatic separator (FBC FA) and one from the bottom of the furnace (FBC BA).

The following physico-mechanical and physico-chemical parameters were selected: the loss on ignition (ČSN 72 0103) showing unburned residues, the bulk density (ČSN 72 2071), the specific surface area and remains on the sieve of 0.090 mm (CSN 72 2072-6). The chemical and mineralogical analyses were also carried out.

In order to monitor the behavior of the samples during the firing process, a special type of annealing microscopy was chosen. Cylinders of 3 mm in cross-section were made. They were placed into an annealing chamber equipped with a camera and backlight to capture the changes in the sample cross-sections during the annealing (10 °C/min, max. 1600 °C). The current temperature and the changes to the sample cross-sectional areas were primarily recorded.

The influence of fly ash on the physico-mechanical properties of a fired ceramic body was determined on the samples fired in a muffle kiln. Fly ash was mixed with water to reach the limit of fluidity. We made samples with the size of 20 mm × 20 mm × 100 mm that were, next day, dried at 60 °C for 2 h and then fired in the muffle kiln. The firing was characterized by the initial temperature of 25 °C, a rate of firing the muffle kiln of 300 °C/h and an isothermal dwell time at 1150 °C of 10 min. After the firing and natural cooling down, the specimens were taken out of the kiln and placed in a desiccator. After a thermal stabilization, their volume weight (ČSN EN 1015-10 and ČSN EN 1015-6), the compressive strength (ČSN EN 14617-15) and the water-absorbing capacity (ČSN EN 1097-6) were determined.

## 3 RESULTS AND DISCUSSION

First of all there are the results characterizing the ashes tested. In **Table 1** you can see the results determining the physico-mechanical and physico-chemical parameters and the results of the chemical analysis.

The analysis of the unburned residues of the tested fly ash shows that apart from fly ash FFA, all the samples fulfill the requirements of the standard (CSN 72 2072-6, 2013) for the maximum loss on ignition of 15 %. Therefore, this fly ash was used as the fuel (FuelFlyAsh) in this work. The determination of the bulk density shows that the fly ash from high-temperature combustion reaches higher values than the fly ash from fluidized-bed combustion. All the values of the high-temperature fly-ash samples and the bottom ash fulfill the requirements of the standard (CSN 72 2072-6, 2013) for the minimum value of 800 kg m<sup>-3</sup>. The low values of the bulk density of samples FFA and FBC show a porous structure of the coal grains.

**Table 1:** Physico-mechanical and physico-chemical parameters of the tested ashes  
**Tabela 1:** Fizikalno-mehanski in fizikalno-kemijski parametri preizkušanih pepelov

|       | Loss on ignition | Bulk density | Specific surface | Remains on the sieve, 0.090 mm | Chemical composition (%) |                    |                                 |            |                  |
|-------|------------------|--------------|------------------|--------------------------------|--------------------------|--------------------|---------------------------------|------------|------------------|
|       |                  |              |                  |                                | %                        | kg m <sup>-3</sup> | m <sup>2</sup> kg <sup>-1</sup> | %          | SiO <sub>2</sub> |
| FA1   | 1.19             | 990          | 329              | 37                             | 47.7                     | 28.2               | 5.6                             | 0.1        | 1.1              |
| FA2   | 1.07             | 1110         | 299              | 33                             | <b>54.6</b>              | 29.5               | 5.5                             | 0.1        | 1.8              |
| FA3s  | 2.39             | 1010         | 234              | 51                             | 50.0                     | 23.4               | <b>14.5</b>                     | 0.3        | 3.4              |
| FA3f  | 1.97             | 940          | 262              | <b>9</b>                       | 48.3                     | 22.8               | <b>16.6</b>                     | 0.5        | 3.7              |
| FFA   | <b>27.12</b>     | <b>830</b>   | 398              | 33                             | 36.0                     | 16.4               | 8.9                             | 0.4        | 5.0              |
| FBCFA | 2.08             | <b>810</b>   | 353              | 32                             | 42.7                     | 26.8               | 5.1                             | <b>3.0</b> | <b>10.2</b>      |
| FBCBA | 4.23             | 1210         | <b>33</b>        | <b>88</b>                      | 42.3                     | 26.7               | 5.2                             | <b>3.1</b> | <b>10.3</b>      |

**Table 2:** Results of the mineralogical analysis of the tested ashes**Tabela 2:** Rezultati mineraloških analiz preizkušanih pepelov

|                    | Quartz<br>SiO <sub>2</sub> | Mullite<br>Al <sub>6</sub> Si <sub>2</sub> O <sub>13</sub> | Hematite<br>Fe <sub>2</sub> O <sub>3</sub> | Anortite<br>CaAl <sub>2</sub> Si <sub>2</sub> O <sub>8</sub> | Lime<br>CaO | Calcite<br>CaCO <sub>3</sub> | Anhydrite<br>CaSO <sub>4</sub> | Amorphous<br>phase |
|--------------------|----------------------------|------------------------------------------------------------|--------------------------------------------|--------------------------------------------------------------|-------------|------------------------------|--------------------------------|--------------------|
| Melting point (°C) | 1470                       | 1810                                                       | 1350                                       | 1550                                                         | 2613        | 825                          | 1400                           | –                  |
| FA1                | 7.0                        | <b>39.3</b>                                                | 1.2                                        | 2.7                                                          | –           | –                            | –                              | <b>39.5</b>        |
| FA2                | 7.8                        | <b>32.3</b>                                                | –                                          | –                                                            | –           | –                            | –                              | <b>58.1</b>        |
| FA3s               | 7.1                        | 18.2                                                       | <b>3.3</b>                                 | <b>8.7</b>                                                   | –           | –                            | –                              | 55.6               |
| FA3f               | 6.8                        | 17.3                                                       | <b>3.5</b>                                 | <b>8.5</b>                                                   | –           | –                            | –                              | 58.4               |
| FFA                | 13.0                       | 12.4                                                       | 2.0                                        | 4.2                                                          | 0.8         | 0.5                          | –                              | 57.5               |
| FBCFA              | 9.5                        | –                                                          | 3.3                                        | –                                                            | <b>3.2</b>  | <b>3.8</b>                   | <b>5.7</b>                     | 63.8               |
| FBCBA              | 8.8                        | –                                                          | 3.4                                        | –                                                            | <b>3.4</b>  | <b>3.6</b>                   | <b>5.9</b>                     | 58.9               |

In most cases, the specific surface corresponds to the results of the granulometry of fly ash. Higher values show a better quality of the reaction in the solid phase and the formation of a stronger structure of the aggregate.

The results of the chemical analysis show that high-temperature ashes usually achieve a higher content of SiO<sub>2</sub>. FA2 has the highest value. The FBC ash samples achieved higher contents of CaO and SO<sub>3</sub> as the sulphate sulphur. This helps us obtain higher strengths of fresh samples.

Because of the SO<sub>3</sub> exceeding limits (CSN 72 2072-6, max. 3 %) it will be necessary to install desulphurization of the production line in the future. The content of Fe<sub>2</sub>O<sub>3</sub> is an important parameter and it acts as a fluxing agent during the firing, enclosing the surface of an aggregate. Consequently, the fumes cannot leave freely and a reductive core is produced. The grains show a more considerable porosity under the surface.<sup>10</sup> This problem can be assumed during the production of the aggregate based on fly ash FA3.

As you can see in **Table 2**, FA1 has the highest percentage of mullite and a lower content of the amorphous phase in comparison with FA2. The mineralogical analysis further confirms that FA3 contains more minerals with a lower melting point and a low content of mullite. Fluidized-bed ashes have almost no content of mullite. The FBC ashes achieve higher contents of the minerals

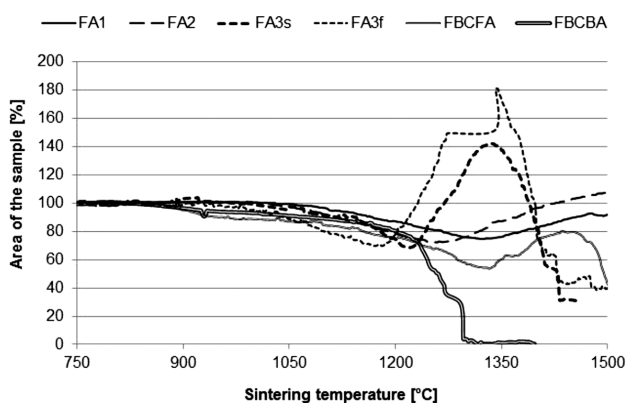


**Figure 1:** Changes to the sample cross-sectional area during annealing  
**Slika 1:** Spremembe prečnega prereza vzorcev med žarjenjem

based on CaO that shorten the sintering interval and decrease the melting point of the material.

In **Figure 1** you can see the results of the annealing microscopy. Specifically, there is a dependence of the area of the sample on the firing temperature. The samples are stable up to 1150 °C. The samples of fly ashes went through a certain sintering phase, followed by the swelling caused by the generated gases. Higher contents of Fe<sub>2</sub>O<sub>3</sub> in FA3s and FA3f, together with the carbon, cause a reduction in FeO, which then functions as a highly active flux.<sup>10</sup> This leads to the sintering of the sample surface and a subsequent significant swelling caused by the generated gases of CO and CO<sub>2</sub>. As you can see, the finer ash of FA3f achieves the highest swelling (180 %). This is one of the reasons why the rate of firing the muffle kiln of 300 °C/h was chosen. A higher firing rate can create samples with unsuitable shapes. At the melting point, the melting starts. The annealing of fluid fly ash is significantly affected by the presence of CaSO<sub>4</sub>, CaCO<sub>3</sub> or CaO alone. The first two minerals show their degradation during the firing and the subsequent percentage of CaO significantly lowers the melting point of the other minerals.

**Figure 2** shows the results of the shrinkage; **Figure 3** shows the compressive strength and **Figure 4** the water absorption of the fired samples.

The highest shrinkage was measured for the samples based on the FBC ashes, exhibiting a higher porosity,

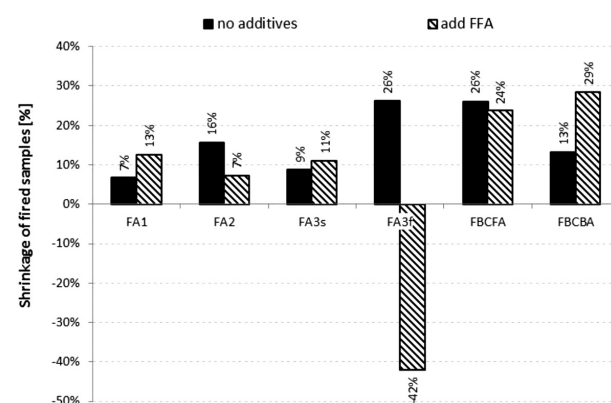


**Figure 2:** Shrinkage of the fired samples  
**Slika 2:** Skrčček žganih vzorcev

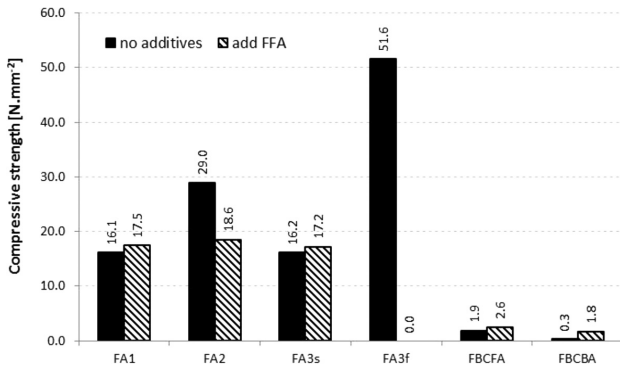


Figure 3: Compressive strength of the fired samples

Slika 3: Tlačna trdnost žganih vzorcev

and a decomposition of the CaO products caused a disintegration of the structure. This is the reason why a low compressive strength was also measured. An addition of high-temperature ash (FBC FA + 24 % FFA; FBC BA + 16 % FFA) increased the strength only on a small scale.

A high shrinkage was also measured for the sample based on FA3f, which had the highest content of the particles under 0.009 mm. Due to a higher content of Fe<sub>2</sub>O<sub>3</sub> the highest compressive strength was measured. The shrinkage and closed porosity caused a very low water absorption. The addition of FFA as a fuel caused a high swelling (negative values for the shrinkage) and the samples then were not useable for the measurement of the physico-mechanical parameters.

The fly ashes from the silo (FA1, FA2, FA3s) had stable structures and achieved a lower shrinkage. A higher content of the amorphous phase and a low content of mullite caused higher compressive strengths of the FA2 samples. An addition of FFA (27 %) in combination with FA2 caused a structural weakening.

As you can see in Figure 4 high-temperature ashes achieved lower values of water absorption in comparison with the FBC ashes.

In Figures 5 and 6 you can see the differences between the samples based on the fly ashes with lower and higher contents of Fe<sub>2</sub>O<sub>3</sub>. Figure 5 shows the closed

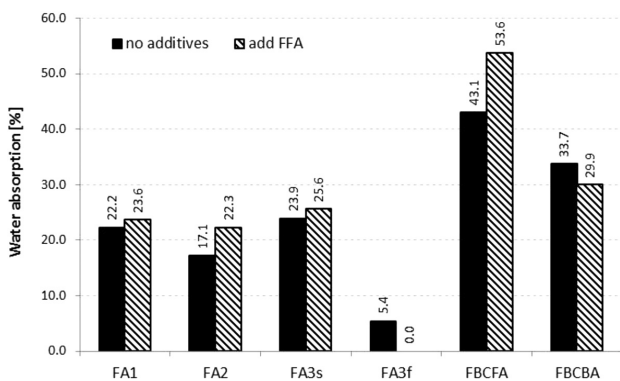


Figure 4: Water absorption of the fired samples

Slika 4: Absorpcija vode žganih vzorcev

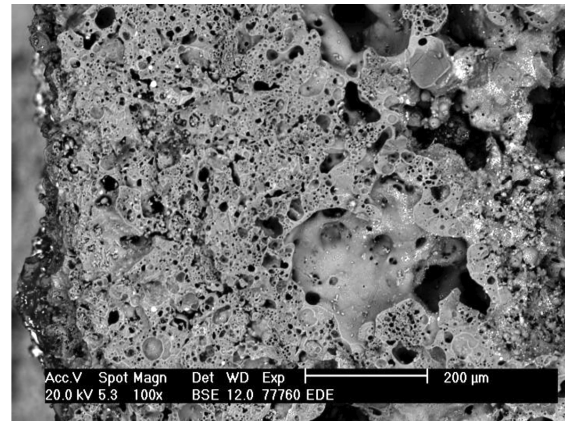


Figure 5: Closed structure of the FA2 sample

Slika 5: Zaprta struktura vzorca FA2

homogeneous structure of FA2 and Figure 6 shows the swollen core of the sample based on FA3s causing an enclosed surface.

#### 4 CONCLUSIONS

When assessing the suitability of fly ash, the main difference can be seen between the high-temperature fly ash and the FBC ash. The first type mainly contains high-temperature minerals like mullite. The FBC ashes mainly contain anhydrite and free lime, which increase the manipulation strength of fresh samples, but they also increase the amount of mixing water, weakening the sintered fly-ash body and creating open porosity. The FBC ashes are not very suitable for sintered aggregates.

When assessing the influence of the quality of high-temperature fly ash on the quality of an ash body, the main parameters are the loss on ignition, the remains on the sieve of 0.009 mm, the contents of SiO<sub>2</sub>, Fe<sub>2</sub>O<sub>3</sub>, quartz, mullite and the amorphous phase. The maximum loss on ignition is 8 %. Higher values classify the ash as a fuel. Finer ashes create more solid structures with small pores at lower temperatures. A higher content of SiO<sub>2</sub> in the amorphous phase ensures a higher strength.

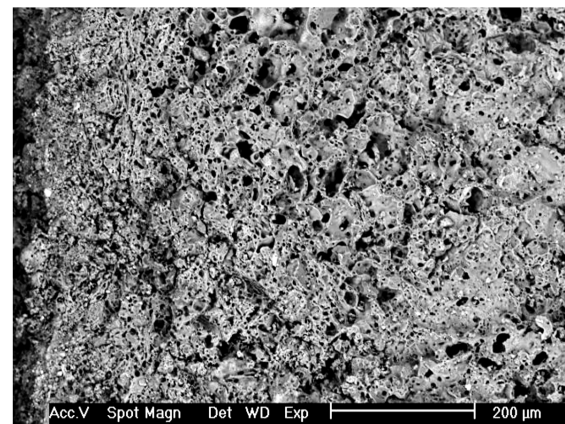


Figure 6: Swollen surface of the FA3s sample

Slika 6: Napihnjena površina vzorca FA3s

A higher content of mullite needs a higher temperature for creating a solid structure. The content of  $\text{Fe}_2\text{O}_3$  together with carbon finally works as a very effective fluxing agent. Thus, the surface of a specimen is sintered faster and the firing product gases of CO and  $\text{CO}_2$  can cause a considerable swelling.

Further work will focus on the influence of a faster temperature rise during the annealing microscopy on the area change and the impact of increasing the firing temperature to 1200 °C on the physico-mechanical parameters and mineralogical changes.

### Acknowledgements

The Czech Science Foundation Project P104-13-30753P "Study of the process of creating fly ash body" and the European Union's "Operational Programme Research and Development for Innovations", No. CZ.1.05/2.1.00/03.0097, as an activity of the regional Centre AdMaS, "Advanced Materials, Structures and Technologies", are gratefully acknowledged.

### 5 REFERENCES

- <sup>1</sup> Act on Waste No. 185/2001 Coll., as amended, Decrees of the Ministry of the Environment No. 376/2001 Coll. and 381/2001 Coll., 2001
- <sup>2</sup> R. Zárubová, Utilisation of coal combustion products from power and heat stations for remediation of open pit mines in the Czech Republic, Proc. of the 1st Symposium on flue gas desulphurization, 4th Symposium on ash, slag and waste landfills in power plants and mines, Palič, 2012, 246–250
- <sup>3</sup> P. Kulhankova, Secondary raw materials policy of the Czech Republic 2012–2030, Proc. of the Inter. Conf. Recycling 2012, Brno, 2012, 72–76
- <sup>4</sup> H. Al-Khaiat, N. Haque, Strength and durability of lightweight and normal weight concrete, Journal of Materials in Civil Engineering, 11 (1999), 231–235, doi:10.1061/(ASCE)0899-1561(1999)11:3(231)
- <sup>5</sup> O. Kayali, M. N. Haque, B. Zhu, Some characteristics of high strength fiber reinforced lightweight aggregate concrete, Cement and Concrete Composites, 25 (2003), 207–213, doi:10.1016/S0958-9465(02)00016-1
- <sup>6</sup> B. Yun, I. Ratiyah, P. A. M. Basheer, Properties of lightweight concrete manufactured with fly ash, furnace bottom ash, and Lytag, International Workshop on Sustainable Development and Concrete Technology, Beijing, 2004, 77–88
- <sup>7</sup> S. Slabaugh, Ch. Swan, R. Malloy, Development and properties of Foamed synthetic Lightweight Aggregates, World of Coal Ash Conference, Kentucky, 2007
- <sup>8</sup> H. Ecke, H. Sakanakura, T. Matsuto, N. Tanaka, A. Lagerkvist, State-of-the-art treatment processes for municipal solid waste incineration residues in Japan, Waste Manag. Res., 18 (2000), 41–51, doi:10.1034/j.1399-3070.2000.00097.x
- <sup>9</sup> A. Mueller, S. N. Sokolova, V. I. Vereshagin, Characteristics of lightweight aggregates from primary and recycled raw materials, Construction and Building Materials, 22 (2008), 703–712, doi:10.1016/j.conbuildmat.2007.06.009
- <sup>10</sup> R. Sokolar, Ceramics, Publishing house VUTIUM, Brno 2006 (in Czech)





## SINTERED BOARD MATERIALS BASED ON RECYCLED GLASS

### SINTRANI PLOŠČATI MATERIALI NA OSNOVI RECIKLIRANEGA STEKLA

**Tomáš Melichar, Jiří Bydžovský**

Brno University of Technology, Faculty of Civil Engineering, Institute of Technology of Building Materials and Components, Veveří 331/95,  
602 00 Brno, Czech Republic  
melichar.t@fce.vutbr.cz

*Prejem rokopisa – received: 2014-08-26; sprejem za objavo – accepted for publication: 2014-09-18*

doi:10.17222/mit.2014.213

Although there are relatively integrated systems and advanced technologies for the recycling of the products and the extraction of certain desirable chemical elements, thereby obtaining relatively high-quality glass, glass factories or other construction-material producers do not show interest in these shards or there is only a partial utilization of cullet. And cullet is the subject of the research presented in this article. The research was focused on the cullet utilisation for the production of glass-based sintered materials. By default, these materials are used as lining and paving elements. The batch was substituted with waste cullet. The study of the properties was focused on the physical and mechanical parameters, possible leaching of harmful elements and also the microstructures of the modified materials. It was found that despite the changes (defects and anomalies) in the microstructure, satisfying qualities of waste-glass-based sintered materials can be obtained.

Keywords: sintering process, waste, glass, parameters, microstructure

Čprav obstajajo relativno integrirani sistemi in napredne tehnologije za recikliranje proizvodov in ekstrakcijo zelenih kemijskih elementov, s čimer dobimo relativno visoko kvaliteto stekla, steklarne in proizvajalci drugih konstrukcijskih materialov ne kažejo zanimanja za te črepinje in se odpadno steklo uporablja samo delno. Odpadno steklo je predmet raziskav, prikazanih v tem članku. Raziskava je bila usmerjena v izdelavo sintranih materialov na osnovi stekla. Navadno se ti materiali uporabljajo kot elementi oblog in tlaka. Osnova je bila nadomeščena z razbitim steklom. Študija je bila namenjena fizikalnim in mehanskim parametrom, morebitnemu izločanju škodljivih elementov in tudi mikrostrukturi modificiranih materialov. Ugotovljeno je bilo, da je kljub spremembam (napake in anomalije) v mikrostrukturi mogoče dobiti zadovoljivo kvaliteto materiala sintranih proizvodov iz odpadnega stekla.

Ključne besede: proces sintranja, odpadki, steklo, parametri, mikrostruktura

## 1 INTRODUCTION

With respect to the glass-production process or the products made from glass, the emphasis is placed, among other features, on their "visual" properties. Considering this fact, recycled glass cannot always be fully applied but only in limited amounts (coloured and clear glass, flat glass from demolitions, car wrecks, etc.). However, some types of recycled glass are not desirable at all for glass works. Here we can mention electrotechnical products like fluorescent tubes, lamps, car lights, etc. Quite a big volume of glass waste is also generated by dismantling old TV sets and monitors. These are older types of CRT screens (cathode-ray tube) which have been replaced by LCD monitors. The characterisation of the waste CRT glass is dealt with, for instance, by the authors of study.<sup>1</sup> In developed countries the majority of older screen types was replaced. However, in developing countries the transition to the LCD technology is not as strong as in the developed world.

The production of glass-based sintered linings (sometimes also called glass silicates or, not quite correctly, glass-crystalline materials) provides a possibility for the utilisation of recycled glass. They are the materials produced by heat treating the cullet with final additions

of admixtures modifying their properties. Sintered-glass-based boards can be used as lining and paving elements in the interior and exterior as well. Thanks to a specifically developed thermal regime, a characteristic texture is obtained during cullet sintering which can result in crystalline materials like stone facings. A high price is the only disadvantage of such elements. Utilisation of recycled glass would result in a welcome price reduction for these elements. Also, a positive impact on the waste management issues, in particular "a relief" for the environment, can also be considered as a positive influence.

There are no relevant researches on the recycled-glass-based sintered boards with a characteristic texture. The studies and papers most closely related to this topic deal with foam glass<sup>2</sup> or glass ceramic.<sup>3</sup> However, these are only related materials. In the technical literature it was found that glass properties should not be notably changed by sintering. Nevertheless, this applies provided a perfect sintering occurs, i.e., without the presence of foreign particles, cracks, pores, cavities, etc. In this respect, very interesting and beneficial outputs are presented in<sup>4-9</sup>.

## 2 METHODOLOGY OF EXPERIMENTAL WORK

As the initial reference, a batch consisting only of the cullet of sodium borosilicate glass with the size of 6 mm was used. This type of glass cullet is used by a Czech producer of sintered boards, R.D.S.–CZ s.r.o. The initial point for the sintering mode was formed with the information provided by the above producer; however, the thermal curve had to be significantly corrected and modified. In addition to the other factors, the differences between the parameters applied in the common production and laboratory furnace aggregates were the reasons for the modification. The modified batch composition consisted of the substitutes for the primary raw materials, involving the following alternative raw materials:

- CRT (cathode-ray tube) glass – face plates with a fraction of 0–16 mm (marked as CRS 0-16),
- CRT glass – a funnel with a fraction of 0–32 mm (marked as CRN 0-32),
- container glass – coloured, with fractions of 0–4 mm and 0–32 mm (marked as COC 0-4, COC 0-32),
- container glass– clear, with a fraction of 0–16 mm (COT 0-16).

With regard to determining different compositions, the temperature in the field of the maximum isothermal dwell time is also included (in the graphic charts and evaluations). At first, i.e., immediately after taking the silicate samples out of the furnaces and cooling them down to the standard laboratory temperature (approximately 20 °C) their texture, or structure, characteristic for the sintered glass boards were evaluated. As required, the characteristic texture was a matrix structure where a separation of the grains was clear (generally bigger than

1–2 mm, because the smaller ones usually melt), with the minimum small-sized pores (approximately within 0.5 mm) and without any spaces. On the basis of this procedure, temperature intervals of the maximum isothermal dwell time were selected. These were used for the production of four sets of specimens, to which the following analyses and settings were applied. The temperature intervals were set with respect to the character of a given raw material and its granulometric composition, for example, with the batch consisting of screen cullet the temperature interval was within a shorter range than in the case of flat glass. Glass sintered boards are commonly used mainly as facings and pavings and, on that ground, the setting of their mechanical and chemical parameters was done mainly in compliance with the set of standards ČSN EN ISO 10545-XX, in particular<sup>10–13</sup>. The examination of the microstructure was carried out using scanning electron microscopy (SEM). The attention was mainly paid to the anomalies and defects in the matrices of the newly produced materials based on recycled cullet.

## 3 RESULTS

In the following table and graphs there are results for both the used raw materials and the newly designed ones. **Table 1** gives the chemical composition of the cullet.

**Table 1:** Chemical compositions of the glass shards used  
**Tabela 1:** Kemijska sestava uporabljenih steklenih črepinj

| Component                      | Shards – content of the component (%) |       |       |       |       |
|--------------------------------|---------------------------------------|-------|-------|-------|-------|
|                                | REF                                   | CRS   | CRN   | COT   | COC   |
| SiO <sub>2</sub>               | 71.97                                 | 60.23 | 51.61 | 71.29 | 69.69 |
| Al <sub>2</sub> O <sub>3</sub> | 7.03                                  | 2.15  | 3.23  | 0.56  | 1.77  |
| Fe <sub>2</sub> O <sub>3</sub> | –                                     | 0.12  | 0.12  | 0.18  | 0.43  |
| BaO                            | 1.96                                  | 9.63  | 1.61  | 0.07  | 0.32  |
| CaO                            | 1.04                                  | 1.44  | 3.54  | 8.72  | 9.38  |
| B <sub>2</sub> O <sub>3</sub>  | 9.94                                  | –     | –     | –     | –     |
| MgO                            | –                                     | 0.26  | 2.21  | 4.33  | 2.30  |
| Na <sub>2</sub> O              | 6.11                                  | 7.47  | 6.26  | 12.75 | 12.14 |
| K <sub>2</sub> O               | 1.94                                  | 7.18  | 7.15  | 0.37  | 0.92  |
| PbO                            | –                                     | 1.59  | 18.99 | –     | –     |
| SrO                            | –                                     | 6.19  | 0.86  | –     | –     |
| Cr <sub>2</sub> O <sub>3</sub> | –                                     | –     | –     | –     | 0.068 |
| ZrO <sub>2</sub>               | –                                     | –     | –     | –     | 0.035 |
| Ann. loss                      | –                                     | 0.02  | 0.01  | 1.24  | 0.92  |

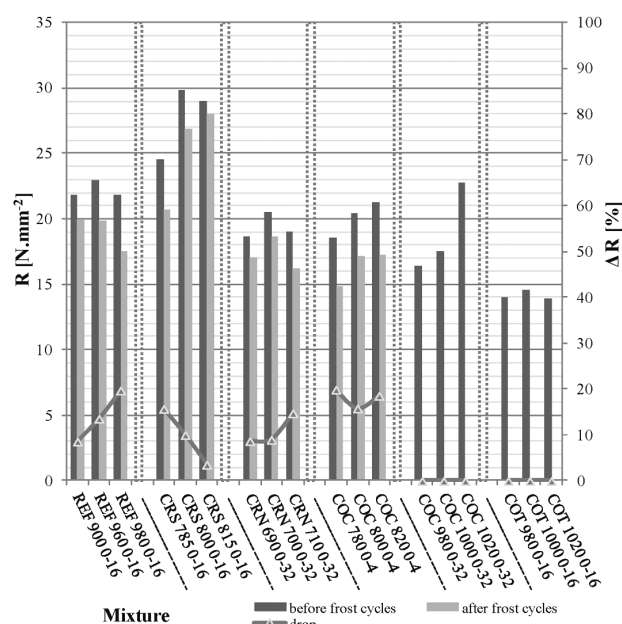


**Figure 1:** Comparison of flexural strengths before and after the frost cycles

**Slika 1:** Primerjava upogibne trdnosti pred ciklji zmrzovanja in po njih

In the case of screen glass, the attention was mainly paid to heavy metals in the forms of BaO, SrO and PbO. With container glass the emphasis was also placed on the presence of burnable materials (loss by ignition).

**Figure 1** shows a comparison between the flexural-strength values before and after the freezing cycles. The course of the strength can be seen here together with the frost influence.

A minimum flexural strength of 15 N mm<sup>-2</sup> was the application criterion. Since the compositions of COT 0-16 and COC 0-32 did not meet the required criteria

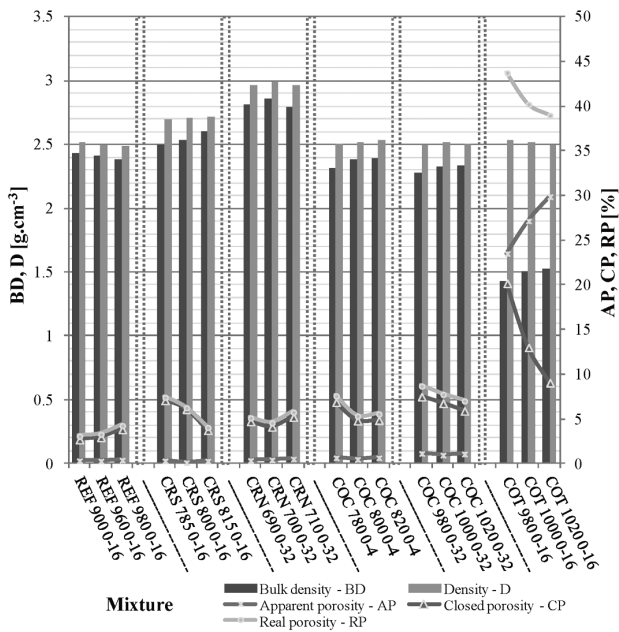


**Figure 2:** Comparison of the values for bulk density, density, apparent porosity, closed porosity and real porosity

**Slika 2:** Primerjava gostote prahu, gostote, navidezne poroznosti, zaprte poroznosti in dejanske poroznosti

(the strength and the required texture), the load tests using frost were not carried out with them.

In **Figure 2** a comparison of the values for density and specific weight is shown including closed, apparent and real porosities. These parameters are essential for characterising the porous system of a given material. A comparison of the average values of the lead migrations from the matrices of the screen- and container-glass-based sintered boards is shown in **Figure 3**.

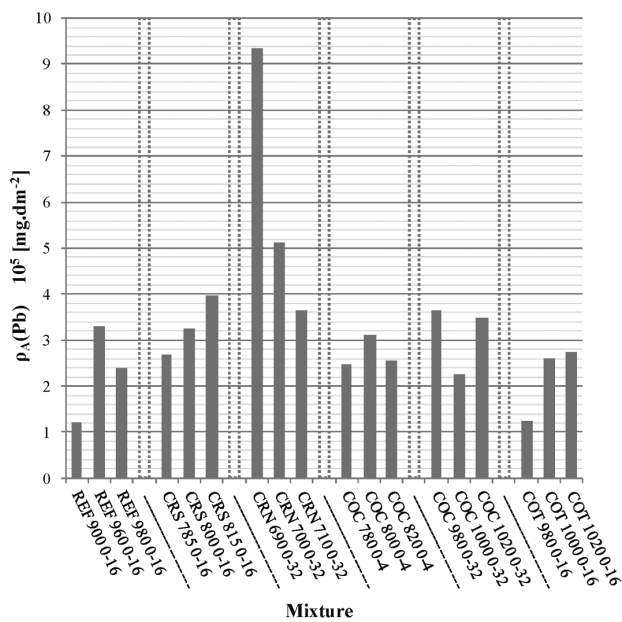


**Figure 3:** Comparison of Pb leach values

**Slika 3:** Primerjava vrednosti izločanja Pb

In addition, there are selected photos of the microstructures of the analysed recycled-cullet-based sintered materials (**Figures 4 to 8**). Considering the characters of the materials, the microstructures were monitored either in the mode of the primary electrons (SE) or in the mode

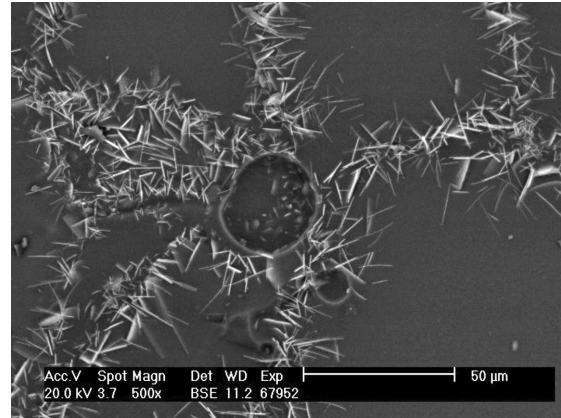


**Figure 4:** Microstructure of sample CRS 815 0-16 (mag. 500-times), SEM

**Slika 4:** Mikrostruktura vzorca CRS 815 0-16 (pov. 500-kratna), SEM



**Figure 5:** Microstructure of sample CRN 850 0-32 (mag. 10-times), SEM

**Slika 5:** Mikrostruktura vzorca CRN 850 0-32 (pov. 10-kratna), SEM

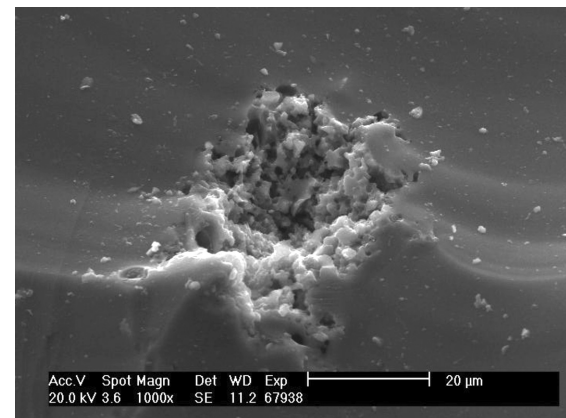


**Figure 6:** Microstructure of sample COC 800 0-4 (mag. 1000-times), SEM

**Slika 6:** Mikrostruktura vzorca COC 800 0-4 (pov. 1000-kratna), SEM



**Figure 7:** Microstructure of sample COC 1020 0-16 (mag. 2000-times), SEM

**Slika 7:** Mikrostruktura vzorca COC 1020 0-16 (pov. 2000-kratna), SEM

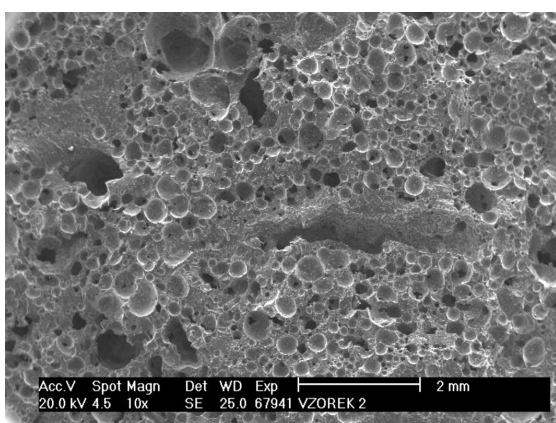


**Figure 8:** Microstructure of sample COT 1000 0-16 (mag. 10-times), SEM

**Slika 8:** Mikrostruktura vzorca COT 1000 0-16 (pov. 10-kratna), SEM

of the secondary ones (BSE). In the case of a display using BSE it can be noted that there are differences in the separation of particular shards with different chemical compositions or phases.

#### 4 DISCUSSION

From the course of the strength it is clear that using recycled glass cullet, the parameters obtained can be even better than the ones for the reference raw material. The comparison related to sample REF 960 0-16. Sample CRS 815 0-16, i.e., the board produced from screen (face plate) glass at the maximum isothermal dwell time at 815 °C and with the fraction of 0–16 mm was assessed as the best. The obtained strength indicates the fact that, in addition to the chemical composition of the cullet, its cleanness and heterogeneity also play important roles. Foreign particles mainly disturb the course of the very important cooling phase. Here, different thermal dilatations occur, thus, causing the formation of microcracks which participate in the decrease in all the parameters.

The heterogeneity of the used cullet is also related to the above. The cullets come from various recycling lines. For instance, even the CRT screen shields have different chemical compositions. Different coefficients of thermal expansion are therefore very essential during the cooling phase. The residues of organic or burnable particles are another negative factor. Thermal disintegration of residual particles results in the formation of a higher percentage of the pores. Further, the cellular-system character can be changed. In the case of the sintered-glass boards, a system of a negligible percentage of closed pores can be seen. Nevertheless, during the thermal disintegration of foreign particles the character of the porous system changes and open pores become more obvious. Sample COT contained such a significant percentage of the porous phase (the real porosity of approximately 45 %) that the strengths markedly decreased. As a result, the frost resistance was not obtained. Sample COC obtained a flexural strength higher than 15 N mm<sup>-2</sup>. However, cavities were identified in the structure (though mainly closed ones) which reached, on average, even 80 % of the thickness of the produced element. On samples COC and COT a partial loss of the characteristic texture was also found. When comparing the curves characterising the strength decrease due to frost and also porosity, it is evident that these correspond to a great extent. Although the glass-based sintered boards contain only a negligible percentage of the pores, these have a significant influence on the other physical/mechanical parameters. Since the screen cullet contains, among other substances, toxic lead, attention was also placed on assessing a possible migration of this element from the matrices of the proposed materials. Subjected to a particular standard<sup>14</sup> a leaching amount of 0.8 mg dm<sup>-2</sup> of lead is permitted. As it can be seen from the value course, all the samples produced from screen cullet met this criterion. It is clear that the sample made from cones (containing even approximately 19 % PbO) obtained the leaching values that were threefold lower than the allowed tolerance.

For the microstructural analysis, the samples with defects in their structures were mainly selected. In the representative sample CRS 815 0-16 a net of crystalline phases was identified; it was situated in the area separating individual shards of the sintered matrix. It is clear from this that, due to the impurities (probably inert ones) contained in the recycled glass, the resulting material properties do not deteriorate with the coexistence of the glass matter with the crystalline particles. Further, sample CRN 850 0-32 was examined in the place where a significant sintering and, thus, a destruction of the texture including a high amount of the porous phase occurred. As it is clear from the BSE display mode (**Figure 5**) it is, with respect to its homogeneity, a very variable matter. In the following figure there is a defect in the COC 800 0-4 structure. Most likely it is a cavity formed after the thermal disintegration of the impurities.

Therefore, the properties were not influenced by this type of defect. **Figure 7** shows the COC 1020 0-16 microstructure. The photo indicates a possible presence of a crystalline phase in the sintered matrix. Most likely this phase originates from the impurities brought to the recycled cullet during its collecting. The last microscopic photo (**Figure 8**) documents a high porosity rate of COT 1000 0-16, which resulted in a significant decrease in the strength parameters and also in a loss of the sintered-material texture.

## 5 CONCLUSIONS

The performed experiments proved that screen-recycled glass and container glass represent very useful alternative raw materials for the production of the sintered boards for the surface treatment of walls and floors. The essential fact is that, in suitably selected conditions, it is possible to reach even better parameters than in the case of the primary raw material – sodium borosilicate glass. However, with the container glass the burnable residues causing an excessive amount of pores showed to be problematic. It would be beneficial to focus on the pre-modification of this secondary raw material (i.e., clear and coloured container glass with bigger fractions). A coexistence of more phases (not targeted) together with small defects in the structures of the newly designed materials, without any significant influence on the physical/mechanical parameters, can be marked as an essential finding. This phenomenon manifested itself mainly with the screen-glass cullet. In the following research it will be necessary to focus on the completion of suitable methods for a more thorough microstructural analysis. Considering the character of the examined materials, it will be necessary to focus on the methods (modified if necessary) for analysing the glass structure or combinations of the methods dealing with silicates and glass.

## Acknowledgements

This paper was prepared with the financial support of the European Union "Operational Programme Research and Development for Innovations", No. CZ.1.05/2.1.00/03.0097, as an activity of the regional Centre AdMaS "Advanced Materials, Structures and Technologies".

This paper was also realized with the financial support from the national budget via the Ministry of Industry and Trade, under project FT-TA5/147 "Sintered products made of by-products for creation of walls and floor surface treatment".

## 6 REFERENCES

- <sup>1</sup> F. Mér, P. Yot, M. Cambon, M. Ribes, The characterization of waste cathode-ray tube glass, *Waste Management*, 26 (2006), 1468–1476, doi:10.1016/j.wasman.2005.11.017
- <sup>2</sup> P. G. Yot, F. O. Méar, Characterization of lead, barium and strontium leachability from foam glasses, *Journal of Hazardous Materials*, 185 (2011) 1, 236–241, doi:10.1016/j.jhazmat.2010.09.023
- <sup>3</sup> Y. H. Yun, Ch. H. Yoon, Y. H. Kim, Ch. K. Kim, S. B. Kim, J. T. Kwon, B. A. Kang, K. S. Hwang, Glass-ceramics prepared by waste fluorescent glass, *Ceramics International*, 28 (2002) 5, 503–505, doi:10.1016/S0272-8842(02)00002-0
- <sup>4</sup> F. Célaríe, M. Ciccotti, C. Marlière, Stress-enhanced ion diffusion at the vicinity of crack tip as evidenced by atomic force microscopy in silicate glasses, *Journal of Non-Crystalline Solids*, 353 (2007), 51–68, doi:10.1016/j.jnoncrysol.2006.09.034
- <sup>5</sup> J. Sheng, K. Kadono, Y. Utagawa, T. Yazawa, X-ray irradiation on the soda-lime container glass, *Applied Radiation and Isotopes*, 56 (2002) 4, 621–626, doi:10.1016/S0969-8043(01)00238-X
- <sup>6</sup> H. Sakamoto, Y. Ohbuch, H. Kuramae, Y. Nakamura, E. Nakamachi, S. Itoh, Visualization of high-speed fracture phenomena of glass container for effective glass recycling technology development, *Procedia Engineering*, 10 (2011), 2472–2477, doi:10.1016/j.proeng.2011.04.407
- <sup>7</sup> S. Y. Marzouk, M. S. Gaarad, Ultrasonic study on some borosilicate glasses doped with different transition metal oxides, *Solid State Communications*, 144 (2007), 478–483, doi:10.1016/j.ssc.2007.09.017
- <sup>8</sup> A. Nishara Begum, V. Rajedran, Structure investigation of TeO<sub>2</sub>-BaO glass employing ultrasonic study, *Materials Letters*, 61 (2007), 2143–2146, doi:10.1016/j.matlet.2006.08.034
- <sup>9</sup> S. Banijamali, B. Eftekhari Yekta, H. R. Rezaie, V. K. Marghussian, Crystallization and sintering characteristics of CaO-Al<sub>2</sub>O<sub>3</sub>-SiO<sub>2</sub> glasses in the presence of TiO<sub>2</sub> and ZrO<sub>2</sub>, *Thermochimica Acta*, 488 (2009), 60–65, doi:10.1016/j.tca.2008.12.031
- <sup>10</sup> ČSN EN ISO 10545-3 Ceramic floor and wall tiles – Determination of water absorption, apparent porosity, apparent relative density and bulk density, ČNI, 1998
- <sup>11</sup> ČSN EN ISO 10545-4 Ceramic tiles – Part 4: Determination of modulus of rupture and breaking strength, ČNI, 2012
- <sup>12</sup> ČSN EN ISO 10545-12 Ceramic tiles – Part 12: Determination of frost resistance, ČNI, 1998
- <sup>13</sup> ČSN EN ISO 10545-15 Ceramic tiles – Part 15: Determination of lead and cadmium given off by glazed tiles, ČNI, 1998
- <sup>14</sup> ČSN EN 14411, ed. 2, Ceramic tiles – Definitions, classification, characteristics and marking, ČNI, 2013



## MECHANICAL AND WETTING PROPERTIES OF NANOSILICA/EPOXY-COATED STAINLESS STEEL

### MEHANSKE IN POVRŠINSKE LASTNOSTI PREMAZA IZ SILICIJEVIH NANODELCEV IN EPOKSIDNE SMOLE NA NERJAVNEM JEKLU

**Marjetka Conradi<sup>1</sup>, Gaber Intihar<sup>1</sup>, Milena Zorko<sup>2</sup>**

<sup>1</sup>Institute of Metals and Technology, Lepi pot 11, 1000 Ljubljana, Slovenia

<sup>2</sup>National Institute of Chemistry, Hajdrihova 19, 1000 Ljubljana, Slovenia  
marjetka.conradi@imt.si

*Prejem rokopisa – received: 2015-03-13; sprejem za objavo – accepted for publication: 2015-04-03*

doi:10.17222/mit.2015.060

Submicron silica particles surface-capped with diglycidyl ether of bisphenol A were dispersed in a solution of epoxy resin, hardener and acetone. The resulting suspension was then spin-coated onto the surface of austenitic stainless steel of type AISI 316L and cured at temperature, generating a thick silica/epoxy coating 300 nm. An epoxy coating without nanosilica was also prepared as a reference in the same manner. The coatings were further functionalized with fluoroalkylsilane (FAS17) for an additional improvement of the non-wetting properties. The mechanical properties of epoxy coatings filled with different combinations of silica particles 30 nm, 200 nm and 600 nm were compared and characterized using scratch-resistance tests. The effects of incorporating the silica particles on the surface characteristics of the epoxy-coated steel were investigated with contact-angle and surface-energy evaluations. The surface morphology of the coatings was characterized with scanning electron microscopy (SEM). The results indicate that the silica particles significantly improved the microstructure of the coating matrix, which was reflected in an increased damage resistance, a reduced degree of delamination and an induced hydrophobicity. We observed the formation of micrometre-size silica agglomerates as a consequence of the epoxy-matrix curing process. We connected the significantly increased hydrophobicity in silica/epoxy coatings 200 nm and (30 + 600) nm to the proper combination of micro- and nano-roughness created by the agglomerates embedded in the epoxy matrix.

Keywords: silica, composite coatings, scratch test, hydrophobicity

Submikrometrске silicijeve delce, prevlečene z diglicidil etrom bisfenola A, smo dispergirali v raztopini epoksidne smole, utrjevalca in acetona. Nastalo suspenzijo smo nato z vrtenjem nanесли na površino avstenitnega nerjavnega jekla tipa AISI 316L in jo dokončno zamrežili pri povišani temperaturi. Dobili smo 300 nm debelo plast prevleke silicij-epoksidna smola. Tako smo za primerjavo lastnosti pripravili tudi prevleko iz čiste epoksidne smole. Vse prevleke smo dodatno funkcionalizirali s fluoroalkilsilanom (FAS17) za povečanje hidrofobnosti površine. Mehanske lastnosti prevlek iz epoksidne smole, obogatene z različnimi kombinacijami silicijevih delcev 30 nm, 200 nm in 600 nm, smo preizkušali z razenjem. Vpliv vključevanja silicijevih delcev v epoksidno smolo na površinske lastnosti prevlek smo analizirali z meritvami stičnih kotov ter površinske energije. Morfološke lastnosti prevlek smo karakterizirali z vrstično elektronsko mikroskopijo (SEM). Rezultati kažejo, da vključitev silicijevih delcev znatno izboljša mikrostrukturo premaza epoksidne matrike, kar se je pokazalo kot povečana odpornost proti poškodbam, zmanjšanje stopnje delaminacije in inducirane hidrofobnosti. Opazili smo tvorbo silicijevih aglomeratov mikrometrске velikosti kot posledico zamreževanja polimera pri povišani temperaturi. Močno povečano hidrofobnost na površini prevlek silicij-epoksidna smola 200 nm in (30 + 600) nm smo povezali z mikro- in nanohrapavostjo, inducirano s tvorbo aglomeratov v matriki epoksidne smole.

Ključne besede: silika, kompozitne prevleke, preizkus razenja, hidrofobnost

## 1 INTRODUCTION

In recent decades, polymer composites have started to see uses in many applications as adhesives and matrix resins. Epoxy resin is one of the most common polymer matrices that are widely used to protect steel reinforcements in concrete structures<sup>1</sup>. It has excellent mechanical properties, chemical resistance, good electrical insulating properties, and in addition, it also provides an effective physical barrier between the metal and the environment containing an aggressive species, such as an enhanced chloride-ion concentration.

The practical use of epoxy coatings in industry, however, is seriously limited by their poor impact resistance and stress-cracking resistance due to a highly cross-

linked structure<sup>2</sup>, as well as by their susceptibility to damage by surface abrasion and wear<sup>3</sup>. To overcome this drawback, researchers have made numerous attempts to improve the properties of epoxy by adding various nanofillers<sup>4-8</sup>. They studied the favourable effects of particle size, volume fraction and the quality of the dispersion on the mechanical response of polymer composites<sup>4,9-14</sup>.

A lot of work has also been done in the field of modifying the surface wettability through the controlled tailoring of the surface morphology and the surface energy<sup>15,16</sup>. In this respect, the surfaces were coated with low-surface-energy compounds<sup>17</sup> and/or their roughness was increased, i.e., by etching or nanoparticle deposition<sup>18,19</sup>. A further technological step is represented by the synthesis of superhydrophobic coatings inspired by

nature (i.e., the lotus leaf). Such coatings are a solution for corrosion, biofouling as well as water- and air-drag reduction applications. Additionally, they improve the mechanical characteristics of the surfaces. For example, nanosilica/epoxy coatings are increasingly attractive and have many potential applications in paints, coatings, sealants, adhesives, etc., due to their low cost, good adhesion to most substrates, good corrosion resistance, good scratch resistance, etc.<sup>13</sup>

Here, we investigate the influence of different sizes of silica nanoparticles (30 nm, 200 nm and 600 nm) on the surface morphology and mechanical characteristics of epoxy coatings on austenitic stainless steel of type AISI 316L. Through the implementation of silica nanoparticles into the epoxy matrix, we focus on a modification of the surface roughness of the epoxy coating that results, in combination with appropriate surface chemistry, in a significantly improved hydrophobicity.

## 2 EXPERIMENTAL

*Materials.* – Epoxy resin (Epikote 816, Momentive Specialty Chemicals B.V.) was mixed with a hardener Epikure F205 (Momentive Specialty Chemicals B. V.) in the mass ratio 100 : 53 % and used as the matrix in the composite. Composite-reinforcing silica (SiO<sub>2</sub>) nanoparticles with mean diameters of 30 nm were provided by Cab-O-Sil, whereas 200 nm and 600 nm particles were synthesized following the Stöber–Fink–Bohn method in our laboratory<sup>20</sup>. Diglycidyl ether of bisphenol A (Sigma-Aldrich) was used as the silica-surface modifier to prevent agglomeration. Imidazole (Sigma-Aldrich) served as a reaction catalyst. Austenitic stainless steel of type AISI 316L was used as a substrate.

*Surface modification of silica.* – Silica and diglycidyl ether of bisphenol A were mixed in the mass ratio 2 : 3 and dispersed in 50 mL of toluene in the presence of imidazole ( $w = 25\%$ ). The mixture was then refluxed at 100 °C for 2 h. To remove the by-product it was centrifuged three times using acetone as a solvent. The remaining silica was then dispersed in acetone and stirred at room temperature for 2–3 h. Finally, the silica was dried in an oven at 110 °C for 2 h.

*Steel-substrate preparation.* – The steel sheet with a thickness of 1.5 mm was cut into discs with diameters of 25 mm. Prior to the application of the coating, the steel discs were diamond polished following a standard mechanical procedure and then cleaned with ethanol in an ultrasonic bath.

*Composite coating preparation.* – Epoxy-based composites were prepared by blending with a mass fraction 2 % of 30 nm/200 nm/600 nm surface-modified SiO<sub>2</sub> particles. To improve the dispersion of the silica particles in the coating, they were dispersed in epoxy resin using acetone as a solvent. Prior to the addition of the silica particles, both the resin and the hardener were separately diluted in acetone in a mass ratio of 1 : 4. The nanopar-

ticles were then dispersed in the epoxy resin/acetone solution using ultrasonification for 20–30 min at room temperature. After adding the hardener/acetone solution in the next step, the mixture was manually stirred for a 5 min. Finally, a drop 19 mg of the silica/epoxy resin/hardener/acetone mixture was poured onto the steel substrate disc and a uniform film was then applied to the substrate by a spin-coating process. The composite coatings were then cured in two steps: first pre-cured at 70 °C for 1 h and then post-cured at 150 °C for another hour. The resulting coatings on the steel-substrate plates were thick 300 nm, as determined by ellipsometry. For comparison, neat epoxy coatings without silica fillers were also prepared and cured in the same process as the composites. Finally, to additionally improve the non-wetting properties, the coatings were functionalized by dip-coating in ethanolic fluoroalkylsilane (FAS17, C<sub>16</sub>H<sub>19</sub>F<sub>17</sub>O<sub>3</sub>Si, Sigma-Aldrich).

*Scanning electron microscopy (SEM).* – SEM analysis using FE-SEM Zeiss SUPRA 35VP was employed to investigate the morphology of the silica/epoxy coatings' surfaces.

*Scratch test.* – The scratch test was performed with a Revetest Scratch tester (CSM Instruments). In the experiment, a scratch length of 10 mm was made using a diamond tip and a linearly increased normal load from 1 N to 5 N at a speed of 5 mm/s. Four tests were performed per sample. A light microscope was employed to analyse the scratches.

*Contact-angle and surface-energy measurements.* – The static contact-angle measurements of water (W) on a clean AISI 316L diamond-polished sample and on the pure epoxy and silica/epoxy composite coatings prepared on an AISI 316L steel substrate were performed using a surface-energy evaluation system (Advex Instruments s. r. o.). Liquid drops of 5 µL were deposited on different spots of the substrates to avoid the influence of roughness and gravity on the shape of the drop. The drop contour was analysed from the image of the deposited liquid drop on the surface and the contact angle was determined by using Young-Laplace fitting. To minimize the errors due to roughness and heterogeneity, the average values of the contact angles of the drop were calculated approximately 30 s after the deposition from at least five measurements on the studied coated steel. All the contact-angle measurements were carried out at 20 °C and ambient humidity. As the contact angles were only available for water, an equation-of-state approach<sup>21,22</sup> was used to calculate the corresponding surface energies.

*Surface roughness.* – A profilometer, model Form Talysurf Series 2 (Taylor-Hobson Ltd.), was employed for the surface analysis. The instrument has a lateral resolution of 1 µm and a vertical resolution of about 5 nm. It measures the surface profile in one direction. TalyMap gold 4.1 software was used for the roughness analysis. The software offers the possibility to calculate



the average surface roughness,  $S_a$ , for each sample, based on the general surface-roughness equation:

$$S_a = \frac{1}{L_x} \frac{1}{L_y} \int_0^{L_x} \int_0^{L_y} |z(x, y)| dx dy \quad (1)$$

where  $L_x$  and  $L_y$  are the acquisition lengths of the surface in the  $x$  and  $y$  directions and  $z(x, y)$  is the height. To level the profile, corrections were made to exclude the general geometrical shape and possible measurement-induced misfits.

### 3 RESULTS AND DISCUSSION

#### 3.1 Scratch resistance

Typical scratches in the 300 nm thick pure epoxy coating and the 300 nm thick epoxy coating filled with 200 nm silica particles are presented in **Figure 1**. The scratch profile as well as the resistance of the other silica/epoxy coatings is analogous to the 200 nm silica/epoxy coating under investigation, and thus not provided here. It is clear that there is much less displaced material in the case of the silica/epoxy coating compared to the pure epoxy coating. It also seems that the pure epoxy coating is much more brittle than the silica/epoxy coating. This, altogether, indicates that the embedded silica particles can improve the scratch resistance and enhance the toughness of the epoxy coating. In addition, the scratch-test results also suggest that the scratch resistance of the coatings is related to the interaction force between the coating and the steel substrate, which is apparently improved for the silica/epoxy coating.

#### 3.2 Wetting properties

To analyse the surface wettability, five static contact-angle measurements with water (W) were performed on different spots all over the sample and used to determine the average contact-angle values with an estimated error in the reading of  $(\theta \pm 1.0)^\circ$  and for the calculation of the surface energy. The wettability, however, was not possible to assess using non-polar liquids for the contact-angle measurements as they spread out on the coatings  $(\theta \pm 0^\circ)$ . The contact angles and the surface energies for the epoxy and silica/epoxy coatings on the AISI 316L substrate in comparison to the clean, diamond-polished AISI 316L sample are reported in **Table 1**.

It was observed that all the investigated silica/epoxy coatings exhibited significantly higher values of static water-contact angles compared to the clean AISI 316L sample, as well as the AISI 316L substrate blended with pure epoxy. This suggests that the microstructure change of the epoxy coating upon adding the silica particles was reflected in an increased surface roughness, which is known to impart a hydrophobic effect to the surface<sup>23</sup>.

The highest values of the static water angles, close to  $120^\circ$ , were however measured in the case of two types of silica/epoxy coatings: 200 nm silica/epoxy coatings and in case of silica/epoxy coatings filled with a combination of 30 nm and 600 nm silica particles. Possible reasons for this observation will be discussed in the following section on surface morphology and surface roughness.

**Table 1:** Surface properties of diamond-polished AISI 316L substrate and AISI 316L substrate when blended with pure epoxy and various types of silica/epoxy coatings. Static contact angles were measured with water ( $\theta^W$ ) and the corresponding surface energies were calculated using an equation-of-state approach.

**Tabela 1:** Površinske lastnosti z diamantno pasto polirane površine podlage AISI 316L in AISI 316L, prevlečne s čisto epoksidno smolo in različnimi prevlekami iz silicij-epoksidne smole. Statični stični koti so bili izmerjeni z vodo ( $\theta^W$ ), ustrezne površinske energije pa so bile izračunane z enačbo stanja.

| Substrate                          | Contact angle $\theta^W/^\circ$ | Surface energy $\gamma^{tot}/(mN/m)$ |
|------------------------------------|---------------------------------|--------------------------------------|
| AISI                               | 68.4                            | 42.7                                 |
| AISI + epoxy                       | 80.2                            | 35.4                                 |
| AISI + 30 nm silica/epoxy          | 110.1                           | 17.0                                 |
| AISI + 200 nm silica/epoxy         | 117.7                           | 12.8                                 |
| AISI + 600 nm silica/epoxy         | 110.1                           | 17.0                                 |
| AISI + (30 + 200) nm silica/epoxy  | 111.7                           | 16.1                                 |
| AISI + (200 + 600) nm silica/epoxy | 111.0                           | 16.5                                 |
| AISI + (30 + 600) nm silica/epoxy  | 118.4                           | 12.5                                 |

As the contact angles were only available for water, an equation-of-state approach<sup>21,22</sup> was used to calculate the surface energies with Equation (1):

$$\cos \theta = -1 + 2 \sqrt{\frac{\gamma_s}{\gamma_1}} e^{-\beta(\gamma_1 - \gamma_s)^2} \quad (2)$$

For a given value of the surface tension of the probe liquid  $\gamma_1$  (i.e., for water  $\gamma_1 = 72.8 \text{ mN/m}$ <sup>24</sup>) and  $\theta^W$  measured on the same solid surface, the constant  $\beta$  and

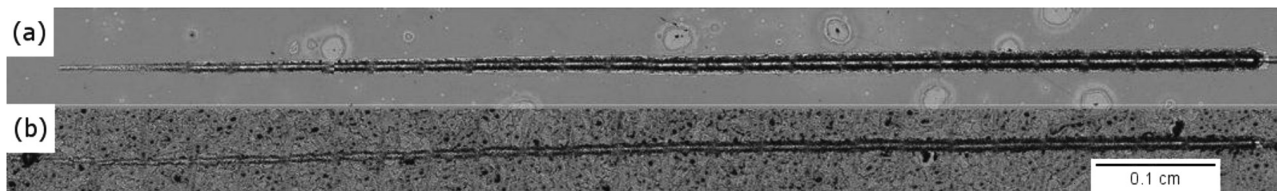


**Figure 1:** Light micrographs revealing the typical morphology of scratches: a) for the thick pure epoxy coating 300 nm on AISI 316L and b) for the thick epoxy coating 300 nm filled with silica particles 200 nm on AISI 316L

**Slika 1:** Svetlobna mikroskopija prikazuje značilno morfologijo prask: a) na 300 nm debeli prevleki iz čiste epoksidne smole in b) na 300 nm debeli prevleki iz epoksidne smole, obogatene s silicijevimi delci 200 nm

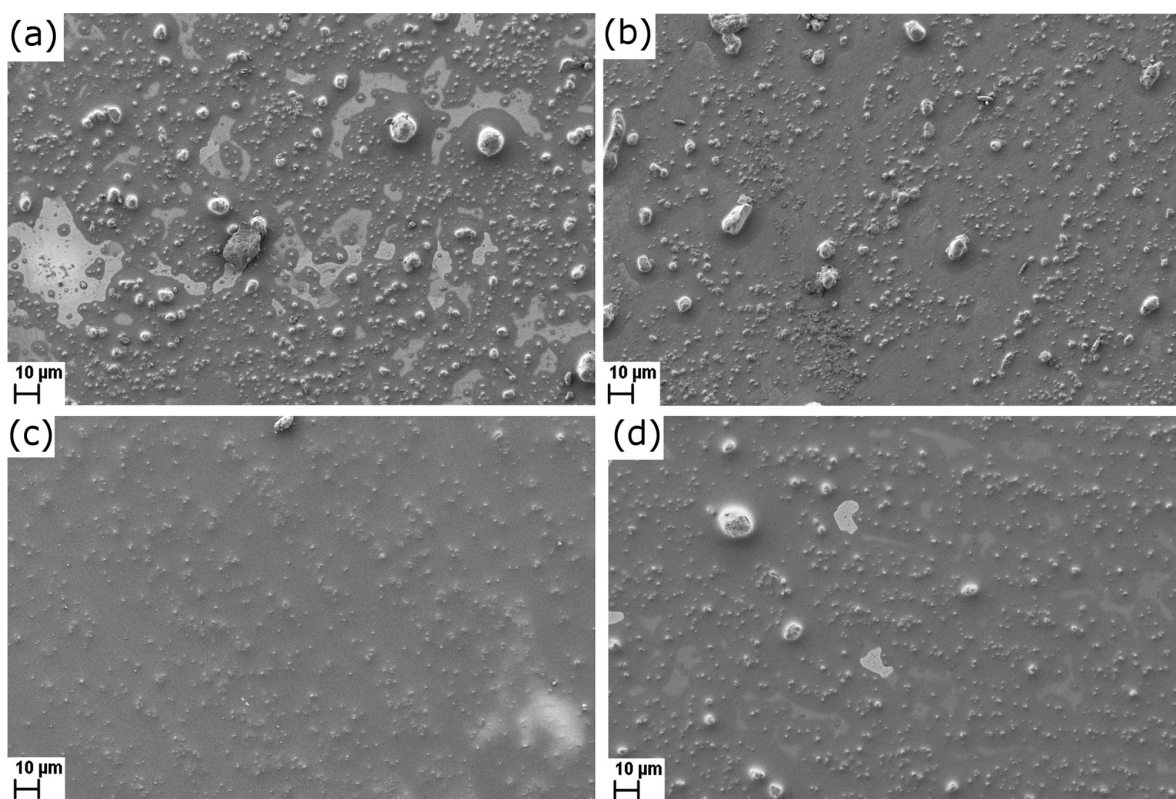


**Figure 2:** SEM images of AISI 316L substrate when blended with: a) silica/epoxy 30 nm, b) silica/epoxy 200 nm, c) silica/epoxy 600 nm and d) silica/epoxy coating (30 + 600) nm

**Slika 2:** SEM-posnetki podlage AISI 316L, prevlečene s prevlekami iz: a) 30 nm silicij-epoksidne smole, b) 200 nm silicij-epoksidne smole, c) 600 nm silicij-epoksidne smole in d) (30 + 600) nm silicij-epoksidne smole

the solid surface-tension  $\gamma_s$  values were determined using the least-squares analysis technique. For the fitting with Equation (2), a literature value of  $\beta = 0.0001234$  ( $\text{mJ/m}^2$ )-<sup>2</sup> was used, as weighted for a variety of solid surfaces<sup>22</sup>. Again, the calculated values of the solid surface energy (**Table 1**) dropped significantly when the clean AISI 316L substrate was covered with silica/epoxy coatings, confirming the induced surface hydrophobicity. The low surface energy of the silica/epoxy coatings is most probably a consequence of the combination of silica-induced surface roughness and the appropriate surface chemistry due to the coatings' functionalization with fluoroalkylsilane.

### 3.3 Surface morphology

**Figure 2** compares the typical morphology of various silica-epoxy coatings. It is clear that in spite of the silica-surface modification with an epoxy-compatible component, we could not prevent silica agglomeration in the coating. After several different attempts we came to the conclusion that the agglomeration appears during the curing process and is most probably a consequence of solvent (acetone) evaporation, together with the formation of a highly cross-linked epoxy structure.

A detailed look at the surface morphology, however, brought us to the conclusion that there exists a typical

average agglomerate size, which depends on the size of the silica fillers in the epoxy matrix. These agglomerates, which are typically in the  $\mu\text{m}$  size range, consequently

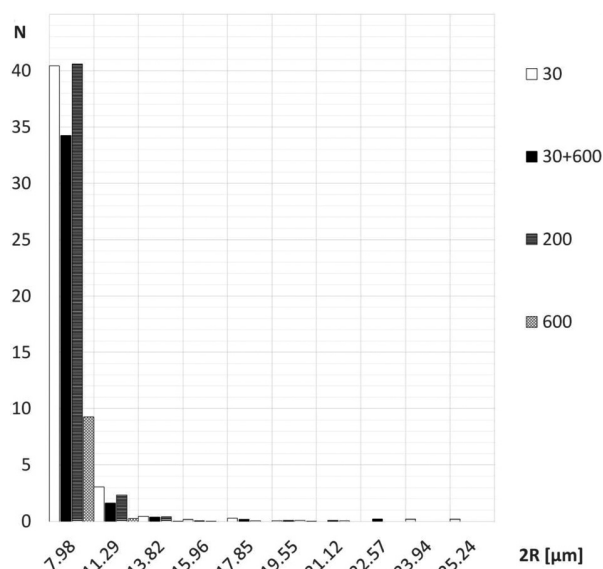


**Figure 3:** Size distribution of silica agglomerates in 30 nm, 200 nm, 600 nm and (30 + 600) nm silica/epoxy coatings

**Slika 3:** Velikostna porazdelitev silicijevih aglomeratov v prevlekah iz epoksidne smole, obogatene s silicijevimi nanodelci 30 nm, 200 nm, 600 nm in (30 + 600) nm

create a micro-roughness on top of the nano-roughness created by the individual silica nanoparticles embedded in the epoxy matrix. As is already known, it is the combination of the two, i.e., the micro- and the nano-roughness, that increases the static water contact angle and makes the surface more hydrophobic<sup>25</sup>.

As reported in **Table 1**, we measured the highest static water contact angles, close to 120 °, only on the surfaces of the 200 nm and (30 + 600) nm silica/epoxy coatings. In **Figure 3** we can see that these two coatings are characterized mostly with agglomerates having diameters of 8 µm and 11 µm. The same holds for the morphology of the 30 nm silica/epoxy coating; however, here we also observe an inconsiderable number of larger agglomerates that most probably influence the proper ratio between the micro- and nano-roughness necessary for an increase of the static water contact angle. This suggests the agglomerate/nanoparticle ratio is extremely sensitive to the appropriate surface roughness that will create a hydrophobic/superhydrophobic surface. This result also confirms the competitive importance of the surface morphology on the wetting properties compared to a low surface energy tailored with the surface chemistry.

### 3.4 Surface Roughness

Finally, we confirmed the morphology observations and determined the effect of the incorporation of silica on the morphology of the epoxy coating, by measuring the average surface roughness of the coatings,  $S_a$ . An examination of the silica/epoxy-coated steel surface with a profilometer revealed that the nanoparticles' size significantly influences the coating's roughness and consequently the morphology of the surface. As listed in **Table 2**,  $S_a$  of 200 nm and (30 + 600) nm silica/epoxy coatings is of the same order of magnitude and in the intermediate regime compared to 30 nm and 600 nm silica/epoxy coatings. This is consistent with the observation of the average size of the agglomerates characterizing the morphology of each coating, as reported in the previous section. Here, we have shown that an intermediate roughness gives the best results in terms of an increased hydrophobicity (**Tables 1** and **2**). Moreover, this confirms the importance of the appropriate surface roughness on the wetting behaviour of the coatings.

**Table 2:** Average surface roughness,  $S_a$ , of various silica/epoxy coatings on an AISI 316L substrate

**Tabela 2:** Povprečna površinska hrapavost  $S_a$  različnih prevlek iz silicij-epoksidne smole na podlagi AISI 316L

| Substrate                         | $S_a$ |
|-----------------------------------|-------|
| AISI + 30 nm silica/epoxy         | 0.65  |
| AISI + 200 nm silica/epoxy        | 0.41  |
| AISI + 600 nm silica/epoxy        | 0.27  |
| AISI + (30 + 600) nm silica/epoxy | 0.46  |

## 4 CONCLUSIONS

Nanosilica particles were homogeneously dispersed in an epoxy matrix at a mass concentration of 2 % and mixtures with different combinations of 30 nm, 200 nm and 600 nm silica were successfully spin coated on austenitic stainless steel of type AISI 316L to form a 300 nm coating. For an additional improvement of the non-wetting properties, the coatings were functionalized by dip-coating in ethanolic fluoroalkylsilane (FAS17).

The mechanical properties of the coatings were evaluated with a scratch test, indicating that the more brittle pure epoxy coating underwent more severe damage, accompanied by a pronounced material displacement compared to the silica/epoxy coating. This indicates that the silica particles enhanced the toughness of the epoxy coating.

The silica nanoparticles changed the microstructure of the epoxy coating, which was reflected in an increased roughness of the silica/epoxy-coated AISI 316L sample. The increased hydrophobicity of the silica/epoxy coatings, on the other hand, was a consequence of the combination of silica-induced surface roughness and the appropriate surface chemistry, due to the coatings' functionalization with fluoroalkylsilane.

The surface morphology of the silica/epoxy coatings was characterized by the formation of micrometre-size silica agglomerates as a consequence of the epoxy-matrix curing process. The significantly increased hydrophobicity in the 200 nm and (30 + 600) nm silica/epoxy coatings was connected to the proper combination of micro- and nano-roughness created by the agglomerates embedded in the epoxy matrix.

## Acknowledgement

This work was carried out within the framework of the Slovenian programme P2-0132, "Fizika in kemija površin kovinskih materialov" of the Slovenian Research Agency, whose support is gratefully acknowledged by M. Conradi.

## 5 REFERENCES

- F. Galliano, D. Landolt, Evaluation of corrosion protection properties of additives for waterborne epoxy coatings on steel, *Prog. Org. Coat.*, 44 (2002), 217–225, doi:10.1016/S0300-9440(02)00016-4
- S. Yamini, R. J. Young, Stability of crack-propagation in epoxy-resins, *Polymer*, 18 (1977) 10, 1075–1080, doi:10.1016/0032-3861(77)90016-7
- B. Wetzel, F. Hauptert, M. Q. Zhang, Epoxy nanocomposites with high mechanical and tribological performance, *Comp. Sci. Tech.*, 63 (2003), 2055–2067, doi:10.1016/S0266-3538(03)00115-5
- A. C. Moloney, H. H. Kausch, T. Kaiser, H. R. Beer, Parameters determining the strength and toughness of particulate filled epoxide-resins, *J. Mat. Sci.*, 22 (1987), 381–393, doi:10.1007/BF01160743
- E. P. Giannelis, Polymer-layered silicate nanocomposites: Synthesis, properties and applications, *App. Org. Chem.*, 12 (1998), 675–680, doi:10.1002/(SICI)1099-0739(199810/11)12:10<11<675::AID-AOC779>3.0.CO;2-V

- <sup>6</sup> T. Lan, T. J. Pinnavaia, Clay-reinforced epoxy nanocomposites, *Chem. Mat.*, 6 (1994), 2216-2219, doi:10.1021/cm00048a006
- <sup>7</sup> R. P. Singh, M. Zhang, D. Chan, Toughening of a brittle thermosetting polymer: Effects of reinforcement particle size and volume fraction, *J. Mat. Sci.*, 37 (2002), 781-788, doi:10.1023/A:1013844015493
- <sup>8</sup> R. A. Pearson, A. F. Yee, Influence of particle-size and particle-size distribution on toughening mechanisms in rubber-modified epoxies, *J. Mat. Sci.*, 26 (1991), 3828-3844, doi:10.1007/BF01184979
- <sup>9</sup> M. Frounchi, T. A. Westgate, R. P. Chaplin, R. P. Burford, Fracture of polymer networks based on diethylene glycol bis(allyl carbonate), *Polymer*, 35 (1994), 5041-5045, doi:10.1016/0032-3861(94)90661-0
- <sup>10</sup> R. T. Quazi, S. N. Bhattacharya, E. Kosior, The effect of dispersed paint particles on the mechanical properties of rubber toughened polypropylene composites, *J. Mat. Sci.*, 34 (1999), 607-614, doi:10.1023/A:1004515300637
- <sup>11</sup> T. Adachi, W. Araki, T. Nakahara, A. Yamaji, M. Gamou, Fracture toughness of silica particulate-filled epoxy composite, *J. App. Polym. Sci.*, 86 (2002), 2261-2265, doi:10.1002/app.11206
- <sup>12</sup> A. Boonyapookana, K. Nagata, Y. Mutoh, Fatigue crack growth behavior of silica particulate reinforced epoxy resin composite, *Comp. Sci. Tech.*, 71 (2011), 1124-1131, doi:10.1016/j.compscitech.2011.02.015
- <sup>13</sup> J. Yuan, S. Zhou, G. Gu, L. Wu, Effect of particle size of nanosilica on the performance of epoxy/silica composite coatings, *J. Mat. Sci.*, 40 (2005), 3927-3932, doi:10.1007/s10853-005-0714-8
- <sup>14</sup> M. Conradi, M. Zorko, A. Kocijan, I. Verpoest, Mechanical properties of epoxy composites reinforced with a low volume fraction of nanosilica fillers, *Mat. Chem. Phys.*, 137 (2013), 910-915, doi:10.1016/j.matchemphys.2012.11.001
- <sup>15</sup> A. Tuteja, W. Choi, M. Ma, J. M. Marby, S. A. Mazzella, G. C. Rutledge, G. G. McKinley, R. E. Cohen, Designing superoleophobic surfaces, *Science*, 318 (2007), 1618-1622, doi:10.1126/science.1148326
- <sup>16</sup> C. H. Xue, S. T. Jia, J. Zhang, L. Q. Tian, H. Z. Chen, M. Wang, Preparation of superhydrophobic surfaces on cotton textiles, *Sci. Technol. Adv. Mater.*, 9 (2008) 3, 035008, doi:10.1088/1468-6996/9/3/035008
- <sup>17</sup> A. Zenerino, T. Darmanin, E. T. deGivenchy, S. Amigoni, F. Guittard, Connector ability to design superhydrophobic and oleophobic surfaces from conducting polymers, *Langmuir*, 26 (2010), 13545-13549, doi:10.1021/la101734s
- <sup>18</sup> N. Salema, D. K. Sarkar, R. W. Paynter, X. G. Cheng, Superhydrophobic aluminum alloy surfaces by a novel one-step process, *ACS Appl. Mater. Interfaces*, 2 (2010), 2500-2502, doi:10.1021/la104979x
- <sup>19</sup> Z. Guo, X. Chen, J. Li, J. H. Liu, X. J. Huang, ZnO/CuO hetero-hierarchical nanotrees array, hydrothermal preparation and self-cleaning properties, *Langmuir*, 27 (2011), 6193-6200, doi:10.1021/la104979x
- <sup>20</sup> W. Stober, A. Fink, E. Bohn, Controlled growth of monodisperse silica spheres in micron size range, *Journal of Colloid and Interface Science*, 26 (1968), 62-69, doi:10.1016/0021-9797(68)90272-5
- <sup>21</sup> D. Li, A. W. Neumann, A reformulation of the equation of state for interfacial-tensions, *Journal of Colloid and Interface Science*, 137 (1990), 304-307, doi:10.1016/0021-9797(90)90067-X
- <sup>22</sup> D. Y. Kwok, A. W. Neumann, Contact angle measurement and contact angle interpretation, *Advances in Colloid and Interface Science*, 81 (1999), 167-249, doi:10.1016/S0001-8686(98)00087-6
- <sup>23</sup> J. Y. Shiu, C. W. Kuo, P. L. Chen, C. Y. Mou, Fabrication of tunable superhydrophobic surfaces by nanosphere lithography, *Chem. Mat.*, 16 (2004), 561-564, doi:10.1021/cm034696h
- <sup>24</sup> Y. Y. Yu, C. Y. Chen, W. C. Chen, Synthesis and characterization of organic - inorganic hybrid thin films from poly(acrylic) and monodispersed colloidal silica, *Polymer*, 44 (2003), 593-601, doi:10.1016/S0032-3861(02)00824-8
- <sup>25</sup> T. J. Athauda, W. Williams, K. P. Roberts, R. R. Ozer, On the surface roughness and hydrophobicity of dual-size double-layer silica nanoparticles, *J. Mater. Sci.*, 48 (2013) 18, 6115-6120, doi:10.1007/s10853-013-7407-5

## DEVELOPMENT OF COMPOSITE SALT CORES FOR FOUNDRY APPLICATIONS

### RAZVOJ KOMPOZITNIH SLANIH JEDER ZA UPORABO V LIVARSTVU

**Jaroslav Beňo, Eliška Adámková, František Mikšovský, Petr Jelínek**

VŠB-Technical University of Ostrava, Faculty of Metallurgy and Materials Engineering, Department of Metallurgy and Foundry,  
17. listopadu 15/2172, 708 33 Ostrava-Poruba, Czech Republic  
jaroslav.beno@vsb.cz

*Prejem rokopisa – received: 2013-09-26; sprejem za objavo – accepted for publication: 2014-09-05*

doi:10.17222/mit.2013.160

For the purpose of increasing the physical/mechanical properties of the cores based on inorganic salts generally destined for pre-casting the cavities and holes of the castings from non-ferrous alloys, the composite salt matrixes are preferably used. The base salt is enriched with the materials of defined properties (granulometry, heat resistance, cooling effect, heat conductivity). This contribution aims at determining the influences of individual additives on the behaviour of the cores prepared with different methods (shooting and squeezing) during a production of the castings with a high surface quality of the pre-cast holes.

Keywords: non-ferrous alloys, salt cores, inorganic salts, die casting, PUR Cold Box, Warm Box, core solubility and stability

Zaradi naraščajočih fizikalno-mehanskih lastnosti jeder na osnovi anorganskih soli se za jedra, najpogosteje namenjena za predhodno litje votlin in praznin v ulitkih iz neželeznih zlitin, uporabljajo kompoziti z osnovo iz soli. Osnovna sol je obogatena z materiali z določenimi lastnostmi (zrnatost, toplotna odpornost, učinek ohlajanja, toplotna prehodnost). Namen tega prispevka je določiti vpliv posameznih dodatkov na vedenje jeder, pripravljenih po različnih metodah (s streljanjem in z brizganjem) med izdelavo ulitkov z veliko kvaliteto površine in predizdelanih odprtin.

Ključne besede: neželezne zlitine, slana jedra, anorganske soli, tlačno litje, PUR Cold Box, Warm Box, topnost jeder in stabilnost

## 1 INTRODUCTION

The application of salt cores for the pre-casting of casting cavities and holes has been known since the 1970s<sup>1</sup>. In the course of time this technology has found its application, above all, in the field of the large-lot production of the castings from Al-alloys (cooling channels of engine pistons) manufactured with the gravity and low-pressure casting methods<sup>2</sup>.

The application of the cores based on water-soluble inorganic salts represents a bonding system associated with easy cleaning of even geometrically complex pre-cast holes, ensuring a dimensional and form complexity and a smoothness of the pre-cast holes of castings. In addition, this binder system is friendly to the living environment and technological equipment. The cores can be manufactured in a closed ecological cycle. During the casting, cooling and solidification the salt cores do not emit any VOC emissions.

The casting process using an increased pressure all the time represents the predominant technology for manufacturing the castings from non-ferrous alloys<sup>3,4</sup> (primarily the use of metal cores). With the growing shape complexity of the castings the requirements for the cleanability of pre-cast cavities and holes are escalating. The application of the cores based on inorganic salts can be a solution of this problem.

Meeting this highly demanding requirement, the application of the cores for the high-pressure casting process (die casting) is complicated due to the extreme conditions to which a core is exposed. The issues that need to be considered are, above all, a high rate of the mold filling leading to the erosion of the cores, metal penetration and a loss of dimensional accuracy under the influence of a closeness of the temperatures of the cast alloys and salt melting.

For these reasons the cores made only of a salt matrix can be replaced with the so-called composite salt cores where the base salt matrix is enriched with the additives with specific properties.

The use of composites, including the additives with a defined granulometry, is aimed at the growth of the primary and secondary strengths that used to be explained with the erosion of long dislocation lines present in a salt matrix with finely dispersed particles (of a high heat resistance). As the melting temperature of the cores from pure salts is near the melt temperatures, the addition of additives increases the heat resistance of the cores, decreasing the possibility of the surface defects of castings. Their influence on the surface quality of castings is also augmented by a higher cooling effect of the cores as a result of the presence of the additives.

The addition of the additives further improves the dimensional and form accuracy, it keeps a good bench

life of the cores and it does not negatively influence their solubility in water.

The properties of the salt cores can be further modified and optimized for individual casting methods by changing the preparation conditions (the intensity of the squeezing pressures, the temperature of the injection in the core box, the choice of a binder, etc.) and the base matrix composition (the salt type, the additives), suitable for the pre-casting of hardly accessible cavities and holes of complex forms.

At present there are many methods of core manufacturing; two processes of manufacturing salt cores were developed in our workshop – high-pressure squeezing with the utilization of the recrystallization process where the strength is achieved by sticking moistened salt grains together and the recrystallization along the grain boundaries, and shooting with the use of inorganic binders, e.g., alkali silicates.

This contribution is aimed at determining the influences of individual additives on the behavior of the cores prepared with different methods (shooting and squeezing) during the production of the castings with a high surface quality of the pre-cast holes.

## 2 MATERIALS AND METHODS

Salt cores based on chemically pure salt (chloride, marked as KCl) and technical salt (chloride, marked as NaCl) and different additives (marked as A, B, C) with the basic parameters summarized in **Table 1** were used as the test cores.

Aluminum alloy AlSi9Cu3(Fe) was used for the experiments. The test casting was cast in operational conditions of the joint-stock company of KOVOLIS HEDVIKOV a. s., CZ, on a casting machine CLH 400 with a squeezing pressure of 76.8 MPa, in a chamber under a casting temperature of 690 °C

The cores were prepared in two ways as follows:

### i) method of high-pressure squeezing of the salts

The cores were squeezed from a mildly moistened composite salt matrix (up to 1 %) with a loading rate of 9 kN/s. The cores were strengthened due to the mechanical deformation of the grains (a conglomeration) and the recrystallization along the grain boundaries. The primary strengths (cold), the strength under high temperatures (650 °C) and the residual (secondary) cold strength after the thermal exposure (650 °C, 1 h) were determined. The primary strengths were evaluated 48 h after the squeezing, but only when the second phase of the hardening – the recrystallization of the salt grain boundaries – was in place;

### ii) injection into core boxes using binders

A mixture of the composite crystalline salt (finely ground and of the original granulometry) and the binder (Na-silicate,  $M = 1.84$ ) was compacted by being injected (7.5–8 bar) into a warm core box (190 °C) with an

injection rate of 7.5 s and a hardening time of 50 s. The shooting machine of the MOREK (PL) firm was used for the injection.

The main criterion was the bending strength  $\sigma_0$  measured on an adapted universal apparatus LRu-2e (MULTISERVIS MOREK, PL).

The seeming porosity  $m$  of the samples of the salt cores was determined according to:

$$m = \frac{\rho_K - \rho_{core}}{\rho_K} \cdot 100(\%) \quad (1)$$

where:

$m$  – porosity (%)

$\rho_K$  – density of matrix KCl (1.981 g/cm<sup>3</sup>)

$\rho_{core}$  – density of the core (g/cm<sup>3</sup>)

The roughness tests of the pre-cast holes were done according to the ISO 1997 standard; a roughness meter of SurfTest SJ-301-Mitutoyo was used. Ten measurements were done for each sample and the resulting value of the mean arithmetic roughness –  $R_a$  (μm) – was obtained as the average of these measurements. Before the testing the castings were fettled of possible coating residues.

**Table 1:** Basic parameters of used additives

**Tabela 1:** Osnovni parametri uporabljenih dodatkov

| Additive | mode $d_{50}/\mu\text{m}$ | SPAN  |
|----------|---------------------------|-------|
| A        | 28.825                    | 2.136 |
| B        | 130.875                   | 4.844 |
| C        | 158.033                   | 0.736 |

Note: SPAN – width of the granulometric curve

## 3 RESULTS AND DISCUSSION

### 3.1 Injection into core boxes using binders

For the purpose of making cores with more complex forms, the manufacturing technology for salt cores using an injection into warm core boxes was developed. Beside the shape complexity, another expected advantage is the utilization of the existing plants for manufacturing sand cores. The method requires a suitable choice of the binder (of an inorganic or organic type) for achieving high strengths (above all, under a high temperature) and an easy solubility in water after a thermal exposure. To meet these requirements, strongly alkaline Na-silicates (sodium silicate) of a low modulus ( $M = 1.84$ ), whose high strengths can be achieved with dehydration, were suggested. The influence of the chemical composition of the mixture and the modifications of the base-matrix granulometry (sample NaCl) on the mean bending strength ( $\sigma_0$ ) and the seeming porosity  $m$  was studied in the framework of the experiment (**Table 2**).

The results of the measurements of the physical properties of the cores shot from pure salts with the Na-silicate binder (**Table 2**) showed the highest strengths for the mixture compositions III, IV (salt NaCl, the

original granulometry); on the contrary, the lowest bending strengths were achieved for the cores with a modified granulometry (under 0.63 mm and 0.4 mm – ground; I, II, V).

**Table 2:** Technological parameters of basic salt-core mixtures  
**Tabela 2:** Tehnološki parametri osnovne slane mešanice jedra

| Composition | Granulometry          | m/%   | $\sigma_b$ /MPa |
|-------------|-----------------------|-------|-----------------|
| I           | $< \phi$ 0.63 mm      | 46–48 | 1.766           |
| II          | $< \phi$ 0.63 mm      | 46–49 | 1.794           |
| III         | original granulometry | 42–56 | 2.332           |
| IV          | original granulometry | 47–51 | 2.115           |
| V           | $< \phi$ 0.4 mm       | 48–52 | 1.332           |

The seeming porosity was high in all the cases (> 42 %). A high porosity of a core enables a high rate of solution in water but it is also a cause for thermal deformations (above 600 °C, the plastic state) and an easy metal penetration.

Therefore, further tests led to a decrease in the porosity of the core faces (protective coatings, sintering of the surface) and an improvement in the strength characteristics by shooting the composite salts.

Additives A and B were used for the salt matrix of the composition of mixture III. The mean values of the results of the experiments determining the bending strengths of individual composite salt cores are summarized in **Figure 1**.

Besides decreasing the core-face porosity (by 17–23 %) neither the A additive nor the B one caused any required strength effect.

The bending strength ranged within 2.93–3.3 MPa (the density of 1.2–1.33 g/cm<sup>3</sup>), corresponding to the values of about 25 % of the bending strength of the squeezed cores.

In this development phase the cores prepared with the injection technology (WARM BOX) are only applicable in the gravity and low-pressure casting technologies.

**3.2 High-pressure squeezing of the salts**

The KCl salt that generally exhibits higher primary and secondary strengths compared to the NaCl technical salt was chosen as the salt matrix for this part of the

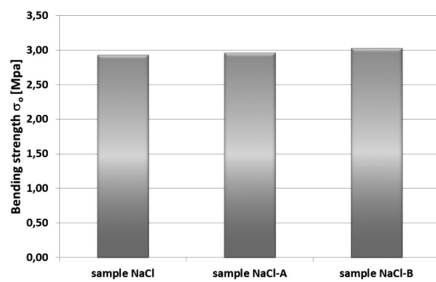


**Figure 1:** Bending strength of the composite salt cores prepared with the WARM-BOX method

**Slika 1:** Upogibna trdnost kompozitnih slanih jedra, pripravljenih po metodi WARM-BOX

experiment<sup>5</sup>. The apparent porosity of the salt cores prepared with high specific pressures was up to 4 %; the results of the bending strength are summarized in **Table 3**.

**Table 3:** Influence of the additive on the bending strength of composite salt cores

**Tabela 3:** Vpliv dodatkov na upogibno trdnost kompozitnih slanih jedra

| Salt matrix KCl                      | A/%   |      | B/% |      | C/% |     |
|--------------------------------------|-------|------|-----|------|-----|-----|
|                                      | 0     | 10   | 0   | 10   | 0   | 10  |
| after 48 h, MPa                      | 7.5   | 7.9  | 7.6 | 8.1  | 6.5 | 7.2 |
| Hot strength (650 °C, 1 h), MPa      | > 8.9 | 13.2 | 8.9 | 10.1 | 8.1 | 8.9 |
| Residual strength (650 °C, 1 h), MPa | 8.5   | 8.7  | 6.8 | 9.9  | 7.9 | 7.8 |

The test showed that the use of the composite salts of a defined granulometry in combination with the KCl salt makes it possible to increase both the primary and secondary strengths and the thermostability of the cores too (an increase in the bending strengths under 650 °C) which is advantageous and desirable in the high-pressure casting of Al-alloy castings. However, the questions about what changes will take place with respect to the bench life (hygroscopicity), the solubility of the composite cores and the surface quality of the pre-cast holes of the test castings as a result of the increased cooling effect of the cores (the presence of additives) remain to be answered.

**3.3 Bench life and the kinetics of solubility of the composite cores**

The hygroscopicity of salt cores (the bench life) and the solubility too belong to the key parameters of the application of salt cores. The hygroscopicity of the composite cores was measured under the conditions defined in advance, simulating the extreme conditions of storing the cores (RV = 100 %, T = 26 °C), with the additions of 30 % of individual additives corresponding to the theoretical maximum concentration of an additive (the economic and technological maximum). The hygroscopicity was defined as the increase in the mass fractions (%) in a given period of time (**Table 4**).

**Table 4:** Storability of composite salt cores

**Tabela 4:** Ustreznost za skladiščenje kompozitnih slanih jedra

| Number of days | K    | K + 30 % A | K + 30 % B | K + 30 % C |
|----------------|------|------------|------------|------------|
| 1              | 0.00 | 0.00       | 0.00       | 0.00       |
| 2              | 0.01 | 0.33       | 0.36       | 0.01       |
| 3              | 0.02 | 0.60       | 0.70       | 0.03       |
| 17             | 0.03 | 0.72       | 0.92       | 0.04       |
| 32             | 0.06 | 2.20       | 2.73       | 0.08       |

Note: K = KCl

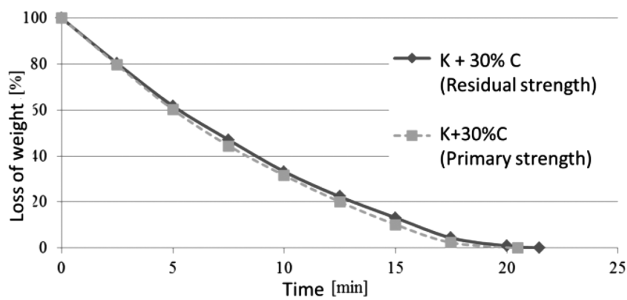


**Figure 2:** Solubility of composite cores (cold hardened and after thermal exposure), K = KCl

**Slika 2:** Topnost kompozitnih jeder (hladno utrjenih in po izpostavi toploti), K = KCl

With regard to the results of the experiment it is evident that the bench life of the salt cores, even under extreme conditions, is very good. No considerable increase in the weight of both the base salt matrix (the KCl sample) and the composite salt cores was observed. Only a low growth in the weight (the moisture) was observed for the cores consisting of the mixtures KCl + 30 % A (2.20 %) and KCl + 30 % B (2.73 %).

The solubility of the salt cores was modeled with the composite salt mixture KCl + 30 % C showing the lowest hygroscopicity during the determination of the core bench life.

The solubility of the composite salts was measured on the composite cores in water at a temperature of 20 °C, namely, in the cases of the cold-hardened ones (the primary strength) and the cores after the thermal exposure (650 °C, 1 h; the residual strength). The solubility was then defined as the weight loss of the cores in time dependence (**Figure 2**).

The results determining the solubility of the composite salt cores showed a high solubility of the composites (totally dissolved in up to 22 min), with no differences with regard to the thermal treatment of the cores.

The whole process can be speeded up with the movement, the temperature and the water pressure; in

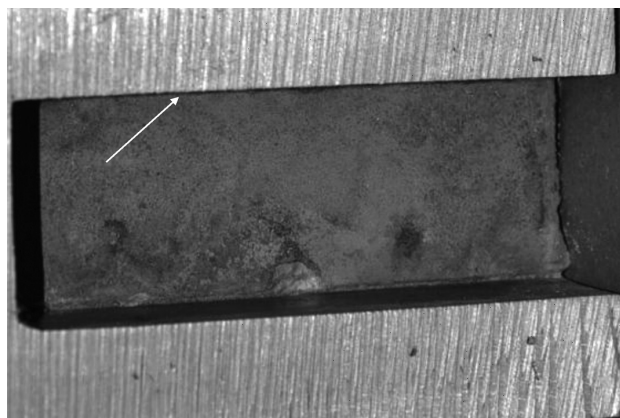


**Figure 3:** Area of a pre-cast hole in a model casting for a determination of the mean arithmetic roughness  $R_a$

**Slika 3:** Področje predizdelane odprtine na modelnem ulitku za določitev srednje aritmetične hrapavosti  $R_a$

spite of this the results showed that, during the storage, the additives or the thermally treated (up to 650 °C) cores influence neither the dissolution kinetics nor the core hygroscopicity.

### 3.4 Surface quality of the test castings

Samples of the composite salt cores with the compositions KCl + 15 % A and KCl + 15 % C prepared with the high-pressure squeezing were chosen for a determination of the surface quality of the pre-cast holes on a test casting (**Figure 3**). In spite of the fact that the apparent porosity of the squeezed cores was up to 4 % different spirituous coatings with different fillers were used for improving of the surface quality of the castings (**Table 5**).

**Table 5:** Basic characterization of the applied coatings

**Tabela 5:** Osnovne značilnosti uporabljenih premazov

| Coating | Filling agent                       |
|---------|-------------------------------------|
| a       | zircon silicate + aluminum silicate |
| b       | corundum                            |
| c       | base of zircon silicate             |

The values of the mean arithmetic roughness  $R_a$  of the test castings are summarized in **Table 6**. Most of the pre-cast holes show the surface roughness ( $R_a = 7.5-18.6 \mu\text{m}$ ) in dependence of the used additive and the coating, too.

**Table 6:** Mean arithmetic roughness of the test castings

**Tabela 6:** Srednja aritmetična hrapavost preizkusnih ulitkov

| Sample     | Coating | $R_a/\mu\text{m}$ |
|------------|---------|-------------------|
| K + 15 % A | c       | 7.5-10.4          |
| K + 15 % C | c       | 15.4              |
| K + 15 % C | b       | 18.6              |
| K + 15 % C | a       | 7.86              |

The best results were achieved in the case of the squeezed composite cores KCl + 15 % A using coating c with the viscosity at a discharge rate of 20 s (F. v.).

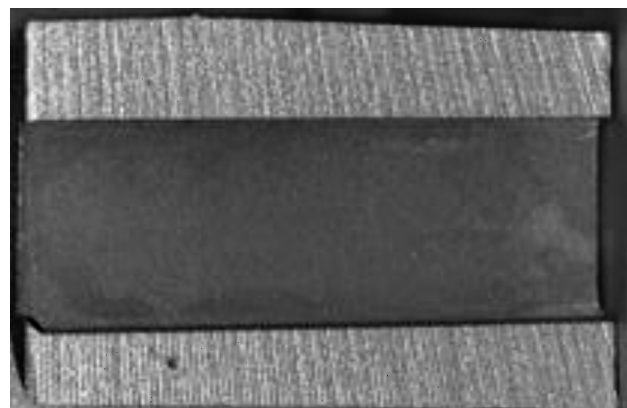


**Figure 4:** Detail of a test casting surface, K+15 % A

**Slika 4:** Detajl površine preizkusnega ulitka, K+15 % A



These castings showed smooth compact surfaces without any coating residues and with the value of  $R_a$  as  $7.5 \mu\text{m}$  (Figure 4).

#### 4 CONCLUSION

This contribution aimed at determining the influences of individual additives on the behaviour of the cores prepared with different methods (an injection and squeezing) during a production of the castings with a high surface quality of the pre-cast holes.

With regard to the results of the experiment involving the salt cores prepared with the warm-core-box method, it can be stated that, in this phase of the development, the cores prepared with this technology are applicable only for the gravity and low-pressure casting technologies.

The cores based on inorganic salts prepared with the high-pressure squeezing method show high primary and secondary strengths. Additions of additives do not influence the solubility of the salt cores (in static water it is up to 22 min). The whole process can be speeded up with mechanical actions, the temperature and the water pressure. On the other hand, the additions of additives

positively influence the surface roughness of the pre-cast holes of the test castings.

#### Acknowledgement

The research was done with the financial support of the Technological Agency of the Czech Republic within the Alfa Programme, TA 02011314.

#### 5 REFERENCES

- <sup>1</sup> P. Stingl, G. Schiller, Leichte und rückstandsfreie Entkernung, Gieserei Erfahrungsaustausch, (2009) 6, 4–8
- <sup>2</sup> P. Jelínek et al., Ověření solných jader na tlakově litém odlitku, Technológ, 4 (2013) 2, 17–22
- <sup>3</sup> P. Lichý, M. Cagala, D. Žáček, Thermomechanical properties of foundry magnesium alloys, Proc. of 20th Anniversary International Metallurgical and Materials Conference METAL 2011, Ostrava, 2011, 890–896
- <sup>4</sup> J. Malík, P. Futaš, I. Vasková, Š. Eperješi, Influence of technological factors of pressure die casting on quality of castings from silumin, Slévárenství, 55 (2007) 5/6, 259–262
- <sup>5</sup> P. Jelínek et al., Influencing the strength characteristics of salt cores soluble in water, Slévárenství, 60 (2012) 3/4, 85–89



# CARBIDE MORPHOLOGY AND FERRITE GRAIN SIZE AFTER ACCELERATED CARBIDE SPHEROIDISATION AND REFINEMENT (ASR) OF C45 STEEL

## MORFOLOGIJA KARBIDOV IN VELIKOST FERITNIH ZRN PO POSPEŠENI SFEROIDIZACIJI IN RAFINACIJI (ASR) JEKLA C45

Jaromir Dlouhy, Daniela Hauserova, Zbysek Novy

COMTES FHT, Prumyslova 995, 334 41 Dobruška, Czech Republic  
jdlohy@comtesfht.cz

*Prejem rokopisa – received: 2013-11-04; sprejem za objavo – accepted for publication: 2014-09-08*

doi:10.17222/mit.2013.270

The pearlite spheroidisation and grain refinement of the C45 steel was investigated. The ASR (accelerated carbide spheroidisation and refinement) process allows us to achieve a microstructure made of fine ferrite grains and globular carbides in seconds or minutes. This paper deals with the ASR process realization via the thermomechanical processing of controlled rolling. Hot rolling is a common part of structural steel processing. A conventional structure after the hot rolling of the C45 steel consists of lamellar pearlite and ferrite. During controlled rolling with a deformation at temperatures around critical temperature  $A_1$ , it is possible to achieve a microstructure of a fine ferritic matrix and globular carbides. The deformation causes a recrystallization of the ferritic matrix – a grain refinement. Furthermore, a high dislocation density during the deformation enhances the diffusion and promotes carbide spheroidisation. The aim of the experimental program was to achieve a microstructure of the C45 steel consisting of fine ferritic grains and homogeneously dispersed cementitic globular particles by processing bars in a laboratory rolling mill. The morphological changes of the cementite after the thermomechanical treatment in comparison with the conventional hot rolling were investigated as well as the ferritic grain refinement. An image analysis was performed to determine the spheroidisation level of the cementite (the aspect ratio of cementite particles) and the ferritic grain size. A proper examination of a cementite morphology can be carried out only by observing the entire cementite particle. A common metallographic analysis relies on a 2D section observation. Thus, deep etching and cementite extraction were performed to study the cementite-particle shape formed during the ASR process.

Keywords: accelerated spheroidisation, carbide morphology, rolling, C45 steel

Preiskovana je bila sferoidizacija perlita in zmanjšanje zrn v jeklu C45. Proces ASR (pospešena sferoidizacija perlita in rafinacija) omogoča v nekaj sekundah ali minutah doseči mikrostrukturo iz drobnih feritnih zrn in globularnih karbidov. Ta članek predstavlja izvedbo ASR-procesa s termomehansko obdelavo pri kontroliranem valjanju. Vročje valjanje je znan postopek pri preoblikovanju jekla. Navadno je mikrostruktura po vročem valjanju jekla C45 iz lamelnega perlita in ferita. Pri kontroliranem valjanju, z deformacijo pri temperaturah okrog kritične temperature  $A_1$ , je mogoče doseči mikrostrukturo iz drobnozrnate feritne osnove in globularnih karbidov. Deformacija povzroči rekristalizacijo feritne osnove in zmanjšanje velikosti zrn. Poleg tega velika gostota dislokacij med deformacijo pospešuje difuzijo in spodbuja sferoidizacijo karbidov. Namen programa preizkusov je bil doseči pri jeklu C45 mikrostrukturo iz drobnih feritnih zrn in homogeno razporejenimi globularnimi cementitnimi delci z valjanjem palic pri laboratorijskem valjanju jekla. Preiskovane so bile spremembe v morfologiji cementita po termomehanski obdelavi v primerjavi z navadnim vročim valjanjem, kot tudi udrobnjenje feritnih zrn. Stopnja sferoidizacije cementita (razmerje med dolžino in debelino cementitnih delcev) in velikosti feritnih zrn je bila izvršena z analizo slik. Pravilen pregled morfologije cementita je lahko izveden samo z opazovanjem celotnega cementitnega delca. Navadne metalografske analize se opirajo na 2D-opazovanje prereza. Za študij oblike cementitnih delcev, ki nastajajo med ASR-procesom, je bilo zato izvršeno globoko jedkanje in ekstrakcija cementita.

Ključne besede: pospešena sferoidizacija, morfologija karbidov, valjanje, jeklo C45

## 1 INTRODUCTION

Carbide spheroidisation is an integral part of processing many types of steel, especially high-carbon steels. The ASR process (accelerated carbide spheroidisation and refinement) can also be used for mild-carbon steels as a way of strengthening them and enhancing their toughness.

To quantify carbide spheroidisation, an image analysis of the micrographs of a metallographic section is usually used. This 2D view of a steel structure cannot provide reliable information about the real 3D shape of cementite particles. A morphological development from carbide lamellae to globular particles includes the exi-

stence of complicated carbide shapes which can only be determined with a 3D view.

A carbide morphology in different stages of spheroidisation is directly observable with SEMs of extracted carbides, 3D tomography using FIB SEM<sup>1</sup> or TEM of extracted carbide particles.<sup>2</sup>

This article describes the cementite morphology in the C45 steel after the ASR process. The experimental steel was thermomechanically treated in order to achieve a different degree of cementite spheroidisation and ferritic grain size. The degree of carbide spheroidisation was determined with the conventional metallographic-section method. A direct observation of the cementite particles

extracted from the ferritic matrix was performed to reveal the spheroidisation mechanism.

## 2 EXPERIMENTAL WORK

### 2.1 Material

The experimental program was performed using structural carbon steel C45 with the chemical composition shown in **Table 1**. The initial state was a hot-rolled bar 50 mm in diameter. The hardness of the as-received material was 180 HV<sub>30</sub>. The initial dimensions of the specimens for the thermomechanical treatment were a length of 330 mm, a width of 50 mm and a height of 30 mm.

**Table 1:** Chemical composition of C45 steel (w/%)

**Tabela 1:** Kemijska sestava jekla C45 (w/%)

| C    | Si   | Mn   | S     | P     | Cr   | Ni   | Cu   | Mo   | W    |
|------|------|------|-------|-------|------|------|------|------|------|
| 0.42 | 0.24 | 0.69 | 0.019 | 0.016 | 0.12 | 0.16 | 0.12 | 0.02 | 0.01 |

### 2.2 Thermomechanical treatment

The thermomechanical treatment was carried out on a laboratory rolling mill at a duo configuration. The roll's diameter was 550 mm, the maximum width of the sheet was 400 mm and the range of the sheet thickness was from 5 mm to 100 mm. The maximum rolling speed was 1.5 m/s. This speed was also chosen for the experiment. The rolling mill was equipped with pyrometers on both sides of the mills monitoring the specimen temperature. The temperature was measured in the specimen centre.

Regimes of the thermomechanical processing were chosen to reveal the influence of the deformation temperature and intensity upon the final ferritic grain size and carbide morphology.

The regimes for the accelerated pearlite spheroidisation consisted of a deformation at temperature  $T_{D1} = 850$  °C (a single thickness reduction from 30 mm to 20 mm) and air cooling of the samples to 675 °C. Then the temperature rose to about 683 °C due to the latent heat of the pearlitic transformation and decreased again. The second deformation was introduced when the temperature of the samples decreased again to  $T_{D2} = 675$  °C after the pearlitic transformation, as seen in **Figure 1**. The second deformation consisted of a single reduction (from the

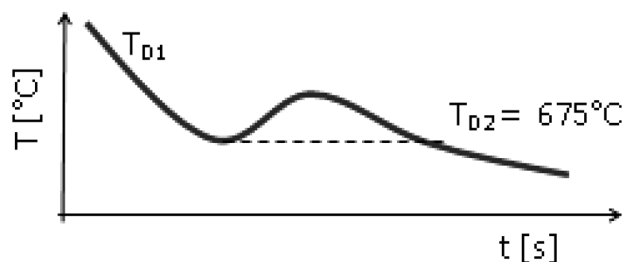


**Figure 1:** Transformation stages, at which deformation was applied  
**Slika 1:** Transformacijske faze, pri katerih je bila izvršena deformacija

thickness of 20 mm to 12 mm) or two reductions (20 mm → 12 mm and 12 mm → 7 mm) introduced in 10 s.

The regimes for a combination of carbide spheroidisation and ferritic grain refinement were also performed. The samples austenitized at 850 °C were cooled on air to 710 °C, deformed (a single thickness reduction from 30 mm to 20 mm) and cooled down. Samples 2, 3, 5 and 6 were deformed at a temperature of 675 °C after the pearlitic transformation with one or two reductions.

### 2.3 Carbide-morphology examination

The metallographic section from each sample was prepared and etched in the Nital etchant. The degree of carbide spheroidisation was quantified with an image analysis of 10 micrographs at a 5000-times SEM magnification. The Nis Element software<sup>3</sup> was used for the image analysis. Each image was turned into a binary image and the carbides were measured. The area, length and width of each carbide particle were measured automatically. The aspect ratio (AR) was computed as the particle length divided by its width. The measured carbides were subsequently divided into categories according to their ARs. The cementite percentage for each category was computed as the area percentage of carbides in each category to the overall cementite area.

The real 3D morphology of cementite particles was revealed by deep etching the samples in Nital for 60 min. Carbide particles were extracted with ultrasound in an alcohol bath, spread onto a copper pad and observed with SEM.

## 3 RESULTS AND DISCUSSION

### 3.1 Metallographic observation

#### 3.1.1 Carbide distribution and the ferritic grain size

The microstructures of samples 1 and 4 (**Table 2**) were ferrite-pearlite with lamellar pearlite. Both ferritic and pearlitic grains were mostly polygonal and equiaxed. The ferritic grains in sample 1 exhibited a uniform size between 10 μm and 20 μm. Sample 4 exhibited two types of ferritic grains. Most of the ferrite was present as equiaxed grains with a diameter from 20 μm to 30 μm. About 15 % of ferrite was in the form of fine equiaxed grains with a diameter from 2 μm to 4 μm. These finely grained areas were about 20 μm large, while the ferritic

**Table 2:** List of schedules

**Tabela 2:** Seznam opravljenih deformacij

| Regime | Preheating       | First deformation       | Second deformation      |
|--------|------------------|-------------------------|-------------------------|
| 1      | 850 °C<br>60 min | 850 °C; $\varphi = 0.4$ | –                       |
| 2      |                  | 850 °C; $\varphi = 0.4$ | 675 °C; $\varphi = 0.5$ |
| 3      |                  | 850 °C; $\varphi = 0.4$ | 675 °C; $\varphi = 1$   |
| 4      |                  | 710 °C; $\varphi = 0.4$ | –                       |
| 5      |                  | 710 °C; $\varphi = 0.4$ | 675 °C; $\varphi = 0.5$ |
| 6      |                  | 710 °C; $\varphi = 0.4$ | 675 °C; $\varphi = 1$   |

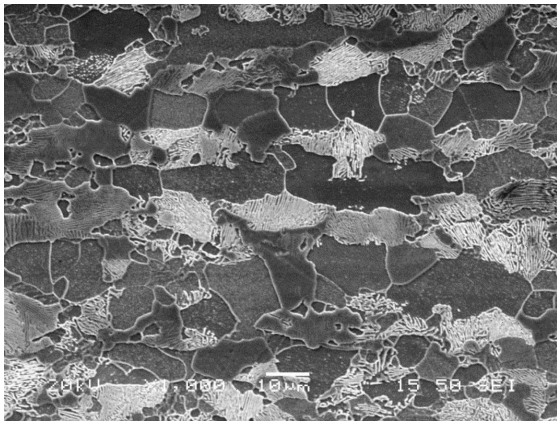


**Figure 2:** Regime 4: ferrite pearlite structure with fine-grained areas  
**Slika 2:** Režim 4: feritno-perlitna struktura s področji drobnostnosti

and pearlitic grains of the same size were mixed together (**Figure 2**). It is assumed that the deformation-induced ferritic transformation took place in these regions during the rolling at 710 °C.

The elongation of the structure was caused by further reduction(s) at the temperature of 675 °C. The cementite was still located in the elongated pearlitic region; the redistribution of the cementite into the originally ferritic areas was not observed. The elongated ferritic grains exhibited a deformation substructure (**Figure 3**).

### 3.1.2 Carbide spheroidisation

The deformation introduced at the temperature of 675 °C after the pearlitic transformation caused a rapid fragmentation of the pearlitic lamellae and a cementite spheroidisation. Samples 2 and 5 exhibited the same cementite morphology and so did samples 3 and 6. Thus, the temperature of the first deformation (850 °C or 710 °C) did not affect the cementite morphology.

Pearlitic lamellae of samples 2 and 5 were fragmented; the image analysis of the metallographic-section micrographs showed a significant amount of cementite

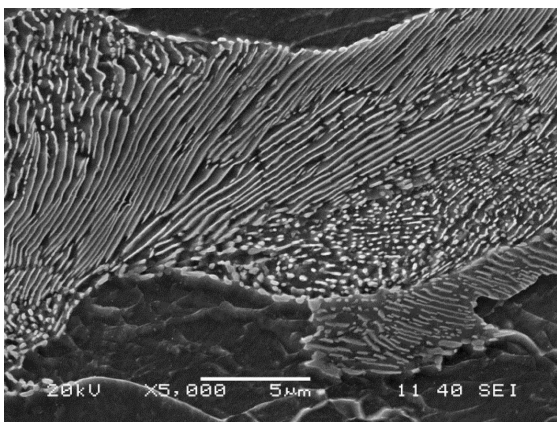


**Figure 3:** Regime 2: metallographic section shows partially fragmented and spheroidised cementite lamellae

**Slika 3:** Režim 2: metalografski prerez prikazuje delno fragmentirane in sferoidizirane cementitne lamele

with a fully spheroidised shape (**Table 3**). However, deep etching and cementite extraction revealed cementite lamellae of a complicated shape with many holes and branches and almost no isolated cementite particles.

**Table 3:** Aspect ratio of cementite particles in samples 2, 3, 5 and 6 deformed in the ferritic-pearlitic state

**Tabela 3:** Razmerje med dolžino in debelino cementitnih delcev v vzorcih 2, 3, 5 in 6, deformiranih v feritno-perlitnem stanju

| Aspect ratio | Fraction (%) |        |        |        |
|--------------|--------------|--------|--------|--------|
|              | Reg. 2       | Reg. 3 | Reg. 5 | Reg. 6 |
| 1–3          | 20.8         | 19.8   | 24.7   | 24.8   |
| 3–6          | 15.9         | 14.9   | 18.3   | 19.0   |
| 6–12         | 20.1         | 19.5   | 22.6   | 23.1   |
| > 12         | 43.2         | 45.8   | 34.3   | 33.1   |

A deformation with intensity  $\varphi = 0.5$  at the temperature of 675 °C (samples 2 and 5) did not cause the main fragmentation of the cementite lamellae into smaller pieces but rather into branches and "lace-like" shapes (**Figure 4**). The cementite lamellae were transformed into a mixture of rods/branches connected together, still following the original shape and size of the cementite lamella. The cementite rods/branches were mostly segmented and were observed as chains of intersecting globular particles. The segments usually had a diameter of 0.1  $\mu\text{m}$  to 0.3  $\mu\text{m}$ .

A deformation with intensity  $\varphi = 1$  at the temperature of 675 °C (samples 3 and 6) caused a pearlitic-structure fragmentation and spheroidisation according to the conventional metallography as well as deep etching and carbide extraction. The cementite lamellae were fragmented into objects, usually of up to 3  $\mu\text{m}$  in the longest direction. These fragments were segmented into globular connected particles. Isolated globular cementitic particles in the same size range were also observed (**Figure 5**).

One third of the pearlite in the structures of samples 3 and 6 (**Table 2**) remained non-fragmented and la-

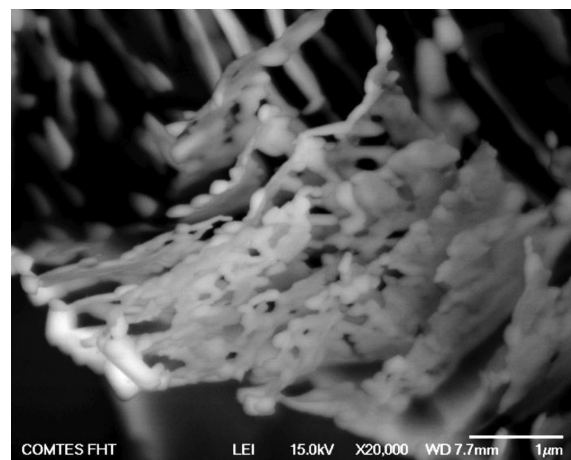


**Figure 4:** Regime 2: deep etching revealed branched remnants of original pearlite lamellae and almost no globular particles

**Slika 4:** Režim 2: globoko jedkanje odkrije razvejane ostanke originalnih perlitnih lamel in skoraj nič globularnih delcev

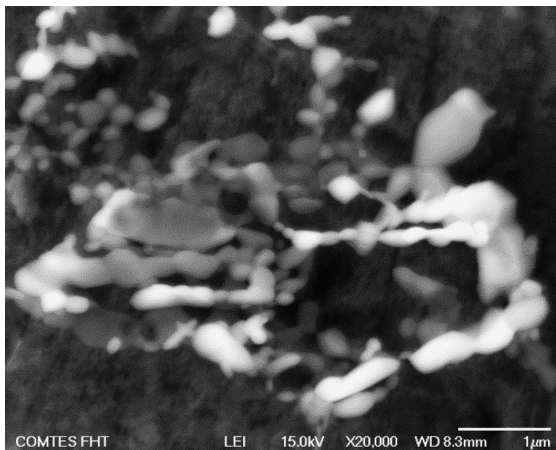


**Figure 5:** Regime 3: extracted cementite; lamella fragments and globular particles

**Slika 5:** Režim 3: izolirani cementit; delci lamel in globularni delci

mellar. The pure lamellar form differs significantly from the predominantly observed highly fragmented or spheroidised morphology. A possible explanation is that the lamellar pearlite could have been formed after the last deformation. The temperature of 675 °C after the temperature peak during the pearlitic transformation was probably not sufficiently low to ensure a complete austenite decomposition.

#### 4 CONCLUSION

The thermomechanical treatment of the C45 steel showed changes in the ferritic grain size and cementite morphology according to the deformation temperature and intensity.

The deformation prior to the pearlitic transformation had a significant influence on the ferritic grain size. A uniform structure with a ferritic grain size of about 15 µm was obtained with the conventional hot rolling at 850 °C. The deformation during the air cooling at a temperature of 710 °C caused a formation of fine ferritic grains

of up to 3 µm in diameter; however, most of the ferrite was formed before in the form of ten-times-larger grains.

The pearlitic transformation of austenite resulted in a lamellar cementite morphology at both temperatures of the austenite deformation (850 and 710 °C – the under-cooled austenite).

The cementite morphology was influenced by the deformation of pearlite. The deformation at 675 °C after the pearlitic transformation caused a fragmentation of the cementite lamellae. The deformation with intensity  $\varphi = 0.5$  induced holes and branching of the original cementite lamellae. The deformation with intensity  $\varphi = 1$  caused a cementite-lamella fragmentation. Fragments with the maximum size of 3 µm were observed in the structure and a significant amount of globular cementite particles, mostly with a diameter of 0.1 µm to 0.3 µm, were also formed.

A more homogeneous dispersion of cementitic globular carbides in the ferritic matrix can be ensured with the formation of fine proeutectoid ferrite. Further experiments will be focused on the ferrite grain refinement with a deformation above temperature  $A_{c1}$ .

#### Acknowledgment

The results presented in this paper were obtained under project West-Bohemian Centre of Materials and Metallurgy CZ.1.05/2.1.00/03.0077, co-funded by the European Regional Development Fund.

#### 5 REFERENCES

- <sup>1</sup> Y. Adachi, K. Nakajima, Y. Sugimoto, Quantitative three-dimensional characterization of pearlite spheroidization, *Acta Materialia*, 58 (2010), 4849–4858, doi:10.1016/j.actamat.2010.05.023
- <sup>2</sup> Y. L. Tian, R. W. Kraft, Mechanisms of Pearlite Spheroidisation, *Metallurgical Transactions A*, 18 (1987) 8, 1403–1414, doi:10.1007/BF02646654
- <sup>3</sup> Nis-Element software, internet site of the producer: <http://www.nis-elements.cz/en/front-page>

# USE OF MICROMACHINING TO SHAPE THE STRUCTURE AND ELECTRICAL PROPERTIES OF THE FRONT ELECTRODE OF A SILICON SOLAR CELL

## UPORABA MIKROOBDELOVANJA ZA OBLIKOVANJE STRUKTURE IN ELEKTRIČNIH LASTNOSTI PREDNJE ELEKTRODE SILICIJEVE SONČNE CELICE

Małgorzata Musztyfaga-Staszuk

Silesian University of Technology, Welding Department, Konarskiego Street 18a, 44-100 Gliwice, Poland  
malgorzata.musztyfaga@polsl.pl

Prejem rokopisa – received: 2014-07-07; sprejem za objavo – accepted for publication: 2014-09-05

doi:10.17222/mit.2014.099

The aim of the work was to study the influence of the front-electrode structure produced with the conventional and unconventional techniques on the electrical properties of silicon solar cells. The investigations were performed on a front electrode produced with the conventional sintering technique in an infrared conveyor furnace and an electrode produced with the unconventional technique of selective laser sintering with a paste based on a silver powder. The investigations of the structure and properties of the front electrodes as well as the electrical properties of the obtained silicon solar cells were performed. The investigations were done on monocrystalline silicon wafers. A special test system was prepared to evaluate the contact resistance of the silver-silicon contact. The front contacts were formed on the surfaces with different morphologies. An optimum model of the front electrode and the area of its connection with the substrate is presented, enabling the best electrical properties of photovoltaic cells. The paper gives a broad general knowledge necessary for solving the problems relating to solar cells.

Keywords: nanosciences and nanotechnologies, selective laser sintering, silicon solar cell, contact resistance, TLM method

Namen dela je bil študij vpliva strukture sprednje elektrode, proizvedene po običajni in neobičajni metodi, na električne lastnosti silicijeve sončne celice. Preiskave so bile izvršene na sprednji elektrodi, izdelani po običajni metodi z infrardečim sintranjem na traku kontinuirne peči, in na elektrodi, izdelani z neobičajno tehniko selektivnega laserskega sintranja s pasto na osnovi srebra v prahu. Izvršene so bile preiskave strukture in lastnosti sprednje elektrode, kot tudi električne lastnosti dobljene silicijeve sončne celice. Preiskave so bile izvršene na monokristalni silicijevi rezini. Za oceno upornosti stika srebro-silicij je bil pripravljen poseben preizkusni sistem. Sprednji kontakt je bil pripravljen na površini z različno morfologijo. Predstavljena sta optimalni model sprednje elektrode in področje njenega stika s podlago, ki omogoča najboljše električne lastnosti fotovoltaične celice. Članek daje izhodišča za novo znanje pri reševanju problemov s področja sončnih celic.

Ključne besede: nanoznanost in nanotehnologija, selektivno lasersko sintranje, silicijeva sončna celica, upornost stika, TLM-metoda

## 1 INTRODUCTION

The whole industry and the life of the average man depend on the electrical energy. One of the methods to acquire the solar energy is the use of photovoltaic cells. For the production of photovoltaic cells we can apply many semiconductor materials, such as silicon (poly- and monocrystalline, amorphous), gallium arsenide, cadmium telluride, cadmium-copper selenide, indium phosphide and conducting polymers.<sup>1-3</sup> For example, monocrystals have very good properties and good cell efficiency in the mass production (14–18 %), but they are expensive. Therefore, research studies are being carried out to find new solutions involving the production technology and indispensable tools used for this purpose, aiming to raise the cell efficiency with the minimum reduction of the material consumption.<sup>1,4-8</sup>

One of such emerging production operations involving photovoltaic cells is the deposition of electrical contacts. As it has been found by numerous research studies,

the electrode coating should satisfy different requirements to ensure a low resistance of the interface zone between the electrode and the substrate. A proper selection of the material (for the electrode and the substrate), the conditions of its fabrication, the shape and size of the electrode, the adhesion of the electrode to the substrate and the substrate morphology are of particular importance. In order to improve the electrical properties

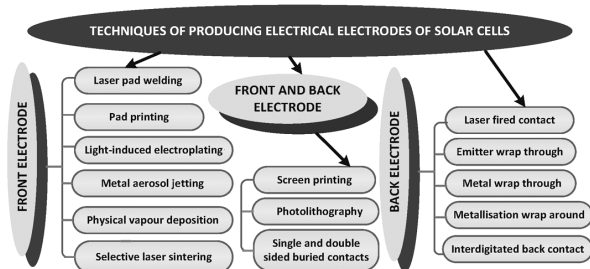


Figure 1: Classification of front and back electrodes<sup>9</sup>  
Slika 1: Klasifikacija prednje in zadnje elektrode<sup>9</sup>

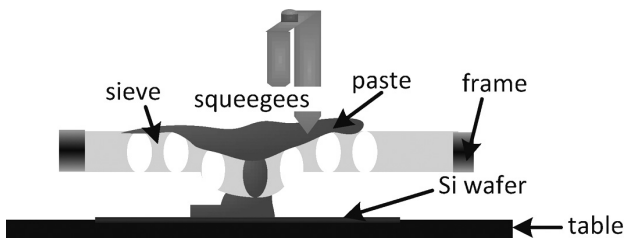


Figure 2: Screen-printing method<sup>10</sup>  
Slika 2: Metoda sitotiska<sup>10</sup>

of the front electrode, various fabrication techniques have already been analyzed (Figure 1), including different imprint techniques and the final connection of the electrode with the substrate surface. This paper summarizes the recent investigations into the front-side metallization achieved with the conventional technique (Figure 2) in comparison with an unconventional technique (Figure 3).<sup>9-11</sup>

2 STUDY MATERIAL AND SAMPLE PREPARATION

The investigations were done on monocrystalline silicon wafers. The basic parameters of these wafers were: the conductivity – the p type; the dopant element – boron; the thickness – (200 ± 20) μm and (330 ± 10) μm; the resistivity – 1–2 Ω cm and ≈ 1 Ω cm; the area – 25 cm<sup>2</sup>. Micromachining was applied to a wafer with a thickness of ≈ 330 μm, and during the co-firing in a furnace its thickness was ≈ 200 μm. For the fabrication of front electrodes, silver pastes were applied (Table 1), experimentally elaborated on the basis of a silver powder with a granulation < 40 nm (Figure 4), an organic carrier and silicon dioxide. The technology to produce solar

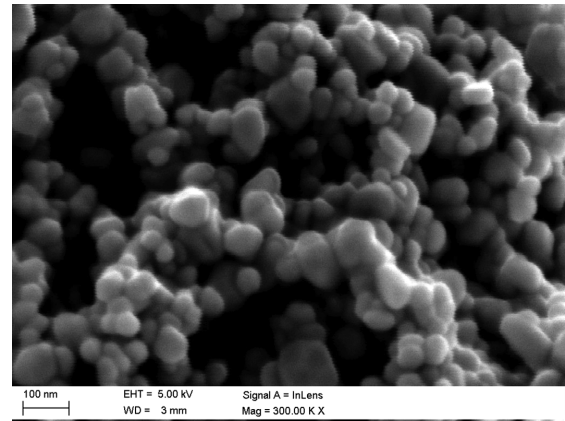


Figure 4: SEM micrograph of silver-powder granulation < 40 nm  
Slika 4: SEM-posnetek granulacije prahu srebra < 40 nm

Table 1: Paste prepared and used for the front metallization  
Tabela 1: Pasta, pripravljena in uporabljena pri srednji metalizaciji

| Paste symbol | Powder size | Applied method (conventional, unconventional) |
|--------------|-------------|-----------------------------------------------|
| H1           | < 40 nm     | Unconventional                                |
| H2           | < 40 nm     | Conventional                                  |

cells was developed at the Institute of Metallurgy and Materials Science in Krakow (Poland). Front contacts were formed on the surfaces of solar cells with various morphologies (textured with a deposited antireflection layer and textured without a deposited antireflection layer, non-textured with a deposited antireflection layer and non-textured without a deposited antireflection layer). Two special test electrode systems were prepared with the screen-printing method in order to determine the suitability of the silver pastes using the two techniques and to evaluate the contact resistance of the metal semiconductor junction, where the sizes of the front paths were X = 2 mm × 10 mm (width × length), with the distances between them being (20, 10, 5 and 2.5) mm, and Y = 5 mm × 10 mm (width × length), with the distances between them being (1, 2, 4 and 8) mm.

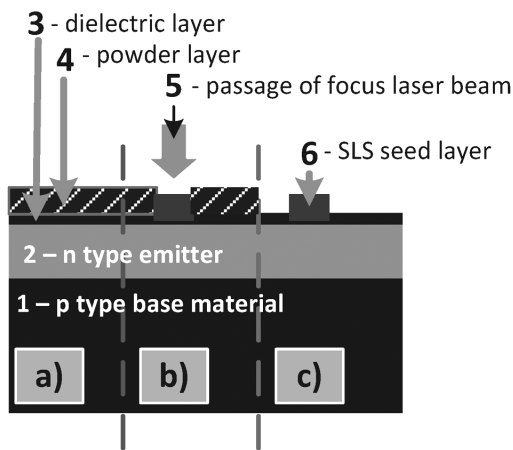


Figure 3: Technology for the formation of front contacts using selective laser sintering (SLS): a) a metallic powder is applied to the Si wafer, b) a laser beam heats the powder locally and melts it into metal lines on the top of the Si wafer, c) the excess metallic powder is moved into the container<sup>9,11</sup>

Slika 3: Tehnologija tvorbe prednjih kontaktov s selektivnim laserskim sintranjem (SLS): a) kovinski prah na Si-rezini, b) laserski žarek ogreva prah lokalno in napravi talilne linije na Si-rezini, c) presežek kovinskega prahu se odvede v zbiralnik<sup>9,11</sup>

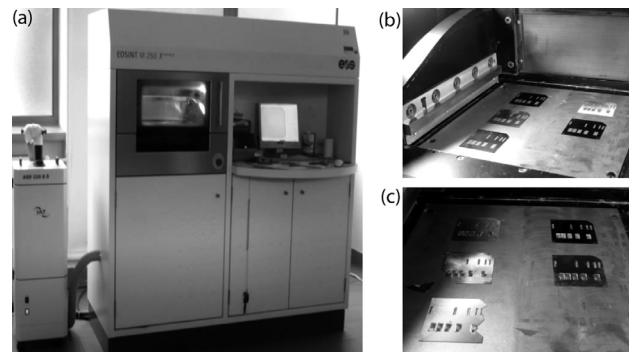


Figure 5: Laser micro-treatment system: a) the EOSINT M 250 Xtended device was equipped with CO<sub>2</sub> laser, b) samples before SLS in a working chamber, c) samples after SLS in a working chamber<sup>12</sup>

Slika 5: Sistem za mikroobdelavo z laserjem: a) naprava EOSINT M 250 Xtended je opremljena s CO<sub>2</sub>-laserjem, b) vzorci pred SLS v delovni komori, c) vzorci po SLS v delovni komori<sup>12</sup>



The laser micromachining conditions for the test electrode system  $X, Y$  were selected for the selective laser sintering (Table 2). Figure 5 presents the laser micro-treatment system.<sup>12</sup>

**Table 2:** Conditions of laser micro-treatment of test electrodes of solar cells

**Tabela 2:** Razmere pri laserski mikroobdelavi preizkusnih elektrod sončnih celic

| Paste symbol | Height of printed front electrode ( $\mu\text{m}$ ) | Feed rate of laser beam, ( $v/(\text{mm/s})$ ) | Laser beam ( $P/W$ ) |
|--------------|-----------------------------------------------------|------------------------------------------------|----------------------|
| H1           | 15                                                  | 38, 41, 43                                     | 50                   |

Table 3 presents some solar cells with the test electrode system  $X, Y$ , prepared for co-firing on conveyor belt IR, which was equipped with fitted tungsten-filament lamps, heating both the top and the bottom of the belt.

**Table 3:** Conditions of co-firing test electrodes of solar cells in the furnace

**Tabela 3:** Razmere pri žganju preizkusnih elektrod sončne celice v peči

| Paste symbol | Height of printed front electrode ( $\mu\text{m}$ ) | Temperature in zone III ( $^{\circ}\text{C}$ ) |
|--------------|-----------------------------------------------------|------------------------------------------------|
| H2           | 15                                                  | 830                                            |
|              |                                                     | 860                                            |
|              |                                                     | 890                                            |
|              |                                                     | 920                                            |
|              |                                                     | 945                                            |

Comparative investigations were performed on the electrical parameters such as the contact resistance, the specific contact resistance ( $\rho_c$ ) and the transfer length ( $L_T$ ) of the front electrodes of the solar cell using the traditional transmission-line-model method (TLM), based on a simultaneous extraction of the electric-current signal ( $I$ ) between the chosen front contacts and the potential difference ( $U$ ) intrinsically generated on them. The resistance  $R$  was measured and a graph of  $R$  against the distance was constructed. From the obtained data the parameters  $R_c, \rho_c, L_T$  were determined. The topographies of both the surfaces and the cross-sections of the front contacts were observed, using a SEM microscope (Zeiss Supra 35). Also, the topography of the textured monocrystalline silicon wafer was observed, using an atomic-force microscope (Park Systems XE 100). The medium size of the pyramids was measured using this microscope.

### 3 RESULTS AND DISCUSSION

The optimum test electrode was selected by the researcher taking into account the paste composition (including the powders with different granulations), the conditions of its fabrication, its shape and size, the lowest resistance value of the joint between the electrode and the substrate, the substrate morphology and the

quality of the structure obtained on the surface and cross-section.

The performance of the front electrodes of the semiconductors can be studied by measuring the value of specific contact resistance  $\rho_c$  (characterized by the connection zone between the contact and the silicon substrate and the regions directly under and below the surface of the phase separation), contact resistance  $R_c$  (Figure 6) and transfer length  $L_T$ . These parameters can be specified with a method based on TLM. The specific contact resistance of the front electrode for given current values of (10, 30, 50) mA were determined, depending on the conditions of the unconventional (Figure 7a) and conventional (Figure 7b) methods.

**The unconventional method:** With the investigations based on the electrical properties, using the TLM method, it was found that the smallest specific-contact-resistance values of test electrodes  $X, Y$  were  $0.1\text{--}12 \Omega \text{ cm}^2$  and  $0.4\text{--}2.2 \Omega \text{ cm}^2$ , respectively, for the solar cells with different morphologies. The minimum value of the specific contact resistance was obtained for test electrode system  $X$  ( $0.1 \Omega \text{ cm}^2; 0.2 \Omega \text{ cm}^2$ ) (min.  $\rho_c = 0.1$

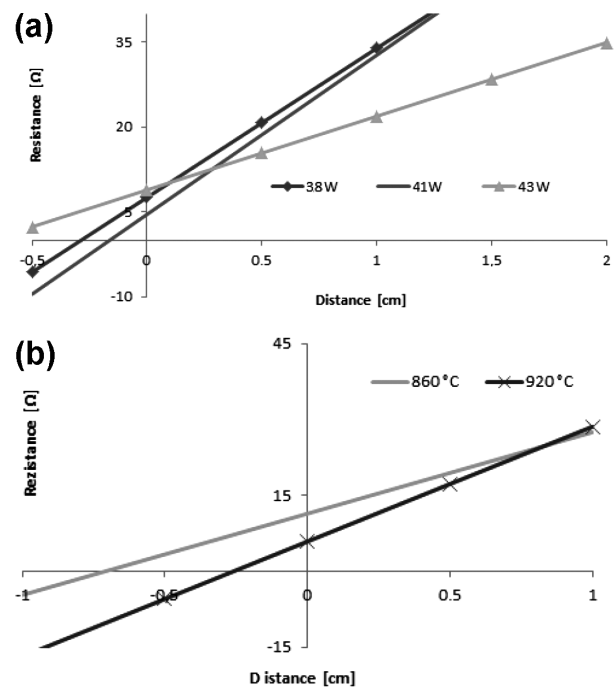


**Figure 6:** Dependence of the contact resistance of the emitter with varying distance  $Y$  between the adjacent special test electrode systems: a) on the laser-beam power for paste H1 on a silicon solar cell with ARC layer and with the texture selectively laser sintered with the feed rate of 50 mm/s, b) on the co-fired temperature for paste H2 on a silicon solar cell without ARC layer and with texture (the example with the smallest parameters –  $\rho_c, L_T$  and  $R_c$  – for a given value of the current: 10 mA)

**Slika 6:** Odvisnost upornosti spoja od oddajnika pri spreminjanju razdalje  $Y$  med mejnima elektrodinima sistemoma: a) na moč laserskega žarka pri pasti H1 na silicijevo sončno celico z ARC-nanosom in s teksturo, selektivno lasersko sintrano s hitrostjo podajanja 50 mm/s, b) na temperaturo žganja pri pasti H2 na silicijevo sončno celico brez ARC-nanosa in s teksturo (izbran primer za najmanjše parametre:  $\rho_c, L_T$  in  $R_c$ , pri dani vrednosti toka: 10 mA)

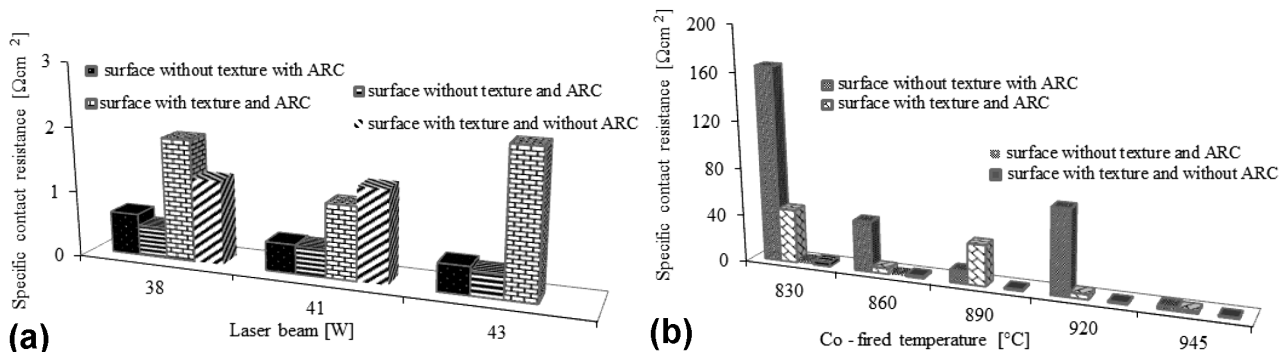


**Figure 7:** Specific contact resistance depending on: a) laser micro-treatment conditions where electrodes were obtained from paste H1, b) conditions of co-firing in the furnace where electrodes were obtained from paste H2 (the example for test electrode system Y)

**Slika 7:** Specifična upornost kontakta, odvisna od: a) razmer pri laserski mikroobdelavi, kjer so bile elektrode pripravljene iz H2-paste, b) dodatno žgano v peči, elektrode pripravljene s H2-pasto (izbrani vzorec za preizkus sistema elektrod Y)

$\Omega \text{ cm}^2$ ,  $P = 41 \text{ W}$ ) on the substrate without texture and the  $\text{TiO}_x$  coating of the solar cell. In the case of test electrode system Y the specific contact resistance was  $0.4\text{--}2.2 \Omega \text{ cm}^2$ . The minimum value of the specific contact resistance was obtained for test electrode system Y ( $0.4 \Omega \text{ cm}^2$ ;  $0.5 \Omega \text{ cm}^2$ ) (min.  $\rho_c = 0.4 \Omega \text{ cm}^2$ ,  $P = 41$

W) on the substrate without texture and the  $\text{TiO}_x$  coating of the solar cell.

**The conventional method:** With the investigations based on the electrical properties, using the TLM method, it was found that the smallest specific-contact-resistance values of test electrode system X, Y were  $1.8\text{--}86.8 \Omega \text{ cm}^2$ ,  $1.1\text{--}165.6 \Omega \text{ cm}^2$ , respectively, for the

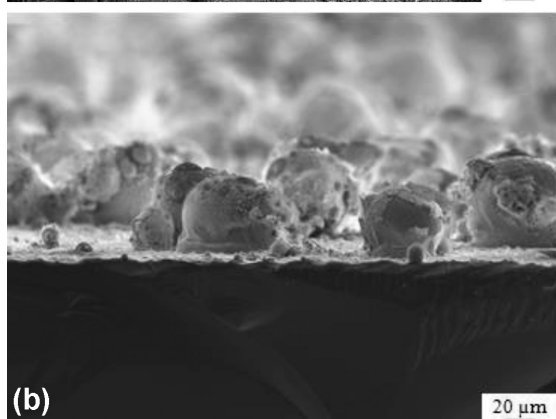
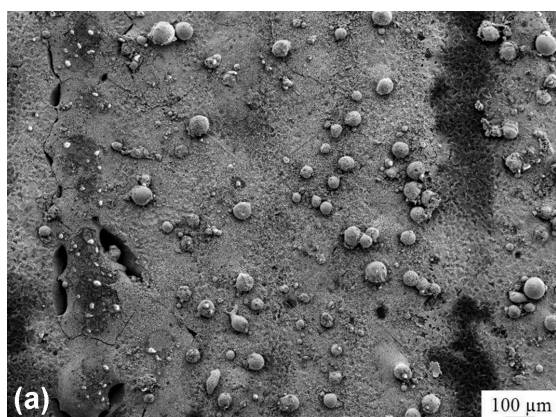


**Figure 8:** SEM of the surface layer obtained from paste H1 on the silicon surface and deposited with the screen-printing method and laser sintered with a laser-beam feed rate of  $50 \text{ mm/s}$  and the maximum laser-beam power of  $41 \text{ W}$ : a) topography image, b) fracture image

**Slika 8:** SEM-posnetka površine, nastale iz H1-paste na površini silicija in nanese na metodo sitotiska, lasersko sintrano z laserskim žarkom s podajanjem  $50 \text{ mm/s}$  in največjo močjo laserja  $41 \text{ W}$ : a) posnetek topografije, b) posnetek preloma

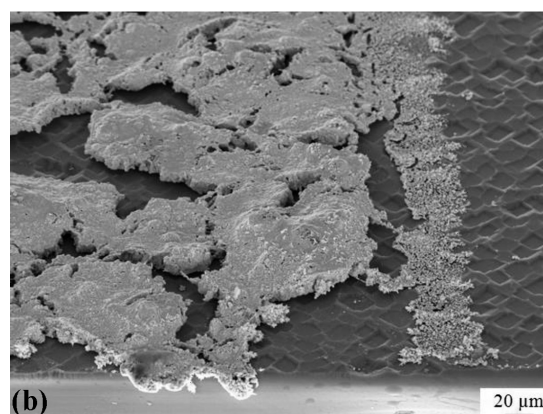
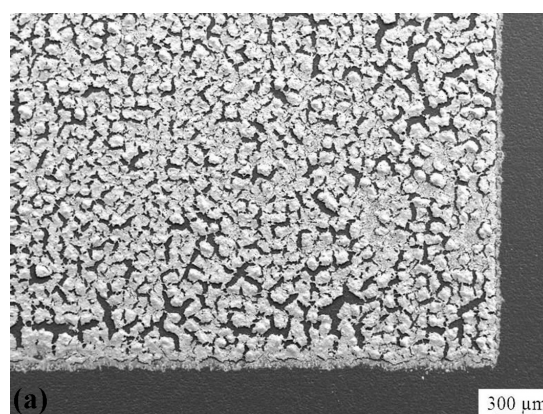


**Figure 9:** SEM of front contact layer obtained from paste H2 and co-fired in the conveyor furnace at  $945 \text{ }^{\circ}\text{C}$  on Si substrate without texture and ARC layer: a) topography image, b) fracture image

**Slika 9:** SEM-posnetka sprednjega sloja kontakta, nastalega iz H2-paste in pri žganju v peči s transporterjem pri  $945 \text{ }^{\circ}\text{C}$  na podlagi iz Si, brez teksture in ARC-nanosa: a) posnetek topografije, b) posnetek preloma

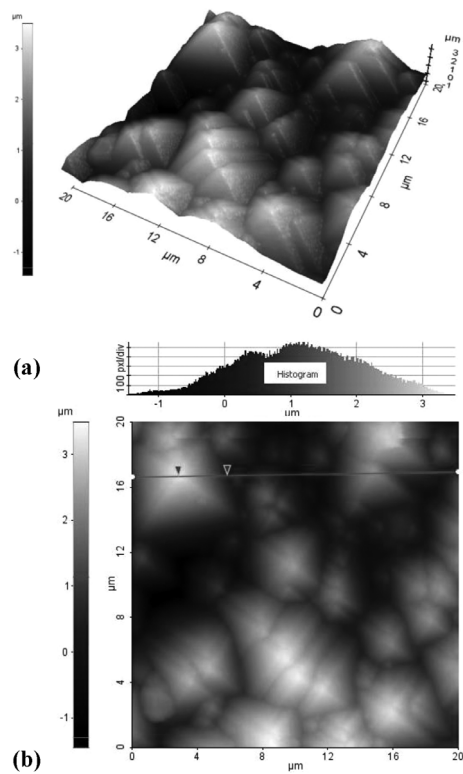


**Figure 10:** Topography of the textured surface of a monocrystalline solar wafer with a thickness of  $\approx 330 \mu\text{m}$  (AFM)

**Slika 10:** Topografija teksturirane površine monokristalne solarne rezine z debljino  $\approx 330 \mu\text{m}$  (AFM)

solar cells with different morphologies. The minimum value of the specific contact resistance was obtained for test electrode system *X* ( $1.8 \Omega \text{ cm}^2$ ;  $2.9 \Omega \text{ cm}^2$ ) (min.  $\rho_c = 1.8 \Omega \text{ cm}^2$ ,  $860 \text{ }^\circ\text{C}$ ) on the substrate with texture and without the  $\text{TiO}_x$  coating of the solar cell. In the case of test electrode system *Y* the specific contact resistance was  $1.1\text{--}165.6 \Omega \text{ cm}^2$ . The minimum value of the specific contact resistance was obtained for test electrode system *Y* ( $1.1 \Omega \text{ cm}^2$ ;  $2.3 \Omega \text{ cm}^2$ ) (min.  $\rho_c = 1.1 \Omega \text{ cm}^2$ ,  $945 \text{ }^\circ\text{C}$ ) on the substrate with texture and without the  $\text{TiO}_x$  coating of the solar cell.

On the basis of these two series, the optimum model structure (the *Y* test electrode system) for the front electrode and the area of its connection with the substrate was found, exhibiting the most satisfactory electrical properties of the photovoltaic cells. Electrical properties of an electrode are closely dependent on the use of particular components of the pastes from which they are made. The conductivity of the investigated silver paste depends on the granulation, the particle shape and the quantity of the powder in its composition. The ceramic glaze combines base-material particles between each other and with the substrate; the rest composes the mixture of the ceramic glaze, which gives the paste a proper viscosity.

With respect to the quality of the test-electrode-system structure, we found a partial evaporation of an electrode, the melting of the elements, and the areas of a

fully exposed silicon substrate of the electrode (**Figure 8a**). The connections of the electrodes obtained from the H1 paste, based on silver nanopowder are pointwise, and the only places close to a continuous connection (**Figure 8b**). **Figure 9a** presents a compound structure containing numerous cracks on the entire electrode surface. This electrode exhibited a porous structure and the porosity grade depended on the co-firing temperature (**Figure 9b**).

In the case of the silicon-substrate morphology, it was found that it has a significant influence on obtaining the minimum resistance values of the electrodes made with selective laser sintering from paste H1. The influence is bigger for the substrate with texture than for the one without texture, which is probably connected with the occurrences of the empty areas under the contacts due to different thicknesses of the pyramids with textured surfaces that we can find in the literature. The topographies of the silicon wafers with texture were observed with the atomic-force microscope. The medium thickness of the pyramids was found to be  $3 \mu\text{m}$  (**Figure 10**), which is consistent with the literature, where the thickness of the pyramids with textured surfaces for Si (100) is in the range from  $3 \mu\text{m}$  to  $9 \mu\text{m}$ .

## 4 CONCLUSION

The investigation studies the fabrication conditions for the front electrodes based on silver powders of various granulations and made with the laser technique, which have become indispensable elements of modern photovoltaic technology. This is an innovative contribution to the solution of the present photovoltaic problems. Hence, the results of the work provide a kind of a guideline for other research workers indicating the focus for further studies.

Based on the results, the following optimum process parameters for manufacturing front electrodes of silicon solar cells were selected: the laser beam ( $41 \text{ W}$ ), the substrate (without texture and antireflection coating) of a solar cell, the minimum value of the specific contact resistance ( $0.4 \Omega \text{ cm}^2$ ) and the paste composition prepared from a nanopowder (H1). It was established that a non-uniformly melted structure caused a pointwise adhesion to the silicon substrate.

## Acknowledgements

The authoress thanks Prof. L. A. Dobrzanski for valuable guidance during the realisation of this work.

## 5 REFERENCES

- <sup>1</sup> P. Panek, M. Lipiński, E. Beltowska-Lehman, K. Drabczyk, R. Ciach, *Opto-electronics Review*, 11 (2003), 269–275
- <sup>2</sup> W. Smolec, *Photothermal conversion of solar energy*, PWN, Warsaw 2000

- <sup>3</sup> Directive 2009/28/EC of the European Parliament and of the Council on the promotion of the use of energy from renewable sources and amending and subsequently repealing Directives 2001/77/EC and 2003/30/EC
- <sup>4</sup> M. T. Sarniak, The basics of photovoltaics, Warsaw University of Technology Publishing, Warsaw 2008
- <sup>5</sup> T. Rodacki, A. Kandyba, The energy processing in a solar station, Silesian University of Technology, Gliwice 2000 (in Polish)
- <sup>6</sup> Z. M. Jarzębski, Solar energy: photovoltaic conversion, PWN, Warsaw 1990
- <sup>7</sup> L. A. Dobrzański, Engineering materials and materials design, Fundamentals of materials science and physical metallurgy, WNT, Warsaw - Gliwice 2006
- <sup>8</sup> D. Janicki, Solid State Phenomena, 199 (2013), 587–592, doi:10.4028/www.scientific.net/SSP.199.587
- <sup>9</sup> L. A. Dobrzański, M. Musztyfaga, Journal of Achievements in Materials and Manufacturing Engineering, 48 (2011) 2, 115–144
- <sup>10</sup> L. A. Dobrzański, M. Musztyfaga, A. Drygala, P. Panek, Journal of Achievements in Materials and Manufacturing Engineering, 41 (2010) 1–2, 57–65
- <sup>11</sup> A. Lisiecki, Proc. of SPIE, Vol. 8703, Laser Technology 2012: Applications of Lasers, 87030S (2013), doi:10.1117/12.2013429
- <sup>12</sup> www.ios.krakow.pl

## FABRICATION OF TiO<sub>2</sub> NANOTUBES FOR BIOAPPLICATIONS

### IZDELAVA TiO<sub>2</sub>-NANOCEVK ZA BIOMEDICINSKO UPORABO

Mukta Kulkarni<sup>1</sup>, Katjuša Mrak-Poljšak<sup>2</sup>, Ajda Flašker<sup>1</sup>, Anca Mazare<sup>3</sup>,  
Patrik Schmuki<sup>3</sup>, Andrej Kos<sup>1</sup>, Saša Čučnik<sup>2,4</sup>, Snežna Sodin-Šemrl<sup>2,4,5</sup>, Aleš Igljič<sup>1</sup>

<sup>1</sup>Faculty of Electrical Engineering, University of Ljubljana, Tržaška cesta 25, 1000 Ljubljana, Slovenia

<sup>2</sup>University Medical Centre, Department of Rheumatology, Ljubljana, Slovenia

<sup>3</sup>Department of Materials Science and Engineering, University of Erlangen-Nuremberg, Erlangen, Germany

<sup>4</sup>Faculty of Pharmacy, University of Ljubljana, Ljubljana, Slovenia

<sup>5</sup>Faculty of Mathematics, Natural Science and Information technology, University of Primorska, Koper, Slovenia  
mukta.kulkarni@fe.uni-lj.si

*Prejem rokopisa – received: 2014-07-31; sprejem za objavo – accepted for publication: 2014-09-29*

doi:10.17222/mit.2014.152

Titanium (Ti), due to its most promising biomaterial properties, can be used in the medical devices that interact with the body tissue, specifically to evaluate, treat, augment or replace any tissue, organ or function of the body. In the present work, we prepared titanium dioxide (TiO<sub>2</sub>) nanotubes with different diameters in the same electrolyte by tailoring different parameters of electrochemical anodization. These structures have more nanorough regions and more surface area that can promote protein binding and cell adhesion in order to increase the lifetime of implants and other medical devices. As an example, we showed the differences in the protein binding of human acute-phase serum amyloid A (SAA) to the TiO<sub>2</sub> nanotubes of different diameters, specifically of 50 nm and 15 nm, as well as comparing it with the binding to the foil alone. We found that SAA binds most prevalently to the nanotubes 50 nm, as opposed to the nanotubes 15 nm or the foil.

Keywords: TiO<sub>2</sub> nanotubes, electrochemical anodization, protein binding

Zaradi dobre biokompatibilnosti se titan (Ti) uporablja pri izdelavi različnih implantatov in medicinskih merilnih priprav, ki so med merjenjem v neposrednem stiku s telesnim tkivom. V tem delu smo prikazali metodo izdelave površin, pokritih z nanocevkami iz titanovega dioksida (TiO<sub>2</sub>), kjer lahko s spreminjanjem parametrov procesa anodizacije spreminjamo premere nastalih nanocevk. Izdelane površine, prekrte z nanocevkami, imajo veliko efektivno površino, kar lahko bistveno vpliva na vezavo proteinov in adhezijo celic, od česar pa je v končni fazi odvisna tudi trajnostna doba implantatov. V prikazanem delu smo kot primer prikazali vezavo proteina serumskega amiloida A (SAA) na TiO<sub>2</sub>-nanocevke premerov 15 nm in 50 nm ter na gladko titanovo površino. Preliminarni rezultati meritev kažejo, da se protein SAA najmočneje veže na površino, prekrto s TiO<sub>2</sub>-nanocevkami 50 nm.

Ključne besede: TiO<sub>2</sub>-nanocevke, elektrokemijska anodizacija, vezava proteinov

## 1 INTRODUCTION

Titanium is considered to be the most biocompatible metal, due to its resistance to body-fluid effects, great tensile strength, flexibility and high corrosion resistance.<sup>1–3</sup> The combination of the strength and biocompatibility of titanium alloys<sup>4</sup> makes them suitable for medical applications.<sup>5–8</sup> Several *in vitro* studies<sup>9–12</sup> have demonstrated that the cells cultured on titanium nanotubular surfaces exhibited high adhesion, proliferation, alkaline phosphatase (ALP) activity and bone matrix deposition. The influence of the nanomorphological features of titanium nanotubes on the cellular response is particularly striking, especially the finding that there is a clear effect of the diameter and that the diameters of 15–20 nm are optimal for an increased cell adhesion and proliferation.<sup>12</sup> Furthermore, the size effect of titanium nanotubes was confirmed for several types of living cells, i.e., mesenchymal stem cells, haematopoietic stem cells, endothelial cells, osteoblasts and osteoclasts.<sup>13,14</sup> The size effect is explained by a specifically tailored nanotubular morphology because the integrin clustering in the cell membrane leads to a focal adhesion complex

with a diameter of about 10 nm, which is a perfect fit for the nanotubes with the diameters of about 15 nm.<sup>15</sup> Irrespective of the location of an implant (a blood-contacting, orthopaedic or dental implant) the first step made after the implantation is the adsorption of proteins from the surrounding tissue or medium. Gongadze et al.<sup>16–18</sup> proposed a mechanism for the adhesion of the cells to a nanorough titanium implant surface with sharp edges, exhibiting more surface area and electric charge than a micro-sized surface. These surface characteristics of a contact surface affect the functional activity of cells. Cells are assumed to bind more strongly to the sharp convex edges or spikes of nanorough regions. Therefore, in order to improve the biological, chemical and mechanical properties and performance of a biomaterial, a surface-modification method such as electrochemical anodization<sup>19</sup> is used to obtain different diameters of nanotubes.

Serum amyloid A (SAA) is a major acute-phase protein in humans that can be elevated, in the circulation, up to 1000 fold during infections or injuries<sup>20</sup> and can represent an invaluable biomarker for inflammation. It has

been implicated in various diseases and pathological states, such as atherosclerosis, rheumatoid arthritis and cancer, among others.<sup>21</sup> When cleaved, SAA products can be deposited into amyloid plaques that can lead to amyloidosis. Due to its expedited and high responsiveness to external stimuli, SAA could be a useful diagnostic and prognostic marker, depending on the disease studied. In this work, we present a fabrication of titanium dioxide nanotubes with different diameters made with electrochemical anodization and an example of protein binding that could be bioapplicable.

## 2 EXPERIMENTAL WORK

### 2.1 Growth of titanium dioxide nanotubes with electrochemical anodization

For the fabrication of different titanium dioxide nanostructures, titanium foils of a thickness 0.1 mm and a purità 99.6 % are used. Before anodization, the titanium foils were degreased using successive ultrasonication in acetone, ethanol and deionized (DI) water for 5 min. Each sample was dried in a nitrogen stream. Ethylene glycol (EG)-based electrolytes were used for growing the nanostructures with specific amounts of water and specific concentrations of hydrofluoric acid (HF) for different nanostructures. The specifications of the electrolyte used and the anodization conditions for obtaining different diameters of nanotubes are listed in **Table 1**. All the anodization experiments were carried out at room temperature ( $\approx 20\text{ }^{\circ}\text{C}$ ) in a two-electrode system with a titanium foil as the working electrode and a platinum gauze as the counter electrode. Different anodization parameters, like the anodization time, the applied voltage, the concentration of chemicals, etc. need to be set to obtain the specific morphologies of the nanostructures.

The formed nanostructures were kept in ethanol for specific time periods to remove all the organic components from the electrolyte, washed with distilled water

and dried in a nitrogen stream. The morphologies of the titanium nanotubes were observed with scanning electron microscopy (SEM).

**Table 1:** Anodization conditions for different TiO<sub>2</sub> nanotubular surfaces

**Tabela 1:** Spreminjanje premerov TiO<sub>2</sub>-nanocevk v odvisnosti od razmer pri anodizaciji

| Nanotube diameter | Electrolyte               | Potential used (V) | Anodization time (h) |
|-------------------|---------------------------|--------------------|----------------------|
| 15 nm             | EG + 8 M water + 0.2 M HF | 10                 | 2.5                  |
| 50 nm             | EG + 8 M water + 0.2 M HF | 20                 | 2.5                  |

Immunofluorescence: Human recombinant serum amyloid A (hrSAA) protein (at a concentration of 1  $\mu\text{g}/\mu\text{L}$ ) was applied as a droplet of 20  $\mu\text{L}$  onto the diameter 50 nm and 15 nm TiO<sub>2</sub> nanotubes and the foil (all 0.5 cm  $\times$  0.5 cm in size). The samples were incubated for 30 min, followed by washing 3-times with PBS for 5 min each. Blocking was performed with bovine serum albumin 1 % and milk 5 % in PBS for 30 min. The blocking buffer was replaced with a primary antibody (an anti-SAA mouse monoclonal antibody, a 1 : 100 dilution) and incubated overnight, followed by washing 3-times in PBS for 5 min. The secondary antibody (a goat anti-mouse IgG conjugated with FITC, a 1 : 800 dilution) was incubated for 30 min, followed by washing 3-times in PBS and immunofluorescent detection (Nikon Eclipse E400, a Nikon Digital Camera DXM1200F).

## 3 RESULTS AND DISCUSSION

### 3.1 Morphology of titanium dioxide nanotubes

By tailoring the anodization conditions (the applied voltage, the anodization time and concentrations of the chemicals) we obtained the nanotubes of diameters 15 nm and 50 nm. SEM images of the top surfaces of diffe-

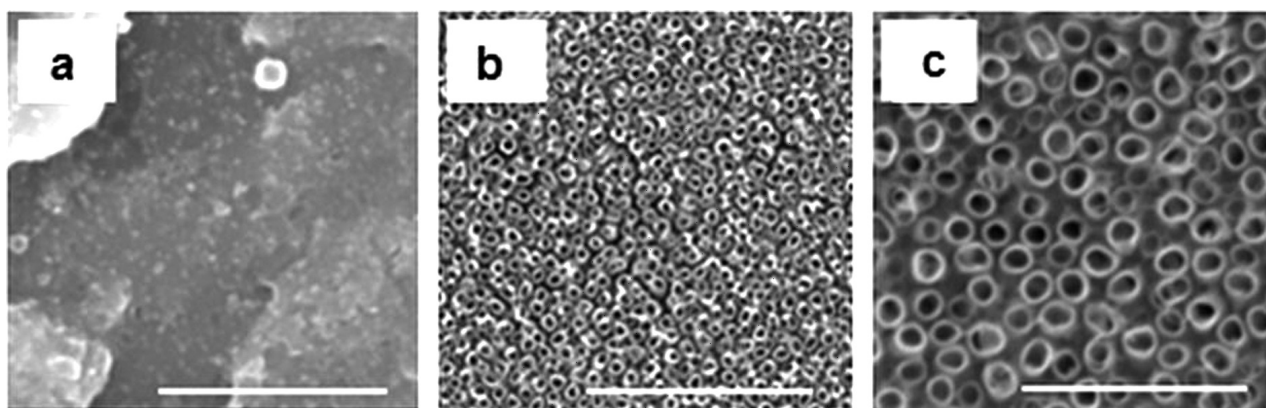


**Figure 1:** SEM images of the top surfaces of: a) Ti foil, b) diameter TiO<sub>2</sub> nanotubes 15 nm and c) diameter TiO<sub>2</sub> nanotubes 50 nm. The scale bar is 500 nm.

**Slika 1:** SEM-posnetki: a) površina titanove folije, b) površina s TiO<sub>2</sub>-nanocevkami premera 15 nm in c) površina s TiO<sub>2</sub>-nanocevkami premera 50 nm. Dolžina črte 500 nm.

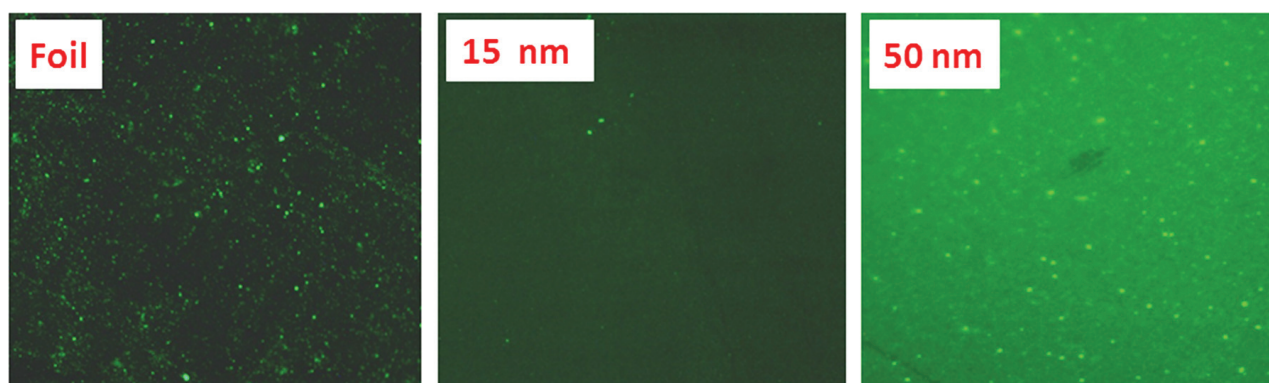


**Figure 2:** Immunofluorescent micrographs of hrSAA protein binding to the foil and TiO<sub>2</sub> nanotubes of diameters 15 nm and 50 nm – examples of protein binding

**Slika 2:** Imunofluorescenčni mikrosposnetki vezave proteina hrSAA na površino folije in na površino z nanocevkami TiO<sub>2</sub> premera 15 nm in 50 nm; primeri vezave proteina

rent nanotube surfaces and the titanium foil are shown in **Figure 1**.

**Immunofluorescence:** The binding of human recombinant SAA protein to the TiO<sub>2</sub> nanotubes and the foil shows a more prevalent signal on the TiO<sub>2</sub> nanotubes 50 nm than on the nanotubes 15 nm or the foil under the same conditions as shown in **Figure 2**.

#### 4 CONCLUSIONS

Different diameters of TiO<sub>2</sub> nanotubes were obtained with electrochemical anodization. Immunofluorescence studies involving SAA were carried out on the TiO<sub>2</sub> nanotubes and compared with the Ti foil. The protein binding to the non-coated titanium dioxide nanotubes, with SAA being the sample protein, is shown to be dependent on the nanotube diameter size, increasing with larger diameters.

#### 5 REFERENCES

- <sup>1</sup> D. F. Williams, *Biomaterials*, 30 (2009) 30, 5897–5909, doi:10.1016/j.biomaterials.2009.07.027
- <sup>2</sup> D. Kowalski, D. Kim, P. Schmuki, *Nano Today*, 8 (2013) 3, 235–264, doi:10.1016/j.nantod.2013.04.010
- <sup>3</sup> D. Mihov, B. Katerska, *Trakia Journal of Sciences*, 8 (2010) 2, 119–125
- <sup>4</sup> D. F. Williams, *Biomaterials*, 29 (2008) 20, 2941–2953, doi:10.1016/j.biomaterials.2008.04.023
- <sup>5</sup> J. M. Macak, M. Zlamal, J. Krysa, P. Schmuki, *Small*, 3 (2007) 2, 300–304, doi:10.1002/smll.200600426
- <sup>6</sup> K. O. Awitor, S. Rafqah, G. Géranton, Y. Sibaud, P. R. Larson, R. S. P. Bokalawela, J. D. Jernigen, M. B. Johnson, *Journal of Photochemistry and Photobiology A: Cehmistry*, 199 (2008) 2–3, 250–254, doi:10.1016/j.jphotochem.2008.05.023
- <sup>7</sup> K. Sasaki, K. Asanuma, K. Johkura, T. Kasuga, Y. Okouchi, N. Ogiwara, S. Kubota, R. Teng, L. Cui, X. Zhao, *Annals of Anatomy*, 188 (2006) 2, 137–142, doi:10.1016/j.aanat.2005.10.003
- <sup>8</sup> X. Liu, P. K. Chu, C. Ding, *Materials Science and Engineering R*, 47 (2004) 3–4, 49–121, doi:10.1016/j.mser.2004.11.001
- <sup>9</sup> M. Bakir, *Journal of Biomaterials Applications*, 27 (2012) 1, 3–15, doi:10.1177/0885328212439615
- <sup>10</sup> S. D. Puckett, T. Erik, T. Raimondo, T. J. Webster, *Biomaterials*, 31 (2010) 4, 706–713, doi:10.1016/j.biomaterials.2009.09.081
- <sup>11</sup> A. P. Ross, T. J. Webster, *International Journal of Nanomedicine*, 8 (2013) 1, 109–117, doi:10.2147/IJN.S36203
- <sup>12</sup> S. Bauer, J. Park, K. von der Mark, P. Schmuki, *European Cells and Materials*, 20 (2010) 3, 16
- <sup>13</sup> S. Bauer, J. Park, J. Faltenbacher, S. Berger, K. von der Mark, P. Schmuki, *Integrative Biology*, 1 (2009) 8–9, 525–532, doi:10.1039/B908196H
- <sup>14</sup> P. Roy, S. Berger, P. Schmuki, *Angewandte Chemie International Edition*, 50 (2011) 13, 2904–2939, doi:10.1002/anie.201001374
- <sup>15</sup> J. Park, S. Bauer, K. von der Mark, P. Schmuki, *Nano Letters*, 7 (2007) 6, 1686–1691, doi:10.1021/nl070678d
- <sup>16</sup> E. Gongadze, D. Kabaso, S. Bauer, T. Slivnik, P. Schmuki, U. van Rienen, A. Igljč, *International Journal of Nanomedicine*, 6 (2011), 1801–1816, doi:10.2147/IJN.S21755
- <sup>17</sup> E. Gongadze, D. Kabaso, S. Bauer, J. Park, P. Schmuki, A. Igljč, *Mini-Reviews in Medicinal Chemistry*, 13 (2013) 2, 194–200, doi:10.2174/138955713804805166
- <sup>18</sup> G. R. Dale, J. W. J. Hamilton, P. S. M. Dunlop, P. Lemoine, J. A. Byrne, *Journal of Nanoscience and Nanotechnology*, 9 (2009) 7, 4215–4219, doi:10.1166/jnn.2009.M35
- <sup>19</sup> K. Vasilev, Z. Poh, K. Kant, J. Chan, A. Michelmore, D. Losic, *Biomaterials*, 31 (2010) 3, 532–540, doi:10.1016/j.biomaterials.2009.09.074
- <sup>20</sup> C. Gabay, I. Kushner, *The New England Journal of Medicine*, 340 (1999) 6, 448–454, doi:10.1056/NEJM199904293401723
- <sup>21</sup> K. Lakota, K. Mrak-Poljšak, B. Rozman, S. Sodin-Šemrl, *Recent Patents on Endocrine Metabolic & Immune Drug Discovery*, 4 (2010) 2, 89–99, doi:10.1371/journal.pone.0110820





# ASSESSMENT OF THE IMPACT-ECHO METHOD FOR MONITORING THE LONG-STANDING FROST RESISTANCE OF CERAMIC TILES

## OCENA METODE IMPACT-ECHO ZA KONTROLO DOLGOTRAJNE ODPORNOSTI KERAMIČNIH PLOŠČIC PROTI ZMRZALI

**Michal Matysik, Iveta Plskova, Zdenek Chobola**

Brno University of Technology, Faculty of Civil Engineering, Institute of Physics, Veveri 331/95, 602 00 Brno, Czech Republic  
matysik.m@fce.vutbr.cz

*Prejem rokopisa – received: 2014-08-01; sprejem za objavo – accepted for publication: 2014-09-11*

doi:10.17222/mit.2014.155

The aim of this paper is to evaluate the possibility of using the impact-echo method for monitoring extremely long-term frost resistance of ceramic tiles. Non-destructive testing methods make it possible to sensitively identify the occurrence and development of defects in materials. Impact-echo methods belong to the family of non-destructive testing methods and can be applied in many branches, among others also in civil engineering. To assess the ceramic-tile frost resistance, a new measurement method was developed based on using the acoustic properties of ceramic tiles. Sets of ceramic tiles of the Ia class were analyzed according to the EN 14 411 B standard. The ceramic tiles under investigation were subjected to degradation due to 500 freeze-thaw cycles in compliance with the relevant EN ISO 10545-12 standard. To verify the correctness of the impact-echo-method results, additional physical properties of the tested ceramic tiles were measured. To analyze the specimen-surface condition, we also used an Olympus LEXT 3100 confocal scanning microscope. It was proved that the impact-echo acoustic method is a sensitive indicator of a structure condition and can be applied to assess the frost resistance of a ceramic cladding element and predict its service life.

**Keywords:** impact-echo, ceramic tiles, frost resistance, confocal microscopy, freeze-thaw cycles

Namen tega članka je oceniti možnosti za uporabo metode Impact-echo za kontrolo ekstremno dolge odpornosti keramičnih ploščic proti zmrzali. Neporušne preiskovalne metode omogočajo selektivno identifikacijo pojava in napredovanja napak v materialu. Metoda Impact-echo pripada skupini neporušnih metod preiskav in je uporabna v mnogih branžah, med drugim tudi v gradbeništvu. Za oceno odpornosti keramičnih ploščic je bila razvita nova merilna metoda, ki temelji na akustičnih lastnostih keramičnih ploščic. Analizirani so bili kompleti keramičnih ploščic kvalitete Ia po standardu EN 14 411 B. Preiskovane keramične ploščice so bile izpostavljene degradaciji pri 500 ciklih zamrznitve-odtaljevanja skladno z odgovarjajočim standardom EN ISO 10545-12. Za preverjanje ustreznosti rezultatov metode Impact-echo so bile izmerjene dodatne fizikalne lastnosti keramičnih ploščic. Za analizo stanja površine vzorca je bil uporabljen konfokalni vrstični mikroskop Olympus LEXT 3100. Dokazano je bilo, da je akustična metoda Impact-echo občutljiv pokazatelj stanja konstrukcije in je uporabna za ugotavljanje odpornosti proti zmrzovanju keramičnih ploščic in za napovedovanje trajnostne dobe ploščic.

**Ključne besede:** Impact-echo, keramične ploščice, odpornost proti zmrzovanju, konfokalna mikroskopija, cikli zmrzovanje-odtaljevanje

## 1 INTRODUCTION

Non-destructive testing methods make it possible to timely identify the occurrence and development of defects in materials and thus ward off a failure or even a breakdown of a structural unit consisting of mechanically or thermally stressed, or corrosion-affected parts. Defect detection, identification and location are the constituents of a diagnosis of an object's technical condition. Impact-echo methods belong to the family of non-destructive testing methods and can be applied in many branches, among others also in civil engineering.<sup>1-5</sup> To assess the ceramic-tile frost resistance, a new measurement method was designed, based on using the acoustic properties of the tiles. The frost resistance of a ceramic product is its capacity to withstand, under specified conditions, a certain number of freeze-thaw cycles without any induced defects in the glaze or the body. Whether the material is used inside (for example, in refrigerating or

freezing plants) or outdoors (rain, snow, ice) it is always exposed to the joint action of frost and water. Water penetrates into the pores and freezes in there. During this transition from the liquid to the solid phase, its volume grows up, resulting in a mechanical stress in the pores, which gives rise to and affects the tension and deformation distribution. Material-integrity defects, such as crevices, cracks, pitting, etc., may occur consequently. The frost may also give rise to the material spalling.<sup>6-9</sup>

## 2 EXPERIMENTAL SECTION

The ceramic tiles under investigation were subjected to freeze-thaw-cycle-based degradation in compliance with the relevant EN ISO 10545-12 standard: Ceramic tiles – Part 12: Determination of frost resistance.<sup>10</sup>

After having been saturated with water, the lining elements were exposed to alternating temperatures of

+5 °C and -5 °C. The lining elements were exposed to the omnidirectional action of the freeze-and-thaw stress treatment in a total of 500 cycles. The ceramic-tile quality was assessed after the completion of 50, 100, 150, 200, 300 and 500 freeze-thaw cycles. Both visual and impact-echo-based analyses of the specimens were carried out.

The impact-echo method makes it possible to detect cracks also in heterogeneous materials. A short-time mechanical impulse is applied to the specimen under test. This impulse propagates throughout the specimen in the form of transversal and longitudinal spherical waves. It also propagates, from the point of its origin, in the form of a surface wave. The transversal and longitudinal waves are reflected on the internal interface (with cracks and defects) or on the external boundary. The response signal therefore carries information of the existence of structural defects. If the test specimen is damaged, energy is dissipated on the defect boundaries. This is reflected in an increased signal attenuation and waveform distortion. The frost-induced damage of the tiles can be assessed on the basis of the signal attenuation and a significant resonance-frequency shift. In our experiments, the response signal was picked up by piezoelectric sensors. The sensor output was fed into the input of a Yokogawa DL1540CL four-channel, eight-bit digital oscilloscope with a GPIB interface. The sampling frequency was 150 MHz. Special software, developed for this type of measurement, was used to further process the signal. When locating the sensors on a measured object, the measured body's geometry and acoustic-signal attenuation are taken into account. To ensure a good acoustic transmission, a layer of a suitable medium (such as paraffin jelly, wax, etc.) is laid on between the sensor and the specimen under test. The sensor output signals are amplified, filtered and saved. What follows is an analysis of the recorded signals using a mathematical analysis method called the Fourier transform, which de-

composes the signals into sine waves of various frequencies and transforms the signal from the time domain into the frequency domain. We look for predominant frequencies in the Fourier spectrum and, particularly, their variations, i.e., their shift towards lower or higher frequencies in each of the load-test stages. Furthermore, it is the coefficient of attenuation  $\lambda$  characterizing the exponential drop in the signal amplitudes. The method can be successfully applied for locating cavities and delamination, determining the depth of the open cracks in a surface or measuring a structure thickness.<sup>11-14</sup>

Another important parameter of the ceramic tiles is the modulus of elasticity expressing the capacity of the material in question to undergo elastic or viscous deformations under the influence of an external load. The materials with a high modulus of elasticity feature low deformations; however, heavy tensions are generated in them even by low deformations. It was the objective of our experiments to determine the moduli of elasticity and deformability for the ceramic tiles. The measurements were carried out on intact specimens as well as on the specimens that had undergone 150, 300 and 500 freeze-thaw cycles. The test procedure was carried out in compliance with the ČSN 73 6174 standard.<sup>15-17</sup>

To determine the strength, elasticity and deformability moduli of the ceramic tiles on the basis of flexural tensile stress tests, a HACKERT/FPZ/100/1 pressing machine was employed. The deflections of each specimen were measured by digital indicators to 0.001 mm.

An Olympus LEXT 3100 laser-type confocal scanning microscope was used to study the surface microgeometry and integrity defects. The microscope uses an Ar laser blue-green spectral line of the wavelength of 488 nm, which makes it possible to attain a very high precision 3D imaging and measurement. The microscope resolution power is as follows: superficial, 120 nm; sectional, 40 nm.

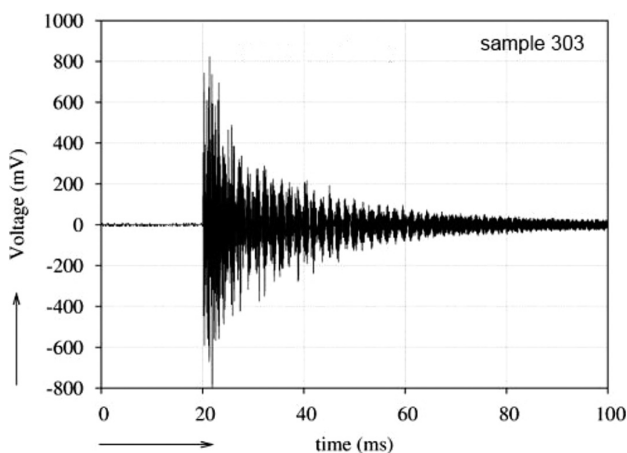


**Figure 1:** Time-response record for tile number 303, prior to freeze-thaw cycles

**Slika 1:** Zapis časovnega odziva ploščice številka 303 pred ciklji zmrzovanje-odtaljevanje

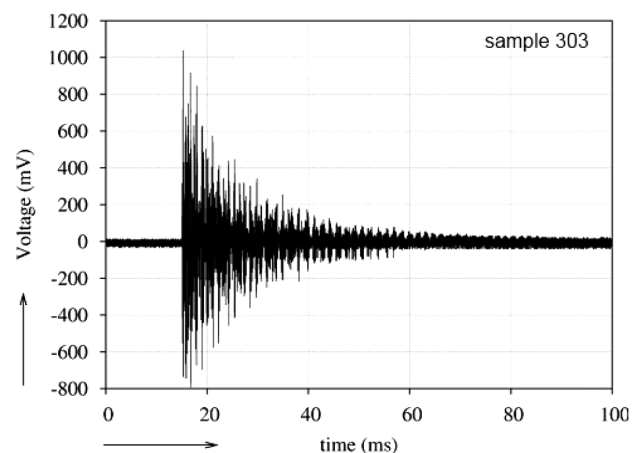


**Figure 2:** Time-response record for tile number 303, after 500 freeze-thaw cycles

**Slika 2:** Zapis časovnega odziva ploščice številka 303 po 500 ciklji zmrzovanje-odtaljevanje

### 3 RESULTS AND DISCUSSION

Figures 1 and 2 show a recording of the time-domain response as picked up at the tile centre of specimen number 303. The measurement was carried out before (Figure 1) and after (Figure 2) the freeze-thaw cycles.

On Figure 3 we can see the power spectral density (in relative unites) versus the frequency plot for specimen number 303 prior to the freeze-thaw cycles. The predominant frequency appears to be  $f_0 = 5.4$  kHz. On Figure 4 we can see the power spectral density for the same specimen after 500 freeze-thaw cycles. The dominant frequency appears to have shifted, being  $f_{500} = 7.2$  kHz.

Figure 5 shows how the average value of attenuation ratio  $\lambda$  changes during 500 freeze-thaw cycles. Figure 6 shows the average value of dominant frequency  $f$  during 500 freeze-thaw cycles.

To verify the correctness of the impact-echo results, the ceramic-tile strength limit, the modulus of elasticity and the modulus of deformability were measured by means of the flexural tensile strength test.

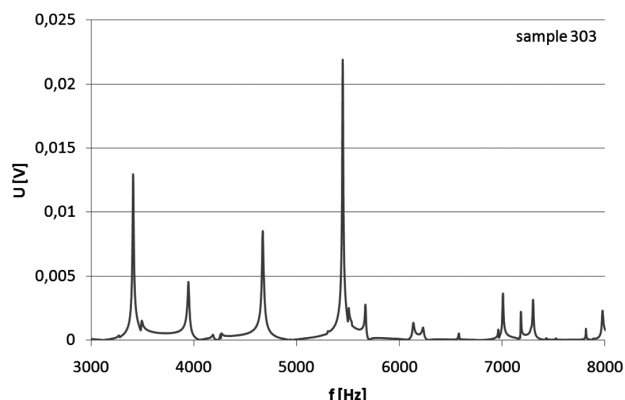


Figure 3: Response frequency spectrum, tile number 303, prior to freeze-thaw cycles

Slika 3: Odgovor frekvenčnega spektra ploščice številka 303 pred cikli zmrzovanje-odtaljevanje

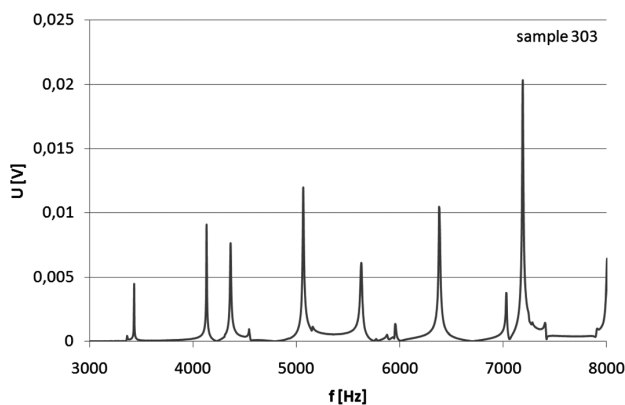


Figure 4: Response frequency spectrum, tile number 303, after a series of 500 freeze-thaw cycles

Slika 4: Odgovor frekvenčnega spektra ploščice številka 303 po seriji 500 ciklov zmrzovanje-odtaljevanje

The ceramic tiles featured the mean tensile strength  $R_{tf} = 33.7$  MPa prior to the degradation tests and then it dropped to  $R_{tf} = 29.2$  MPa (by about 13.3 % of the initial value) after the completion of 500 freeze-thaw cycles (Figure 7).

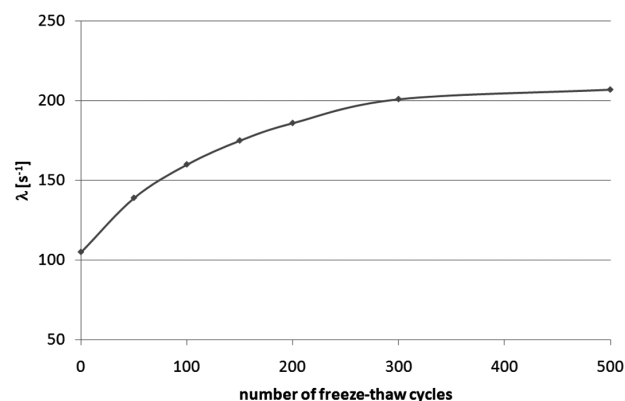


Figure 5: Change in the average value of attenuation ratio  $\lambda$  during 500 freeze-thaw cycles

Slika 5: Spreminjanje povprečne vrednosti razmerja slabljenja  $\lambda$  med 500 cikli zmrzovanje-odtaljevanje

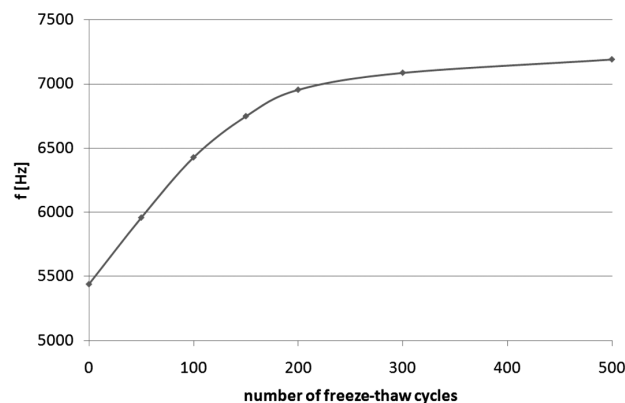


Figure 6: Change in the average value of dominant frequency  $f$  during 500 freeze-thaw cycles

Slika 6: Spreminjanje srednje vrednosti prevladujoče frekvence  $f$  med 500 cikli zmrzovanje-odtaljevanje

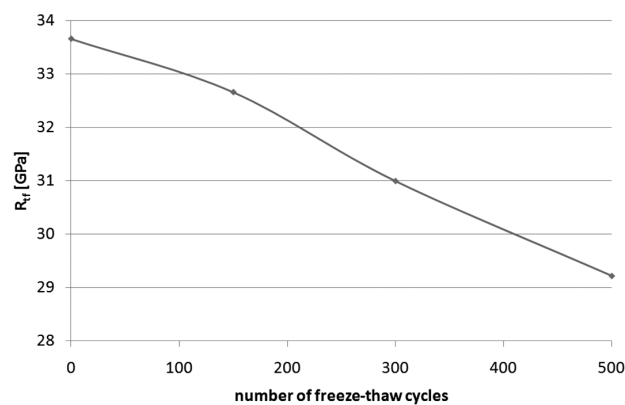
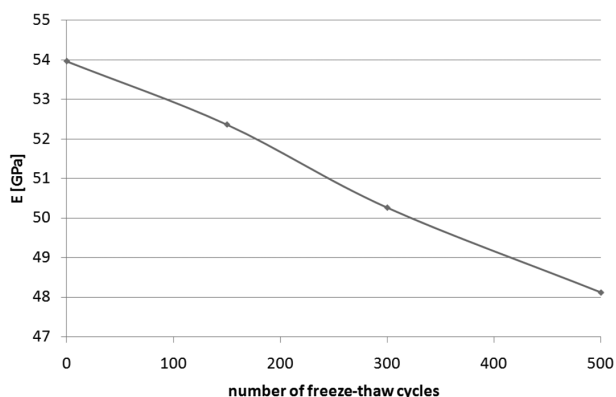


Figure 7: Change in the average value of tensile strength  $R_{tf}$  during 500 freeze-thaw cycles

Slika 7: Spreminjanje povprečne vrednosti natezne trdnosti  $R_{tf}$  med 500 cikli zmrzovanje-odtaljevanje



**Figure 8:** Change in the average value of modulus of elasticity  $E$  during 500 freeze-thaw cycles

**Slika 8:** Spreminjanje povprečne vrednosti modula elastičnosti  $E$  med 500 cikli zmrzovanje-odtaljevanje

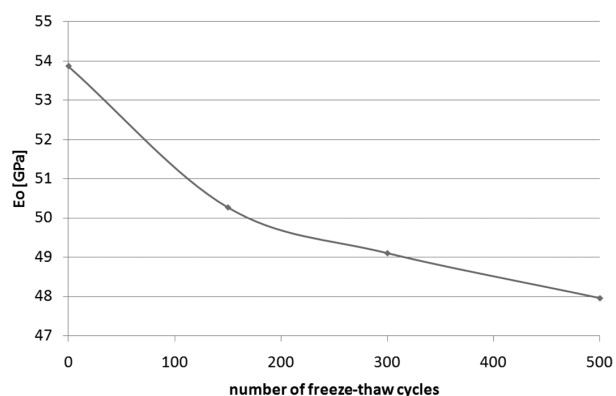


**Figure 9:** Change in the average value of modulus of deformability  $E_0$  during 500 freeze-thaw cycles

**Slika 9:** Spreminjanje povprečne vrednosti modula deformabilnosti  $E_0$  med 500 cikli zmrzovanje-odtaljevanje

Similarly to the tensile-strength values, moduli of elasticity  $E$  also dropped after the application of the freeze-thaw cycles. The average value of modulus of elasticity  $E$  of the ceramic tiles dropped from 53.9 GPa

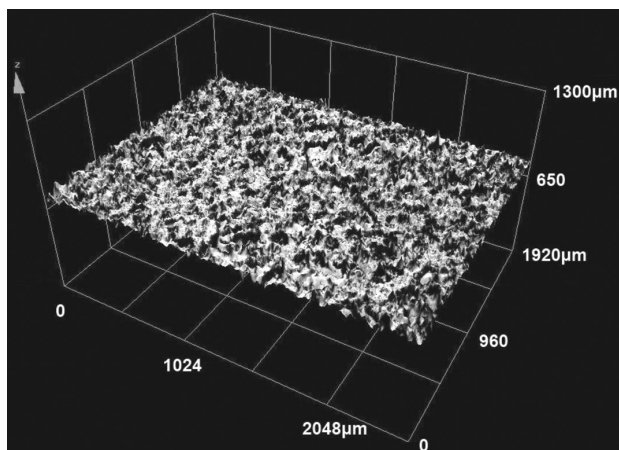


**Figure 10:** Surface relief before applying the stress test  
**Slika 10:** Relief površine pred izvajanjem napetostnih preizkusov

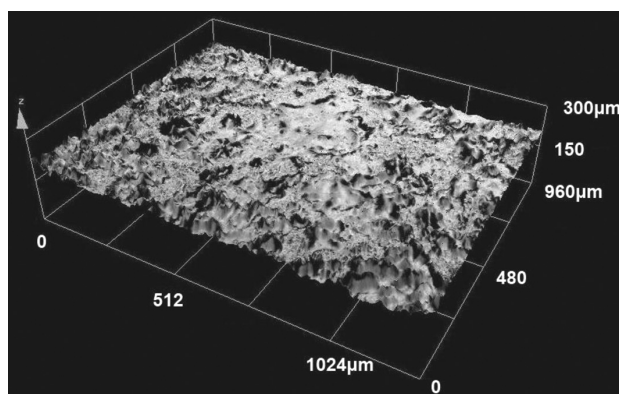


**Figure 11:** State of the surface after 500 freeze-thaw cycles

**Slika 11:** Stanje površine po 500 ciklih zmrzovanje-odtaljevanje

to 48.1 GPa (by about 10.8 % of the initial value) (**Figure 8**).

From **Figure 9** we can see the change in the average value of modulus of deformability  $E_0$  during 500 freeze-thaw cycles.

Using the confocal microscope LEXT 3100, we monitored the state of the surfaces of the ceramic tiles during the degradation caused by 500 freeze-thaw cycles. **Figure 10** illustrates the surface relief before applying the stress test. **Figure 11** shows the state of the surface after 500 freeze-thaw cycles. We can see that at the beginning the surface roughness was significantly higher and reached the average roughness  $R_a = 6.9 \mu\text{m}$ . Individual peaks covered the surface area of over  $60 \mu\text{m}$ . After 500 freeze-thaw cycles the roughness decreased to  $R_a = 4.4 \mu\text{m}$  and individual peaks were not higher than  $40 \mu\text{m}$ .

#### 4 CONCLUSIONS

The present paper deals with the application potential of the impact-echo method to assess and predict the service life of ceramic lining elements and presents the respective results. Sets of 60 ceramic tiles were tested. The ceramic tiles were subjected to degradation tests consisting of 500 freeze-thaw cycles within a temperature interval from  $+5 \text{ }^\circ\text{C}$  to  $-5 \text{ }^\circ\text{C}$  and the degradation-test-induced variations in their properties were tracked.

The average value of the dominant frequency during 500 freeze-thaw cycles increased by 33 %. To verify the correctness of the impact-echo results, we measured the ceramic-tile strength limit and the modulus of elasticity, resulting from the flexural tensile strength tests. During the degradation tests consisting of 500 freeze-thaw cycles the strength limit decreased by more than 13.3 % and the elasticity modulus decreased by about 10.8 %. Using the confocal microscope LEXT 3100 we found that the surface roughness of the ceramic tiles decreased.

The strong correlation between the variations in the classical parameters such as the strength limit, the elasticity modulus and the dominant frequency shifts upward, and the attenuation-coefficient growth also

convincingly shows that the impact-echo method is a convenient tool for assessing the quality and service life of ceramic tiles. The impact-echo method can also be recommended as a continuous screening tool for automated ceramic-tile production lines.

### Acknowledgments

This research was carried out with the financial support of the European Union's "Operational Programme Research and Development for Innovations", No. CZ.1.05/2.1.00/03.0097, as an activity of the regional Centre AdMaS "Advanced Materials, Structures and Technologies", and with the financial support of the Czech Science Foundation through project GA13-18870S and VUT FAST-S-13-2149 No. 23688.

### 5 REFERENCES

- <sup>1</sup> H. S. Limaye, R. J. Krause, *Materials Evaluation*, 49 (1991) 10, 1312–1315, doi:10.1016/S0963-8695(97)88984-0
- <sup>2</sup> M. T. Liang, P. J. Su, *Cement and Concrete Research*, 31 (2001) 10, 1427–1436, doi:10.1016/S0008-8846(01)00569-5
- <sup>3</sup> G. Epasto, E. Proverbio, V. Venturi, *Materials and Structures*, 43 (2010) 1–2, 235–245, doi:10.1617/s11527-009-9484-0
- <sup>4</sup> L. Pazdera, L. Topolar, *Russian Journal of Nondestructive Testing*, 50 (2014) 2, 127–132, doi:10.1134/S1061830914020065
- <sup>5</sup> M. Krause, M. Barmann, R. Frielinghaus, *NDT & E International*, 30 (1997) 4, 195–204, doi:10.1016/S0963-8695(96)00056-4
- <sup>6</sup> D. N. Boccaccini, M. Maioli, M. Cannio, M. Romagnoli, P. Veronesi, C. Leonelli, A. R. Boccaccini, *Engineering Fracture Mechanics*, 76 (2009) 11, 1750–1759, doi:10.1016/j.engfracmech.2009.03.008
- <sup>7</sup> M. Korenska, M. Manychova, L. Pazdera, *Russian Journal of Nondestructive Testing*, 49 (2013) 9, 530–537, doi:10.1134/S1061830913090040
- <sup>8</sup> E. Cam, S. Orhan, M. Luy, *NDT & E International*, 38 (2005) 5, 368–373, doi:10.1016/j.ndteint.2004.10.009
- <sup>9</sup> EN 14411:2006 Ceramic tiles - Definitions, classification, characteristics and marking, European Committee for Standardization, Brussels, 2007
- <sup>10</sup> EN ISO 10545-12:1997 Ceramic tiles - Part 12: Determination of frost resistance, European Committee for Standardization, Brussels, 1998
- <sup>11</sup> K. E. A. Van Den Abeele, A. Sutin, J. Carmeliet, P. A. Johnson, *NDT and E International*, 34 (2001) 4, 239–248, doi:10.1016/S0963-8695(00)00064-5
- <sup>12</sup> M. Korenska, L. Pazdera, M. Manychova, *International Journal of Materials & Product Technology*, 42 (2011) 3–4, 209–218, doi:10.1504/IJMPT.2011.045468
- <sup>13</sup> J. J. Wang, T. P. Chang, B. T. Chen, H. C. Lin, H. Wang, *Journal of Nondestructive Evaluation*, 29 (2010) 2, 111–121, doi:10.1007/s10921-010-0070-8
- <sup>14</sup> T. Ficker, L. Topolar, I. Kusak, *Magazine of Concrete Research*, 65 (2013) 24, 1480–1485, doi:10.1680/macr.13.00195
- <sup>15</sup> CSN 73 6174 Determination of the modulus of elasticity and modulus of deformation by testing concrete for flexural strength, Czech Office for Standards, Metrology and Testing, Praha, 1994
- <sup>16</sup> I. Kusak, M. Lunak, *Advanced Materials Research*, 897 (2014), 131–134, doi:10.4028/www.scientific.net/AMR.897.131
- <sup>17</sup> ISO 4013 Concrete - Determination of flexural strength of test specimens, International Organization for Standardization, Geneva, 1978



# INVESTIGATION ON NEW CREEP- AND OXIDATION-RESISTANT MATERIALS

## PREISKAVA NOVEGA MATERIALA, ODPORNEGA PROTI LEZENJU IN OKSIDACIJI

**Omid Khalaj<sup>1</sup>, Bohuslav Masek<sup>1</sup>, Hana Jirkova<sup>1</sup>, Andrea Roneso<sup>1</sup>,  
Jiri Svoboda<sup>2</sup>**

<sup>1</sup>Research Centre of Forming Technology, University of West Bohemia, Univerzitní 22, 306 14 Pilsen, Czech Republic

<sup>2</sup>Institute of Physics of Materials, Academy of Sciences of the Czech Republic, Žitkova 22, 616 62 Brno, Czech Republic  
khalaj@vctt.zcu.cz

*Prejem rokopisa – received: 2014-08-25; sprejem za objavo – accepted for publication: 2014-10-02*

doi:10.17222/mit.2014.210

The specific mechanical property and structure of a material can be achieved by combining various types of materials and technologies. The main aim of this research is to develop new creep- and oxidation-resistant materials (ODS) (new ODS Fe-Al based alloys and ODS composites) applicable at high temperatures of up to about 1100 °C. The new ODS composites consist of a ferritic Fe-Al matrix strengthened with about volume fractions 2 % to 30 % of Al<sub>2</sub>O<sub>3</sub> particles. In order to find the optimum material structure, different oxide amounts were added to three different containers. Also, to find the influence of the temperature on the obtained structures, three processing temperatures of (26, 750 and 1150) °C were used with the specific deformation profile. An analysis of the structures was performed using different analytical methods such as light microscopy, scanning electron microscopy and X-ray diffraction analysis.

Keywords: ODS steel, alloys, composite, creep, Fe-Al

Posebne mehanske lastnosti in strukturo materiala je mogoče doseči s kombinacijo različnih vrst materialov in tehnologij. Glavni namen tega članka je razviti nov material, odporen proti lezenju in oksidaciji (ODS), tj. novo ODS-zlitino na osnovi Fe-Al in ODS-kompozite, uporabne pri visokih temperaturah do 1100 °C. Novi ODS-kompozit je sestavljen iz feritne Fe-Al-osnove, ojačane z okrog volumenskim deležem od 2 % do 30 % delcev Al<sub>2</sub>O<sub>3</sub>. Da bi dobili optimalno strukturo materiala, je bil v tri vsebnike primešan različen delež oksida. Za ugotovitev vpliva temperature na dobljeno strukturo so bile uporabljene tri temperature izdelave (26, 750 in 1150) °C s posebnim profilom deformacije. Analiza strukture je bila izvršena z različnimi metodami, kot so svetlobna mikroskopija, vrstična elektronska mikroskopija in rentgenska difrakcija.

Ključne besede: ODS-jeklo, zlitine, kompozit, lezenje, Fe-Al

## 1 INTRODUCTION

A new unconventional structure with specific mechanical and physical properties and new application possibilities in some areas of the industry can be obtained, using the conventional materials, with innovative technological techniques. One of these techniques includes a combination of powder metallurgy with the processing of materials in the semi-solid state or a creation of a microstructure consisting of a metal matrix and dispersed stable particles in order to develop a new material resistant to the high-temperature creep. For making intricately shaped components from such materials, represented by oxide-dispersion-strengthened (ODS) alloys, new processes must be found to allow near-net-shape products to be manufactured in a simple and rapid manner. The ODS alloys are of interest mainly because of their outstanding microstructural stability that is also the basis for superior creep properties.

The ODS alloys that were commercially produced at the end of the 20<sup>th</sup> Century and at the beginning of the 21<sup>st</sup> Century include MA 956 or MA 957<sup>1</sup>, PM 2000 or PM 2010<sup>2</sup>, ODM alloys<sup>3</sup> and 1DK or 1DS<sup>4</sup> with a ferritic

matrix, ODS Eurofer steel with a tempered ferritic-martensitic matrix<sup>5</sup> and austenitic Ni-ODS PM 1000 or Ni-ODS PM 3030<sup>6</sup>. The volume fraction of dispersed spherical oxides (usually Y<sub>2</sub>O<sub>3</sub>) is typically below 1 % and the oxides typically have the mean size of 5–30 nm. Because of a lower diffusion coefficient, austenitic ODS alloys show a better creep resistance for the same oxide volume fraction and contain minimum chromium and/or aluminium contents to guarantee a sufficient oxidation resistance. However, the resistance to the coarsening of the oxides (and, thus, the stability of the creep properties) is due to the solubility of oxygen in the matrix and its diffusion coefficient<sup>7</sup>; this factor is more advantageous for the ferritic ODS alloys. This is probably the reason why the application of the ferritic ODS steels is the dominant one. The excellent creep properties of the ODS alloys are due to an attractive interaction of dislocations with oxides described in the well-known model by Rösler and Arzt<sup>8</sup>. Creep usually exhibits the threshold stress, which correlates well with the Orowan theory according to which, at a given temperature, the threshold stress is inversely proportional to the distance of the oxides. Thus, any coarsening of the oxides causes a

degradation of the creep properties. The typical creep strength of the ferritic ODS alloys is estimated, in the available literature, to be 60 (40) MPa for coarse-grained structures and 20 (6) MPa for fine-grained structures at 1000 (1100) °C<sup>9</sup>. New ODS ferritic steels are currently in development at Oak Ridge National Laboratories<sup>10-13</sup>. Sufficient amounts of Al and/or Cr in the ODS alloys are crucial for their oxidation resistance.<sup>14-16</sup>

On the basis of the thermomechanical and microstructure analyses, this paper presents the development of the new ODS Fe-Al based alloys and ODS composites applicable at high temperatures of up to about 1100 °C. The new ODS composites consist of a ferritic Fe-Al matrix strengthened with about volume fractions from 6 % to 10 % of Al<sub>2</sub>O<sub>3</sub> particles. The new ODS alloys and ODS composites produced with a combination of mechanical alloying and hot consolidation, are new types of materials with a promising property spectrum. The experimental programme was carried out in order to get a more detailed insight into these new groups of materials, to better understand their processing behaviour and their operational properties.

## 2 EXPERIMENTAL PROCEDURE

Mechanically alloyed powders consisting of a mass fraction Fe 10 % Al matrix and volume fractions from 6 % to 10 % of Al<sub>2</sub>O<sub>3</sub> particles were deposited into a steel container which was not evacuated before the welding and was sealed by welding. The mechanically alloyed powders were prepared in a Pulverisette 6 planetary ball mill (produced by Fritsch), equipped with a steel milling container with a volume of 1 dm<sup>3</sup> filled with steel balls with a diameter of 20 mm. The steel container with the mechanically alloyed powder was rolled by a rolling machine at the average temperature of 900 °C and a force of 1200 kN (**Figure 1**). These experiments were performed in order to check the applicability of the semi-products prepared by mechanical alloying in the semi-solid process.

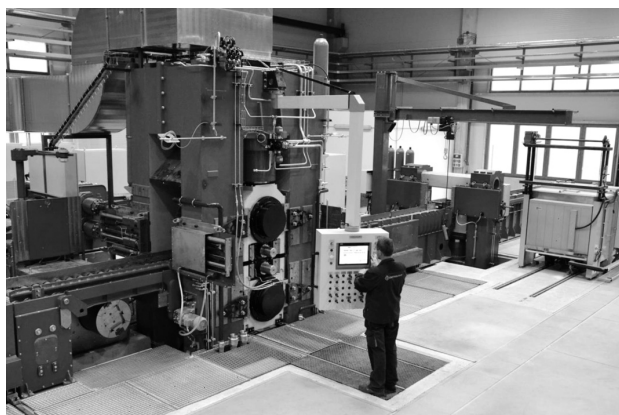


**Figure 1:** Hot rolling mill  
**Slika 1:** Ogradnje za vroče valjanje

A number of metallographic methods were used to evaluate the initial powder and the resulting structures; the volume fractions of individual phases were determined using an X-ray diffraction analysis and the local chemical composition was measured using an EDX detector. The measurement was completed by determining the hardness. In order to investigate the thermomechanical treatment of the specimens, a thermomechanical simulator (**Figure 2**) was used, demonstrating various temperature-deformation paths necessary for finding the conditions leading to the most effective grain coarsening due to recrystallization. Multi-step thermomechanical procedures stimulating a more effective grain coarsening were also tested. Several procedures of the thermomechanical treatment were designed and carried out, differing in the number of deformation steps characterized by different strains, strain rates and temperatures. The thermomechanical simulator also allows a combination of tensile and compressive deformations, thus accumulating a high plastic deformation (and a high dislocation density) in a specimen. The experimental results of the thermomechanical simulator provided the basis for the characterization of the influence of the accumulated plastic deformation and temperature on the grain coarsening and recrystallization.

## 3 TEST PROGRAMME

The test programme was divided into preliminary tests and original tests. The preliminary tests were performed to find the appropriate specimen shapes for the heat field and the original tests were performed to investigate the thermomechanical treatment of the materials (**Table 1**).

Material 1 is a composite with the mass fraction  $w(\text{Fe}) = 10\%$  Al ferritic matrix and a volume fraction  $\varphi(\text{Al}_2\text{O}_3) = 10\%$  of particles with the typical size of 300 nm. Material 2 is an ODS alloy with the  $w(\text{Fe}) = 10\%$  Al ferritic matrix and  $\varphi(\text{Al}_2\text{O}_3) = 6\%$  of Al<sub>2</sub>O<sub>3</sub> particles

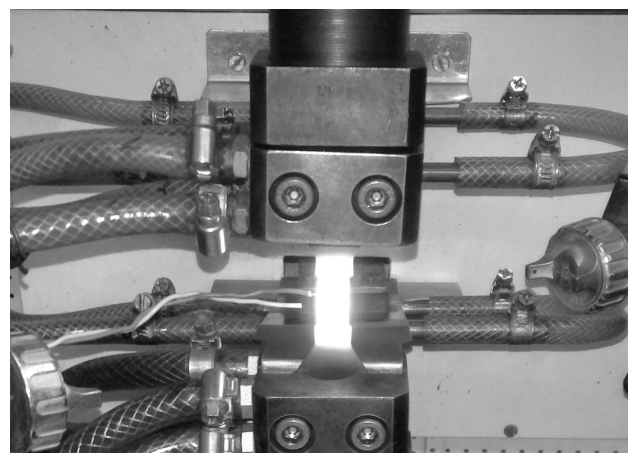


**Figure 2:** Thermomechanical simulator  
**Slika 2:** Termomehanski simulator



**Table 1:** Parameters of test programme  
**Tabela 1:** Parametri programa preizkusov

| Test series | Material No. | Specimen shape No. | Treatment No. | Maximum temperature (°C)       | Number of tests | Purpose of the tests                                                 |
|-------------|--------------|--------------------|---------------|--------------------------------|-----------------|----------------------------------------------------------------------|
| A           | Steel        | 1, 2, 3, 4, 5, 6   | 1             | 1150                           | 7*              | To achieve the optimum temperature field                             |
| B           | 1            | 5                  | 2             | 1200, 1100, 1000, 900, 800, 30 | 6               | To check the material mechanical behaviour at different temperatures |
| C           | 2            | 5                  | 2             | 1200, 1100, 1000, 900, 800, 30 | 6               | To check the material mechanical behaviour at different temperatures |

\* One more test to control the side temperature field

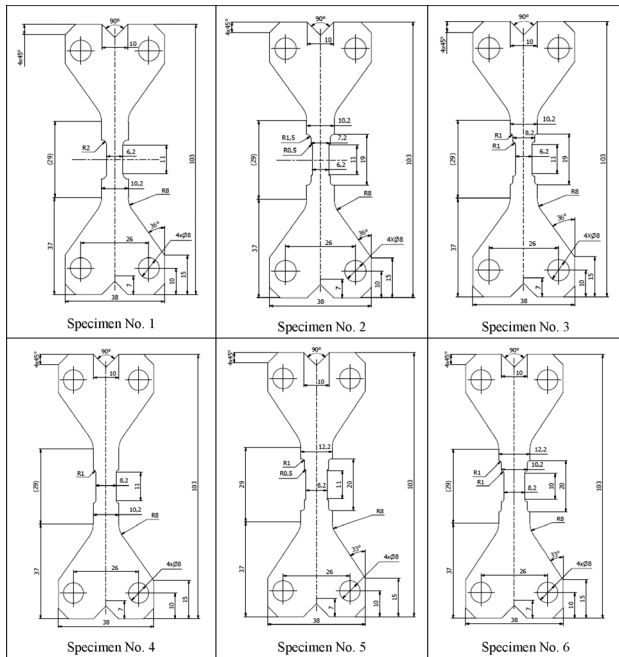


**Figure 3:** Six different specimen types for test series A  
**Slika 3:** Tri različne vrste vzorcev za preizkusno serijo A

with the typical size of 50 nm. Test series A was performed to find the optimum temperature field for the specimens. In this case, six types of different specimen shapes (Figure 3) made from steel were tested under treatment number 1 (Figure 4). In this treatment, the temperature raised to 1150 °C in 3 min, being stable for 3 min and then it fell down to room temperature over 3 min.

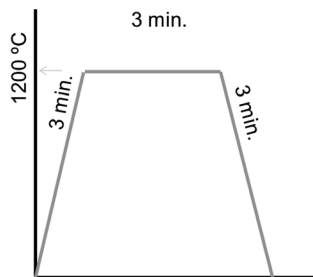


**Figure 4:** Treatment No. 1  
**Slika 4:** Obdelava št. 1

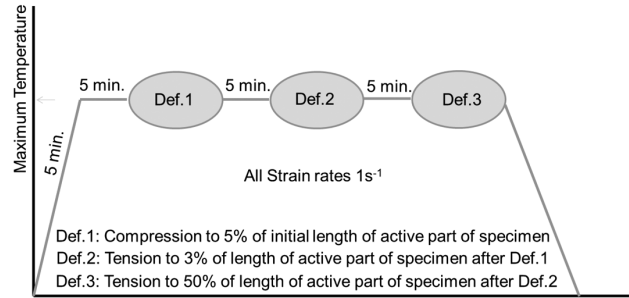


**Figure 5:** Treatment No. 2  
**Slika 5:** Obdelava št. 2

Test series B was carried out to investigate the thermomechanical behaviour of Material 1 under treatment No. 2 (Figure 5), at different temperatures more precisely as the results of test series C showed that this material is rather sensitive to the temperature changes.

Test series C was performed on Material 2 (the ODS alloy) to investigate its thermomechanical behaviour under treatment No. 2 (Figure 5), at different heating temperatures.

## 4 RESULTS AND DISCUSSION

### 4.1 Series A

The results achieved with this series show that the homogeneity of the temperature field is more homogeneous for specimen shapes 2 and 5 than for the others. Regarding several experiences with the specimen-shape selection we decided to choose these two specimen

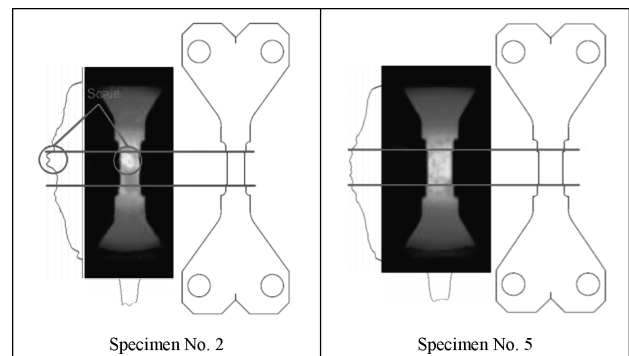


**Figure 6:** Thermo camera detailed results at 1150 °C  
**Slika 6:** Detajli rezultatov, dobljenih s termokamero pri 1150 °C

shapes for the testing of Materials 1 and 2. The difference between the shapes of Specimens 2 and 5 is only in the temperature-field width. Specimen 5 has a larger cross-section in order to obtain a better sample for the microstructure investigation. **Figure 6** shows the vertical and horizontal thermo-profiles of Specimens 2 and 5. The results indicate high temperature homogeneity in the middle parts of the specimens regardless of the scale.

#### 4.2 Series B and C

In the last tested series the number of the tested temperatures was increased and the temperatures used were also higher than in the previous tests. In series E Material 2 was tested. The stress-strain curves from individual deformation steps are depicted in **Figures 7 to 9**. **Figure 7** shows the stress-strain curves for Materials 1 and 2 during a 5 % compression at different temperatures. It can be seen that at high temperatures (1200 °C and 1100 °C), both materials show the same behaviour as the maximum stress values are approximately 50 MPa and 100 MPa for 1200 °C and 1100 °C, respectively. As the temperature decreases, Material 2 shows a more sustainable stress than Material 1. For example, at 30 °C, the maximum stress for Materials 1 and 2 is 300 MPa and 500 MPa, respectively. No fracture occurs in any tests.

The curves for a tension of 3 % were also investigated (**Figure 8**). It can be seen that at high temperatures

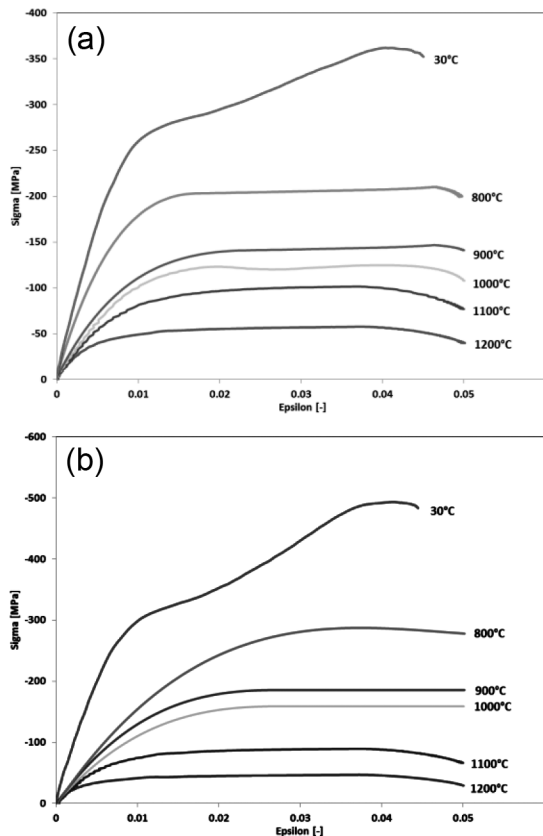


**Figure 7:** Stress-strain curves for 5 % compression  
**Slika 7:** Krivulja napetost – raztezek pri tlačni obremenitvi 5 %

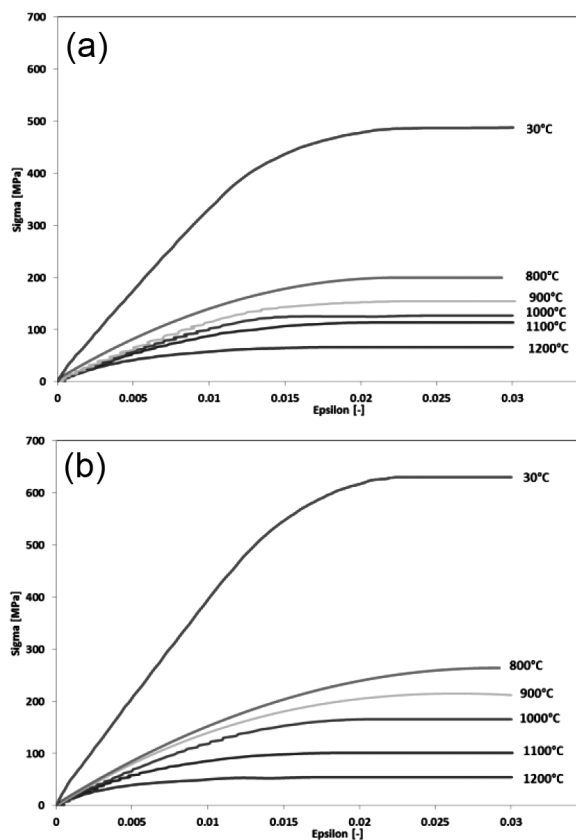


**Figure 8:** Stress-strain curves for 3 % tension  
**Slika 8:** Krivulja napetost – raztezek pri natezni obremenitvi 3 %

(1200 °C and 1100 °C) both materials show the same behaviour as the maximum stress values are approximately 50 MPa and 100 MPa for 1200 °C and 1100 °C, respectively. As the temperature decreases, Material 2 shows a more sustainable stress than Material 1. For example, at 800 °C, the maximum stress for Materials 1 and 2 is 100 MPa and 250 MPa, respectively. No fracture occurs in any tests.

**Figure 9** shows the stress-strain curves of Materials 1 and 2 for a tension of 50 % at different temperatures. It can be seen that at high temperatures (1200, 1100 and 1000) °C both materials show the same behaviour as the maximum stress values are approximately (50, 100 and 130) MPa for (1200, 1100 and 1000) °C, respectively. As the temperature decreases, this trend also continues but with a slight difference, for example, at 800 °C the maximum stress for Material 1 is approximately 250 MPa but for Material 2 it is approximately 200 MPa. For all the specimens, fracturing occurred at a strain of 35–45 %, except for Material 1 at 800 °C which may due to the non-homogeneity of the material along the sheet.<sup>17–22</sup>

#### 4.2.1 Metallographic Analysis

For a better understanding of the behaviour of the composite material, a metallographic analysis was performed on the fracture point of the sample that had

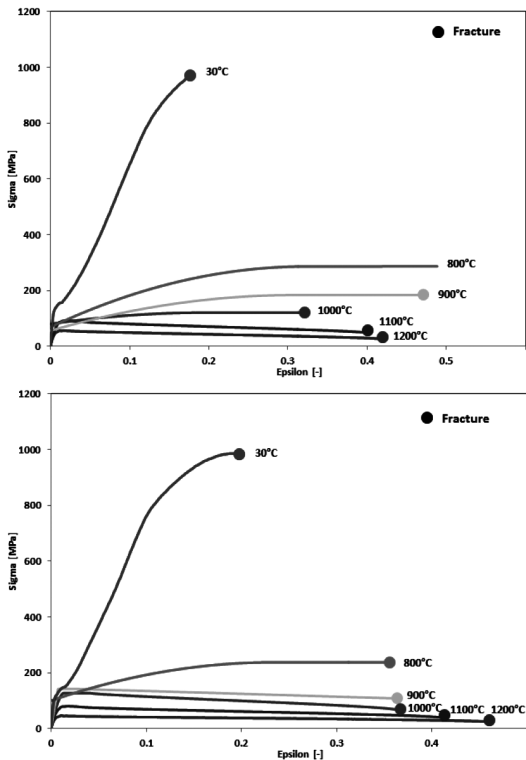


Figure 9: Stress-strain curve at 50 % tension  
 Slika 9: Krivulja napetost – raztezek pri natezni obremenitvi 50 %

most of the local deformation and on the other side of the sample where the deformation was zero. A fractographic analysis was also performed to describe the character of the fracture area.

Material 1 – Test series B

Figure 10 shows the structure of Material 1 (the  $w(\text{Fe}) = 10\%$  Al ferritic matrix and  $\varphi(\text{Al}_2\text{O}_3) = 10\%$  of the particles with the typical size of 300 nm) which was formed in all the cases of solid solution Fe-Al, iron aluminide and dispersed  $\text{Al}_2\text{O}_3$  particles. Iron aluminide was mostly found around the grains of the solid solution, creating a network around the grains. Also, the particles of  $\text{Al}_2\text{O}_3$  were, in most cases, concentrated in the area around the grains of the solid solution. With the decreasing heating temperature, which indicated a lower break temperature, a stronger impact of deformation was observed, causing an elongation of the grains.

In all the cases, the analysis of the fracture area showed a ductile mode of the fracture. Even in the case of a RT fracture there was no evidence of brittle failure. Only the grains stretched due to the deformation were seen.

Material 2 – Test Series B

In the same way a microstructural evaluation was done for test series B, involving Material 2 (the  $w(\text{Fe}) =$

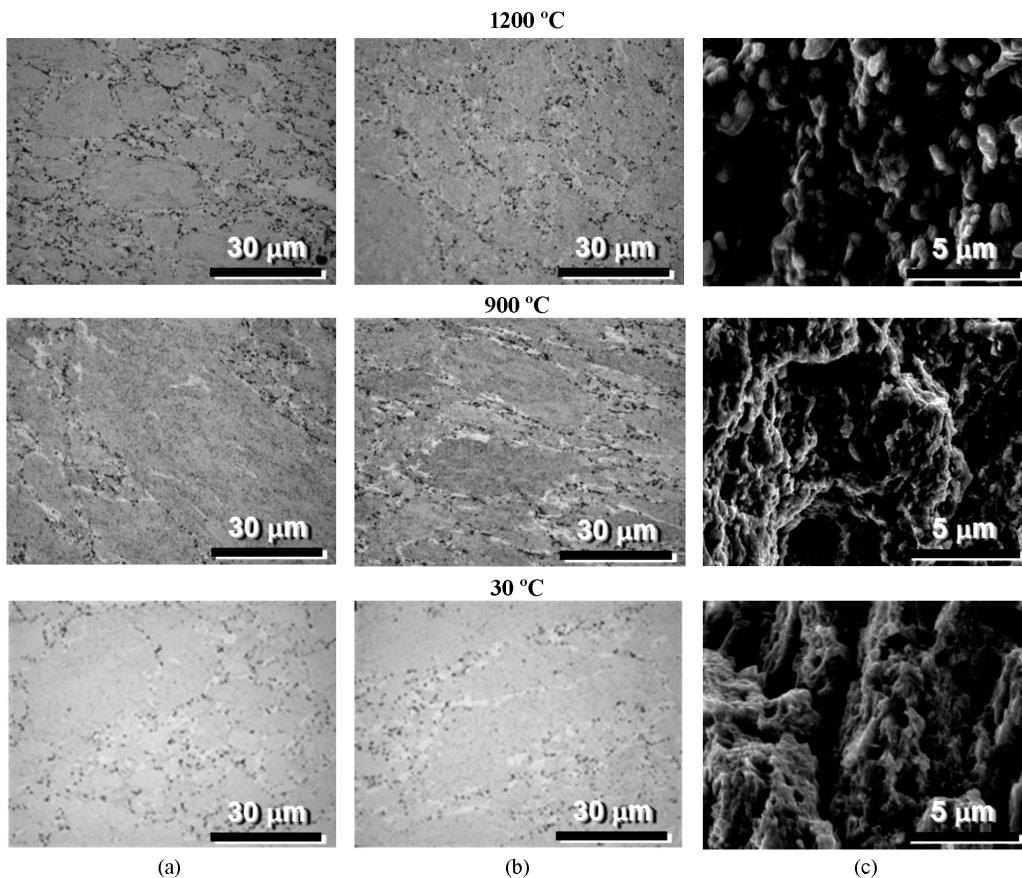
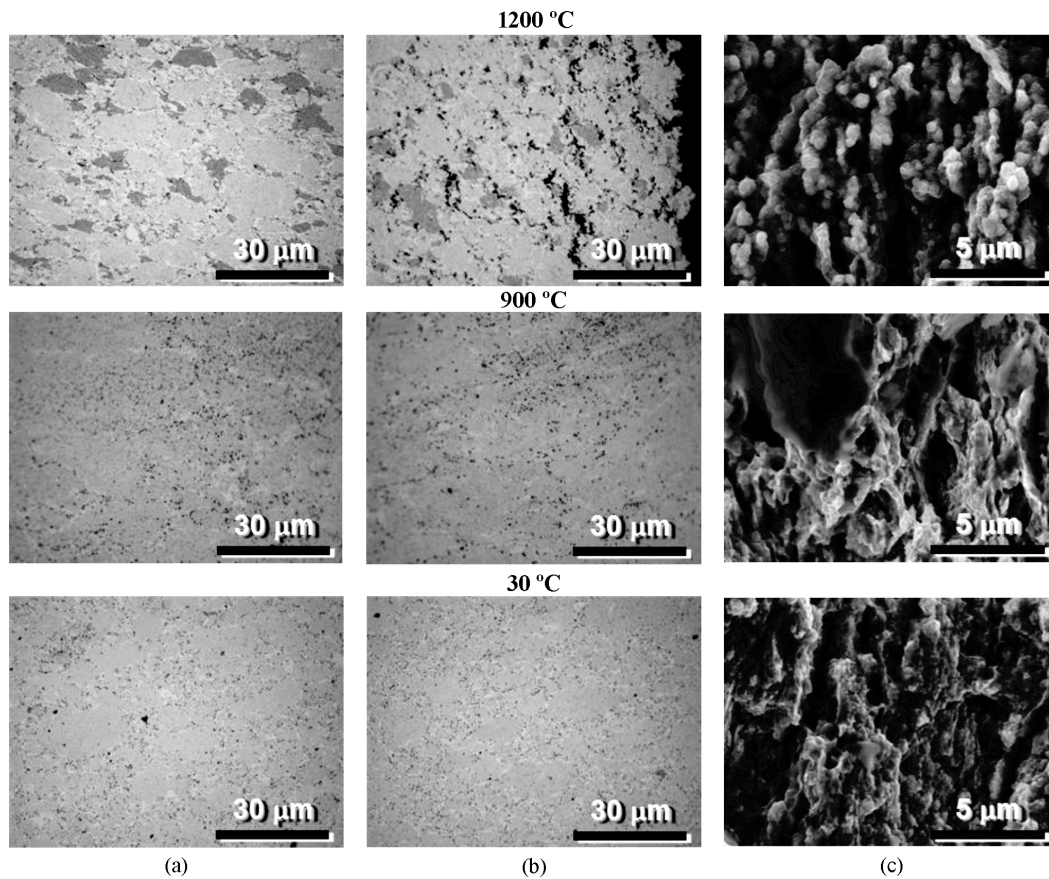


Figure 10: Microstructure of Material 1: a) area with a regular deformation, b) area close to fracture, c) fracture  
 Slika 10: Mikrostruktura materiala 1: a) področje z deformacijo, b) področje blizu preloma, c) prelom



**Figure 11:** Microstructure of Material 2: a) area with a regular deformation, b) area close to fracture, c) fracture  
**Slika 11:** Mikrostruktura materiala 2: a) področje z deformacijo, b) področje blizu preloma, c) prelom

10 % Al ferritic matrix with  $\varphi(\text{Al}_2\text{O}_3) = 6\%$  of the particles with the typical size of 50 nm, in which there was a reduction in  $\text{Al}_2\text{O}_3$  (Figure 11). Also, the size of the particles was reduced from 300 nm to 50 nm. The structure was similar to that in the previous case. The particles of  $\text{Al}_2\text{O}_3$  were more uniformly distributed at the lower processing temperatures and they were also found within the grains of the Fe-Al solid solution.

#### 4.2.2 Hardness

In order to compare the material stiffness values, a Vickers-hardness test was performed on both materials within HV10. As Figure 12 shows, by increasing the temperature, both materials show a lower amount of hardness caused by the changes made to the microstructures of the elements. Regarding the metallographic results, the porosity of both materials increased due to the high temperature which led to a loose interlocking of the grains.

## 5 CONCLUSION

The results of the experiments show the characterization of the thermomechanical behaviour of the new-generation ODS alloys and composites. The difference between the two materials is in the amount and size of the oxides embedded in the ferritic matrix. The advan-

tages of both materials are their low costs and creep, corrosion and oxidation resistances due to the Fe-Al based ferritic matrix of the ODS alloys and composites. The matrix should substantially retain its uniformity during its short transition through the semi-solid state and the oxides should not coalesce. The materials of this type have the required potential for a production of intricately shaped miniature parts by mini-thixoforming. This paper shows that this particular process chain has a

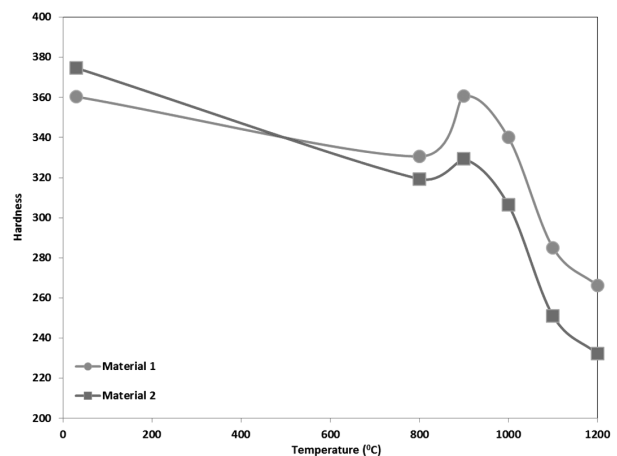


**Figure 12:** Vickers-hardness test (HV10)  
**Slika 12:** Meritve trdote po Vickersu (HV10)

large potential. Using a metallographic analysis, discontinuities and pores were detected in some areas of the samples heated at 800 °C. The heating to 1000 °C and 1200 °C led to a minimizing of the discontinuities. A compact structure was formed due to the Al<sub>2</sub>O<sub>3</sub> particles dispersed within the plastic matrix created by a solid solution of iron and aluminium. Follow-up research tasks will focus on shortening the heating and semi-solid processing times to inhibit the diffusion and oxide-oxide interactions, which stimulate the undesirable coalescence, the coarsening and clustering of the oxide particles.

### Acknowledgements

The paper includes the results achieved within project GAČR 14-24252S "Preparation and optimization of creep resistant submicron-structured composite with Fe-Al matrix and Al<sub>2</sub>O<sub>3</sub> particles", funded from the specific resources of the state budget for research and development. The research was also supported through the projects of "EXLIZ – Excellence in human resources as a source of competitiveness" CZ.1.07/2.3.00/30.0013 and "West-Bohemian Centre of Materials and Metallurgy" CZ.1.05/2.1.00/03.0077, co-funded by the European Regional Development Fund.

### 6 REFERENCES

- <sup>1</sup> Inco Alloys Limited, Material data sheet, INCOLOY, alloy MA 956, INCOLOY, alloy MA 957, Hereford, UK, 2001
- <sup>2</sup> G. Korb, M. Rühle, H. P. Martinz, Proceedings of the International Gas Turbine and Aeroengine Congress and Exposition, Orlando (FL), 1991
- <sup>3</sup> B. Kazimierzak, J. M. Prignon, R. I. Fromont, *Materials and Design*, 13 (1992), 67–70, doi:10.1016/0261-3069(92)90109-U
- <sup>4</sup> S. Ukai, M. Harada, H. Okada, M. Inoue, S. Nomura, S. Shikakura, T. Nishida, M. Fujiwara, K. Asabe, *J. Nucl. Mat.*, 204 (1993), 74–80, doi:10.1016/0022-3115(93)90201-9
- <sup>5</sup> R. Schaeublin, T. Leguey, P. Spätig, N. Baluc, M. Victoria, *J. Nucl. Mat.*, 307–311 (2002), 778–782, doi:10.1016/S0022-3115(02)01193-5
- <sup>6</sup> Werkstoffdatenblätter der Fa. PM Hochtemperaturmetall GmbH, Reutte (A), 1992
- <sup>7</sup> F. D. Fischer, J. Svoboda, P. Fratzl, *Phil. Mag.*, 83 (2003), 1075–1093, doi:10.1080/0141861031000068966
- <sup>8</sup> J. Rösler, E. Arzt, *Acta Metall.*, 38 (1990), 671–683, doi:10.1016/0956-7151(90)90223-4
- <sup>9</sup> R. Herzog, *Mikrostruktur und Mechanische Eigenschaften der Eisenbasis-ODS-Legierungen PM 2000*, PhD. Thesis, Forschungszentrum Jülich, Germany, 1997
- <sup>10</sup> K. M. Miller, K. F. Russel, D. T. Hoelzer, *J. Nucl. Mat.*, 351 (2006), 261–268, doi:10.1016/j.jnucmat.2006.02.004
- <sup>11</sup> M. J. Alinger, G. R. Odette, D. T. Hoelzer, *Acta Mater.*, 57 (2009), 392–406, doi:10.1016/j.actamat.2008.09.025
- <sup>12</sup> M. C. Brandes, L. Kovarik, M. K. Miller, G. S. Daehm, M. J. Mills, *Acta Mater.*, 60 (2012), 1827–1839, doi:10.1016/j.actamat.2011.11.057
- <sup>13</sup> M. C. Brandes, L. Kovarik, M. K. Miller, M. J. Mills, *J. Mater. Sci.*, 47 (2012), 3913–3923, doi:10.1007/s10853-012-6249-x
- <sup>14</sup> I. Kubena, T. Kruml, *Fatigue life and microstructure of ODS steels*, *Eng. Fract. Mech.*, 103 (2013), 39–47, doi:10.1016/j.engfracmech.2012.10.011
- <sup>15</sup> I. Kubena, B. Fournier, T. Kruml, *Journal of Nuclear Materials*, 424 (2012), 101–108, doi:10.1016/j.jnucmat.2012.02.011
- <sup>16</sup> B. Fournier, A. Steckmeyer, A. L. Rouffié, J. Malaplate, J. Garnier, M. Ratti, P. Wident, L. Ziolk, I. Tournié, V. Rabeau, J. M. Gentz-bittel, T. Kruml, I. Kubena, *Journal of Nuclear Materials*, 430 (2012), 142–149, doi:10.1016/j.jnucmat.2012.05.048
- <sup>17</sup> M. Palm, *Intermetallics*, 13 (2005), 1286–1295, doi:10.1016/j.intermet.2004.10.015
- <sup>18</sup> F. Stein, M. Palm, G. Sauthoff, *Intermetallics*, 13 (2005), 1275–1285, doi:10.1016/j.intermet.2004.08.013
- <sup>19</sup> D. G. Morris, M. A. Muñoz-Morris, *Materials Science and Engineering A*, 462 (2007), 45–52, doi:10.1016/j.msea.2005.10.083
- <sup>20</sup> S. Milenkovic, M. Palm, *Intermetallics*, 16 (2008), 1212–1218, doi:10.1016/j.intermet.2008.07.007
- <sup>21</sup> D. G. Morris, *Intermetallics*, 6 (1998), 753–758, doi:10.1016/S0966-9795(98)00028-4
- <sup>22</sup> M. A. Morris-Muñoz, *Intermetallics*, 7 (1999), 653–661, doi:10.1016/S0966-9795(98)00079-X



## EFFECT OF PREHEATING ON MECHANICAL PROPERTIES IN INDUCTION SINTERING OF METAL-POWDER MATERIAL Fe AND $w(\text{Cu}) = 3 \%$

### VPLIV PREDGREVANJA NA MEHANSKE LASTNOSTI INDUKCIJSKO SINTRANEGA MATERIALA, IZDELANEGA IZ KOVINSKEGA PRAHU Fe IN $w(\text{Cu}) = 3 \%$

Göksan Akpınar<sup>1</sup>, Enver Atik<sup>2</sup>

<sup>1</sup>Celal Bayar University, Hasan Ferdi Turgutlu Faculty of Technology, Manufacturing Engineering Department, 45400 Turgutlu/Manisa, Turkey  
<sup>2</sup>Celal Bayar University, Engineering Faculty, Mechanical Engineering Department, 45040 Manisa, Turkey  
goksanakpinar105@hotmail.com

*Prejem rokopisa – received: 2014-08-29; sprejem za objavo – accepted for publication: 2014-09-24*

doi:10.17222/mit.2014.215

In this study, the sintering process of iron-based powder-metal parts through induction and in a classic resistance furnace was analyzed experimentally and theoretically. Within the scope of the study, the Högenas ASC 100.29 iron powder containing mass fractions  $w(\text{Cu}) = 3 \%$ ,  $0.5 \%$  graphite and, as a lubricant,  $0.8 \%$  Kenolub was used. The effects of preheating, sintering time, conveyor-belt speed and gradual cooling on the sintering with induction, and the effects of the sintering parameters on the mechanical properties of the samples were analyzed experimentally and numerically. In the study, preheating with the induction adjustable at a low or mid (2.5–5 kHz) frequency was tested. By means of applying preheating and sintering in an atmosphere of argon gas, the thermal shock on the samples was blocked and superior physical and mechanical properties were achieved.

Keywords: powder metallurgy, sintering with induction, preheating, classical furnace, finite-element method, resistivity

V tej študiji smo eksperimentalno in teoretično analizirali proces sintranja kovinskih delov na osnovi železovega prahu. Uporabljen je bil komercialni Högenasov železov prah ASC 100,29, ki je vseboval masne deleže  $w(\text{Cu}) = 3 \%$ ,  $0,5 \%$  grafita in  $0,8 \%$  maziva Kenolub. Vpliv predgrevanja, časa sintranja, hitrosti pomikanja traku in postopno ohlajanje pri indukcijskem sintranju na mehanske lastnosti vzorcev so bili analizirani eksperimentalno in numerično. V študiji je bilo preizkušeno predgreje z regulirano indukcijo pri nizki in srednji frekvenci (2,5–5 kHz). S predgrevanjem in postopkom sintranja v atmosferi argona je bil preprečen toplotni šok pri vzorcih in dobljene so bile boljše fizikalne in mehanske lastnosti.

Ključne besede: metalurgija prahov, indukcijsko sintranje, predgrevanje, klasična peč, metoda končnih elementov, upornost

## 1 INTRODUCTION

The PM manufacturing method is the process of producing metal powders and transforming the produced powders into desired parts. This method consists of a series of stages including powder production, mixing of the powders produced, powder pressing, sintering and optional processes (infiltration, oil impregnation, dewaxing, etc.).<sup>1</sup>

Sintering is a process of heating which results in a considerable resistance increase due to the bonding of particles and in improved characteristics. Sintering enables the particles to contact each other so as to bond at high temperatures. This bonding may occur due to the atom movements (the diffusion) in the solid state below the melting temperature. However, in many cases, it is accompanied by the formation of the liquid phase.<sup>2</sup> Prior to sintering, the polymers used as binders or lubricants should be removed. The polymer-combustion process occurs during the heating of the polymer up to the decomposition temperatures at which it loses stability and decomposes into its components. The heat initially melts the polymer and afterwards enables the emergence

of small molecules that are separated, due to evaporation, from the crude parts. The atmosphere in the combustion process is important since the active gases result in either an easy separation of the polymer or a reaction with the powders. A weight decrease shows that during the heating of the mass of the pressed stainless-steel powder at a  $10 \text{ }^\circ\text{C}/\text{min}$  rate, the lubricating polymers do not gradually separate from the mass. If a proper time-dependent heat input is not provided to the powder materials during the sintering process, the polymer is likely to be still included in the mass of the material. Thus, the time-dependent heat input should be set very well during the sintering. Most of the lubricants used in powder metallurgy are melted below  $1500 \text{ }^\circ\text{C}$ , but they are not vaporized up to a temperature of  $300\text{--}500 \text{ }^\circ\text{C}$ . To prevent damage to the raw part, the heating speed at the stage with a weight loss should be slow. The combustion process is shown in different atmospheres at a fixed heating rate. When carrying out a complete combustion of argon and hydrogen, a weight increase after the combustion occurs since air and nitrogen enter into a reaction. In the applications where crude density is very high, the

heating rate should be slow since the polymer/lubricator evaporation is difficult because of open porosity.<sup>2</sup>

Compared to the conventional heating systems, the heating with induction has advantages such as a considerably shorter processing time, no environmental heat distribution, being clean and highly productive, being controllable and repeatable, being subjected to a precise temperature control, no air pollution due to the gases used in the furnaces and during the combustion, no by-products in the heating area, minimum ventilation and smoke output thanks to the absence of the combustion by-products and radiation and being a secure system not causing the events such as explosions. As a result of these benefits, the use of this heating system in the industry has increased recently. Induction is used for many purposes in the industry. It is widely used in the processes such as hard soldering, surface hardening, welding, forging, annealing, heat treatment and smelting.<sup>3,4</sup>

In recent years, powder metallurgy has led to major innovations in different areas in order to meet the demand for more mechanical features and competitive production costs for steel components. Recently, researches have focused on the materials achieving a high-performance with low costs. For this purpose, for particular powder compositions, new processes are continually developed for the pre-sintering, sintering and after-sintering stages. High-quality PM components are a result of these researches involving the induction-sintering process. Since the inner structures of powder-metal materials are porous, their electrical features are quite different compared to the bulk material. The extent of the porosity of the internal structure of a powder-metal material also strongly affects the mechanical properties by lowering the density and the Young's modulus of the material. In this study, we analyze how the changes in the parameters of the sintering with induction affect the interior structures of powder-metal materials; we also determine the internal structures and stress conditions under the ideal sintering conditions by analyzing the behaviors of the micro-stresses that occur within the internal structure of a material as a result of the loading conditions. In this context, it is considered that this study will shed light on the parameters of induction sintering of powder-metal particles in the industry and their usage conditions.

## 2 MATERIALS AND METHODS

In this study, the mechanical and micro-structural features of iron-based powder-metal samples sintered with induction and in a furnace at (0.2, 0.3 and 0.5) mm/s conveyor speeds were analyzed. In addition, the effect of the preheating process at a frequency 2.5 kHz during the sintering with induction on the microstructures and mechanical features of the PM samples was investigated. The samples obtained from the Högenas ASC 100.29 iron powder, whose chemical, physical and sieve features are given in **Table 1**, were subjected to the sintering process with induction and to the sintering in a furnace at different conveyor speeds. The samples were processed by preheating with induction at a medium and low frequency (2.5 kHz) and by sintering at a medium frequency (45 kHz). The test was conducted as a loca-

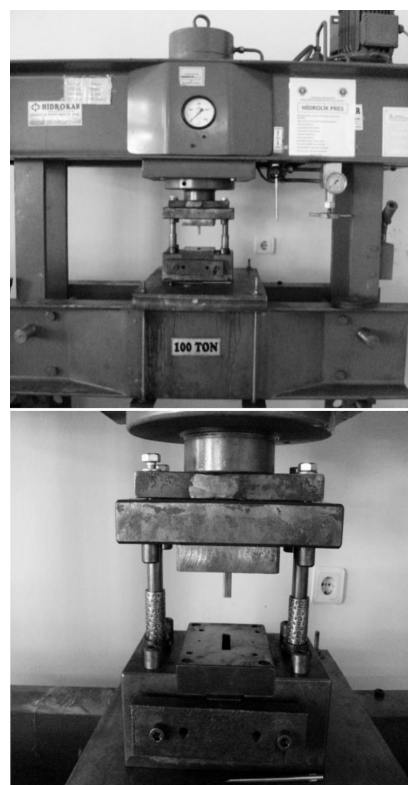


**Figure 1:** Images of the hydraulic press and the mold  
**Slika 1:** Fotografija hidravlične stiskalnice in modela

**Table 1:** PM-sample codes and applied procedures

**Tabela 1:** Oznake vzorcev in uporabljeni postopki

| Sample No. | Sample code | Sintering process | Protective atmosphere | Conveyor-belt speed (mm/s) | Preheating duration (min) | Sintering time (min) | Density (g/cm <sup>3</sup> ) |
|------------|-------------|-------------------|-----------------------|----------------------------|---------------------------|----------------------|------------------------------|
| 1          | K 0.2       | Induction         | Argon                 | 0.2                        | –                         | 17.08                | 7.457                        |
| 2          | K 0.3       | Induction         | Argon                 | 0.3                        | –                         | 11.38                | 7.197                        |
| 3          | K 0.5       | Induction         | Argon                 | 0.5                        | –                         | 6.83                 | 7.135                        |
| 4          | Ö 0.3       | Induction         | Argon                 | 0.3                        | 11.27                     | 11.38                | 7.485                        |
| 5          | Ö 0.5       | Induction         | Argon                 | 0.5                        | 6.76                      | 6.83                 | 7.318                        |
| 6          | F 1         | Furnace           | Argon                 | –                          | 15                        | 45                   | 7.211                        |
| 7          | F 2         | Furnace           | None                  | –                          | 15                        | 45                   | 7.184                        |



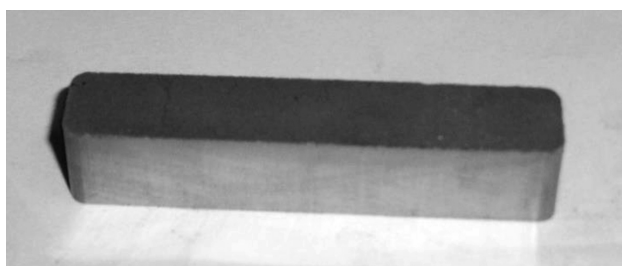


**Figure 2:** Cold-pressed sample of 10 mm × 10 mm × 55 mm in size  
**Slika 2:** Hladno stiskan vzorec dimenzij 10 mm × 10 mm × 55 mm

tion- and speed-controlled procedure through a controlled conveyor using a programmable logic controller (plc).

In the beginning of the experimental study, the powders were weighed as 37.37 grams on a Sartorius BL 210S sensitive balance, filled into a mold cavity of 10 mm × 10 mm × 55 mm in size, and cold pressed in the mold at a pressure 600 MPa via a Hidrokar hydraulic press for 10 s. Graphite powder was used as the mold lubricant. The samples were then sintered with induction at three different conveyor speeds of (0.2, 0.3 and 0.5) mm/s. Also, in order to observe the effect of preheating with induction, some samples were treated with the preheating process. The concentrations of the PM samples were measured according to Archimedes' principle. The images of the press, the mold and the obtained sample are given in **Figure 1**. An image of the cold-pressed sample is given in **Figure 2**.

**Table 1** gives the code names and test conditions for the samples sintered at different parameters, and **Table 2** gives the Högenas ASC 100.29 iron powder, its chemical and physical properties as well as the sieve-analysis results.<sup>5</sup>

In order to prevent the harmful effects of the ambient atmosphere during the sintering of the PM samples with induction, the samples were passed through a heat-resistant quartz-glass tube and pure argon gas was sent to the environment. By means of the holes drilled into the quartz-glass tube, the evaporation of the lubricants and a direct measurement with the laser heat readers were ensured. In **Figure 3**, the quartz-glass tube, the heat readers and the procedure for removing the lubricant at 600 °C are shown.

The samples obtained from the iron-based ASC 100.29 powder were subjected to the sintering process

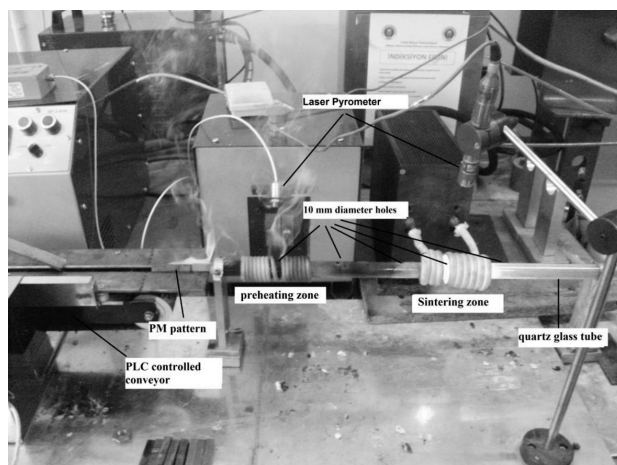


**Figure 3:** Induction test device  
**Slika 3:** Indukcijska preizkusna naprava

with induction at the conveyor speeds of (0.2, 0.3 and 0.5) mm/s and constantly in the furnace. Eight units were produced from each sample and they were used for the necessary mechanical, physical and microstructural analyses. The samples sintered with induction at different conveyor speeds (at different times) and in the furnace were subjected to metallographic and mechanical tests. The preheating temperature was defined as 600 °C and the sintering temperature as 1120 °C. For the sintering of the PM samples at 1120 °C, we used an induction device with a coil with a diameter of 8 mm, a tunnel with a length of 95 mm, a frequency of 45 kHz with 9 wrappings, a power of 12 kW and a current intensity of 17.5 A.



**Figure 4:** 45-kHz-frequency induction device  
**Slika 4:** Indukcijska naprava s frekvenco 45 kHz

**Table 2:** Högenas ASC 100.29 iron powder, its chemical and physical properties and sieve analysis<sup>5</sup>

**Tabela 2:** Högenas ASC 100,29 Fe-prah: kemijske in fizikalne lastnosti ter sejalne analize<sup>5</sup>

| Chemical properties % |                   | Physical properties  |                        | Sieve analysis % |    |
|-----------------------|-------------------|----------------------|------------------------|------------------|----|
| C                     | 0.01              | Apparent density     | 2.42 g/cm <sup>3</sup> | < 45 μm          | 23 |
| O                     | 0.07              | Flow (Hall)          | 31 s/50 g              | 45–150 μm        | 69 |
| Cu                    | 3.0               | Compression pressure | 5.5 kbar (40 tsi)      | 150–180 μm       | 8  |
| Lubricant             | 0.8               |                      |                        | > 180 μm         | 0  |
| Iron                  | Balancing element |                      |                        |                  |    |

In **Figure 4**, an image of the induction device for the 1120 °C sintering section is given. When sintering the PM samples with induction and without preheating, it was observed that the lubricators separated fast on the samples and combusted because of the rapid heating. This adversely affected the mechanical and physical properties of the samples. The processing depth of the sintering area was detected through a numerical analysis. All the tests involving the sintering of the PM samples with induction were conducted in a protective atmosphere of argon gas.

### 3 RESULTS

#### 3.1 Three-point-bending test results for the powder-metal samples

Three-point-bending tests of the powder-metal samples subjected to different sintering processes were conducted on the Shimadzu equipment. A three-point-bending device is shown in **Figure 5**. The average values were obtained by conducting four separate tests for each sample.

In the three-point-bending test, the dimensions of each sample were entered into the computer before the testing. The zeroing and calibration procedures were conducted at the start of each test. After placing the

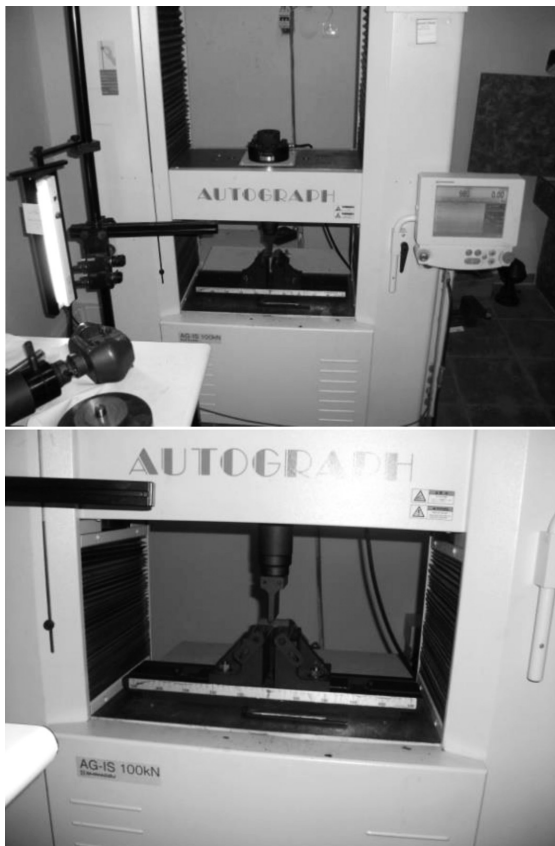


**Figure 5:** Three-point-bending test device  
**Slika 5:** Tritočkovna upogibna naprava

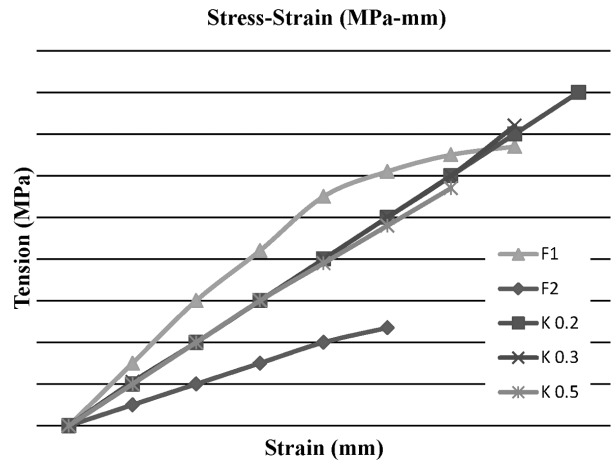


**Figure 6:** Three-point-bending test graphs of the samples sintered with induction without preheating in the furnace

**Slika 6:** Rezultati tritočkovnega upogibnega preizkusa indukcijsko sintranih vzorcev brez predgrevanja v peči

samples at a support distance 44 mm, the pressure was applied at a bending speed 10 mm/min and under a load 12 kN until they were broken. The stress-strain (MPa mm) curves obtained from the average values of the three-point-bending test of the samples are given in **Figures 6** and **7**.

In order to view the results of the three-point-bending test of the samples sintered with induction and in the furnace, they are shown in a single graph. The preheating duration for the samples processed with the preheating with induction at 600 °C is 11.38 min for the sample at the conveyor speed of 0.3 mm/s and 6.83 min for the sample at the conveyor speed 0.5 mm/s.

#### 3.2 Hardness-test results

The surface-hardness values for the PM samples were measured using the Brinell-hardness testing method. After the grinding of each sample, the load was applied using a diameter ball 2.5 mm end for 10 s. By conduct-

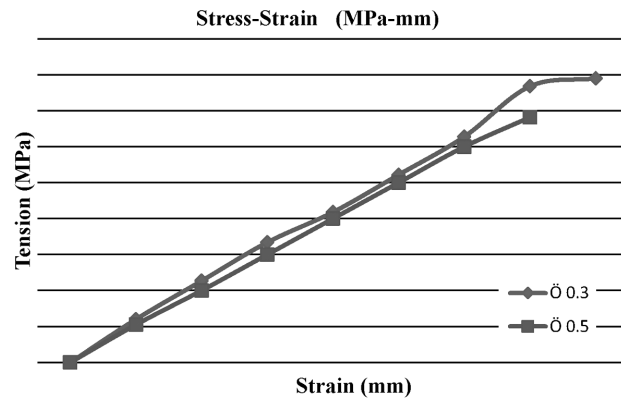


**Figure 7:** Three-point-bending test graphs of the samples sintered with induction and with preheating

**Slika 7:** Rezultati tritočkovnega upogibnega preizkusa indukcijsko sintranih vzorcev s predgrevanjem

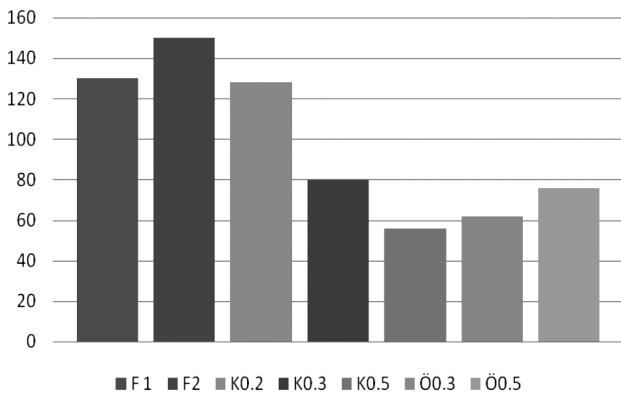


**Figure 8:** Brinell hardness of individual samples  
**Slika 8:** Trdota po Brinellu posameznih vzorcev

ing four hardness tests on the samples, the average values were obtained. The test results are given in **Figure 8**.

### 3.3 Electrical analyses

Due to the porous internal structure of the powder-metal samples, their resistivity is quite different compared to the bulk samples. In order to view the changes in the resistance of the powder-metal materials due to the temperature, a Hioki 3541 resistance-measuring device was used. After obtaining the real resistance-heat graphs for the iron-based powder-metal samples of 10 mm × 10 mm × 55 mm in size and calculating the real resistivity values, these results were used in the numerical models. In this manner, we attempted to obtain the optimum sintering parameters. The resistivity of the PM samples greatly affects the sintering parameters and the heat generation in the material and processing depth. In **Figure 9**, the Hioki 3541 resistance-measuring device can be seen.

A Högenas ASC 100.29 iron-powder resistance-temperature graph and the average values are given in **Figure 10** and **Table 3**.

The resistivity of the bulk metals, unlike that of the powder-metal materials, increases in direct proportion to



**Figure 9:** Temperature-dependent resistance-meter device  
**Slika 9:** Merilna naprava za merjenje specifične električne upornosti v odvisnosti od temperature

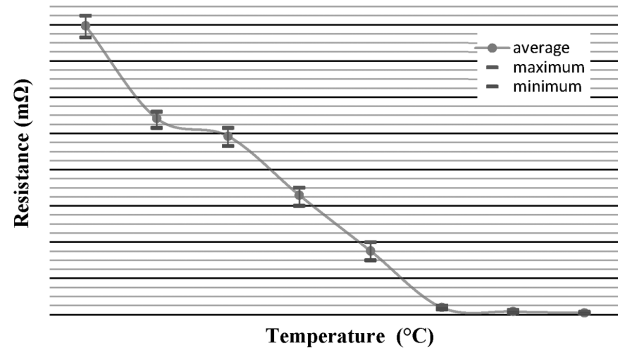


**Figure 10:** Resistance-temperature graph of ASC 100.29 powder-metal material with dimensions of 10 mm × 10 mm × 55 mm  
**Slika 10:** Upornost v odvisnosti od temperature sintranega izdelka iz prahu ASC 100,29 z dimenzijami 10 mm × 10 mm × 55 mm

**Table 3:** Resistance-temperature average values for the ASC 100.29 powder-metal material with the dimensions of 10 mm × 10 mm × 55 mm

**Tabela 3:** Povprečne vrednosti upornosti na izbrani temperaturi za surovce 10 mm × 10 mm × 55 mm iz prahu ASC 100,29

| Temperature, T/°C | Resistance, R/mΩ |
|-------------------|------------------|
| 20                | 159.4            |
| 50                | 108.32           |
| 100               | 98.507           |
| 200               | 65.953           |
| 300               | 35.14            |
| 400               | 3.953            |
| 500               | 1.72             |
| 600               | 0.942            |

the temperature. While sintering the PM materials with induction, different heat is generated in their inner structures based on their resistivity, compared to the bulk materials, and this affects the sintering with induction. The resistivity values calculated with these resistance values obtained from the PM samples were used in the numerical solutions of the sintering process with induction. The temperature-location graphs of the PM samples were obtained by means of numerical analyses in the

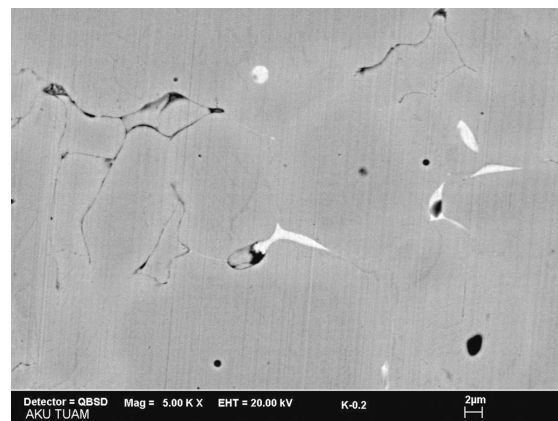


**Figure 11:** SEM image of K-0.2 sample, magnification of 5000-times  
**Slika 11:** SEM-posnetek mikrostrukture vzorca K-0.2, povečava 5000-kratna

depths of the penetration in the preheating and sintering areas.

### 3.4 Metallographic analyses

In order to examine the PM samples in the SEM BEC mode, they were cut in the dimensions of 1 cm × 1 cm × 1 cm. The cut samples were sanded and polished with

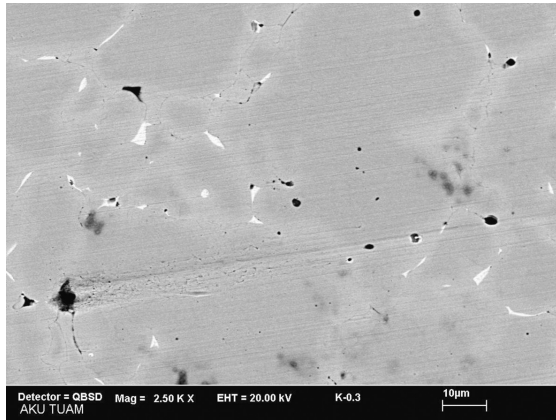


**Figure 12:** SEM image of K-0.3 sample, magnification of 2500-times  
**Slika 12:** SEM-posnetek mikrostrukture vzorca K-0.3, povečava 2500-kratna

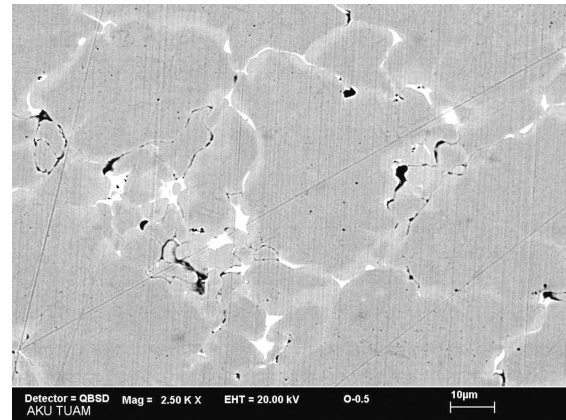


**Figure 15:** SEM image of Ö-0.5 sample, magnification of 2500-times  
**Slika 15:** SEM-posnetek mikrostrukture vzorca Ö-0.5, povečava 2500-kratna

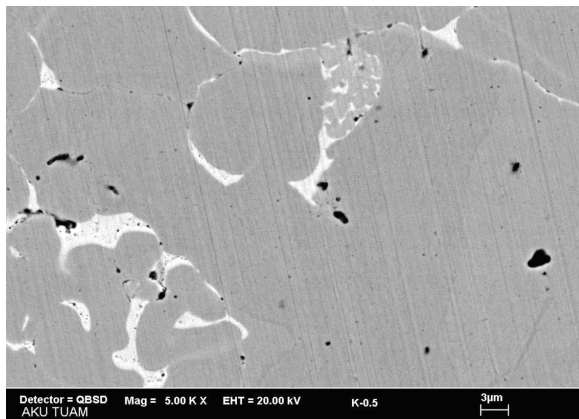


**Figure 13:** SEM image of K-0.5 sample, magnification of 5000-times  
**Slika 13:** SEM-posnetek mikrostrukture vzorca K-0.5, povečava 5000-kratna

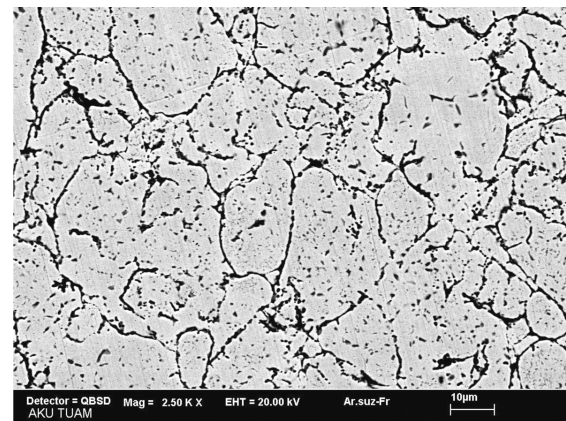


**Figure 16:** SEM image of F-2 sample, magnification of 2500-times  
**Slika 16:** SEM-posnetek mikrostrukture vzorca F-2, povečava 2500-kratna

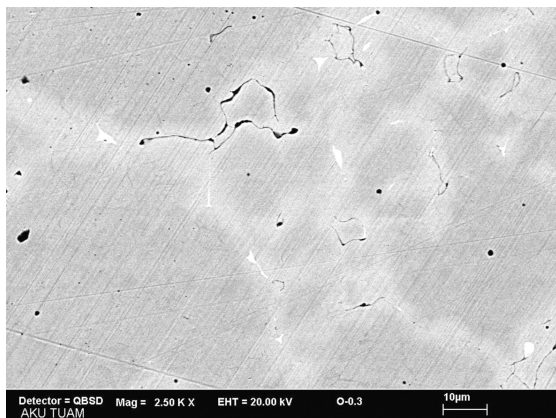


**Figure 14:** SEM image of Ö-0.3 sample, magnification of 2500-times  
**Slika 14:** SEM-posnetek mikrostrukture vzorca Ö-0.3, povečava 2500-kratna

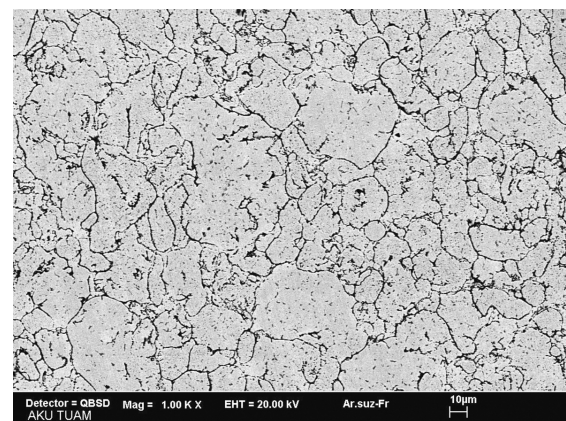


**Figure 17:** SEM image of F-2 sample, magnification of 1000-times  
**Slika 17:** SEM-posnetek mikrostrukture vzorca F-2, povečava 1000-kratna

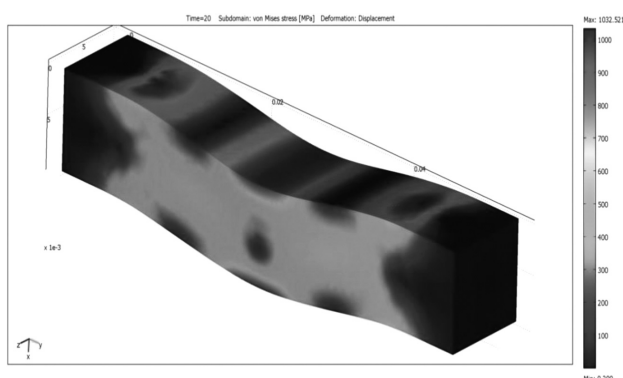


Figure 18: Three-point-bending strain numerical analysis

Slika 18: Numerična analiza tritočkovnega upogibnega preizkusa the grits 240-400-600-800. The polished samples were analyzed with a scanning electron microscope (SEM). The SEM results of the PM samples are given in Figures 11 to 17.

### 3.5 Theoretical studies

In the theoretical studies, three-point-bending strength-strain (displacement) analyses of the PM samples were conducted. In addition, the penetration-depth calculations for the samples were conducted using the program numerically. In the numerical studies, the Comsol Multiphysics finite-element-analysis program was used. The obtained numerical data were compared with the experimental results.

### 3.6 Mechanical analysis

The three-point-bending test results for the samples were supported with the numerical three-point-bending analyses. The elasticity module and the Poisson rate connected with the density of the samples were obtained through the R-A approach.<sup>6</sup> In Figure 18, an example of the three-point-bending numerical model established for each specimen is given (the bulk-sample Von Mises stress-strain model).

The three-point-bending and stain graphs for the samples modeled in the actual sizes and in the experi-

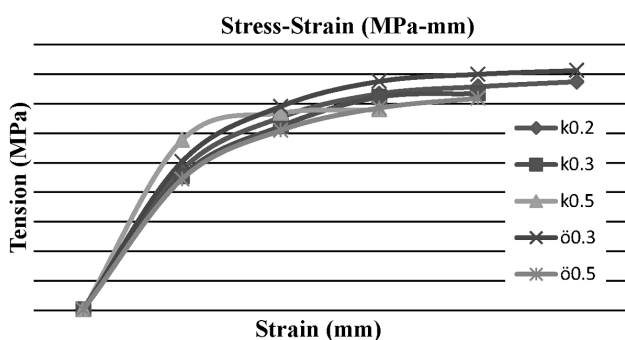


Figure 19: Numerical stress-strain curves of the samples sintered with induction

Slika 19: Numerično določene krivulje napetost – deformacija indukcijsko sintranih vzorcev

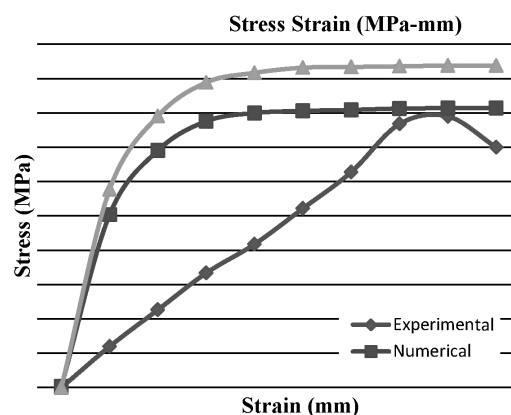


Figure 20: Experimental and numerical three-point-bending strain-resistance results for the Ö0.3 sample

Slika 20: Eksperimentalno in numerično določeni rezultati tritočkovnega upogibnega preizkusa na vzorcu z oznako Ö0.3

mental boundary conditions are given in Figure 19. In the analyses, the elasticity module and the Poisson rate of the PM samples were obtained using the values from the R-A approach, accepting the isotropic-material features.

In Figure 20, the experimental and numerical three-point-bending resistance results for the Ö0.3 samples are compared.

### 3.7 Numerical analysis of the penetration depth

The resistivity values calculated with the resistance values obtained from the experimental data were used in the numerical analyses and the penetration depths occurring in the preheating and sintering areas were calculated. In Figure 21, magnetic-flux lines are given for the preheating and sintering zones, and in Table 4, the parameters used in the program for the preheating and sintering zones are given. In the preheating process,

Table 4: Parameters used in the calculations

Tabela 4: Parametri, uporabljeni v izračunih

| Variables                               | Preheating zone                        | Sintering zone                         |
|-----------------------------------------|----------------------------------------|----------------------------------------|
| Current                                 | 10 A                                   | 17.5 A                                 |
| Coil diameter                           | 0.004 m                                | 0.008 m                                |
| Number of windings                      | 15                                     | 9                                      |
| Reference temperature                   | 20 °C                                  | 20 °C                                  |
| Resistivity<br>$T = T_0 = 20\text{ °C}$ | $289 \times 10^{-6}\ \Omega\ \text{m}$ | $289 \times 10^{-6}\ \Omega\ \text{m}$ |
| Density of argon                        | 1.784 g/cm <sup>3</sup>                | 1.784 g/cm <sup>3</sup>                |
| Argon heat capacity                     | 0.52 kJ/(kg K)                         | 0.52 kJ/(kg K)                         |
| Thermal conductivity of argon           | 0.01772 W/(m K)                        | 0.01772 W/(m K)                        |
| Density of crude iron                   | 6720 kg/m <sup>3</sup>                 | 6720 kg/m <sup>3</sup>                 |
| Heat capacity of iron                   | 25.1 J/(mol K)                         | 25.1 J/(mol K)                         |
| Thermal conductivity of iron            | 58 W/(m K)                             | 58 W/(m K)                             |
| Iron permeability                       | $8.75 \times 10^{-4}\ \text{H/m}$      | $8.75 \times 10^{-4}\ \text{H/m}$      |
| Frequency                               | 2.5 kHz                                | 45 kHz                                 |

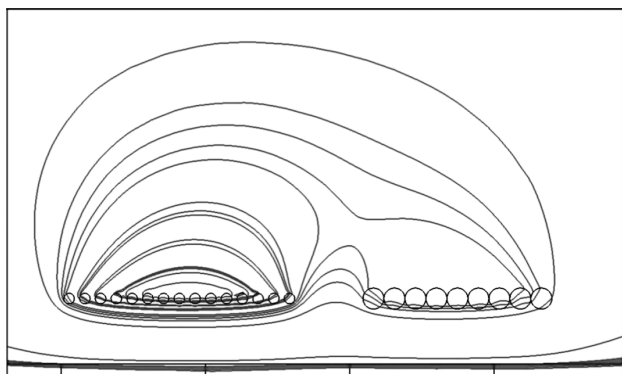


**Figure 21:** Magnetic-field lines in the preheating and sintering zones  
**Slika 21:** Magnetne silnice v conah predgrevanja in sintranja

a processing depth of 3.751 mm was obtained on the samples by means of a coil of a diameter 4 mm. In the sintering zone, a penetration depth 2.56 mm was reached by means of a diameter coil 8 mm.

#### 4 DISCUSSION

Within the scope of the study, a continuous test rig was designed for the preheating and sintering with induction. The iron-based PM samples sintered with induction and in the furnace at (0.2, 0.3 and 0.5) mm/s conveyor speeds were investigated experimentally and theoretically.

The highest resistance and strain values were observed in the samples processed with the preheating at the 0.3 mm/s conveyor speed and in the samples processed without preheating and at the conveyor speed of 0.2 mm/s (Figures 6 and 7). The preheat application not only prevented the thermal shock on the samples but also allowed the lubricators to separate from the structure more stably. In the samples sintered with induction at the speeds slower than 0.5 mm/s, we obtained a higher level of resistance and a larger settling amount compared to the samples sintered in the furnace. In the atmospheric environment, it was observed that corrosion occurred on the samples sintered in the furnace and, thus, the three-point-bending resistances decreased.

The lowest hardness value was detected in the sample sintered with induction at the 0.3 mm/s preheating speed. This result was understood to arise from the hard oxide layer formed on the surfaces of the samples sintered in the furnace (Figure 8).

In the studies related to the resistances of the PM samples, the resistances of the samples sintered at room temperature and at high temperatures showed considerable differences. In the conducted experimental studies, the resistance-temperature graph for the Högensas ASC 100.29 iron-based powder was revealed. Contrary to the bulk metallic materials, an increase in the temperature of the PM samples decreased the resistivity. This reduction of a high proportion resulted in a decrease in the depth of penetration in the heating with induction for the PM materials. The resistivity values of the 10 mm × 10 mm

× 55 mm iron-based powder-metal particles are recorded in the literature. In the numerical analyses, the measured actual resistivity values for the PM samples were used.

The highest density value of 99.704 % was measured for the sample sintered with induction at the conveyor speed of 0.3 mm/s applied with the preheating. The internal structures of the samples sintered in the atmospheric environment of the furnace are quite different from those of the samples sintered with induction. In the samples sintered in the furnace, a heterogeneous distribution of the internal structure is observed, stemming from the harmful effects of the environment atmosphere (Figures 16 and 17). The induction current enabled the formation of a more uniform internal structure by ensuring a gradual and homogenous heating of the powder particles through a formation of a 3.751 mm processing depth, especially in the preheating zone of the 10 mm × 10 mm sample section.

With the numerical three-point-bending results, the RA<sup>6</sup> approach and the porosity-based elasticity modulus were obtained for each sample, and these values were used in the numerical analyses. Analyzing experimental and numerical three-point-bending resistance graphs for the PM samples, it was seen that the results overlap. However, these differences can be considered to stem from the orthotropic mechanical properties of the PM samples (Figure 20). As expected, not only in the experimental results but also in the numerical results, the resistance values of the samples were increased due to the increase in the duration of the sintering with induction. The highest three-point-bending resistance values were found for samples K0.2 and Ö0.3. Although the Ö0.3 sample was sintered faster than the K0.2 sample, the reason why it is denser is the extra preheating applied for 11.38 min at 600 °C. For the Ö0.3 sample, the preheating process and the conveyor speed were observed to have positive effects on the mechanical properties and the microstructure. Although it is known that if the conveyor speed is further decreased, the density increases, it should be noted that this process also increases the costs. Therefore, it is concluded that in the induction sintering, rather than increasing the conveyor speed, preheating is better in terms of energy costs and an improvement in the mechanical and physical properties of the PM materials.

In the preheating zone, an area of about 2.49 mm within the sample was sintered with heat transfer. A positive effect of preheating on the internal structure and mechanical properties was supported with the experimental and numerical results. For the Ö0.3 sample processed with preheating, it was observed that the mechanical features similar to the ones of the K0.2 sample were achieved. Based on this result, it was observed that it could be possible to shorten the sintering duration by including preheating in the induction sintering of the PM parts and, therefore, decreasing the energy costs.

## 5 CONCLUSIONS

The effects of the preheating process with induction at a medium/low frequency (2.5 kHz) on the microstructural, mechanical and physical properties were investigated experimentally and numerically, and the following results were obtained:

- In the three-point-bending tests of the PM samples sintered with induction, an increase in the three-point-bending resistance values was observed due to a conveyor-speed reduction (an increase in the sintering time) (**Figures 6 and 7**).
- Considering the Brinell surface-hardness test results, a higher surface hardness was observed for the samples sintered in the furnace compared to the samples sintered with induction. The lowest hardness value was detected for the sample sintered with induction at a 0.3 mm/s preheating speed.
- In the metallographic studies, the microstructure (SEM) images of the samples were found to be quite different. In the case of the K0.2 sample where the conveyor speed was the lowest, it was observed that copper filled in the microcavities through the phase sintering (**Figure 11**). Furthermore, it was observed that the pores decreased with the conveyor-speed

reduction (an increase in the sintering time) and the density increased.

- Using the resistivity values obtained for the PM samples in the numerical analysis, the penetration depths in the preheating and sintering zones were calculated. In the numerical analyses conducted on the basis of the axis of symmetry, a processing depth of 3.751 mm in the preheating zone and a depth of 2.56 mm in the sintering zone were obtained.

## 6 REFERENCES

- <sup>1</sup> A. Lawley, Atomization: The production of metal powders, Metal Powder Industries Federation, Princeton, New Jersey, USA 1992
- <sup>2</sup> R. M. German, Powder metallurgy and particulate materials processing, translation: Sarıtaş-Türker-Durlu, Turkish Powder Metallurgy Association, Ankara 2007, 150–151
- <sup>3</sup> B. H. Yüksel, The Use of Third Harmonic High Frequency Induction Furnace Design, Master's Thesis, Electrical Education, Gazi University Institute of Science, Ankara, Turkey, 2006
- <sup>4</sup> Ç. Sevilay, One Phase Induction Heating System Analysis and Design, Master's Thesis, Pamukkale University, Institute of Science and Technology, Denizli/Turkey, 2005
- <sup>5</sup> www.hoganas.com, Available from the World Wide Web: 13.06.2013
- <sup>6</sup> N. Ramakrishnan, V. S. Arunachalam, Effective Elastic Moduli of Ceramic Materials, Journal of the American Ceramic Society, 76 (1993), 2745–2752, doi:10.1111/j.1151-2916.1993.tb04011.x

